

**Design and synthesis of fluorescent probes for
detection of different metal ions: crystal structure
elucidation and biological application**

**Thesis Submitted for the Degree of
Doctor of Philosophy (Science)
2022**



Submitted By

JAYANTA MANDAL

INDEX NO. 77/16/Chem./24 of 2016

**Department of Chemistry
Jadavpur University**

Under the Supervision of

Dr. Amrita Saha

Professor

**Department of Chemistry
(Inorganic Section)
Jadavpur University
Kolkata-700032**

যাদবপুর বিশ্ববিদ্যালয়
কলকাতা-৭০০ ০৩২, ভারত



*JADAVPUR UNIVERSITY
KOLKATA-700032, INDIA

FACULTY OF SCIENCE : DEPARTMENT OF CHEMISTRY : INORGANIC CHEMISTRY SECTION

CERTIFICATE FROM THE SUPERVISOR

This is to certify that the thesis “**Design and synthesis of fluorescent probes for detection of different metal ions: crystal structure elucidation and biological application**” submitted by Mr. Jayanta Mandal, M.Sc. (Chemistry), who got his name registered on 28.04.2016 (Index No. **77/16/Chem./24 of 2016**) for the award of Ph.D. (Science) degree of Jadavpur University, is absolutely based upon his own work under the supervision of Dr. Amrita Saha and that neither this thesis nor any part of it has been submitted for either any degree/diploma or any other academic award anywhere before.

Amrita Saha

(Dr. Amrita Saha)
Professor
Department of Chemistry
(Inorganic Section)
Jadavpur University
Kolkata-700032

Date: 22/11/2022



Dr. Amrita Saha
Professor
Department of Chemistry
Jadavpur University
Kolkata-700032

*Established on and from 24th December, 1955 vide Notification No. 10986-Edn/IU-42/55 dated 6th December, 1955 under Jadavpur University Act, 1955 (West Bengal Act XXXIII of 1955) followed by Jadavpur University Act, 1981 (West Bengal Act XXIV of 1981)

দূরভাষ : ২৪১৪-৩৩৩৩/৩১২৪/৩৩৪৩/৩৪২৪/৩৪৪৩ প্রসারণ : ২৪৩৯
দূরবার্তা : (৯১)-০৩৩-২৪১৪-৩৪১৪/৩২১০/২৪১০-৭১২১

Website : www.jadavpur.edu
E-mail : registrar@admin.jdvu.ac.in

Phone : 2414-6666/6194/6643/6495/6443 Extn. 2469
Fax : (91)-033-2414-6414/6210/2413-7121

*Dedicate to My
Family*

ACKNOWLEDGEMENTS

It is a great pleasure and honor for me that by grace of almighty, I am about to submit my Ph.D. thesis entitled “**Design and synthesis of fluorescent probes for detection of different metal ions: crystal structure elucidation and biological application**” that includes solely my research activities performed in the Department of Chemistry, Jadavpur University. In this regard, I would like to express my deep sense of thanks and gratitude to all those persons who helped me and contributed to my experience during this time.

First of all, I would also like to express my sincere gratitude to my mentor, philosopher and guide **Dr. Amrita Saha**, Inorganic Section, Professor, Department of Chemistry, Jadavpur University. Her dedication, keen interest and above all her overwhelming attitude to help her students has been solely and mainly responsible for completing my work. Her timely advice and meticulous scrutiny, scholarly advice and scientific approach has helped a lot in every way during my work. Apart from many scientific lessons, she taught me to be focused and be patient in future. Without her resourceful and continuous untiring supervision, this work would not have been possible.

I express my sincere gratitude to Prof. S.K. Bhattacharya, (Head of the Department) and Prof. S. Das (Section-In-Charge) of Jadavpur University for their kind help, co-operation and suggestion. I am also grateful to Prof. C. Sinha, Prof. S. Bhattacharya, Prof. S. Koner, Prof. K. Pramanik, Prof. K. K. Rajak, Prof. S. Baitalik, Prof. M. Ali, Prof. P. Roy, Dr. B. B. Show, Dr. P. Mahata (Inorganic Chemistry Section), Prof. T. Bhaumik (Organic Chemistry Section) and Prof. P. P. Parui (Physical Chemistry Section) for their spontaneous help and co-operation.

I heartily acknowledge Dr. Paula Brandão, Prof. A. Frontera, Prof. Carlos J. Gómez García, Prof. Parimal Karmakar and Dr. A. Panja, for their kind collaboration.

I convey my gratefulness to Dr. Narayan Ch. Jana and many others for their suggestions and scientific support.

I am thankful to my lab mates, Dr. Saikat Banerjee, Mr. Pravat Ghorai, Mr. Subhomoy Malike and Miss. Mohafuza Khatun Research scholar, Department of Chemistry, Jadavpur University, who have in various ways shared the task for preparing the present thesis and have provided their invaluable co-operation and suggestions throughout the progress of the work.

I am privileged to thank my parents and my entire family members for their kind understanding, encouragement, and moral supports throughout my life.

Last but not least, I thank almighty God for providing me strength and courage to undergo this task.

Jayanta Mandal.

Date: 22.11.2022

(JAYANTA MANDAL)
Department of Chemistry
Jadavpur University
Kolkata-700032

Contents

	Page No.
Preface	xv-xvi
List of Abbreviations	xvii- xviii
Chapter 1 : General Introduction	1-44
Abstract	3
1.1 Introduction:	5
1.2 The significance of metal ions sensing: a brief discussion	5-10
1.3 Analytical methods and advantages of fluorescence technique	10
1.4 Fluorescent chemosensors and their classification	11-13
1.4.1 Turn-on fluorescent chemosensor	12
1.4.2 Turn-off fluorescent chemosensor	12
1.4.3 Ratiometric fluorescent chemosensor	12-13
1.4.4 Chemodosimeter	13
1.5. Fluorescence sensing mechanisms	14-19
1.5.1 Paramagnetic fluorescence quenching	14
1.5.2 Photo-induced electron transfer (PET)	14-15
1.5.3 Chelation enhanced fluorescence (CHEF) and Chelation enhanced quenching (CHEQ)	15-16
1.5.4 Intra and intermolecular charge transfer (ICT)	16-17
1.5.5 Fluorescence resonance energy transfer (FRET)	17-18
1.5.6 Excited-state intramolecular proton transfer (ESIPT)	18-19
1.6. A concise literature survey on recent fluorescent chemosensors	19-31
1.6.1 4-Methyl-2,6-diformylphenol (DFP) based sensors	19-23
1.6.2 3-Hydroxy-2-methylpyridine based vitamers sensors	23-28
1.6.3 Rhodamine based chemosensors	28-31
1.7 Concluding remarks and aim of my research work	32-33
1.8 Physical measurement	33-35
1.9 References	35-44
Chapter 2 : Development of rhodamine 6G based fluorescent chemosensors for Al³⁺ ion detection: effect of ring strain and substituent in enhancing its sensing Performance	45-112
Abstract	47
2.1 Introduction	49-53
2.2 Experimental section	53-75
2.2.1 Materials and physical measurements description	53
2.2.2 X-ray crystallography	54-55
2.2.3 Synthesis of N-(Rhodamine-6G)lactam-hydrazine and N-(Rhodamine-6G)lactam-propylenediamine	55
2.2.4 Preparation of chemosensor (H ₃ L2.1)	55-58
2.2.5 Preparation of chemosensor (H ₃ L2.2)	58-60
2.2.6 Preparation of chemosensor (H ₃ L2.3)	61-63
2.2.7 Preparation of chemosensor (H ₃ L2.4)	63-65
2.2.8 Synthesis of complex (2.1)	65-68

	Page No.
2.2.9 Synthesis of complex (2.2)	69-71
2.2.10 Synthesis of complex (2.3)	71-73
2.2.11 Synthesis of complex (2.4)	73-75
2.2.12 UV-visible and fluorescence spectroscopic experiment	76
2.2.13 Binding stoichiometry (Job's plot) studies	76
2.2.14 Cell culture	76-77
2.2.15 Cell visualisation studies	77
2.2.16 Computational method	77
2.3 Results and discussion	77-79
2.3.1 Syntheses and IR spectroscopy	77-78
2.3.2 Crystal structure descriptions of chemosensors (H ₃ L2.1-H ₃ L2.4)	78-81
2.3.3 NMR studies	81-82
2.3.4 Absorption spectral analysis	83-84
2.3.5 Fluorescence properties analysis	85-94
2.3.6 Life time and quantum yield study	94-96
2.3.7 Mechanism of fluorescence intensity enhancement...	96-98
2.3.8 Biocompatibility study of the ligands	98-99
2.3.9 Cell imaging	99-100
2.3.10 DFT study	100-102
2.3.11 TDDFT study	102-104
2.4 Conclusion	105-106
2.5 References	107-111
Chapter 3 : Rhodamine-azo based two fluorescent probes for recognition of trivalent metal ions: crystal structures elucidation and biological application	113-184
Abstract	115
3.1 Introduction	117-122
3.2 Experimental section	122-144
3.2.1 Materials and physical measurements description	122-123
3.2.2 X-ray crystallography	123-125
3.2.3 Synthesis of N-(rhodamine-6G)lactam-hydrazine and azo-aldehydes	125
3.2.4 Preparation of chemosensor HL _{3.1}	125-128
3.2.5 Synthesis of chemosensor HL _{3.2}	128-131
3.2.6 Synthesis of [Al(L1) ₂](NO ₃)•3DMF•2H ₂ O] (3.1)	131-134
3.2.7 Synthesis of [Cr(L3.1) ₂](NO ₃) (3.2)	135
3.2.8 Synthesis of [Fe(L3.1) ₂](NO ₃) (3.3)	136
3.2.9 Synthesis of [Al(HL3.2)(L3.2)](NO ₃) ₂ •4H ₂ O] (3.4)	137-140
3.2.10 Synthesis of [Cr(L3.2) ₂](NO ₃) (3.5)	141
3.2.11 Synthesis of [Fe(L3.2) ₂](NO ₃) (3.6)	142
3.2.12 UV-visible and fluorescence spectroscopic experiment	143
3.2.13 Binding stoichiometry (Job's plot) studies	143
3.2.14 Protocol of real sample analysis	143
3.2.15 Cell culture	144
3.2.16 Cell interbalisation studies	144
3.2.17 Computational method	144
3.3 Results and discussion	145-178
3.3.1 Synthesis and characterization	145

	Page No.
3.3.2 Crystal structure descriptions of chemosensors	145-146
3.3.3 Crystal structure descriptions of complexes	147-149
3.3.4 NMR studies	150-152
3.3.5 Absorption spectral analysis	152-155
3.3.6 Fluorescence properties analysis	155-165
3.3.7 Life time and quantum yield study	165-166
3.3.8 Mechanism of fluorescence intensity enhancement in chemosensors in presence of trivalent metal ions	166-167
3.3.9 Biocompatibility study of the ligands	167-168
3.3.10 Cell imaging	168-169
3.3.11 DFT and TDDFT study	169-176
3.3.12 Natural transition orbital (NTO) study	176-177
3.3.13 Electrochemical study	177-178
3.4 Conclusion	178-179
3.5 References	180-184
Chapter 4 : 2-hydroxy-5-methylisophthalaldehyde based fluorescent-colorimetric chemosensor for dual detection of Zn²⁺ and Cu²⁺ with high sensitivity and application in live cell imaging	185-226
Abstract	187
4.1 Introduction	189-190
4.2 Experimental section	191-195
4.2.1 Materials and physical measurements	191
4.2.2 Synthesis of 2-hydroxy-5-methylisophthalaldehyde (DFP)	191
4.2.3 Synthesis of chemosensor [HL4.1=4-methyl-2,6-bis((E)-((2-(piperazin-1-yl)ethyl)imino)methyl)phenol]	191-192
4.2.4 Synthesis of complex [Zn ₂ (L4.1)(OH ₂)(OH)(NO ₃)](NO ₃) (4.1)	192-193
4.2.5 Synthesis of complex [Cu ₂ (L4.1)(OH ₂)(OH)(NO ₃)](NO ₃) (4.2)	193
4.2.6 UV-visible and fluorescence spectroscopic studies	193-194
4.2.7. Binding stoichiometry (Job's plot)	194
4.2.8 Cell line culture	194
4.2.9 Cell imaging	194-195
4.2.10. Computational method	195
4.3 Results and discussion	195-222
4.3.1 Synthesis and characterization	195-198
4.3.2 Absorption spectral studies	199-201
4.3.3 NMR studies	201-203
4.3.4 Fluorescence properties	204-212
4.3.5 Life time and quantum yield measurements	213-214
4.3.6 Cell imaging	214
4.3.7 DFT study	215-218
4.3.8 TDDFT study	218-222
4.4 Conclusion	222-223
4.5 References	223-226

	Page No.
Chapter 5 : Aza-crown based macrocyclic probe design for "PET-off" multi-Cu²⁺ responsive and "CHEF-on" multi-Zn²⁺ sensor: application in biological cell imaging, and theoretical studies	227-290
Abstract	229
5.1 Introduction	231-233
5.2 Experimental Section	233-240
5.2.1 Materials and physical measurements	233
5.2.2 X-ray crystallography	233-234
5.2.3 Synthesis of 2,6-diformyl-4-methylphenol (DFP)	235
5.2.4 Synthesis of chemosensor 1,16-dihydroxy-tetraaza-30-crown-8 (H ₂ DTC5.1)	235
5.2.5 Synthesis of Complex (5.1) [Zn ₄ (DTC5.1)(OH) ₂ (NO ₃) ₄]	235-236
5.2.6 Synthesis of Complex (5.2) {[Cu ₄ (DTC5.1)(OCH ₃) ₂ (NO ₃) ₄].H ₂ O} _n	236-237
5.2.7 UV-visible and fluorescence spectroscopic studies	237
5.2.8 EMF measurements	237-238
5.2.9 Cell culture	238
5.2.10 Cell imaging	239
5.2.11 Cell survivability assay	239
5.2.12 Computational method	240
5.3 Results and discussion	240-283
5.3.1 Synthesis and characterization	240-243
5.3.2 Crystal structure description of complex 5.1	243-244
5.3.3 Crystal structure description of complex 5.2	244-246
5.3.4 NMR studies	247-250
5.3.5 Absorption spectral studies	251-252
5.3.6 ESI-MS ⁺ analysis	252-256
5.3.7 Fluorescence properties	256-267
5.3.8 Life time and quantum yield measurements	267-269
5.3.9 pH-potentiometric titrations	269-274
5.3.10 Stability constants determination from UV-Vis and fluorometric titrations	274-277
5.3.11 Cell imaging study	277-278
5.3.12 Cell survival assay of H ₂ DTC5.1	278-280
5.3.13 Computational study of the ligand	280-283
5.4 Conclusion	283-284
5.5 References	285-290
Chapter 6 : Two pyridoxal derived Schiff base chemosensors design for fluorescence turn-on sensing of Zn(II) ion in pure aqueous medium	291-332
Abstract	293
6.1 Introduction	295-296
6.2 Experimental section	297-309
6.2.1 Materials and physical measurements	297
6.2.2 Synthesis of chemosensor HL6.1	297-300
6.2.3 Synthesis of Chemosensor HL6.2	300-302

	Page No.
6.2.4 Synthesis of complex (6.1)	303-305
6.2.5 Synthesis of complex (6.2)	305-307
6.2.6 UV-visible and fluorescence spectroscopic studies	307-308
6.2.7 Binding stoichiometry (Job's plot)	308
6.2.8 Cell culture	308
6.2.9 Cell imaging	309
6.2.10 Computational method	309
6.3 Results and discussion	309-328
6.3.1 Synthesis and characterization	309-311
6.3.2 Absorption spectral studies	311-312
6.3.3 NMR studies	313
6.3.4 Fluorescence properties	313-319
6.3.5 Life time and quantum yield measurements	319-320
6.3.6 Cell imaging	321
6.3.7 DFT study	321-326
6.3.8 TDDFT study	326-328
6.4 Conclusion	328
6.5 References	329-332

Appendix I : List of Publication and Seminar Attended

Appendix II : Thesis Related Published Paper

PREFACE

Design and synthesis of fluorescence chemosensors is an extremely interdisciplinary area of research now-a-days because of their importance and application in several different fields, such as chemistry, biology, medicine and environmental studies etc. Literature survey helps that fluorescent sensors have been designed, synthesized and applied for the selective detection of various metal ions in biologically and environmentally. The newly developed chemosensors are thoroughly characterized by several spectroscopic techniques like $^1\text{H-NMR}$, UV-Vis, FT-IR, and Mass analysis. Structure of the representative probes are confirmed by single crystal X-ray diffraction method. This thesis consists of six chapters based on the synthesis, characterization and extensive study of sensing properties of the newly constructed molecular probes. The sensing mechanisms of the probes are supported by theoretical calculations based on Density Functional Theory (DFT).

Chapter 1 represents a brief introduction on the basic definition of chemosensor with several possible mechanistic pathways for selective detection of several biologically and environmentally relevant ions. A concise literature survey of various reported chemosensors based on different fluorophoric (Rhodamine, DFP and Pyridoxal) platforms.

Chapter 2 presents the design, synthesis and characterization of four new rhodamine 6G based chemosensors for selective detection of Al^{3+} ion in organic-aqueous medium. The chemical structures as well as the photophysical properties of the probes are thoroughly studied by spectroscopic methods. Electronic structure of the probe is also studied through the theoretical calculation based on DFT/B3LYP method.

Chapter 3 includes another two rhodamine and azo based chemosensors have been synthesized for colorimetric and fluorometric detection of three trivalent metal ions, Al^{3+} , Cr^{3+} and Fe^{3+} . The chemosensors are thoroughly characterized by different spectroscopic

techniques and X-ray crystallography. Chemosensors are detect intracellular Al^{3+} , Cr^{3+} and Fe^{3+} ions in cervical cancer cell line HeLa.

Chapter 4 deals with the fabrication of a new chemosensor for dual sensing of Zn^{2+} and ions Cu^{2+} distinctly in methanol/water (1:9) medium. Both the ions are detected colorimetric and fluorometric. Biological studies are performed in MDA-MB-468 cell line.

Chapter 5 represents a rare example of an aza-crown DFP based macrocyclic chemosensor for selective detection of both Zn^{2+} and Cu^{2+} in HEPES buffer medium (pH 7.4). The changes in photophysical property of the Schiff-base molecule in the presence of both ions and cell imaging studies are discussed.

Chapter 6 covers the synthesis of two pyridoxal-based novel Schiff base compounds as a chemosensor for Zn^{2+} ions. Living cell imaging studies using these two compounds were discussed, herein. Electronic structures of the probes are also studied through the theoretical calculation based on DFT/B3LYP method.

The entire work of the thesis entitled “**Design and synthesis of fluorescent probes for detection of different metal ions: crystal structure elucidation and biological application**” has been carried out in the Department of Chemistry, Jadavpur University.

In keeping with the general practice of reporting scientific observation, due acknowledgement has been made whenever the work described as based on the findings of other investigators. I must take the responsibility of any unintentional oversights and errors which might have crept in spite of due precautions.

Jayanta Mandal.

(JAYANTA MANDAL)

List of Abbreviations and symbols

τ	: Fluorescence Lifetime
Φ	: Quantum yield
π	: Pi
σ	: Sigma
Δr	: Charge transfer index
σ_s	: Hole-electron overlapping indices
a	: Crystallographic distance along 'x' axis of a unit cell (in angstrom)
b	: Crystallographic distance along 'y' axis of unit cell (in angstrom)
c	: Crystallographic distance along 'z' axis of unit cell (in angstrom)
α	: Crystallographic angle in a unit cell between b and c (in degree)
β	: Crystallographic angle in a unit cell between c and a (in degree)
γ	: Crystallographic angle in a unit cell between a and b (in degree)
ρ	: Density (in g cm^{-3})
Mo-K α	: Molybdenum K α radiation
$F(000)$: Crystallographic (000) plane
Å	: Angstrom
BH	: Benesi Hildebrand
DFT	: Density functional theory
TDDFT	: Time dependent functional theory
DMSO- d_6	: Deuterated dimethyl sulfoxide
K_{sv}	: Stern-Volmer constant
I	: Fluorescence intensity
ex	: Excitation
em	: Emission
UV	: Ultraviolet
vis	: Visible
λ	: Wavelength
%T	: Percentage of transmittance
h	: Hour(s)
KBr	: Potassium bromide
CHCl ₃	: Chloroform
ACN	: Acetonitrile
MeOH	: Methanol
DCM	: Dichloromethane

DMF/dmf	: <i>N,N</i> -Dimethylformamide
DMSO/dmso	: Dimethyl sulfoxide
DMSO- <i>d</i> ₆	: Deuterated dimethyl sulfoxide
mL	: Milliliter
μM	: Micromolar
nM	: Nanomolar
eV	: Electron-volt
ESI MS	: Electron Spray Ionization Mass spectrometry
FTIR	: Fourier Transform Infrared Spectroscopy
EPR	: Electron Paramagnetic Resonance
NMR	: Nuclear Magnetic Resonance
PXRD/XRPD	: Powder X-ray Diffraction/X-ray Powder Diffraction
CT	: Charge Transfer
PET	: Photo-Induced Electron Transfer
PCT	: Photo-Induced Charge Transfer
ICT	: Internal Charge Transfer
ET	: Energy Transfer
FRET	: Fluorescence Resonance Energy Transfer
ESIPT	: Excited-State Intramolecular Proton Transfer
HOMO	: Highest Occupied Molecular Orbital
LUMO	: Lowest Unoccupied Molecular Orbital
NTO	: Natural transition orbital
CHEF	: Chelation Enhanced Fluorescence
CHQF	: Chelation-quenched fluorescence
K _f / K _a	: Association constant
K _d	: Dissociation constant
HeLa	: Human epithelial carcinoma cell
PBS	: Phosphate-buffered saline
Tris	: Tris(hydroxymethyl)aminomethane
LOD	: Limit of Detection
EDTA	: Ethylenediaminetetraacetic acid
HEPES	: 4-(2-Hydroxyethyl)piperazine-1-ethanesulfonic acid
eV	: Electron volt
ORTEP	: Oak Ridge Thermal Ellipsoid Plot

Chapter 1

General Introduction

Abstract

Here, a brief discussion has been made on different chemosensing pathways for the selective detection of several biologically and environmentally relevant metal ions. Also, a concise literature survey has been furnished on various reported Rhodamine, DFP and Pyridoxal based fluorophoric platforms to recognize the different metal ions.

1.1. Introduction

In, 1852 English physicist and mathematician **Sir George G. Stokes** first invent the word fluorescence. A fluorescent probe is a compound that keeps an intrinsic ability to release fluorescent photons after excitation with a suitable wavelength. Fluorescent probes cover broad applications rang like as high-throughput screening for the detection of nucleic acids, pharmaceutical research, clinical diagnostics, enzymes, cytoskeleton proteins, organelles, antibodies, avidins, lipids, proteins, and many others in the fields of cell biology, immunology, molecular biology, neurobiology, and biophysics.

Metal ions are essential in keeping the human body healthy. In a living system, numerous critical biological functions depend on the presence of metal ions, and the absence or insufficiency of this may also lead to many diseases. However, heavy metal ions, such as lead, mercury, arsenic, cadmium, chromium, etc. are dangerous for their toxic effects. The presence of essential metal ions is crucial for survival but can also be toxic if not present in the requisite concentration. Among the metals that are essential for biological activists in humans is potassium (K), sodium (Na), calcium (Ca) and magnesium (Mg), which belong to the main group of elements, and chromium (Cr), vanadium (V), manganese (Mn), iron (Fe), copper (Cu), zinc (Zn), nickel (Ni), molybdenum (Mo), and cobalt (Co), those belong to transition metal group in the periodic table. ^{1.1,1.2}

1.2. The significance of metal ions sensing: a brief discussion

In biological processes, potassium and sodium ions play major roles due to their participation in metabolism. In Earth's crust, sodium is the sixth most abundant element (abundance 2.83%). Sodium ions can be used in opposition to potassium ions in animals to allow electrostatic charge transportation on cell membranes and then allow the transmission of nerve impulses. Hence, sodium is classified as a dietary inorganic macro-mineral for animals. But, excess sodium intake can damage kidneys and increase high blood pressure.^{1.3} Potassium

is required for both plants and animals. In fertilizers and crops, potassium salt is a common constituent and the concentration of magnesium may decrease by excessive use of potassium fertilizers.^{1.4} An increase in the concentration of intracellular free Ca^{2+} ions causes the abnormal release of neurotransmitters from synaptic vesicles in neuronal synapses.^{1.5,1.6} Many changes in neuronal function including gene expression, effects on neuronal survival, modulation of ion channels, apoptosis, etc. can occur due to alterations in the concentration of Ca^{2+} . Mg^{2+} , the main part of chlorophyll, regulates photosynthesis and plays an important role in cellular processes like enzyme-driven biochemical reactions, stabilization of DNA conformation in human cells, proliferation of cells, etc.^{1.7-1.9} Mg^{2+} participates in some biological processes like congestive muscle dysfunction, heart failure, lung cancer, cerebral infarction, etc.^{1.10-1.13}

As a heavy metal, Lead is a highly poisonous metal to humans and the environment. For children, lead poisoning is a main environmental health problem. Exposure of lead to the children in the age range 1–5 can affect the organ system in the body which increases the risks of brain damage and hamper the nervous system, as a result, growth becomes slow, and behavior in learning problems may occur and may cause hearing and speaking deficiencies.^{1.14,1.15} Lead is a growing toxicant that affects hematological, neurological, gastrointestinal, cardiovascular and renal systems. Chronic exposure usually causes anemia, headache, lethargy, convulsions, irritability, ataxia, tremors, weakness in the muscle, and even paralysis. Acute exposure causes gastrointestinal disturbances like nausea, anorexia, abdominal pain, vomiting, etc. which lead to convulsions and even death. Mercury and its derivatives are very much toxic, causing contamination of ecosystems.^{1.16-1.18} The presence of mercury (Hg^{2+}) in water is hazardous to human health and as well as environment. The surface and groundwater get polluted mostly by industrial wastes, untreated sewage water, battery wastes, gasoline, pigments, medical waste, poor sanitation management, electroplated

steel, and electronic spares. These metals cause several diseases like neurological, cardiac disorders, and several developmental illnesses.^{1.19} Cadmium is a highly toxic and heavy metal having a long biological half-life of 10–20 years, easy to consume in organisms but hard to destroy.^{1.20} It interacts with the thiol groups in the proteins and cadmium-metallothionein is formed. Cd poisoning causes a series of illnesses like liver and kidney failure, itai-itai disease, osteoporosis, respiratory and immune system diseases, reproductive disorders, and even cancers.^{1.21,1.22} The International Agency for Research on Cancer (IARC) recommends cadmium as a carcinogen in the human body.^{1.23} On the other hand, the presence of higher concentrations of arsenic was reported in water resources because of geochemical conditions, anthropogenic activities, and hydrogeological events, which affected the populations in around 70 regions including the United States, India, Bangladesh, Hungary, and China.^{1.24,1.25} As(III) is the most harmful out of the different oxidation states for ecological systems and the environment. The regular consumption of arsenic-contaminated water is likely to cause many severe human health-related problems including heart, kidney, nervous, gastrointestinal, and liver diseases in addition to lung and skin cancer.^{1.26} The 25% population in West Bengal, India, is exposed to arsenic pollution. Neurological, physiological, and sensory processing disorders may result from chronic exposure to arsenic. The toxicity of arsenic causes by the biotransformation in which arsenic compounds are methylated by fungi, bacteria, algae, and humans. In oceans, vanadium is the second most abundant transition metal and seawater holds vanadium in form of $\text{Na}^+\text{H}_2\text{VO}_4^-$ with a concentration between 30 and 35 nM. Oral uptake of vanadium contains compound, and speciation occurs by the saliva, in the stomach and in the intestinal tract. In few organisms, large amount of vanadium ions are found as a toxin. Some other salts of vanadium in addition with its oxide have moderate toxicity.^{1.27} In the human body, chromium appears at trace levels and the more stable oxidation state is +3 existing in soil and water. In the human body, Cr(III) regulates the action of insulin through

glucose tolerance factors (GTFs), activates certain enzymes, and stabilize nucleic acids and proteins.^{1.28} By intracellular reducing agents Cr(VI) is reduced to Cr(III), which coordinated with DNA by guanine N7 and the phosphate group backbone.^{1.29} Insufficiency of chromium can increase the threats of sugar, nervous system disorders, heart diseases, etc., and the higher levels of Cr³⁺ may cause cancer.^{1.30,1.31} On the earth's shell, manganese is the third most abundant transition metal and an essential trace element for the human body.^{1.32} For many enzymes which are involved in the metabolic processes of humans, plants, and animals, manganese plays a very important role in their activation.^{1.33} Manganese has different applications including batteries, ceramics, fertilizers, electrical coils, etc., and is also an essential micronutrient for different organisms.^{1.34} But, high concentrations of manganese can cause some problems in the nervous and respiratory systems.^{1.35} In cellular systems, Fe³⁺ is the most abundant transition metal and plays a crucial role in biological processes like enzyme catalysis, cellular metabolism, and electron-transfer reactions.^{1.36} Fe³⁺ transports oxygen in all the tissues in the form of hemoglobin.^{1.37} The deficiency and also the overdose of Fe³⁺ ions induce serious diseases (Huntington's disease).^{1.38,1.39} Among the most important heavy metal, cobalt is one of them found in Earth's crust and used in different products and developments like electroplating, due to its hardness and resistance to oxidation, magnet, and battery manufacturing, electric cable manufacturing, mining, pigments, automotive industries, stainless steels alloys, coloring, catalysts, etc.^{1.40,1.41} Hence, this is one of useful metal for industries. Again, cobalt is beneficial for the human body as a part of vitamin B12. Therefore, the presence of Co(II) in trace amounts is necessary for life but a higher concentration may be harmful to human health. Compared to other heavy metals, nickel is a moderate toxic element and has diverse applications in various industries. It is widely used in the steel industry due to its abundant usage in electroplating for excellent alloying metal.^{1.42,1.43} Furthermore, in the structure of enzyme urease contains nickel ion which plays

an effective role for domestic animals and plants.^{1.44} Although it's a critical role in human life, exposure to nickel compounds in higher concentrations causes severe disorders to the human organism like respiratory system cancer, nickel-eczema, etc.^{1.45} Copper is an essential transition metal ion in human health and plays a significant role in several biological processes.^{1.46} The Cu^{2+} ion regulates a decisive role in catalytic cofactor for some metalloenzymes, including cytochrome c oxidase, superoxide dismutase, and tyrosinase.^{1.47-1.49} Hence, daily consumption of Cu^{2+} is necessary for keeping good health. At high concentrations, Cu^{2+} reacts with oxygen to generate reactive oxygen species (ROS; O^{2-} , O_2^{2-} , $\cdot\text{OH}$) that cause oxidative damage to proteins, lipids, and nucleic acids.^{1.50-1.52} Numerous studies show that the cellular toxicity of copper ions causes Alzheimer's disease, prion disease, Indian childhood cirrhosis (ICC), Menkes and Wilson diseases.^{1.53-1.55} Furthermore, Cu^{2+} can also cause pollution in drinking water. In the human body, zinc is the second transition metal ion after iron and plays a significant role in several biological processes^{1.56}, like immune function,^{1.57} pathology,^{1.58,1.59} brain function, gene transcription,^{1.60} mammalian reproduction, and muscle contraction.^{1.61} Zinc constituent of more than 300 biomolecules also causes some diseases in the nervous system, such as Alzheimer's disease,^{1.62} ischemic stroke, Parkinson's disease, amyotrophic lateral sclerosis,^{1.63} infantile diarrhea, and epileptic seizures.^{1.64} For plant growth, molybdenum is essential and has been known since the 1930.^{1.65-1.67}

Metal ions are essential for healthy life but they are toxic after a limit of consumption. World Health Organization (WHO), Central Pollution Control Board (CPCB), Indian Standard Institution (ISI), and Indian Council of Medical Research (ICMR) defined the safe limits or maximum contaminant levels of ions in drinking water (**Table 1.1**).

From the above discussion, it is clear that the detection and quantification of these metal ions are very crucial and thus, it is emerging as a significant research topic.

Table 1.1. Permissible limits of drinking water quality (in the unit of mg/liter)

Parameters	WHO	ICMR	ISI
Iron	0.1	1.0	0.3
Copper	1.0	1.5	0.05
Magnesium	50	-	30
Sodium	200	1100-3300 mg/day	-
potassium	-	1100-3750 mg/day	-
Calcium	75	200	75
Cadmium	0.005	0.01	0.01
Lead	0.05	0.05	0.10
Mercury	0.001	0.001	0.001
Arsenic	0.05	0.05	0.05
Zinc	5.0	0.10	5.0
Chromium	-	-	0.05
Selenium	0.01	-	-

1.3. Analytical Methods and Advantages of Fluorescence Technique

Different analytical methods (volumetric, electrochemical, spectrophotometric and gravimetric etc.) are used for quantitative analyses of ions and elements. But, elemental analysis was carried out by different techniques like inductively coupled plasma-atomic emission spectrometry (ICP-AES),^{1.68,1.69} voltammetry,^{1.70} flame or graphite furnace atomic absorption spectroscopy (AAS),^{1.71} flame atomic absorption spectroscopy (FAAS),^{1.72} inductively coupled plasma mass spectrometry (ICPMS),^{1.73} thin chitosan films^{1.74,1.75} and various functionalized metal nanoparticles^{1.76,1.77} etc. UV-visible and fluorescence spectroscopic methods are commonly used ways in addition with the most advantageous methods to recognize environmentally and physiologically important analytes and this importance may be due to their low detection limits (LOD) and also applicable for cell imaging in biological mediums. In biochemical and chemical research, fluorescence-based techniques are important tools due to its appropriate and valuable criteria of a non-invasive nature, appreciable detection selectivity, quick response, high intrinsic sensitivity, cost-effectiveness, operational simplicity, easy signal detection and high temporal resolution.

1.4. Fluorescent chemosensors and their classification:

Fluorescent chemosensors are specially devised in such a way that they can generate information about the recognition of the target chemical species by the means of fluorescence emission. As stated earlier fluorescent chemosensors are composed of three components, the receptor part, the signaling moiety, which is termed fluorophore here and sometimes there is a spacer that links the other two units. When the target analyte is an ion, the receptor in the fluorescent chemosensor is termed ionophore and the fluorescent chemosensor is termed fluoroionophore. At present fluorescent chemosensors are vastly used by scientists and even for industrial means owing to their high sensitivity for the target analytes, very economical and easy operational methods for detection, easy monitoring, and fast response ability. Fluorophore can give rise to two types of signaling changes, quenching of fluorescence emission and enhancement of fluorescence emission.

i) Quenching of fluorescence emission- in this process by the means of chelation with the target analyte or due to the collision with other molecules (which can be analyte also) in the surroundings the emission of the sensor gets quenched which is termed as chelation enhanced quenching (CHEQ) effect.

ii) Enhancement of fluorescence emission- in this process the emission of the sensor gets enhanced as a consequence of binding with the analytes. This effect is known as chelation enhanced fluorescence (CHEF).

Again, on the basis of the nature of the fluorescence signaling occurred upon analyte binding and the reversible or irreversible nature of the mechanism of the interaction with the target analyte fluorescent sensors can be classified into four discrete groups: (i) Turn-off, (ii) Turn-on (iii) Ratiometric and (iv) Chemodosimeters (**Figure 1.1**).

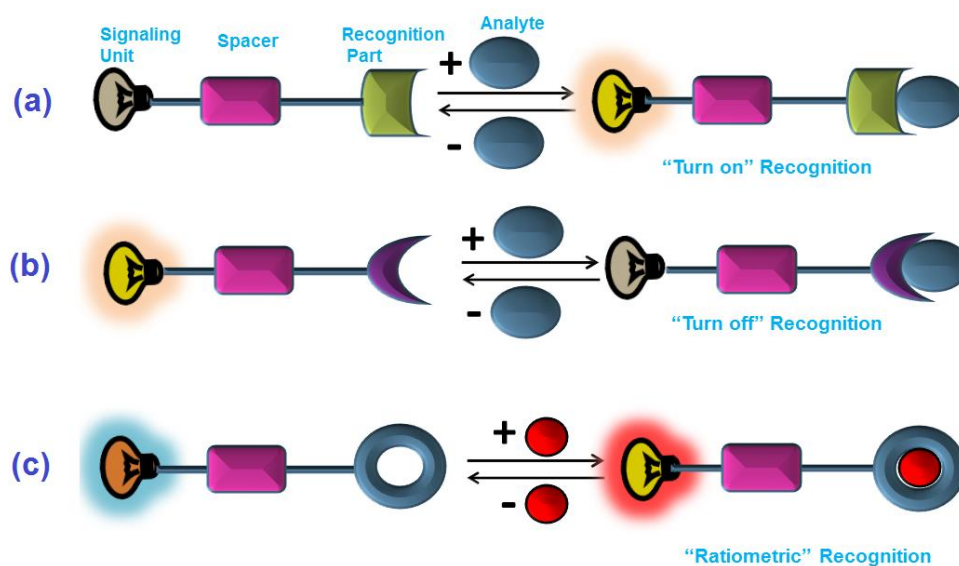


Figure 1.1 Simplified illustration of (a) turn-on, (b) turn-off and (c) ratiometric fluorescent chemosensors.

1.4.1. Turn-on fluorescent chemosensor: These type of chemosensors exhibits an amplification in the fluorescence emission as a consequence of binding with the target analyte. It can be either non-fluorescent or weakly fluorescent which turns into highly emissive compound after the chelation with the analyte. In this case the analyte binding process is reversible in nature. If some strong chelating agent like EDTA or other apposite anion is added externally to the solution of the chelated complex of the metal ion and the ligand, it can snatch out the metal ions from metal complexes and as a result, the emission gets quenched.

1.4.2 Turn-off fluorescent chemosensor: these types of chemosensors are generally highly emissive. The fluorescence emission gets quenched upon the binding with the analyte. This process is also reversible in nature.

1.4.3. Ratiometric fluorescent chemosensor: The fluorescent chemosensors of the previous two types exhibit an increase or decrease in the emission intensity as a result of binding with the target analyte. Now, as here the only detectable signal is the fluorescence intensity, several factors like the instrumental efficiency, illumination intensity, environmental

conditions, the effective thickness of the cell in the optical beam and chemosensor concentration can affect the signal output. It is advantageous to use a ratiometric fluorescent measurement to get rid of these effects. Ratiometric sensors have an edge over typical fluorescence chemosensor as the later work on the basis of monitoring of emission intensity at a single wavelength for precise analysis. It is advantageous to have an indicator that shifts wavelengths at the same time maintaining strong emission while responding to the target analyte. Ratiometric detection collates the emission intensity ratios at two different wavelengths before and after recognition of the target analytes. The ratio of the emission at two properly chosen wavelengths would then cancel out most or all of the plausible variability as stated above.^{1.78-1.81}

1.4.4. Chemodosimeter: Chemodosimeters are abiotic molecules used for analyte recognition associated with the irreversible transduction of an observable signal. Chemodosimeters are designed in such a way that the target analyte which can be anion, cation or neutral molecule can induce a specific reaction involving both making and breaking of the covalent bonds (**Figure 1.2**). Therefore, chemodosimeters are often advantageous being associated with high selectivity. Products formed in this process are different from the designed chemodosimeter which exhibit optically different properties.^{1.82,1.83}

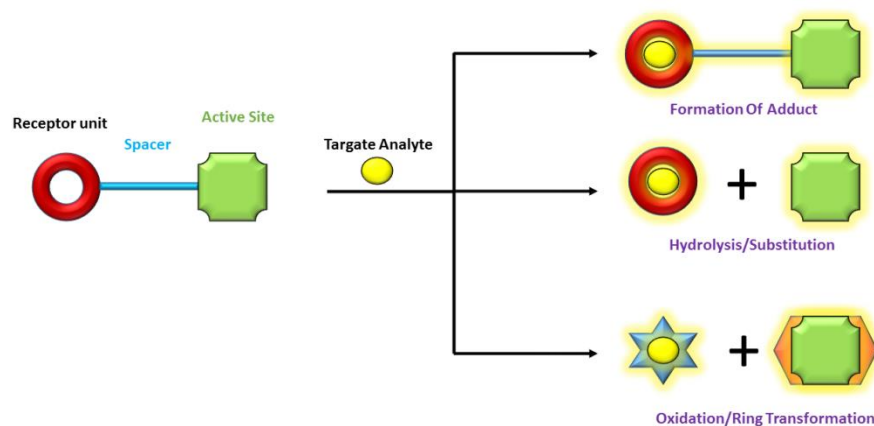


Figure 1.2 Pictorial representation of various types of fluorescent Chemodosimeter.

1.5. Fluorescence sensing mechanisms

An ideal fluorescent sensor must have the three basic requirements; as given in **Figure 1.1**. Normally, ‘Turn-On’ and ‘Turn-Off’ type fluorescence sensing are observed. ‘Turn-On’ type may have any of three different categories *viz.* normal fluorescence enhancement, ratiometric enhancement and wavelength shift. But in ‘Turn-Off’ type only quenching of fluorescence is observed.

1.5.1. Paramagnetic fluorescence quenching: It is a ‘Turn-Off’ type fluorescence process and in this method existence of a paramagnetic metal ion to the fluorophore, the generally forbidden Intersystem Crossing (ISC) becomes faster and it is termed as the paramagnetic effect. Metal complexes undergo ISC from S_1 to T_1 state of the fluorophore upon excitation and accordingly deactivated through non-radiative processes (**Figure 1.3**).^{1,84}

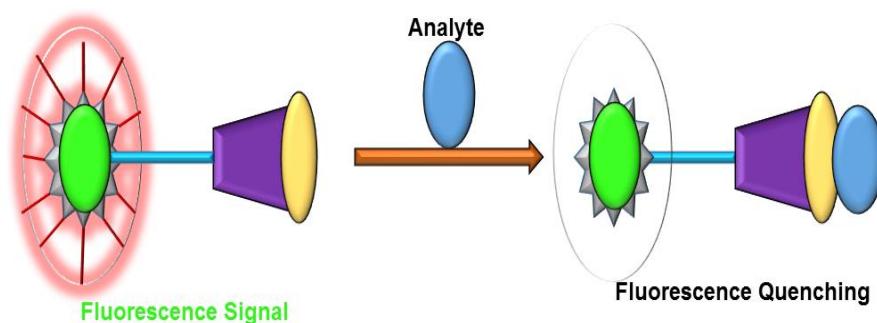


Figure 1.3 Diagram showing binding of a paramagnetic ion (eg. Fe^{3+} , analyte) with fluorophore, fluorescence quenching phenomenon.

1.5.2. Photo-induced electron transfer (PET): A Photo-induced electron transfer (PET) fluorescent probe is contained of fluorophore-spacer-receptor compartments and a small aliphatic spacer present between the fluorophore and receptor units. Usually, PET occurs from O, S, N and P donor centers with lone pair of electrons to the HOMO. After excitation,

an electron of the free receptor from HOMO is transferred to LUMO of fluorophore, which an intramolecular electron transfer happens in the unbound state and no fluorescence is observed. However, the bounded receptor caused the electron pair to interact with analyte, which makes the HOMO of receptor to lower in energy than that of the fluorophore i.e. when the donor atom of the lone pair binds with the metal ion, the PET process is prevented and the fluorescence ‘switch-ON’ occurs (**Figure 1.4**).^{1.85} Furthermore, the PET effect depends on solvent polarity if the solvent polarity is increased then electron transfer is easier.

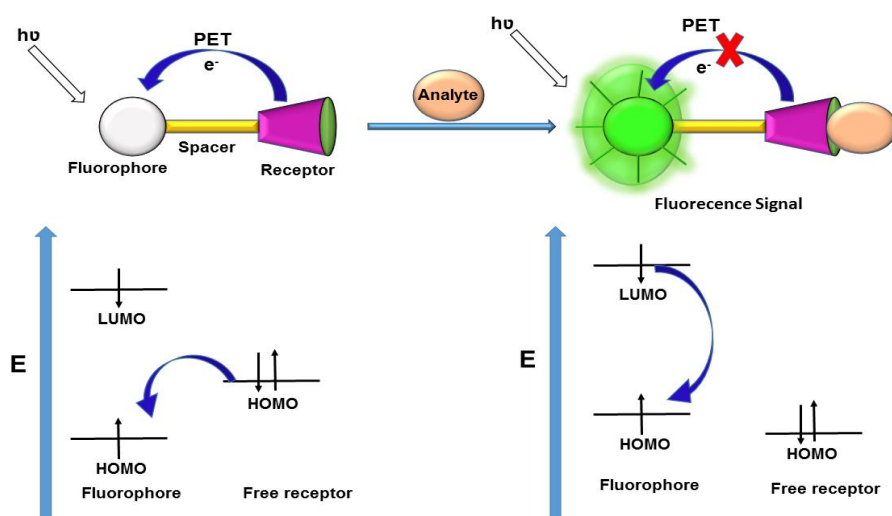


Figure 1.4 Schematic diagram for PET mechanism.

1.5.3. Chelation enhanced fluorescence (CHEF) and Chelation enhanced quenching (CHEQ):

In a fluorescent probe, when a metal ion binds with receptor, emission intensity may increase or quenched and accordingly named as chelation enhanced fluorescence (CHEF) or chelation enhance quenching (CHEQ) respectively causing blue or red shift of the fluorescence band (**Figure 1.5**).^{1.86} In CHEF, when analyte coordinated with receptor, the molecule becomes more rigid and energy is then transferred by radiative pathway. In quenching process, the spin-forbidden intersystem crossing (ISC) become faster due to paramagnetic metal ion is in the proximity of the fluorophore. Metal complexes upon

excitation undergo ISC from S_1 to T_1 state of the fluorophore and subsequently deactivated through the non-radiative processes.

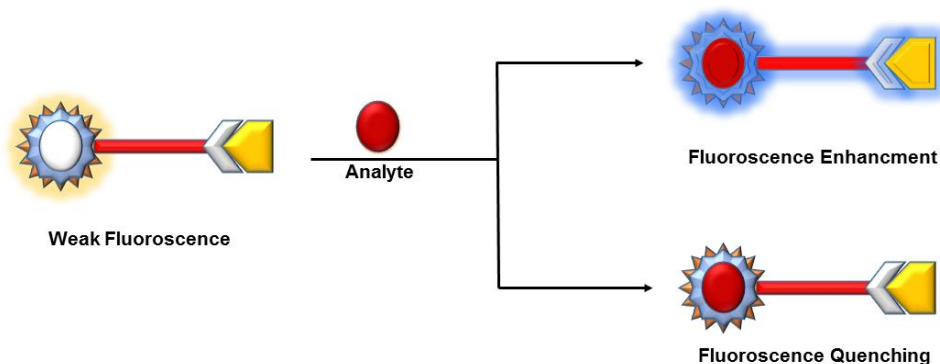


Figure 1.5 Schematic diagram shows CHEF and CHEQ processes.

1.5.4. Intra and intermolecular charge transfer (ICT): In an ICT system, a fluorophore is in direct interaction with a receptor; one terminal is electron rich and the other terminal is electron poor resulting a ‘push–pull’ system (**Figure 1.6**). The fluorophore electron density is affected during the recognition processes of coordination between the recognition group and the analyte and changes of luminescence emission is observed. Intra and intermolecular charge transfer (ICT) causes substantial shifts in the absorption and fluorescence emission properties. Between PET and ICT probes, there is a difference only in the way of fluorescence responds during the recognition processes. In PET process, there are no exact spectral shifts, but, ICT shows clear ratiometric shifts in the fluorescence emission band during the binding courses.^{1.87}

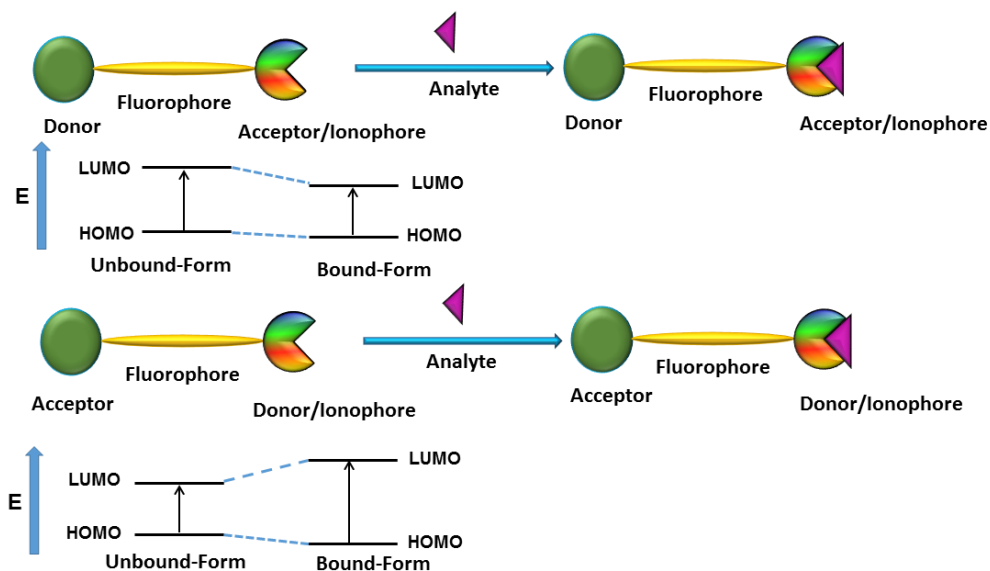


Figure 1.6 Schematic diagram shows mechanism of ICT.

1.5.5. Fluorescence resonance energy transfer (FRET): FRET results in a transfer of excitation energy by the interaction between donor and acceptor. The whole process includes several factors like the spectral overlaps between the absorbance of donor and emission of acceptor, the dipole moment of the molecules, the distance between donor and acceptor etc. Here, the spectrum overlap between the absorption spectrum of fluorophore 1 (Acceptor) and the emission spectrum of fluorophore 2 (Donor) is vital to allow FRET process (**Figure 1.7**). In FRET, the energy is transferred from the excited Donor to Acceptor having longer-wavelength ($A + D^* \rightarrow A^* + D$), which is coupled in resonance and acceptor emits light with a loss of emission from the donor.^{1.88,1.89}

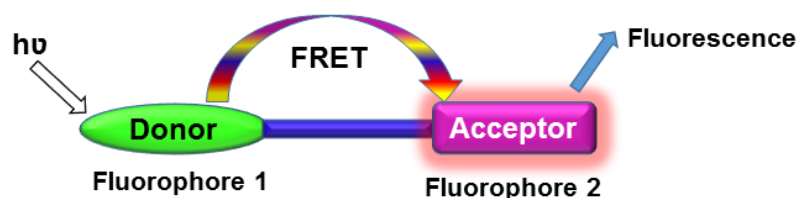
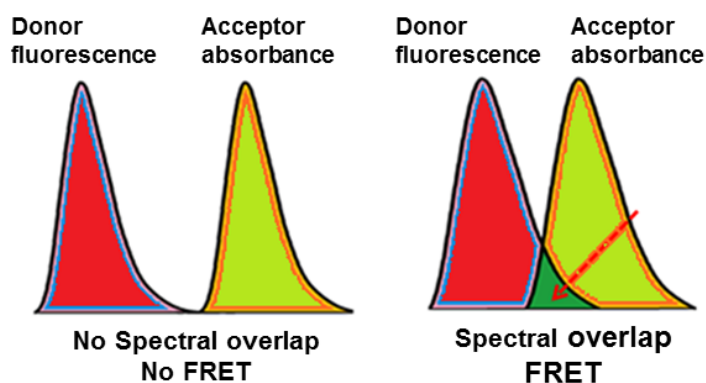


Figure 1.7 Schematic diagram of FRET process

1.5.6. Excited-state intramolecular proton transfer (ESIPT): ESIPT process commonly occurs in the molecules having a five/six membered ring which undergoes tautomerization and is based on the large Stokes' shift (**Figure 1.8**). Generally, the enol (E) form of molecules exist as unexcited in which five/six membered ring with intramolecular hydrogen-bond is formed and upon photo excitation it undergoes tautomerization process to a keto form (${}^1E^* \rightarrow {}^1K^*$) at very fast. Then, ESIPT process occurs and the intramolecular hydrogen bond also stabilizes the keto form. Both the radiative decay and the deactivation path lead to exciting keto (K^*) form into the ground state keto (K) forms. Subsequently, the radiative decay is slower than ESIPT and the emission of ESIPT chromophores is very often.^{1.90}

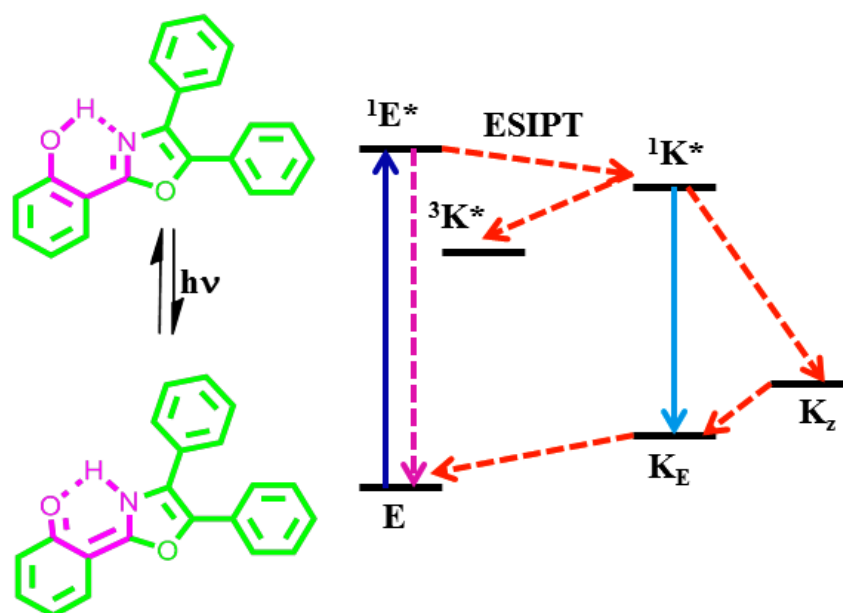


Figure 1.8 Schematic diagram for ESIPT process.

1.6. A concise literature survey on recent fluorescent chemosensors:

Chemosensors of different types have been reported for different metal ions, e.g. Al^{3+} , Zn^{2+} , Fe^{3+} , Cr^{3+} , Cu^{2+} , etc. over several years. Many of these have been crafted by embodying various fluorophoric units such as pyridoxal, rhodamine, DFP, quinoline, anthracene, BODIPY, coumarin, pyrene, etc. A concise literature survey on the recently published reports on different chemosensors for cations on the basis of the fluorophore used are epitomized afterward.

1.6.1. 4-Methyl-2,6-diformylphenol (DFP) based sensors:

4-Methyl-2,6-diformylphenol (DFP) is extensively used to synthesis acyclic as well as macrocyclic ligands. These ligands are produce tremendous type of transition metal complexes and widely used fluorophoric constituent for the fabrication of probes for various analytes. The DFP base products have been capable to sense cations (like Al^{3+} , Zn^{2+} , Cu^{2+} , Mg^{2+} , Hg^{2+} . etc.) anions (like N_3^- , H_2PO_4^- , PO_4^{3-} , CH_3COO^- , ClO^- , H_2AsO_4^- , AsO_3^{3-} etc.) and small neutral molecules (like cysteine, mandelic acid and glutathione).^{1.91-1.99} DFP holds two aldehyde groups, there is sufficiently of choice to scheme effective fluorophoric probes

for a specific species. A strong knowledge will lead to synthesis the future fluorophoric probes.

Bhanja *et al.*^{1.92} reported a DFP based aza-crown Schiff base ligand (**DFP 1, Chart 1.1**). The chemosensor was selectively sensing Al^{3+} and Zn^{2+} in DMSO water medium by turn-on fluorescence at 580 nm (Al^{3+}) and 505 nm (Zn^{2+}), emission wavelengths. The limit of detections was calculated as 1.2 μM (Al^{3+}) and 21 nM (Zn^{2+}), respectively. Cell-imaging study of the probe was done in *SCC084 (Human Oral carcinoma)* cell lines to explore its efficacy to identify Zn^{2+} and Al^{3+} ions in a living cell. The probe was also explored for theoretical DFT study and building logic gates (OR and NOT).

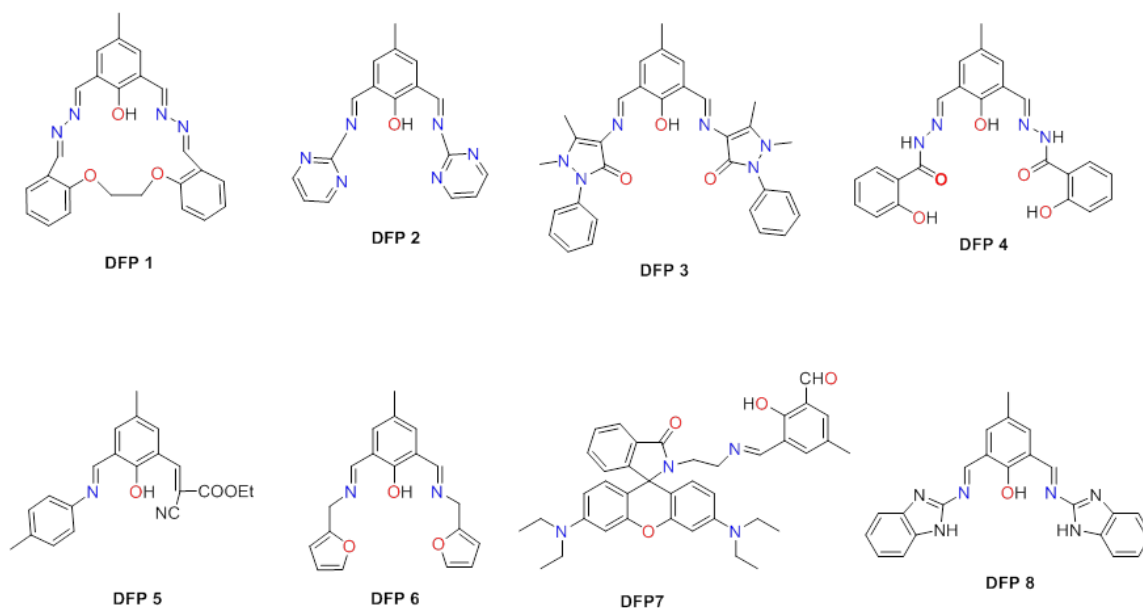


Chart 1.1: DFP based chemosensors.

Hazra *et al.*^{1.93} reported a Schiff base **DFP 2 (chart 1.1)** derivative of DFP and 2-aminopyrimidine which was applied for the fluorescence turn-on sensing of Al^{3+} in DMSO : water (v/v, 9:1, 10 mM HEPES buffer at pH 7.4) medium. The limit of detection was calculated as 1.27 μM . In the presence of Al^{3+} ion, the fluorescence intensity was enhanced 12 times at 493 nm. The chemosensor was explored to identify Al^{3+} in a real sample.

Dey *et al.*^{1.94} reported a DFP based dual signaling Schiff base ligand (**DFP 3, Chart 1.1**) which was found to exert fluorescence and colorimetric turn on sensing towards the Zn^{2+} and Al^{3+} ions. The chemosensor showed an aggregation induced emission (AIE) phenomenon by manipulating the THF water solvent ratio which exerted robust green emissive fluorogenic aggregates. Fluorescence increment by 195-times and 168-times in presence of Al^{3+} and Zn^{2+} was observed at 480 nm and 508 nm, respectively. PET and CHEF processes were responsible for fluorescence enhancement. The binding constants and stoichiometry were calculated as $7.63 \times 10^4 \text{ M}^{-1}$, $3.42 \times 10^4 \text{ M}^{-1}$ and 1: 1 for both Al^{3+} and Zn^{2+} , respectively. The probe showed a high sensitivity for the detection of Al^{3+} and Zn^{2+} ions with low limits of detection values like 21 nM and 30 nM, respectively. Besides this the probe was used as a chemosensor for explosive 2,4,6-trinitrophenol (TNP) with a LOD value of 1.74 μM .

Mistri *et al.* reported a DFP base zinc sensor (**DFP 4, Chart 1.1**) with N_3O_2 donors which was obtained from the condensation reaction between DFP and salicylhydrazide (1:2) in acetic acid and ethanol medium.^{1.95} The chemosensor showed weak emission at 512 nm wavelength ($\lambda_{\text{ex}}=390\text{nm}$) in water : THF (v/v, 4:6, HEPES buffer at pH 7.0) medium. Upon the addition of Zn^{2+} ions, the fluorescence intensity enhancement was 680 times at 486 nm. The binding stoichiometry (1:2) was confirmed by X-ray diffraction analysis of the zinc-probe complex. The ligand dissociation constant (K_d) value was calculated as 0.85 pM^2 . Limit of detection value was 2.88 ng/L for zinc ions. Chemosensor was explored to identify Zn^{2+} ions in A375 human melanoma cancer cells.

Parua *et al.* reported a new chemosensor **DFP 5 (chart 1.1)** which was obtained from the condensation reaction between p-toluidine and DFP followed by ethyl cyanoacetate in the presence of Et_3N (triethylamine).^{1.96} The probe exhibited strong emission at 595 nm (λ_{ex} : 400 nm) in water : acetonitrile (v/v, 1:4, HEPES buffer at pH 6.8). Significant quenching of the fluorescence in presence of Cu^{2+} ion has occurred which inhibits the ESIPT process. The

quantum yields were found as 0.090 and 0.015 for the probe and Cu-bound probe, respectively. The binding stoichiometry 1:2 was confirmed from single crystal X-ray structure of the Cu-complex. It showed the binding side of the probe, which was phenolic oxygen and imine nitrogen atom from each of the probes. The binding constant was calculated as 2.19×10^4 and 1.03×10^5 for Cu^{2+} and S^{2-} , respectively. The limit of detection value was found as 7.92×10^{-7} M. Upon the addition of sulfide anion, the Cu-bound chemosensor fluorescence intensity was enhanced at 595 nm. The limit of detection value was calculated as 5.87×10^{-7} M for sulfide anion. The chemosensor was applied to fabricate the molecular logic gate.

Another DFP based Schiff base chemosensor **DFP 6**, synthesized (**Chart 1.1**) for selective detection of both Zn^{2+} and Cu^{2+} was reported by Ghorai *et al.*^{1.97} The chemosensor showed rapid response through colorimetric and fluorescence changes for both the ions. Both of the metal ions formed complexes with the probe with 1:1 stoichiometry as indicated by the Job's Plot. The probe bound the metal ions in reversible manner. The detection limit values were determined for Cu^{2+} and Zn^{2+} as 2.29 nM and 3.67 nM, respectively. The cell-imaging experiment of the probe was done in *Candida albicans* cells to explore its efficiency to identify both Zn^{2+} and Cu^{2+} ions in the cell imaging study. Molecular logic gates were fabricated using the system.

Roy *et al.* constructed a chemosensor (**DFP7, chart 1.1**) combining rhodamine and DFP unit for sensing trivalent metal ions (Al^{3+} , C and Fe^{3+}) in methanol : water (v/v, 9:1, HEPES buffer at pH 7.4).^{1.98} The chemosensor showed a response through colorimetric and fluorescence changes for these cations. Also, the fluorescence intensity of the chemosensor was enhanced at 550 nm by 800(Fe^{3+})-, 588(Cr^{3+})- and 1465(Al^{3+})-times in presence of trivalent metal ions. The binding constant values were calculated as 8.74×10^4 , 1.47×10^5 and 6.24×10^4 M^{-1} , for Fe^{3+} , Al^{3+} and Cr^{3+} , respectively. The quantum yield of the chemosensor

and metal bound chemosensors with Fe^{3+} , Al^{3+} and Cr^{3+} were measured as 0.00036, 0.1473, 0.2428 and 0.1296, respectively. The LOD values were calculated as 14.00, 6.97 and 15.80 nM for Fe^{3+} , Al^{3+} and Cr^{3+} , respectively. The chemosensor was explored to detect Al^{3+} , Cr^{3+} and Fe^{3+} ions in SH-SY5Y cells.

In another work, Dey *et al.* reported a new zinc sensor (**DFP8**, **chart 1.1**), synthesized from a 1:1 condensation reaction of 2-aminobenzimidazole with DFP in acetonitrile.^{1.99} It showed weak emission at 528 nm (λ_{ex} : 445 nm) in methanol : water (v/v, 9:1, HEPES buffer at pH 7.2). The enhancement of fluorescence intensity was increased eight fold due to the binding with the Zn^{2+} ion, which was attributed to the PET-off process. Zn^{2+} ions formed complexes with the probe with 1 : 1 binding stoichiometry. CHEF process was responsible for fluorescence enhancement. The binding constant value was measured as $4.38 \times 10^4 \text{ M}^{-1}$. The quantum yields of the probe and Zn-bound probe were shown as 0.02 and 0.18, respectively. The LOD value of the Zn^{2+} ion was measured as 0.832 nM. Chemosensor was explored for the cell-imaging study of Zn^{2+} ions on A549 human lung cancer cell lines.

1.6.2. 3-hydroxy-2-methylpyridine based vitamers sensors:

3-hydroxy-2-methylpyridine based vitamers are water-soluble and naturally occurring. Namely, pyridoxamine, pyridoxal, pyridoxine and their phosphorylated products, are called vitamin B₆. This vitamer contributes to around 140 enzymatic reactions in human body like racemization, decarboxylation and transamination. Pyridoxal is also used as anticancer agent. It has been widely used in the areas of sensing and biosensing due to its bioactivity, solubility in aqueous medium, water solubility, attractive photophysical properties good chelating ability, and easy structural modifications.^{1.100-1.110}

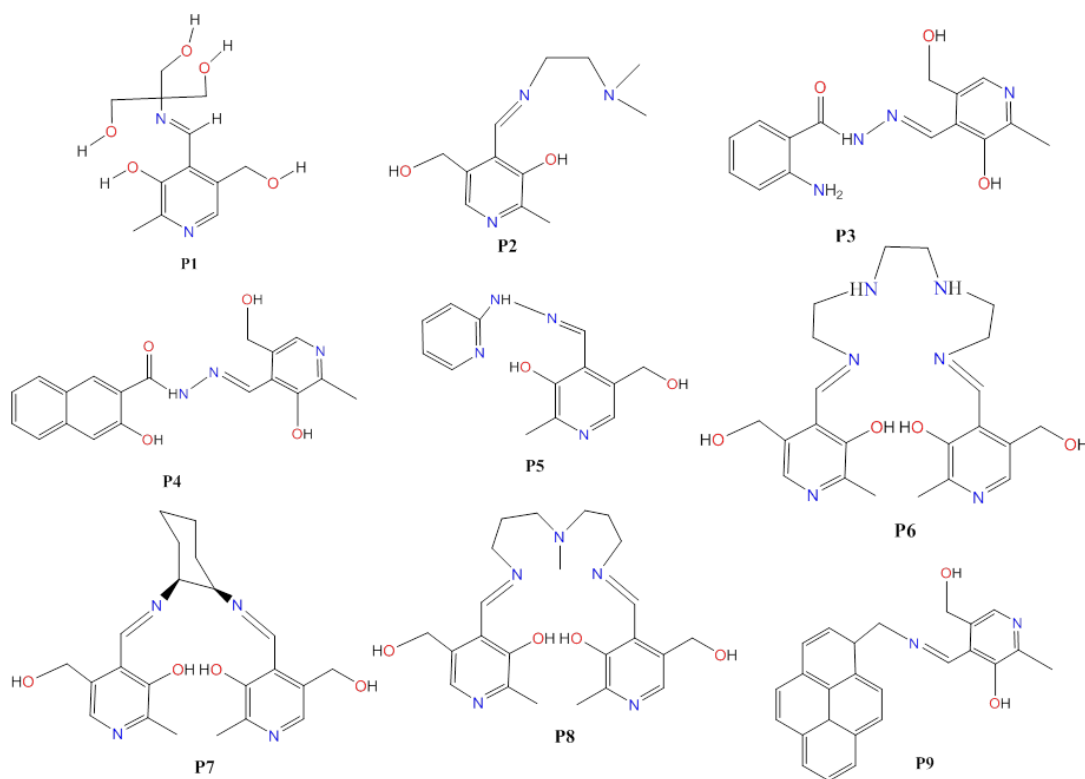


Chart 1.2: Pyridoxal based chemosensors.

A turn-off fluorescent pyridoxal based chemosensor (**P 1**, **chart 1.2**) was reported by Hussain *et al.*^{1,100} for the sensing of Zn^{2+} ions in a aqueous buffer solution. Probe **P1** exhibited weak fluorescence and the addition of Zn^{2+} ion enhanced the fluorescence intensity 12 times at 470 nm. Ligand **P1** formed a complex between Zn^{2+} and **P1** in a 1 : 2 binding stoichiometry. The LOD and association constant values were calculated as 2.77×10^{-8} M and 1.2×10^9 M⁻², respectively. They reported two single crystal structures and also, done reversibility experiment with EDTA. Additionally, the capability of the probe to detect Zn^{2+} in human embryonic kidney (HEK293) cells was studied.

In another work, Mondal *et al.* reported a new pyridoxal derivative **P2** (**chart 1.2**) was obtain by refluxing with an equal molar of N,N-dimethylethylenediamine. It exhibited Zn^{2+} selective turn-on emission at 483 nm with excitation at 411 nm in water-ethanol medium (v/v, 1:4, 25 mM Tris buffer at pH 7.4).^{1,101} The emission intensity enhanced due to the

inhibition of excited state intramolecular proton transfer (ESIPT), C=N isomerization and chelation-enhanced fluorescence (CHEF). The limit of detection value was calculated as 4.078 mM for Zn^{2+} . Jobs plot analysis was proved 1:1 metal:probe binding stoichiometry. Probe **P2** was explored to the cell-imaging study of intracellular Zn^{2+} in human lung cancer A549 cells. In further study, a penta-coordinated Zn^{2+} complex was produced and characterized by using X-ray diffraction analysis.^{1.102} Here, Zn^{2+} was binding with two nitrogen and one oxygen donor atoms from **P2**, one water molecule and one azide ligand. The Zn-complex exhibited 17 times higher emission intensity at 462 nm than **P2** in water : methanol (v/v, 1:9, 10 mM, Tris-HCl at pH 7.4.). The LOD value was calculated as 0.295 mM for Zn^{2+} ions from emission titration. Also, Probe **P2** was valid for live cell imaging in various cell lines (pollen, bacteria and fungi). The same probe (**P2**) exhibited fluorescence quenching at 500 nm for the sensing of Cu^{2+} ions in a methanolic medium. This quenching occurred due to the CHEQ effect. The limit of detection value was calculated as 10 mM for Cu^{2+} .^{1.103} The probe was explored to detect Cu^{2+} ions in live HeLa cells.

A new Schiff base chemosensor **P3** (**chart 1.2**) was obtained from a condensation reaction between pyridoxal and 2-aminobenzohydrazide. The probe exhibited weak fluorescence at 415 nm in water-DMSO medium.^{1.104} In the presence of Zn^{2+} , the probe showed a 7.5 times emission increment at 415nm due to the CHEF process. The binding stoichiometry between **P3** and Zn^{2+} was 1:1, which inhibited the C=N isomerization at the excited state. The LOD value was calculated as 0.32 mM for Zn^{2+} . Probe **P3** was explored to identify Zn^{2+} ions in live HeLa cells. Again, probe **P3** exhibited a 12.5 times emission intensity enhancement at 480 nm upon the addition of CN^- anions. The limit of detection value was calculated as 0.153 mM for CN^- . In addition, probe **P3** detected CN^- anions as colorimetrically and changed from colourless to lime yellow. A new absorbance band of **P3** was observed at 431 nm upon the addition of CN^- . The limit of detection was calculated as

0.17 mM from UV–vis titration. Further, This group synthesized a Schiff base **P4** (**chart 1.2**) with refluxing 3-hydroxy-2-naphthoic hydrazide and pyridoxal for the sensing of Zn^{2+} and Cysteine in water-DMSO medium.^{1.105} The interaction of **P4** with Zn^{2+} caused fluorescence quenching at 475 nm with excitation at 375 nm, which permitted the ratiometric sensing of Zn^{2+} ions and the limit of detection value was calculated as 0.873 mM. The complexation between **P4** and Zn^{2+} in a 1:1 binding ratio due to the interaction with imine–N, Pyridoxal–OH and carbonyl–O. Probe **P4** was applied for the intracellular cell-imaging of Zn^{2+} ions in HeLa cells. Also, the Zn-bound probe showed fluorescence quenching at 525 nm in the presence of Cys and LOD value was calculated as 0.663 mM. Cys is coordinated with the additional coordination sites available in the **P4**– Zn^{2+} complex. In addition, the absorbance at 435 nm of the complex **P4**– Zn^{2+} was quenched upon the addition of Cys with a visible colour difference from light yellow to colourless. The complex **P4**– Zn^{2+} showed a sensitivity limit of 0.286 mM for Cys.

Anand *et al.* reported, a pyridoxal-2-hydrazinopyridine Schiff base **P5** (**chart 1.2**), which was working for the emission turn-on sensing to detect Zn^{2+} ions in an aqueous solution of DMSO : water (v/v, 1:99, 10 mM Tris at pH 7.4).^{1.106} The complex formation between **P5** and Zn^{2+} in a 1:1 stoichiometry ratio caused a selective emission enhancement at 470 nm with excitation at 402 nm. The limit of detection was calculated as 70 nM for Zn^{2+} ions. Probe **P5** was explored to detect Zn^{2+} ions in live HeLa cells.

The six coordinated ligand N1,N4-bis(pyridoxylidene)triethylenetetramine **P6** (**chart 1.2**) was designed for complex formation with Zn^{2+} , Cd^{2+} , Ni^{2+} and Mn^{2+} in the solid state. The presence of Zn^{2+} in a methanol-water medium (v/v, 9:1, at pH 7.5) exhibited as 3 times luminescence intensity enhancement at 460 nm due to CHEF process.^{1.107} The fluorescence enhancement caused complexation and inhibited PET process. The limit of detection value was calculated as 10 nM from 3- σ method.

A novel Schiff base **P7** (chart 1.2) derivative of pyridoxal and 1,2-diaminocyclohexane exhibited emission enhancement at 475 nm upon the accumulation of Zn^{2+} in a water-ethanol (v/v, 1:4, HEPES buffer at pH 7.4).^{1.108} The limit of detection value was determined as 5.9 mM for Zn^{2+} ions and a linearity range of 5 to 45 mM. Probe **P7** has real-world application to detect Zn^{2+} in cell-imaging of human gastric adenocarcinoma (AGS) cells. Further, the Zn-bound chemosensor was efficient to mimic the phosphatase activity.

Another, pyridoxal base **P8** (chart 1.2), complexes with Zn^{2+} , was reported and its DNA binding and insulin-enhancing activity were explored.^{1.109} Receptor **P8** was detect Zn^{2+} ions in methanol-water (v/v, 98:2, , pH = 7.5 Tris-HCl buffer) medium. The weakly fluorescent probe **P8** showed fluorescence enhancement at 469 nm with excitation 265nm, upon the addition of Zn^{2+} with a limit of detection 400 mM. The monomer-excimer based probe **P8** was produced by refluxing 1-aminomethylpyrene with pyridoxal and used for the detection of Zn^{2+} in water-DMSO medium.^{1.110} Probe **P9** exhibited weak fluorescence at 417, 397 and 378 nm because of the monomeric pyrene. The complexation between **P9** and Zn^{2+} in a 2:1 stoichiometry and the monomer bands were increased because of the inhibition of PET. Then, a new band was observed at 485 nm due to the construction of excimer upon face-to-face π - π stacking of pyrene moieties and the colour was changed from blue to bluish green for different emissions. The Zn bound probe was used for the fluorescence sensing of $H_2PO_4^-$ and cysteine. The addition of $H_2PO_4^-$ and cysteine showed fluorescence enhancement due to the snatching of Zn^{2+} from the **P9** bound- Zn^{2+} compound. In contrast to $H_2PO_4^-$, the addition of cysteine exhibited emission enhancement of the monomer bands due to non-covalent interactions between the probe and cysteine, which inhibited the PET effect. The limit of detection values were calculated as 2.3 mM, 0.159 mM and 0.218 mM for Zn^{2+} ,

cysteine and H_2PO_4^- , respectively. Probe **P9** was explored to detect Zn^{2+} ions in living HeLa cells.

1.6.3. Rhodamine based chemosensors:

Rhodamine-based probes are efficient in both fluorescence emission and naked eye detection. They are nonfluorescent and colorless due to the close spirolactam ring. When the spirolactam ring is open, the dye is coordinated with a cation. Then, the closed spirolactam ring opens up causing a strong emission, typically, an emission band at greater than 550 nm. Two types of rhodamine derivatives are generally used in this purpose, namely, Rhodamine-2B and Rhodamine-6G.

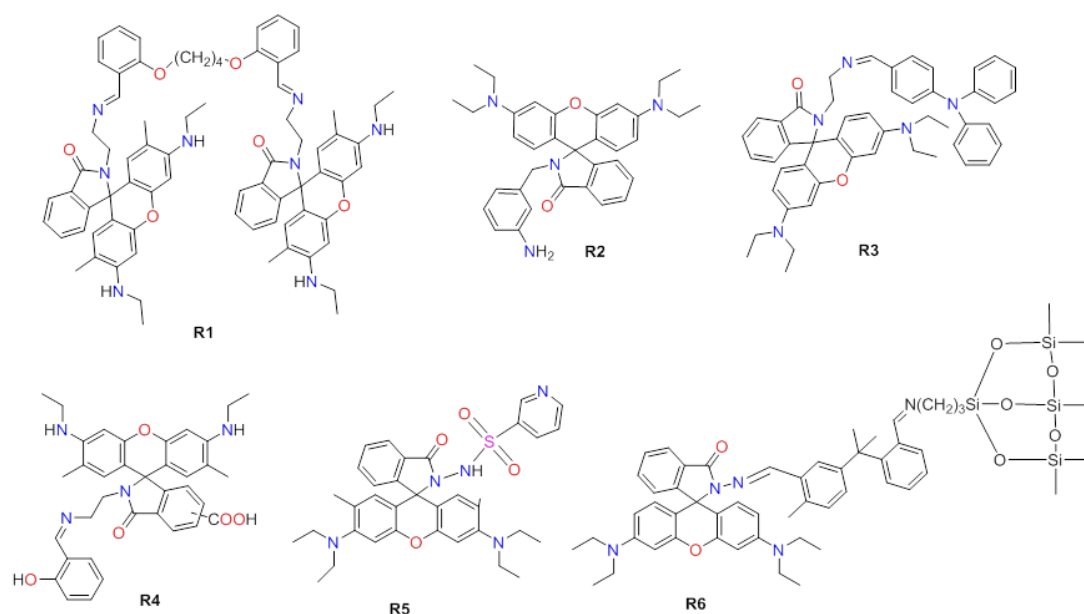


Chart 1.3: Rhodamine based chemosensors.

Das *et al.*^{1.111} synthesized a rhodamine 6G-based chemosensor (**R1**, **chart 1.3**). The probe was selective and sensitive towards trivalent metal ions Al^{3+} (653-fold), Fe^{3+} (669-fold), and Cr^{3+} (667-fold) in water/acetonitrile (7 : 3, v/v, at pH 7.2) medium. The detection limits were determined by 3σ methods and found to be 2.57 μM , 0.78 μM and 0.47 μM , for Fe^{3+} , Al^{3+} and Cr^{3+} , respectively. The probe was explored in advanced level of molecular logic gate devices.

Another fluorescence probe (**R2**, **chart 1.3**) was synthesized by Kan et al.^{1.112} which showed notable selectivity and sensitivity towards the Al^{3+} ion. The sensor exhibited a sheer enhancement in the absorbance and fluorescence spectra along with a change in color from colorless to pink with the addition of Al^{3+} ions in methanol/water (1:1, v/v) medium with a pretty short response time. The reversible nature of the chemosensor's recognition mechanism was proved by adding EDTA to the solution containing the probe and Al^{3+} ion, which took the edge off the emission intensity. The probe was found to have a low limit of detection as $0.314\mu\text{M}$. Again, the sensor was applied for the recognition of Al^{3+} ion in real life environmental water samples with a decent recovery rate. It was also applied to image Al^{3+} ions in soybean root tissue, zebrafish, human breast cells and natural water samples.

The Schiff base (**R3**, **chart 1.3**) derivative of a rhodamine-B and triphenylamine was applied for the fluorescence resonance energy transfer (FRET) ratiometric fluorescence specific sensing of Al^{3+} over other important metal ions in methanol/water (v/v, 1/4, pH 7.2, HEPES buffer (10 mM)).^{1.113} The complex was formed between **R3** and Al^{3+} in a 1:1 binding ratio, which caused FRET fluorescence enhancement with a sensitivity limit of 67 nM. The probe **R3** was explored to detect Al^{3+} in biological systems (such as human peripheral blood mononuclear cells, PBMCs) and the probe was used for INHIBIT logic gate.

Qiu *et al.*^{1.114} was reported two aqueous soluble chemosensor, based on 5-carboxyl rhodamine and 6-carboxyl rhodamine (**R4**, **chart 1.3**). In aqueous medium, 5-carboxyl substituent shows fabulous selectivity for Fe^{3+} over different common metal ions and detection limit of 5.2 mM. The Probe was realistic for the intracellular cell-imaging of Fe^{3+} in living HeLa cells. But, 6-carboxyl substituent was not sensed to detect in Fe^{3+} ion. They conclude that the fluorescence performance of xanthene-based probes was dependent on substituent position.

A rhodamine B based fluorescent probe (**R 5**, **chart 1.3**) was reported by Wang *et al.*^{1.115} for the “turn-on” detection of Fe³⁺ ion with profound selectivity and sensitivity. The detection limit and binding constant values of the probe towards Fe³⁺ ions were calculated as 75.9 nM and 0.608 ×10⁴ M⁻¹, respectively. 1:1 binding stoichiometry was confirmed from Job’s plot analysis. The probe was successfully used to identify Fe³⁺ ions in Hela cells and zebrafish.

A mesoporous silica rhodamine framework base compound (**R6**, **chart 1.3**) was reported by Singha *et al.*,^{1.116} which senses multi metal ions like Al³⁺, Cr³⁺, Fe³⁺ and Cu²⁺ in ethanol medium. The fluorescence enhancement of the chemosensor increased at 550 nm by 36, 17, 40 and 89 times in the presence of Al³⁺, Cr³⁺, Fe³⁺ and Cu²⁺, respectively. The quantum yield of the chemosensor and metal bound chemosensors with Al³⁺, Cr³⁺, Fe³⁺ and Cu²⁺ were measured as 0.057, 0.389, 0.275, 0.348 and 0.557, respectively. The LOD values were calculated as 3.79×10⁻⁷ M, 1.48×10⁻⁶ M, 3.27×10⁻⁷ M and 7.4×10⁻⁸ M for Al³⁺, Cr³⁺, Fe³⁺ and Cu²⁺, respectively. Another benefit that the compound was used to remove of Hg²⁺ and Cu²⁺ in an aqueous solution. Same group in 2019, was reported another silica Rhodamine base compound (**R7**, **chart 1.4**) which selectively detected Al³⁺, Cr³⁺, Fe³⁺ ions in water/ethanol (14:1, v/v) medium.^{1.117} The limit of detection values were calculated as 23.5 nM, 13.4 nM and 69.7 nM for Al³⁺, Cr³⁺ and Fe³⁺, respectively.

In another work, Guo *et al.* reported a rhodamine 6G-based fluorescent probe (**R8**, **chart 1.4**)^{1.118} with a t-butyl pyrrole moiety as recognition site. Photophysical studies showed that **R8** exhibited excellent selectivity and sensitivity towards Cu²⁺ ion over other metal ions via ‘turn-on’ sensing in neutral acetonitrile aqueous media with detection limit of 0.38 μM and the mechanism showed recognition process may due to Cu²⁺ promoted hydrolysis reaction of **R8**.

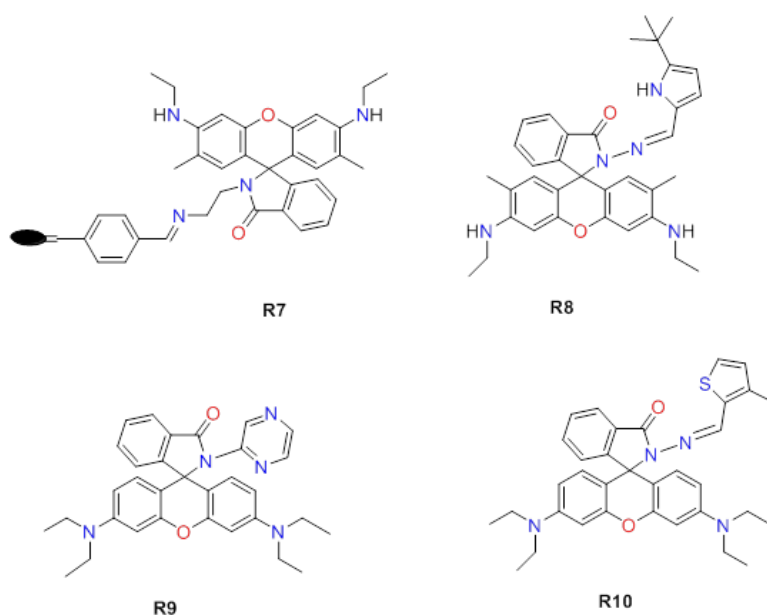


Chart 1.4: Rhodamine based chemosensors.

A rhodamine-6G based chemosensor (**R9**, **chart 1.4**) was developed and characterized as a reversible switch by Cheng *et al.*^{1.119}. The probe had high selectivity for Fe^{3+} ions in water/ ethanol (V/V, 1/1, Tris-HCl at pH = 7.4). The spirolactam ring opening mechanism of the rhodamine was prompted by fluorescence enhancement and Fe^{3+} ion binding. The limit of detection was calculated as 1.093×10^8 mol/L for Fe^{3+} ion, and colour of the chemosensing probe changed from colourless to pale-pink in the presence of Fe^{3+} ions. It was efficiently applied to microscopic imaging for the identification of Fe^{3+} in L929 cells.

A fluorescent probe (**R 10**, **chart 1.4**) containing 3-methyl-2-thiophenecarboxaldehyde and rhodamine B moieties was synthesized for selective recognition ions by Li *et al.*^{1.120}. The sensor exerted highly selective and sensitive “off-on” emissive responses toward the Hg^{2+} ion. The LOD value was 1.5 ppb for Hg^{2+} ions. Further, the probe was utilized as a sensing material to detect Hg^{2+} ions in MCF-7 cells.

1.7. Concluding remarks and aim of my research work

During last three decades of research in physical sciences, chemical sciences, biotechnology, neurobiology, engineering, technology etc., the chemosensing-based spectrophotometric and electrochemical analytical techniques are advancing very fast. The above discussion demonstrates the importance of fluorescence probes for biologically important analyte detection. Considering the importance of techniques in the selective sensing, our laboratory is also investing intellectual emotion in the design and application of sensors on ions and small molecule analyses. A Schiff base has been widely explored for various industrial applications and due to the biological activity; this class of compounds still requires further exploration. The Schiff bases and their metal complexes both are very interesting research area that constantly provides us with new information about recently created compounds. To detect metal ions at very low concentration (μM to nM), there are numbers of analytical instruments present, and these are very costly and also suffer limitations in case of real-time detection on the field monitoring. In this thesis, some Schiff base ligands have been synthesized (**Chart 1.5**) bearing different moieties, like as imine ($-\text{C}=\text{N}-$), azo ($-\text{N}=\text{N}-$), amide ($\text{O}=\text{C}-\text{NH}$) etc. of 4-Methyl-2,6-diformylphenol, pyridoxal and rhodamine derivatives. The probes and sometimes their coordination complexes are synthesized by facile, green and economically cheap synthetic route followed by complete spectral characterization and also confirmation of some structures by X-Ray analysis. The Schiff base molecules are used as chemosensor for the detection of several biologically as well as environmentally important ions such as Zn^{2+} , Al^{3+} , Cu^{2+} , Fe^{3+} and Cr^{3+} . All the Schiff bases as well as their metal complexes have been characterized by various spectroscopic techniques (FT-IR, NMR, Mass, micro analytical data) and have been used as metal ion sensor and also use for live cell imaging studies. The structures are also confirmed by X-ray diffractometric measurement whenever possible. Some of the studies also embraced

preliminary computational studies using density functional theory (DFT) to procure some breadth of view of the molecular level interactions between the probe and analytes. HeLa cells and human breast cancer cells (MDA-MB-468) are used for bio-cell imaging.

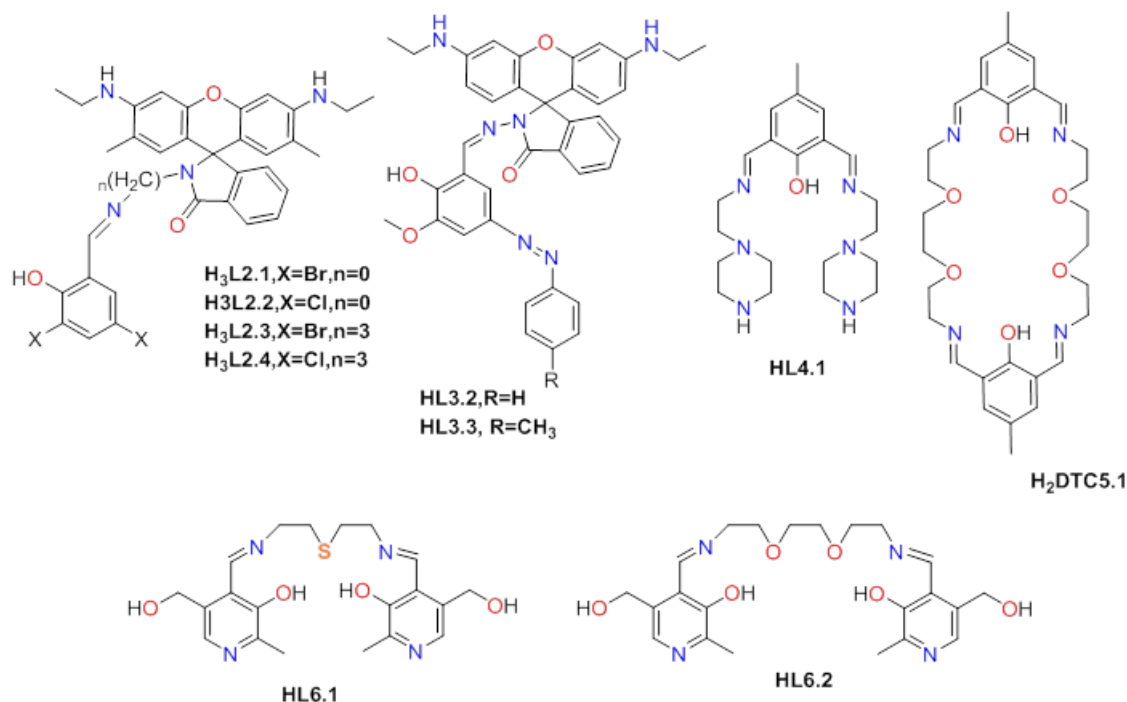


Chart 1.5: Design of target Schiff base probes.

I.7. Physical measurement:

(i) **Elemental analysis:** Micro analytical data (C, H, N) were collected on Perkin Elmer 2400 Series-II CHN analyzer, USA elemental analyzer using the pure solid sample.

(ii) **FT-IR spectra:** FT-IR spectra (KBr disk, $4000-400\text{ cm}^{-1}$) by Perkin Elmer LX-1 FTIR spectrophotometer with samples prepared as KBr pellets.

(iii) **1H NMR spectra:** 1H NMR spectra were obtained from Bruker 400 MHz spectrometer or Bruker 300 MHz spectrometer using $DMSO-d_6$, CD_3OD and $CDCl_3$ as solvent and tetramethylsilane as internal standard.

(iv) **Single crystal X-ray diffraction study:** Attempts will be made to obtain single crystals of the ligands and their complexes by slow evaporation of solvent from solution, or from the diffusion of another solvent into the solution. Data will be collected on a Bruker SMART Apex CCD area detector by graphite monochromated Mo K_{α} radiation with wavelength of 0.71073 Å. X-ray data reduction, structure solution and refinement were done by using ORTEP-32,^{1.121} SHELXL-97,^{1.122} and WinGX^{1.123} programs. The structures were solved by direct method.

(v) **Mass Spectroscopy:** A Water HRMS model XEVO-G2QTOF#YCA351 spectrometer was used to record ESI mass spectra.

(vi) **UV-Vis spectra:** UV-Vis spectra were recorded by Cary 60 spectrophotometer (Agilent) using the solution as required concentration. Solution will be kept in a quartz cell with 1 cm path length and absorption spectra were recorded starting from visible to UV region.

(vii) **Fluorescence spectra:** Steady-state fluorescence measurements were accomplished with HORIBA Fluoromax-4 spectrofluorimeter and Duetta-fluorescence and absorbance spectrometer, HORIBA.

(viii) **Estimation of Quantum Yield:** Fluorescence quantum yields (Φ) were calculated by integrating the area under the fluorescence curves using the following equation,

$$\Phi_{\text{sample}} = \left\{ \frac{(\text{OD}_{\text{standard}} \times A_{\text{sample}} \times \eta_{\text{sample}}^2)}{(\text{OD}_{\text{sample}} \times A_{\text{standard}} \times \eta_{\text{standard}}^2)} \right\} \times \Phi_{\text{standard}}$$

In the above equation, A is the area under the emission spectral curve, OD is the optical density of the compound at the excitation wavelength and η is the refractive index of the solvent. Φ_{standard} value is taken as 0.52 (for Quinine Sulfate).

(vii) **Life time measurement:** The steady-state fluorescence lifetime measurements were executed using a TCSPSC (time-correlated single photon counting) set up from Horiba Jobin-Yvon. The luminescence decay data were collected on a Hamamatsu MCP photomultiplier (R3809) and were analyzed using the IBH DAS6 software.

(viii) Theory and Computational Methods:

Optimization of ground-state structures and energy calculations for all the fluorescence probe and their complexes were carried out by DFT (density functional theory) method using the Gaussian 09 package, where CAM-B3LYP or B3LYP was chosen as the basis function.^{1.124,1.125} For C, H, N, O and S the 6-31G^{1.126-132} basis set were assigned, while for Zn, Cu, and Al the LanL2DZ^{1.133} basis set with effective core potential were employed. Vibrational frequency calculations were performed for confirmation the optimized geometries which represent the local minima, and these only yielded positive eigenvalues. Time Dependent Density Functional Theory (TD-DFT) was also performed by the use of conductor-like polarizable continuum model (CPCM),^{1.134-1.136} from this theoretical UV-Vis spectral transitions are observed. The fraction of contributions of various groups in each molecular orbital were calculated by carrying out GAUSSSUM.^{1.137}

(ix) Live cell imaging: Cell images were taken using fluorescence microscope.

1.8 References

- (1.1) D. R. Williams, *The metals of life*, Van Nostrand, London, 1971.
- (1.2) I. Bertini, H. B. Gray, S. J. Lippard, J. S. Valentine, *Bioinorganic Chemistry*, University Science Books, Mill Valley, California, 1994.
- (1.3) M. Constantin, I. Alexandru, *The role of sodium in the body*, *Balneo-Research Journal*, Vol.2, Nr.1, 2011.
- (1.4) Potassium and Sodium (In Biological Systems), <https://doi.org/10.1002/0471743984.vse5720>, 2005.
- (1.5) G. Augustine, *Curr. Opin. Neurobiol.*, 2001, **11**, 320–326.
- (1.6) R. D. Burgoyne and A. Morgan, *Trends Neurosci.*, 1995, **18**, 191–196.
- (1.7) H. Rubin, *Arch. Biochem. Biophys.*, 2007, **458**, 16–23.

- (1.8) F. I. Wolf, A. Torsello, A. Fasanella and A. Cittadini, *Mol. Aspects Med.*, 2003, **24**, 11–25.
- (1.9) J. R. Moll, A. Acharya, J. Gal, A. A. Mir and C. Vinson, *Nucleic Acids Res.*, 2002, **30**, 1240–1246.
- (1.10) O. B. Stepura and A. I. Martynow, *Int. J. Cardiol.*, 2009, **134**, 145–147.
- (1.11) S. C. Larsson, M. J. Virtanen, M. Mars, S. Maññisto, P. Pietinen, D. Albanes and J. Virtamo, *Arch. Intern. Med.*, 2008, **168**, 459–465.
- (1.12) S. Mahabir, Q. Y. Wei, S. L. Barrera, Y. Q. Dong, C. J. Etzel, M. R. Spitz and M. R. Forman, *Carcinogenesis*, 2008, **29**, 949–956.
- (1.13) F. H. Nielsen and H. C. Lukaski, *Magnesium Res.*, 2006, **19**, 180–189.
- (1.14] D. Satcher, Screening Young Children for Lead Poisoning: Guidance for State and Local Public Health Officials. Center for Disease Control and Prevention; Atlanta, GA, USA: 1997.
- (1.15) Center for Disease Control and Prevention, Blood Lead Levels in Residents of Homes with Elevated Lead in Tap Water-District of Columbia, 2004, Volume 53. Center for Disease Control and Prevention; Washington, DC, USA: 2004, pp. 268–270.
- (1.16) M. Barakat, *Arabian J. Chem.*, 2011, **4**, 361–377.
- (1.17) M. Castro-González and M. Méndez-Armenta, *Environ. Toxicol. Pharmacol.*, 2008, **26**, 263–271.
- (1.18) S. Majumder, G. Gangadhar, S. Raghuvanshi and S. Gupta, *J. Water Process Eng.*, 2015, **6**, 136–143.
- (1.19) K. Karthikeyan and L. Sujatha, *IEEE SENSORS JOURNAL*, 2018, **18**, 5225–5231.
- (1.20) L. Li, L. F. Liao, Y. P. Ding and H. Y. Zeng, *RSC Adv.*, 2017, **7**, 10361–10368.

- (1.21) G. F. Nordberg and R. F. M. Herber, L. Alessio (Eds.), *Cadmium in the Human Environment: Toxicity and Carcinogenicity*, International Agency for Research on Cancer, Lyon, 1992.
- (1.22) D. M. Templeton and Y. Liu, *Chem. Biol. Interact.*, 2010, **188**, 267–275.
- (1.23) Y. Xue, H. Zhao, Z. J. Wu, X. J. Li, Y. J. He and Z. B. Yuan, *Analyst*, 2011, **136**, 3725–3730.
- (1.24) D. K. Nordstrom, *Science*, 2002, **296**, 2143–2145.
- (1.25) P. L. Smedley and D. G. Kinniburgh, *Appl. Geochem.*, 2002, **17**, 517–568.
- (1.26) A. A. Duker, E. J. M. Carranza and M. Hale, *Environ. Int.*, 2005, **31**, 631–641.
- (1.27) D. Rehder, *Metallomics*, 2015, **7**, 730–742.
- (1.28) A. K. Singh, V. K. Gupta and B. Gupta, *Anal. Chim. Acta*, 2007, **585**, 171–178.
- (1.29) H. Arakawa, R. Ahmad, M. Naoui, H. Ali and T. Riahi, *J. Biol. Chem.*, 2000, **275**, 10150–10153.
- (1.30) J. B. Vincent, *Nutr. Rev.*, 2000, **58**, 67–72.
- (1.31) M. Zhang, Z. Chen, Q. Chen, H. Zou, J. Lou and J. He, *Mutat. Res., Genet. Toxicol. Environ. Mutagen.*, 2008, **654**, 45–51.
- (1.32) P. A. Cox, *The Elements on Earth: Inorganic Chemistry in the Environment*, Oxford University Press, New York, 1995.
- (1.33) L. Wang, D. Ding, R. Salvi and J. A. Roth, *Neurobehav. Toxicol.*, 2014, **40**, 65–74.
- (1.34) T. G. Kazi, H. I. Afridi, N. Kazi, M. K. Jamali, M. B. Arain, N. Jalbani and G. A. Kandhro, *Biol. Trace Elem. Res.*, 2008, **122**, 1–18.
- (1.35) Y. Liu, S. H. Wu, C. Hua and X. Han, *Desalin. Water Treat.*, 2014, **52**, 4183–4189.
- (1.36) S. K. Sahoo, D. Sharma, R. K. Bera, G. Crisponi and J. F. Callan, *Chem. Soc. Rev.*, 2012, **41**, 7195–7227.
- (1.37) D. Touati, *Arch. Biochem. Biophys.*, 2000, **373**, 1–6.

- (1.38) L. Zecca, M. B. H. Youdim, P. Riederer, J. R. Connor and R. R. Crichton, *Nat. Rev. Neurosci.*, 2004, **5**, 863–873.
- (1.39) D. Berg and H. Hochstrasser, *Mov. Disord.*, 2006, **21**, 1299–1310.
- (1.40) P. Rafighi, M. Yaftian and N. Noshiranzadeh, *Sep. Purif. Technol.*, 2010, **75**, 32–38.
- (1.41) A. Ahmadpour, M. Tahmasbi, T. R. Bastami, J. A. Besharati, *J. Hazard. Mater.*, 2009, **166**, 925–930.
- (1.42) Y. A. Iyaka, *Sci. Res. Essays*, 2011, **6**, 6774–6777.
- (1.43) A. W. Lothongkum, Y. Khemglad, N. Usomboon and U. Pancharoen, *J. Alloys Comp.*, 2009, **476**, 940–949.
- (1.44) K. Alizadeh, H. Nemati, S. Zohrevand, P. Hashemi, A. Kakanejadifard, M. Shamsipur, M. R. Ganjali and F. Faridbod, *Mater. Sci. Eng. C*, 2013, **33**, 916–922.
- (1.45) M. J. Zirwas and M. A. Molenda, *J. Clin. Aesthet. Dermatol.*, 2009, **2**, 39–43.
- (1.46) J. A. Cowan, *Inorganic Biochemistry: An Introduction*, Wiley VCH, New York, 1997, pp. 133–134.
- (1.47) W. Wang, A. Fu, J. You, G. Gao, J. Lan and L. Chen, *Tetrahedron*, 2010, **66**, 3695–3701.
- (1.48) A. K. Mahapatra, G. Hazra, N. K. Das and S. Goswami, *Sensor. Actuat. B Chem.*, 2011, **156**, 456–462.
- (1.49) P. Kaur, S. Kaur and K. Singh, *Inorg. Chem. Commun.*, 2009, **12**, 978–981.
- (1.50) J. S. Valentine and P. J. Hart, *Proc. Natl. Acad. Sci. U.S.A.*, 2003, **100**, 3617–3622.
- (1.51) L. I. Bruijn, T. M. Miller and D. W. Cleveland, *Annu. Rev. Neurosci.*, 2004, **27**, 723–749.
- (1.52) M. Sonawane, K. Tayade, S. K. Sahoo, C. P. Sawant and A. Kuwar, *J. Coord. Chem.*, 2016, **69**, 2785–2792.

- (1.53) K. J. Barnham, C. L. Masters and A. I. Bush, *Nat. Rev. Drug Discovery*, 2004, **3**, 205–214.
- (1.54) S. H. Hahn, M. S. Tanner, D. M. Danke and W. A. Gahl, *Biochem. Mol. Med.*, 1995, **54**, 142–145.
- (1.55) D. J. Waggoner, T. B. Bartnikas and J. D. Gitlin, *Neurobiol. Dis.*, 1999, **6**, 221–230.
- (1.56) P. Jiang and Z. Guo, *Coord. Chem. Rev.*, 2004, **248**, 205–229.
- (1.57) L. T. Sun and S. S. Jeng, *Fish Physiol. Biochem.*, 1999, **20**, 313–324.
- (1.58) J. M. Berg and Y. Shi, *Science*, 1996, **271**, 1081–1085.
- (1.59) C. J. Frederickson, *Int. Rev. Neurobiol.*, 1989, **31**, 145–238.
- (1.60) X. Xie and T. G. Smart, *Nature*, 1991, **349**, 521–524.
- (1.61) A. R. Kay, *Trends Neurosci.*, 2006, **29**, 200–206.
- (1.62) A. Takeda, *BioMetals*, 2001, **14**, 343–351.
- (1.63) J. H. Weiss, S. L. Sensi and J. Y. Koh, *Trends Pharmacol. Sci.*, 2000, **21**, 395–401.
- (1.64) Z. Xu, J. Yoon and D. R. Spring, *Chem. Soc. Rev.*, 2010, **39**, 1996–2006.
- (1.65) E. J. Hewitt, *Biol. Rev.*, 1959, **34**, 333–375.
- (1.66) E. J. Underwood, *Trace Elements in Human and Animal Nutrition*, 4th Edn., Academic Press, New York, 1977
- [67] C. F. Mills and I. Bremner, Nutritional aspects of molybdenum in animals. In Coughlan, M. P. (ed.) *Molybdenum and Molybdenum-containing Enzymes*, Pergamon, Oxford, 1980, pp. 517–542.
- (1.68) K. Pomazal, C. Prohaska, I. Steffan, G. Reich and J. F. K. Huber, *Analyst*, 1999, **124**, 657–663.
- (1.69] P. Vanloot, B. Coulomb, C. Brach-Papa, M. Sergent and J. L. Boudenne, *Chemosphere*, 2007, **69**, 1351–1360.
- (1.70) C. M. G. Berg, *Anal. Chem.*, 2006, **78**, 156–163.

- (1.71) G. Cerchiaro, T. M. Manieri and F. R. Bertuchi, *Metallomics*, 2013, **5**, 1336–1345.
- (1.72) T. Shamspur, I. Sheikhshoae and M. H. Mashhadizadeh, *J. Anal. At. Spectrom.*, 2005, **20**, 476–478.
- (1.73) A. A. Ammann, *J. Mass Spectrom.*, 2007, **42**, 419–427.
- (1.74) H. A. McIlwee, C. L. Schauer, V. G. Praig, R. Boukherroub and S. Szunerits, *Analyst*, 2008, **133**, 673–677.
- (1.75) T. I. Nasution, I. Nainggolan, D. Dalimunthe, M. Balyan, R. Cuana and S. Khanifah, *IOP Conf. Ser.: Mater. Sci. Eng.*, 2018, **309**, 012080.
- (1.76) V. N. Mehta, S. K. Kailasa and H. F. Wu, *New J. Chem.*, 2014, **38**, 1503–1511.
- (1.77) Z. Z. Yin, Y. Li, L. P. Jiang, R. K. Rana and J. J. Zhu, *Anal. Chim. Acta*, 2013, **781**, 48–53.
- (1.78) S. K Sahoo, D. Sharma, R. K. Bera, G. Crisponic, J. F. Callan, *Chem. Soc. Rev.*, 2012, **41**, 7195.
- (1.79) G. Grynkwicz, M. Poenie, R. Y. Tsien, *The Journal of Biological Chemistry*, 1985, **260**, 3440.
- (1.80) S. Banthia, A. Samanta, *J. Phys. Chem. B* 2006, **110**, 6437.
- (1.81) H. J. Jung, N. Singh, D. O. Jang, *Tetrahedron Lett.*, 2008, **49**, 2960–2964.
- (1.82) S. K. Sahoo, D. Sharma, R. K. Bera, G. Crisponi, J. F. Callan, *Chem. Soc. Rev.*, 2012, **41**, 7195.
- (1.83) K. Kaur, R. Saini, A. Kumar, V. Luxami, N. Kaur, P. Singh and S. Kumar, *Coord. Chem. Rev.*, 2012, **256**, 1992.
- (1.84) J. H. Chang, Y. M. Choi and Y. K. Shin, *Bull. Korean Chem. Soc.*, 2001, **22**, 527–530.
- (1.85) R. A. Marcus, *Angew. Chem. Int. Edit.*, 1993, **32**, 1111–1121.

- (1.86) P. Li, X. Zhou, R. Huang, L. Yang, X. Tang, W. Dou, Q. Zhao and W. Liu, *Dalton Trans.*, 2014, **43**, 706–713.
- (1.87) Y. Jiao, B. Zhu, J. Chen and X. Duan, *Theranostics*, 2015, **5**, 173–187.
- (1.88) M. A. Rizzo, G. H. Springer, B. Granada and D. W. Piston, *Nat. Biotechnol.*, 2004, **22**, 445–449.
- (1.89) W. M. Shih, Z. Gryczynski, J. R. Lakowicz and J. A. Spudich, *Cell*, 2000, **102**, 683–694.
- (1.90) T. Iijima, A. Momotake, Y. Shinohara, T. Sato, Y. Nishimura and T. Arai, *J. Phys. Chem. A*, 2010, **114**, 1603–1609.
- (1.91) P. Roy, *Coord. Chem. Rev.*, 2021, **427**, 213562.
- (1.92) A. K. Bhanja, C. Patra, S. Mondal, S. Mishra, K. D. Saha and C. Sinha, *Sensors and Actuators B*, 2017, **252**, 257–267.
- (1.93) A. Hazra and P. Roy, *Inorganic Chemistry Communications*, 2021, **130**, 108694.
- (1.94) S. Dey, A. Maity, M. Shyamal, D. Das, S. Maity, P. k. Giri, N. Mudi, S. S. Samanta, P. Hazra and A. Misra, *Photochem. Photobiol. Sci.*, 2019, **18**, 2717.
- (1.95) T. Mistri, M. Dolai, D. Chakraborty, A.R. Khuda-Bukhsh, K.K. Das, M. Ali, *Org. Biomol. Chem.*, 2012, **10**, 2380.
- (1.96) S.P. Parua, D. Sinha, K.K. Rajak, *Chemistry Select*, 2018, **3**, 1120.
- (1.97) P. Ghorai, S. Banerjee, D. Nag, S. K. Mukhopadhyay and A. Saha, *Journal of Lumin.*, 2019, **205**, 197.
- (1.98) A. Roy, S. Das, S. Sacher, S.K. Mandal, P. Roy, *Dalton Trans.*, 2019, **48**, 17594–17604.
- (1.99) S. Dey, A. Roy, G.P. Maiti, S.K. Mandal, P. Banerjee, P. Roy, *New J. Chem.*, 2016, **40**, 1365.

(1.100) A. Hussain, K. Mariappan, D. C. Cork, L. D. Lewandowski, P. K. Shrestha, S. Giri, X. Wang and A. G. Sykes, *RSC Adv.*, 2021, **11**, 34181-34192.

(1.101) S. Mandal, Y. Sikdar, D. K. Maiti, G. P. Maiti, S. K. Mandal, J. K. Biswas and S. Goswami, *RSC Adv.*, 2015, **5**, 72659–72669.

(1.102) S. Mondal, M. Chakraborty, A. Mondal, B. Pakhira, S. K. Mukhopadhyay, A. Banik, S. Sengupta and S. K. Chattopadhyay, *New J. Chem.*, 2019, **43**, 5466–5474.

(1.103) S. Mandal, S. K. Mandal, A. R. Khuda-Bukhsh and S. Goswami, *J. Fluoresc.*, 2015, **25**, 1437–1447.

(1.104) S. Mandal, S. K. Mandal, A. R. Khuda-Bukhsh and S. Goswami, *J. Fluoresc.*, 2015, **25**, 1437–1447.

(1.105) T. Anand, A. S. K. Kumar and S. K. Sahoo, *Chemistry Select*, 2017, **2**, 7570–7579.

(1.106) T. Anand, A. S. K. Kumar and S. K. Sahoo, *Photochem. Photobiol. Sci.*, 2018, **17**, 414–422.

(1.107) S. Mondal, P. Adak, C. Das, S. Naskar, B. Pakhira, A. L. Rheingold, E. Sinn, C. S. Eribal and S. K. Chattopadhyay, *Polyhedron*, 2014, **81**, 428–435.

(1.108) S. Mandal, Y. Sikdar, D. K. Maiti, R. Sanyal, D. Das, A. Mukherjee, S. K. Mandal, J. K. Biswas, A. Bauza, A. Frontera and S. Goswami, *J. Photochem. Photobiol.*, A, 2017, **334**, 86–100.

(1.109) T. Mukherjee, J. C. Pessoa, A. Kumar and A. R. Sarkar, *Dalton Trans.*, 2012, **41**, 5260–5271

(1.110) Y. Upadhyay, T. Anand, L. T. Babu, P. Paira, G. Crisponi, S. K. Ashok Kumar, R. Kumar and S. K. Sahoo, *Dalton Trans.*, 2018, **47**, 742–749.

(1.111) D. Das, R. Alam and M. Ali, *analyst*, 2022, **147**, 471–479.

- (1.112) C. Kan, X. Wang, X. Shao, L. Wu, S. Qiu and J. Zhu, *New J. Chem.*, 2021, **45**, 8918–8924.
- (1.113) S. Das, P. P. Das, J. W. Walton, K. Ghoshal, L. Patra and M. Bhattacharyya, *New J. Chem.*, 2021, **45**, 1853—1862.
- (1.114) J. Qiu, C. Zhong, M. Liu, Y. Yuan, H. Zhu and Y. Gao, *New J. Chem.*, 2021, **45**, 5184–51949.
- (1.115) X. Wang, J. Huang, H. Wei, L. Wu, H. Xing, J. Zhu and Chun Kan, *Journal of Molecular Structure*, 2022, **1270**, 133979.
- (1.116) D. Singha, A. Pal, H. Uyama, P. Roy and M. Nandi, *Dalton Trans.*, 2021, **50**, 12478–12494.
- (1.117) D. Singha, T. Das, L. Satyanarayana, P. Roy and M. Nandi, *New J. Chem.*, 2019, **43**, 15563–15574.
- (1.118) Z. Guo, X. Wang, P. Wei, Y. Gao and Q. Li, *J. Anal. Methods Chem.*, Volume 2019, Article ID 8130767, 7 pages.
- (1.119) Z. Cheng, X. Liu, L. Zheng, Y. Xu and H. He, *Anal. Methods*, 2022, **14**, 2277–2283.
- (1.120) B. Li, F. Tian and Y. Hua, *RSC Adv.*, 2022, **12**, 21129–21134.
- (1.121) L. J. Farrugia, *J. Appl. Crystallogr.*, 1997, **30**, 565–565.
- (1.122) G. M. Sheldrick, *Acta Crystallogr., Sect. A: Found. Crystallogr.*, 2008, **64**, 112–122.
- (1.123) A. L. Spek, *J. Appl. Cryst.*, 2003, **36**, 7–13.
- (1.124) M. J. Frisch, G. W. Trucks, H. B. Schlegel, P. M. W. Gill, B. G. Johnson, M. A. Robb, J. R. Cheeseman, T. A. Keith, G. A. Petersson, J. A. Montgomery, K. Raghavachari, M. A. Al-Laham, V. G. Zakrzewski, J. V. Ortiz, J. B. Foresman, J. Cioslowski, B. B. Stefanov, A. Nanayakkara, M. Challacombe, C. Y. Peng, P. Y. Ayala,

W. Chen, M. W. Wong, J. L. Andres, E. S. Replogle, R. Gomperts, R. L. Martin, D. J. Fox, J. S. Binkley, D. J. Defrees, J. Baker, J. P. Stewart, M. Head-Gordon, C. Gonzalez, J. A. Pople, Gaussian 98, Gaussian Inc. Pittsburgh, PA, (1998).

- (1.125) C. Lee, W. Yang and R. G. Parr, *Phys. Rev. B*, 1988, **37**, 785–789.
- (1.126) H. G. Korth, M. I. De Heer and P. Mulder, *J. Phys. Chem. A*, 2002, **106**, 8779–8789.
- (1.127) B. G. Johnson, P. M. W. Gill and J. A. Pople, *J. Chem. Phys.*, 1993, **98**, 5612–5626.
- (1.128) P. K. Chowdhury, *J. Phys. Chem. A*, 2003, **107**, 5692–5696.
- (1.129) V. Chis, *Chem. Phys.*, 2004, **300**, 1–11.
- (1.130) A. Asensio, N. Kobko and J. J. Dannenberg, *J. Phys. Chem. A*, 2003, **107**, 6441–6443.
- (1.131) A. Müller, M. Losada and S. Leutwyler, *J. Phys. Chem. A*, 2004, **108**, 157–165.
- (1.132) N. S. Goncalves, R. Cristiano, M. G. Pizzolatti and F. da Silva Miranda, *J. Mol. Struct.*, 2005, **733**, 53–61.
- (1.133) P. J. Hay and W. R. Wadt, *J. Chem. Phys.*, 1985, **82**, 270–283.
- (1.134) A. D. Becke, *J. Chem. Phys.*, 1993, **98**, 5648–5652.
- (1.135) M. Cossi and V. Barone, *J. Chem. Phys.*, 2001, **115**, 4708–4717.
- (1.136) M. Cossi, N. Rega, G. Scalmani and V. Barone, *J. Comput. Chem.*, 2003, **24**, 669–681.
- (1.137) N. M. O'Boyle, A. L. Tenderholt and K. M. Langner, *J. Comput. Chem.*, 2008, **29**, 839–845.

Chapter 2

Development of rhodamine 6G based fluorescent chemosensors for Al^{3+} ion detection: effect of ring strain and substituent in enhancing its sensing Performance

Abstract

Four rhodamine 6G based chemosensors (**H₃L2.1-H₃L2.4**) are designed for selective detection of Al³⁺ ion. They are characterized using various spectroscopic techniques and X-ray crystallography. All absorption and emission spectral studies have performed in 10 mM HEPES buffer solution at pH 7.4 in H₂O/MeOH (9:1 v/v) at 25 °C. In absorption spectra, chemosensors exhibit intense band around 530 nm in the presence of Al³⁺ ion. Chemosensors (**H₃L2.1-H₃L2.4**) are nonfluorescent when excited around 490 nm. Presence of Al³⁺ ion enhances emission intensity (555 nm) in many times. Formation of complexes **2.1-2.4** is established with the aid of different spectroscopic techniques. Limit of detection value obtains in the nanomolar range confirm high sensitivity of the probes towards Al³⁺ ion. It has been observed that the presence of aliphatic spacers in the diamine part and different halogen substituents in the salicylaldehyde part strongly influence selectivity of the chemosensors towards Al³⁺ ion. The propensity of the chemosensors to identify intracellular Al³⁺ ions in triple negative human breast cancer cell line MDA-MB-468 by fluorescence imaging is also examined in this study.

2.1 Introduction

Metal ions play a crucial role in human life and in the environment. Therefore, their detection is of immense importance to the biologists, chemists and environmentalists.^{2.1} Scientists emerge in the development of new methodologies for recognition of these cations.^{2.2-2.5} Design and synthesis of new chemosensors for selective detection of biologically and environmentally important cations needs special mention in this context.^{2.6,2.7} Aluminium is the highest abundant metal in the earth's crust.^{2.8-2.10} Materials prepared from aluminum are widely used in our society. They are used in food additives, textile industry, water treatment plants, paper industry, production of light alloys, medicines (antacids), cookware, etc. Aluminum toxicity causes Alzheimer's and Parkinson's diseases.^{2.11} Other Al-contaminated diseases are amyotrophic lateral sclerosis, microcytic hypochromic anaemia, osteomalacia and breast cancer.^{2.12-2.17} Preparation of chemosensor for selective detection of Al³⁺ ion is a challenging task owing to its weak coordination ability, strong hydration ability and interferences from other trivalent ions like Cr³⁺ and Fe³⁺. Up to date, a considerable number of organic probes for Al³⁺ ion^{2.18-2.23} have been synthesized, most of the probes suffer from some drawbacks like insolubility in aqueous solution, synthetic procedures with multiple steps, poor sensitivity and selectivity with target metal ions etc.^{2.24-2.26} Al³⁺ sensing organic probes consist of important fluorophoric unit like rhodamine, anthraquinone, BODIPY, salicylaldehyde, fluorescein, coumarin, etc.^{2.27-2.33} Rhodamine based chemophores are colourless and nonfluorescent due to presence of spirolactam ring. Sensing mechanism is basically opening of spirolactam ring resulting strong emission. Low pH or acidic condition also initiates opening of spirolactam ring. Therefore, selective choice of metal ion can initiates spirolactam ring opening of rhodamine based probe. Literature study reveals that rhodamine based probes can selectively detect various metal ions like Al³⁺, Fe³⁺, Cr³⁺, Hg²⁺, Cu²⁺, etc.^{2.34-2.43} Some recently reported rhodamine based important chemosensors are

collected in Chart 2.1. Chart 2.1 clearly shows that chemosensors reported in this present work have certain advantages regarding crystal structure, real sample analysis and cell imaging study in comparison with previously reported data.^{2.44} G. Yang et al.^{2.44a} reported two rhodamine-pyrazole-based both colorimetric and turn-on fluorescent chemosensors for dual detection of Ni²⁺ and Al³⁺ ions in alcohol and aqueous DMF medium. J. W. Jeong et al.^{2.44b} have synthesized rhodamine-chloronicotinaldehyde -based “OFF–ON” chemosensor for colorimetric and fluorescent detection of Al³⁺ in acetonitrile medium. S. Chemate and coworkers have used two rhodamine based OFF–ON fluorescent chemosensors for dual detection of Hg²⁺ and Al³⁺ in aqueous solution.^{2.44c} S. B. Maity and coworkers have prepared a rhodamine-1,2,3-Triazole based chemosensor for dual detection of Al³⁺ and fluoride or acetate ions in CH₃OH–H₂O (9:1) medium.^{2.44d} Above examples did not report crystal structures of the chemosensors and their biological cell imaging studies. In this work we have successfully elucidated crystal structures of all four chemosensors and also perform their biological studies. In an interesting work A. Roy and coworkers have synthesized a rhodamine based dual chemosensor for detection of Al³⁺ and Zn²⁺ Ions in HEPES buffer.^{2.44e} M. Ghosh and coworkers have prepared a chemosensor using rhodamine unit for detection and discrimination of Al³⁺ and Hg²⁺ ions in HEPES buffer.^{44f} R. Alam and coworkers have synthesized a rhodamine based trivalent fluorescent sensor which can selectively detect Fe³⁺, Al³⁺ and Cr³⁺ ions in CH₃OH–H₂O (1:1).^{2.44g} These works clearly show that these chemosensors did not achieve their selectivity towards Al³⁺ ions, whereas, our synthesized chemosensors show selectivity only towards Al³⁺ ions. Y. Fu and coworkers^{2.44h} have synthesized a rhodamine 6G containing fluorescent probe for Al³⁺ ion. A. Sahana et al. reported a rhodamine–pyrene compound for selective colorimetric and fluorimetric detection of Al³⁺ ion and living cell imaging study.^{2.44i} In above chemosensors the LOD values are observed in micro molar range, interestingly, our reported chemosensors give LOD values in

nano molar range. A. Roy et al. have reported a rhodamine-based fluorescent chemosensor^{2.44j} for selective detection of Al³⁺ ions in H₂O/MeOH = 1 : 9 (v/v) medium. B. Sen and coworkers have also reported a rhodamine-based Al³⁺ ion sensing organic compound^{2.44k} in EtOH–water, 1 : 3 (v/v) medium. A. Sahana and group have synthesized a rhodamine-based fluorescent probe^{2.44l} for selective detection of Al³⁺ ions in EtOH–water, 4 : 1 (v/v) medium. In all these examples medium is mainly organo-aqueous, whereas, our Al³⁺ ions sensing studies are performed in MeOH–water, 1 : 9 (v/v) medium.

In this work, we have chosen hydrazine and 1,3 diaminopropane as amines, 3,5 dichlorosalicylaldehyde and 3,5 dibromosalicylaldehyde as aldehydes to prepare four different rhodamine 6G based chemosensors **H₃L2.1**, **H₃L2.2**, **H₃L2.3** and **H₃L2.4**, respectively. All four chemosensors selectively detect Al³⁺ both colorimetrically and fluorimetrically. Structure property relationship is established in this work. Variation of amines and halogen substituents in the salicylaldehyde part control the extent of selectivity towards Al³⁺ ion. Significant variation in different sensing parameters such as LOD, binding constant and necked eye detection of Al³⁺ ion are observed during this study. These biocompatible chemosensors (**H₃L2.1-H₃L2.4**) also exhibit cell permeability and sense intracellular Al³⁺ ion present in breast cancer cell line, *MDA-MB-468* cells.

Chart 2.1. Literature survey of rhodamine based derivatives used in sensing of Al³⁺ ion.

Sl. No.	Probe	Sensing of metal ion(s)	Sensing Media	Binding constant	Limit of detection (LOD)	Biological study	Refs.
1.	pyrazole-based chemosensor (Pry-R6G)	Al ³⁺	(DMF/H ₂ O, 1/99, v/v)	-	2.61×10 ⁻⁸ M	No	44a
2.	rhodamine B-2-chloronicotinaldehyde derivative (RBCN)	Al ³⁺	CH ₃ CN	2.96×10 ⁻⁵ M ⁻¹	2.86×10 ⁻⁸ M	No	44b
3.	3',6'-Bis(diethylamino)-2-(2-isothiocyanatoethyl)spiro-[isoindoline-1,9'-xanthen]-3-one (2)	Al ³⁺	CH ₃ CN:H ₂ O (1:1, v/v)	4.5×10 ⁻⁴ M ⁻¹	1.1×10 ⁻⁸ M	No	44c
4.	1,2,3-triazole-ringappended rhodamine dye (L)	Al ³⁺	CH ₃ OH–H ₂ O, 9:1 (v/v)	2.55×10 ⁴ M ⁻¹	-	No	44d

5.	2-(2-((3-(tert-butyl)-2-hydroxybenzylidene)amino)ethyl)-3'-6'-bis(ethylamino)-2',7'-dimethylspiro-[indoline-1,9'-xanthen]-3-one (HL-t-Bu)	Al ³⁺ and Zn ²⁺	10 mM HEPES buffer (methanol/water mixture) (9:1, pH = 7.4)	9.38×10 ³ M ⁻¹ and 4.75×10 ⁴ M ⁻¹	10.98×10 ⁻⁹ M and 76.92×10 ⁻⁹ M	Yes	44e
6.	3', 6'- bis(diethylamino)-2-(2-((2-hydroxybenzylidene)amino)phenylthio)ethyl) spiro[isoindoline 1,9' xanthen]-3-one (L)	Al ³⁺ and Hg ²⁺	HEPES-buffered (20 mM, MeOH/H ₂ O, 4/1, v/v, pH 7.4)	4.66×10 ⁶ M ⁻¹ -	0.005×10 ⁻⁶ M and 0.05×10 ⁻⁶ M	Yes	44f
7.	(3-(3,5-dimethyl-pyrazol-1-ylmethyl)-2-hydroxy-5-methylbenzaldehyde (HL ⁵))	Al, Fe and Cr	methanol/H ₂ O (1 : 1, v/v, pH 7.2)	8.2 ×10 ⁴ M ⁻¹ , 6.7 ×10 ⁴ M ⁻¹ and 6.0×10 ⁴ M ⁻¹	0.34×10 ⁻⁶ M, 0.29×10 ⁻⁶ M and 0.31×10 ⁻⁶ M	Yes	44g
8.	rhodamine-based derivative (L)	Al ³⁺	H ₂ O–EtOH (4 : 1, v/v)	3.14×10 ⁵ M ⁻¹	3.26×10 ⁻⁶ M	Yes	44h
9.	(E)-3',6'-bis(diethylamino)-2-(2-(pyren-4-ylmethyleneamino)ethyl)spiro[isoindoline-1,9'- xanthen]-3-one (L)	Al ³⁺	HEPES buffer (0.1 M; EtOH–H ₂ O, 4 : 1 v/v; pH 7.4)	1.19×10 ⁴ M ⁻¹	0.02×10 ⁻⁶ M	Yes	44i
10	3',6'-bis(ethylamino)-2-(2-(2-hydroxy-5-methylbenzylideneamino)ethyl)-2',7'-dimethylspiro[isoindoline-1,9'-xanthen]-3-one (HL-Me)	Al ³⁺	10 mM HEPES buffer, pH 7.4, H ₂ O/MeO H = 1 : 9 (v/v)	2.05×10 ⁵ M ⁻¹	2.8×10 ⁻⁹ M	Yes	44j
11	rhodamine Schiff base (L)	Al ³⁺	HEPES buffer (1 mM, pH 7.4; EtOH–water, 1 : 3 v/v)	8.13×10 ⁴ M ⁻¹	60×10 ⁻⁹ M	Yes	44k
12	Rhodamine-diformyl p-cresol conjugate (L)	Al ³⁺	HEPES-buffered (0.1 M) EtOH:water (4:1, v/v), pH 7.4	9.1×10 ⁶ M ⁻²	5×10 ⁻⁹ M	Yes	44l
13	2-((3,5-dibromo-2-hydroxybenzylidene)amino)-3',6'-bis(ethylamino)-2',7'-dimethylspiro[isoindoline-1,9'-xanthen]-3-one, (H3L2.1)	Al ³⁺	10 mM HEPES buffer, pH 7.4, (H ₂ O/MeO H) (9:1 v/v)	8.00×10 ⁵ M ⁻¹	2.50×10 ⁻⁹ M	Yes	This Work
14	2-((3,5-dichloro-2-hydroxybenzylidene)amino)-3',6'-bis(ethylamino)-2',7'-dimethylspiro[isoindoline-1,9'-xanthen]-3-one, (H3L2.2)	Al ³⁺	10 mM HEPES buffer, pH 7.4, (H ₂ O/MeO	6.90×10 ⁵ M ⁻¹	1.40×10 ⁻⁹ M	Yes	This Work

			H) (9:1 v/v)				
15	2-(3-((3,5-dibromo-2-hydroxybenzylidene)amino)propyl)-3',6'-bis(ethylamino)-2',7'-dimethylspiro[isindoline-1,9'-xanthen]-3-one, (H3L2.3)	Al ³⁺	10 mM HEPES buffer, pH 7.4, (H ₂ O/MeOH) (9:1 v/v)	1.37×10 ⁴ M ⁻¹	0.053×10 ⁻⁹ M	Yes	This Work
16	2-(3-((3,5-dichloro-2-hydroxybenzylidene)amino)propyl)-3',6'-bis(ethylamino)-2',7'-dimethylspiro[isindoline-1,9'-xanthen]-3-one, (H3L2.4)	Al ³⁺	10 mM HEPES buffer, pH 7.4, (H ₂ O/MeOH) (9:1 v/v)	1.03×10 ⁴ M ⁻¹	0.040×10 ⁻⁹ M	Yes	This Work

2.2 Experimental section

2.2.1 Materials and physical measurements description

All reagent or analytical grade chemicals and solvents were collected from commercial sources and used without further purification. Elemental analysis was carried out using a Perkin–Elmer 240C elemental analyzer. Infrared spectra (400–4000 cm⁻¹) were recorded using KBr pellets on a Nicolet Magna IR 750 series-II FTIR spectrophotometer. Absorption spectral data were collected using a Cary 60 spectrophotometer (Agilent) with a 1-cm-path-length quartz cell. Electron spray ionization mass (ESI-MS positive) spectra were noted using a MICROMASS Q-TOF mass spectrometer. Fluoromax-4 spectrofluorimeter was used to collect emission spectral data at room temperature (298 K) in HEPES buffer at pH=7.4 solution under degassed condition. A time-resolved spectrofluorometer from IBH, UK was used to collect fluorescence lifetime data of ¹H and ¹³C NMR spectral data were collected using a Bruker 400 and 300 spectrometers in DMSO-*d*₆ solvent.

2.2.2 X-ray crystallography

Single crystal X-ray data of chemosensors (**H₃L2.1-H₃L2.4**) were collected on a Bruker SMART APEX-II CCD diffractometer the aid of graphite mono chromated Mo K α radiation ($\lambda = 0.71073 \text{ \AA}$) at room temperature. Data processing, structure solution, and refinement were examined using Bruker Apex-II suite program. All available reflections data in $2\theta_{\max}$ range were harvested and corrected for Lorentz and polarization factors with Bruker SAINT plus.^{2.45} Reflections were then corrected for absorption, inter-frame scaling, and different systematic errors with SADABS.^{2.46} The structures were solved by the direct methods and refined with the help of full matrix least-square technique based on F² with SHELX-2017/1 software package.^{2.47} All the non hydrogen atoms were refined with anisotropic thermal parameters. C-H hydrogen atoms were attached at geometrical positions with $U_{\text{iso}} = 1/2U_{\text{eq}}$ to those they are attached. Crystal data and details of data collection and refinement for **H₃L1-H₃L4** were collected in **Table 2.1**.

Table 2.1. Crystal parameters and selected refinement details for the chemosensors (**H₃L2.1-H₃L2.4**).

Complex	H₃L2.1	H₃L2.2	H₃L2.3	H₃L2.4
Empirical formula	C ₃₃ H ₃₀ Br ₂ N ₄ O ₃	C ₃₃ H ₃₀ Cl ₂ N ₄ O ₃	C ₃₆ H ₃₆ Br ₂ N ₄ O ₃	C ₃₆ H ₃₆ Cl ₂ N ₄ O ₃
Formula weight	690.43	601.51	732.51	643.59
Temperature (K)	273(2)	273(2)	273(2)	273(2)
Crystal system	triclinic	triclinic	monoclinic	monoclinic
Space group	<i>P</i> -1	<i>P</i> -1	<i>P</i> 2 ₁ / <i>c</i>	<i>P</i> 2 ₁ / <i>c</i>
<i>a</i> (Å)	9.5600(16)	9.5793(10)	13.6753(18)	13.513(2)
<i>b</i> (Å)	12.335(2)	12.2135(12)	9.5139(12)	9.3806(17)
<i>c</i> (Å)	13.635(2)	13.5543(14)	26.448(4)	25.521(5)
α (°)	92.659(4)	92.238(3)	90	90
β (°)	106.547(4)	107.023(3)	97.271(4)	94.479(6)
γ (°)	95.976(4)	96.087(3)	90	90
Volume (Å ³)	1528.1(4)	1503.7(3)	3413.4(8)	3225.2(10)
Z	2	2	4	4
<i>D</i> _{calc} (g cm ⁻³)	1.501	1.329	1.425	1.325
Absorption coefficient (mm ⁻¹)	2.693	0.257	2.415	0.244

<i>F</i> (000)	700	628	1496	1352
θ Range for data collection (°)	27.126- 2.191	27.257- 2.322	25.08-2.98	2.286-27.285
Reflections collected	69311	49439	49611	28853
Independent reflection / R_{int}	4237/0.0845	5048/ 0.0335	2356/0.1199	5615/0.1020
Data / restraints / parameters	6741/ 0/ 396	6688/0/ 383	7514/0/414	7061/0/406
Goodness-of-fit on F^2	1.040	1.028	1.025	1.110
Final R indices [$I > 2\sigma(I)$]	$R1 = 0.0678$, $wR2 = 0.1662$	$R1 = 0.0889$, $wR2 = 0.2717$	$R1 = 0.1080$, $wR2 = 0.2952$	$R1 = 0.1981$, $wR2 = 0.5034$
R indices (all data)	$R1 = 0.1127$ $wR2 = 0.1915$	$R1 = 0.1093$, $wR2 = 0.2983$	$R1 = 0.2709$, $wR2 = 0.4043$	$R1 = 0.2126$, $wR2 = 0.5103$
Largest diff. peak / hole ($e \text{ \AA}^{-3}$)	1.692/ -1.177	1.351/ -0.687	1.248/ -1.204	1.001/-0.882

2.2.3 Synthesis of N-(Rhodamine-6G)lactam-hydrazine and N-(Rhodamine-6G)lactam-propylenediamine

N-(Rhodamine-6G)lactam-hydrazine and N-(Rhodamine-6G)lactam-propylenediamine were prepared by following literature procedure.^{2,48}

2.2.4 Preparation of chemosensor (H₃L2.1) [H₃L2.1 = 2-((3,5-dibromo-2-hydroxybenzylidene)amino)-3',6'-bis(ethylamino)-2',7'-dimethylspiro[isoindoline-1,9'-xanthen]-3-one]

A mixture of N-(Rhodamine-6G)lactam-hydrazine (2.0 mmol, 0.8564 g) and 3,5-Dichlorosalicylaldehyde (2.0 mmol, 0.5598 g) was heated in refluxing condition for *ca.* 4 h in acetonitrile solvent. Very light yellow colour crystal was collected after evaporation of the solvent.

Yield: 1.008 g (84%). Anal. Calc. for C₃₃H₃₀Br₂N₄O₃: C 57.41%; H 4.38%; N 8.11%. Found: C 57.18%; H 4.30%; N 8.02%. IR (cm⁻¹, KBr): ν (C=N) 1621s; ν (O-H) 3408s ν (C=O)1663s (**Figure 2.1**). ESI-MS (positive) in MeOH: The molecular ion appeared at $m/z =$

691.11, consistent to [H₃L2.1+1]⁺ (Figure 2.2). UV-Vis, λ_{\max} (nm), (ϵ (dm³mol⁻¹cm⁻¹)) in HEPES buffer at pH= 7.4: 345 (14020).

¹H NMR (400 MHz, d₆-DMSO) δ ppm: 1.20 (-CH₃) (t, 6H, $J_1=7.2$ Hz, $J_2=6.8$ Hz), 1.84 (Ar-CH₃) (s, 6H), 3.13 (-CH₂) (q, 4H), 5.11 (NH)(t, 2H, $J_1=4.8$ Hz, $J_2=5.2$ Hz), 6.20 (Ar-CH) (s, 2H), 6.34 (Ar-CH) (s, 2H), 7.06 (Ar-CH) (d, 1H, $J=7.2$ Hz), 7.53 (Ar-CH) (s, 1H), 7.56-7.72 (Ar-CH) (m, 2H), 7.94 (Ar-CH) (d, 1H, $J=7.2$ Hz), 8.90 (-CH=N) (s, 1H), 11.56 (-OH) (s, 1H) (Figure 2.3).

¹³C NMR (d₆-DMSO, 75 MHz) δ ppm:

14.59, 17.44, 37.92, 66.24, 96.32, 104.13, 106.13, 114.16, 119.04, 121.58, 123.78, 124.36, 127.20, 128.26, 129.47, 132.40, 134.90, 136.25, 148.47, 151.48, 151.88, 161.87, 164.27, 166.13 (Figure 2.4).

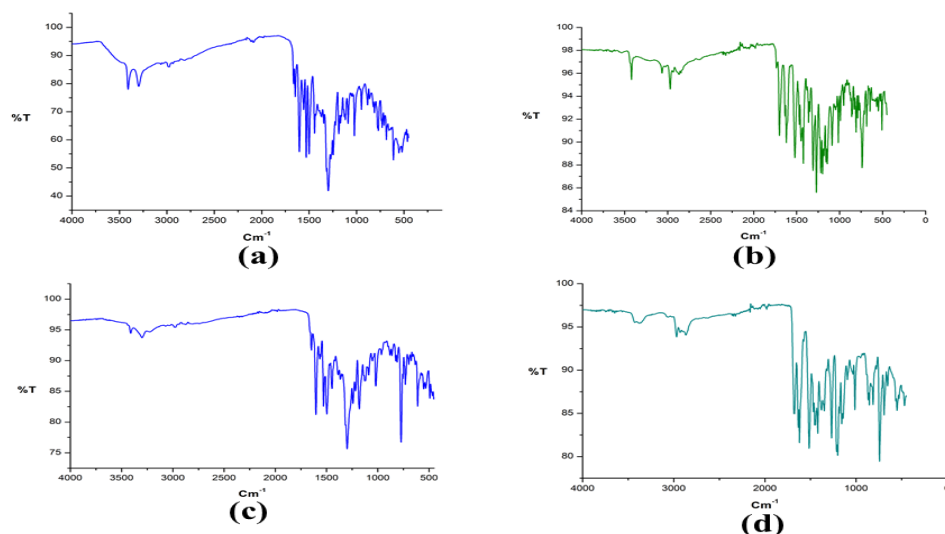


Figure 2.1. FTIR spectra of chemosensors (a) H₃L2.1, (b) H₃L2.2, (c) H₃L2.3 and (d) H₃L2.4.

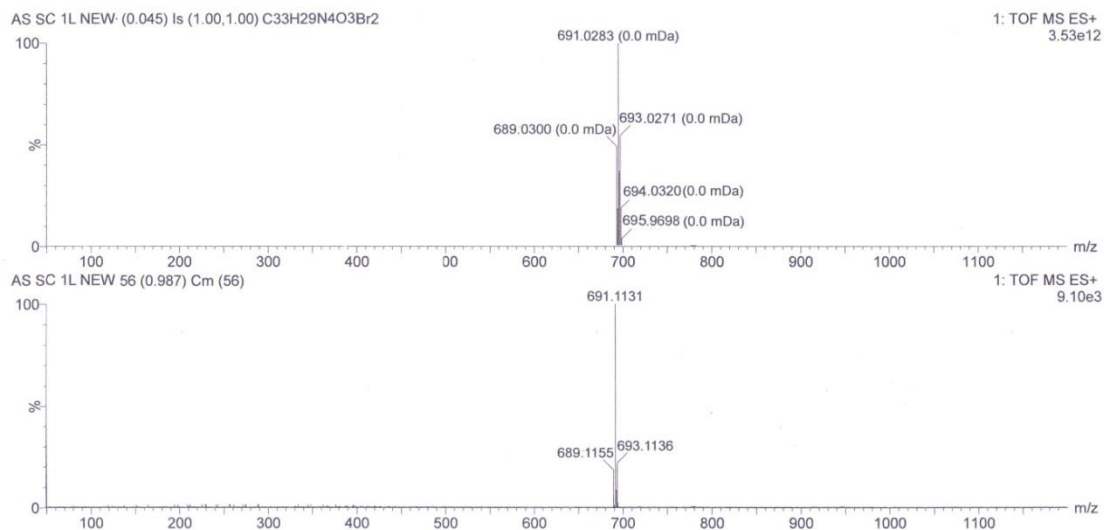


Figure 2.2. ESI-mass spectrum of chemosensor **H₃L2.1** (above is simulated pattern and below is experimental finding).

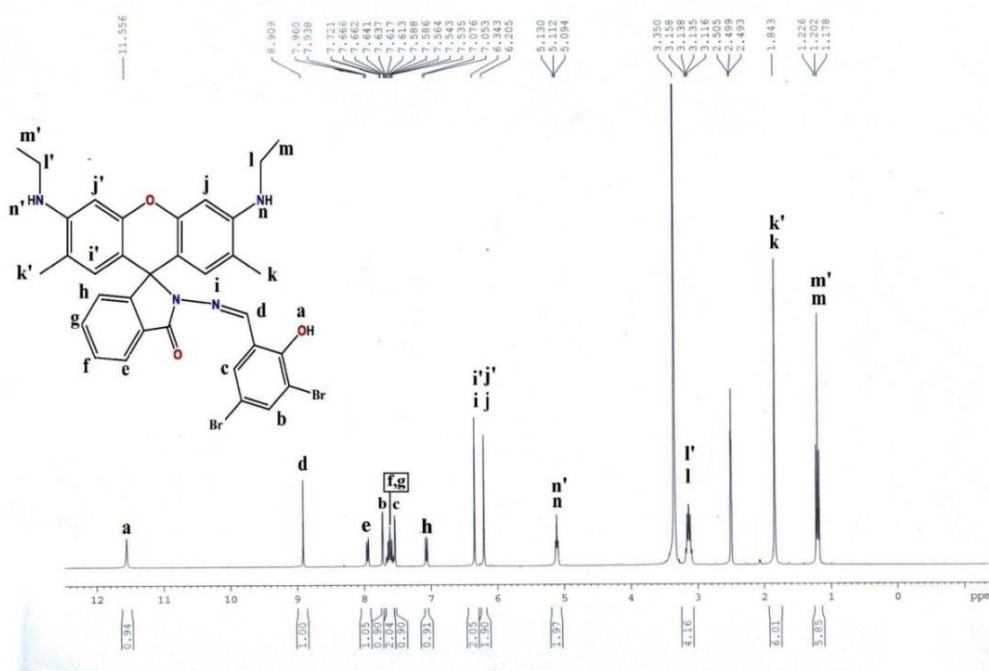


Figure 2.3 ¹H-NMR of the chemosensor **H₃L2.1** in DMSO-d₆ recorded on a 400 MHz Bruker NMR spectrometer.

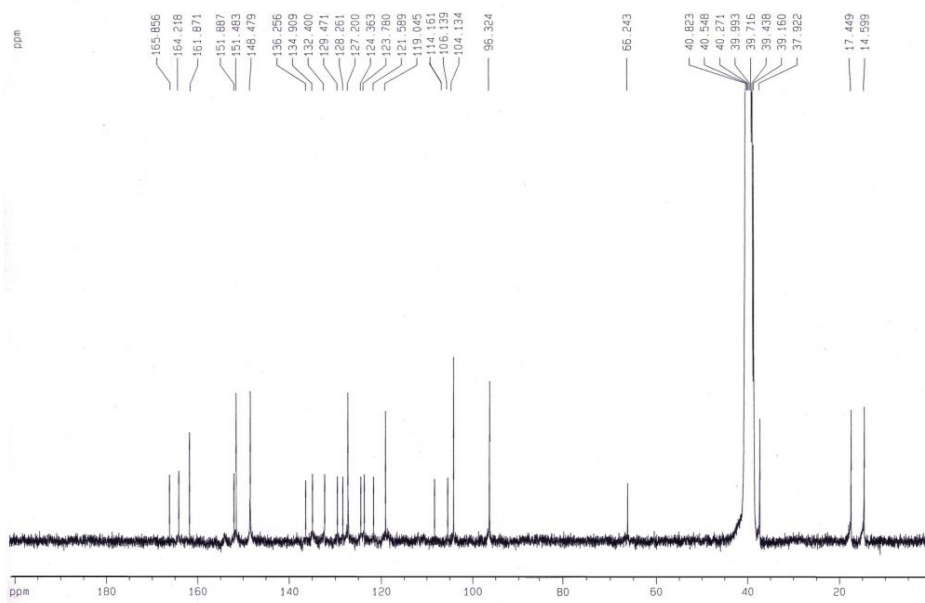


Figure 2.4. ¹³C NMR spectrum of **H₃L2.1** in DMSO-*d*₆.

2.2.5 Synthesis of chemosensor (**H₃L2.2**) [**H₃L2.2**=2-((3,5-dichloro-2-hydroxybenzylidene)amino)-3',6'-bis(ethylamino)-2',7'-dimethylspiro[isoindoline-1,9'-xanthen]-3-one]

A mixture of N-(Rhodamine-6G)lactam-hydrazine (2.0 mmol, 0.8564 g) and 3,5-Dichlorosalicylaldehyde (2.0 mmol, 0.3820 g) was heated in refluxing condition for *ca.* 4 h in acetonitrile solvent. Very light yellow colour crystal was collected after evaporation of the solvent.

Yield: 1.200g (87%). Anal. Calc. for C₃₃H₃₀Cl₂N₄O₃: C 65.89%; H 5.03%; N 9.31%. Found: C 65.68%; H 4.88%; N 9.29%. IR (cm⁻¹, KBr): ν(C=N) 1619s; ν(O-H) 3421s ν(C=O) 1699s (**Figure 2.1**). ESI-MS (positive) in MeOH: The base peak was appeared at *m/z* = 623.18, corresponding to [**H₃L2.2**+1]⁺ (**Figure 2.5**). UV-Vis, λ_{max} (nm), (ε (dm³mol⁻¹cm⁻¹)) in HEPES buffer (10mM) at pH= 7.4: 345 (20440).

¹H NMR (400 MHz, d₆-DMSO) δ ppm: 1.20 (-CH₃) (t, 6H, $J_1=7.2\text{Hz}$, $J_2=6.8\text{Hz}$), 1.84 (Ar-CH₃) (s, 6H), 3.15-3.09 (-CH₂) (m, 4H), 5.11 (NH)(t, 2H, $J=5.2\text{Hz}$), 6.20 (Ar-CH) (s, 2H), 6.33 (Ar-CH) (s, 2H), 7.40 (Ar-CH) (s, 1H), 7.51 (Ar-CH) (d, 1H, $J=7.2\text{Hz}$), 7.56-7.65 (Ar-CH) (m, 2H), 7.94 (Ar-CH) (d, 1H, $J=7.2\text{Hz}$), 8.96 (-CH=N) (s, 1H), 11.32 (-OH) (s, 1H) (Figure 2.6).

¹³C NMR (d₆-DMSO, 75 MHz) δ ppm:

14.59, 17.44, 37.92, 66.24, 96.32, 104.13, 106.13, 114.13, 119.04, 121.58, 123.78, 124.36, 127.20, 128.26, 129.47, 132.40, 134.90, 136.25, 148.47, 151.48, 151.88, 154.27, 166.13 (Figure 2.7).

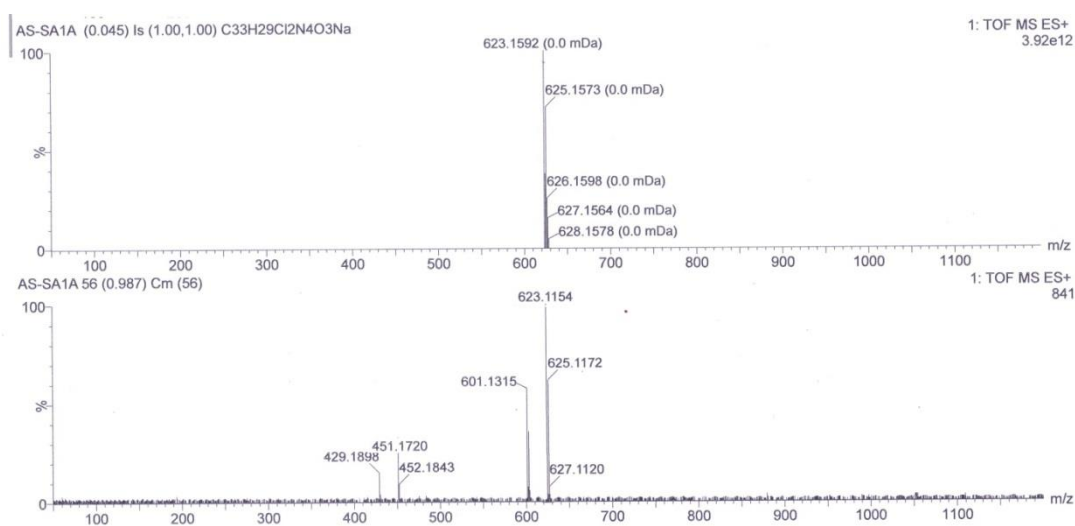


Figure 2.5 ESI-mass spectrum of chemosensor **H₃L2.2** (above is simulated pattern and below is experimental finding).

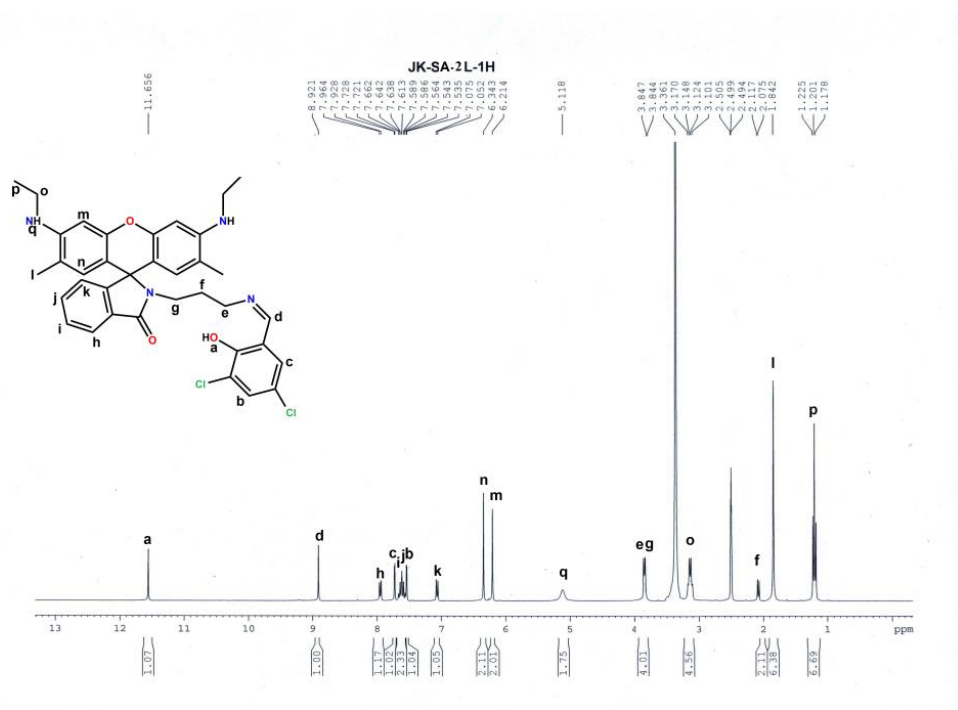


Figure 2.6. ^1H -NMR of the free ligand **H₃L2.2** in $\text{DMSO-}d_6$ recorded on a 400 MHz Bruker NMR spectrometer.

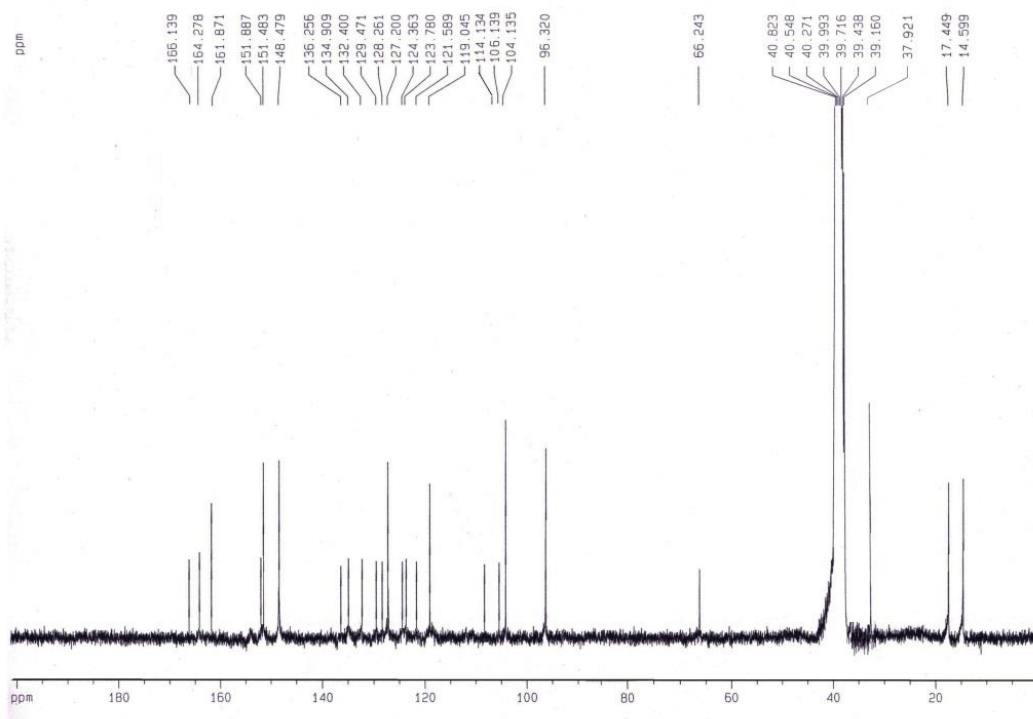


Figure 2.7 ^{13}C NMR spectrum of **H₃L2.2** in $\text{DMSO-}d_6$.

2.2.6 Synthesis of chemosensor (H₃L2.3) [H₃L2.3=2-(3-((3,5-dibromo-2-hydroxybenzylidene)amino)propyl)-3',6'-bis(ethylamino)-2',7'-dimethylspir[isindoline-1,9'-xanthen]-3-one]

A mixture of N-(Rhodamine-6G)lactam-propylenediamine (2.0 mmol, 0.9128g) and 3,5-Dichlorosalicylaldehyde (2.0 mmol, 0.5598 g) was heated to in refluxing condition for *ca.* 4 h in acetonitrile solvent. Yellow colour crystal was collected after evaporation of the solvent.

Yield: 1.171 g (80%). Anal. Calc. for C₃₆H₃₆Br₂N₄O₃: C 59.03%; H 4.95%; N 7.65%. Found: C 58.88%; H 4.78%; N 9.29%. IR (cm⁻¹, KBr): ν (C=N) 1621s; ν (O-H) 3401s ν (C=O) 1663s (**Figure 2.1**). ESI-MS (positive) in MeOH: The base peak was appeared at m/z = 755.01, corresponding to [H₃L2.3+Na]⁺ (**Figure 2.8**). UV-Vis, λ_{\max} (nm), (ϵ (dm³mol⁻¹cm⁻¹)) in HEPES buffer at pH= 7.4: 420 (47570).

¹H NMR (400 MHz, d₆-DMSO) δ ppm: 1.20 (-CH₃) (t, 6H, $J_I=9.6$ Hz, $J_I=9.2$ Hz), 1.84 (Ar-CH₃) (s, 6H), 2.09 (-CH₂) (d, 2H, $J=16.8$ Hz), 3.13 (-CH₂) (q, 4H), 5.11 (NH)(s, 2H), 6.20 (Ar-CH) (s, 2H), 6.34 (Ar-CH) (s, 2H), 7.06 (Ar-CH) (d, 1H, $J=9.2$ Hz), 7.54 (Ar-CH) (s, 1H), 7.54-7.72 (Ar-CH) (m, 2H), 7.72 (Ar-CH) (s, 1H), 7.95 (Ar-CH) (d, 1H, $J=8.8$ Hz), 8.90 (-CH=N) (s, 1H), 11.66 (-OH) (s, 1H) (**Figure 2.9**).

¹³C NMR (d₆-DMSO, 75 MHz) δ ppm:

14.74, 16.74, 29.11, 37.54, 38.92, 54.60, 65.10, 96.64, 106.06, 107.72, 113.74, 118.00, 118.97, 122.76, 123.89, 128.17, 128.37, 131.16, 132.60, 132.81, 137.90, 147.54, 151.79, 153.42, 160.96, 163.82, 168.52 (**Figure 2.10**).

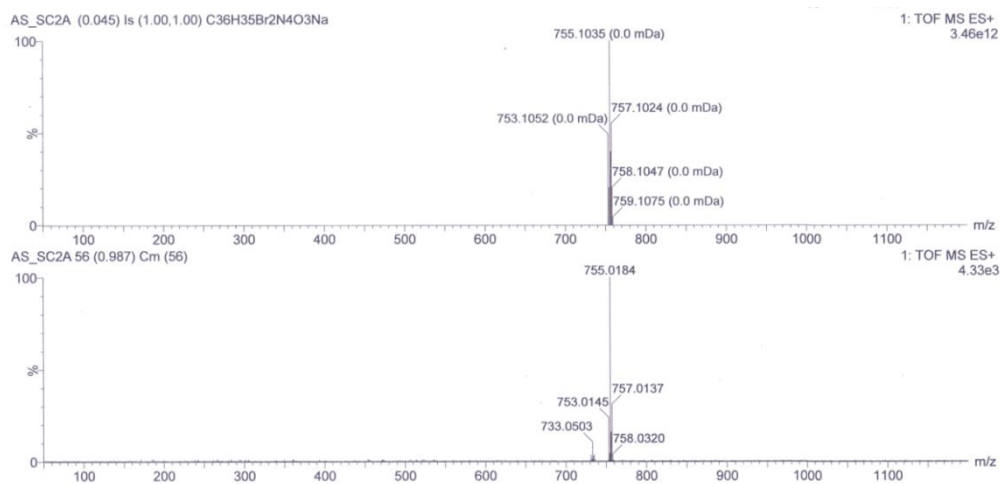


Figure 2.8 ESI-mass spectrum of chemosensor **H₃L2.3** (above is simulated pattern and below is experimental finding).

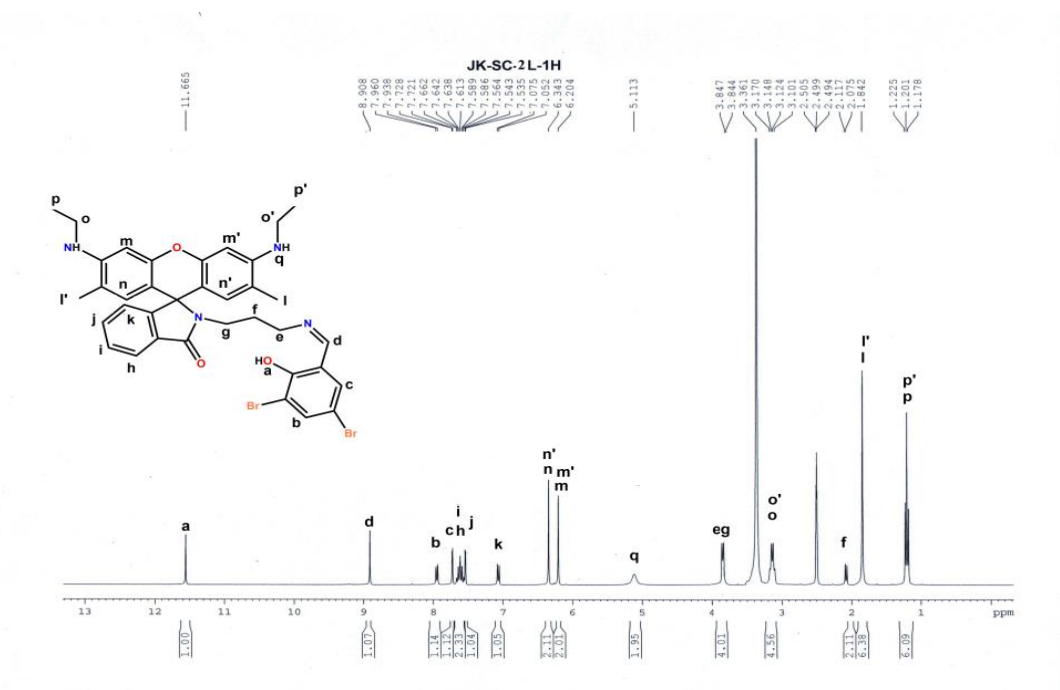


Figure 2.9 ¹H-NMR of the free ligand **H₃L2.3** in DMSO-*d*₆ recorded on a 400 MHz Bruker NMR spectrometer.

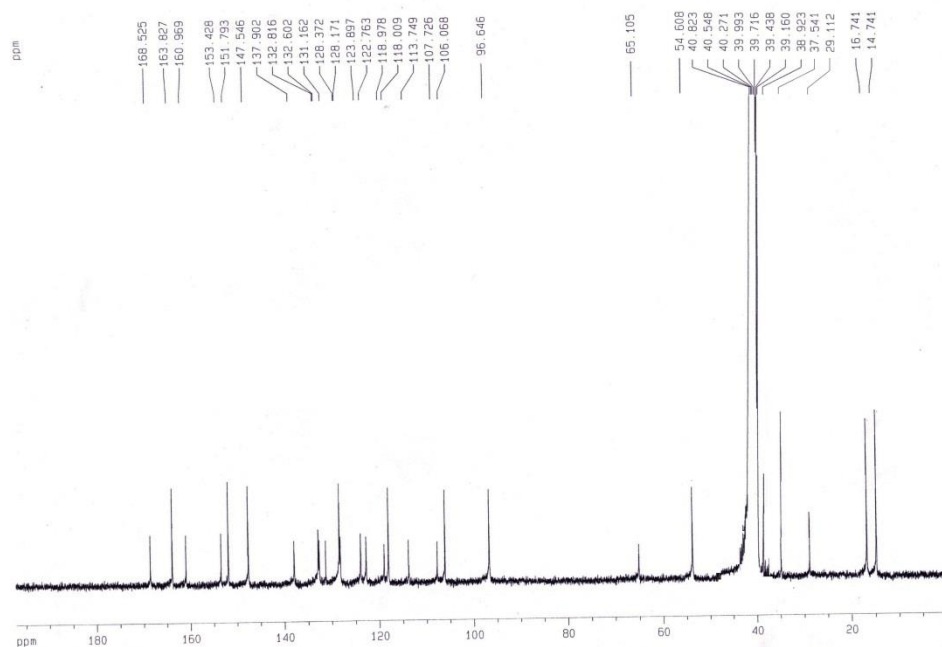


Figure 2.10 ^{13}C NMR spectrum of **H₃L2.3** in $\text{DMSO-}d_6$.

2.2.7 Synthesis of chemosensor (**H₃L2.4**) [**H₃L2.4**=2-(3-((3,5-dichloro-2-hydroxybenzylidene)amino)propyl)-3',6'-bis(ethylamino)-2',7'-dimethylspir[isindoline-1,9'-xanthen]-3-one]

A mixture of N-(Rhodamine-6G)lactam-propylenediamine (2.0 mmol, 0.9128 g) and 3,5-Dichlorosalicylaldehyde (2.0 mmol, 0.3820 g) was heated in refluxing condition for *ca.* 4 h in acetonitrile solvent. Yellow colour crystal was obtained after evaporation of the solvent.

Yield: 1.008 g (84%). Anal. Calc. for $\text{C}_{36}\text{H}_{36}\text{Cl}_2\text{N}_4\text{O}_3$: C 67.18%; H 5.64%; N 8.71%. Found: C 67.18%; H 5.58%; N 8.59%. IR (cm^{-1} , KBr): $\nu(\text{C}=\text{N})$ 1634s; $\nu(\text{O}-\text{H})$ 3430s $\nu(\text{C}=\text{O})$ 1674s (**Figure 2.1**). ESI-MS (positive) in MeOH: The base peak was appeared at $m/z = 665.13$, corresponding to $[\text{H}_3\text{L2.4}+\text{Na}]^+$ (**Figure 2.11**). UV-Vis, λ_{max} (nm), (ϵ ($\text{dm}^3\text{mol}^{-1}\text{cm}^{-1}$)) in HEPES buffer(10mM) at pH= 7.4: 420 (47570).

^1H NMR (400 MHz, d_6 -DMSO) δ ppm: 1.20 (-CH₃) (t, 6H, $J_1=9.6\text{Hz}$, $J_2=9.2\text{Hz}$), 1.84 (Ar-CH₃) (s, 6H), 2.09 (-CH₂) (d, 2H, $J=16.8\text{Hz}$), 3.14 (-CH₂) (q, 4H), 5.118 (NH)(s,2H), 6.21

(Ar-CH) (s, 2H), 6.34 (Ar-CH) (s, 2H), 7.06 (Ar-CH) (d, 1H, $J=9.2\text{Hz}$), 7.54 (Ar-CH) (s, 1H), 7.54-7.72 (Ar-CH) (m, 2H), 7.72 (Ar-CH) (s, 1H), 7.94 (Ar-CH) (d, 1H $J=14.4\text{Hz}$), 8.92 (-CH=N) (s, 1H), 11.66(-OH) (s, 1H) (**Figure 2.12**).

¹³C NMR (d₆-DMSO, 75 MHz) δ ppm:

14.71, 16.72, 29.11, 37.54, 38.92, 54.60, 65.10, 96.65, 106.10, 117.99, 118.68, 121.13, 122.76, 123.61, 123.88, 128.15, 128.38, 128.99, 131.18, 132.57, 147.54, 151.79, 153.43, 159.18, 163.87, 168.49

(**Figure 2.13**).

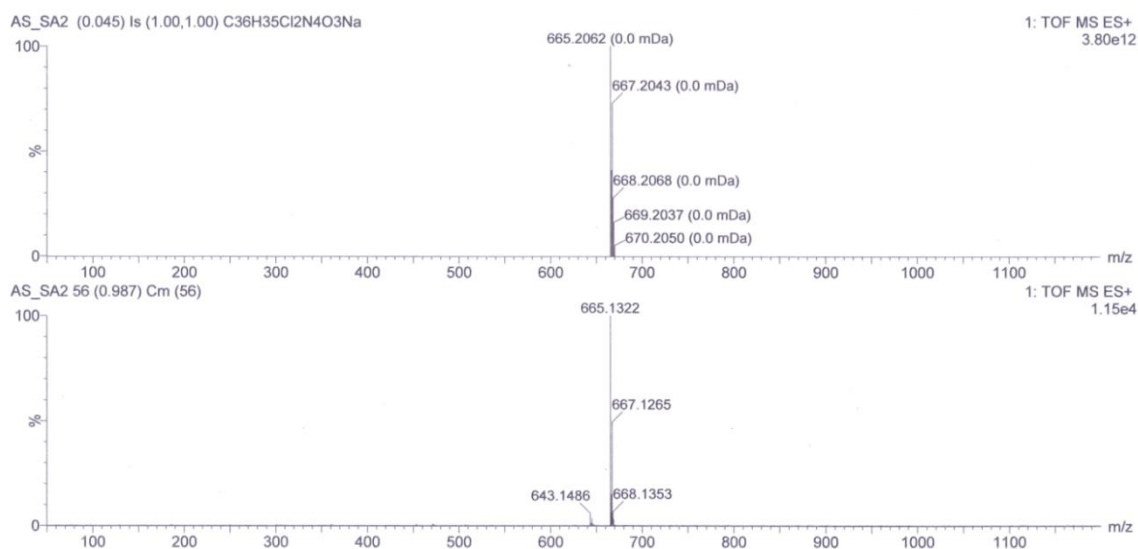


Figure 2.11 ESI-mass spectrum of chemosensor **H₃L2.4** (above is simulated pattern and below is experimental finding).

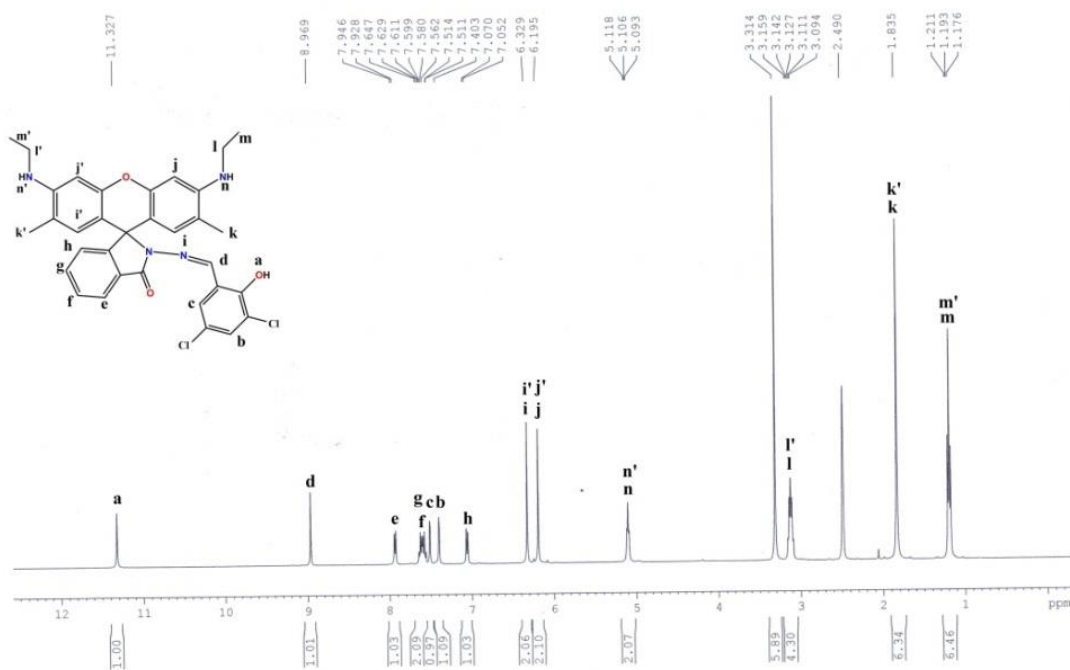


Figure 2.12 ¹H-NMR of the free ligand H₃L_{2.4} in DMSO-*d*₆ recorded on a 400 MHz Bruker NMR spectrometer

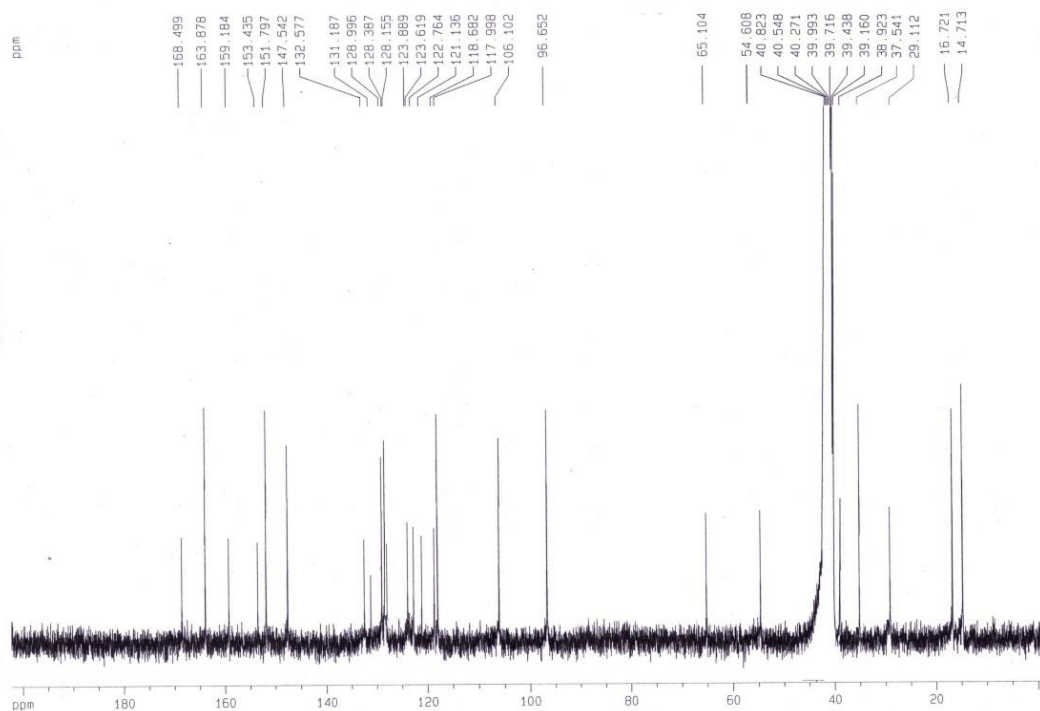


Figure 2.13 ¹³C NMR spectrum of H₃L_{2.4} in DMSO-*d*₆.

2.2.8 Synthesis of complex (2.1) $\{[Al(HL2.1)(NO_3)]=N-(3,5\text{-dibromo-2-oxidobenzylidene)-2-(6-(ethylamino)-3-(ethylimino)-2,7-dimethyl-3H-xanthen-9-yl)benzohydrionate nitratoaluminium(III)}\}$

A 2 mL methanolic solution of Aluminum nitrate nonahydrate (1.0 mmol, 0.375 g) was added carefully to 20 mL acetonitrile solution of **H₃L2.1** (1.0 mmol, 0.690 g) followed by addition of triethylamine (1.0 mmol, ~0.2 mL) and the resultant reaction mixture was stirred for ca. 3 h. red colour solid mass was collected in high yield after slow evaporation of the solvent.

Yield: 0.512 g (78%). Anal. Calc. for C₃₃H₂₈AlBr₂N₅O₆:C 50.99%; H 3.63%; N, 9.01%; Found: C 50.55%; H 3.51%; N 8.91%. IR (cm⁻¹, KBr): $\nu(C=N)$ 1601s; $\nu(NO_3^-)$ 1300s and 809s; $\nu(C=O)$ 1655 s (**Figure 2.14**). ESI-MS (positive) in MeOH: The base peak was observed at $m/z = 778.06$, corresponding to $[Al(HL2.1)(NO_3)+1]^+$ (**Figure 2.15**). UV-Vis, λ_{max} (nm), (ϵ (dm³mol⁻¹cm⁻¹)) in HEPES buffer at pH= 7.4: 490(27500).

¹H NMR (400 MHz, d₆-DMSO) δ ppm: 1.22 (-CH₃) (t, 6H, $J=5.6Hz$), 1.87 (Ar-CH₃) (s, 6H), 3.50 (-CH₂) (t, 4H, $J=5.2Hz$), 5.11 (NH)(s,1H), 6.10 (Ar-CH) (s, 2H), 6.27 (Ar-CH) (s, 2H), 6.97-6.95 (Ar-CH) (m, 2H), 7.52-7.50 (Ar-CH) (m, 2H), 7.61 (Ar-CH) (s, 1H), 7.81-7.80 (Ar-CH) (m, 2H), 9.30(-CH=N) (s, 1H) (**Figure 2.16**).

¹³C NMR (d₆-DMSO, 75 MHz) δ ppm:

14.59, 17.44, 37.92, 96.32, 104.13, 106.13, 114.16, 119.04, 121.58, 123.78, 124.36, 127.20, 128.26, 129.47, 132.40, 134.90, 136.25, 148.47, 151.48, 151.88, 163.37, 165.90, 167.58 (**Figure 2.17**).

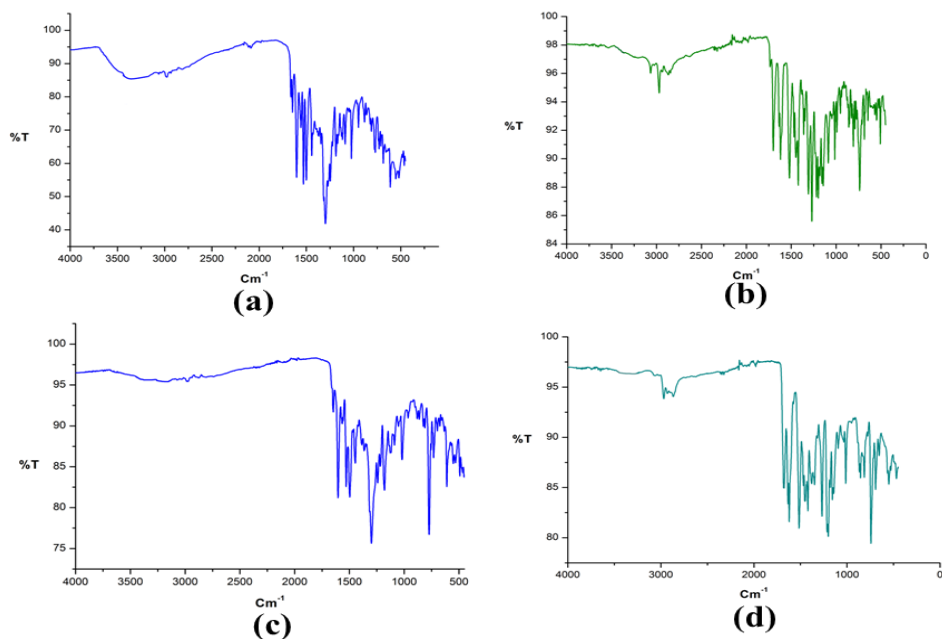


Figure 2.14 FTIR spectra of (a) complex **2.1**, (b) complex **2.2**, (c) complex **2.3** and (d) complex **2.4**.

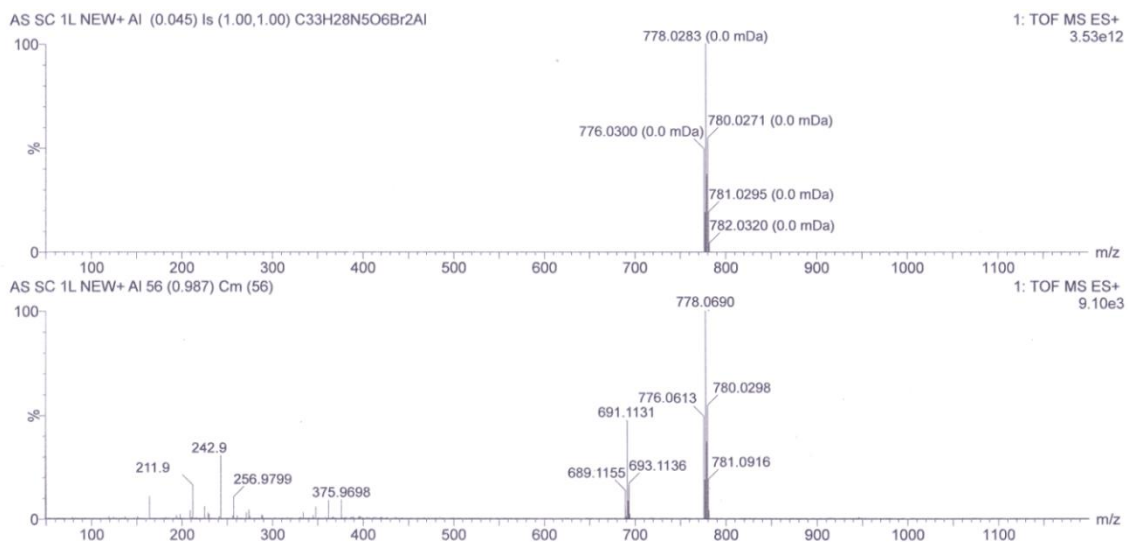


Figure 2.15 ESI-mass spectrum of complex **2.1** (above is simulated pattern and below is experimental finding).

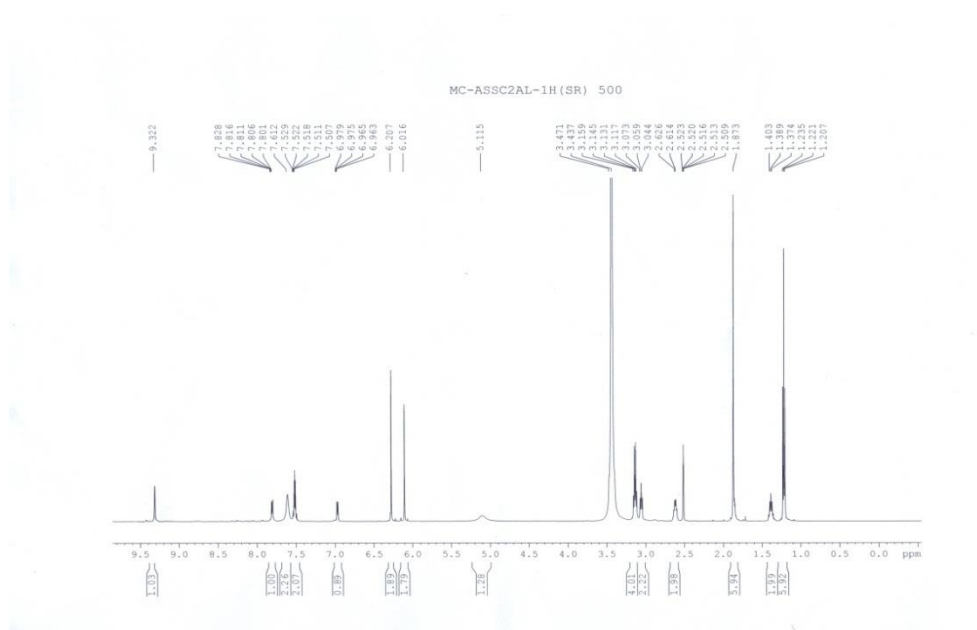


Figure 2.16 ¹H-NMR of the complex **2.1** in DMSO-*d*₆ recorded on a 400 MHz Bruker NMR spectrometer

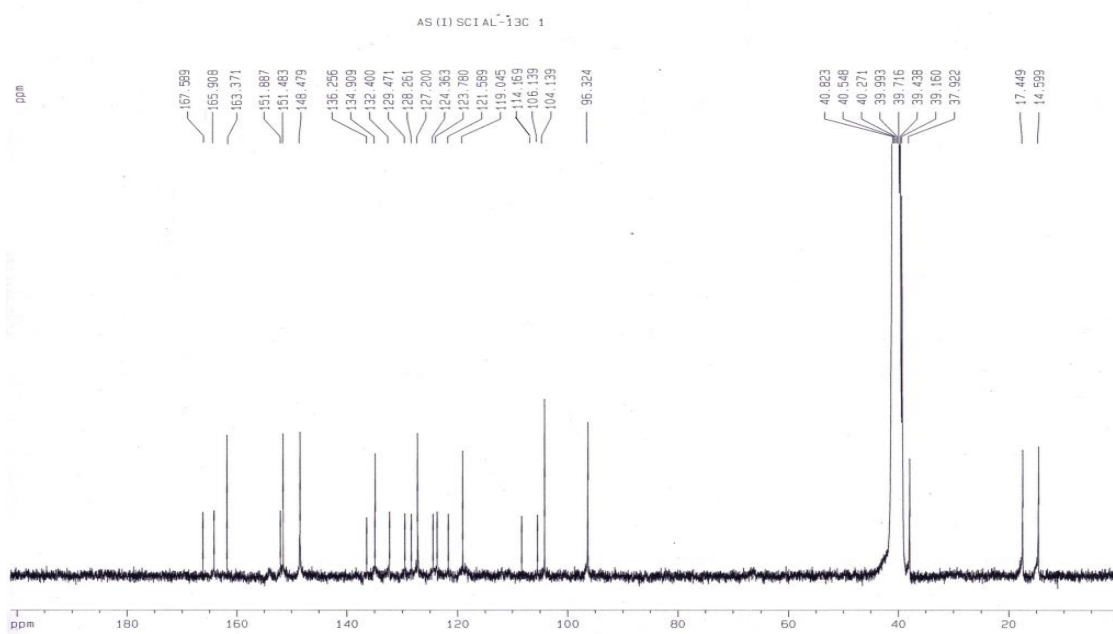


Figure 2.17 ¹³C NMR spectrum of complex **2.1** in DMSO-*d*₆.

2.2.9 Synthesis of complex (2.2) {[Al(HL2.2)(NO₃)]= N-(3,5-dichloro-2-oxidobenzylidene)-2-(6-(ethylamino)-3-(ethylimino)-2,7-dimethyl-3H-xanthen-9-yl)benzohydrazonate nitratoaluminium(III)}

A 2 mL methanolic solution of Aluminum nitrate nonahydrate (1.0 mmol, 0.375 g) was added carefully to 20 mL acetonitrile solution of **H₃L2.2** (1.0 mmol, 0.690 g) followed by addition of triethylamine (1.0 mmol, ~0.2 mL) and the resultant reaction mixture was stirred for ca. 3 h. red colour solid mass was isolated in high yield after slow evaporation of the solvent.

Yield: 0.512 g (78%). Anal. Calc. for C₃₃H₂₈AlCl₂N₅O₆: C 50.99%; H 3.63%; N, 9.01%; Found: C 50.55%; H 3.51%; N 8.91% IR (cm⁻¹, KBr): $\nu(\text{C}=\text{N})$ 1603s; $\nu(\text{NO}_3^-)$ 1300s and 810s; $\nu(\text{C}=\text{O})$ 1646 s (**Figure 2.14**). ESI-MS (positive) in MeOH: The base peak was appeared at $m/z = 696.22$, corresponding to [Al(HL2.2)(NO₃)+Li]⁺ (**Figure 2.18**). UV-Vis, λ_{max} (nm), (ϵ (dm³mol⁻¹cm⁻¹)) in HEPES buffer at pH= 7.4: 415(19670).

¹H NMR (400 MHz, d₆-DMSO) δ ppm: 1.22 (-CH₃) (t, 6H, $J=5.6\text{Hz}$), 1.87 (Ar-CH₃) (s, 6H), 3.50 (-CH₂) (t, 4H, $J=5.2\text{Hz}$), 5.12 (NH)(s, 1H), 6.12 (Ar-CH) (s, 2H), 6.28 (Ar-CH) (s, 2H), 6.97-6.95 (Ar-CH) (m, 2H), 7.52-7.50 (Ar-CH) (m, 2H), 7.61 (Ar-CH) (s, 1H), 7.82-7.80 (Ar-CH) (m, 2H), 9.33(-CH=N) (s, 1H) (**Figure 2.19**).

¹³C NMR (d₆-DMSO, 75 MHz) δ ppm:

14.59, 17.44, 37.92, 96.32, 105.10, 106.13, 114.13, 119.04, 121.58, 123.78, 124.36, 127.20, 128.26, 129.47, 132.40, 134.88, 136.25, 149.47, 152.48, 152.90, 162.87, 165.27, 169.13 (**Figure 2.20**).

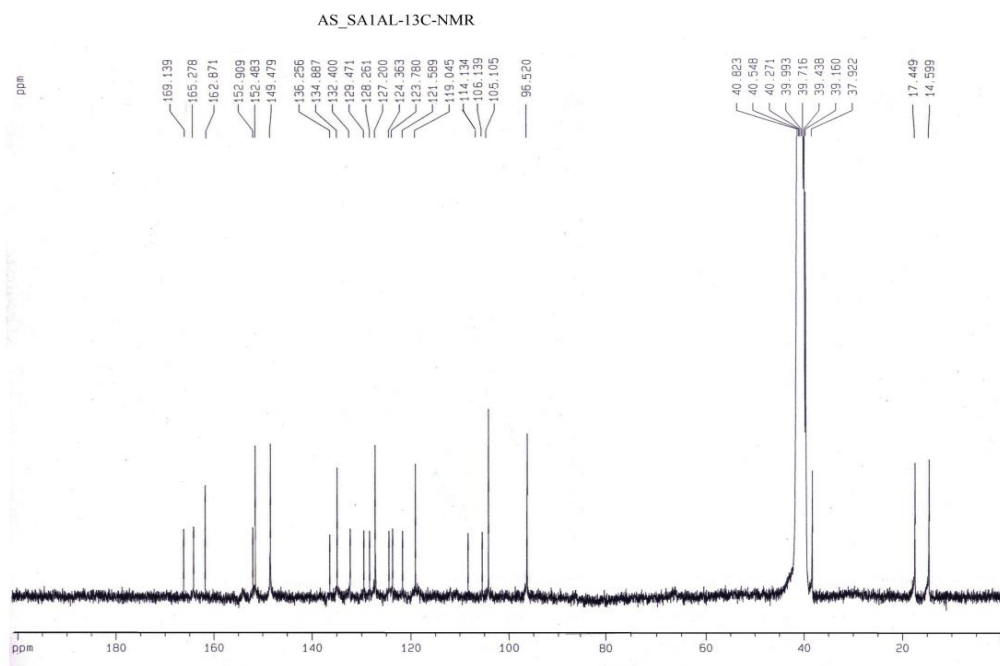


Figure 2.18 ESI-mass spectrum of complex **2.2** (above is simulated pattern and below is experimental finding).

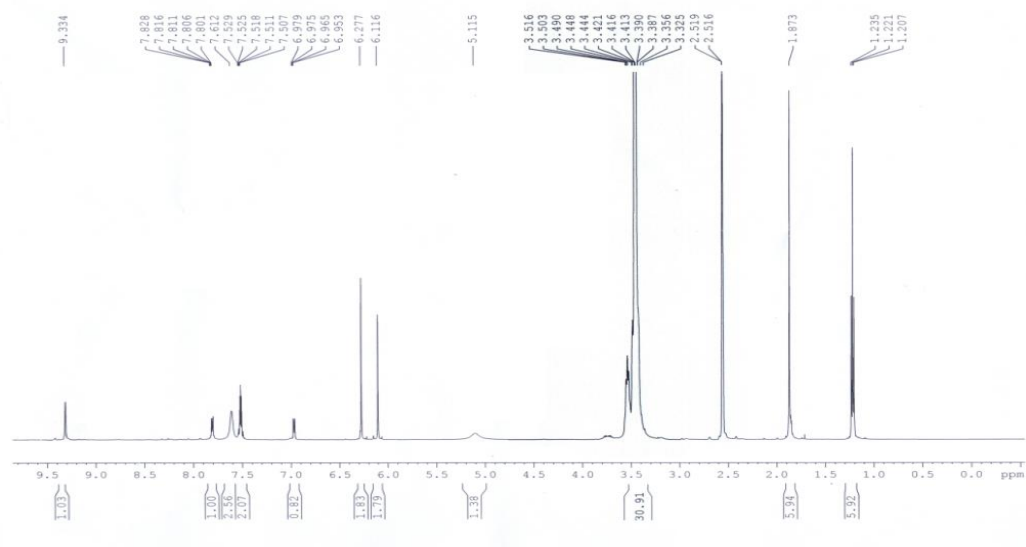


Figure 2.19 ¹H-NMR of the complex **2.2** in DMSO-*d*₆ recorded on a 400 MHz Bruker NMR spectrometer.

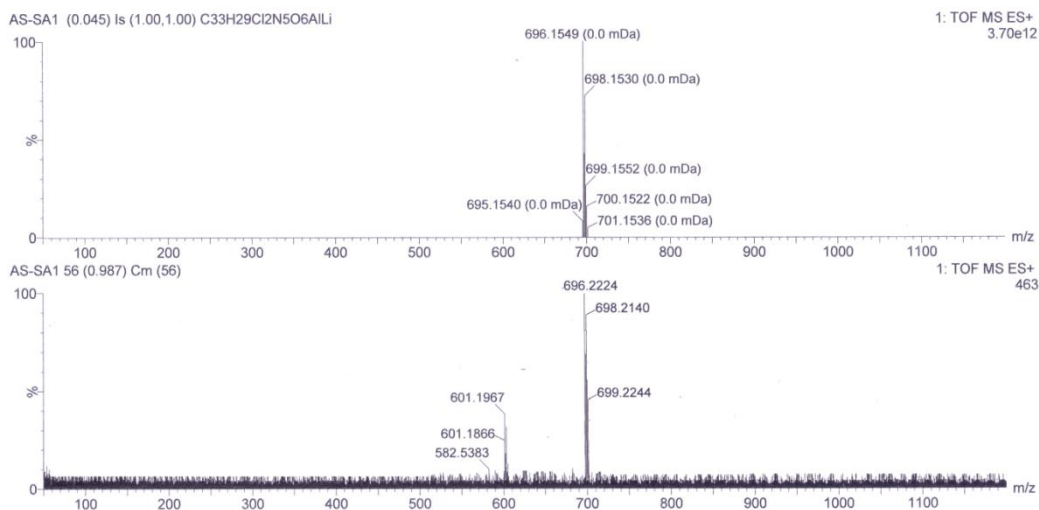


Figure 2.20 ¹³C NMR spectrum of complex **2.2** in DMSO-*d*₆.

2.2.10 Synthesis of complex (2.3) {[Al(L2.3)(NO₃)]=N-(-3-((-3,5-dibromo-2-oxidobenzylidene)amino)propyl)-2-(-6-(ethylamino)-3-(ethylimino)-2,7-dimethyl-3H-xanthen-9-yl)benzimidatenitratoaluminium(III)}

A 2 mL methanolic solution of Aluminum nitrate nonahydrate (1.0 mmol, 0.375 g) was added carefully to 20 mL acetonitrile solution of **H₃L2.3** (1.0 mmol, 0.690 g) followed by addition of triethylamine (1.0 mmol, ~0.2 mL) and the resultant reaction mixture was stirred for ca. 3 h. red colour solid mass was isolated in high yield after slow evaporation of the solvent.

Yield: 0.512 g (78%). Anal. Calc. for C₃₆H₃₅AlBr₂N₅O₆: C 52.63%; H 4.42%; N 8.53%. Found: C 52.55%; H 4.31%; N 8.47%. IR (cm⁻¹, KBr): ν(C=N) 1630s; ν(NO₃⁻)1300s and 811s; ν(C=O) 773 s (**Figure 2.14**). ESI-MS (positive) in MeOH: The base peak was appeared at *m/z* = 822.09, corresponding to [Al(**HL2.3**)(NO₃)+1]⁺ (**Figure 2.21**). UV-Vis, λ_{max} (nm), (ε (dm³mol⁻¹cm⁻¹)) in HEPES buffer at pH= 7.4: 490(28160).

¹H NMR (400 MHz, *d*₆-DMSO) δ ppm: 1.22 (-CH₃) (t, 6H, *J*=5.6Hz), 1.38(-CH₂) (t, 2H, *J*₁=5.6Hz, *J*₂=5.2Hz), 1.87 (Ar-CH₃) (s, 6H), 2.62(-CH₂) (d, 2H, *J*=3.6Hz), 3.05(-CH₂) (t, 2H, *J*₁=4.2Hz, *J*₂=4.5Hz), 3.13 (-CH₂) (q, 4H), 5.11 (NH)(t,1H), 6.01 (Ar-CH) (s, 2H), 6.20 (Ar-

CH) (s, 2H), 6.97-6.96 (Ar-CH) (m, 2H), 7.52-7.50 (Ar-CH) (m, 2H), 7.61 (Ar-CH) (s, 1H), 7.82-7.80 (Ar-CH) (m, 2H), 9.32 (-CH=N) (s, 1H) (**Figure 2.22**).

¹³C NMR (d₆-DMSO, 75 MHz) δ ppm:

14.74, 16.74, 29.21, 37.54, 38.92, 54.80, 96.64, 106.06, 107.72, 113.74, 118.00, 118.97, 122.76, 123.89, 128.17, 128.37, 131.16, 132.60, 132.81, 137.90, 147.54, 151.79, 153.42, 160.96, 163.82, 168.52 (**Figure 2.23**).

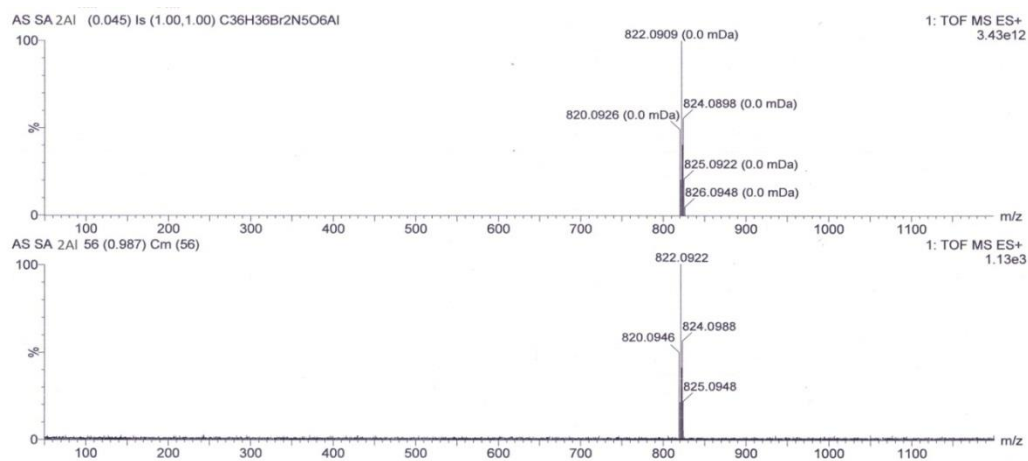


Figure 2.21 ESI-mass spectrum of complex **2.3** (above is simulated pattern and below is experimental finding).

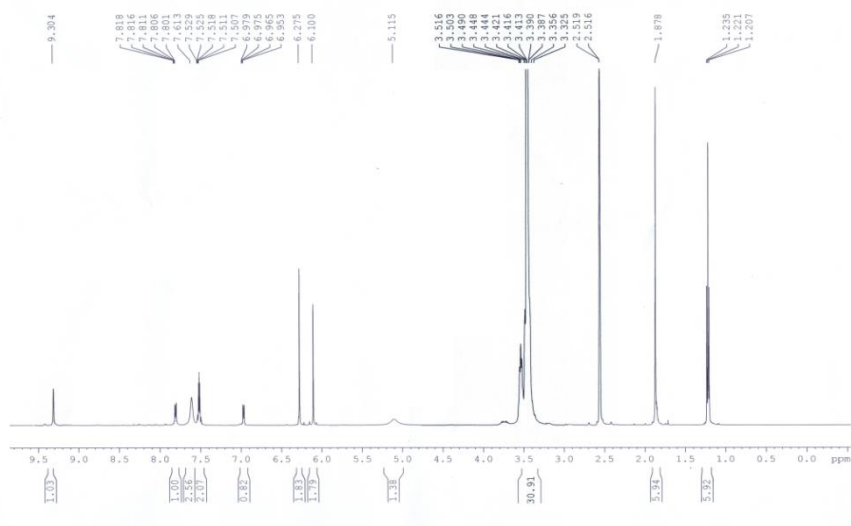


Figure 2.22 ¹H-NMR of the complex **2.3** in DMSO-*d*₆ recorded on a 400 MHz Bruker NMR spectrometer.

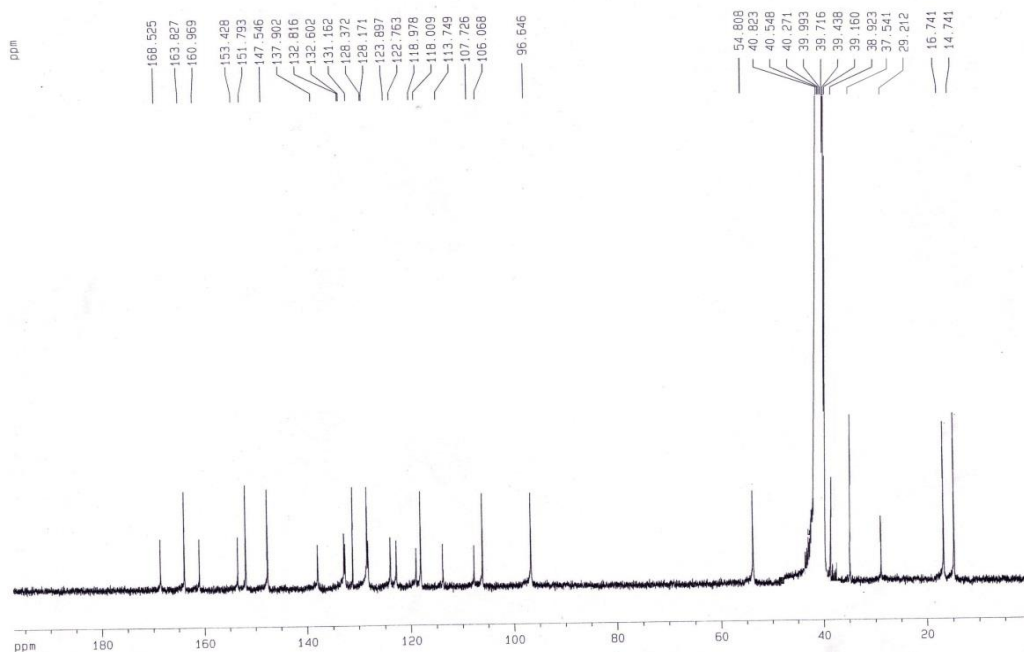


Figure 2.23 ¹³C NMR spectrum of complex **2.3** in DMSO-*d*₆.

2.2.11 Synthesis of complex (2.4) {[Al(HL2.4)(NO₃)]=N-(3-((-3,5-dichloro-2-oxidobenzylidene)amino)propyl)-2-(-6-(ethylamino)-3-(ethylimino)-2,7-dimethyl-3H-xanthen-9-yl)benzimidatenitratoaluminium(III)}

A 2 mL methanolic solution of Aluminum nitrate nonahydrate (1.0 mmol, 0.375 g) was added carefully to 20 mL acetonitrile solution of **H₃L2.4** (1.0 mmol, 0.690 g) followed by addition of triethylamine (1.0 mmol, ~0.2 mL) and the resultant reaction mixture was stirred for ca. 3 h. red colour solid mass was isolated in high yield after slow evaporation of the solvent.

Yield: 0.512 g (78%). Anal. Calc. for C₃₆H₃₅AlCl₂N₅O₆: C 59.02%; H 4.95%; N 9.56%.

Found: C 58.85%; H 4.81%; N 9.21%. IR (cm⁻¹, KBr): ν(C=N) 1621s; ν(NO₃⁻) 1310s and 813s; ν(C=O) 1634 s (**Figure 2.14**). ESI-MS (positive) in MeOH: The base peak was appeared at *m/z* = 732.16, corresponding to [Al(HL2.4)(NO₃)+1]⁺ (**Figure 2.24**). UV-Vis, λ_{max} (nm), (ε (dm³mol⁻¹cm⁻¹)) in HEPES buffer at pH= 7.4: 490(13019).

¹H NMR (400 MHz, d₆-DMSO) δ ppm: 1.29 (-CH₃) (t, 6H $J=4.2$ Hz), 1.38(-CH₂) (t, 2H $J_1=4.2$ Hz, $J_2=4.5$ Hz), 1.87 (Ar-CH₃) (s, 6H), 2.62(-CH₂) (d, 2H, $J=3.6$ Hz), 3.05(-CH₂) (t, 2H, $J_1=4.2$ Hz, $J_2=4.5$ Hz), 3.13 (-CH₂) (q, 4H), 5.11 (NH)(s,1H), 6.10 (Ar-CH) (s, 2H), 6.27 (Ar-CH) (s, 2H), 6.97-6.94 (Ar-CH) (m, 2H), 7.52-7.50 (Ar-CH) (m, 2H), 7.61 (Ar-CH) (s, 1H), 7.87-7.85 (Ar-CH) (m, 2H), 9.35(-CH=N) (s, 1H) (**Figure 2.25**).

¹³C NMR (d₆-DMSO, 75 MHz)δ ppm:

14.71,16.72,29.11,37.54,54.60,96.65,106.10,117.99,118.68,121.13,122.76,,123.61,123.88,128.15,128.38,128.99,131.88, 132.57,147.74,151.59,153.73,160.18,164.57,169.45 (**Figure 2.26**).

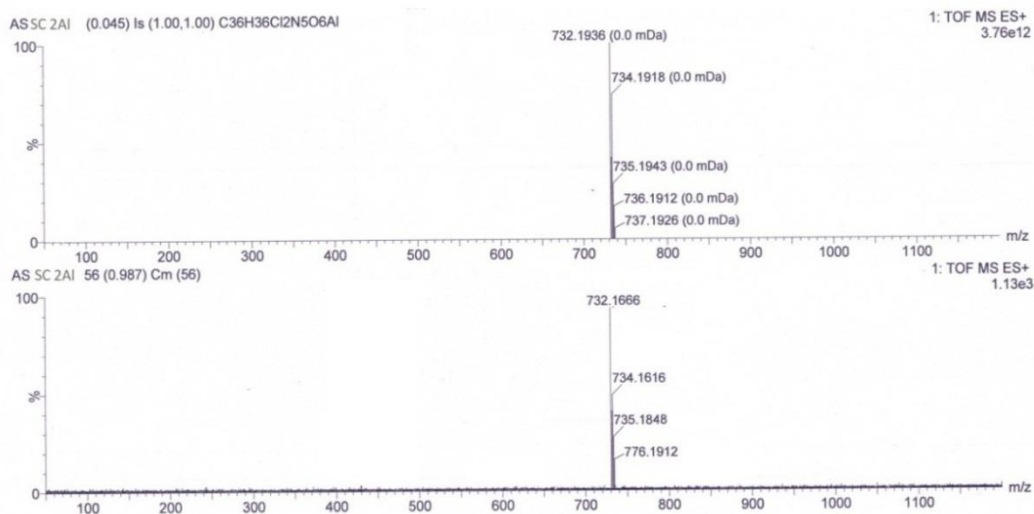


Figure 2.24 ESI-mass spectrum of complex 2.4 (above is simulated pattern and below is experimental finding).

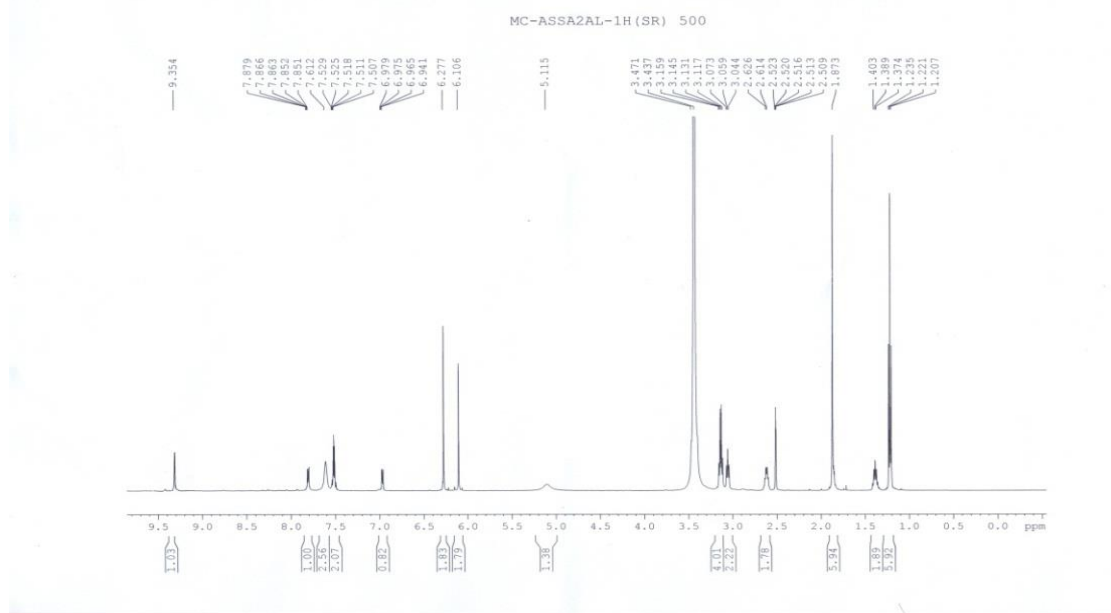


Figure 2.25 ¹H-NMR of the complex **2.4** in DMSO-*d*₆ recorded on a 400 MHz Bruker NMR spectrometer.

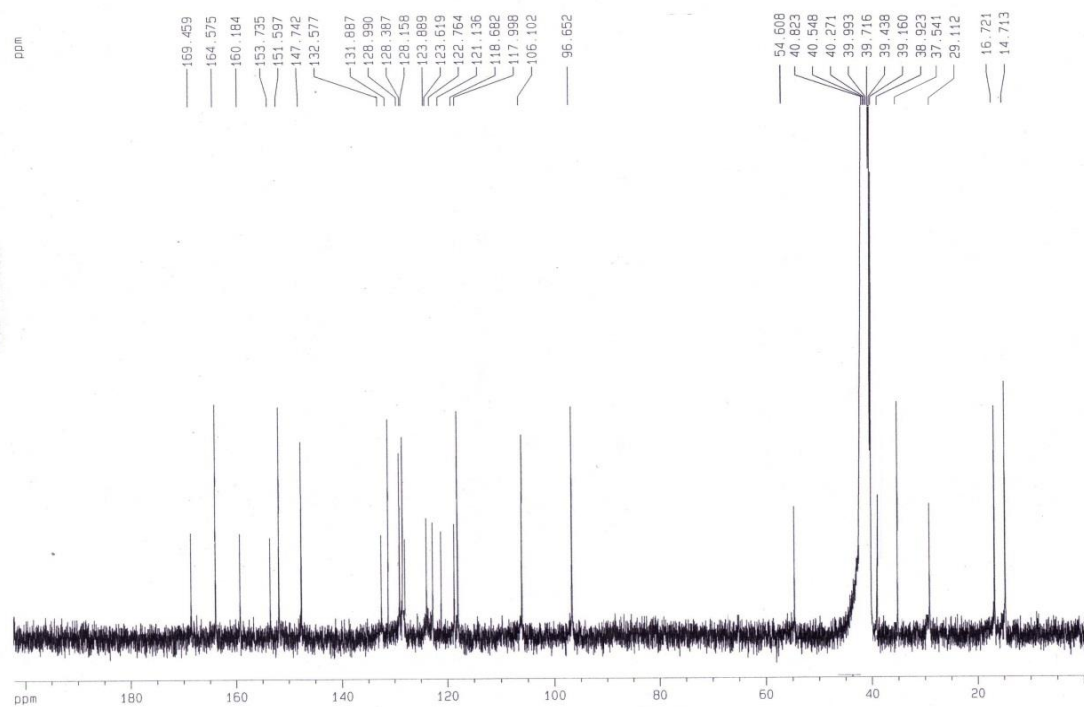


Figure 2.26 ¹³C NMR spectrum of complex **2.4** in DMSO-*d*₆.

2.2.12 UV-visible and fluorescence spectroscopic experiment

Stock solutions of different ions (1×10^{-3} M) were prepared in deionized water medium. A stock solution of the chemosensors (**H₃L2.1-H₃L2.4**) (1×10^{-3} M) was prepared in methanol medium. The chemosensors (**H₃L2.1-H₃L2.4**) solution was then diluted to 1×10^{-5} M as per requirement. Competitive assay of various cations and anions and other spectroscopic experiments were performed in aqueous- methanolic HEPES buffer (10mM) medium at pH 7.4. In competitive assay experiments, the test samples were prepared by mixing appropriate amounts of the cations stock in 3 mL of chemosensors (**H₃L2.1-H₃L2.4**) solution (1×10^{-5} M).

2.2.13 Binding stoichiometry (Job's plot) studies

Binding stoichiometry of the chemosensors with that of Al³⁺ ions are determined by Job's continuation method using absorption spectroscopy. At 25°C temperature, the absorbance was recorded for solutions where the concentrations of both chemosensor and Al³⁺ ions are varied but the sum of their concentrations was kept constant at 1×10^{-5} M. Relative change in absorbance ($\Delta A/A_0$) against mole fraction of chemosensor. The break point in the resulting plot represents the mole fraction of chemosensor in Al³⁺ complex. From the break point the stoichiometry were determined. The final results reported were average of at least three experiments.

2.2.14 Cell culture

The triple negative breast cancer cells of human origin, MDA-MB-468 are procured from the National Center for Cell Science (NCCS) Pune, India. The cells were cultured in an enriched cell culture medium, DMEM (Dulbecco's Modified Eagle Medium), supplemented with 10% FBS (Fetal Bovine Serum) and a mixture of appropriate antibiotics (streptomycin

and penicillin at dose of 100units/ml. The cells were incubated at a temperature of 37°C and in the prevalence of 5%CO₂.

2.2.15 Cell visualisation studies

The human breast cancer cells, MDA-MB-468 cells were cultured on coverslips for a period of 24hrs. Then these cells were either left untreated or were exposed to a dose of ligands (10µM) and Al³⁺ salt(10µM). These treated cells were then incubated for 24 hrs at a temperature of 37°C. Afterwards the cells were thoroughly washed with the help of 1×PBS. Ultimately the cells were envisaged with the help of fluorescence microscope (Leica) following the mounting of the cells on a glass slide.

2.2.16 Computational method

All computations were studied using the GAUSSIAN09 (G09)^{2.49} software package. For optimization process we used the density functional theory method at the B3LYP level^{2.50,2.51} and the standard 6-31+G(d) basis set for C, H, N and O atoms^{2.52,2.53} and the lanL2DZ effective potential (ECP) set of Hay and Wadt^{2.54-2.56} for zinc and copper atoms have been selected for optimization .

TDDFT calculation was studied with the optimized geometry to ensure only positive eigen values. Time-dependent density functional theory (TDDFT)^{2.57-2.59} was examined using conductor-like polarizable continuum model (CPCM)^{2.60-2.62} and the same B3LYP level and basis sets in methanolic solvent system. GAUSSSUM^{2.63} was utilized to calculate the fractional contributions of various groups to each molecular orbital.

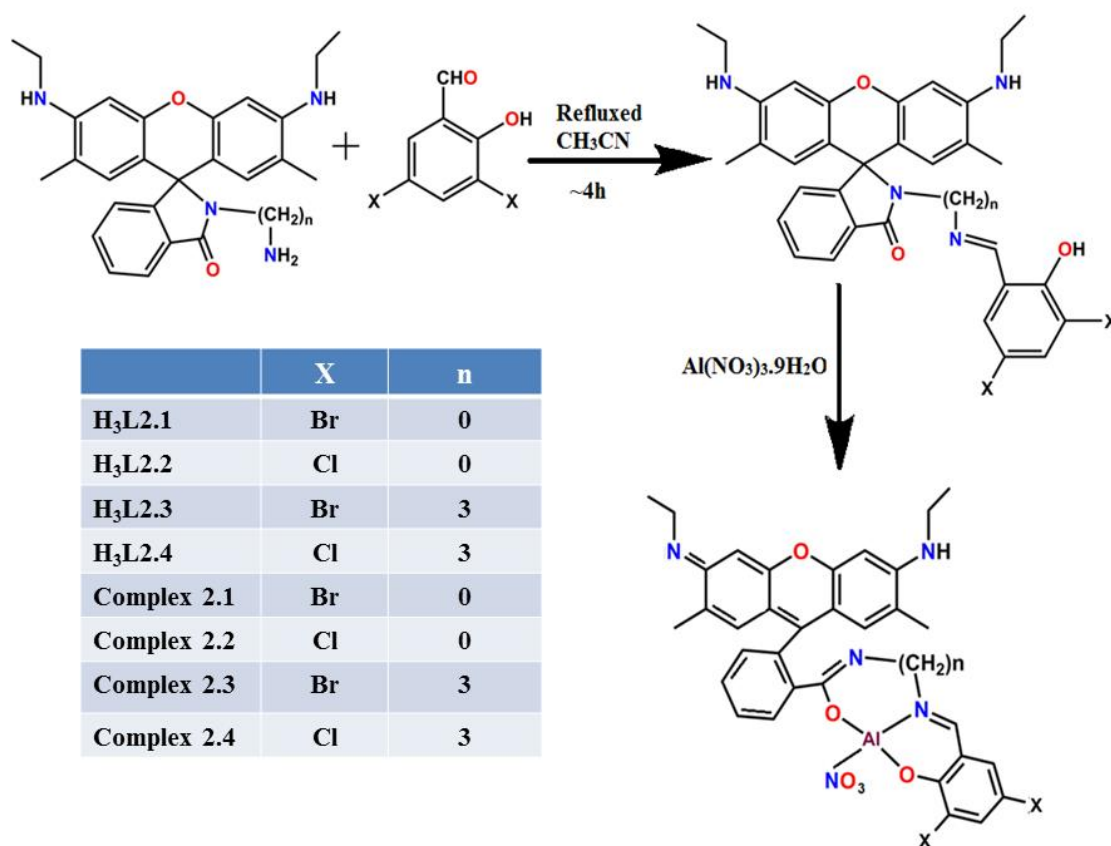
2.3 Results and discussion

2.3.1 Synthesis and characterization

N-(Rhodamine-6G)lactam-hydrazine and N-(Rhodamine-6G)lactam-propylenediamine have been synthesized according to a published procedure.^{2.48} The

chemosensors (**H₃L2.1-H₃L2.4**) are synthesized by Schiff base condensation reaction using rhodamine-6G based amine and 3,5-Dibromosalicylaldehyde or 3,5-Dichlorosalicylaldehyde. They are carefully characterized using different spectroscopic techniques (UV-Vis, FT-IR and NMR) and purity has verified with ESI-mass and C, H, N analysis.

H₃L2.1-H₃L2.4 react with Al(NO₃)₃·9H₂O in 1:1 ratio to produce complexes **2.1-2.4** (**Scheme 2.1**). They are characterized by ¹H NMR, ¹³C NMR, FT-IR spectroscopy, C, H, N and ESI-MS analyses. The experimentally obtained ESI-MS data are well matched with their simulated result. Detail data are presented in the experimental section.



Scheme 2.1 Route of preparation of chemosensors (**H₃L2.1-H₃L2.4**) and complexes **2.1-2.4**.

2.3.2 Crystal structure descriptions of chemosensors (**H₃L2.1-H₃L2.4**)

We are successfully developed X-ray quality crystals of **H₃L2.1**, **H₃L2.2** and **H₃L2.3**, **H₃L2.4** is poorly diffracted. **H₃L2.1** and **H₃L2.2** are formed with triclinic crystal system with

P -1 space group whereas **H₃L2.3** and **H₃L2.4** crystals are developed in monoclinic system with *P* 2₁/*c* space group (**Table 2.1**). ORTEP views of the chemosensors are shown in **Figure 2.26** (**H₃L2.1-H₃L2.4**, respectively). Important bond distances and bond angles are collected in **Table 2.2** and **2.3**, respectively. The organic molecule is non planer and it confirms Schiff base condensation reaction along with presence of spiro lactam ring and xanthene unit within the molecule. The C-O and C-N bond distances of the chemosensors vary within the range 1.217-1.381 Å and 1.274-1.441 Å, respectively.

Table 2.2. Selected Bond lengths (Å) and Bond angles (°) for **H₃L2.1** and **H₃L2.2**.

H₃L2.1	X-ray	Calculated	H₃L2.2	X-ray	Calculated
O1-C6	1.377(6)	1.368	O1-C12	1.378(4)	1.371
O1-C18	1.383(5)	1.368	O1-C5	1.381(4)	1.371
O2-C32	1.204(6)	1.224	O3-C26	1.217(4)	1.225
O3-C11	1.321(6)	1.345	N1-N2	1.376(4)	1.355
N1-N2	1.381(6)	1.356	N1-C26	1.377(4)	1.392
N1-C32	1.384(6)	1.290	N1-C10	1.497(4)	1.513
N1-C8	1.488(6)	1.517	N2-C27	1.274(5)	1.296
N2-C9	1.256(7)	1.396	N3-C14	1.372(4)	1.387
N3-C16	1.361(6)	1.314	N3-C18	1.438(5)	1.456
N3-C15	1.438(7)	1.445	N4-C2	1.441(7)	1.456
N4-C4	1.381(7)	1.314	N4-C3	1.385(5)	1.386
N4-C2	1.455(10)	1.448	N1-C10-C6	111.5(2)	111.78
N1-C8-C19	110.9(3)	107.47	N1-C10-C11	110.6(2)	110.58
N1-C8-C26	99.4(3)	100.02	C6-C10-C11	110.7(2)	110.40
C19-C8-C26	111.6(4)	111.17	N1-C10-C20	99.4(2)	99.60
N1-C8-C7	111.5(4)	111.09	C6-C10-C20	112.5(2)	112.70
C19-C8-C7	110.9(4)	107.47	C1- C10-C20	111.7(3)	112.07
C26-C8-C7	112.1(4)	113.54			

Table 2.3. Selected Bond lengths (Å) and Bond angles (°) for **H₃L2.3** and **H₃L2.4**.

H₃L2.3	X-ray	Calculated	H₃L2.4	X-ray	Calculated
O1-C2	1.339(13)	1.332	O1-C20	1.383(11)	1.372
O2-C11	1.228(14)	1.227	O1-C21	1.407(11)	1.372
O3-C25	1.381(9)	1.372	O2-C37	1.221(13)	1.227
O3-C31	1.381(9)	1.372	O3-C3	1.340(14)	1.332
N1-C7	1.257(12)	1.281	N1-C9	1.446(13)	1.455
N1-C8	1.479(13)	1.456	N1-C10	1.497(11)	1.498
N2-C11	1.394(15)	1.382	N1-C37	1.375(13)	1.378
N2-C10	1.440(13)	1.455	N2-C14	1.376(12)	1.387
N2-C18	1.489(11)	1.498	N2-C15	1.435(15)	1.455
N3-C23	1.375(11)	1.387	N3-C25	1.379(12)	1.382
N3-C33	1.500(16)	1.459	N3-C26	1.432(13)	1.456
N4-C29	1.364(12)	1.374	N4-C5	1.245(16)	1.281
N4-C35	1.450(14)	1.456	N4-C7	1.485(15)	1.456
N2-C18 C19	112.3(6)	112.86	N1-C10-C11	110.2(7)	111.96
N2-C18 C17	99.3(7)	100.23	N1-C10-C22	111.1(7)	111.46
C19-C18-C17	111.1(7)	111.98	N1-C10-C31	101.0(7)	100.23
N2-C18-C26	110.4(7)	110.94	C22-C10-C31	111.1(8)	111.98
C17-C18-C26	112.4(7)	111.96	C31-C10-C11	112.6(7)	112.02
C19-C18-C26	110.8(7)	111.45	C22-C10-C11	110.5(7)	110.94

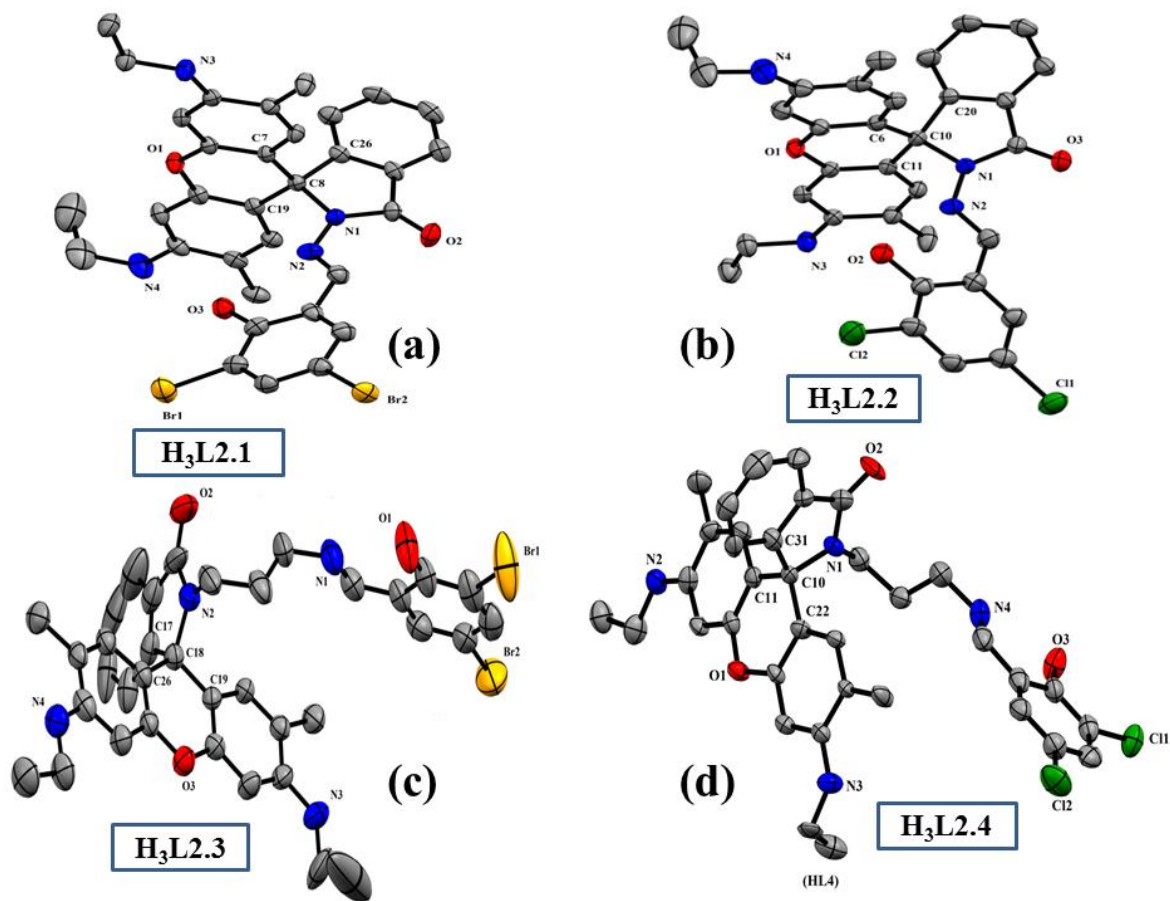


Figure 2.26 ORTEP view of the chemosensors (a) **H₃L2.1**, (b) **H₃L2.2**, (c) **H₃L2.3** and (d) **H₃L2.4**. Atoms are shown as 30% thermal ellipsoids. Here, H atoms are omitted for clarity.

2.3.3 NMR studies

All the chemosensors and Al³⁺- probe complexes give well resolved ¹H NMR spectra in DMSO-*d*₆ solvent. In **H₃L2.1**, the phenolic OH and imine proton appear as a sharp singlet at 11.56 and 8.90 ppm, respectively. Aromatic protons appear in the region 7.94-6.20 ppm. Aliphatic amine (-NH) protons appear as triplet at 5.11 ppm. Aliphatic CH₂ protons appear as quartet at 3.13 ppm. Aromatic CH₃ protons appear as singlet at 1.84 ppm whereas; aliphatic CH₃ protons appear as triplet at 1.20 ppm (**Figures 2.3, 2.6, 2.9** and **2.13**).

In complex **2.1**, the phenolic -OH peak disappears due to complexation, Imine proton shifted to downfield and appears as a sharp singlet at 9.30 ppm. We also observe significant

changes in aromatic peak positions and broadening of the peaks due to complexation. During complexation one NH proton of the aliphatic part disappears and the other appears as a broad peak at 5.11 ppm. Aliphatic CH₂ protons merged with water molecules appear as multiplet at 3.50 ppm. Aromatic CH₃ protons appear as singlet at 1.87 ppm and aliphatic CH₃ protons appear as triplet at 1.22 ppm, respectively (**Figure 2.16**).

All the chemosensors and probe bound Al³⁺ complexes give clean ¹³C NMR spectra in DMSO-*d*₆ solvent. In **H₃L2.1**, spirolactam amide carbon appears at 165.58 and phenolic carbon appears at 164.21 ppm. Imine carbon appears at 161.87 ppm. Aromatic carbons present in the region 151.88-96.32 ppm. Carbon atom connecting the xanthene part and spirolactam ring is *sp*³ hybridized and appears at 66.24 ppm. Aromatic CH₃ carbons appear with double intensity at 37.92 ppm. Aliphatic CH₂ and CH₃ carbons appear with double intensity at 17.44 and 14.59 ppm, respectively (**Figure 2.4**).

In complex **2.1**, spirolactam amide carbon appears at 167.58 and phenolic carbon appears at 165.90 ppm. Imine carbon appears at 163.37 ppm. These three peaks are shifted to downfield due to metal coordination. Aromatic carbons appear within 151.88-96.32 ppm. Since, metal coordination results spirolactam ring opening, the *sp*³ hybridized carbon atom connecting xanthene part and spirolactam ring now become *sp*² hybridized and appears at 134.90 ppm. Aromatic CH₃ carbons appear with double intensity at 37.92 ppm. Aliphatic CH₂ and CH₃ carbons appear with double intensity at 17.44 and 14.59 ppm, respectively (**Figure 2.17**)

2.3.4 Absorption spectral analysis

The UV-Vis spectra of chemosensors (**H₃L2.1-H₃L2.4**) are first examined in 10 mM HEPES buffer solution at pH 7.4 (9 : 1, water : methanol, v/v). Chemosensors, **H₃L2.1** and **H₃L2.2** exhibit well-resolved bands at ~ 290 and ~ 345 nm whereas **H₃L2.3** and **H₃L2.4** show well-defined band at ~ 420 nm. Peaks are represented as $\pi \rightarrow \pi^*$ and $n \rightarrow \pi^*$ type of transitions. Interestingly upon successive addition of Al³⁺ ions (0-11 μ M, 10 mM HEPES buffer solution; pH 7.4; 9:1, water: methanol, v/v) to the chemosensor (10 μ M), a new peak appears at ~ 530 nm with significant changes in the spectra of all chemosensors (**H₃L2.1-H₃L2.4**). In **H₃L2.1** and **H₃L2.2** absorbance of peaks at ~ 290 and ~ 345 nm gradually increase whereas, in **H₃L2.3** and **H₃L2.4** absorbance of peak at ~ 420 nm gradually decreases (**Figure 2.27**). In the presence of Al³⁺, spirolactam ring opening occurs followed by the coordination of the cation. Here, Al³⁺ ion binds with phenoxido oxygen, imine nitrogen and amide oxygen of the chemosensor. Spirolactam ring opening results in reorientation of protons within the aromatic ring and consequently removal of one primary amine proton. Generation of a new peak at ~ 530 nm in the presence of Al³⁺ ions also confirms structural rearrangement within the organic molecule. Colour of the solution turns to fluorescent pinkish yellow. Saturation has been observed in presence of 1.1 equivalents of Al³⁺ ions to the chemosensor. The 1:1 binding stoichiometry of the chemosensors with Al³⁺ ions has been confirmed by Job's plot analysis (**Figure 2.28**). These results have been further supported by ESI-MS analysis. It is important to mention that, the addition of different cations (Cd²⁺, Hg²⁺, Pb²⁺, Zn²⁺, Ag⁺, Mn²⁺, Fe³⁺, Co²⁺, Ni²⁺, Na⁺, K⁺, Mg²⁺ and Ca²⁺) did not change the initial absorption spectrum of the chemosensor appreciably.

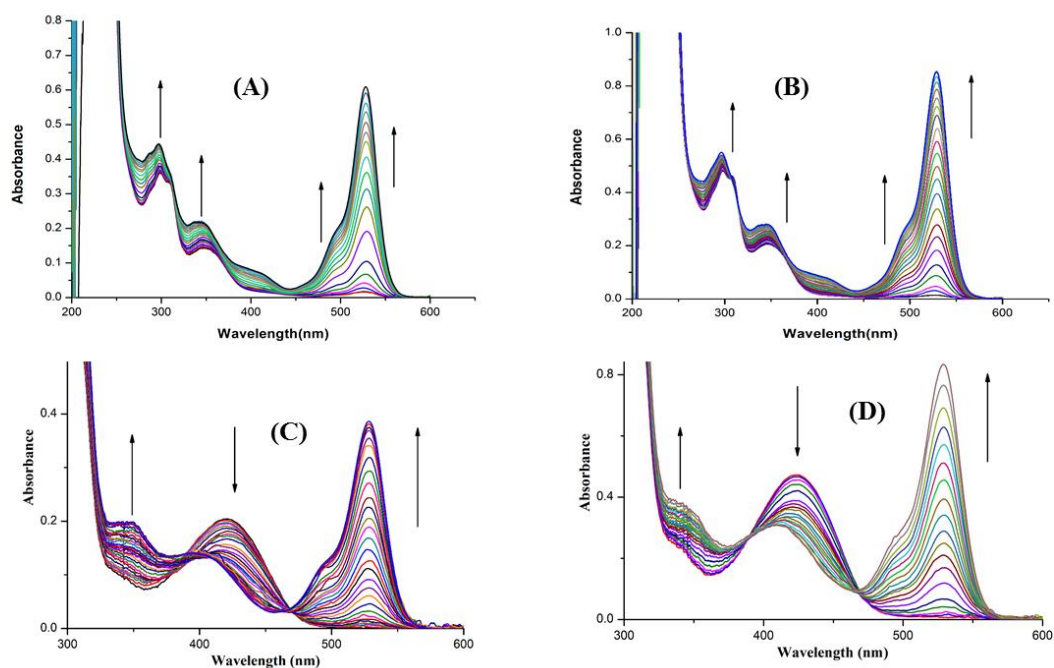


Figure 2.27 Absorption titration study of (A)=**H₃L2.1**, (B)=**H₃L2.2**, (C)=**H₃L2.3** and (D)=**H₃L2.4** (10 μ M) with gradual addition of Al^{3+} , 0-11 μ M in 10 mM HEPES buffer at pH 7.4.

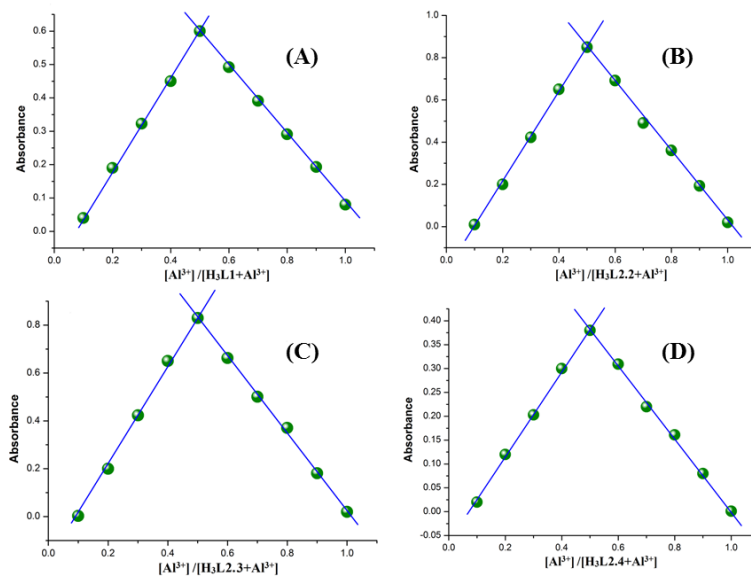


Figure 2.28 1:1 binding stoichiometry has shown by Job's plot of complex (A)=**2.1**, (B)=**2.2**, (C)=**2.3** and (D)=**2.4**. Symbols and solid lines represent the experimental and simulated profiles, respectively.

2.3.5 Fluorescence properties analysis

The experiment is performed in 10mM HEPES buffer at pH = 7.4 (9:1, water : methanol, v/v) at ambient conditions. When excited at 345 nm, probes (10 μ M) are non-fluorescent. Upon successive addition of Al³⁺ ions (0-11 μ M) to the probe an enormous fluorescence enhancement is observed at 555 nm (**Figure 2.29-2.32**). The fluorescence enhancement has a steady growth and finally reaches a maximum at 1.1 equivalents of Al³⁺ ions. In fact, metal ions initiate opening of spirolactam ring followed by a long conjugation of π -electronic system within the probe (**Figure 2.42**). Generation of a fluorescence peak at 555 nm in the presence of Al³⁺ ions also proves the above fact. Interestingly, the values of increment in emission spectra are not equal for all the probes. In case of **H₃L2.1** and **H₃L2.2**, the emission enhancement is 780 and 725 fold whereas for **H₃L2.3** and **H₃L2.4**, enhancement is 425 and 391 fold.

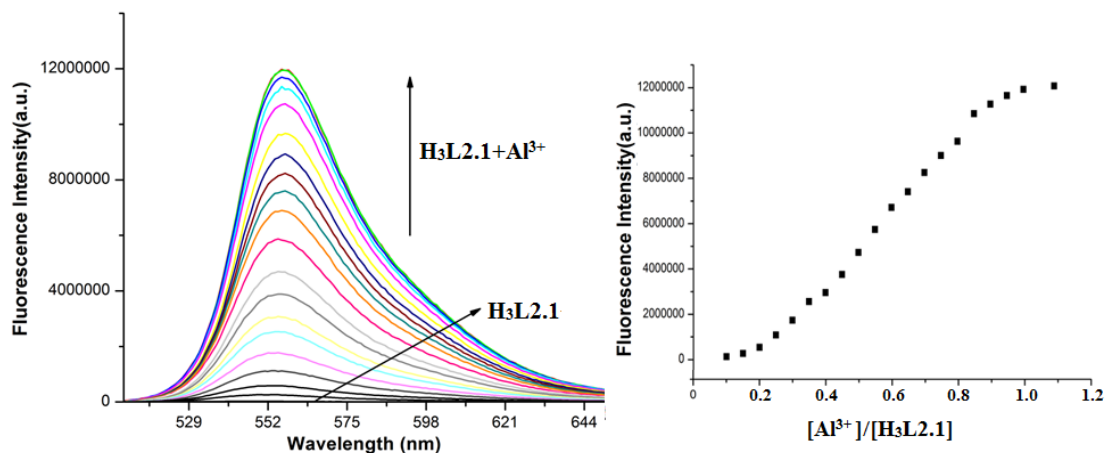


Figure 2.29 Fluorescence titration of **H₃L2.1** (10 μ M) in 10 mM HEPES buffer at pH =7.4 by successive addition of Al³⁺ (0–11 μ M) with λ_{em} = 555 nm (1/1 slit).

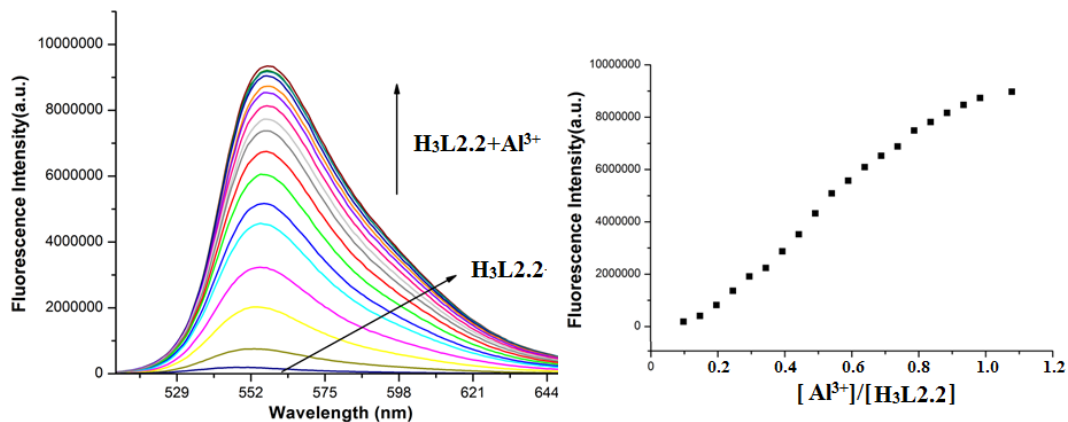


Figure 2.30 Fluorescence titration of $\text{H}_3\text{L}2.2$ ($10 \mu\text{M}$) in 10 mM HEPES buffer at $\text{pH} = 7.4$ by successive addition of Al^{3+} (0 – $11 \mu\text{M}$) with $\lambda_{\text{em}} = 555 \text{ nm}$ ($1/1$ slit).

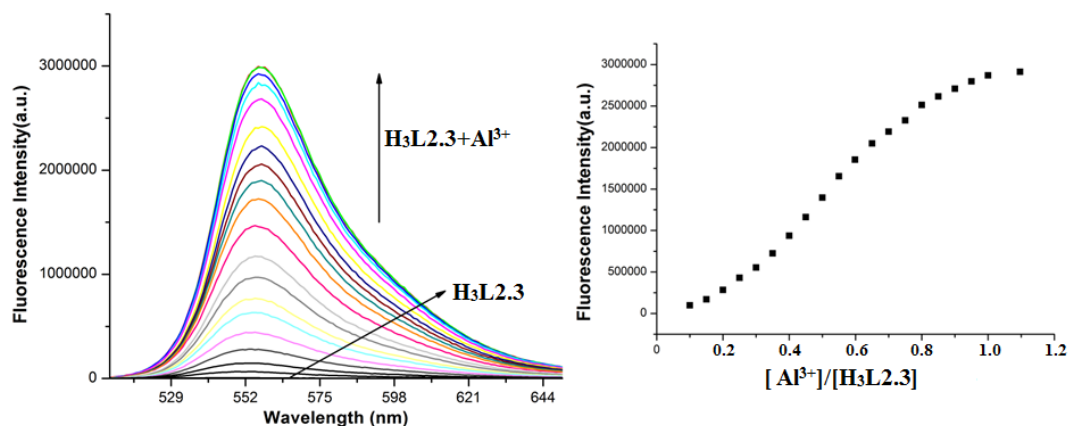


Figure 2.31 Fluorescence titration of $\text{H}_3\text{L}2.3$ ($10 \mu\text{M}$) in 10 mM HEPES buffer at $\text{pH} = 7.4$ by successive addition of Al^{3+} (0 – $11 \mu\text{M}$) with $\lambda_{\text{em}} = 555 \text{ nm}$ ($1/1$ slit).

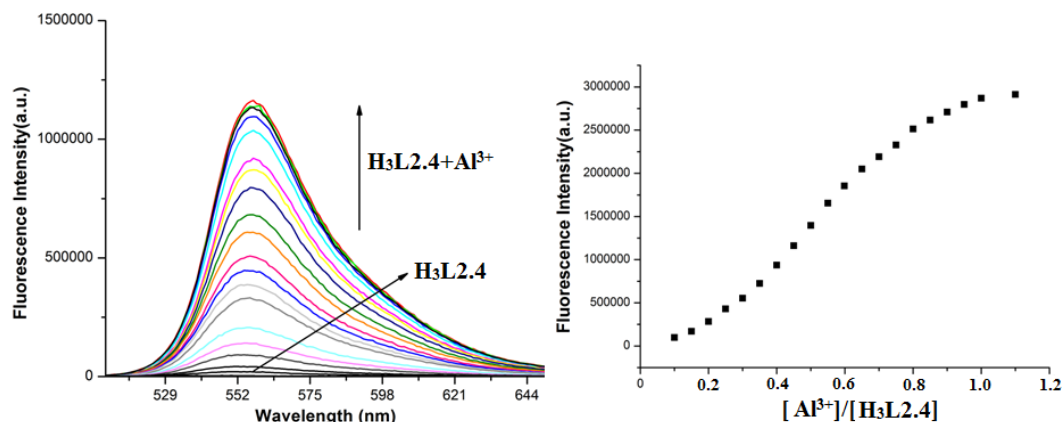


Figure 2.32 Fluorescence titration of **H₃L2.4** (10 μ M) in 10 mM HEPES buffer at pH =7.4 by successive addition of Al³⁺ (0–11 μ M) with λ_{em} = 555 nm (1/1 slit).

Binding ability of the chemosensors towards Al³⁺ ions has been calculated using Benesi-Hildebrand equation (Equation 1) involving fluorescence titration curve.^{2,64}

$$1/(F - F_0) = 1/(F_{max} - F_0) + (1/K[C])\{1/(F_{max} - F_0)\} \dots\dots\dots(1)$$

Here, F_{max} , F_0 and F_x are fluorescence intensities of chemosensors (**H₃L2.1-H₃L2.4**), in presence of metal ions at saturation, free chemosensors (**H₃L2.1-H₃L2.4**), and any intermediate metal ions concentration, respectively. K is denoted as the binding constant of the complexes, and concentration of Al³⁺ ions are represented by C . The value of binding constant (K) of the complexes has been determined using the relation, $K=1/\text{slope}$. Binding constant values as $8.00 \times 10^5 \text{M}^{-1}$, $6.90 \times 10^5 \text{M}^{-1}$, $1.37 \times 10^4 \text{M}^{-1}$ and $1.03 \times 10^4 \text{M}^{-1}$, respectively for the chemosensors **H₃L2.1-H₃L2.4** towards Al³⁺ ions (**Figure 2.33**). We have also performed fluorescence titrations of the chemosensors in the presence of Al³⁺ ions in aprotic solvent such as tetrahydrofuran (THF) to determine the binding constant in THF and to compare the difference of binding constant values determined in protic and aprotic solvents. The calculated binding constant values in THF are close with the previously calculated values measured at HEPES buffer solution (9:1, water : methanol, v/v) (**Table 2.4**). Therefore, we can conclude that free chemosensors, **H₃L2.1-H₃L2.4** do not undergo deprotonation in

solution (protic or aprotic). Al³⁺ ions can promote deprotonation of **H₃L2.1-H₃L2.4** both in aqueous or non aqueous solution.

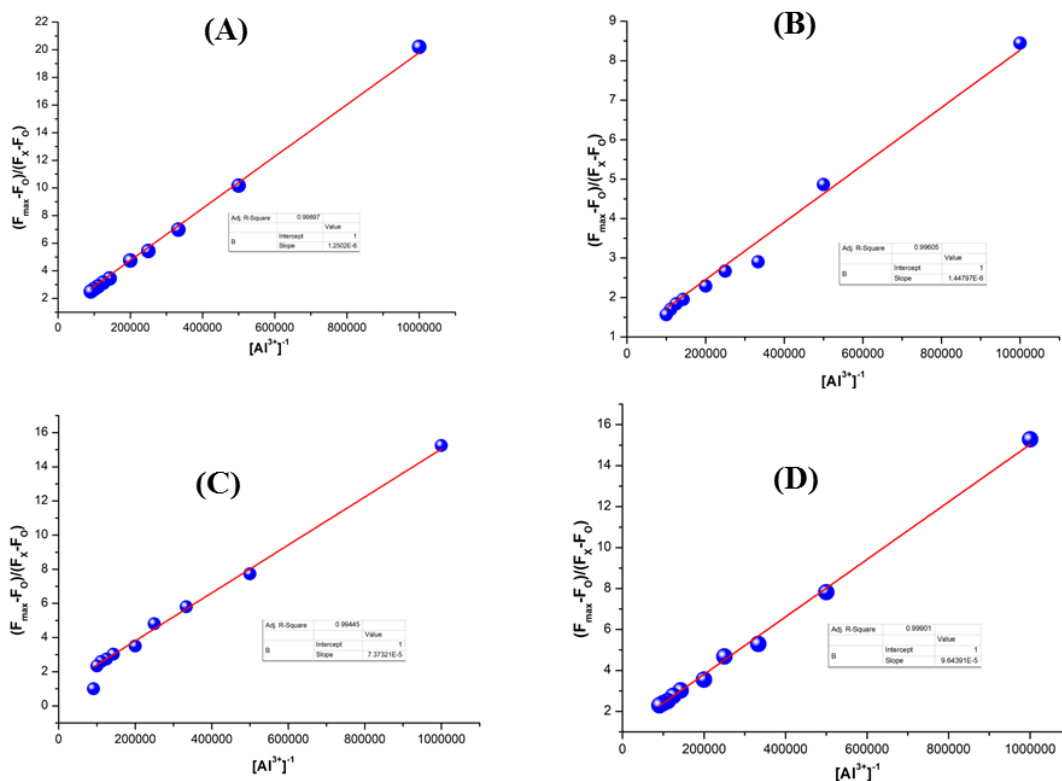


Figure 2.33 Benesi-Hildebrand plot for complex (A) **2.1**, (B) **2.2**, (C) **2.3** and (D) **2.4**. The plot is obtained after adding 10 μ M Al³⁺ solution to the **H₃L2.1-H₃L2.4** solution (10 μ M) (in 10 mM HEPES buffer medium, pH 7.4).

Table 2.4. Binding constant values of chemosensors in presence of Al³⁺ ions in different solvent system.

Chemosensors	Binding constant in 9:1 water: methanol (v/v) medium(M ⁻¹)	Binding constant in THF medium(M ⁻¹)
H₃L2.1	8.00×10^5	6.84×10^5
H₃L2.2	6.90×10^5	4.83×10^5
H₃L2.3	1.37×10^4	1.44×10^4
H₃L2.4	1.03×10^4	1.10×10^4

High selectivity of the chemosensors toward Al³⁺ ions is again established by competition assay experiment. Here in presence of chemosensor and Al³⁺ ions (1.0 equiv.) different metal ions (Cd²⁺, Hg²⁺, Pb²⁺, Zn²⁺, Ag⁺, Mn²⁺, Fe³⁺, Co²⁺, Ni²⁺, Na⁺, K⁺, Mg²⁺ and Ca²⁺) (**Figure 2.34**) and common anions (S₂O₃²⁻, S²⁻, SO₃²⁻, HSO₄⁻, SO₄²⁻, SCN⁻, N₃⁻, OCN⁻, AsO₄³⁻, H₂PO₄⁻, HPO₄²⁻, PO₄³⁻, ClO₄⁻, AcO⁻, NO₃⁻, F⁻, Cl⁻, PF₆⁻ and P₂O₇⁴⁻) are added in excess amount (4.0 equiv.) in 10 mM HEPES buffer solution at pH 7.4. Competition assay experiments clearly express high fluorescent recognition of chemosensors (**H₃L2.1-H₃L2.4**) for Al³⁺ ions over most of the metal ions and all common anions (**Figure 2.35** and **2.36**). It is important to mention that in presence of Cr³⁺, Mg²⁺, Cu²⁺ and Fe³⁺ ions little quenching in fluorescence intensity has been observed.

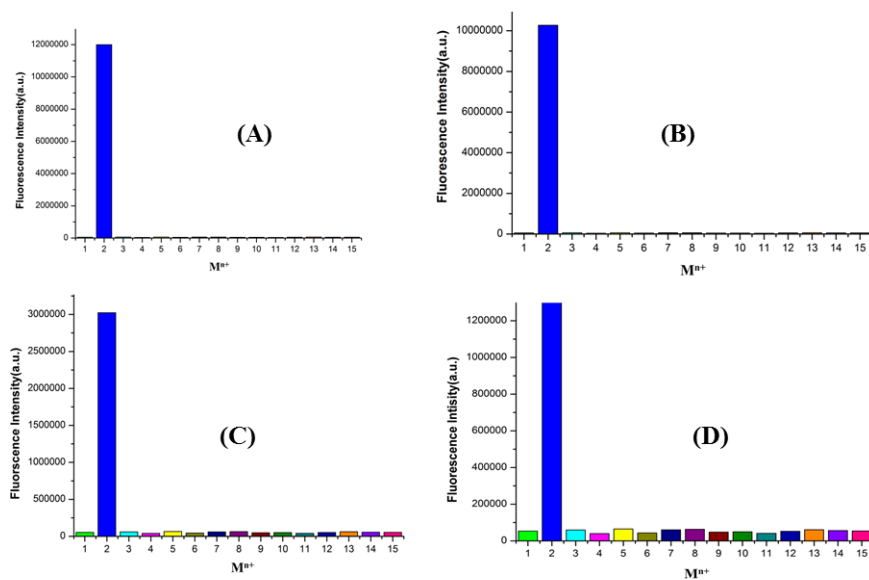


Figure 2.34. Relative fluorescence intensity diagram of chemosensor (A)=H₃L2.1, (B)=H₃L2.2, (C)=H₃L2.3 and (D)=H₃L2.4 in the presence of different cations in HEPES buffer at pH 7.4. [1=only H₃L2.1/ H₃L2.2/ H₃L2.3/ H₃L2.4 (10 μM); H₃L2.1/ H₃L2.2/ H₃L2.3/ H₃L2.4 (10 μM) + Mⁿ⁺(10 μM), where Mⁿ⁺=2–Al³⁺, 3–Cu²⁺, 4–Cr³⁺, 5–Fe³⁺, 6–Hg²⁺, 7–K⁺, 8–Mn²⁺, 9–Na⁺, 10–Ni²⁺, 11–Mg²⁺, 12–Pb²⁺, 13–Ca²⁺, 14–Fe²⁺, 15–Cd²⁺].

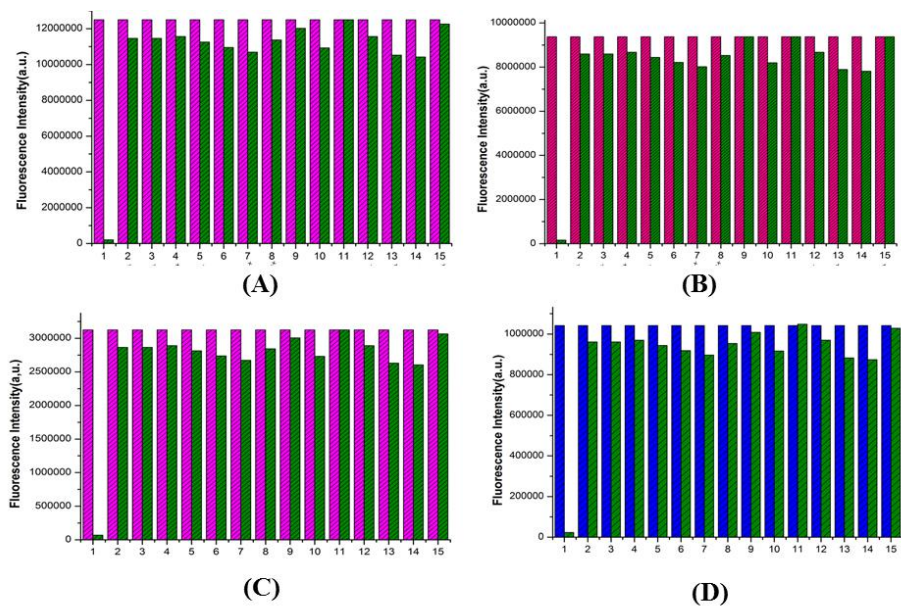


Figure 2.35 Relative fluorescence intensity diagram of [(A)=**H₃L2.1**-Al³⁺, (B)=**H₃L2.2**-Al³⁺, (C)=**H₃L2.3**-Al³⁺, (D)=**H₃L2.4**-Al³⁺] system in the presence of different cations in 10 mM HEPES buffer at pH 7.4. [1=only **H₃L2.1**/ **H₃L2.2**/ **H₃L2.3**/ **H₃L2.4** and (2-15)= **H₃L2.1**/ **H₃L2.2**/ **H₃L2.3**/ **H₃L2.4** (10 μ M) + Al³⁺(10 μ M) + Mⁿ⁺(40 μ M), where Mⁿ⁺=2-Ca²⁺, 3-Co²⁺, 4-Hg²⁺, 5-Zn²⁺, 6-Cr³⁺, 7-Mg²⁺, 8-Mn²⁺, 9-Na⁺, 10-Ni²⁺, 11-K⁺, 12-Pb²⁺, 13-Cu²⁺, 14-Fe³⁺, 15-Cd²⁺].

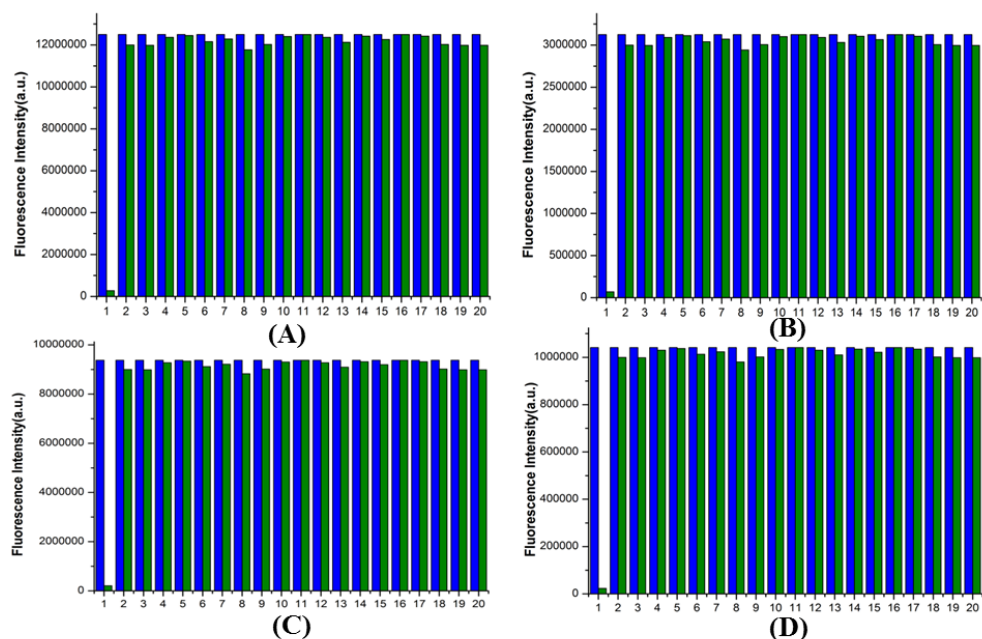


Figure 2.36 Relative fluorescence intensity diagram of [(A)=**H₃L2.1**-Al³⁺, (B)=**H₃L2.2**-Al³⁺, (C)=**H₃L2.3**-Al³⁺, (D)=**H₃L2.4**-Al³⁺] system in the presence of different anions in HEPES buffer medium (10 mM) at pH 7.4. [1=only **H₃L2.1**/ **H₃L2.2**/ **H₃L2.3**/ **H₃L2.4** (10 μ M) and (2-20)= **H₃L2.1**/ **H₃L2.2**/ **H₃L2.3**/ **H₃L2.4** (10 μ M) + Al³⁺(10 μ M) + Anions (40 μ M), Anions = 2-S₂O₃²⁻, 3-S²⁻, 4-SO₃²⁻, 5-HSO₄⁻, 6-SO₄²⁻, 7-SCN⁻, 8-N₃⁻, 9-OCN⁻, 10-AsO₄³⁻, 11-

H₂PO₄⁻, 12-HPO₄²⁻, 13-PO₄³⁻, 14-ClO₄⁻, 15-AcO⁻, 16-NO₃⁻, 17-F⁻, 18-Cl⁻, 19-PF₆⁻, 20-P₂O₇⁴⁻].

Interestingly all the chemosensors, **H₃L2.1-H₃L2.4** also act as colorimetric probe for selective detection of Al³⁺ ions. In presence Al³⁺ ions all the probes exhibits fluorescent pinkish yellow colouration whereas it is almost colourless in presence of common ions. The intensity of Al³⁺- chemosensor increases in the order **H₃L2.1>H₃L2.2>H₃L2.3>H₃L2.4**. Thus, the chemosensors will be a good choice for selective colorimetric detection of Al³⁺ ions both in environmental and biological fields (**Figure 2.37**). We have used saloon waste water and our laboratory tap water for real sample analysis. Al³⁺ ions present in saloon waste water and laboratory tap water are successfully detected by our chemosensors through naked eye and under UV-lamp (**Figure 2.38**).

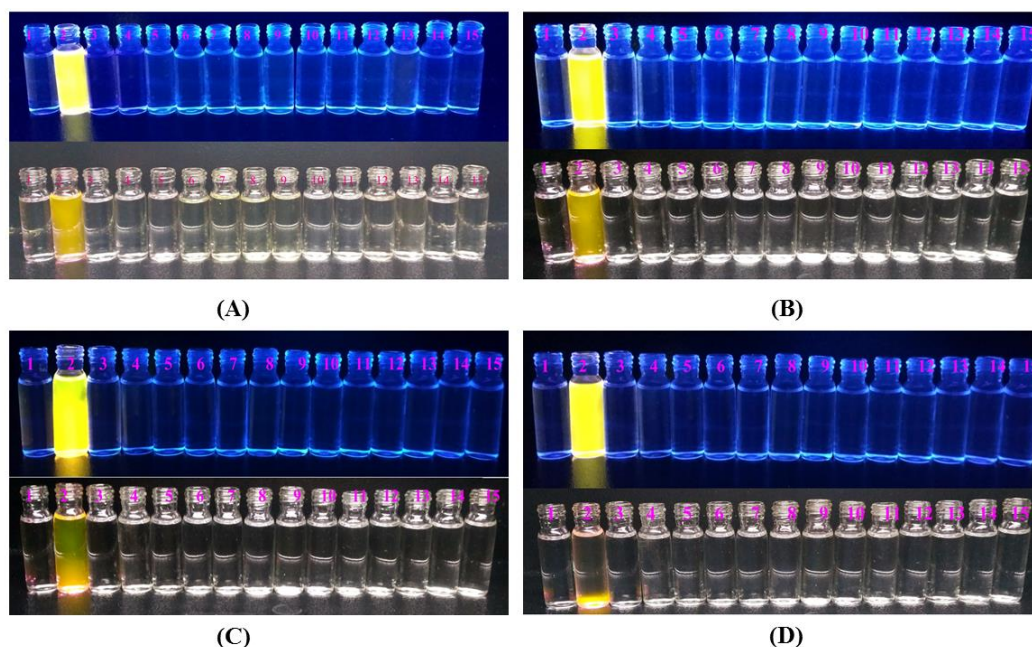


Figure 2.37 Visual colour changes of chemo sensor (A)=**H₃L2.1**, (B)=**H₃L2.2**, (C)=**H₃L2.3** and (D)=**H₃L2.4** (10 μ M) in presence of common metal ions (1equivalent) in 10 mM HEPES buffer (pH 7.4). The images in below row and above row were taken under visible light and UV light respectively. Where 1= only **H₃L2.1/ H₃L2.2/ H₃L2.3/ H₃L2.4**, 2-15= **H₃L2.1/**

H₃L2.2/ H₃L2.3/ H₃L2.4 + different metal ions (Al³⁺, Cu²⁺, Cd²⁺, Pb²⁺, Hg²⁺, Mn²⁺, Fe³⁺, Co²⁺, Ni²⁺, K⁺, Na⁺, Mg²⁺, Ca²⁺ and Zn²⁺ respectively).

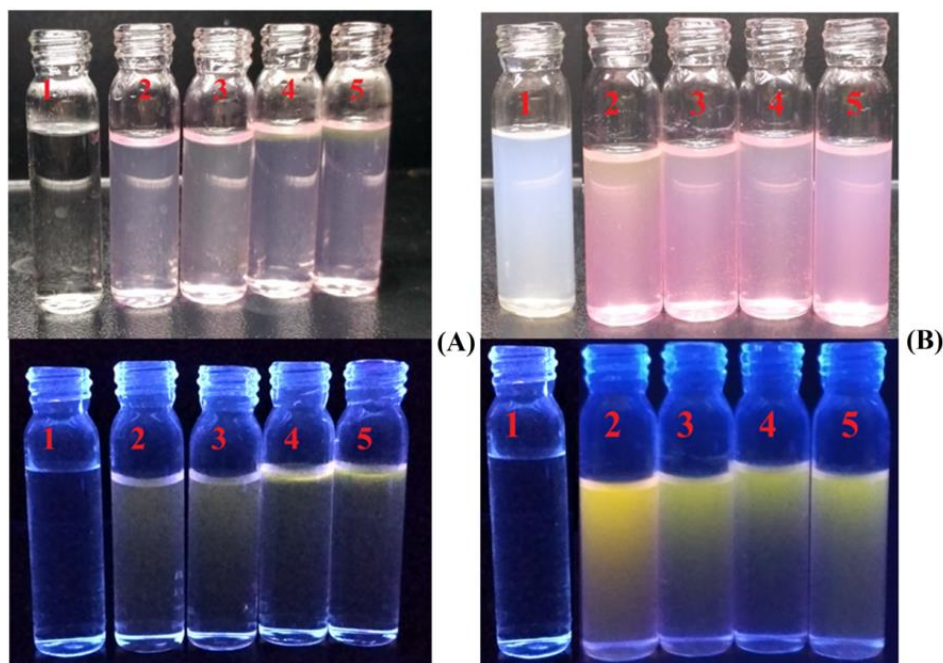


Figure 2.38 Visual colour changes of real samples under normal light (above) and UV lamp (below) in presence of chemosensors (**H₃L2.1- H₃L2.4**). (A) Laboratory tap water (1= Only laboratory tap water, 2-5=laboratory tap water + **H₃L2.1- H₃L2.4**). (B) Saloon waste water, (1= Only saloon waste water, 2-5= Saloon waste water + **H₃L2.1- H₃L2.4**).

Reversibility and regeneration are the two important factors for real time application of the chemosensor. This is tested with the aid of sodium salt of ethylenediaminetetraacetic acid (Na₂EDTA) solution. The fluorescent pinkish yellow colour of probe-Al³⁺ complex disappears after addition of one equivalent of Na₂EDTA with simultaneous decrease in fluorescence intensity which clearly indicates the regeneration of the free chemosensor. Again, addition of Al³⁺ ions to the probe gives back fluorescent pinkish yellow colouration. The whole cycle repeat for at least five times to establish reversibility and regeneration point (**Figure 2.39**).

Limit of detection (LOD) of the chemosensors towards Al³⁺ ions are estimated using 3 σ method.^{2,65} The detection limit of the chemosensors (**H₃L2.1-H₃L2.4**) for the Al³⁺ ions are 1.4×10^{-9} M, 2.50×10^{-9} , 0.40×10^{-8} M and 0.53×10^{-8} M, respectively.

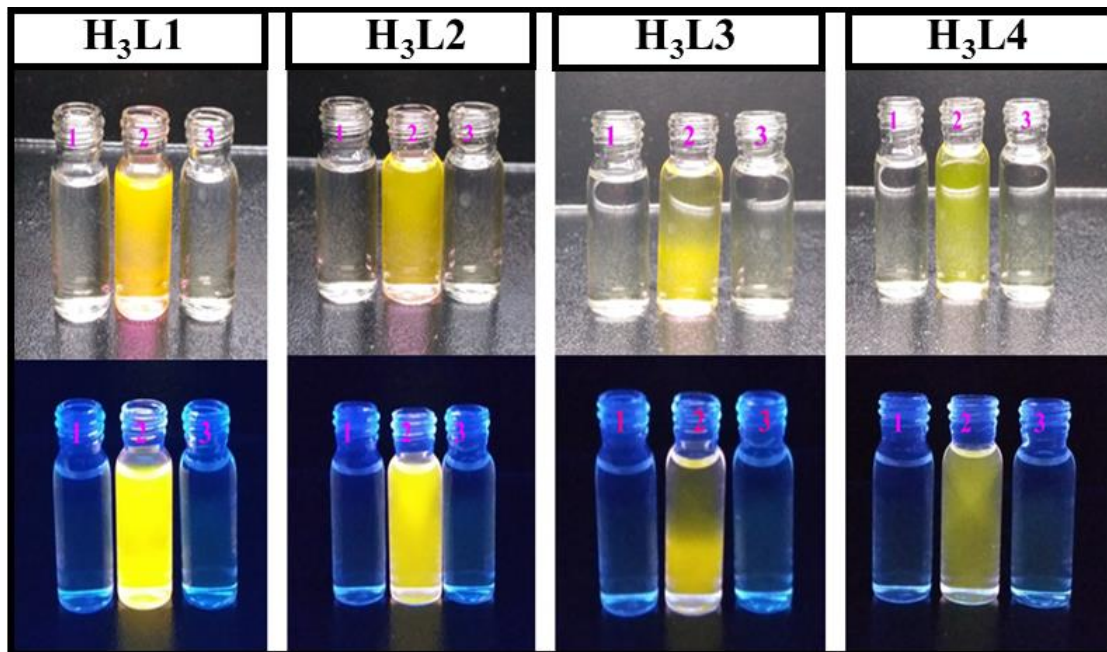


Figure 2.39 Visual colour changes in reversibility experiments. For **H₃L2.1-H₃L2.4**, 1= Only **H₃L2.1-H₃L2.4** (10 μ M), 2= **H₃L2.1-H₃L2.4** (10 μ M) + Al³⁺(10 μ M), 3= **H₃L2.1-H₃L2.4** (10 μ M) + Al³⁺(10 μ M) + EDTA²⁻(10 μ M) under UV and normal light, respectively.

The effect of pH on chemosensors (**H₃L2.1-H₃L2.4**) both in free condition and in presence of Al³⁺ ions are studied fluorimetrically. It is well known that in acidic condition spirolactam ring of the chemosensor opens. Similar observation is also noticed in presence of Al³⁺ ions. Therefore, both free chemosensor and chemosensor -Al³⁺ adduct will exhibit high fluorescence intensity at pH 2-4. At pH 5 a sharp decrease in fluorescence intensity of free chemosensor is observed. After pH 5 to pH 11 its fluorescence intensity is very weak and remains unchanged. This observation suggests reconstruction of spirolactam ring in neutral and basic condition. In presence of Al³⁺ ions fluorescence intensity of the chemosensor decrease a little after pH 4 and then it maintain a constant value up to pH 8. At pH 9 a sharp decrease in fluorescence intensity of chemosensor is observed. After pH 9 to pH 11, very

weak fluorescence intensity observed. This is probably due to generation of Al(OH)₃ and free chemosensor at higher pH. Rest of the probes (**H₃L2.1-H₃L2.4**) and probe-Al³⁺ adducts are also followed a similar trend in fluorescence intensity at different pH values (**Figure 2.40**). The pH experiments show that these chemosensors can act as a selective fluorescent probe to recognize Al³⁺ ions in presence of other metal ions in biological system under physiological condition.

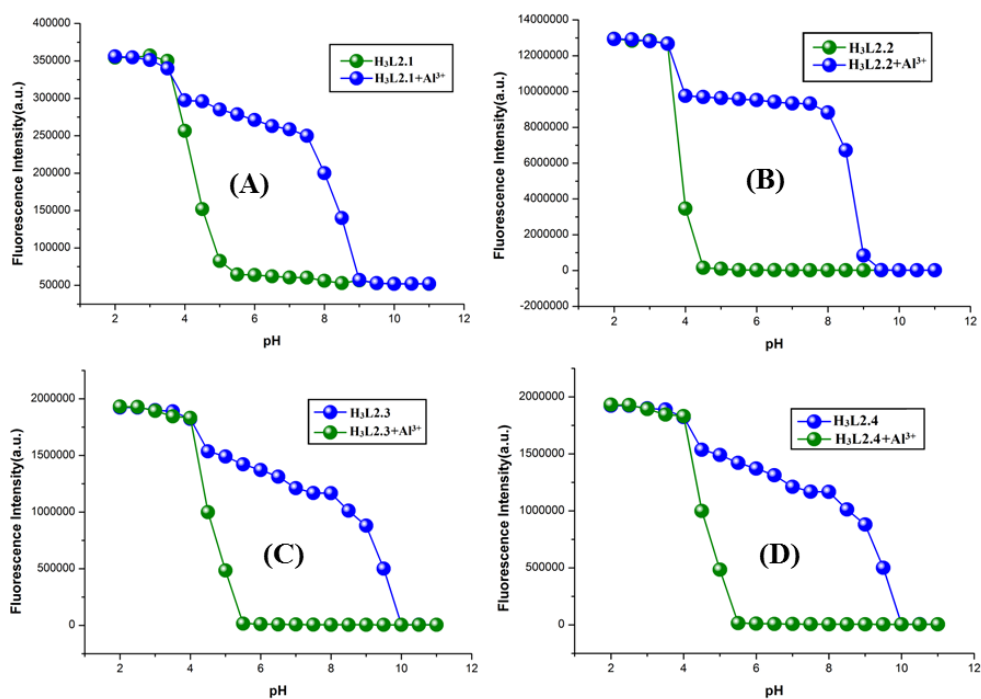


Figure 2.40 Fluorescence intensity of **H₃L2.1-H₃L2.4** (10 μ M) in the absence and presence of Al³⁺ ions (10 μ M) at different pH values in 10 mM HEPES buffer [(A)=**H₃L2.1**, (B)=**H₃L2.2**, (C)=**H₃L2.3** and (D)=**H₃L2.4**].

2.3.6 Life time and quantum yield study

Lifetime measurement for the chemosensors (**H₃L2.1-H₃L2.4**) and complexes **2.1-2.4** are studied at 25°C in 10 mM HEPES buffer (pH= 7.4) medium. The average values of fluorescence decay life time of the chemosensors and complexes **2.1-2.4** have been measured using the given formula ($\tau_f = a_1\tau_1 + a_2\tau_2$, where a_1 and a_2 are relative amplitude of decay

process). The average values of fluorescence lifetime of the chemosensors (**H₃L2.1-H₃L2.4**) and complexes **2.1-2.4** are 3.95, 2.56, 1.58, 1.06 ns and 6.8, 4.58, 4.53, 4.38, respectively (**Figure 2.41, Table 2.5**).

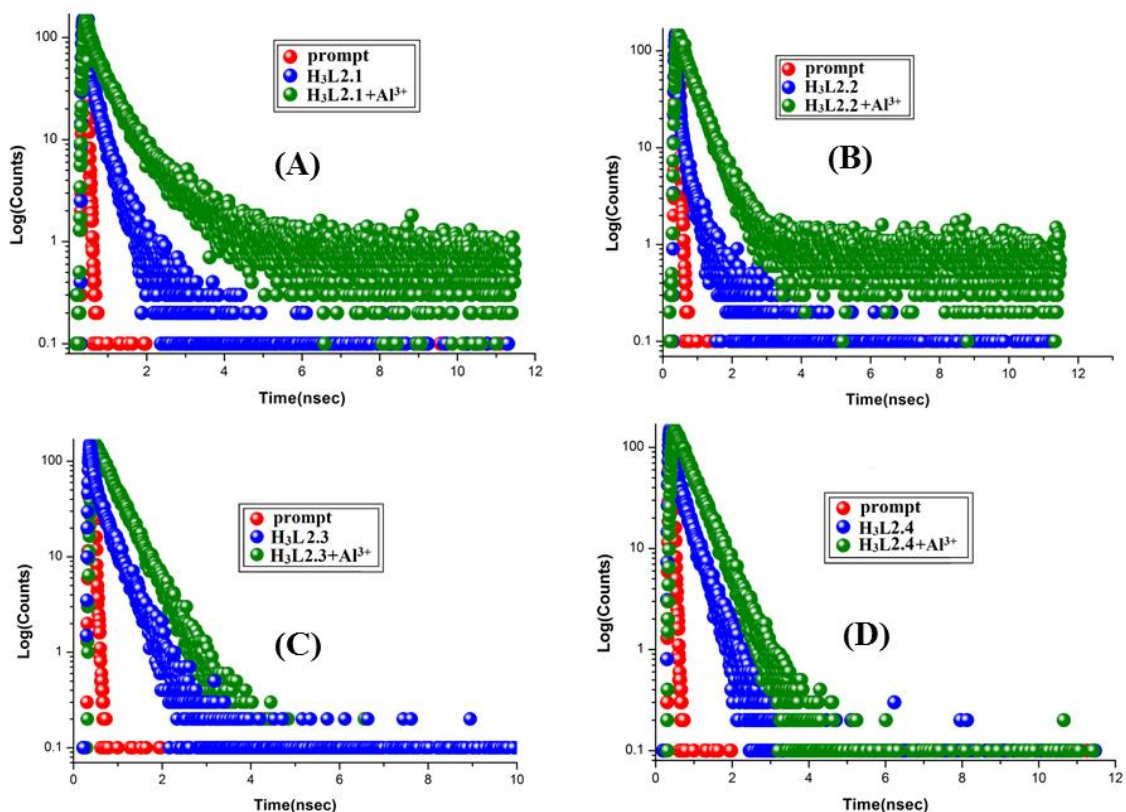


Figure 2.41. Time-resolved fluorescence decay curves (logarithm of normalized intensity vs time in ns) of **H₃L2.1-H₃L2.4** in the absence (●) and presence (●) of Al³⁺ion, (●) indicates decay curve for the scattered [(A)=**H₃L2.1**, (B)=**H₃L2.2**, (C)=**H₃L2.3** and (D)=**H₃L2.4**].

Fluorescence quantum yield (Φ) has been calculated as follows:

$$\Phi_{\text{sample}} = \left\{ \frac{(\text{OD}_{\text{standard}} \times A_{\text{sample}} \times \eta_{\text{sample}}^2)}{(\text{OD}_{\text{sample}} \times A_{\text{standard}} \times \eta_{\text{standard}}^2)} \right\} \times \Phi_{\text{standard}}$$

In the above equation, A is the area under the emission spectral curve, OD is the optical density of the compound at the excitation wavelength and η is the refractive index of the solvent. Φ_{standard} value is taken as 0.52 (for Quinine Sulfate).

The values of Φ for **H₃L2.1-H₃L2.4** and probe-Al³⁺ complexes **2.1-2.4** are estimated to be 0.004, 0.003, 0.002, 0.004 and 0.24, 0.18, 0.13, 0.11, respectively (**Table 2.5**).

Table 2.5. Lifetime, quantum yield, LOD and binding constant values of chemosensors (**H₃L2.1-H₃L2.4**) and complexes (**2.1-2.4**).

	Lifetime (ns) ($\tau_{av.}$)	Quantum Yield (Φ)	LOD (nM)	Binding Constant (M^{-1})
H₃L2.1	3.95	0.004	-	-
H₃L2.2	2.56	0.003	-	-
H₃L2.3	1.58	0.002	-	-
H₃L2.4	1.06	0.004	-	-
Complex 2.1	6.80	0.24	1.40	8.00×10^5
Complex 2.2	4.58	0.18	2.50	6.90×10^5
Complex 2.3	4.53	0.13	4.00	1.37×10^4
Complex 2.4	4.38	0.11	5.30	1.03×10^4

2.3.7 Mechanism of fluorescence intensity enhancement in chemosensors in the order **H₃L2.1>H₃L2.2>H₃L2.3>H₃L2.4** in presence of Al³⁺ ions

In this work sensing behavior of four rhodamine 6G based chemosensors towards Al³⁺ ions are explored. Fluorescence intensity of the chemosensors increases abruptly in presence of Al³⁺ ions due to opening of the spirolactam ring (Scheme 2.1). This mechanistic process has been supported by spectroscopic techniques such as ¹H, ¹³C NMR and FT-IR spectroscopy.^{31,34,36-38,40} In presence of Al³⁺ ions appreciable changes are observed in their ¹H NMR spectrum of free chemosensors. Presence of Al³⁺ ion initiates spirolactam ring opening followed by rearrangement of double bonds. This results disappearance of one aliphatic amine (-NH) proton. Disappearance of phenolic -OH peak and downfield shift of imine proton (9.30 ppm) establish coordination of phenoxido oxygen and imine nitrogen atom with the metal center. Changes in spectral pattern of both aromatic and aliphatic protons are also observed after addition of Al³⁺. In free chemosensor, the carbon atom connecting the xanthene part and spirolactam ring is *sp*³ hybridized and it appears at 66.24 ppm.

Interestingly, during metal coordination, spiro lactam ring opens, as a result the sp^3 hybridized carbon atom become sp^2 hybridized and appears at 134.90 ppm. Free chemosensors exhibit FT-IR stretching frequency of amide 'C=O' bond and imine bond at ~ 1699 and ~ 1674 cm^{-1} , respectively, which are shifted significantly to lower value and appear at ~ 1663 and ~ 1646 cm^{-1} , respectively, after complexation. Sharp -OH peak at 3408 cm^{-1} also disappears after complexation. This observation suggests Al³⁺ ion coordination with phenoxido oxygen, amide oxygen and imine nitrogen of the chemosensor. Therefore, FT-IR data also supports spiro lactam ring opening in presence of Al³⁺ ion.

All chemosensors are colourless and nonfluorescent in visible light. Presence of Al³⁺ ions initiates opening of spiro lactam ring and colour become intense, pinkish yellow. The intensity of colour is not similar. In presence of Al³⁺ ions intensity increases in the order **H₃L2.1**>**H₃L2.2**>**H₃L2.3**>**H₃L2.4**. Again, **H₃L2.1**, **H₃L2.2**, **H₃L2.3** and **H₃L2.4** exhibit around 780, 725, 425 and 391 times increase of fluorescence intensity in presence of Al³⁺ ions. The LOD values are 1.4×10^{-9} M, 2.50×10^{-9} M, 0.40×10^{-8} M and 0.53×10^{-8} M, respectively. The values of binding constant of the probes towards Al³⁺ ions are 8.00×10^5 M⁻¹, 6.90×10^5 M⁻¹, 1.37×10^4 M⁻¹ and 1.03×10^4 M⁻¹ respectively. Here, enhancement in fluorescence intensity of the chemosensors in presence of Al³⁺ ions and binding constant values of the probes towards Al³⁺ ions follow the same order **H₃L2.1**>**H₃L2.2**>**H₃L2.3**>**H₃L2.4**. All these facts can be well explained by considering two factors, influence of ring strain during interaction between chemosensors and Al³⁺ ions and electron withdrawing effect (-I effect) of the halogen substituent present in the chemosensors. Interestingly, the first effect is more pronounced. **H₃L2.1** and **H₃L2.2** form more stable five member chelate rings with Al³⁺ ions whereas **H₃L2.3** and **H₃L2.4** form eight member chelate rings in presence of Al³⁺ ions (**Figure 2.42**). Also, in presence of bromo substituent coordination ability of the imine nitrogen and phenoxido oxygen of the respective

chemosensor is relatively high in comparison with chloro substituent due to $-I$ effect. Therefore, due to formation of most stable H_3L1-Al^{3+} complex, the intensity of the complex solution under visible light is maximum, binding constant is the highest and LOD value is the lowest among four chemosensors.

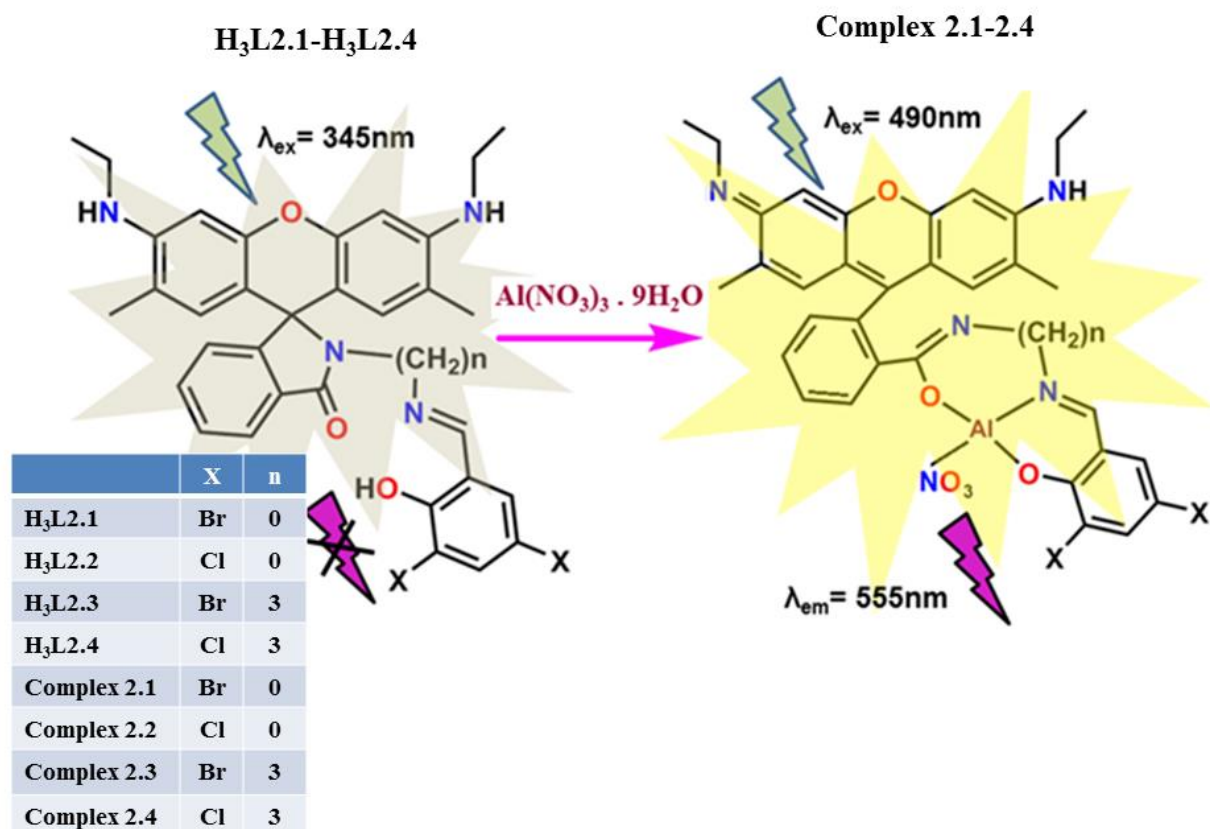


Figure 2.42 Pictorial representation of spiro-lactam ring opening in presence of Al³⁺ ions.

2.3.8 Biocompatibility study of the ligands

The cellular toxicity of the ligands (**H₃L2.1**, **H₃L2.2**, **H₃L2.3** and **H₃L2.4**) are envisaged to determine the compatibility against the normal human lung fibroblast cells, WI-38. The cells are exposed with various concentrations (20 - 100 μ M/ml) of the ligands. Then the cells are incubated for 24 hrs and then the cellular survivability is determined with the help of MTT assay. From the results, no significant toxicity is observed even at enhanced concentrations of 100 μ M (as seen in **Figure 2.43**). Hence, the results clearly depict the

biocompatibility of the ligands and also suggest that these ligands have the potential to emerge as promising tools for application in biomedical fields.

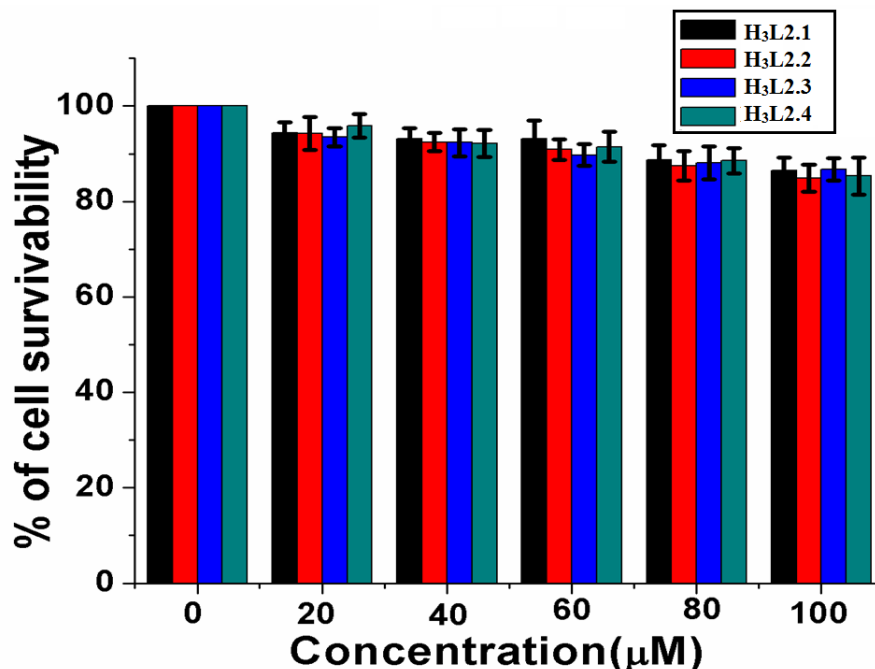


Figure 2.43 Survivability of WI38 cells exposed to H₃L2.1-H₃L2.4.

2.3.9 Cell imaging

The cellular internalization of the chemosensors (H₃L2.1-H₃L2.4) (10 μM) and Al³⁺ salt (10 μM) has been determined with the aid of detailed fluorescence microscopy studies. The fluorescence microscopic images reveal the presence of a promiscuous red fluorescent signal in the microscope (**Figure 2.44**). Henceforth the results suggest that the ligands and the Al³⁺ salts are promptly internalized by the cells which in turn are responsible for the emergence of red fluorescent signal.

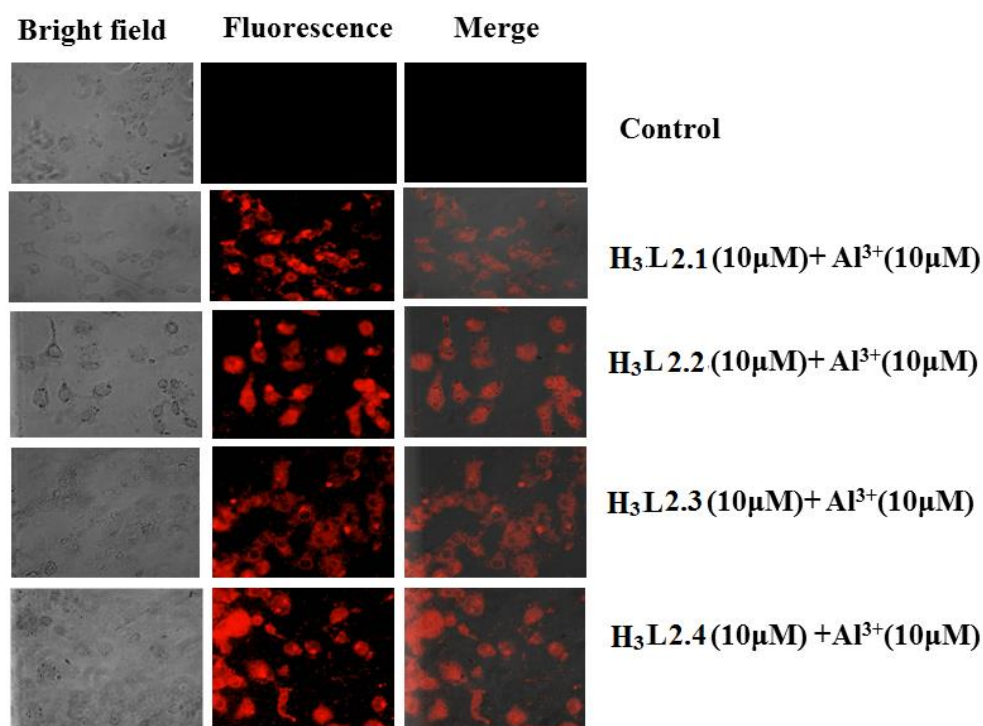


Figure 2.44 Bright field, fluorescence and merged microscopic images of untreated MDA-MB-468 (Control), cells in presence of with chemosensor (**H₃L2.1-H₃L2.4**) (10 μM) + Al³⁺ (10 μM).

2.3.10 DFT study

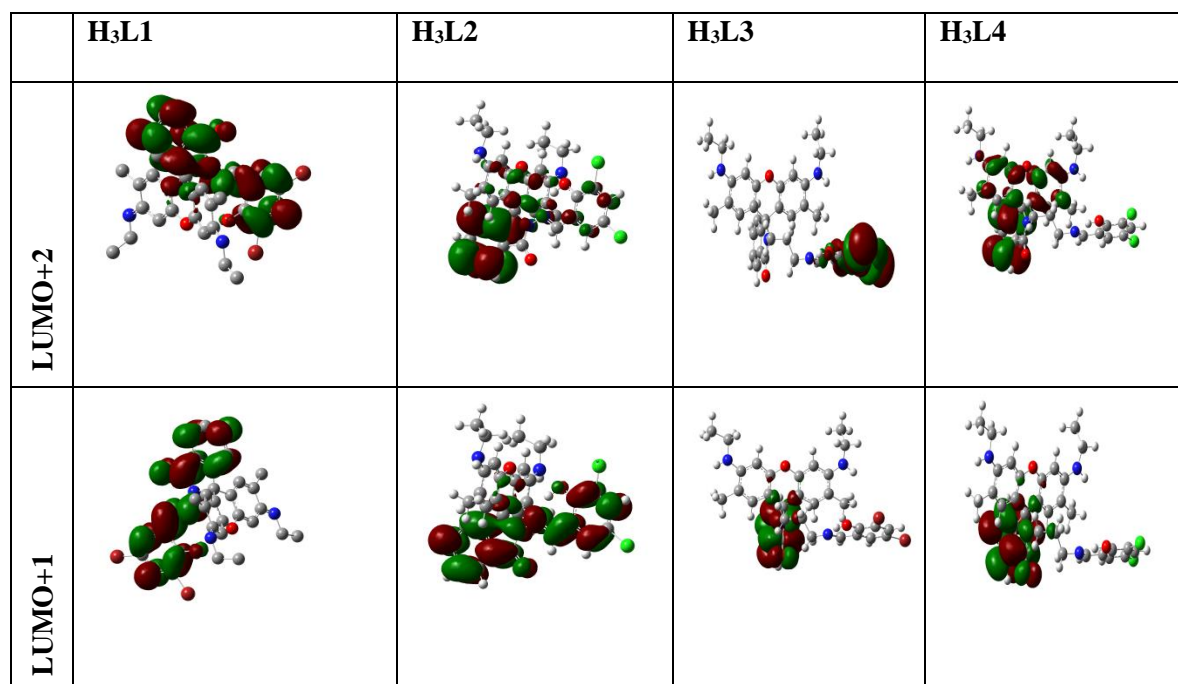
DFT and TDDFT studies are performed to establish structural and electronic parameters of probes. Furthermore, to understand nature, origin and contribution of M.O.s for electronic transitions TDDFT study was performed. This study gives idea of quantity of energy associated with every individual transition. In each individual M.O. the contribution from both chemosensor and metal center has been computed. Therefore, DFT and TDDFT analysis play an important role to support and understand structural and electronic parameters of complexes.

Here, geometry optimization of the chemosensors (**H₃L2.1-H₃L2.4**) has been performed using DFT/B3LYP process. Some important bond distances and bond angles of all the chemosensors (**H₃L2.1-H₃L2.4**) are listed in **Table 2.2** and **2.3**. Energy (eV) of some

selected M.O.s are included in **Table 2.6**. Contour plots of some selected molecular orbital of the chemosensors are depicted in **Figure 2.45**. Theoretical calculations reveal that in **H₃L2.1** electron density in LUMO is mainly distributed over the xantheno part and electron density in HOMO is mainly distributed over the xantheno part and spirolactam ring. In **H₃L2.2** electron density in LUMO is mainly distributed over the salicyl part and spirolactam ring adjacent aromatic moiety and electron density in HOMO is mainly distributed over the xantheno part. LUMOs of both **H₃L2.3** and **H₃L2.4** are mainly salicyl part based, whereas, HOMOs are mainly xantheno moiety based.

Table 2.6. Energy (eV) of selected M.O.s of chemosensors (**H₃L2.1-H₃L2.4**).

	H₃L2.1	H₃L2.2	H₃L2.3	H₃L2.4
LUMO+2	-1.03	-0.52	-0.44	-0.41
LUMO+1	-1.91	-0.99	-1	-1
LUMO	-2.99	-2.76	-1.7	-1.7
HOMO	-4.82	-5.34	-5.26	-5.26
HOMO-1	-6.06	-5.46	-5.37	-5.38
HOMO-2	-6.2	-5.96	-5.91	-5.91



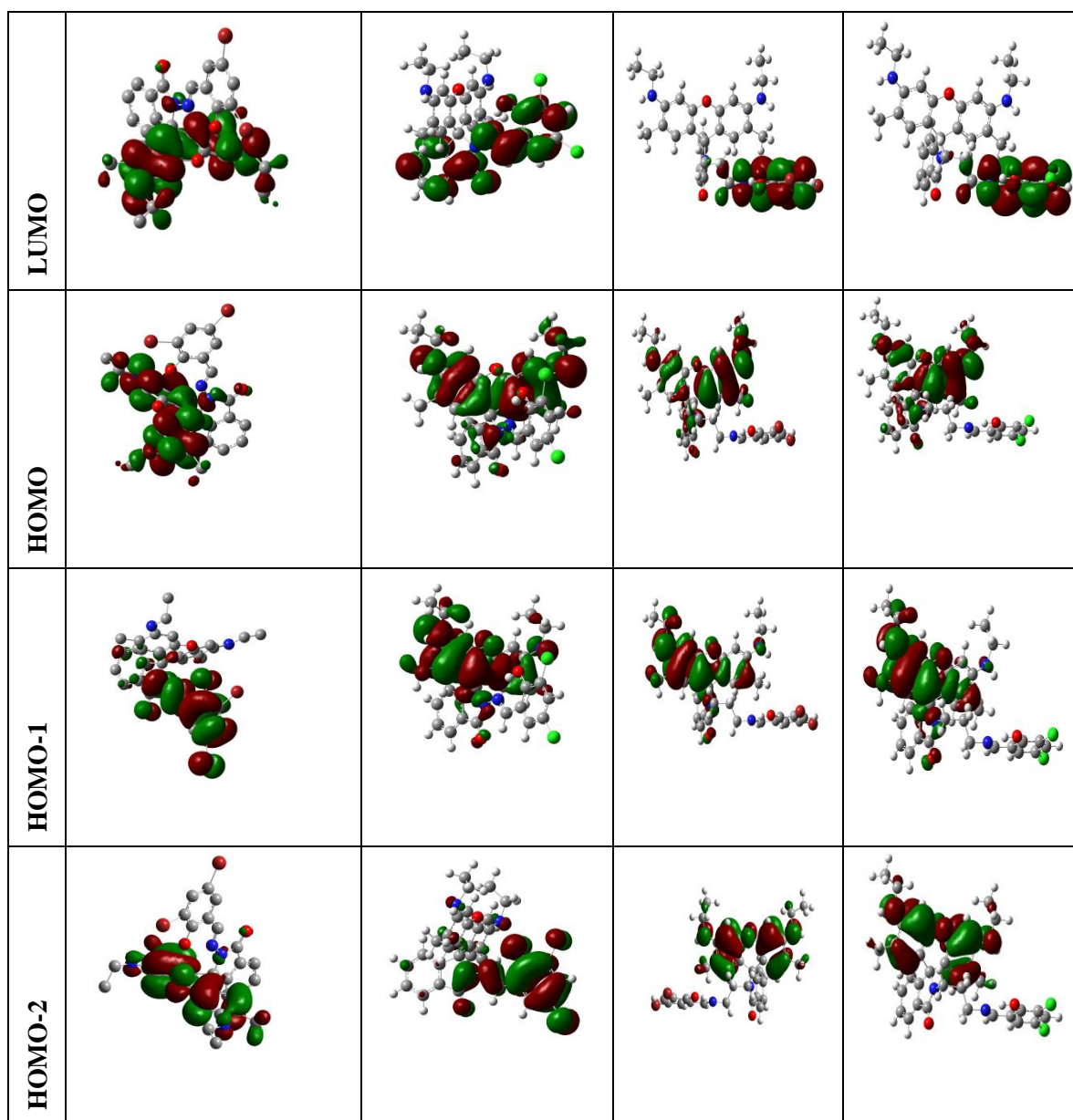


Figure 2.45 Selected contour plots of molecular orbitals of **H₃L2.1-H₃L2.4**.

2.3.11 TDDFT study

Electronic transitions in chemosensors (**H₃L2.1-H₃L2.4**) are theoretically studied using TDDFT, B3LYP/CPCM method. Important electronic transitions are given in **Table 2.7**. In theoretical calculations, for **H₃L2.1** and **H₃L2.2** intense absorption bands found at around 355 and 345 nm, respectively. Major transitions for **H₃L2.1** are HOMO-2→LUMO (88%) and HOMO-1→LUMO (74%) (**Figure 2.46**) whereas for **H₃L2.2**, the key transitions

are HOMO-2→LUMO (99%) and HOMO-3→LUMO (96%), respectively (**Figure 2.46**). In case of **H₃L2.3** and **H₃L2.4**, two major bands observe at around 420 nm and 400 nm which correspond to the HOMO→LUMO (96%) and HOMO-1→LUMO (95%) (**H₃L2.3**) (**Figure 2.47**) and HOMO→LUMO (97%) and HOMO-1→LUMO (96%) (**H₃L2.4**), respectively (**Figure 2.47**).

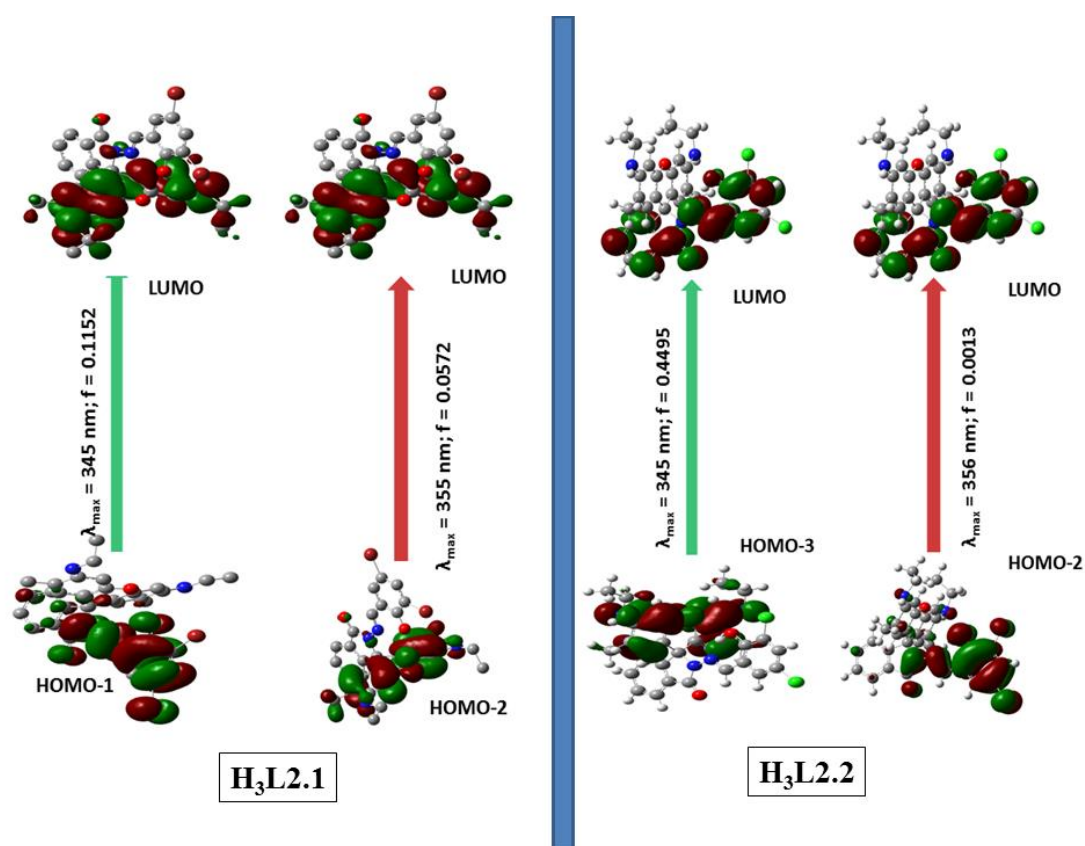


Figure 2.46 Pictorial representation of key transitions involved in UV-Vis absorption of chemosensor **H₃L2.1** and **H₃L2.2**.

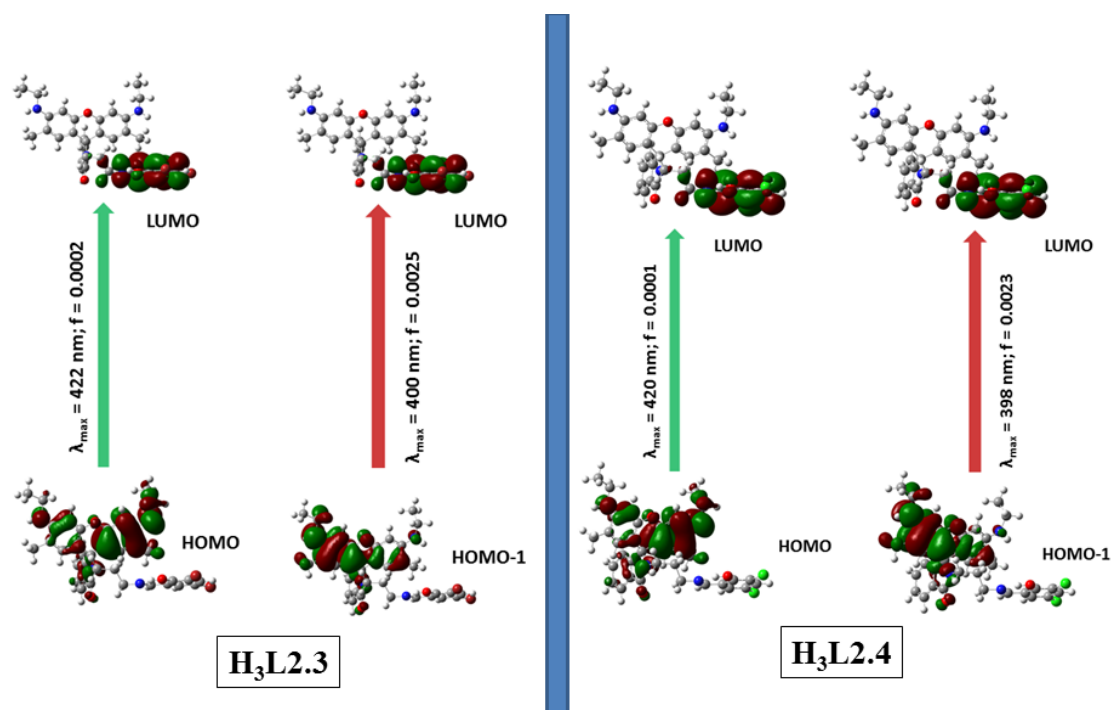


Figure 2.47 Pictorial representation of key transitions involved in UV-Vis absorption of chemosensor **H₃L2.3** and **H₃L2.4**.

Table 2.7. Electronic transition calculated by TDDFT using B3LYP/CPCM method in water solvent of chemosensors (**H₃L1-H₃L4**).

	$E_{\text{excitation}}$ (eV)	$\lambda_{\text{excitation}}$ (nm)	Osc. Strength (f)	Key transition
H₃L2.1	3.48	355	0.0572	HOMO-2 \rightarrow LUMO(88%)
	3.58	345	0.1152	HOMO-1 \rightarrow LUMO(74%)
H₃L2.2	3.49	356	0.0013	HOMO-2 \rightarrow LUMO(99%)
	3.58	345	0.4495	HOMO-3 \rightarrow LUMO(96%)
H₃L2.3	3.12	422	0.0002	HOMO \rightarrow LUMO(96%)
	3.35	400	0.0025	HOMO-1 \rightarrow LUMO(95%)
H₃L2.4	3.10	420	0.0001	HOMO \rightarrow LUMO (97%)
	3.35	398	0.0023	HOMO-1 \rightarrow LUMO(96%)

2.4 Conclusion

In this work, we have successfully developed four new rhodamine 6G based fluorescent and colorimetric chemosensors **H₃L2.1–H₃L2.4** for rapid and selective detection of Al³⁺ ions. In naked eyes, the intensity of the colour of probe-Al³⁺ ions increase in the order **HL2.4-Al³⁺** < **HL2.3-Al³⁺** < **HL2.2-Al³⁺** < **HL2.1-Al³⁺**. All four chemosensors form 1:1 complex with Al³⁺ ions which have been proved by fluorescence measurements, ESI-MS analysis and NMR studies. In fluorescence competition assay experiments selectivity of the probes towards Al³⁺ ions is established. Moreover, the reversibility is also achieved by addition of Na₂EDTA solution. **H₃L2.1**, **H₃L2.2**, **H₃L2.3** and **H₃L2.4** exhibit around 780, 725, 425 and 391 times enhancement in fluorescence intensity in presence of Al³⁺ ions. Al³⁺ is detected in nanomolar scale and the LOD values are 1.4×10^{-9} M, 2.50×10^{-9} M, 0.40×10^{-8} M and 0.53×10^{-8} M, respectively. All the probes are suitable for real-time quantitative detection of Al³⁺ ions in the field of environmental samples and biological systems. The values of binding constant of the probes towards Al³⁺ ions are 8.00×10^5 M⁻¹, 6.90×10^5 M⁻¹, 1.37×10^4 M⁻¹ and 1.03×10^4 M⁻¹, respectively. In this work we have also established influence of ring strain and electron withdrawing effect (-I effect) of the halogen substituents present in the chemosensors during interaction between chemosensors and Al³⁺ ions. Interestingly, the first effect is more pronounced compare to the other. Colour intensity difference of the probes in presence of Al³⁺ ions under visible light, different binding constant, quantum yields and LOD values of the probes towards Al³⁺ ions can be well explained in the light of the above two factors. **H₃L2.1** and **H₃L2.2** form more stable five member chelate ring with Al³⁺ ions whereas **H₃L2.3** and **H₃L2.4** form eight member chelate ring in presence of Al³⁺ ions (**Figure 2.42**). Also, in presence of bromo substituent coordination ability of the imine nitrogen and phenoxido oxygen of the respective chemosensor is relatively high in comparison with chloro substituent due to less -I effect. We are also successful to reveal its practical application by

performing cell imaging study of chemosensors (**H₃L2.1-H₃L2.4**) using MDA-MB-468 cells. Furthermore, the probes are applied to detect intracellular Al³⁺ ions in live cells with no significant cytotoxicity. We have compared different factors like elucidation of crystal structure of the chemosensors, solubility of chemosensors in the aqueous medium for biological and real sample analyses, selectivity of the chemosensors towards Al³⁺ ions and nanomolar range of LOD values between chemosensors reported in this work and previously reported results. Interestingly, our chemosensors have successfully covered all the points mentioned above in comparison with previously reported results presented in **chart 2.1**.

Performing cell imaging study of chemosensors (**H₃L2.1-H₃L2.4**) using MDA-MB-468 cells. Furthermore, the probes are applied to detect intracellular Al³⁺ ions in live cells with no significant cytotoxicity. We have compared different factors like elucidation of crystal structure of the chemosensors, solubility of chemosensors in the aqueous medium for biological and real sample analyses, selectivity of the chemosensors towards Al³⁺ ions and nanomolar range of LOD values between chemosensors reported in this work and previously reported results. Interestingly, our chemosensors have successfully covered all the points mentioned above in comparison with previously reported results presented in **chart 2.1**.

2.5 References

- (2.1) J. J. Du, M. M. Hu, J. L. Fang, X. J. Peng, *Chem. Soc. Rev.* 2012, **41**, 4511–4535.
- (2.2) A. P. S. Gonzales, M. A. Firmino, C.S. Nomura, F. R. P. Rocha, P. V. Oliveira, I. Gaubeur, *Anal. Chim. Acta.* 2009, **636**, 198–204.
- (2.3) P. Pathirathna, Y. Y. Yang, K. Forzley, S. P. McElmurry, P. Hashemi, *Anal. Chem.* 2012, **84**, 6298–6302.

- (2.4) J. S. Becker, M. V. Zoriy, C. Pickhardt, N. Palomero-Gallagher, K. Zilles, *Anal. Chem.* 2005, **77**, 3208–3216.
- (2.5) Y. Liu, P. Liang, L. Guo, *Talanta*. 2005, **68**, 25–30.
- (2.6) Y. Zhou, Y. Zhang, J. F. Yoon, *J. Chem. Rev.* 2014, **114**, 5511–5571.
- (2.7) J. F. Zhang, Y. Zhou, J. Yoon, J. S. Kim, *Chem. Soc. Rev.* 2011, **40**, 3416–3429.
- (2.8) G. Muller, V. Bernuzzi, D. Desor, *Teratology*. 1990, **42**, 253-261.
- (2.9) J. M. Donald, M. Golub, *SNeurotoxicol. Teratol.* 1989, **11**, 231-235.
- (2.10) R. J. P. Williams, *Chem. Rev.* 2002, **228**, 93-97.
- (2.11) R. A. Yokel, *Coord. Chem. Rev.* 2002, **228**, 97-113.
- (2.12) M. Baral, S. K. Sahoo, B. K. J. Kanungo, *Inorg. Biochem.* 2008, **102**, 1581-1688.
- (2.13) M. Kawahara, K. Muramoto, K. Kobayashi, H. Mori, Y. Kroda, *Biochem. Biophys. Res. Commun.* 1994, **198**, 531-535.
- (2.14) S. R. Paik, J. H. Lee, D. H. Kim, C. S. Chang, J. Kim, *Arch. Biochem. Biophys.* 1997, **344**, 325-334.
- (2.15) J. L. Lin, M. T. Kou, M. L. Leu, *Nephron*. 1996, **74**, 33-38.
- (2.16) P. F. Good, C. W. Olanow, D. P. Perl, *Brain Res.* 1992, **593**, 343-346.
- (2.17) P. D. Darbre, *J. Inorg. Biochem.* 2005, **99**, 1912-1919.
- (2.18) D. K. Singha, P. Mahata, *Inorg. Chem.* 2015, **54**, 6373–6379.
- (2.19) Q. Diao, P. Ma, L. Lv, T. Li, Y. Sun, X. Wang, D. Song, *Sens. Actuators B.* 2016, **229**, 138–144.
- (2.20) B. Naskar, R. Modak, Y. Sikdar, D. K. Maiti, A. Bauzá, A. Frontera, A. Katarkar, K. Chaudhuri, S. Goswami, *Sens. Actuators B.* 2017, **239**, 1194–1204.
- (2.21) V. K. Gupta, A. K. Singh, L. K. Kumawat, *Sens. Actuators B.* 2014, **195**, 98–108.
- (2.22) V. K. Gupta, N. Mergu, L. K. Kumawat, A. K. Singh, *Talanta*. 2015, **144**, 80–89.

- (2.23) V. K. Gupta, A. K. Jain, G. Maheshwari, *Talanta*. 2007, **72**, 1469–1473.
- (2.24) Y. Ding, W. Zhu, Y. Xu, X. Qian, *Sens. Actuators B*. 2015, **220**, 762–771.
- (2.25) X. Wan, T. Liu, H. Liu, L. Gu, Y. Yao, *RSC Adv*. 2014, **4**, 29479–29484.
- (2.26) L. Wang, H. Li, D. Cao, *Sens. Actuators B*. 2013, **181**, 749–755.
- (2.27) Y. Lu, S. Huang, Y. Liu, S. He, L. Zhao, X. Zeng, *Org. Lett.* 2011, **13**, 5274-5277.
- (2.28) (a) Y. Tachapermpon, S. Thavornpradit, A. Charoenpanich, J. Sirirak, K. Burgess, N. Wanichacheva, *Dalton Trans*. 2017, **46**, 16251-16256. (b) T. Liu, Y. Dong, X. Wan, W. Li, Y. Yao, *RSC Adv*. 2015, **5**, 76939-76942.
- (2.29) (a) L. Hou, J. Feng, Y. Wang, C. Dong, S. Shuang, Y. Wang, *Sens. Actuators B*, 2017, **247**, 451-460; (b) J. -c. Qin, L. Fan, B. -d. Wang, Z. -y. Yang, T. -r. Li, *Anal. Methods*. 2015, **7**, 716-722.
- (2.30) X. Chen, T. Pradhan, F. Wang, J. S. Kim, J. Yoon, *Chem. Rev.* 2012, **112**, 1910-1956.
- (2.31) H. N. Kim, M. H. Lee, H. J. Kim, J. S. Kim, J. Yoon, *Chem. Soc. Rev.* 2008, **37**, 1465-1472.
- (2.32) V. Dujols, F. Ford, A.W. Czarnik, *J. Am. Chem. Soc.* 1997, **119**, 7386-7387.
- (33) D. T. Quang, J. S. Kim, *Chem. Rev.* 2010, **110**, 6280-6301.
- (2.34) X.-M. Li, R. -R. Zhao, Y. Yang, X. W. Lv, Y. -L. Wei, R. Tan, J. -F. Zhang, Y. Zhou, *Chinese Chem. Lett.*, 2017, **28**, 1258-1261.
- (2.35) J. Y. Kwon, Y. J. Jang, Y. J. Lee, K. M. Kim, M. S. Seo, W. Nam, J. Yoon, *J. Am. Chem.* 2005, **127**, 10107-10111.
- (2.36) Y. Wang, H. -Q. Chang, W. -N. Wu, X. -J. Mao, X. -L. Zhao, Y. Yang, Z. -Q. Xu, Z. -H. Xu, L. Jia, *J. Photochem. Photobiol. A*, 2017, **335**, 10-16.
- (2.37) R. Alam, R. Bhowmick, A. S. M. Islam, A. katarkar, K. Chaudhuri, M. Ali, *New J. Chem.*, 2017, **41**, 8359-8369.

- (2.38) J. W. Jeong, B. A. Rao, Y. -A. Son, *Sens. Actuators B*, 2015, **208**, 75-84.
- (2.39) V. K. Gupta, N. Mergu, L. K. Kumawat, *Sens. Actuators B*. 2016, **223**, 101-113.
- (2.40) K.-S. Ku, P. Muthukumar, S. Angupillai, Y.-A. Son, *Sens. Actuators B*, 2016, **236**, 184-191.
- (2.41) L. Hou, J. Feng, Y. Wang, C. Dong, S. Shuang, Y. Wang, *Sens. Actuators B*. 2017, **247**, 451-460.
- (2.42) M. Maniyazagan, R. Mariadasse, M. Nachiappan, J. Jeyakanthan, N.K. Lokanath, S. Naveen, G. Sivaraman, P. Muthuraja, P. Manisankar, T. Stalin, *Sens. Actuators B*. 2018, **254**, 795-804.
- (2.43) Q. Huang, Q. Zhang, E. Wang, Y. Zhou, H. Qiao, L. Pang, F. Yu, *Spectrochimica Acta Part A*. 2016, **152**, 70-76.
- (2.44) (a) G. Yang, X. Meng, S. Fang, L. Wang, Z. Wang, F. Wang, H. Duan, A. Hao, *New J. Chem.* 2018, **42**, 14630–14641. (b) J. W. Jeong, B. A. Rao, Y. Son, *Sensors and Actuators B* 2015, **208**, 75–84. (c) S. Chemate, N. Sekar, *Sensors and Actuators B* 2015, **220**, 1196–1204. (d) S. B. Maity, P. Bharadwaj, *Inorg. Chem.* 2013, **52**, 1161–1163. (e) A. Roy, U. Shee, A. Mukherjee, S. K. Mandal, P. Roy, *ACS Omega* 2019, **4**, 6864–6875. (f) M. Ghosh, S. Mandal, S. Ta, D. Das, *Sensors and Actuators B* 2017, **249**, 339–347. (g) R. Alam, R. Bhowmick, A. S. M. Islam, A. katarkar, K. Chaudhuri, M. Ali, *New J. Chem.* 2017, **41**, 8359–8369. (h) Y. Fu, X. -J. Jiang, Y. -Y. Zhu, B. -J. Zhou, S. -Q. Zang, M. -S. Tang, H. -Y. Zhang, T. C. W. Maka, *Dalton Trans.* 2014, **43**, 12624–12632. (i) A. Sahana, A. Banerjee, S. Lohar, A. Banik, S. K. Mukhopadhyay, D. A. Safin, M. G. Babashkina, M. Bolte, Y. Garcia, D. Das, *Dalton Trans.* 2013, **42**, 13311–13314. (j) A. Roy, R. Mukherjee, B. Dam, S. Dam, P. Roy, *New J. Chem.* 2018, **42**, 8415–8425. (k) B. Sen, M. Mukherjee, S. Banerjee, S. Pal, P. Chattopadhyay, *Dalton Trans.* 2015, **44**, 8708–8717. (l) A. Sahana, A. Banerjee, S. Lohar, B. Sarkar, S. K. Mukhopadhyay, D. Das, *Inorg. Chem.* 2013, **52**, 3627–3633.

- (2.45) G. M. Sheldrick, SAINT, Version 6.02, SADABS, Version 2.03, Bruker AXS Inc., Madison, Wisconsin, **2002**.
- (2.46) G. M. Sheldrick, SADABS: Software for Empirical Absorption Correction, University of Gottingen, Institute fur Anorganische Chemieder Universitat, Gottingen, Germany, **1999-2003**.
- (2.47) G. M. Sheldrick, Crystal structure refinement with *SHELXL*. *ActaCryst.* 2015, **C71**, 3-8.
- (2.48) X. F. Yang, X. Q. Guo, Y. B. Zhao, Development of a novel rhodamine-type fluorescent probe to determine peroxyxynitrite. *Talanta.* 2002, **57**, 883-890.
- (2.49) M. J. Frisch, G. W. Trucks, H. B. Schlegel, G. E. Scuseria, M. A. Robb, J. R. Cheeseman, G. Scalmani, V. Barone, B. Mennucci, G. A. Petersson, H. Nakatsuji, M. Caricato, X. Li, H. P. Hratchian, A. F. Izmaylov, J. Bloino, G. Zheng, J. L. Sonnenberg, M. Hada, M. Ehara, K. Toyota, R. Fukuda, J. Hasegawa, M. Ishida, T. Nakajima, Y. Honda, O. Kitao, H. Nakai, T. Vreven, Montgomery, J. A. Peralta, J. E. Jr. F. Ogliaro, M. Bearpark, J. Heyd, J. E. Brothers, K. N. Kudin, V. N. Staroverov, R. Kobayashi, J. Normand, K. Raghavachari, A. Rendell, J. C. Burant, S. S. Iyengar, J. Tomasi, M. Cossi, N. Rega, J. M. Millam, M. Klene, J. E. Knox, J. B. Cross, V. Bakken, C. Adamo, J. Jaramillo, R. Gomperts, R. E. Stratmann, O. Yazyev, A. J. Austin, R. Cammi, C. Pomelli, J. W. Ochterski, R. L. Martin, K. Morokuma, V. G. Zakrzewski, G. A. Voth, P. Salvador, J. J. Dannenberg, S. Dapprich, A. D. Daniels, Ö. Farkas, J. B. Foresman, J. V. Ortiz, J. Cioslowski, D. J. Fox, GAUSSIAN09, Revision D.01, Gaussian Inc. Wallingford, CT, **2009**.
- (2.50) A. D. Becke, *J. Chem. Phys.* 1993, **98**, 5648-5652.
- (2.51) C. Lee, W. Yang, R. G. Parr, *Phys. Rev.*, 1988, **B 37**, 785-789.
- (2.52) P. J. Hay, W. R. Wadt, *J. Chem. Phys.*, 1985, **82**, 270-283.

- (2.53) W. R. Wadt, P. Hay, *J. Chem. Phys.* 1985, **82**, 284-298.
- (2.54) P. J. Hay, W. R. Wadt, *J. Chem. Phys.* 1985, **82**, 299-310.
- (2.55) G. A. Petersson, A. Bennett, T. G. Tensfeldt, M. A. Al-Laham, W. A. Shirley, J. Mantzaris, *J. Chem. Phys.* 1988, **89**, 2193-2218.
- (2.56) G. A. Petersson, M. A. Al-Laham, *J. Chem. Phys.* 1991, **94**, 6081-6090.
- (2.57) R. Bauernschmitt, R. Ahlrichs, *Chem. Phys. Lett.*, 1996, **256**, 454-464.
- (2.58) R. E. Stratmann, G. E. Scuseria, M. Frisch, *J. J. Chem. Phys.*, 1998, **109**, 8218-8224.
- (2.59) M. E. Casida, C. Jamorski, K. C. Casidaand, D. R. Salahub, *J. Chem. Phys.* 1998 , **108**, 4439-4449.
- (2.60) V. Barone, M. Cossi, *J. Phys. Chem. A.* 1998, **102**, 1995-2001.
- (2.61) M. Cossiand, V. Barone, *J. Chem. Phys.* 2001, **115**, 4708-4717.
- (2.62) M. Cossi, N. Rega, G. Scalmani, V. Barone, *J. Comput.Chem.* 2003, **24**, 669-681.
- (2.63) N. M. O'Boyle, A. L. Tenderholt, K. M. Langner, *J. Comput. Chem.* 2008, **29**, 839-845.
- (2.64) H. A. Benesi, J. H. Hildebrand, *J. Am. Chem. Soc.* 1949, **71**, 2703-2707.
- (2.65) A. B. Pradhan, S. K. Mandal, S. Banerjee, A. Mukherjee, S. Das, A. R. K. Bukhsh, A. Saha, *Polyhedron* 2015, **94**, 75-82.

Chapter 3

**Rhodamine-azo based two
fluorescent probes for recognition of
trivalent metal ions: crystal
structures elucidation and biological
application**

Abstract

Two rhodamine and azo based chemosensors, (**HL3.1** = (3',6'-bis(ethylamino)-2-((2-hydroxy-3-methoxy-5-(phenyldiazenyl)benzylidene)amino)-2',7'-dimethylspiro[isindoline-1,9'-xanthen]-3-one) and **HL3.2** = (3',6'-bis(ethylamino)-2-(((2-hydroxy-3-methoxy-5-(p-tolyldiazenyl)benzylidene)amino)-2',7'-dimethylspiro[isindoline-1,9'-xanthen]-3-one) have been synthesized for colorimetric and fluorometric detection of three trivalent metal ions, Al^{3+} , Cr^{3+} and Fe^{3+} . The chemosensors have been thoroughly characterized by different spectroscopic techniques and X-ray crystallography. They are non-fluorescent due to the presence of a spirolactam ring. The trivalent metal ions initiate an opening of spirolactam ring when excited at 490 nm in Britton Robinson buffer solution ($\text{H}_2\text{O}/\text{MeOH}$ 1:9 v/v; pH 7.4). Opening of the spirolactam ring increases conjugation within the probe, which is supported by an intense fluorescent pinkish-yellow colouration and an enhancement of fluorescence intensity of the chemosensors by ~400 times in presence of Al^{3+} and Cr^{3+} ions and by ~100 times in presence of Fe^{3+} ions. Such type of enormous fluorescence enhancement is rarely observed in other chemosensors for the detection of trivalent metal ions. A 2:1 binding stoichiometry of the probes with the respective ions has been confirmed by Job's plot analysis. Elucidation of crystal structures of Al^{3+} bound chemosensors (1 and 4) also justify 2:1 binding stoichiometry and the presence of open spirolactam ring within the chemosensor framework. The limit of detection (LOD) values for both the chemosensors towards the respective metal ions are in the order of $\sim 10^{-9}$ M which supports their application in the biological field. The biocompatibility of the ligands has been studied with the help of MTT assay. Results show that no significant toxicity was observed up to 100 μM of chemosensors concentration. The capability of our synthesized chemosensors to detect intracellular Al^{3+} , Cr^{3+} and Fe^{3+} ions in cervical cancer cell line HeLa was evaluated with the aid of fluorescence imaging.

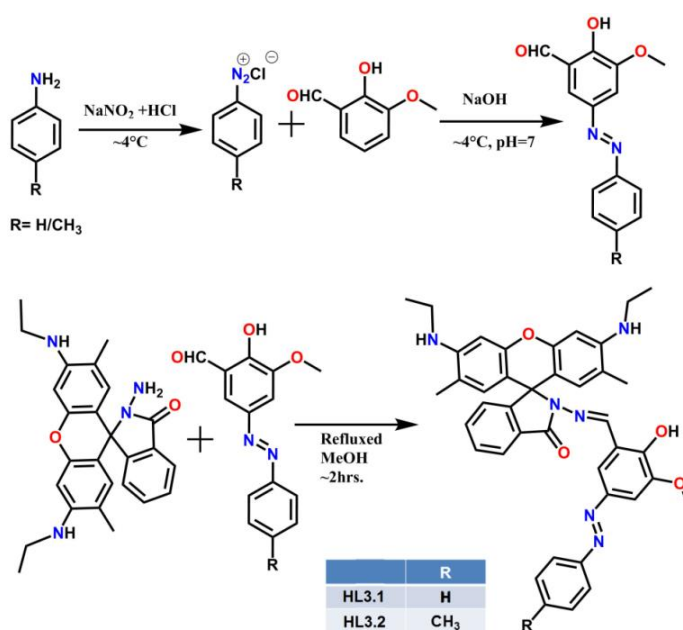
3.1 Introduction

Colorimetric and fluorescent chemosensors which are designed for selective detection of metal ions play crucial role in the development of medicinal and environmental research.^{3.1-3.3} Various techniques such as atomic absorption spectroscopy,^{3.4} inductively coupled plasma-mass spectroscopy,^{3.5} plasma emission spectrometry,^{3.6} neutron activation analysis,^{3.7} chromatography^{3.8} and voltammetry^{3.9} are available for detection of different metal ions in food, biological systems, environmental and industrial samples. Most of these detection techniques are expensive and users face challenges in sample preparation, instrument handling and its costly maintenance charges. In this regard fluorescence study is highly sensitive, user friendly, low cost and real time monitoring process. Among different metal ions, trivalent metal ions, Al^{3+} , Cr^{3+} and Fe^{3+} need special mention. Extensive application of these metals in industry and daily life results their diffusion and contamination in living system and causes a wide variety of diseases.^{3.10} Aluminium is the most abundant metal in the earth's crust and used vastly in domestic purpose. The excessive concentration of Al^{3+} in human body causes myopathy, encephalopathy, microcytic hypochromic anemia, Parkinson's disease and Alzheimer's disease.^{3.11} Iron is an important dietary element since it is present in the active site of different metalloenzymes which play crucial roles in different physiological processes, such as oxygen uptake,^{3.12} oxygen metabolism^{3.13} and electron transfer^{3.14} etc. Therefore, iron deficiency lead to low blood pressure, anemia etc.^{3.15,3.16} whereas, excess iron storage can generate reactive oxygen species, which can damage lipids, proteins and nucleic acids.^{3.17,3.18} Cr^{3+} is an essential nutritional trace element for the human body and its deficiency causes cardiovascular disease, diabetes and affects the glucose and lipid metabolism resulting nervous system disorder.^{3.19} Again, Cr^{3+} from industrial waste causes damage towards environment and living system. Generally, chemosensors designed for sensing individual metal ions are well known in the literature, only a handful example of

dual or multi metal ion sensing chemosensors are reported. Such type of chemosensor reduces synthesis cost and analytical time.

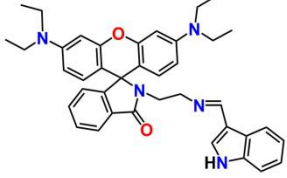
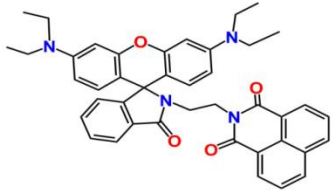
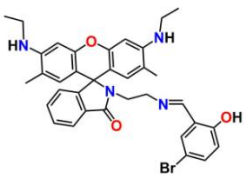

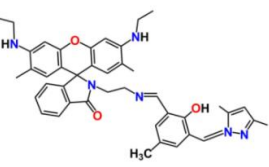
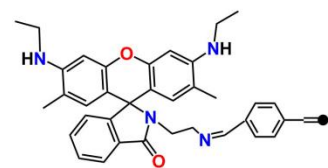
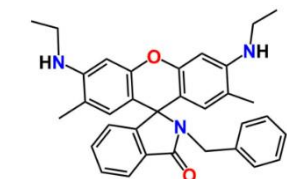
Here, we have demonstrated rhodamine and azo containing fluorescent as well as colorimetric probes **HL3.1** and **HL3.2** [**HL3.1** = 3',6'-bis(ethylamino)-2-((2-hydroxy-3-methoxy-5-(p-phenyldiazenyl)benzylidene)amino)-2',7'-dimethylspiro[isoinoline-1,9'-xanthen]-3-one and [**HL3.2**= 3',6'-bis(ethylamino)-2-((2-hydroxy-3-methoxy-5-(p-tolyldiazenyl)benzylidene)amino)-2',7'-dimethylspiro[isoinoline-1,9'-xanthen]-3-one] for monitoring trivalent ions, Al^{3+} , Cr^{3+} and Fe^{3+} (**Scheme 3.1**). Common fluorophoric units present in fluorescent chemosensors are coumarin, pyrene, 1,8-naphthalimide, rhodamine, squaraine, cyanine, boron dipyrromethene difluoride (BODIPY), nitrobenzofurazan etc. Among them rhodamine-based chemosensors are capable of both naked eye detection and fluorescence emission. They have excellent photo physical properties with greater photo stability, visible wave-length emission, high extinction coefficient and quantum yield. Their off/on-type of sensing property is owing to its structural property. Presence of proton or metal ions initiate opening of its spiro lactam ring resulting in colorimetric response and strong fluorescence emission.^{3,20} In the chemosensors, an azo unit is introduced due to its high photosensitivity and it may also initiates longer conjugation.^{3,21} Recently two rhodamine and azo based chemosensors are reported which selectively detect Al^{3+} and Cu^{2+} ions. In case of Al^{3+} , rhodamine 2B and nitro substituted azo units are present in the chemosensor.^{3,22} Rhodamine 2B and simple azo units are present in case of Cu^{2+} sensor.^{3,23} Interestingly, replacement of rhodamine 2B unit with rhodamine 6G unit and simple azo or methyl substituted azo unit result chemosensors **HL3.1** and **HL3.2** which selectively detect trivalent metal ions. Chemosensors **HL3.1** and **HL3.2** result ~400, ~400 and ~100 times enhancement of fluorescence intensity at 555 nm wavelength in presence of Al^{3+} , Cr^{3+} and Fe^{3+} , respectively. The permissible limit of Al^{3+} , Cr^{3+} and Fe^{3+} ions in water is 2.9 mg/L, 0.3

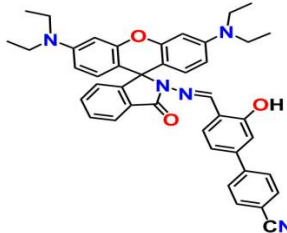
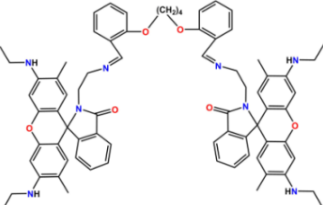
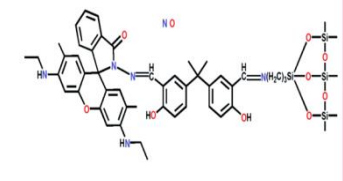
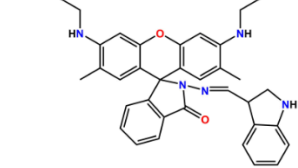
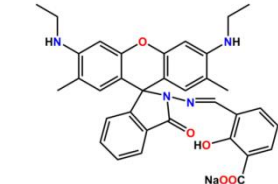
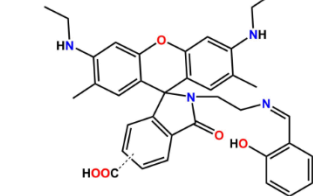
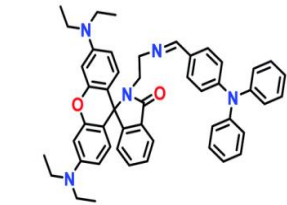
mg/L, 0.05 mg/L, respectively. Therefore, low detection limit (LOD) of **HL3.1** and **HL3.2** against Al^{3+} , Cr^{3+} and Fe^{3+} ions ($\sim 10^{-9}$ M order) will allow us to use them in real world applications and cell imaging study. We have successfully elucidated X-ray crystal structures of both the chemosensors and their Al^{3+} bound complexes. X-ray crystal structures confirm 1:2 binding stoichiometry between metal ion and chemosensors. Crystal structures of Al^{3+} bound rhodamine-based chemosensor complexes are scarce in literature. Some recently reported rhodamine-based chemosensors are collected in **Chart 3.1**.^{3,24} A literature survey on previously reported rhodamine based chemosensors^{3,24-3,26} (both single metal ion and multiple metal ion detectors) and other chemosensors^{3,27-3,30} (both single metal ion and multiple metal ion sensors) reveals that our reported chemosensors, which simultaneously detect three trivalent metal ions, have certain advantages like easy synthetic procedure involving less expensive chemicals, high fluorescence enhancement in presence of metal ions, low LOD values (10^{-9} M order), duel sensing character (colorimetric and fluorescence), X-ray structures of both free chemosensors and its metal bound form and the real world and biological applications. One main drawback of these chemosensors is their partial solubility in aqueous medium^{3,31,3,32,3,24m}.

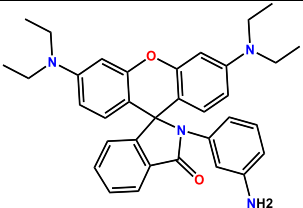
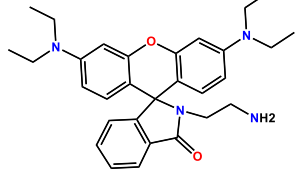
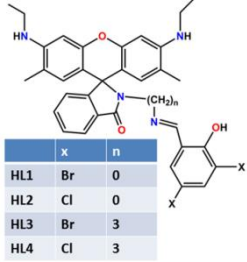


Scheme 3.1. Route to preparation of azo-aldehyde and chemosensors (**HL3.1** and **HL3.2**).

Chart 3.1 Literature survey of rhodamine based derivatives used in sensing of Al^{3+} , Cr^{3+} and Fe^{3+} ions.

Sl. No.	Probe	Sensing Medium	Limit of detection (LOD)	Biological study	Fluorescence intensity enhancement	Refs.
1.		$CH_3CN:H_2O$ (1:1, v/v)	12×10^{-6} M (Al^{3+}), 15×10^{-6} M (Cr^{3+}), 20×10^{-6} M (Fe^{3+})	No	--	24a
2.		$MeOH-H_2O$ (6:4, v/v)	1.74×10^{-9} M (Al^{3+}), 2.36×10^{-6} M (Cr^{3+}), 2.90×10^{-6} M (Fe^{3+})	No	62 (Al^{3+}), 1.7 (Cr^{3+}), 1.47 (Fe^{3+})	24b
3.		$H_2O: methanol$ (3:7, v/v)	1.18×10^{-9} M (Al^{3+}), 1.80×10^{-6} M (Cr^{3+}), 4.04×10^{-6} M (Fe^{3+})	No	98 (Al^{3+}), 50 (Cr^{3+}), 38 (Fe^{3+})	24c
4.		CH_3OH-H_2O , (9:1, v/v)	6.87×10^{-9} M (Al^{3+}), 15.8×10^{-6} M (Cr^{3+}), 14.0×10^{-6} M (Fe^{3+})	Yes	1465 (Al^{3+}), 588 (Cr^{3+}), 800 (Fe^{3+})	24d
5.		methanol/ H_2O (1 : 1, v/v, pH 7.2)	0.34×10^{-6} M (Al^{3+}), 0.29×10^{-6} M (Cr^{3+}), 0.31×10^{-6} M (Fe^{3+})	Yes	14 (Al^{3+}), 10 (Cr^{3+}), 21 (Fe^{3+})	24e
6.		water/ethanol (14:1, v/v)	23.5×10^{-9} M (Al^{3+}), 13.4×10^{-9} M (Cr^{3+}), 69.7×10^{-9} M (Fe^{3+})	NO	145 (Al^{3+}), 174 (Cr^{3+}), 30 (Fe^{3+})	24f
7.		H_2O/CH_3CN (4:1), v/v	1.34×10^{-6} M (Al^{3+}), 2.28×10^{-6} M (Cr^{3+}), 1.28×10^{-6} M (Fe^{3+})	Yes	31 (Al^{3+}), 26 (Cr^{3+}), 41 (Fe^{3+})	24g

8.		HEPES-buffered MeOH/H ₂ O	1.61×10^{-7} M (Al ³⁺), 8.91×10^{-8} M (Cr ³⁺), 8.74×10^{-8} M (Fe ³⁺)	No	--	24h
9.		H ₂ O/CH ₃ CN (7:3, v/v, pH 7.2, 20 mM HEPES buffer)	0.74×10^{-6} M (Al ³⁺), 0.47×10^{-6} M (Cr ³⁺), 2.57×10^{-6} M (Fe ³⁺)	No	653 (Al ³⁺), 667 (Cr ³⁺), 669 (Fe ³⁺)	24i
10.		EtOH water/acetone (14 : 1, v/v) (pH 7.2, 10 mM HEPES buffer)	3.79×10^{-7} M (Al ³⁺), 14.8×10^{-7} M (Cr ³⁺), 3.29×10^{-7} M (Fe ³⁺), 0.74×10^{-7} M (Cu ²⁺)	No	36 (Al ³⁺), 17 (Cr ³⁺), 40 (Fe ³⁺), 89 (Cu ²⁺)	24j
11		aqueous medium	24×10^{-9} M (Al ³⁺), 27×10^{-9} M (Cr ³⁺),	No	--	24k
12.		H ₂ O–EtOH (4 : 1, v/v)	3.26×10^{-6} M (Al ³⁺)	Yes	--	24l
13.		Water, 10 mM with Tris–HCl buffer solution (pH = 7.4).	5.2×10^{-6} M (Fe ³⁺)	Yes	>200 (Fe ³⁺)	24m
14.		MeOH/H ₂ O (1/4, v/v), HEPES buffer (10 mM), pH 7.2	6.7×10^{-8} M (Al ³⁺),	Yes	--	24n

15.		MeOH/H ₂ O (1 : 1, v/v, HEPES, 0.5 mM, pH = 7.35	0.314×10^{-6} M (Al ³⁺)	Yes	---	24o															
16.		Ethanol	40×10^{-6} M (Fe ³⁺)	No	--	24p															
17.	 <table border="1" data-bbox="185 703 342 829"> <thead> <tr> <th></th> <th>X</th> <th>n</th> </tr> </thead> <tbody> <tr> <td>HL1</td> <td>Br</td> <td>0</td> </tr> <tr> <td>HL2</td> <td>Cl</td> <td>0</td> </tr> <tr> <td>HL3</td> <td>Br</td> <td>3</td> </tr> <tr> <td>HL4</td> <td>Cl</td> <td>3</td> </tr> </tbody> </table>		X	n	HL1	Br	0	HL2	Cl	0	HL3	Br	3	HL4	Cl	3	water:methanol (9:1, v/v)	$\sim 10^{-9}$ M (Al ³⁺)	Yes	780(HL1) (Al ³⁺) 725(HL2) (Al ³⁺) 425(HL3) (Al ³⁺) 391(HL4) (Al ³⁺)	24q
	X	n																			
HL1	Br	0																			
HL2	Cl	0																			
HL3	Br	3																			
HL4	Cl	3																			
18.	HL3.1	water:methanol (1:9, v/v)	2.86×10^{-8} M (Al ³⁺), 2.67×10^{-8} M (Cr ³⁺), 5.62×10^{-6} M (Fe ³⁺)	Yes	400 (Al ³⁺), 380 (Cr ³⁺), 100 (Fe ³⁺)	This work															
19.	HL3.2	water:methanol (1:9, v/v)	2.78×10^{-8} M (Al ³⁺), 2.61×10^{-8} M (Cr ³⁺), 6.14×10^{-6} M (Fe ³⁺)	Yes	396 (Al ³⁺), 390 (Cr ³⁺), 100 (Fe ³⁺)	This work															

3.2 Experimental section

3.2.1 Materials and physical measurements description

All reagent or analytical grade chemicals and solvents were collected from commercial sources and used without further purification. Elemental analysis was carried out using a Perkin–Elmer 240C elemental analyzer. Infrared spectra (400–4000 cm⁻¹) were recorded using KBr pellets on a Nicolet Magna IR 750 series-II FTIR spectrophotometer. Absorption spectral data were collected using a Cary 60 spectrophotometer (Agilent) with a 1-cm-path-length quartz cell. Electron spray ionization mass (ESI-MS positive) spectra were

noted using a MICROMASS Q-TOF mass spectrometer. Fluoromax-4 spectrofluorimeter was used to collect emission spectral data at room temperature (298 K) in Britton Robinson buffer at pH= 7.4 solution under degassed condition. A time-resolved spectrofluorimeter from IBH, UK was used to collect fluorescence lifetime data. ^1H and ^{13}C NMR spectral data were collected using Bruker 300 and Bruker 400 spectrometers in CD_3OD and $\text{DMSO-}d_6$ solvent. Cyclic voltammetric experiments were performed using a PC-controlled PAR model 273A electrochemical system under a nitrogen atmosphere using an Ag/AgCl reference electrode, with a Pt disk working electrode and a Pt wire auxiliary electrode in acetonitrile containing supporting electrolyte, 0.1 M Bu_4NClO_4

3.2.2 X-ray Crystallography

Single crystal X-ray data of chemosensors (**HL3.1** and **HL3.2**) were collected on a Bruker SMART APEX-II CCD diffractometer aid of graphite mono-chromated $\text{Mo K}\alpha$ radiation ($\lambda = 0.71073 \text{ \AA}$) at room temperature. Data processing, structure solution, and refinement were examined using Bruker Apex-II suite program. All available reflections data in $2\theta_{\text{max}}$ range were harvested and corrected for Lorentz and polarization factors with Bruker SAINT plus.^{3.33} Reflections were then corrected for absorption, inter-frame scaling, and different systematic errors with SADABS.^{3.34} The structures were solved by the direct methods and refined with the help of full matrix least-square technique based on F^2 with SHELX-2017/1 software package.^{3.35} All the non hydrogen atoms were refined with anisotropic thermal parameters. C–H hydrogen atoms were attached at geometrical positions with $U_{\text{iso}} = 1/2U_{\text{eq}}$ to those they are attached. Some restraints were applied when refining disordered DMF molecules and nitrate ion to make it reasonable. One of dichloromethane molecules present as solvent of crystallization in **HL3.1** is highly disordered, which was very difficult to model, and thus the final contribution of them to the R value was excluded

through the SQUEEZE procedure. Similarly in complex **3.1**, two water and two DMF molecules present as solvent of crystallization are highly disorder and it is very difficult produce a good model to resolve the issue and thereby their contributions were removed by squeeze procedure from the final R values. Crystal data and details of data collection and refinement for chemosensors (**HL3.1** and **HL3.2**) and complexes (**3.1** and **3.4**) were collected in **Table 3.1**.

Table 3.1 Crystal parameters and selected refinement details for **HL3.1**, **HL3.2**, complex **3.1** and complex **3.4**.

sample	HL 3.1	HL3.2	complex 3.1	complex 3.4
CCDC	2051844	2051845	2051846	2051847
Empirical formula	$C_{42}H_{38}Cl_6N_6O_4$	$C_{42}H_{38}Cl_3N_6O_4$	$C_{89}H_{97}AlN_{17}O_{15}$	$C_{164}H_{150}Al_2N_{28}O_{36}$
Formula weight	903.48	797.13	1671.81	3143.07
Temperature (K)	273(2)	273(2)	273(2)	293(2)
Crystal system	monoclinic	triclinic	Monoclinic	triclinic
Space group	<i>P21/c</i>	<i>P-1</i>	<i>P21/c</i>	<i>P-1</i>
<i>a</i> (Å)	23.1315(19)	9.2184(7)	13.9132(12)	16.651(16)
<i>b</i> (Å)	11.7069(10)	13.4158(10)	16.3851(14)	20.317(19)
<i>c</i> (Å)	17.5826(15)	17.3821(13)	19.9383(17)	28.03(3)
α (°)	90	84.617(3)	92.089 (3)	106.557(14)
β (°)	110.173(3)	78.146(3)	106.005(3)	94.278(18)
γ (°)	90	76.103(3)	90.341(3)	114.051(14)
Volume (Å ³)	4469.3(7)	2040.0(3)	4365.6(7)	8101(13)
Z	4	2	2	2
D_{calc} (g cm ⁻³)	1.343	1.298	1.272	1.288
Absorption coefficient (mm ⁻¹)	0.432	0.273	0.098	0.103
<i>F</i> (000)	1864	830	1766	3288
θ Range for data collection (°)	1.97-27.11	1.92- 27.15	1.66-27.19	1.61-27.12
Reflections collected	9827	9010	19326	35653
Independent reflection / R_{int}	4996/0.1022	5171/0.0898	12734/0.0695	14083/0.1302

Data / restraints / parameters	9827/0/581	9010/0/500	19326/0/1072	35653/0/2132
Goodness-of-fit on F^2	1.026	1.022	1.036	1.024
Final indices [$I > 2\sigma(I)$]	R1= 0.0936 wR1= 0.2212	R1= 0.1062 wR1= 0.0761	R1=0.0812 wR1= 0.2388	R1=0.0941 wR1= 0.2572
R indices (all data)	R1= 0.1700 wR2= 0.2707	R1= 0.1062 wR2= 0.3072	R1= 0.1190 wR2= 0.2844	R1= 0.2280 wR2= 0.3493
Largest diff. peak / deepest hole ($e \text{ \AA}^{-3}$)	0.297/-0.369	0.957/-0.663	0.858/-0.828	1.163/-0.328

3.2.3 Synthesis of N-(rhodamine-6G)lactam-hydrazine and azo-aldehydes

N-(rhodamine-6G)lactam-hydrazine and azo-aldehydes were prepared by following literature procedures.^{3,24h,3, 21}

3.2.4 Preparation of chemosensor HL3.1

A mixture of N-(rhodamine-6G)lactam-hydrazine (2.0 mmol, 0.8564 g) and 2-hydroxy-5-(phenyldiazenyl)benzaldehyde (2.0 mmol, 0.512 g) was heated in refluxing condition for *ca.* 2 h in methanol-chloroform (9:1,v/v). Light yellow colour crystals were formed from slow evaporation of methanol-chloroform solvent mixture.

Yield: 1.094 g (80%). Anal. Calc. for $C_{42}H_{40}N_6O_4Cl_6$: C 55.71%; H 4.45%; N 9.28%; Found: C 55.69%; H 4.40%; N 9.26%. IR (cm^{-1} , KBr): $\nu(\text{C}=\text{N})$ 1624s; $\nu(\text{O}-\text{H})$ 3433s; $\nu(\text{C}=\text{O})$ 1690s (**Figure 3.1**). ESI-MS (positive) in MeOH: The base peak was appeared at $m/z = 689.27$, corresponding to $[\text{HL3.1}+\text{Na}]^+$ (**Figure 3.2**). UV-Vis, λ_{max} (nm), (ϵ ($\text{dm}^3\text{mol}^{-1}\text{cm}^{-1}$)) in Britton Robinson buffer at pH= 7.4: 307 (39020).

^1H NMR (300 MHz, d_6 -DMSO) δ ppm: 1.20 (-CH₃) (t, 6H, $J=7.2\text{Hz}$), 1.86 (Ar-CH₃) (s, 6H), 3.34-3.099 (-CH₂) (m, 4H), 3.84 (-OCH₃) (s, 3H), 5.09 (NH) (t, 2H, $J_1=4.8\text{Hz}$, $J_2=5.1\text{Hz}$), 6.23 (Ar-CH) (s, 2H), 6.34 (Ar-CH) (s, 2H), 7.06 (Ar-CH) (d, 1H, $J=6.2\text{Hz}$), 7.44 (Ar-CH) (s, 1H), 7.49-7.67 (Ar-CH) (m, 4H), 7.82-7.96 (Ar-CH) (m, 3H), 8.32 (Ar-CH₃) (s, 1H), 9.05 (-CH=N) (s, 1H), 11.55 (-OH) (s, 1H) (**Figure 3.3a**).

^1H NMR (400 MHz, $\text{d}_4\text{-CD}_3\text{OD}$) δ ppm: 1.31 ($-\text{CH}_3$) (t, 6H), 1.92 (Ar-CH_3) (s, 6H), 3.21-3.27 ($-\text{CH}_2$) (m, 4H), 3.91 ($-\text{OCH}_3$) (s, 3H), 6.29 (Ar-CH) (s, 2H), 6.49 (Ar-CH) (s, 2H), 7.53-8.29 (Ar-CH) (m, 11H), 8.84 ($-\text{CH}=\text{N}$) (s, 1H), 11.54 ($-\text{OH}$) (s, 1H) (**Figure 3.3**).

^{13}C NMR ($\text{d}_6\text{-DMSO}$, 75 MHz) δ ppm:

14.62, 17.47, 37.94, 56.36, 66.08, 96.29, 104.06, 104.70, 118.92, 119.28, 119.77, 122.74, 123.63, 124.31, 127.27, 128.71, 128.96, 129.32, 129.85, 131.33, 134.59, 145.06, 146.67, 147.40, 148.39, 149.26, 150.56, 151.47, 151.99, 152.35, 164.27 (**Figure 3.4**).

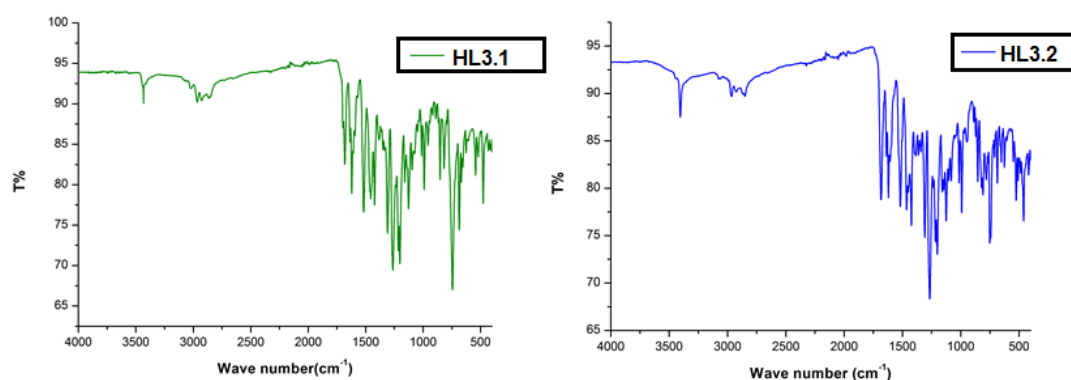


Figure 3.1 FTIR spectra of chemosensor **HL3.1** and **HL3.2**.

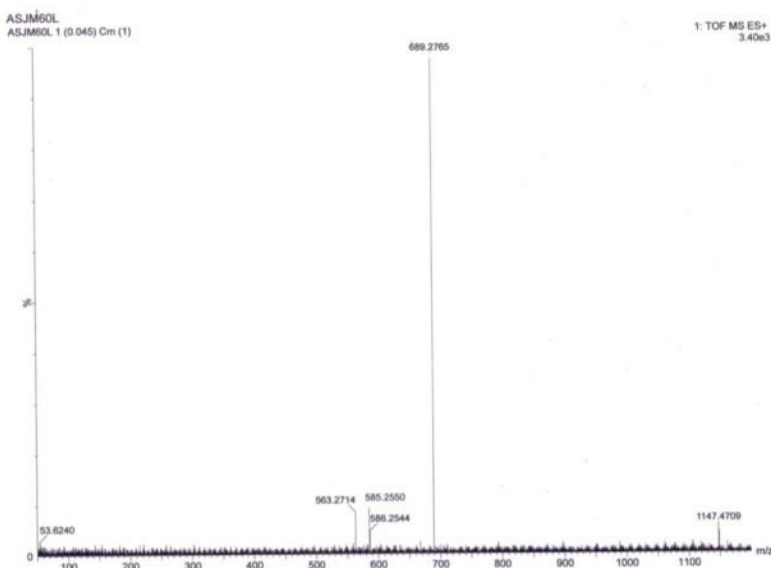


Figure 3.2 ESI-mass spectrum of chemosensor **HL3.1**

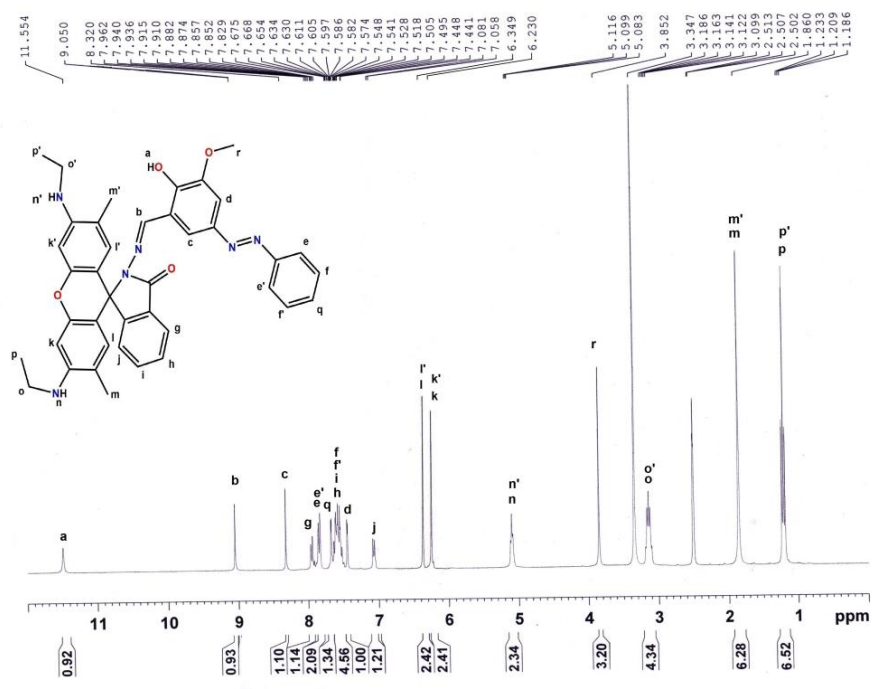


Figure 3.3(a) $^1\text{H-NMR}$ spectrum of the chemosensor **HL3.1** in DMSO-d_6 recorded on a 300 MHz Bruker NMR spectrometer.

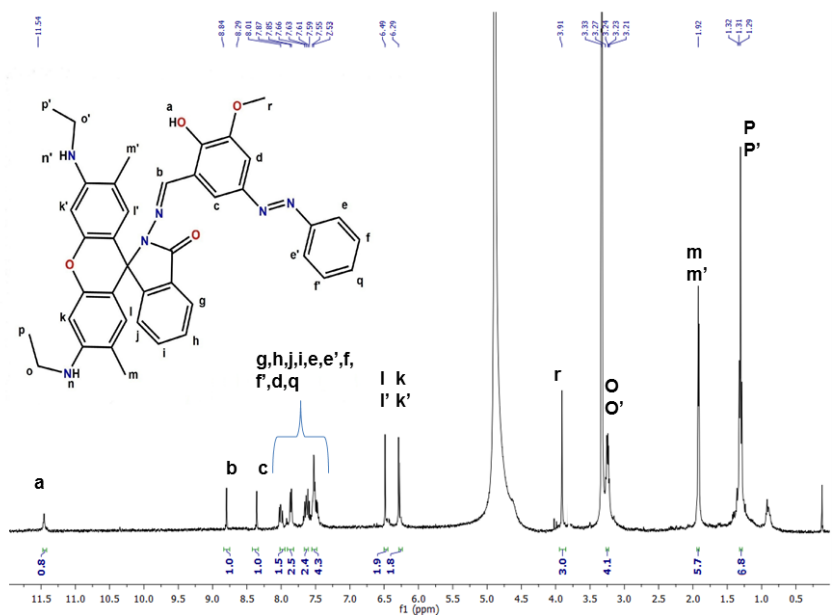


Figure 3.3(b) $^1\text{H-NMR}$ spectrum of the chemosensor **HL3.1** in CD_3OD recorded on a 400 MHz Bruker NMR spectrometer.

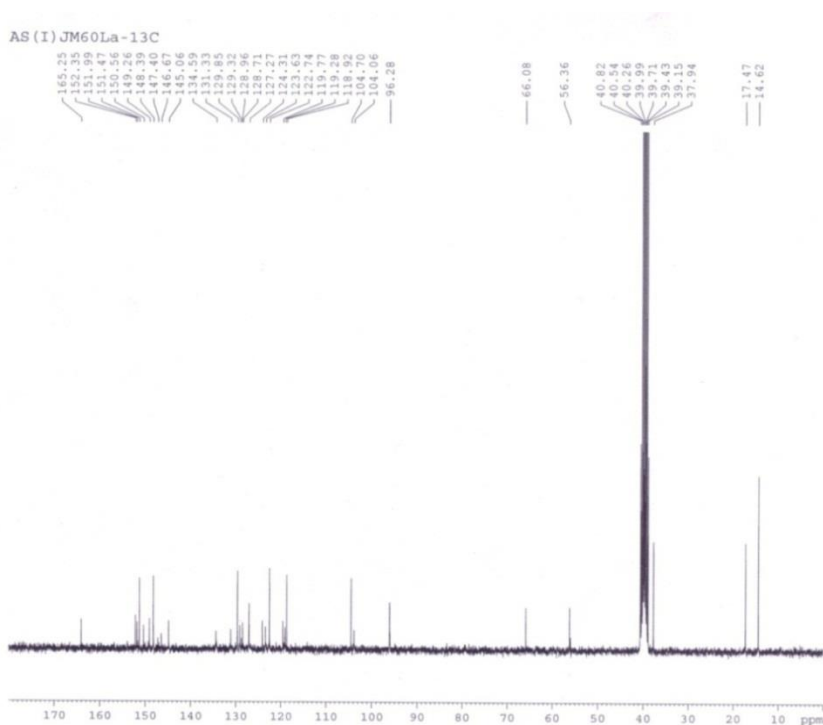


Figure 3.4 ^{13}C NMR spectrum of **HL3.1** in DMSO-d_6 .

3.2.5 Synthesis of chemosensor **HL3.2**

A mixture of N-(rhodamine-6G)lactam-hydrazine (2.0 mmol, 0.8564 g) and 2-hydroxy-3-methoxy-5-(p-tolyldiazenyl)benzaldehyde (2.0 mmol, 0.540 g) was heated in refluxing condition for *ca.* 2 h in methanol-chloroform (9:1,v/v). Light yellow colour crystals were formed from slow evaporation of methanol-chloroform solvent mixture.

Yield: 1.201g (86%). Anal. Calc. for $\text{C}_{42}\text{H}_{41}\text{N}_6\text{O}_4\text{Cl}_3$: C 63.04%; H 5.16%; N 10.50%.

Found: C 62.98%; H 5.10%; N 10.46%. IR (cm^{-1} , KBr): $\nu(\text{C}=\text{N})$ 1621s; $\nu(\text{O}-\text{H})$ 3421s; $\nu(\text{C}=\text{O})$ 1696s (**Figure 3.1**). ESI-MS (positive) in MeOH: The molecular ion peak was appeared at $m/z = 681.27$, corresponding to $[\text{HL3.2}+1]^+$ (**Figure 3.5**). UV-Vis, λ_{max} (nm), (ϵ ($\text{dm}^3\text{mol}^{-1}\text{cm}^{-1}$)) in Britton Robinson buffer (10mM) at pH= 7.4: 310 (38440).

^1H NMR (300 MHz, d_6 -DMSO) δ ppm: 1.211 (- CH_3) (t, 6H), 1.86 (Ar- CH_3) (s, 6H), 2.39 (Ar- CH_3) (s, 3H), 3.18-3.09 (- CH_2) (m, 4H), 3.85 (- OCH_3)(s,3H), 5.09 (NH)(t, 2H, $J_1=4.5,\text{Hz}$ $J_2=5.4\text{Hz}$), 6.22 (Ar-CH) (s, 2H), 6.34 (Ar-CH) (s, 2H), 7.06 (Ar-CH) (d, 1H,

$J=6.6$ Hz), 7.36 (Ar-CH) (d, 2H, $J=8.4$ Hz), 7.42 (Ar-CH) (s, 1H), 7.65-7.56 (Ar-CH) (m, 2H), 7.75 (Ar-CH) (d, 2H, $J=8.1$ Hz), 7.94 (Ar-CH) (d, 2H, $J=6.6$ Hz), 8.32 (Ar-CH) (s, 1H), 9.03 (-CH=N) (s, 1H), 11.51(-OH) (s,1H) (**Figure 3.6a**).

^1H NMR (400 MHz, $\text{d}_4\text{-CD}_3\text{OD}$) δ ppm: 1.29 (-CH₃) (t, 6H), 1.92 (Ar-CH₃) (s, 6H), 2.42 (Ar-CH₃) (s, 3H), 3.26-3.21 (-CH₂) (m, 4H), 3.89 (-OCH₃)(s,3H), 6.26 (Ar-CH) (s, 2H), 6.44 (Ar-CH) (s, 2H), 8.02-7.30 (Ar-CH) (m, 9H), 8.30 (Ar-CH) (s, 1H), 8.82 (-CH=N) (s, 1H), 11.50(-OH) (s,1H) (**Figure 3.6b**).

^{13}C NMR ($\text{d}_6\text{-DMSO}$, 75 MHz) δ ppm:

14.62,17.47,21.92,37.94,56.36,66.08,96.29,104.06,104.70,118.92,119.28,119.77,122.74,123.63,124.31,127.27,128.71,128.96,129.32,129.85,131.33,134.59,145.06,146.67,147.40,148.39, 149.26,150.56,151.47 151.99,152.35,164.27 (**Figure 3.7**).

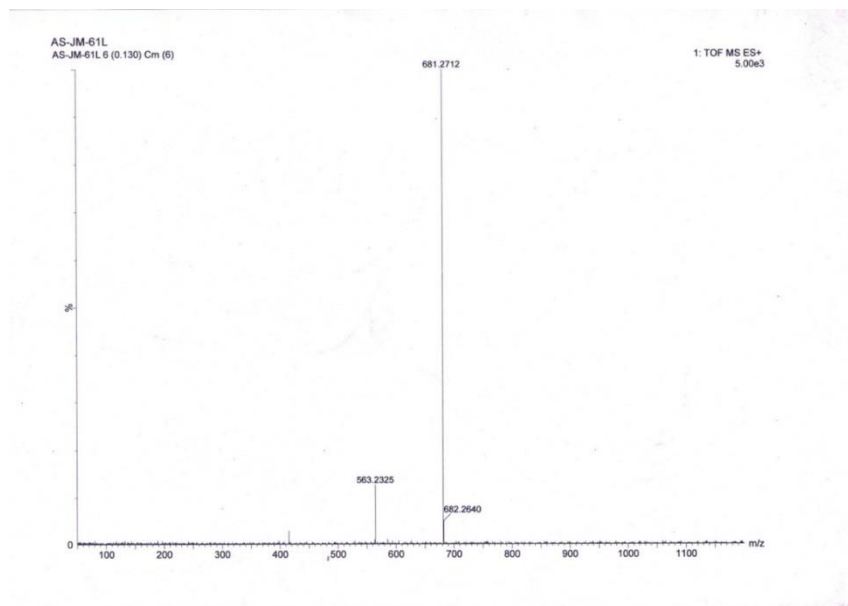


Figure 3.5 ESI-mass spectrum of chemosensor **HL3.2**.

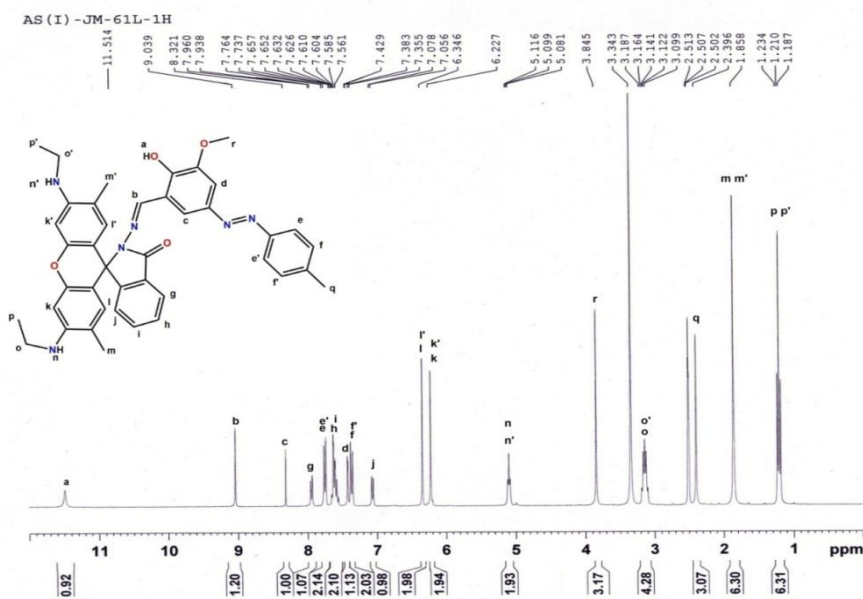


Figure 3.6(a) $^1\text{H-NMR}$ spectrum of the chemosensor **HL3.2** in DMSO-d_6 recorded on a 300 MHz Bruker NMR spectrometer.

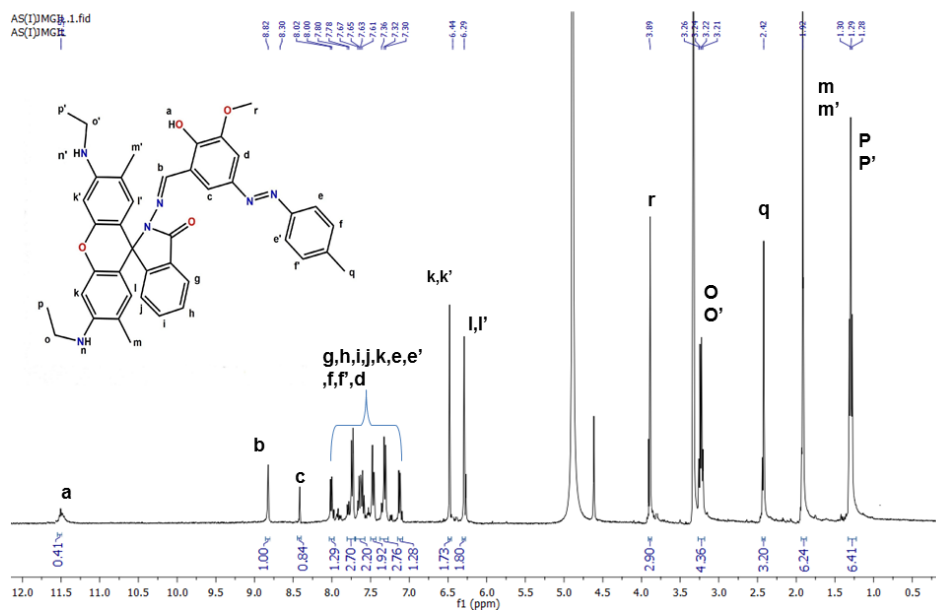


Figure 3.6(b) $^1\text{H-NMR}$ spectrum of the chemosensor **HL3.2** in CD_3OD recorded on a 400 MHz Bruker NMR spectrometer.

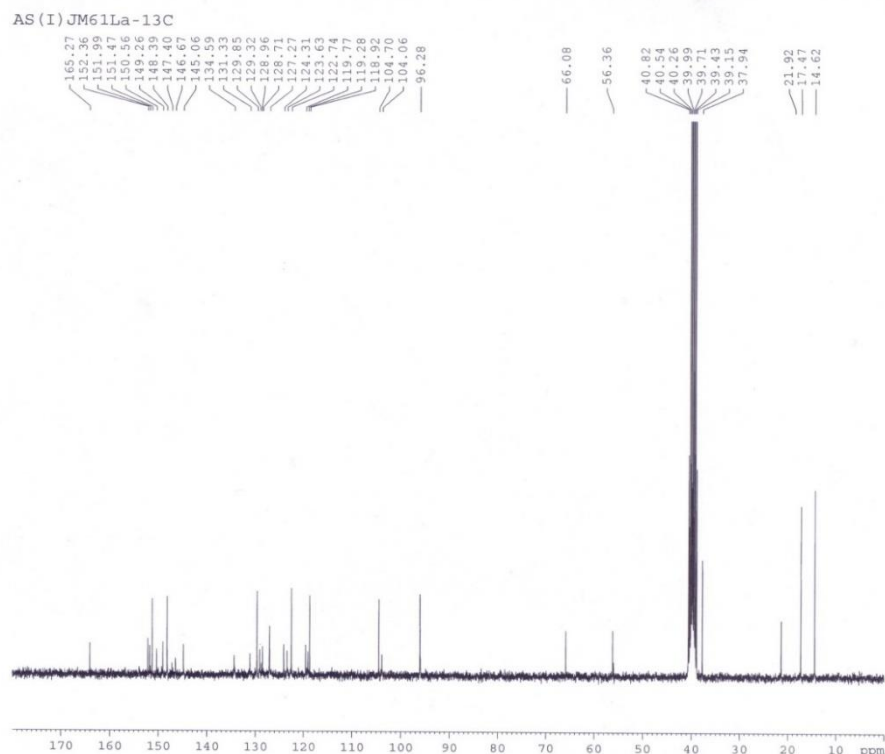


Figure 3.7 ^{13}C NMR spectrum of **HL3.2** in DMSO-d_6 .

3.2.6 Synthesis of $[\text{Al}(\text{L}3.1)_2](\text{NO}_3)\cdot 3\text{DMF}\cdot 2\text{H}_2\text{O}$ (**3.1**)

A 2 mL methanolic solution of aluminum nitrate nonahydrate (1.0 mmol, 0.375 g) was added carefully to 20 mL methanol-chloroform (9:1,v/v) solution of **HL3.1** (2.0 mmol, 1.332 g). Then, the reaction mixture was stirred for ca. 3 h. Red colour crystals were collected in high yield after slow evaporation of the methanol-DMF solvent mixture.

Yield: 1.348 g (79%). Anal. Calc. for $\text{C}_{89}\text{H}_{99}\text{AlN}_{16}\text{O}_{16}$: C 63.79%; H 5.95%; N 13.37%; Found: C 63.68%; H 5.86%; N 13.29%. IR (cm^{-1} , KBr): $\nu(\text{C}=\text{N})$ 1601s; $\nu(\text{NO}_3^-)$ 1300s and 809s; $\nu(\text{C}=\text{O})$ 1646s (**Figure 3.8**). The molecular ion peak was appeared at $m/z = 1357.37$ and 679.26, corresponding to $[\text{Al}(\text{L}3.1)_2]^+$ and $[\text{Al}(\text{L}3.1)_2+\text{H}]^{2+}$, respectively (**Figure 3.9**). UV-Vis, λ_{max} (nm), (ϵ ($\text{dm}^3\text{mol}^{-1}\text{cm}^{-1}$)) in Britton Robinson buffer at pH= 7.4: 525(59558).

^1H NMR (400 MHz, d_6 -DMSO) δ ppm: 1.20(-CH₃) (t, 6H, $J=7.2\text{Hz}$), 1.87 (Ar-CH₃) (s, 6H), 3.12-3.19 (-CH₂) (m, 4H), 5.93 (NH)(s,1H), 6.29 (Ar-CH) (d, 2H, $J=6\text{Hz}$), 6.40 (Ar-CH) (d,

2H, $J=6.3\text{Hz}$), 7.47-7.61 (Ar-CH) (m, 6H), 7.63-7.88 (Ar-CH) (m, 4H), 8.41 (NH) (d, 2H), 9.07(-CH=N) (s, 1H) (**Figure 3.10a**).

^1H NMR (400 MHz, $\text{d}_4\text{-CD}_3\text{OD}$) δ ppm: 1.32(-CH₃) (t, 6H), 2.09 (Ar-CH₃) (s, 6H), 3.12-3.19 (-CH₂) (m, 4H), 6.53 (NH)(s,1H), 6.89 (Ar-CH) (d, 4H), 7.42-8.45 (Ar-CH) (m, 10H), 8.90(-CH=N) (s, 1H) (**Figure 3.10b**).

^{13}C NMR ($\text{d}_6\text{-DMSO}$, 75 MHz) δ ppm:

14.55,17.9,38.10,56.35,96.62,104.16,105.21,118.29,119.09,119.67,122.41,122.74,123.63,124.30,125.12,127.34,128.74,129.35,130.33,134.60,141.42,145.08,148.17,149.22,150.23,150.40, 151.47,151.91,156.01,157.22,164.47,168.07 (**Figure 3.11**).

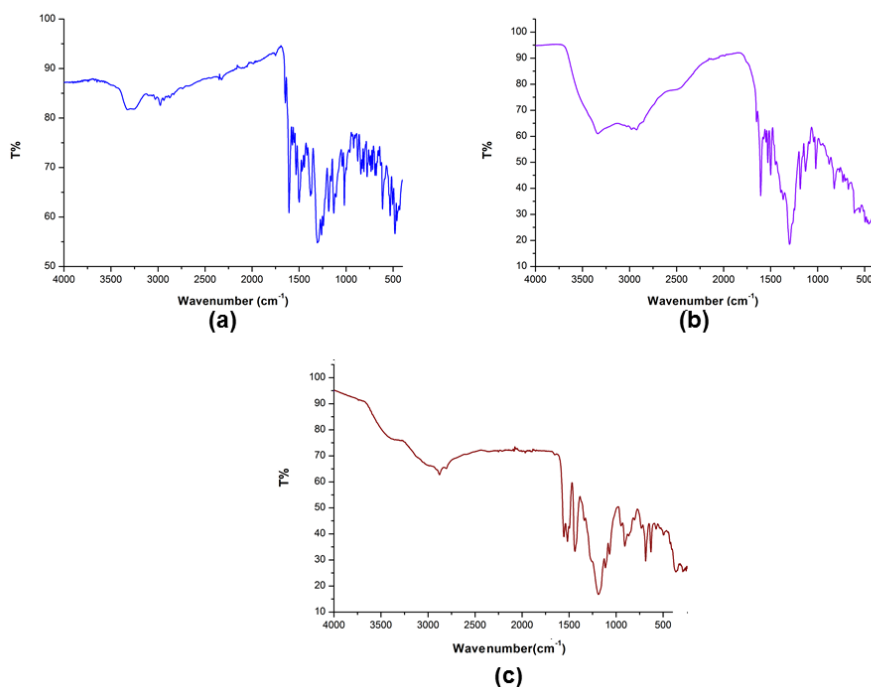


Figure 3.8 FTIR spectra of (a) complex **3.1**, (b) complex **3.2** and (c) complex **3.3**.

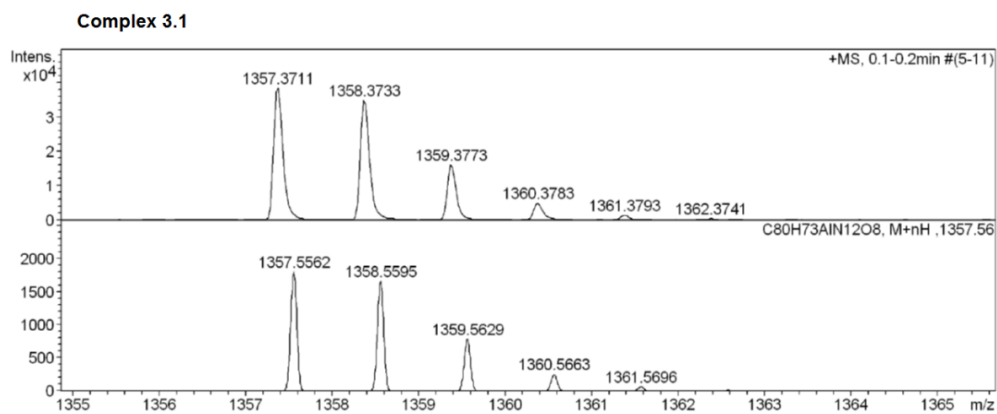


Figure 3.9(a) ESI-mass spectrum of $[\text{Al}(\text{L}3.1)_2]^+$ (complex **3.1**).

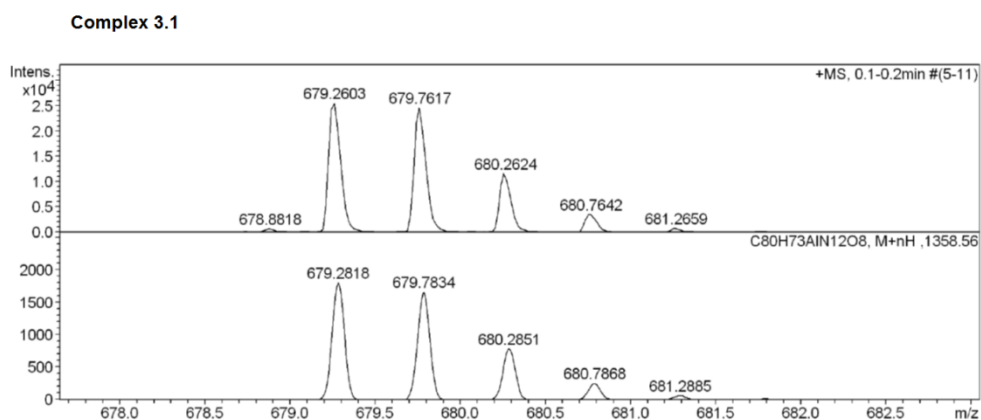


Figure 3.9(b) ESI-mass spectrum of $[\text{Al}(\text{L}3.1)_2 + \text{H}]^{2+}$ (complex **3.1**).

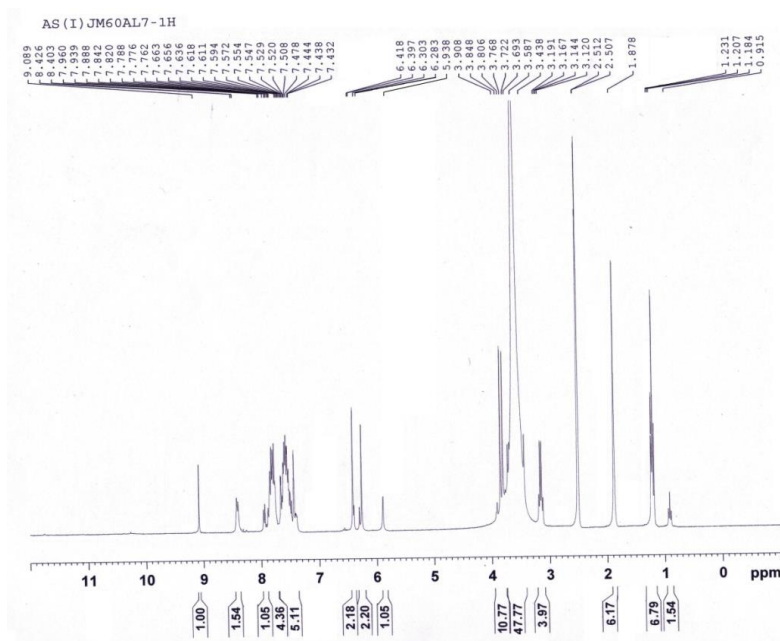


Figure 3.10(a) ^1H -NMR spectrum of complex **3.1** in DMSO-d_6 recorded on a 300 MHz Bruker NMR spectrometer.

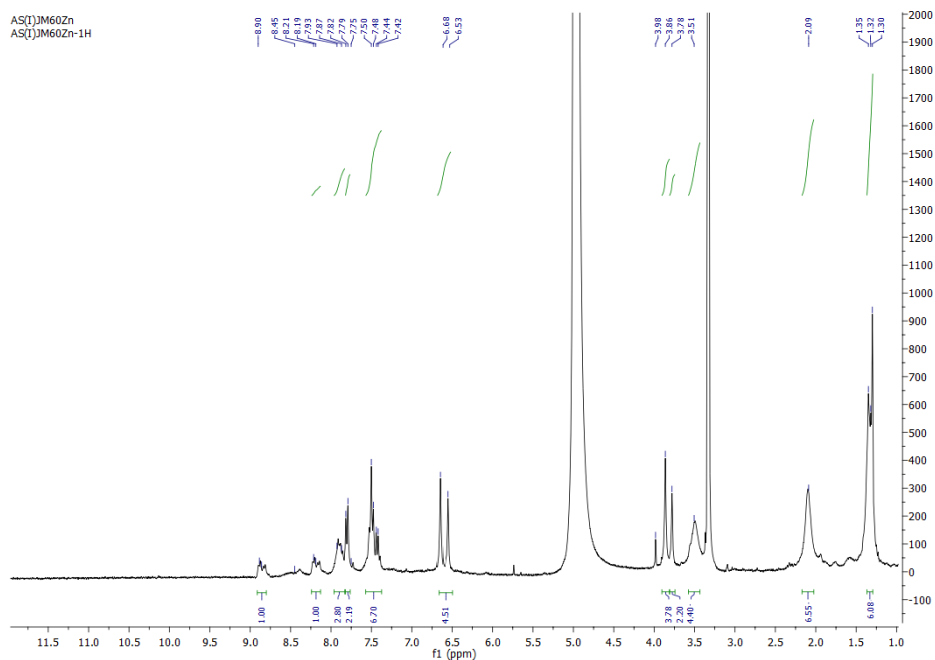


Figure 3.10(b) $^1\text{H-NMR}$ spectrum of complex **3.1** in CD_3OD recorded on a 400 MHz Bruker NMR spectrometer.

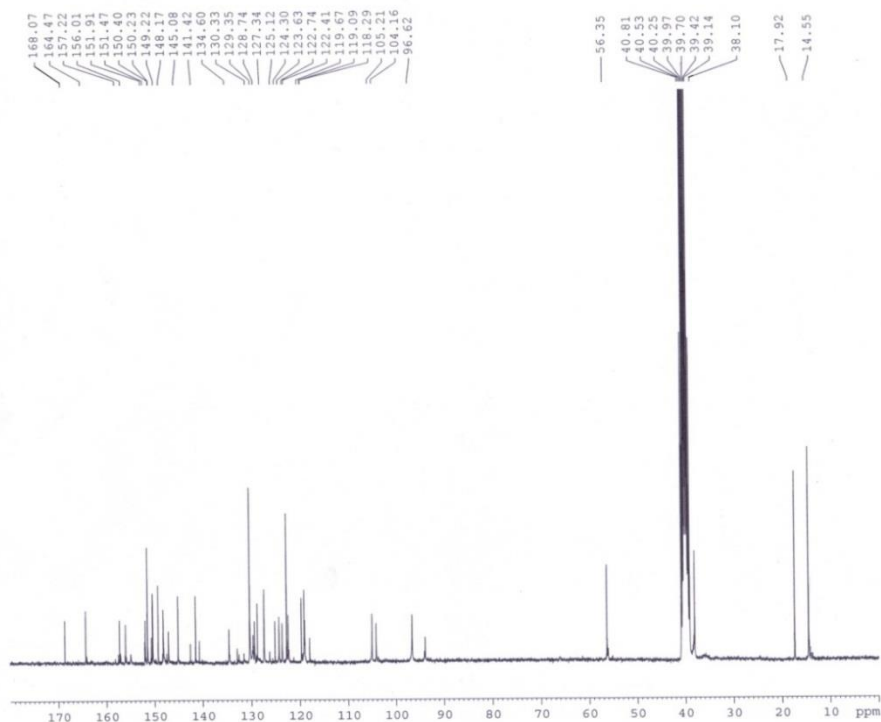


Figure 3.11 ^{13}C NMR spectrum of complex **3.1** in DMSO-d_6

3.2.7 Synthesis of $[\text{Cr}(\text{L3.1})_2](\text{NO}_3)$ (3.2)

A 2 mL methanolic solution of chromium nitrate nonahydrate (1.0 mmol, 0.400 g) was added carefully to 20 mL methanol-chloroform (9:1,v/v) solution of **HL3.1** (2.0 mmol, 1.332 g). Then, the reaction mixture was stirred for ca. 3 h. Red colour microcrystals were collected in high yield after slow evaporation of the solvent.

Yield: 1.385 g (80%). Anal. Calc. for $\text{C}_{80}\text{H}_{74}\text{CrN}_{13}\text{O}_{11}$: C 66.74%; H 5.16%; N 12.60%; Found: C 66.65%; H 5.01%; N 12.50%. IR (cm^{-1} , KBr): $\nu(\text{C}=\text{N})$ 1601s; $\nu(\text{NO}_3^-)$ 1300s and 810s; $\nu(\text{C}=\text{O})$ 1655 s (**Figure 3.8**). The molecular ion peak was appeared at $m/z = 1382.51$ and 691.76, corresponding to $[\text{Cr}(\text{L3.1})_2]^+$ and $[\text{Cr}(\text{L1})_2+\text{H}]^{2+}$, respectively (**Figure 3.12**).

UV-Vis, λ_{max} (nm), (ϵ ($\text{dm}^3\text{mol}^{-1}\text{cm}^{-1}$)) in Britton Robinson buffer at pH= 7.4: 525(80235).

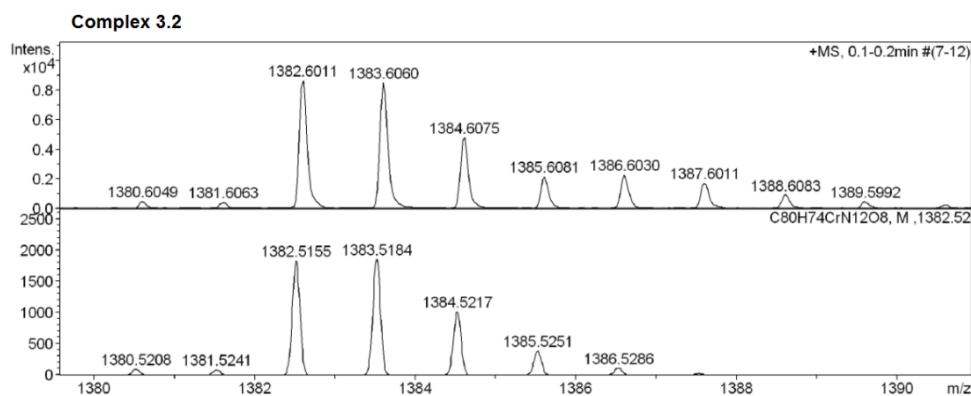


Figure 3.12(a) ESI-mass spectrum of $[\text{Cr}(\text{L1})_2]^+$ (complex 3.2).

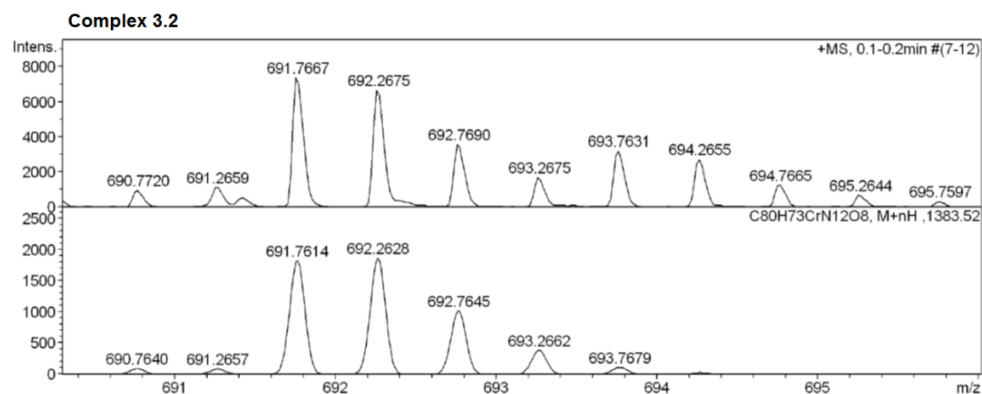


Figure 3.12(b) ESI-mass spectrum of $[\text{Cr}(\text{L3.1})_2+\text{H}]^{2+}$ (complex 3.2).

3.2.8 Synthesis of $[\text{Fe}(\text{L3.1})_2](\text{NO}_3)$ (3.3)

A 2 mL methanolic solution of ferric nitrate nonahydrate (1.0 mmol, 0.404 g) was added carefully to 20 mL methanol-chloroform (9:1,v/v) solution of **HL3.1** (2.0 mmol, 1.332 g). Then, the reaction mixture was stirred for ca. 3 h. Red colour powder were collected in high yield after slow evaporation of the solvent.

Yield: 1.302 g (75%). Anal. Calc. for $\text{C}_{80}\text{H}_{74}\text{FeN}_{13}\text{O}_{11}$: C 66.74%; H 5.15%; N 12.56%; Found: C 66.55%; H 5.01%; N 12.41%. IR (cm^{-1} , KBr): $\nu(\text{C}=\text{N})$ 1603s; $\nu(\text{NO}_3^-)$ 1300s and 809s; $\nu(\text{C}=\text{O})$ 1641s (**Figure 3.8**). The molecular ion peak was appeared at $m/z = 1386.51$ and 693.83, corresponding to $[\text{Fe}(\text{L3.1})_2]^+$ and $[\text{Fe}(\text{L3.1})_2+\text{H}]^{2+}$, respectively (**Figure 3.13**). UV-Vis, λ_{max} (nm), (ϵ ($\text{dm}^3\text{mol}^{-1}\text{cm}^{-1}$)) in Britton Robinson buffer at pH= 7.4: 525(80470).

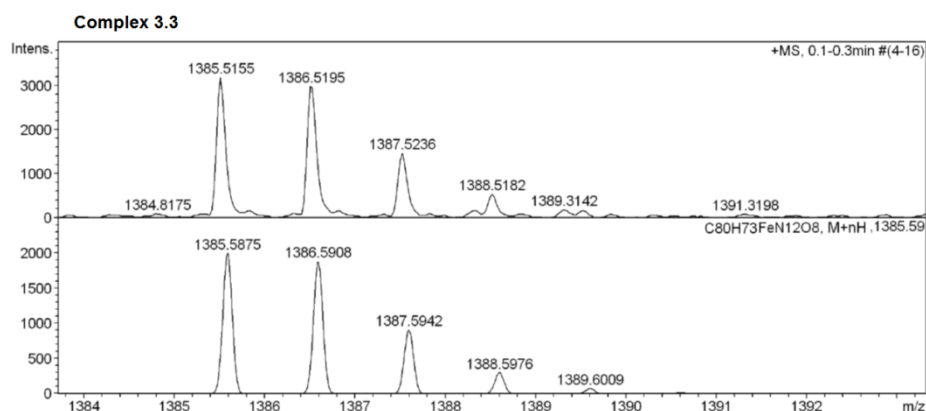


Figure 3.13(a) ESI-mass spectrum of $[\text{Fe}(\text{L3.1})_2]^+$ (complex 3.3).

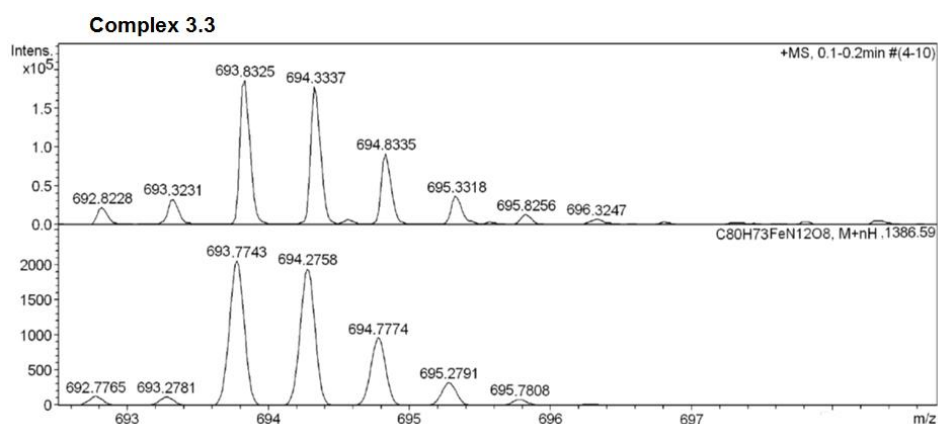


Figure 3.13 (b) ESI-mass spectrum of $[\text{Fe}(\text{L3.1})_2+\text{H}]^{2+}$ (complex 3.3).

3.2.9 Synthesis of [Al(HL3.2)(L3.2)](NO₃)₂•4H₂O (3.4)

A 2 mL methanolic solution of aluminum nitrate nonahydrate (1.0 mmol, 0.375 g) was added carefully to 20 mL methanol-chloroform (9:1,v/v) solution of **HL3.2** (2.0 mmol, 1.362 g). Then, the reaction mixture was stirred for ca. 3 h. red colour crystals were collected in high yield after slow evaporation of the solvent.

Yield: 0.802 g (76%). Anal. Calc. for C₈₂H₈₇AlN₁₄O₁₈: C 62.19%; H 5.54%; N 12.38%; Found: C 62.01%; H 5.29%; N 12.07%; IR (cm⁻¹, KBr): $\nu(\text{C}=\text{N})$ 1608s; $\nu(\text{NO}_3^-)$ 1300s and 822s; $\nu(\text{C}=\text{O})$ 1640s (**Figure 3.14**). The molecular ion peak was appeared at $m/z = 1385.58$ and 693.29, corresponding to [Al(L2)₂]⁺ and [Al(L3.2)₂+H]²⁺, respectively (**Figure 3.15**). UV-Vis, λ_{max} (nm), (ϵ (dm³mol⁻¹cm⁻¹)) in Britton Robinson buffer at pH= 7.4: 525(59847).

¹H NMR (400 MHz, d₆-DMSO) δ ppm: 1.20(-CH₃) (t, 6H, $J=7.2\text{Hz}$), 1.87 (Ar-CH₃) (s, 6H), 2.39 (Ar-CH₃) (s, 3H), 3.12-3.19 (-CH₂) (m, 4H), 5.93 (NH)(s,1H), 6.29 (Ar-CH) (d, 2H, $J=6\text{Hz}$), 6.40 (Ar-CH) (d, 2H, $J=6.3\text{Hz}$), 7.47-7.61 (Ar-CH) (m, 4H), 7.63-7.88 (Ar-CH) (m, 4H), 8.41 (Ar-CH) (d, 1H), 9.07(-CH=N) (s, 1H) (**Figure 3.16a**).

¹H NMR (400 MHz, d₄-CD₃OD) δ ppm: 1.34 (-CH₃) (t, 6H), 2.09 (Ar-CH₃) (s, 6H), 2.68 (Ar-CH₃) (s, 3H), 3.04-2.90 (-CH₂) (m, 4H), 6.24 (Ar-CH) (s, 2H), 6.46 (Ar-CH) (s, 2H), 7.43-8.18 (Ar-CH) (m, 10H), 8.45 (Ar-CH) (d, 1H), 8.99 (-CH=N) (s, 1H) (**Figure 13.6b**).

¹³C NMR (d₆-DMSO, 75 MHz) δ ppm:

14.55,17.91,21.91,38.10,56.34,96.60,104.16,105.01,118.99,119.09,119.67,122.41,122.74,123.63,124.30,125.12,127.34,128.74,129.35,130.33,134.60,141.46,145.08,148.17,149.23,150.23,150.40,151.47,151.91,156.01,157.25,164.27,168.27 (**Figure 3.17**).

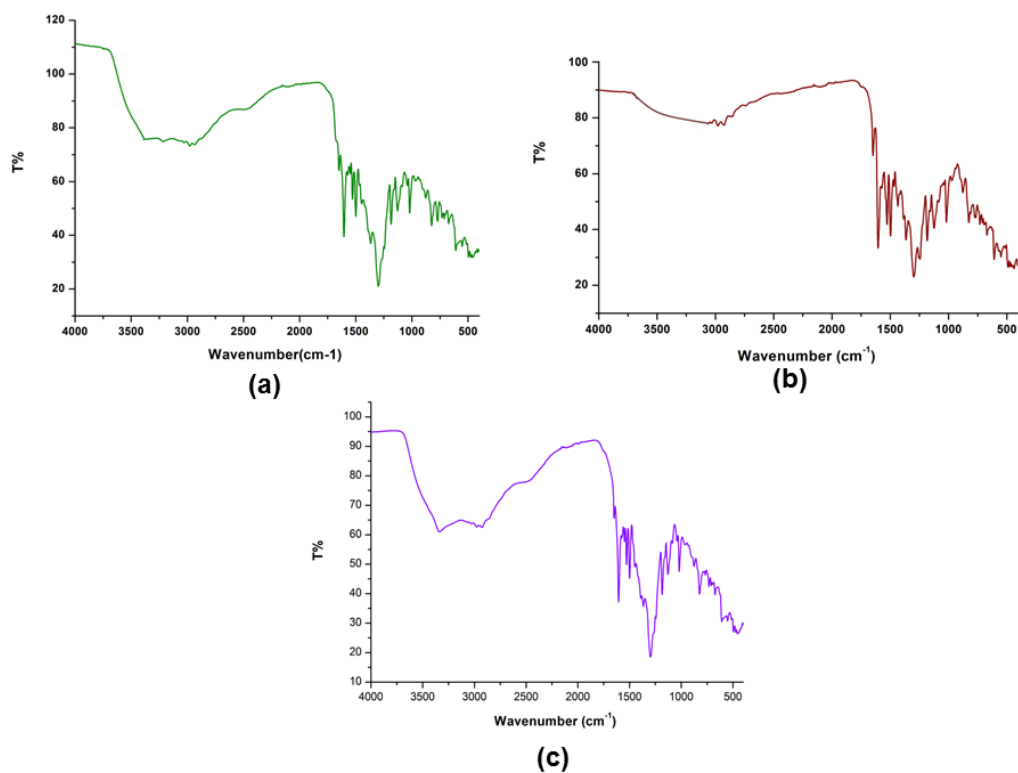


Figure 3.14 FTIR spectra of (a) complex 3.4, (b) complex 3.5 and (c) complex 3.6.

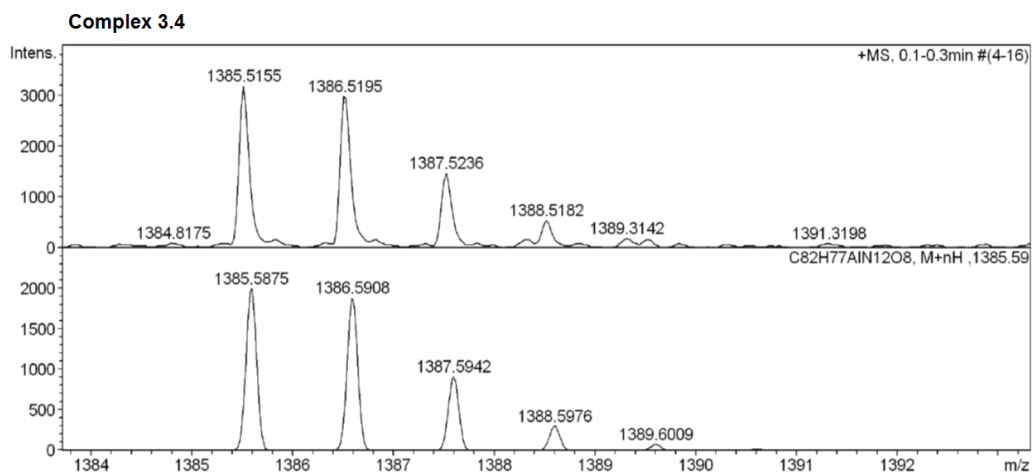


Figure 3.15 (a) ESI-mass spectrum of [Al(L3.2)₂]⁺ (complex 3.4).

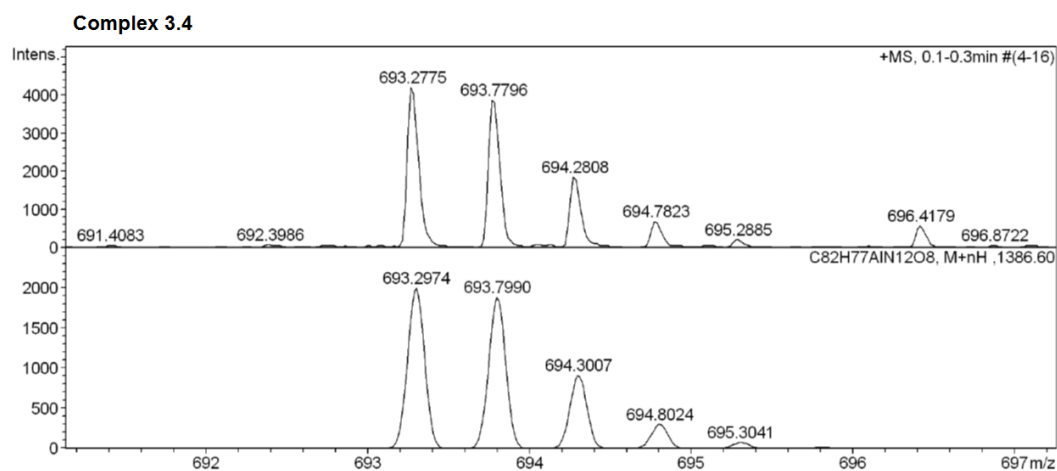


Figure 3.15 (b) ESI-mass spectrum of $[Al(L3.2)_2+H]^+$ (complex 3.4).

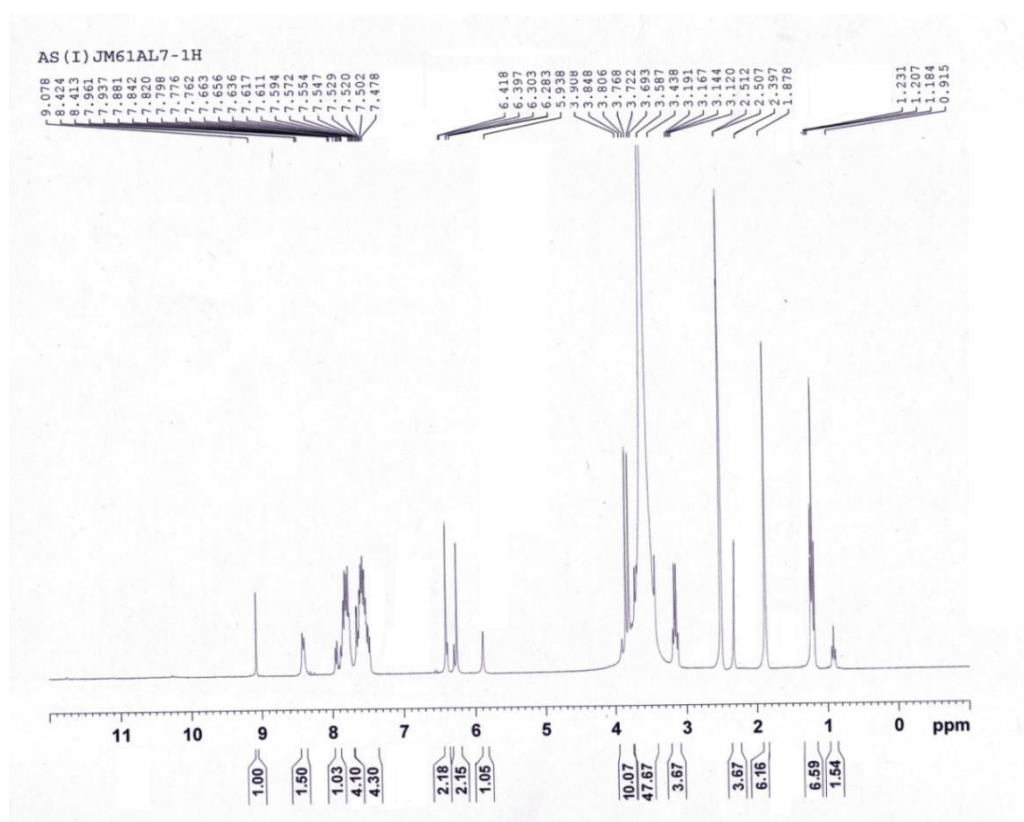


Figure 3.16(a) 1H -NMR spectrum of complex 3.4 in $DMSO-d_6$ recorded on a 300 MHz Bruker NMR spectrometer.

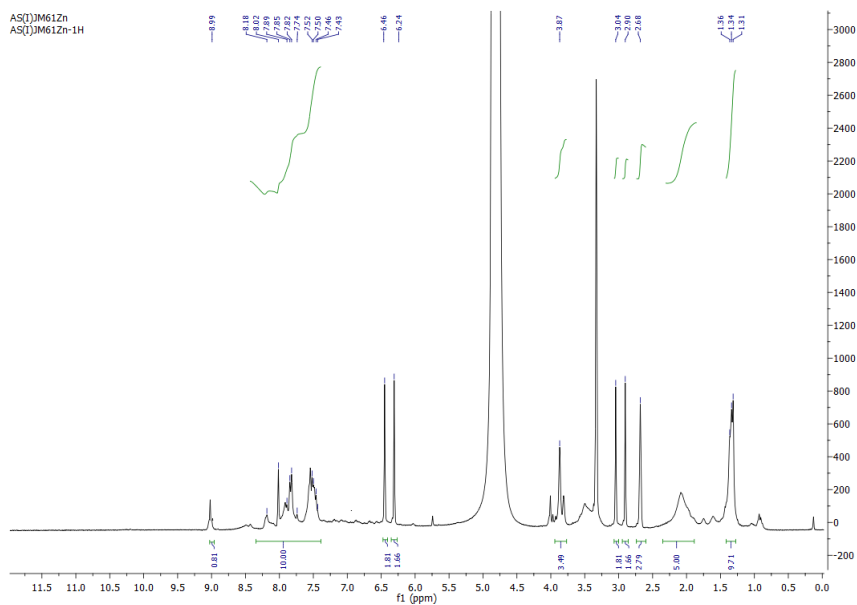


Figure 3.16(b) $^1\text{H-NMR}$ spectrum of complex **4** in CD_3OD recorded on a 400 MHz Bruker NMR spectrometer.

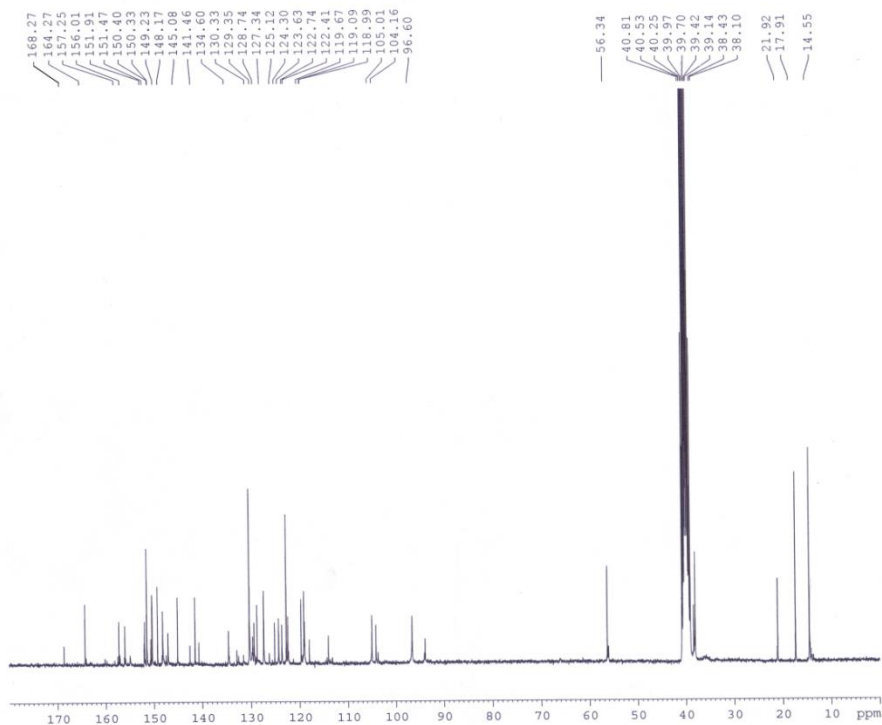


Figure 3.17 ^{13}C NMR spectrum of complex **3.4** in DMSO-d_6 .

3.2.10 Synthesis of $[\text{Cr}(\text{L3.2})_2](\text{NO}_3)$ (3.5)

A 2 mL methanolic solution of chromium nitrate nonahydrate (1.0 mmol, 0.400 g) was added carefully to 20 mL methanol-chloroform (9:1,v/v) solution **HL3.2** (2.0 mmol, 1.362g). Then, the reaction mixture was stirred for ca. 3 h. Red colour microcrystals were collected in high yield after slow evaporation of the solvent.

Yield: 1.448 g (82%). Anal. Calc. for $\text{C}_{82}\text{H}_{78}\text{CrN}_{13}\text{O}_{11}$: C 66.84%; H 5.34%; N, 12.36%; Found: C 66.75%; H 5.28%; N 12.31%; IR (cm^{-1} , KBr): $\nu(\text{C}=\text{N})$ 1600s; $\nu(\text{NO}_3^-)$ 1312s and 811s; $\nu(\text{C}=\text{O})$ 1641s (**Figure 3.14**). The molecular ion peak was appeared at $m/z = 1411.55$ and 706.28, corresponding to $[\text{Cr}(\text{L3.2})_2]^+$ and $[\text{Cr}(\text{L3.2})_2+\text{H}]^{2+}$, respectively (**Figure 3.18**). UV-Vis, λ_{max} (nm), (ϵ ($\text{dm}^3\text{mol}^{-1}\text{cm}^{-1}$)) in Britton Robinson buffer at pH= 7.4: 525(80235).

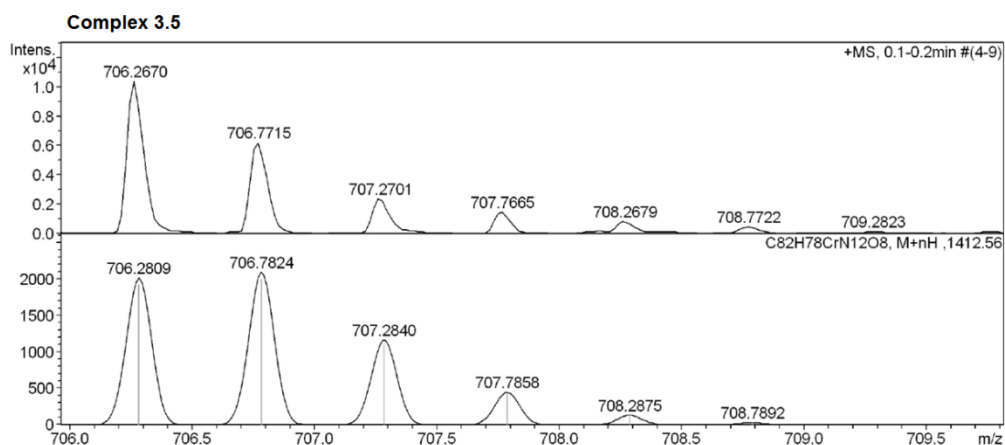


Figure 3.18 (a) ESI-mass spectrum of $[\text{Cr}(\text{L3.2})_2]^+$ (complex 3.5).

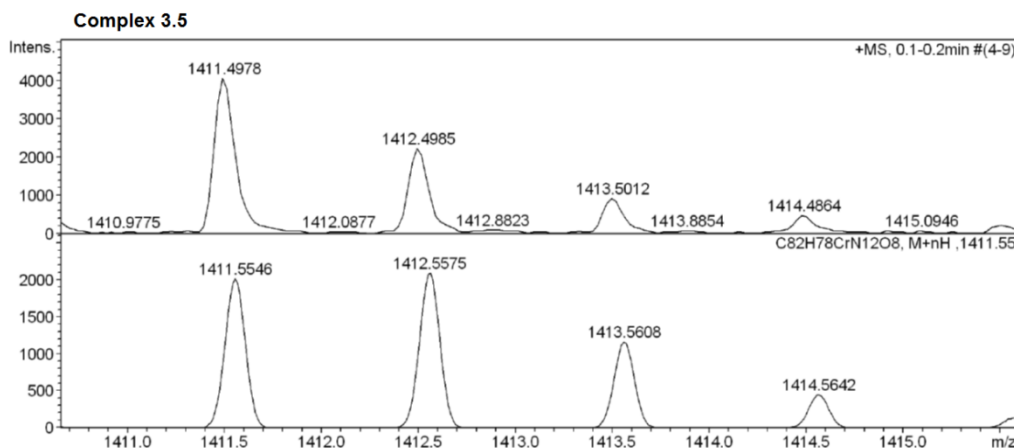


Figure 3.18 (b) ESI-mass spectrum of $[\text{Cr}(\text{L3.2})_2+\text{H}]^{2+}$ (complex 3.5).

3.2.11 Synthesis of $[\text{Fe}(\text{L3.2})_2](\text{NO}_3)$ (3.6)

A 2 mL methanolic solution of ferric nitrate nonahydrate (1.0 mmol, 0.404 g) was added carefully to 20 mL methanol-chloroform (9:1,v/v) solution of **HL3.2** (2.0 mmol, 1.362g). Then, the reaction mixture was stirred for ca. 3 h. red colour powder was collected in high yield after slow evaporation of the solvent.

Yield: 1.377 g (78%). Anal. Calc. for $\text{C}_{82}\text{H}_{78}\text{FeN}_{13}\text{O}_{11}$: C 66.66%; H 5.32%; N, 12.32%; Found: C 66.55%; H 5.25%; N 12.30%; IR (cm^{-1} , KBr): $\nu(\text{C}=\text{N})$ 1605s; $\nu(\text{NO}_3^-)$ 1300s and 812s; $\nu(\text{C}=\text{O})$ 1642s (**Figure 3.14**). The molecular ion peak was appeared at $m/z = 1414.54$ and 707.77, corresponding to $[\text{Fe}(\text{L3.2})_2]^+$ and $[\text{Fe}(\text{L3.2})_2+\text{H}]^{2+}$, respectively (**Figure 3.19**).

UV-Vis, λ_{max} (nm), (ϵ ($\text{dm}^3\text{mol}^{-1}\text{cm}^{-1}$)) in Britton Robinson buffer at pH= 7.4: 525(82471).

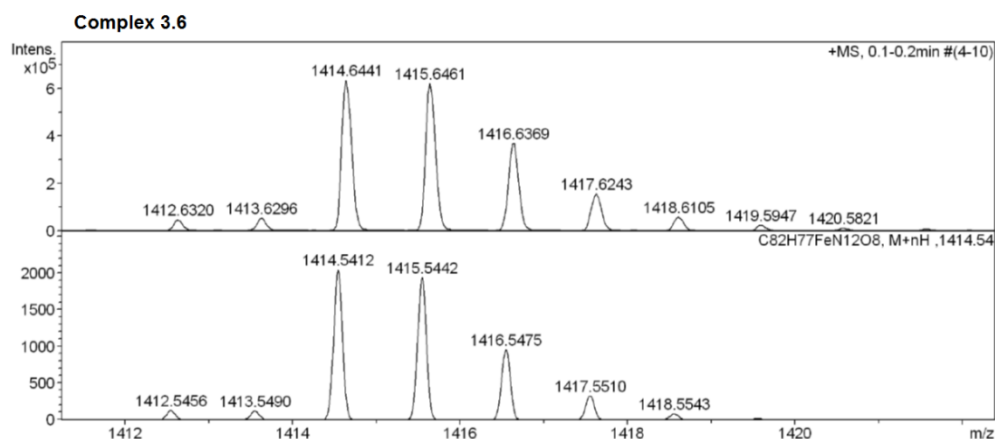


Figure 3.19 (a) ESI-mass spectrum of $[\text{Fe}(\text{L3.2})_2]^+$ (complex 3.6).

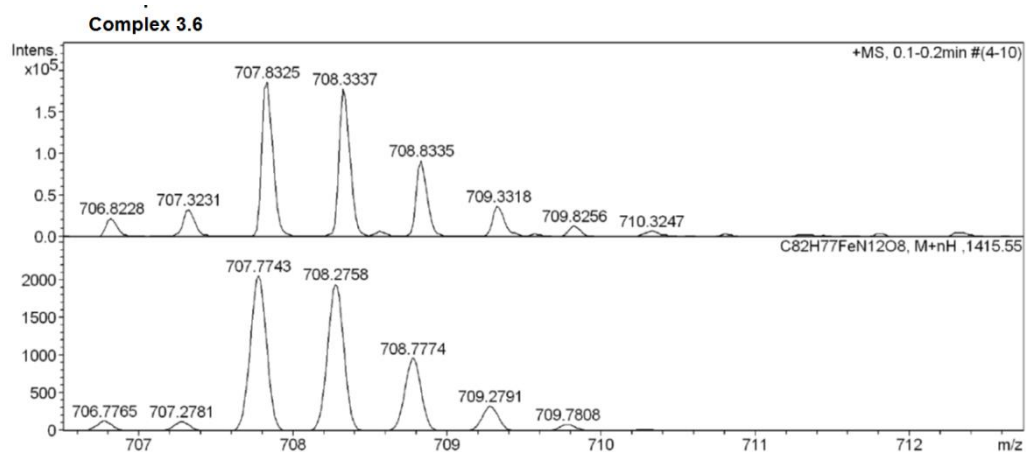


Figure 3.19 (b) ESI-mass spectrum of $[\text{Fe}(\text{L3.2})_2+\text{H}]^{2+}$ (complex 3.6).

3.2.12 UV-visible and fluorescence spectroscopic experiment

Stock solutions of different ions (1×10^{-3} M) were prepared in deionized water medium. A stock solution of the chemosensor (**HL3.1** and **HL3.2**) (1×10^{-3} M) was prepared in methanol medium. The chemosensor (**HL3.1** and **HL3.2**) solution was then diluted to 1×10^{-5} M as per requirement. Competitive assay of various cations and anions and other spectroscopic experiments were performed in aqueous- methanolic Britton Robinson buffer (10mM) medium at pH 7.4. In competitive assay experiments, the test samples were prepared by mixing appropriate amounts of the cations stock in 3 mL of chemosensors (**HL3.1** and **HL3.2**) solution (1×10^{-5} M).

3.2.13 Binding stoichiometry (Job's plot) studies

Binding stoichiometry of the chemosensors with that of Al^{3+} , Cr^{3+} and Fe^{3+} ions are determined by Job's Continuous Variation Method using absorption spectroscopy. At 25 °C temperature, the absorbance was recorded for solutions where the concentrations of both chemosensors and Al^{3+} , Cr^{3+} and Fe^{3+} ions are varied but the sum of their concentrations was kept constant at 1×10^{-5} M. Relative change in absorbance ($\Delta A/A_0$) was plotted against mole fraction. The break point in the resulting plot represents the mole fraction of chemosensor in Al^{3+} , Cr^{3+} and Fe^{3+} complexes. From the break point the stoichiometry was determined. The final results were average of at least three experiments.

3.2.14 Protocol of real sample analysis

A stock solution of the chemosensor (**HL3.1** and **HL3.2**) (1×10^{-2} M) was prepared in methanol:H₂O (9:1) medium. 3mL real sample (Saloon waste water or Laboratory tap water) was taken in a vial and 3 μL stock solution of chemosensor (**HL3.1** and **HL3.2**) was added to it. Instantaneous colour change observed. After that, we took images of the vials under UV-lamp and visible light.

3.2.15 Cell culture

The cervical cancer cell line *HeLa* were procured from the National Center for Cell Science (NCCS) Pune, India. The cells were cultured in an enriched cell culture medium, DMEM (Dulbecco's Modified Eagle Medium), supplemented with 10% FBS (Fetal Bovine Serum) and a mixture of appropriate antibiotics (streptomycin and penicillin) at dose of 100 units/ml. The cells were incubated at a temperature of 37 °C and in the prevalence of 5% CO₂.

3.2.16 Cell interbalisation studies

The cervical cancer cell line *HeLa* were cultured on coverslips for a period of 24 h. Then these cells were either left untreated or were exposed to a dose of ligands (10 μM) and Al³⁺ salt (5 μM), Cr³⁺ salt (5 μM), Fe³⁺ salts (5 μM). These treated cells were then incubated for 24 h. at a temperature of 37 °C. Afterwards the cells were thoroughly washed with the help of 1×PBS. Ultimately the cells were envisaged with the help of fluorescence microscope (Leica) following the mounting of the cells on a glass slide.

3.2.17 Computational method

All computations were performed using the GAUSSIAN 09 (G09)^{3.37} software package. For optimization, we used the density functional theory method at the CAM-B3LYP level^{3.38,3.39} and the standard 6-31+G(d) basis set for C, H, N and O atoms.^{3.40,3.41} TDDFT calculation was performed with the optimized geometry to ensure only positive eigen values. Time-dependent density functional theory (TDDFT)^{3.42-3.44} was performed using the conductor-like polarizable continuum model (CPCM)^{3.45-3.47} and the same CAM-B3LYP level and basis sets in methanol solvent system. GAUSSSUM^{3.48} was used to calculate the fractional contributions of various groups to each molecular orbital.

3.3 Results and discussion

3.3.1 Synthesis and characterization

N-(rhodamine-6G)lactam-hydrazine and azo-aldehyde were prepared following published procedures.^{3.24h,3.21} Schiff base condensation reaction between rhodamine-6G based amine and 2-hydroxy-5-(phenyldiazenyl)benzaldehyde or 2-hydroxy-3-methoxy-5-(p-tolyldiazenyl)benzaldehyde finally generate the chemosensors, **HL3.1** and **HL3.2**, respectively (**Scheme 3.1**). Different spectroscopic techniques (UV-Vis, FT-IR and NMR), X-ray crystallography, ESI-mass and elemental analysis were utilized for their complete characterization (**Figures 3.1-3.23**).

Reaction between $M(\text{NO}_3)_3 \cdot 9\text{H}_2\text{O}$ (where, $M^{3+} = \text{Al}^{3+}$, Cr^{3+} and Fe^{3+}) and **HL3.1/HL3.2** in 1:2 ratio produce complexes **3.1-3.6**, respectively. They were characterized by ^1H NMR, ^{13}C NMR, FT-IR spectroscopy, X ray-crystallography, and C, H and N analysis. In ESI-MS analysis both the chemosensors exhibit base peak at m/z 689.27 and 681.27, corresponding to $[\text{HL3.1}+\text{Na}]^+$ and $[\text{HL3.2}+1]^+$, respectively. All the six complexes **3.1-3.6** give ESI-MS peaks at 1357.37, 1382.60, 1386.51, 1385.51, 1411.49, 1414.64 corresponding to $[\text{M}(\text{L3.1/L3.2})_2]^+$ (where $M = \text{Al}, \text{Cr}, \text{Fe}$) species. Interestingly, all the experimental data are well matched with their simulated patterns.

3.3.2 Crystal structure descriptions of chemosensors (**HL3.1** and **HL3.2**)

X ray-crystallographic analysis reveals that **HL3.1** is crystallized in the monoclinic system with $P2_1/c$ space group, while **HL3.2** in the triclinic system with $P\bar{1}$ space group (**Table 3.1**). Crystal structure of chemosensor **HL3.1** is presented in **Figure 3.20**, while **HL3.2** is depicted in **Figure 3.21**. Both chemosensors are non planer and crystal structures confirm imine bond formation, presence of spirolactam ring, xanthene unit and azo chromophore within the molecules. The C–O and C–N bond distances of the **HL3.1** vary within the range 1.220-1.425 Å and 1.280-1.494 Å, respectively.

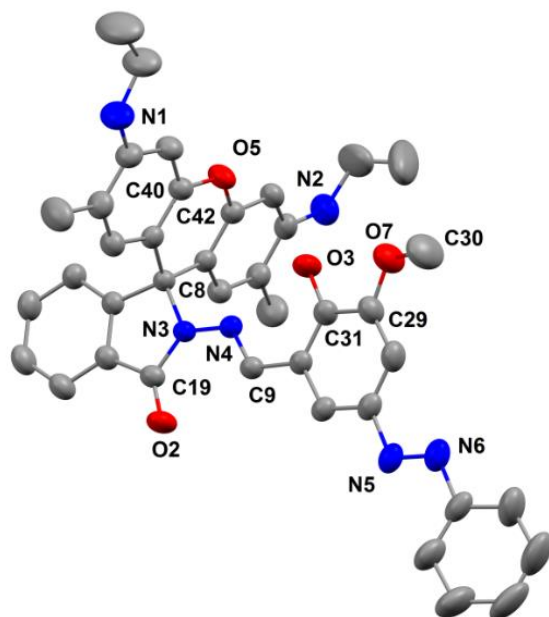


Figure 3.20 Crystal structure of chemosensor **HL3.1**. Atoms are shown as 30% thermal ellipsoids. H atoms and solvent molecule are omitted for clarity.

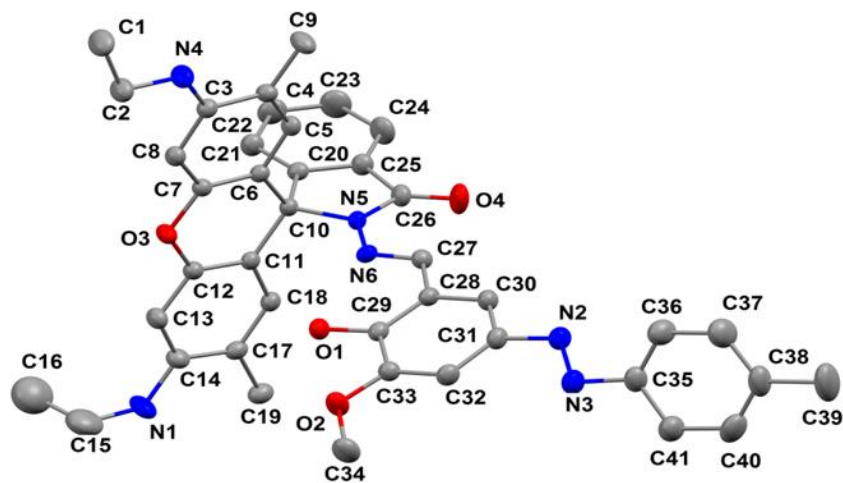


Figure 3.21 Crystal structure of the chemosensor **HL3.2**. Atoms are shown as 30% thermal ellipsoids. Here, H and solvent molecule atoms are omitted for clarity.

3.3.3 Crystal structure descriptions of complexes 3.1 and 3.4

Crystals of complex **3.1** were developed from methanol-DMF solvent mixture whereas, crystals of complex **3.4** were collected from chloroform-methanol solvent mixture. Complex **3.4** crystallized in the triclinic system with space group $P\bar{1}$ where the asymmetric unit consists of two complex cations and four non-coordinating nitrate anions together with four water molecules as solvent of crystallization. Crystal structure of one of the complex cations is shown in **Figure 3.22**. Crystallographic data are collected in **Table 3.1** and important bond lengths and angles in are given in **Table 3.2**. Crystal structure of complex **3.4** confirms presence of open spirolactam ring within the chemosensor and 2:1 binding stoichiometry between the chemosensor and Al^{3+} ion. The structures of complex cations in the asymmetric unit are eventually similar and structure of only one unit briefly described here. In the complex cations, the metal centre is distorted octahedral being coordinated with two imine N-atoms (N4 and N10), two phenoxide O-atoms atoms (O3 and O7) of both ligands and two O-atoms of open spirolactam amide (O2 and O6) of chemosensor in meridional fashion. The Al^{3+} -O_{phenoxide}, Al^{3+} -N_{imine} bond distances vary within the range 1.807–1.929(3) Å, 1.811–1.863(2) Å and 1.957–2.000(3) Å, respectively. In complex **3.4**, spirolactam amide present as amide form in one chemosensor and in iminolate form in other one. Presence of both amide and iminolate form of spirolactam amide further supported by shorter C–O (C67–O6, 1.247(5) Å) and longer C–N (C67–N9, 1.348(6) Å) bond distances in one chemosensor unit and relatively longer C–O (C26–O2, 1.297(5) Å) and shorter C–N (C26–N3, 1.323(5) Å) bond distances in another chemosensor unit. The azo bonds (N11–N12 and N5–N6) exhibit a double bond character with distances of 1.265(6) Å and 1.277(6) Å, repetitively. In the complex the azo bound phenyl ring is slightly twisted with respect to the phenolate ring. The dihedral angles between these two phenyl rings are 21.91° and 36.92° for complex **3.4** (**Figure 3.22**).

Complex **3.1** crystallized in the same crystal system as complex **3.4** does but the asymmetric unit of complex **3.1** consists of a complex cation, comprising with an Al^{3+} ion

and two chemosensors, and one non-coordinating nitrate anion. Three DMF and two water molecules are also present as solvents of crystallization. In complex **3.1**, spirolactamide present exclusively in iminolate form. Presence of the iminolate form is confirmed by longer C–O (C10–O1=1.290 Å, C11–O2=1.291 Å) and shorter C–N (C10–N10=1.312 Å, C11–N2=1.307 Å) bond distances within the complex cation (**Figure 3.23** and **Table 3.2**).

Table 3.2 Selected Bond lengths (Å) and Bond angles (°) for **HL3.1**, **HL3.2**, complex **3.1** and complex **3.4**.

HL3.1		HL3.2		complex 3.1		complex 3.4	
N4-C9	1.282(4)	C27-N6	1.221(4)	Al1-O1	1.889(2)	Al1-O2	1.863(4)
N4-N3	1.370(4)	N6-N5	1.361(5)	Al1-O2	1.893(2)	Al1-O3	1.811(4)
O2-C19	1.229(4)	C26-N5	1.367(2)	Al1-O6	1.850(2)	Al1-O6	1.929(4)
O3-C31	1.356(4)	C10-N5	1.489(3)	Al1-O7	1.840(2)	Al1-O7	1.807(4)
O5-C40	1.371(4)	C26-O4	1.230(4)	Al1-N3	1.985(2)	Al1-N3	1.957(4)
O5-C32	1.375(4)	C29-O1	1.335(4)	Al1-N9	1.992(2)	Al1-N10	2.000(4)
N3-C19	1.374(4)	C10-C11	1.511(5)	O2-C11	1.291(3)	O6-C67	1.251(5)
N3-C8	1.510(4)	C10-C6	1.512(4)	O1-C10	1.290(3)	O2-C26	1.294(5)
N5-N6	1.241(4)	C27-N6	1.282(6)	N2-C11	1.307(3)	N9-C67	1.334(6)
N5-C12	1.446(5)	C14-N1	1.382(3)	N10-C10	1.312(3)	N3-C26	1.322(5)
O7-C29	1.375(5)	C3-N4	1.361(4)	N6-N7	1.265(4)	N11-N12	1.265(6)
O7-C30	1.436(6)	N4-C3	1.371(5)	N2-N3	1.401(3)	N5-N6	1.277(6)
N1-C4	1.392(5)	N4-C2	1.454(6)	O7-Al1-O1	168.75(9)	O2-Al-O3	170.38(15)
N6-C14	1.434(5)	N2-N3	1.261(5)	O6-Al1-O2	169.39(9)	N4-Al-N10	170.19(17)
N2-C36	1.446(7)	N1-C15	1.489(9)	N3-Al1-N9	167.36(10)	O7-Al-O6	168.23(14)
N3-C8-C100	109.9(3)	N5-C10-C20	99.6(3)	O7-Al1-O6	91.10(10)	N4-Al1-O2	80.43(15)
N3-C8-C7	110.5(3)	N5-C10-C6	109.6(3)	O2-Al1-N9	90.24(9)	N4-Al1-O3	92.43(17)
C100-C8-C7	110.6(3)	C20-C10-C6	111.4(3)	O6-Al1-O1	90.21(10)	N10-Al1-O3	92.15(15)
N3-C8-C25	98.7(2)	N5-C10-C11	111.3(3)	O7-Al1-N3	97.59(9)	N10-Al1-O2	94.01(14)

C100-C8-C25	113.8(3)	C20-C10-C11	114.1(3)	O6-A11-N3	90.13(9)	N10-A11-O6	78.87(15)
C7-C8-C25	112.7(3)	C6-C10-C11	110.4(3)	O1-A11-N3	93.58(9)	N10-A11-O6	89.78(14)
				O2-A11-N3	79.29(9)	N4-A11-O6	92.69(15)
				O7-A11-N9	89.60(9)	N4-A11-O7	98.38(17)

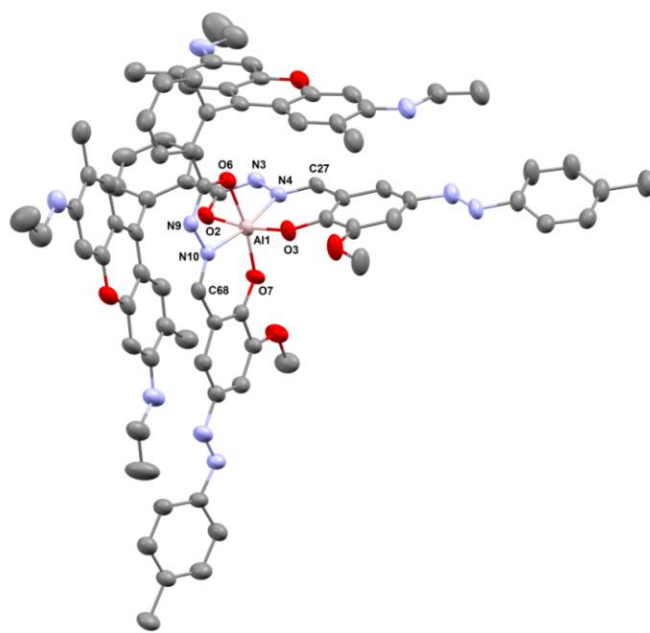


Figure 3.22 Crystal structure of one of the complex cations of **3.4**. Atoms are shown as 30% thermal ellipsoids. H atoms are omitted for clarity.

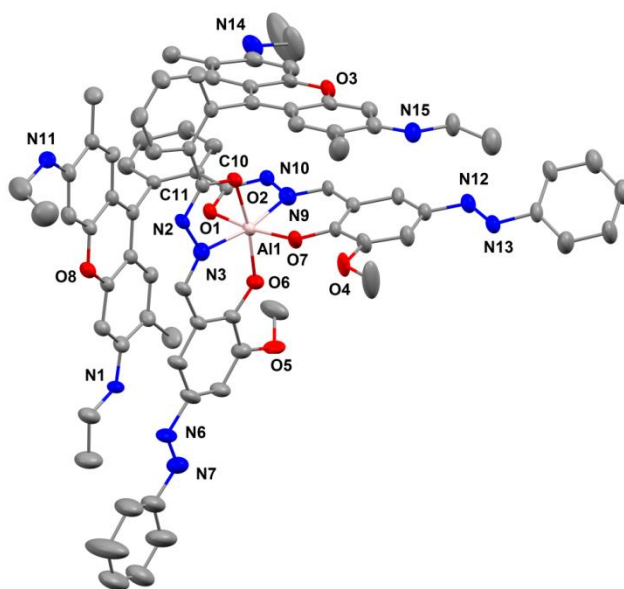


Figure 3.23 Crystal structure of complex cation of **3.1**. Atoms are shown as 30% thermal ellipsoids. Here, H atoms are omitted for clarity.

3.3.4 NMR studies

All ^1H NMR spectra are recorded in $\text{DMSO-}d_6$ solvent. ^1H NMR spectrum of **HL3.2** is discussed as a representative example. Here, both phenolic -OH and imine proton appear as sharp singlet at 11.51 and 9.04 ppm, respectively. Aromatic protons appear as singlet at 8.32 and 7.42 ppm, represent azo-aromatic part, doublet at 7.74 and 7.36 ppm, represent *O*-vanillin part. Aromatic protons adjacent to the spirolactam ring appear as doublets at 7.94 and 7.06 ppm and multiplet within 7.65-7.56 ppm. Aromatic protons present in xanthene part appear as sharp singlet with double intensity at 6.34 and 6.22 ppm. Aliphatic amine (-NH) protons appear as triplet at 5.09 ppm. Aromatic -OCH₃ protons appear as singlet at 3.84 ppm. Aliphatic CH₂ protons appear as multiplet within 3.18-3.09 ppm. Aromatic CH₃ protons appear as singlet at 2.39 and 1.85 ppm whereas, aliphatic CH₃ protons appear as triplet at 1.21 ppm (**Figure 3.6**). ^1H NMR spectrum data of **HL3.1** is collected in experimental section (**Figure 3.3**).

Both Al^{3+} - probe complexes (**3.1** and **3.4**) give clean and similar type of ^1H NMR spectra in $\text{DMSO-}d_6$ solvent. In complex **3.4**, coordination of metal with chemosensors result disappearance of phenolic -OH proton, whereas position of imine proton (singlet, 9.08 ppm) remain almost unchanged. We also observe down field shift of aromatic protons and broadening of the peaks. Aromatic protons adjacent to the open spirolactam ring, azo-aromatic moiety and *o*-vanillin part appear as multiplet within range 7.96-7.47 ppm. Protons present in xanthene part appear as doublet at 6.40 and 6.29 ppm, respectively. Aliphatic CH₂ protons appear as multiplet within 3.19-3.12 ppm and aromatic OCH₃ protons (merged with water molecules) appear as multiplet within 3.90-3.69 ppm region. During complexation one aliphatic -NH proton disappears, other aliphatic amine get protonated (-NH₂⁺) and appears at 5.93 ppm. In complex **3.4**, amide group is present in iminolate form in one chemosensor and amide form in another chemosensor for which proton appears at 8.42 ppm. Interestingly,

positions of aromatic and aliphatic CH₃ protons are almost unchanged upon complexation (2.39, 1.87 and 1.20 ppm, respectively) (**Figure 3.12**). ¹H NMR spectral data of complex **3.1** is collected in experimental section (**Figure 3.9**).

¹³C NMR spectra are also recorded in DMSO-d₆ solvent and collected in experimental section. In **HL3.2**, spirolactam amide carbon appears at 165.25 and phenolic carbon appears at 152.35 ppm. Imine carbon appears at 151.99 ppm. In complex **3.4**, metal coordination results downfield shift of spirolactam amide carbon, phenolic carbon and imine carbon positions at 168.27, 164.27 and 157.25 ppm respectively. In free chemosensor, carbon atom connecting the xanthene part and spirolactam ring is sp³ hybridized and appears at 66.08 ppm. Al³⁺ coordination results spirolactam ring opening, therefore, carbon atom connecting xanthene part and spirolactam ring has changed hybridization from sp³ to sp² and appears at 141.46 ppm. Interestingly, position of OCH₃ carbon, aliphatic CH₂ and CH₃ carbon atoms remain almost unchanged (appear at 56.34, 17.91 and 14.54 ppm, respectively) both in free and Al³⁺ bound chemosensor (**Figures 3.11** and **3.17**).

We have also performed ¹H NMR titration in DMSO-d₆ solvent. Gradual addition of Al³⁺ (0-2 equivalent) to the chemosensor (**HL3.1/HL3.2**) solution shows gradual disappearance of phenolic-OH proton and aliphatic -NH proton confirming opening of spirolactam ring followed by complexation through phenoxide oxygen, amide oxygen and imine nitrogen atoms. Broadening of both aromatic and aliphatic protons is also observed during this titration process (**Figures 3.24** and **3.25**). Since all the sensing experiments are studied in methanol:water solution, we have performed ¹H NMR of free chemosensors and complexes **3.1** and **3.4** in CD₃OD. Well resolved NMR spectra are presented in experimental section (**Figures 3.10b** and **3.16b**).

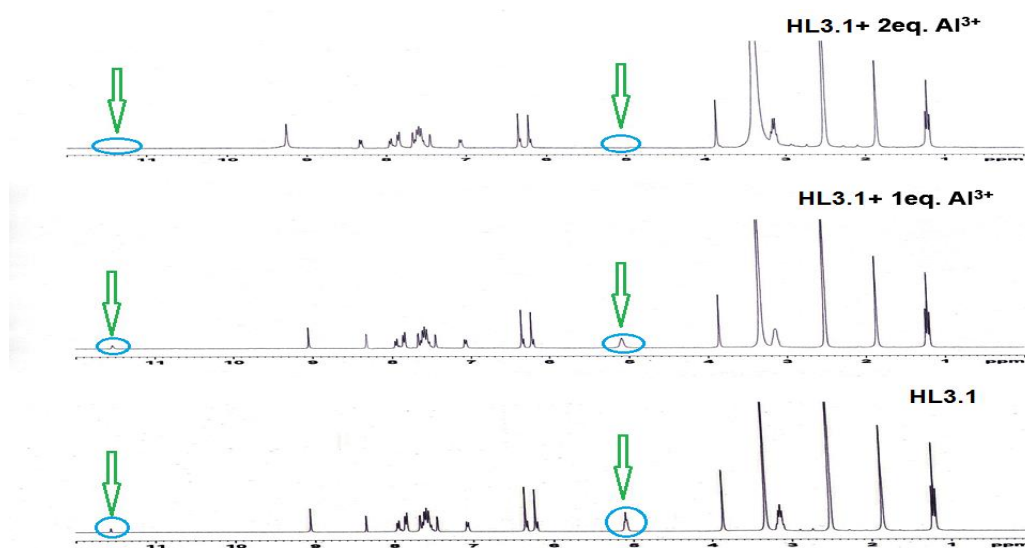


Figure 3.24 $^1\text{H-NMR}$ titration of the free ligand (**HL3.1**) and with the addition of 1 and 2 equivalent of Al^{3+} in DMSO-d_6 recorded on a 300 MHz Bruker NMR spectrometer.

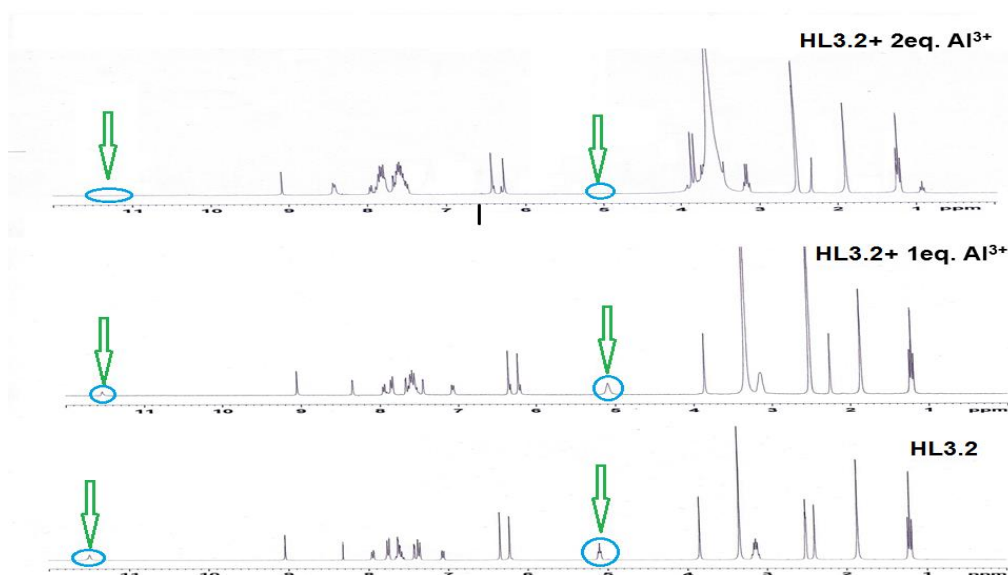


Figure 3.25 $^1\text{H-NMR}$ titration of the free ligand (**HL3.2**) and with the addition of 1 and 2 equivalent of Al^{3+} in DMSO-d_6 recorded on a 300 MHz Bruker NMR spectrometer.

3.3.5 Absorption spectral analysis

The UV-Vis spectra of chemosensors (**HL3.1** and **HL3.2**) are first examined in 10 mM Britton Robinson buffer solution at pH 7.4 (1 : 9, water : methanol, v/v). Chemosensors, **HL3.1** and **HL3.2** exhibit well-resolve bands at ~ 307 and ~ 360 nm, responsible for $\pi \rightarrow \pi^*$

and $n \rightarrow \pi^*$ type of transitions. Interestingly upon successive addition of Al^{3+} , Fe^{3+} and Cr^{3+} ions (0-6 μM , 10 mM Britton Robinson buffer solution; pH 7.4; 1:9, water: methanol, v/v) to the chemosensor (10 μM), a new peak appears at ~ 525 nm with significant changes in the spectra of all chemosensors (**HL3.1** and **HL3.2**). In case of Fe^{3+} an additional peak appears at ~ 395 nm (**Figures 3.26 and 3.27**). Presence of Al^{3+} , Cr^{3+} and Fe^{3+} ions initiate spirolactam ring opening followed by the coordination with the chemosensors, resulting its colour change from faint yellow to intense fluorescent yellowish pink in visible light. Spirolactam ring opening increases delocalization of π electrons within ligand framework followed by charge transfer transitions. Saturation has been observed in presence of 0.5 equivalents of trivalent metal ions to the chemosensors. 2:1 binding stoichiometry of the chemosensors with Al^{3+} , Cr^{3+} and Fe^{3+} ions has been confirmed by Job's plot analysis at $\lambda = 525$ nm (**Figures 3.28 and 3.29**).

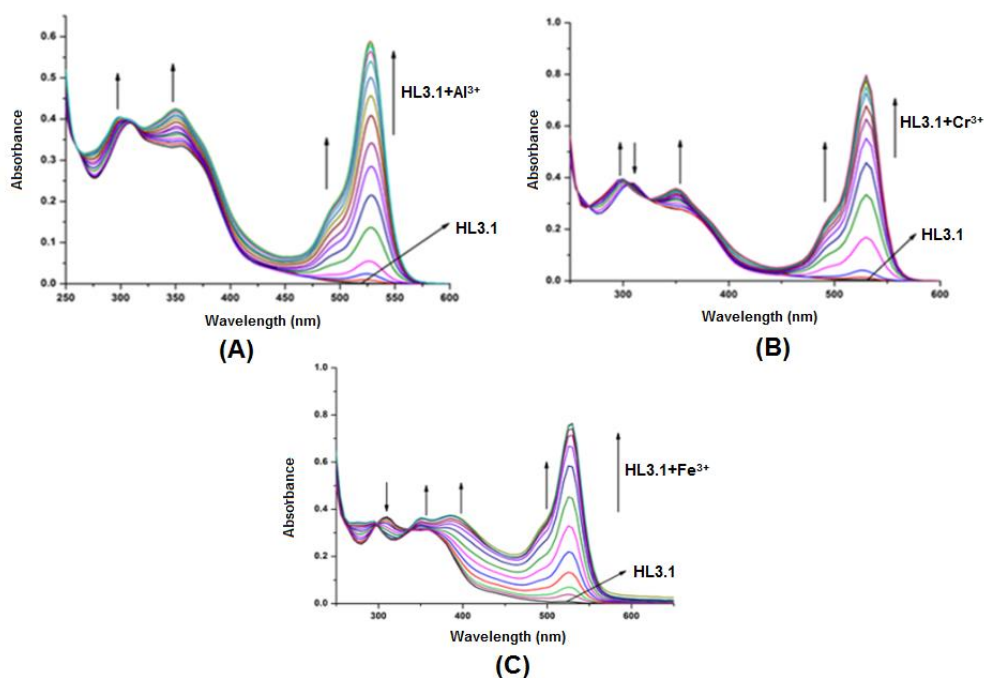


Figure 3.26 Absorption titration study of **HL3.1** (10 μM) with gradual addition of metal ions (Al^{3+} , Cr^{3+} and Fe^{3+}) (A-C) 0-6 μM in 10 mM Britton Robinson buffer at pH 7.4.

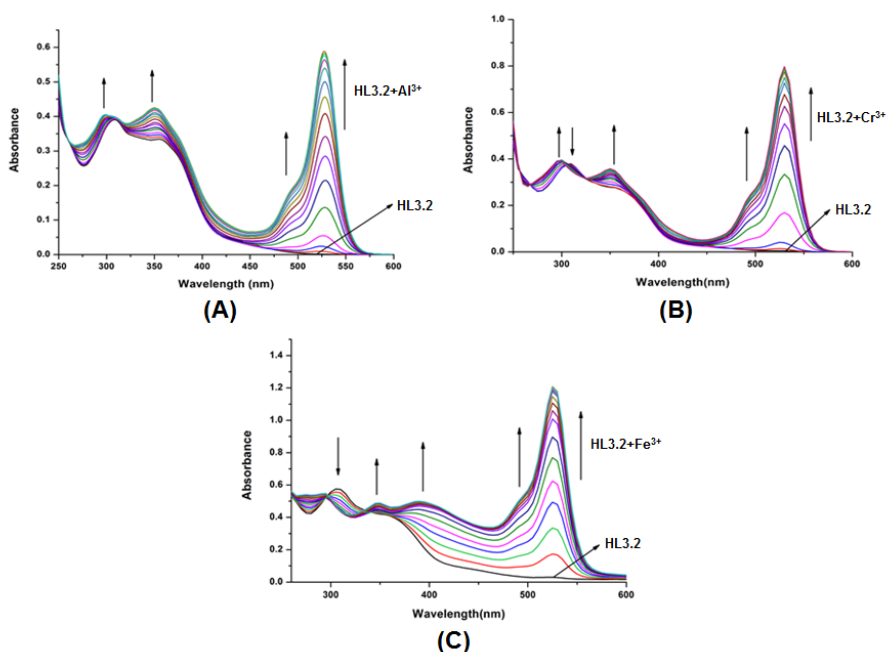


Figure 3.27 Absorption titration study of **HL3.2** (10 μM) with gradual addition of metal ions (Al³⁺, Cr³⁺ and Fe³⁺) (a-c) 0-6 μM in 10 mM Britton Robinson buffer at pH 7.4.

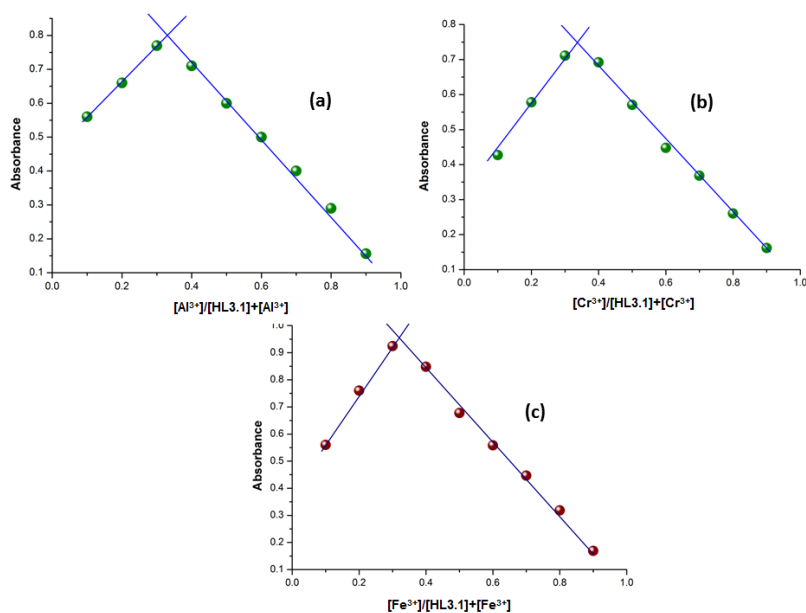


Figure 3.28 2:1 (Ligand:Metal) binding stoichiometry has shown by Job's plot of complex 3.1-3.3 (a-c) (at λ = 525 nm). Symbols and solid lines represent the experimental and simulated profiles, respectively

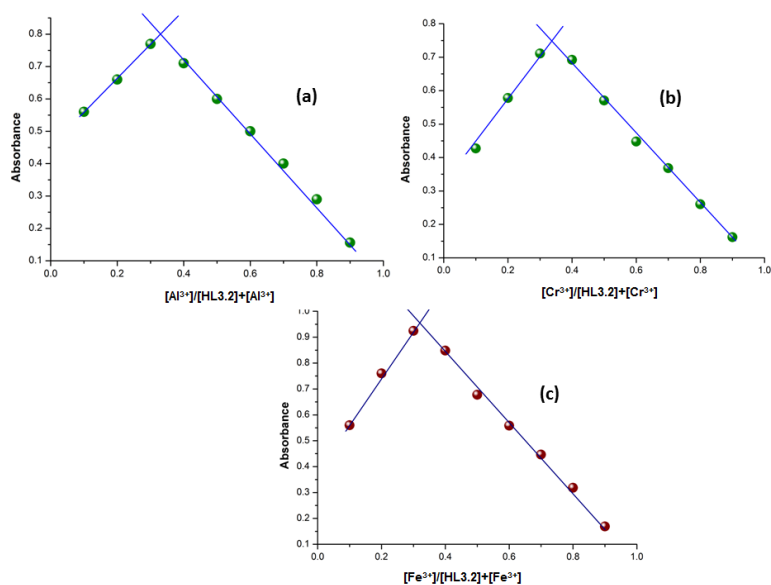


Figure 3.29 2:1 (Ligand:Metal) binding stoichiometry has shown by Job's plot of complex 3.4-3.6(a-c) (at $\lambda = 525$ nm). Symbols and solid lines represent the experimental and simulated profiles, respectively.

3.3.6 Fluorescence properties analysis

Both chemosensors ($10 \mu M$) are non-fluorescent when excited at 360 nm in $10mM$ Britton Robinson buffer (1:9, water : methanol, v/v; $pH = 7.4$) medium. Presence of trivalent metal ions (Al^{3+} , Cr^{3+} and Fe^{3+} ions; $0-6 \mu M$) to the probe results enormous fluorescence enhancement at 555 nm (**Figures 3.30** and **3.31**). Fluorescence increases steadily and reaches a maximum at 0.5 equivalents of every trivalent metal ion. Free chemosensors are non-fluorescent due to presence of closed spirolactam ring. Metal coordination with imine N-atoms, phenoxide O-atoms and O-atoms of open spirolactam amide (CHEF on) initiates fluorescence enhancement due to opening of the spirolactam ring. In case of Al^{3+} and Cr^{3+} the emission enhancement is ~ 400 fold, whereas for Fe^{3+} enhancement is ~ 100 fold.

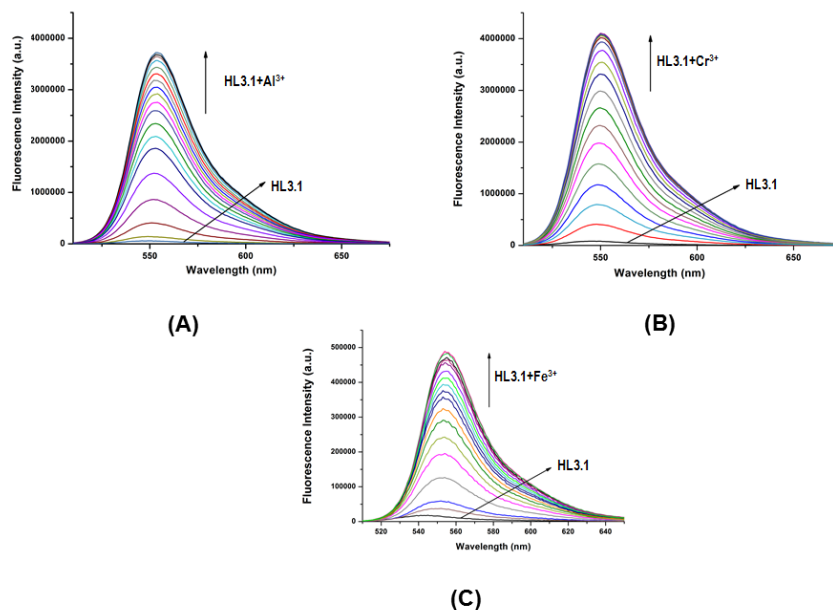


Figure 3.30 Fluorescence titration of **HL3.1** (10 μM) in 10 mM Britton Robinson buffer at pH = 7.4 by successive addition of metal ions (Al^{3+} , Cr^{3+} and Fe^{3+}) (A-C) (0–6 μM) with $\lambda_{\text{em}} = 555$ nm.

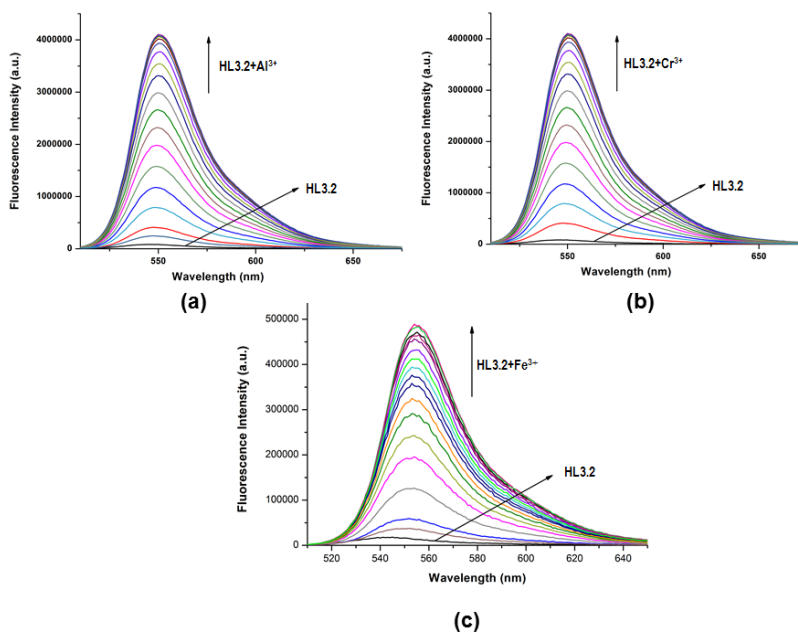


Figure 3.31 Fluorescence titration of **HL3.2** (10 μM) in 10 mM Britton Robinson buffer at pH = 7.4 by successive addition of metal ions (Al^{3+} , Cr^{3+} and Fe^{3+}) (0–6 μM) with $\lambda_{\text{em}} = 555$ nm.

Binding ability of the chemosensors towards Al^{3+} , Cr^{3+} and Fe^{3+} ions has been calculated using Benesi-Hildebrand equation (Equation 1) involving fluorescence titration curve.^{3,36}

$$1/(F - F_0) = 1/(F_{\max} - F_0) + (1/K[C])\{1/(F_{\max} - F_0)\} \dots\dots\dots(1)$$

Here, F_{\max} , F_0 and F_x represent fluorescence intensities of each chemosensor (**HL3.1/HL3.2**) in presence of metal ions at saturation, free chemosensor (**HL3.1/HL3.2**) and any intermediate metal ion concentration, respectively. K is denoted as the binding constant of the complexes and concentration of respective metal ion is represented by C . The value of binding constant (K) has been determined using the relation, $K=1/\text{slope}$. Binding constant values are $5.14 \times 10^5 \text{ M}^{-2}$, $4.91 \times 10^5 \text{ M}^{-2}$, $3.37 \times 10^4 \text{ M}^{-2}$ and $5.03 \times 10^5 \text{ M}^{-2}$, $4.86 \times 10^5 \text{ M}^{-2}$, $3.95 \times 10^4 \text{ M}^{-2}$, respectively for the chemosensors **HL3.1** and **HL3.2** towards Al^{3+} , Cr^{3+} and Fe^{3+} ions (**Figures 3.32** and **3.33**).

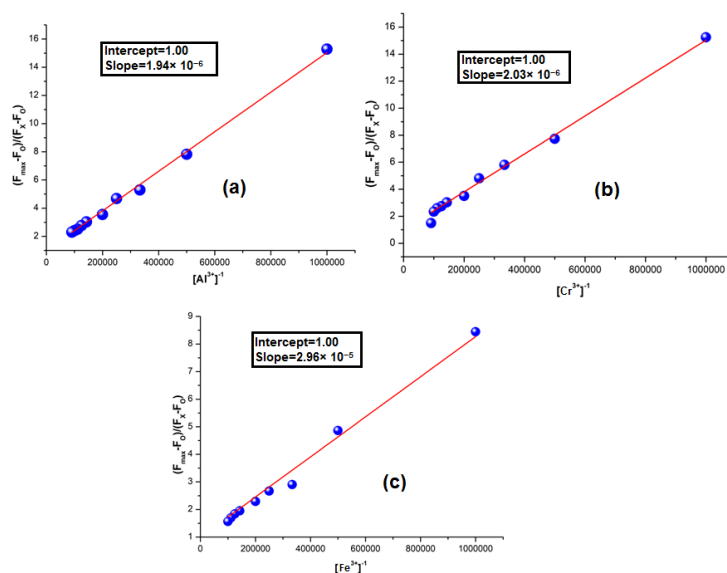


Figure 3.32 Benesi-Hildebrand plot for complex **3.1-3.3** (a-c). The plot is obtained after adding $5 \mu\text{M}$ Al^{3+} Cr^{3+} and Fe^{3+} solution to the **HL3.1** solution ($10 \mu\text{M}$) (in 10 mM HEPES buffer medium, pH 7.4).

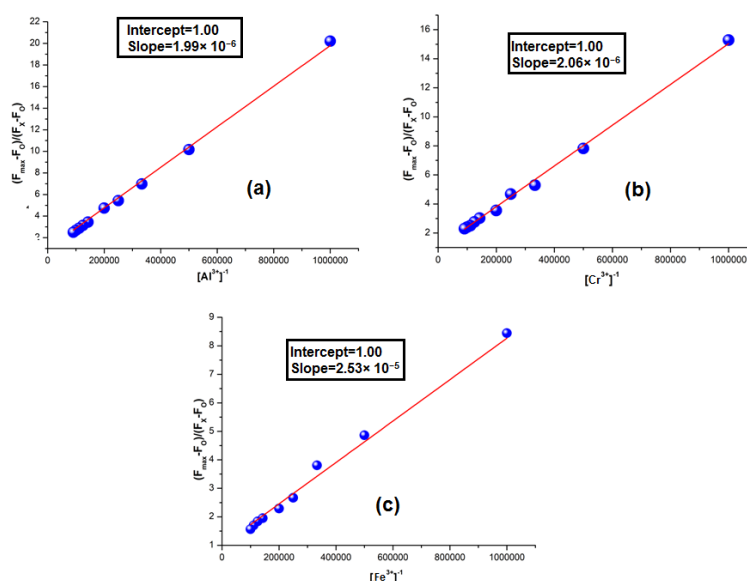


Figure 3.33 Benesi-Hildebrand plot for complex **3.4-3.6** (a-c). The plot is obtained after adding 5 μ M Al^{3+} , Cr^{3+} and Fe^{3+} solution to the **HL3.2** solution (10 μ M) (in 10 mM HEPES buffer medium, pH 7.4).

High selectivity of the chemosensors toward respective metal ions (Al^{3+} , Cr^{3+} and Fe^{3+}) are again established by competition assay experiment. Here in presence of chemosensor and respective metal (Al^{3+} , Cr^{3+} and Fe^{3+}) ion, (0.5 equiv.) different metal ions (Cd^{2+} , Hg^{2+} , Pb^{2+} , Zn^{2+} , Ag^{+} , Mn^{2+} , Fe^{2+} , Co^{2+} , Ni^{2+} , Na^{+} , K^{+} , Mg^{2+} , Cu^{2+} , Ca^{2+} , As^{3+} , Ga^{3+} , In^{3+} and Tl^{3+}) (**Figures 3.34** and **3.35**) and common anions ($S_2O_3^{2-}$, S^{2-} , SO_3^{2-} , HSO_4^{-} , SO_4^{2-} , SCN^{-} , N_3^{-} , OCN^{-} , AsO_4^{3-} , $H_2PO_4^{-}$, HPO_4^{2-} , PO_4^{3-} , ClO_4^{-} , AcO^{-} , NO_3^{-} , F^{-} , Cl^{-} , PF_6^{-} , $P_2O_7^{4-}$ and ROS such as $NaOCl$, KO_2 , H_2O_2) are added in excess amount (10.0 equiv.) in 10 mM Britton Robinson buffer solution at pH 7.4. Competition assay experiments clearly express high fluorescent recognition of chemosensors (**HL3.1** and **HL3.2**) for Al^{3+} , Cr^{3+} and Fe^{3+} ions over most of the metal ions and all common anions. (**Figures 3.36** and **3.37**).

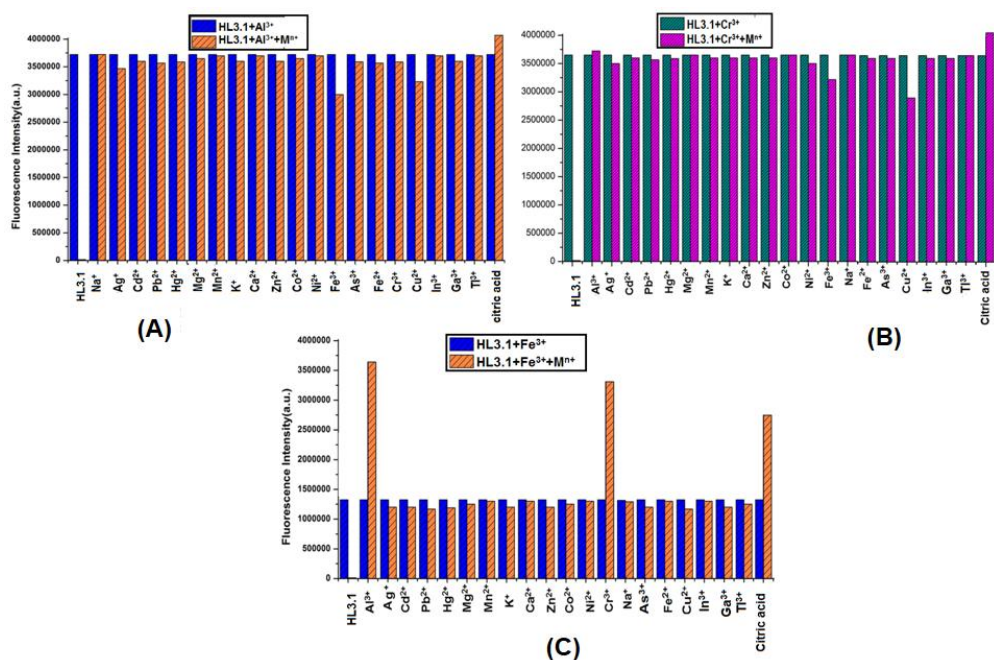


Figure 3.34 Relative fluorescence intensity diagram of [HL3.1-Al³⁺], [HL3.1-Cr³⁺] and [HL3.1-Fe³⁺] (A-C) system in the presence of different cations in 10 mM Britton Robinson buffer at pH 7.4.

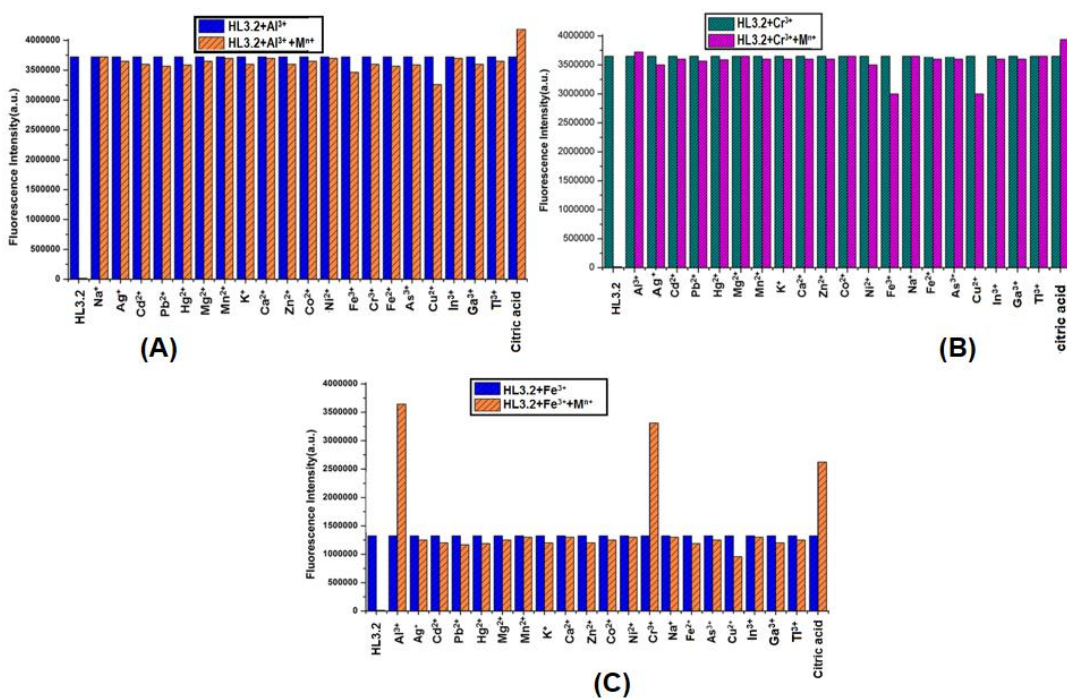


Figure 3.35 Relative fluorescence intensity diagram of [HL3.2-Al³⁺], [HL3.2-Cr³⁺] and [HL3.2-Fe³⁺] (A-C) system in the presence of different cations in 10 mM Britton Robinson buffer at pH 7.4.

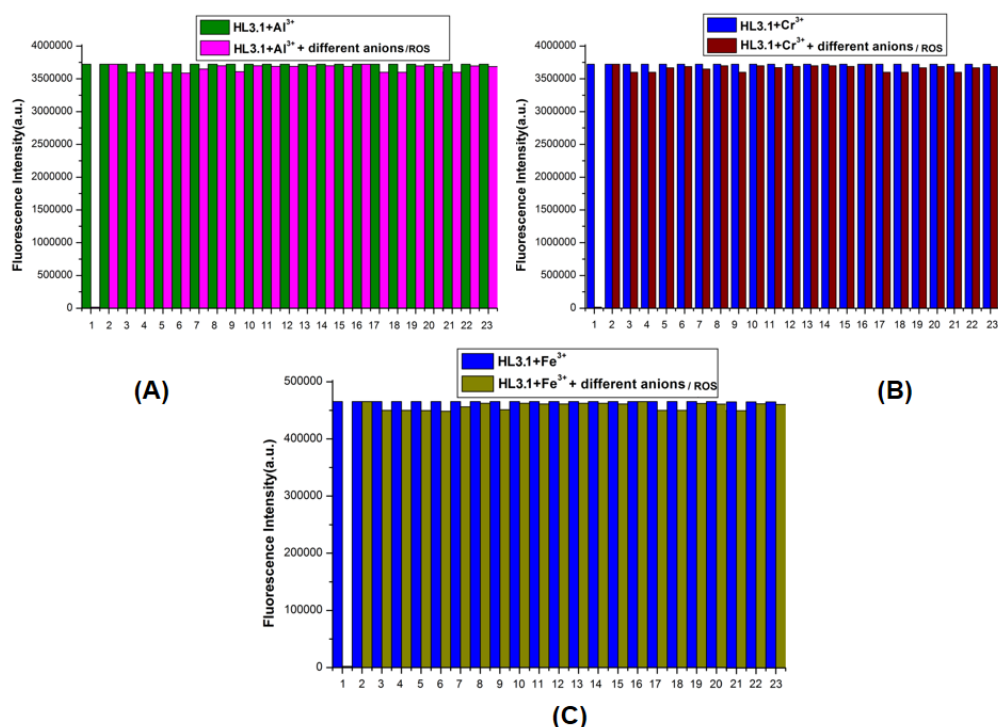


Figure 3.36 Relative fluorescence intensity diagram of [HL3.1-Al³⁺], [HL3.1-Cr³⁺] and [HL3.1-Fe³⁺](A-C) system in the presence of different anions in Britton Robinson buffer medium (10 mM) at pH 7.4. 1=only HL3.1 (10 μM) and (2-23)= HL3.1 (10 μM) + Al³⁺/Cr³⁺/Fe³⁺(5 μM) + Anions (50 μM), Anions = 2-S₂O₃²⁻, 3-S²⁻, 4-SO₃²⁻, 5-HSO₄⁻, 6-SO₄²⁻, 7-SCN⁻, 8-N₃⁻, 9-OCN⁻, 10-AsO₄³⁻, 11-H₂PO₄⁻, 12-HPO₄²⁻, 13-PO₄³⁻, 14-ClO₄⁻, 15-AcO⁻, 16-NO₃⁻, 17-F⁻, 18-Cl⁻, 19-PF₆⁻, 20-P₂O₇⁴⁻, 21NaOCl, 22KO₂, 23H₂O₂.

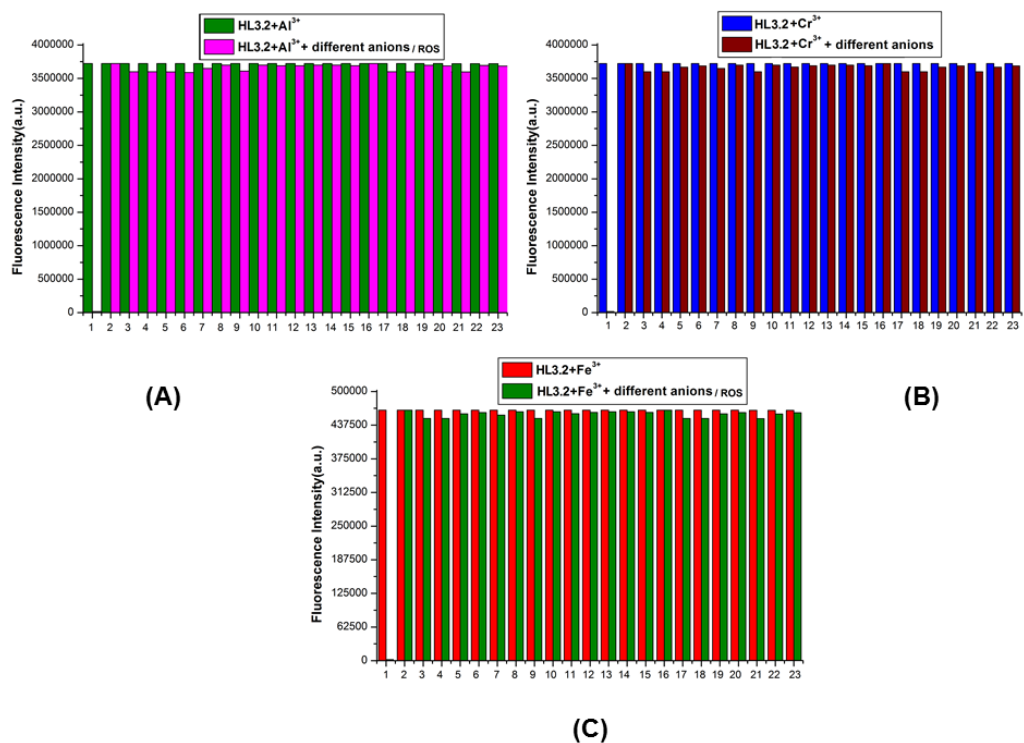


Figure 3.37 Relative fluorescence intensity diagram of $[\text{HL3.2-Al}^{3+}]$, $[\text{HL3.2-Cr}^{3+}]$ and $[\text{HL3.2-Fe}^{3+}]$ (A-C) system in the presence of different anions in Britton Robinson buffer medium (10 mM) at pH 7.4. 1=only **HL3.2** (10 μM) and (2-23)= **HL3.2** (10 μM) + $\text{Al}^{3+}/\text{Cr}^{3+}/\text{Fe}^{3+}$ (5 μM) + Anions (50 μM), Anions = 2- $\text{S}_2\text{O}_3^{2-}$, 3- S^{2-} , 4- SO_3^{2-} , 5- HSO_4^- , 6- SO_4^{2-} , 7- SCN^- , 8- N_3^- , 9- OCN^- , 10- AsO_4^{3-} , 11- H_2PO_4^- , 12- HPO_4^{2-} , 13- PO_4^{3-} , 14- ClO_4^- , 15- AcO^- , 16- NO_3^- , 17- F^- , 18- Cl^- , 19- PF_6^- , 20- $\text{P}_2\text{O}_7^{4-}$, 21- NaOCl , 22- KO_2 , 23- H_2O_2 .

Interestingly both the chemosensors, **HL3.1** and **HL3.2**, also act as colorimetric probe for selective detection of Al^{3+} , Cr^{3+} and Fe^{3+} ions. Al^{3+} , Cr^{3+} and Fe^{3+} ions exhibit fluorescent pinkish yellow colouration in presence of both probes. Some common cations show light yellow colour in presence of the chemosensors. The intensity of chemosensors increases in the order $\text{Al}^{3+} \approx \text{Cr}^{3+} > \text{Fe}^{3+}$. Thus, the chemosensors will be a good choice for colorimetric detection of Al^{3+} , Cr^{3+} and Fe^{3+} ions both in environmental and biological fields (**Figure 3.38**).

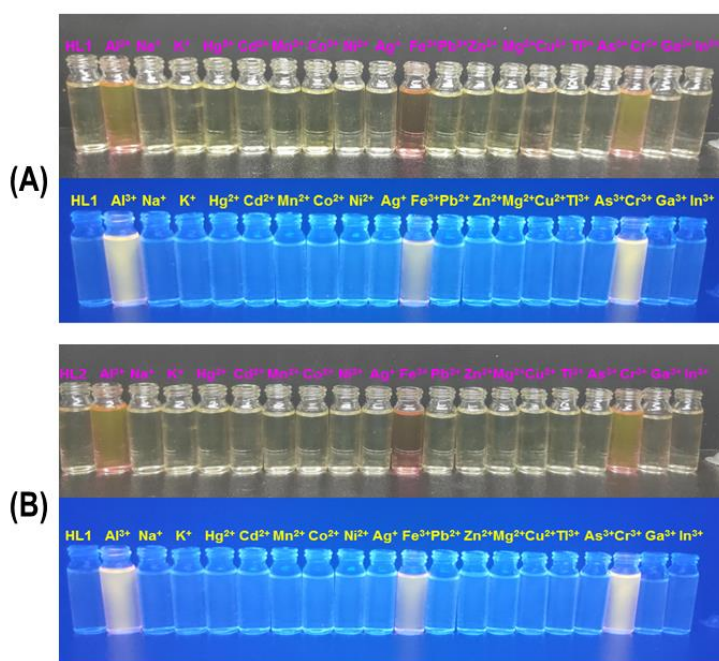


Figure 3.38 Visual colour changes of chemosensor **[HL3.1 (A) and HL3.2 (B)]** (10 μM) in presence of common metal ions (0.5 equivalent) in 10 mM Britton Robinson buffer (pH 7.4).

The images in above row and below row were taken under visible light and UV light respectively.

On-field applicability of these colorimetric sensors has also been tested. We have performed paper strip experiment to support colorimetric as well as fluorescence sensing abilities of both the chemosensor. We have used saloon waste water and our laboratory tap water for real sample analysis. Presence of Al^{3+} ions in saloon waste water and laboratory tap water are successfully detected by our chemosensors through naked eye and under UV-lamp (**Figures 3.39** and **3.40**). Although the chemosensors have low solubility in water but use of aqueous-methanol solution of **HL3.1/HL3.2** in the system and low LOD values of the chemosensors help such type of detection. Both the chemosensors are highly photo-stable. In photostability experiments, 10^{-3} M aqueous solutions of **HL3.1** and **HL3.2** were irradiated with a tungsten lamp light (emission in the 400–700 nm range, power 60 W/220V) over a period of one hour. Interestingly, fluorescence intensity of the chemosensors remains unchanged over a period of time (**Figure 3.41**).

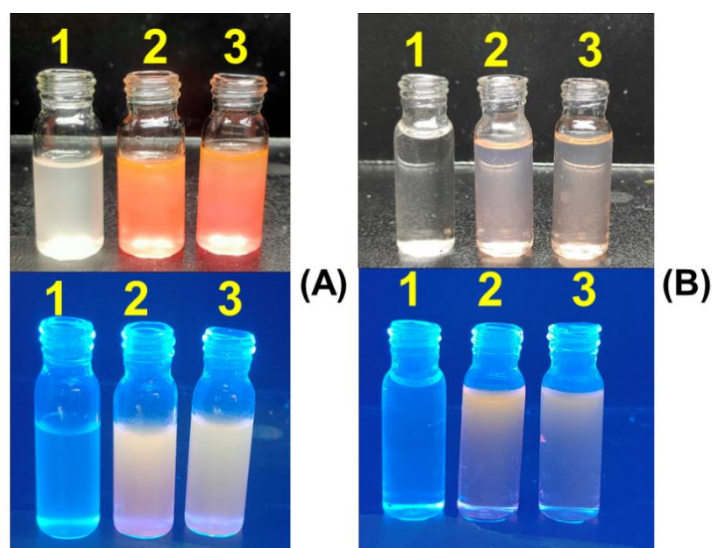


Figure 3.39 Visual colour changes of real samples under normal light (above) and UV light (below) in presence of chemosensors (**HL3.1** and **HL3.2**). (A) Saloon waste water, (1= Only

saloon waste water, 2 and 3= Saloon waste water + **HL3.1/HL3.2**). (B) Laboratory tap water (1= Only laboratory tap water, 2 and 3=laboratory tap water + **HL3.1/HL3.2**).

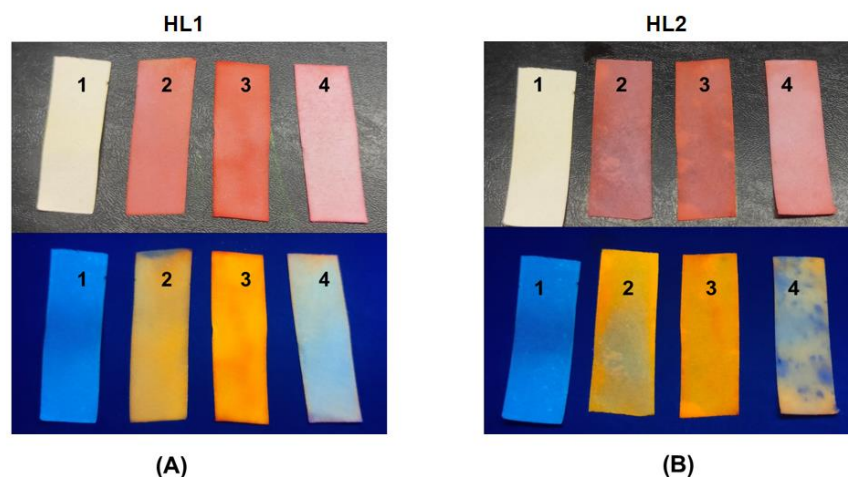


Figure 3.40 Colour changes of paper strip under normal light (above) and UV light (below) in presence of chemosensors **HL3.1** (A) and **HL3.2** (B) [1=only **HL3.1/HL3.2**; 2-4= **HL3.1/HL3.2** + Cr^{3+} , Al^{3+} and Fe^{3+} , respectively].

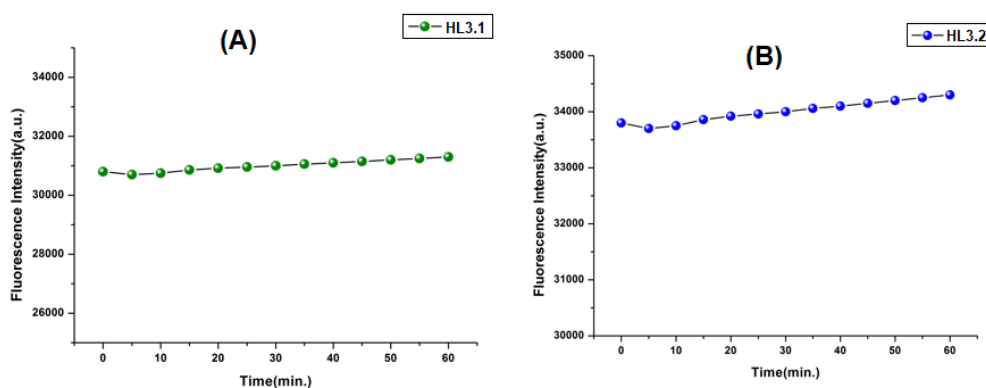


Figure 3.41 The photostability of chemosensors [**HL3.1**(A) and **HL3.2**(B)] (10 μM) in 10 mM Britton Robinson buffer at pH 7.4. ($\lambda_{\text{exc}} = 450 \text{ nm}$).

Limit of detection (LOD) of the chemosensors towards Al^{3+} , Cr^{3+} and Fe^{3+} ions are estimated using 3σ method.^{3,49} The detection limit of the chemosensors (**HL3.1** and **HL3.2**)

for Al^{3+} , Cr^{3+} and Fe^{3+} ions are 2.86×10^{-8} M, 2.67×10^{-8} M, 5.62×10^{-6} M, 2.78×10^{-8} M, 2.61×10^{-8} M and 6.14×10^{-6} M, respectively.

The effect of pH on chemosensors (**HL3.1** and **HL3.2**) both in free condition and in presence of Al^{3+} , Cr^{3+} and Fe^{3+} ions are studied fluorometrically. It is well known that in acidic condition spirolactam ring of the chemosensor opens. Similar observation is also noticed in presence of Al^{3+} , Cr^{3+} and Fe^{3+} ions. Therefore, both free chemosensor and chemosensor- Al^{3+} , Cr^{3+} , Fe^{3+} adduct exhibit high fluorescence intensity at pH 2-4. At pH 5 a sharp decrease in fluorescence intensity of free chemosensor is observed. After pH 5 to pH 11 its fluorescence intensity is very weak and remains unchanged. This observation suggests reconstruction of spirolactam ring in neutral and basic condition. In presence of Al^{3+} , Cr^{3+} and Fe^{3+} ions fluorescence intensity of the chemosensor decrease a little after pH 4 and then it maintain a constant value up to pH 8. At pH 9 a sharp decrease in fluorescence intensity of chemosensor is observed. After pH 9 to pH 11, very weak fluorescence intensity is observed. This is probably due to generation of metal hydroxide and free chemosensor at higher pH (**Figure 3.42**). Interestingly, effect of pH is more pronounced in case of Fe^{3+} -chemosensor adduct. The pH experiment shows that these chemosensors can act as a selective fluorescent probe for Al^{3+} , Cr^{3+} and Fe^{3+} ions in presence of other metal ions in biological system under physiological condition.

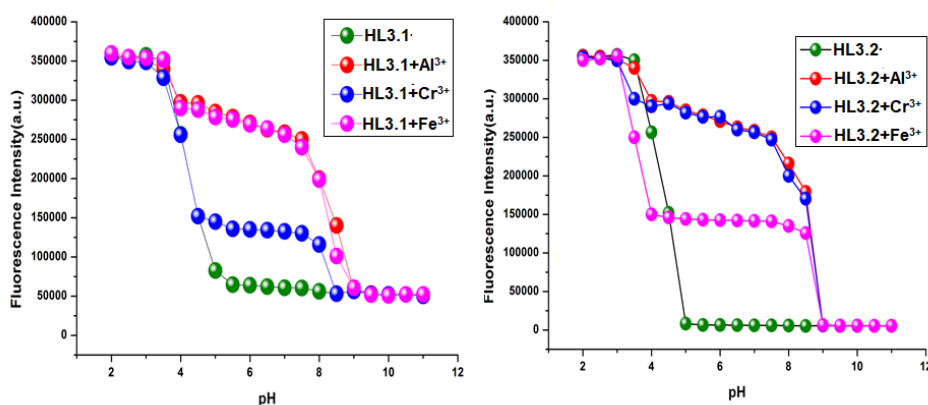


Figure 3.42 Fluorescence intensity of chemosensors (**HL3.1** and **HL3.2**) (10 μM) in the

absence and presence of metal ions (Al^{3+} , Cr^{3+} and Fe^{3+}) ($5 \mu\text{M}$) at different pH values in 10 mM Britton Robinson buffer.

3.3.7 Life time and quantum yield study

Lifetime measurement for the chemosensors (**HL3.1** and **HL3.2**) and complexes **3.1-3.6** are studied at $25 \text{ }^\circ\text{C}$ in 10 mM Britton Robinson buffer (pH= 7.4) medium. The average values of fluorescence decay life time of the chemosensors and complexes **3.1-3.6** have been measured using the given formula ($\tau_f = a_1\tau_1 + a_2\tau_2$, where a_1 and a_2 are relative amplitude of decay process). The average value of fluorescence lifetime of the chemosensors (**HL3.1** and **HL3.2**) and complexes **3.1-3.6** are 2.26, 2.21 ns and 4.56, 3.77, 2.14, 4.24, 3.59 and 2.12ns, respectively (**Figure 3.43** and **Table 3.3**).

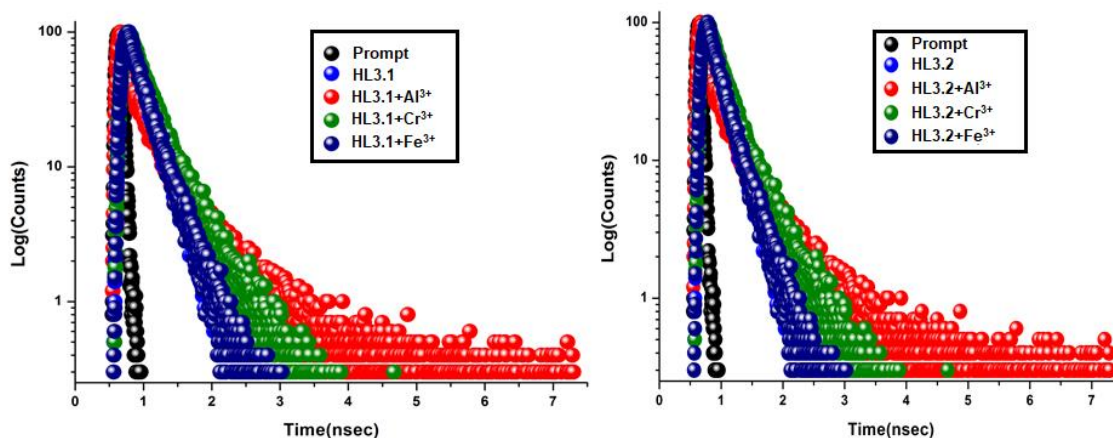


Figure 3.43 Time-resolved fluorescence decay curves (logarithm of normalized intensity vs time in ns) of **HL3.1** and **HL3.2**.

Table 3.3 Lifetime, quantum yield, LOD and binding constant values of chemosensors (**HL3.1** and **HL3.2**) and complexes (**3.1-3.6**).

	Lifetime (ns) ($\tau_{av.}$)	Quantum Yield (Φ)	LOD (M)	Binding Constant (M^{-1})
HL3.1	2.26	0.005	-	-
HL3.2	2.21	0.006	-	-
complex 3.1	4.56	0.26	2.86×10^{-8} M	5.14×10^5
complex 3.2	3.77	0.24	2.67×10^{-8} M	4.91×10^5
complex 3.3	2.14	0.027	5.62×10^{-6} M	3.37×10^4
complex 3.4	4.24	0.25	2.78×10^{-8} M	5.03×10^5
complex 3.5	3.59	0.23	2.61×10^{-8} M	4.86×10^5
complex 3.6	2.12	0.022	6.14×10^{-6} M	3.95×10^4

Fluorescence quantum yield (Φ) has been calculated as follows:

$$\Phi_{\text{sample}} = \left\{ \frac{(\text{OD}_{\text{standard}} \times A_{\text{sample}} \times \eta_{\text{sample}}^2)}{(\text{OD}_{\text{sample}} \times A_{\text{standard}} \times \eta_{\text{standard}}^2)} \right\} \times \Phi_{\text{standard}}$$

In the above equation, A is the area under the emission spectral curve, OD is the optical density of the compound at the excitation wavelength and η is the refractive index of the solvent. Φ_{standard} value is taken as 0.52 (for Quinine Sulfate).

The values of Φ for **HL3.1**, **HL3.2** and complexes **3.1-3.6** are estimated to be 0.005, 0.006 and 0.26, 0.24, 0.02, 0.25, 0.23, 0.02 respectively (**Table 3.3**).

3.3.8 Mechanism of fluorescence intensity enhancement in chemosensors in presence of trivalent metal ions

Free chemosensors are non fluorescent due to presence of spirolactam ring. Fluorescence intensity of the chemosensor increases ~400 times in presence of Al^{3+} and Cr^{3+} ions and ~100 times in presence of Fe^{3+} ions due to opening of its spirolactam ring followed by complexation with the respective metal ions. 1H , ^{13}C NMR and FT-IR spectroscopy and X-ray crystallographic techniques are used to explain the mechanistic pathway. Crystal

structures of complexes **3.1** and **3.4** prove presence of open spirolactam ring in Al^{3+} bound chemosensors. Presence of phenoxide oxygen, amide oxygen and imine nitrogen in the coordination environment is also observed in the crystal structures. In ^1H NMR spectra of free chemosensors phenolic $-\text{OH}$ peak, imine and aliphatic $-\text{NH}$ protons appear around 11.5, 9.0 and 5.0 ppm. Whereas, in presence of Al^{3+} ions disappearance of phenolic $-\text{OH}$ peak and aliphatic $-\text{NH}$ proton, downfield shift of imine protons and aromatic protons, establish opening of spirolactam ring and coordination of phenoxide oxygen and imine nitrogen atom with the metal center. In ^{13}C NMR spectra of free chemosensor, sp^3 hybridized carbon atom connecting the xanthene part and spirolactam ring appears at 66.08 ppm. Interestingly, spirolactam ring opening followed by metal coordination results change of sp^3 hybridization into sp^2 hybridization and new peak appears at 141.46 ppm (**Figures 3.11** and **3.17**). In FT-IR spectrum free chemosensors exhibit stretching frequency of amide 'C=O' bond and imine bond at ~ 1696 and $\sim 1621\text{ cm}^{-1}$, respectively. These values are shifted significantly to lower value and appear at ~ 1640 and $\sim 1600\text{ cm}^{-1}$, respectively for all metal bound complexes (**Complex 3.1-3.6**). Apart from that sharp $-\text{OH}$ peak appears around 3500 cm^{-1} in free chemosensor is also disappeared after complexation. Such type of changes in FT-IR spectral pattern again confirms opening of spirolactam ring and coordination of phenoxide oxygen, imine nitrogen and amide oxygen atoms with the metal centers. Therefore, using above spectroscopic and X-ray crystallographic results, we can easily establish coordination of metal centers (Al^{3+} / Cr^{3+} / Fe^{3+}) with the chemosensor followed by charge transfer within the ligand framework resulting strong colorimetric changes and huge fluorescence enhancement.

3.3.9 Biocompatibility study of the ligands

The cellular toxicity of the ligands (**HL3.1** and **HL3.2**) was envisaged to determine the compatibility against the normal human lung fibroblast cells, WI-38. The cells were exposed with various concentrations (20 - 100 $\mu\text{M}/\text{ml}$) of the ligands. Then the cells were

incubated for 24 h. and then the cellular survivability was determined with the help of MTT assay. From the results, no significant toxicity was observed even at enhanced concentrations of 100 μM (as seen in **Figure 3.44**). Hence the results clearly depict the biocompatibility of the ligands and also suggest that these ligands have the potential to emerge as promising tools for application in biomedical fields.

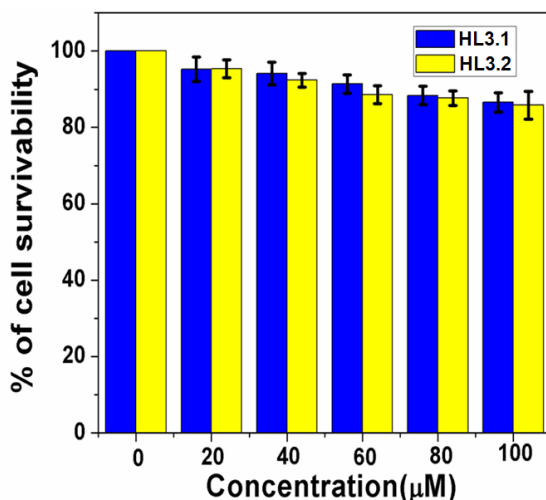


Figure 3.44 Survivability of WI38 cells exposed to **HL3.1** and **HL3.2**.

3.3.10 Cell imaging

The cellular internalization of the chemosensors (**HL3.1** and **HL3.2**) (10 μM) and Cr^{3+} salt (5 μM), Fe^{3+} salt (5 μM) and Al^{3+} salt (5 μM) has been determined in detail with the aid of fluorescence microscopy studies. The fluorescence microscopic images reveal the presence of a promiscuous red fluorescent signal (**Figure 3.45**). Henceforth the results suggest that the ligands and the Cr^{3+} salt (5 μM), Fe^{3+} salt (5 μM), Al^{3+} salts (5 μM) are promptly internalized by the cells which in turn is responsible for the emergence of red fluorescent signal.

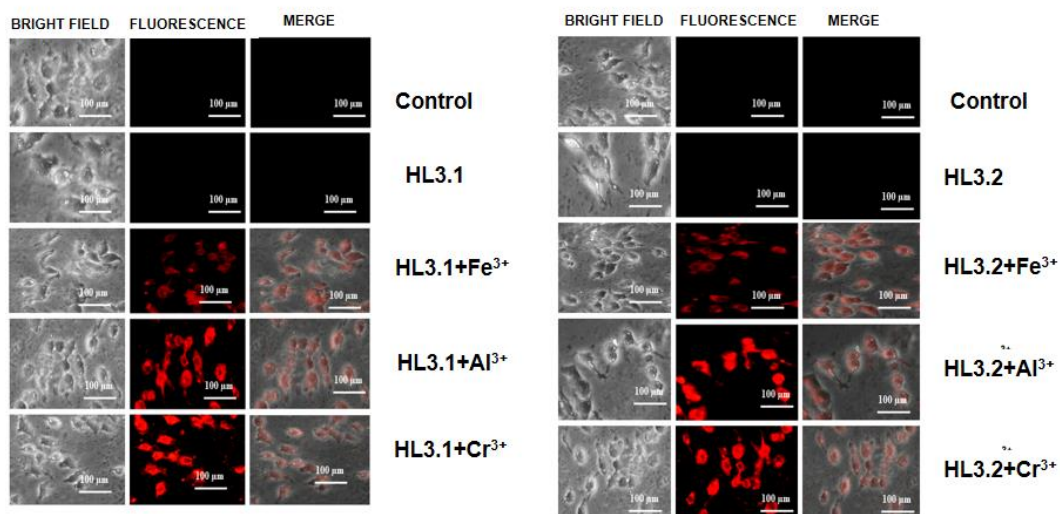


Figure 3.45 Bright field, fluorescence and merged microscopic images of untreated HeLa (Control), cells in presence of chemosensors (**HL3.1** and **HL3.2**) ($10\mu\text{M}$) + M^{3+} (Al^{3+} , Cr^{3+} and Fe^{3+}) ($5\mu\text{M}$).

3.3.11 DFT and TDDFT study

We have performed DFT and TDDFT studies to support the structure of the chemosensors. The TDDFT studies also help to understand the nature, origin and contribution of the FMOs which are involved in the electronic transitions, and quantity of energy associated with each transition. Here, the optimization of **HL3.1** and **HL3.2** was performed using the DFT at Coulomb attenuating method CAM-B3LYP (**Figure 3.46**). The optimized energies (eV) of some selected FMOs are presented in **Table 3.4**. The contour plots of some selected molecular orbitals of the chemosensors are presented in **Figures 3.47** and **3.48**. Both the ligands **HL3.1** and **HL3.2** can exist in keto or enol form in solution. The results show that the in the keto and enol forms of **HL3.1** and only keto form of **HL3.2**, the electron density in the HOMO and LUMO are distributed over azo aromatic part. In case of enol form of **HL3.2**, electron density in HOMO and LUMO are mainly distributed on rhodamine part.

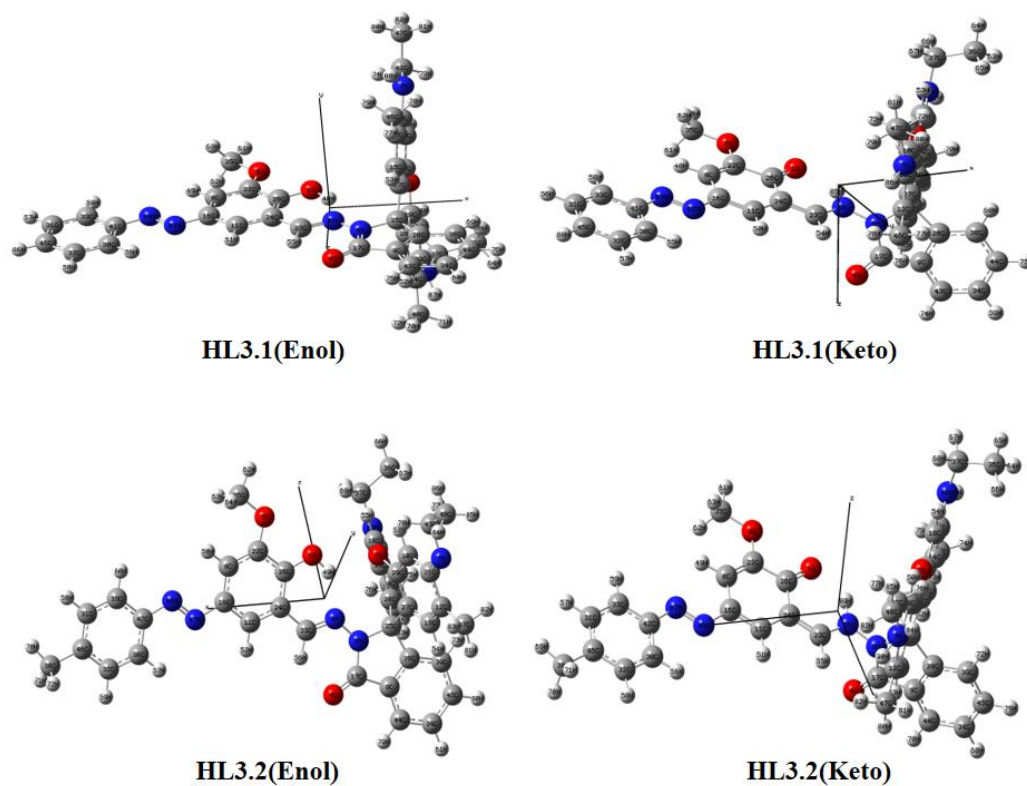


Figure 3.46 (a) DFT optimized structure of **HL3.1** and **HL3.2** (Enol and Keto form).

Table 3.4. Energy (eV) and composition (%) of selected M.O.s of **HL3.1** and **HL3.2**.

M.O.s	HL3.1 Energy(eV)		HL3.2 Energy(eV)	
	Enol	Keto	Enol	Keto
LUMO+3	1.05	0.84	0.43	0.86
LUMO+2	0.79	0.21	-0.37	0.23
LUMO+1	-0.12	-0.04	-0.6	0
LUMO	-0.53	-0.5	-3.19	-0.45
HOMO	-6.43	-6.06	-5.68	-6
HOMO-1	-6.57	-6.67	-6.55	-6.66
HOMO-2	-6.64	-6.79	-7.35	-6.78
HOMO-3	-7.18	-7.32	-7.61	-7.31

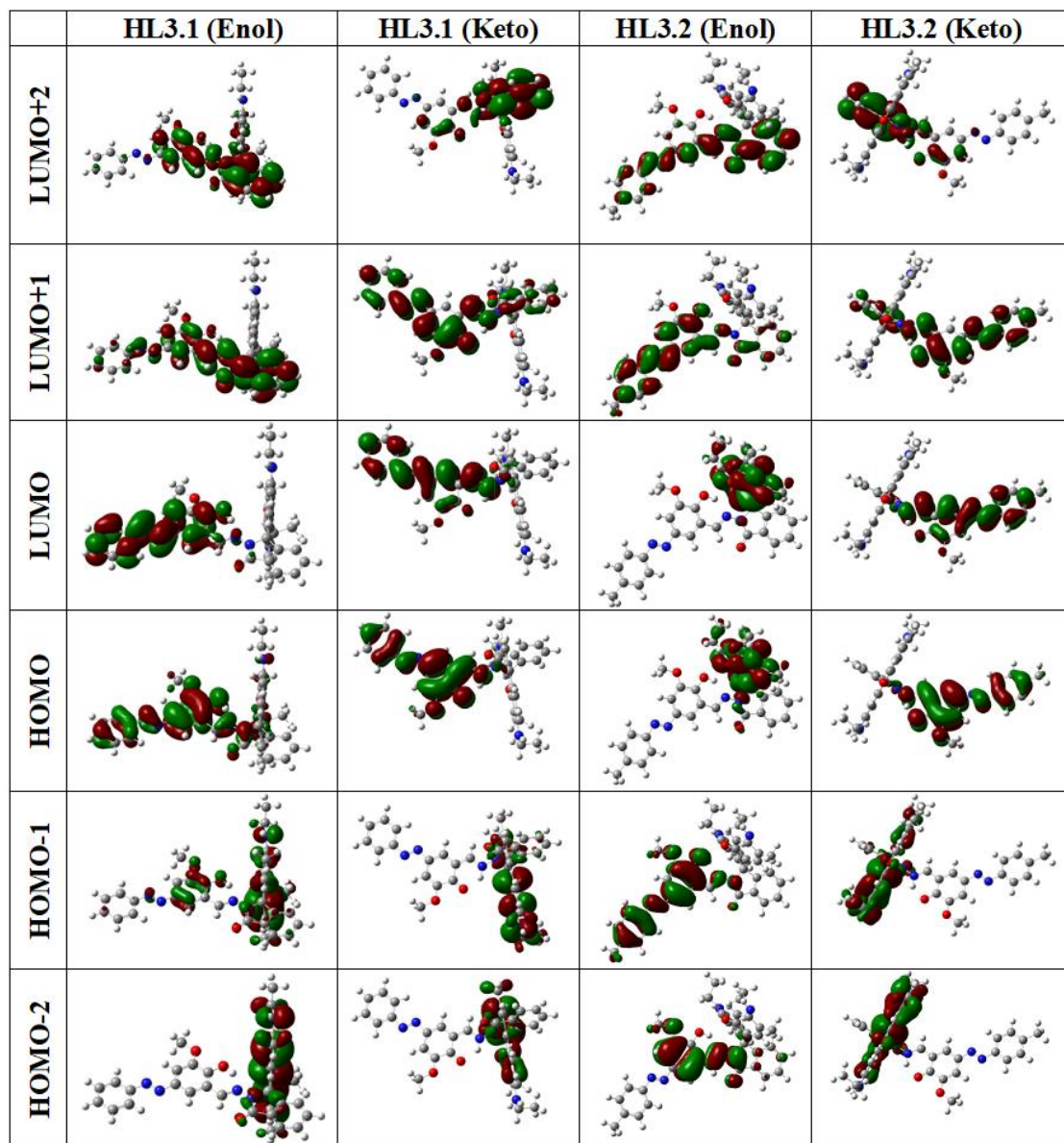


Figure 3.47 Selected contour plots of molecular orbitals of HL3.1 and HL3.2.

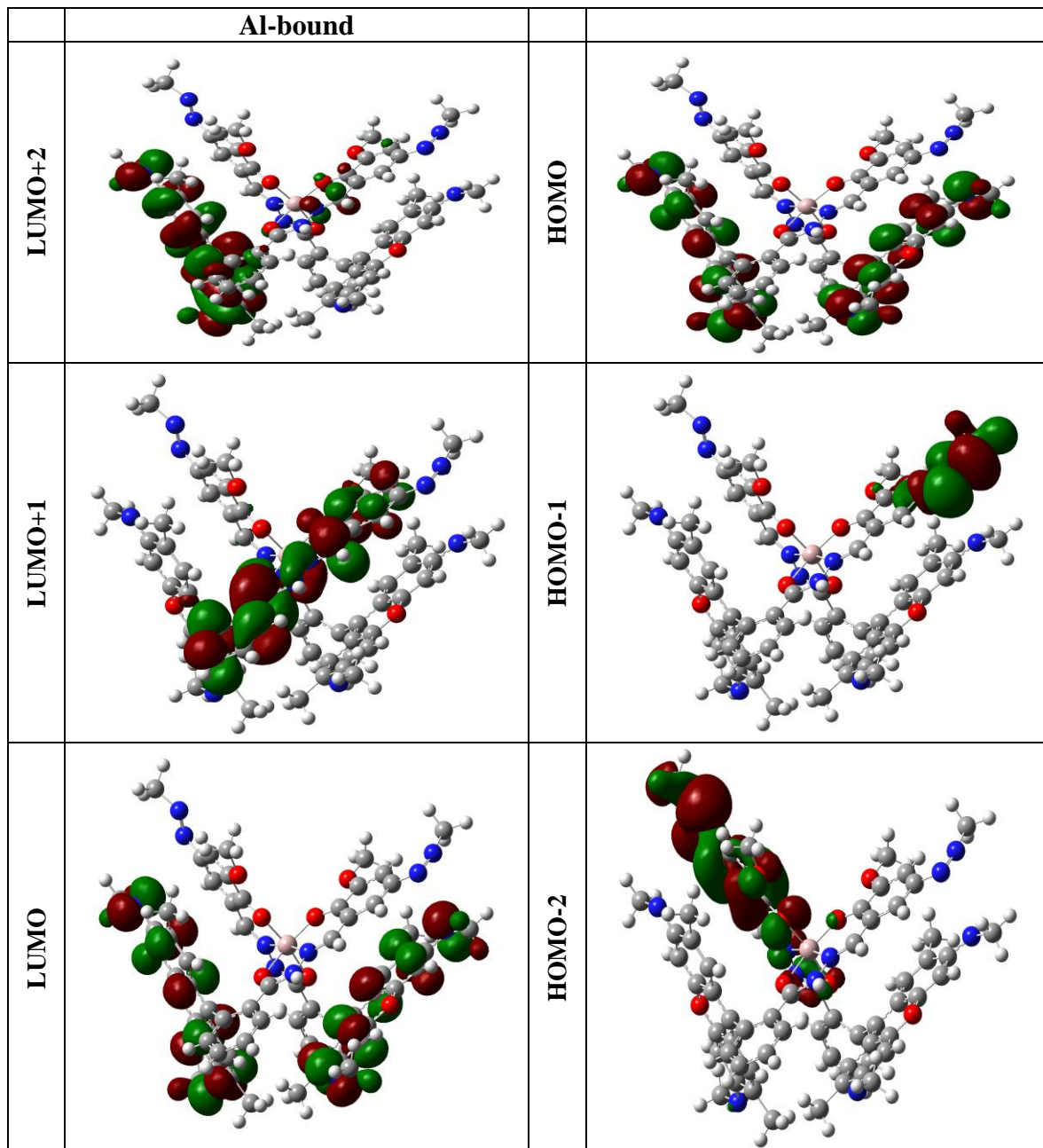


Figure 3.48 Selected contour plots of molecular orbitals of **Al-bound** chemosensor.

In TDDFT, CAM-B3LYP/CPCM method was used with the same basis sets in methanol. The calculated electronic transitions are presented in **Table 3.5**. The theoretical calculations showed that keto and enol form of both chemosensors exhibit intense absorption bands at around 310 and 365 nm for the ligand based $\pi \rightarrow \pi^*$ and $n \rightarrow \pi^*$ transitions,

respectively, which is well matched with experimental observations. The major transitions for **HL3.1** are H-2→L (89%), H-2→L+1 (56%) (for enol form) and H-2→L (83%), H→L+1 (80%), H-9→L+1(27%) (for keto form) based, whereas for **HL3.2**, the key transitions are H-2→L (89%), H-2→L+1 (53%)(for enol form) and H→L (86%), H→L+1 (84%), H-9→L+1 (32%) (for keto form) (**Figure 3.49**).

Table 3.5 Electronic transition calculated by TDDFT using CAM-B3LYP/CPCM method in methanol solvent of chemosensors enol form (**HL3.1** and **HL3.2**) (Used number of states = 20).

Probe	E _{excitation} (ev)	λ _{excitation} (nm)	Osc. frequency	Key transation	Experimantal
HL3.1 (enol)	29575.75	338.1149	0.9577	HOMO-2→LUMO (89%)	360
	32361.61	309.0081	0.6827	HOMO-2→LUMO+1 (56%), HOMO→LUMO+1 (12%)	310
HL3.2 (enol)	29370.08	340.4826	1.0739	HOMO-2→LUMO (89%)	360
	32192.23	310.634	0.6948	HOMO-2→LUMO+1 (53%) HOMO→LUMO+1(14%)	310
HL3.1 (Keto)	26710.04	374.391	0.728	HOMO-2→LUMO (83%), HOMO→LUMO+1 (10%)	360
	29282.16	341.5049	0.6714	HOMO→LUMO (10%), HOMO→LUMO+1 (80%)	360
	32425.33	308.4009	0.0104	HOMO-11→LUMO+1 (11%), HOMO-9→LUMO (10%), HOMO-9→LUMO+1 (27%)	310
HL3.2 (Keto)	26624.55	375.5933	0.7514	HOMO→LUMO (86%)	360

	29166.02	342.8648	0.7536	HOMO→LUMO+1 (84%)	360
				HOMO-11→LUMO+1 (11%) HOMO-9→LUMO (15%), HOMO-9→LUMO+1 (32%), HOMO-6→LUMO+1 (10%)	310
	32407.58	308.5698	0.0097		

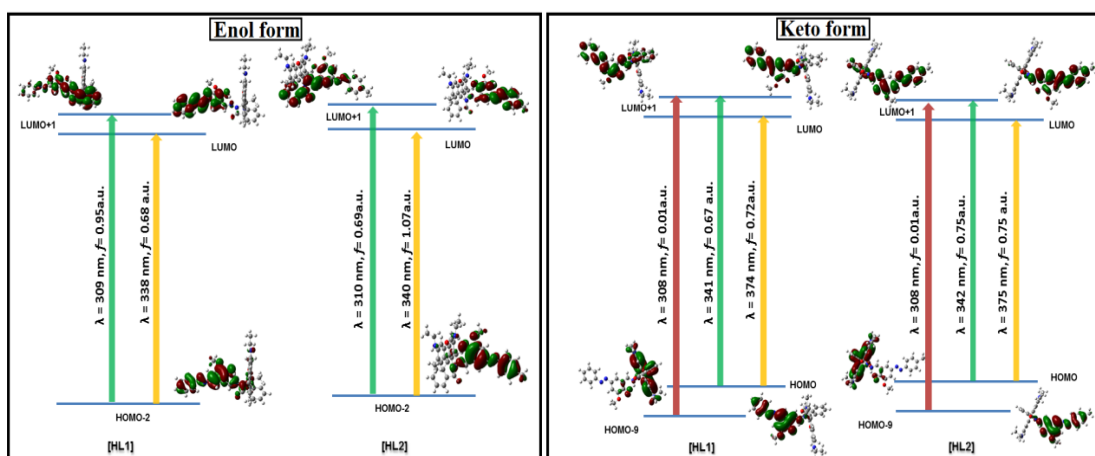


Figure 3.49 Pictorial representation of key transitions of chemosensors **HL3.1** and **HL3.2**.

To investigate the mechanism of emission behavior of the Al-complex, the structures of the S_0 and S_1 states, were optimized at the DFT level using the Coulomb attenuating method CAM-B3LYP hybrid functional and the split-valence 6-31+G(d) basis set for all atoms. Time dependent DFT (TD-DFT) approach over 60 states to compute the vertical excitations also using the CAM-B3LYP functional to minimize deviations in charge-transfer excitation energies.³⁻⁵⁰ To avoid the computational time, we have truncated the structure slightly of the Al-complex. The solvation effects were applied via a Conductor-like Screening Model (CPCM) using methanol as solvents.

The results show that the two strong low-energy transitions are associated to H-2 to L+2 (58%) at 525 nm ($f = 0.48$ a.u.) and H-2 to L+3 (63%) at 519 nm ($f = 0.45$ a.u.). This is in good agreement with the experimental results at 555 nm. Further analyses (**Figure 3.50**

and **Table 3.6**) of these FMOs show that H-2 is localized (93%) on azo aromatic part of the chemosensor (1st part, marked with red colour) (see **Figure 3.51**), L+2 is localized (96%) on the open spirolactam ring of rhodamine unit (2nd part, marked with sky colour), and L+3 is delocalized over both open spirolactam ring of rhodamine part (1st part, marked with green colour) (72%) and azo aromatic part of chemosensor (2nd part, marked with blue colour) (22%). Thus, the peak 525 nm originated from an electron transition from azo aromatic part of (marked with red colour) to rhodamine part (marked with sky colour) of chemosensors. Another peak at 519 nm can be assigned as a transition from azo part of ligand (marked with red colour) to both the fragments: rhodamine (marked with green colour) and azo aromatic part of chemosensors (marked with blue colour).

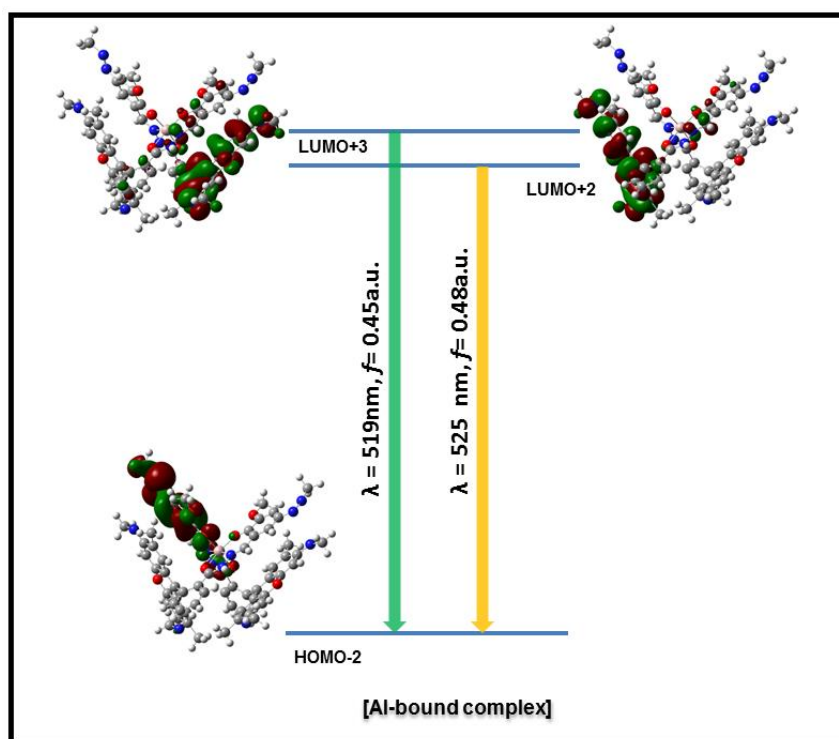


Figure 3.50 Pictorial representation of lowest energy vertical excitation of the Al-bound complex

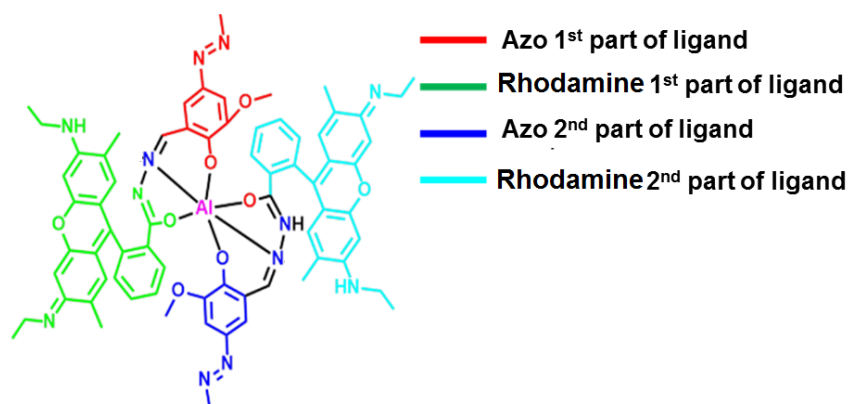


Figure 3.51 Naming of fragments of Al-bound complex as used in **Table 3.6**

Table 3.6 Composition (%) of the FMOs in terms of the central metal and the fragments of the attached ligands for the Al-complex.

FMOs	Energy (eV)	Al	1 st part		2 nd part	
			Azo (red)	Rhodamine (green)	Azo (blue)	Rhodamine (sky)
L+3	-1.75	0	1	72	22	5
L+2	-1.91	0	0	0	3	96
L+1	-2.62	0	1	1	27	71
LUMO	-3.83	0	0	30	20	49
HOMO	-4.13	0	0	29	21	50
H-1	-4.28	0	0	0	100	0
H-2	-4.8	0	93	5	0	1
H-3	-5.17	1	77	19	1	3

3.3.12 Natural transition orbital (NTO) study

Additionally, analysis on the electronic structure of the excited states employing NTO representation showed that the S1 state can be mainly characterized by an intra-ligand charge-transfer (ILCT) transitions, by populating the highest-occupied (HO)NTO and the lowest-unoccupied (LU)NTO describe the hole and the excited electron state, respectively. The charge transfer index (Δr) between HONTO and LUNTO, and hole-electron overlapping indices (σ_s) were calculated to identify the charge transition in the excited-states. The Δr value is a quantitative measure of charge-transfer (CT) length of electron excitation, higher

Δr indices and smaller σ_S indices imply longer CT distance, whereas, smaller Δr value and larger σ_S value are indicators of local-excitation. Here, the computed values of Δr and σ_S are 2.47 Å and 0.51 indicates that fluorophore originated from the charge transfer within the Schiff base. As shown in **Figure 3.52**, both HONTOs and LUNTOs are mainly localized on the ligand Schiff base.

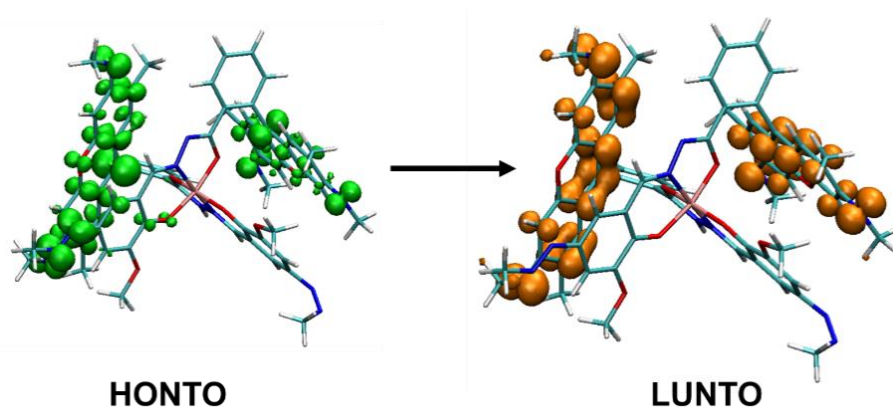


Figure 3.52 The HONTO and LUNTO of the strongest low-energy emission.

Therefore, theoretical studies clearly reveal that in metal bound chemosensor presence of metal ion (Al^{3+}) initiates opening of spirolactam ring of the chemosensor followed by charge transfer within the ligand framework resulting strong colorimetric changes and huge fluorescence enhancement.

3.3.13 Electrochemical study

The electrochemical behavior of the metal bound chemosensor complexes (**3.1-3.6**) was studied in acetonitrile medium containing 0.1 M tetrabutylammonium perchlorate as a supporting electrolyte in a conventional three-electrode configuration using a Pt disk working electrode, Pt auxiliary electrode and Ag/AgCl reference electrode. All electrochemical data are collected in **Table 3.7**. Interestingly we are only able to collect data for Fe^{3+} and Cr^{3+} bound chemosensor complexes (**3.2**, **3.3**, **3.5** and **3.6**) and all the peaks are irreversible in nature. The reductive response at -0.44 V and the oxidative response at 1.26 V may be

assigned to Fe^{III}/Fe^{II} and Fe^{III}/Fe^{IV} couple. The lowest potential cathodic response occurs near -0.59 V has been assigned to the Cr(III)/Cr(II) couple. Rest of the oxidative peaks appears in all the compounds are probably due to ligand based oxidations.

Table 3.7 Energy (eV) and composition (%) of selected M.O.s of **HL3.1** and **HL3.2**.

Complex	E _p (V)
HL3.1	0.33, 0.90, 1.33
HL3.2	0.31, 1.16, 1.33
3.2	0.33, 0.92, -0.59
3.3	0.877, 1.48, 1.26, -0.44
3.5	0.33, 0.95, 1.15, 1.51, -0.58
3.6	0.32, 0.90, 1.28, 1.49, -0.44

3.4 Conclusions

Here, we have reported two new fluorescent and colorimetric chemosensors containing rhodamine 6G and azo units (**HL3.1** and **HL3.2**) which selectively detect trivalent metal ions Al³⁺, Cr³⁺ and Fe³⁺. Crystal structures of both chemosensors show closed spirolactam ring, which make them non fluorescent. Both chemosensors form 2:1 complexes with trivalent metal ions which have been established by Job's plots. Crystal structures of Al³⁺ bound chemosensors prove presence of open spirolactam ring resulting visual colouration and enhancement of fluorescence intensity of the system. Al³⁺ and Cr³⁺ ions exhibit ~400 times enhancement of fluorescence intensity in presence of chemosensors whereas, ~100 times enhancement has been observed in case of Fe³⁺ ions. Such huge enhancement of fluorescence intensity is rarely observed in other trivalent metal ions sensing chemosensors. LOD values of the trivalent ions Al³⁺, Cr³⁺ and Fe³⁺ are 2.86×10^{-8} M, 2.67×10^{-8} M, 5.62×10^{-6} M, and 2.78×10^{-8} M, 2.61×10^{-8} M, 6.14×10^{-6} M, respectively. The values of binding constant of the probes towards respective metal (Al³⁺, Cr³⁺ and Fe³⁺) ions are $5.14 \times 10^5 \text{ M}^{-2}$, $4.91 \times 10^5 \text{ M}^{-2}$, $3.37 \times 10^4 \text{ M}^{-2}$ and $5.03 \times 10^5 \text{ M}^{-2}$, $4.86 \times 10^5 \text{ M}^{-2}$, $3.95 \times 10^4 \text{ M}^{-2}$

respectively. We are also successful to reveal its practical application by performing cell imaging study of chemosensors (**HL3.1** and **HL3.2**) using *HeLa* cells. Furthermore, the probes are applied to detect intracellular Al^{3+} , Cr^{3+} and Fe^{3+} ions in live cells with no significant cytotoxicity. A comparison of different experimental findings like crystal structure elucidation of free chemosensors and its metal (particularly Al^{3+}) bound complexes, biological applications, LOD values, enhancement of fluorescence intensity in presence of metal ions etc. between chemosensors reported earlier with present probes (**chart 3.1**) have been performed. Interestingly, our chemosensors have successfully covered most of the criteria especially crystal structure study of Al^{3+} bound chemosensors complexes which are rare in literature.

3.5 References

- (3.1) J. S. Kim and D. T. Quang, *Chem. Rev.*, 2007, **107**, 3780–3799.
- (3.2) H. N. Kim, M. H. Lee, H. J. Kim, J. S. Kim and J. Yoon, *Chem. Soc. Rev.*, 2008, **37**, 1465–1472.
- (3.3) X. Chen, T. Pradhan, F. Wang, J. S. Kim and J. Yoon, *Chem. Rev.*, 2012, **112**, 1910–1956.
- (3.4) Y. Yamini, N. Alizadeh and M. Shamsipur, *Anal. Chim. Acta*, 1997, **355**, 69–74.
- (3.5) C. F. Harrington, S. A. Merson and T. M. D. D'Silva, *Anal. Chim. Acta*, 2004, **505**, 247–254.
- (3.6) S. L. C. Ferreira, A. S. Queiroz, M. S. Fernandes and H. C. dos Santos, *Spectrochim. Acta B*, 2002, **57**, 1939–1950.
- (3.7) J. C. Yu, J. M. Lo and K. M. Wai, *Anal. Chim. Acta*, 1983, **154**, 307–312.
- (3.8) A. Ali, H. Shen and X. Yin, *Anal. Chim. Acta*, 1998, **369**, 215–223.
- (3.9) A. Bobrowski, K. Nowak and J. Zarebski, *Anal. Bioanal. Chem.*, 2005, **382**, 1691–1697.
- (3.10) W. Shotyk, D. Weiss, P. Appleby, A. Cheburkin, R. Frei and M. Gloor, *Science*, 1998, **281**, 1635–1640.
- (3.11) V. K. Gupta, A. K. Jain and G. Maheshwari, *Talanta*, 2007, **72**, 1469–1473.
- (3.12) G. C. Kabat and T. E. Rohan, *Cancer Causes Contro*, 2007, **118**, 1047–1053.
- (3.13) P. Aisen, C. Enns and M. Wessling-Resnick, *Int. J. Biochem. CellBiol.*, 2001, **33**, 940–959.
- (3.14) K. J. Hintze and E. C. Theil, *Proc. Natl. Acad. Sci. U.S.A.*, 2005, **102**, 15048–15052.

- (3.15) L. Huang, F. Hou, J. Cheng, P. Xi, F. Chen, D. Bai and Z. Zeng, *Org. Biomol. Chem.*, 2012, **10**, 9634–9638.
- (3.16) H. Kim, K. B. Kim, E. J. Song, I. H. Hwang, J. Y. Noh, P. -G. Kim, K. -D. Jeong and C. Kim, *Inorg. Chem. Commun.*, 2013, **36**, 72–76.
- (3.17) J. Wang, D. Zhang, Y. Liu, P. Ding, C. Wang, Y. Ye and Y. Zhao, *Sens. Actuators B*, 2014, **191**, 344–350.
- (3.18) P. Xie, F. Guo, R. Xia, Y. Wang, D. Yao, G. Yang and L. Xie, *J. Lumin.*, 2014, **145**, 849–854.
- (3.19) H. Wu, P. Zhou, J. Wang, L. Zhao and C. Duan, *New J. Chem.*, 2009, **33**, 653.
- (3.20) X. Q. Chen, T. Pradhan, F. Wang, J. S. Kim and J. Y. Yoon, *Chem. Rev.*, 2012, **112**, 1910–1956.
- (3.21) (a) S. Banerjee, A. Dey, P. Ghorai, P. Brandao, J. Ortega-Castro, A. Frontera, P. P. Ray and A. Saha, *New J. Chem.*, 2018, **42**, 13430-13441. (b) M. Yang, W. Meng, X. Liu, N. Su, J. Zhou and B. Yang, *RSC Adv.*, 2014, **4**, 22288-22293.
- (3.22) S. Mabhai, M. Dolai, S. Dey, A. Dhara, B. Das and A. Jana, *New J. Chem.*, 2018, **42**, 10191–10201.
- (3.23) M. Yang, W. Meng, X. Liu, N. Su, J. Zhou and B. Yang, *RSC Adv.*, 2014, **4**, 22288–22293.
- (3.24) (a) S. Samanta, T. Ray, F. Haque and G. Das, *J. Lumin.*, 2016, **171**, 13–18. (b) S. Paul, A. Manna and S. Goswami, *Dalton Trans.*, 2015, **44**, 11805–11810. (c) S. Dey, S. Sarkar, D. Maity and P. Roy, *Sens. Actuators B*, 2017, **246**, 518–534. (d) A. Roy, S. Das, S. Sacher, S. K. Mandal and P. Roy, *Dalton Trans.*, 2019, **48**, 17594–17604. (e) R. Alam, R. Bhowmick, A. S. M. Islam, A. katarkar, K. Chaudhuri and M. Ali, *New J. Chem.*, 2017, 8359-8369. (f) D. Singha, T. Das, L. Satyanarayana, P. Roy and M. Nandi, *New J. Chem.*, 2019, **43**, 15563-

15574. (g) D. Das, R. Alam, A. Katarkar and M. Ali, *Photochem. Photobiol. Sci.*, 2019, **18**, 242-252. (h) X. Tang, Y. Wang, J. Han, L. Ni, H. Zhang, C. Li, J. Lid and Y. Qiu, *Dalton Trans.*, 2018, **47**, 3378–3387. (i) D. Das, R. Alam and M. Ali, *analyst*, 2022(DOI: 10.1039/D1AN01788H). (j) D. Singha, A. Pal, H. Uyama, P. Roy and M. Nandi, *Dalton Trans.*, 2021, **50**, 12478-12494. (k) N. Dey, N. Kumari and S. Bhattacharya, *Tetrahedron*, 2021, **85**, 132007. (l) Y. Fu, X. J. Jiang, Y. Y. Zhu, B. J. Zhou, S. Q. Zang, M. S. Tang, H. Y. Zhang and T. C. W. Mak, *Dalton Trans.*, 2014, **43**, 12624–12632. (m) J. Qiu, C. Zhong, M. Liu, Y. Yuan, H. Zhu and Y. Gao, *New J. Chem.*, 2021, **45**, 5184–51949. (n) S. Das, P. P. Das, J. W. Walton, K. Ghoshal, L. Patra and M. Bhattacharyya, *New J. Chem.*, 2021, **45**, 1853–1862. (o) C. Kan, X. Wang, X. Shao, L. Wu, S. Qiu and J. Zhu, *New J. Chem.*, 2021, **45**, 8918–8924. (p) Z. Qin, W. Su, P. Liu, J. Ma, Y. Zhang and T. Jiao, *ACS Omega*, 2021, **6**, 25040–25048. (q) J. Mandal, P. Ghorai, K. Pal, T. Bhaumik, P. Karmakar and A. Saha, *ACS Omega*, 2020, **5**, 145–157.

(3.25) A. Hazra, P. Ghosh and P. Roy, *Spectrochim. Acta Part A*, 2022, **271**, 120905.

(3.26) A. Hazra and P. Roy, *Anal. Chim. Acta*, 2022, **1193**, 339378.

(3.27) M. B. Maitya, B. Dutta, A. Rahaman, N. Sahu, D. P. Mandal, S. Bhattacharjee and C. Sinha, *J. Mole. Structure*, 2022, **1250**, 131870.

(3.28) T. T. Liu, S. J. Li, H. Fu, Z. N. Tian, X. J. Sun and Z. Y. Xing, *J. Photochem. Photobiol.*, 2020, **403**, 112865.

(3.29) S. O. Tumay, A. Senocak and A. Mermer, *New J. Chem.*, 2021, **45**, 18400–18411.

30 R. Kaushik, R. Sakla, N. Kumar, A. Ghosh, V. D. Ghule and D. A. Jose, *Sens. Actuators B*, 2021, **328**, 129026.

(3.31) L. Hou, T. Liu, Y. Gong, J. Li, C. Deng, C. Zhang, Y. Wang, S. Shuang and W. Liang, *New J. Chem.*, 2020, **44**, 19642–19649.

(3.32) a) L. Wang, W. Li, W. Zhi, Y. Wang, J. Han, Z. Cao, L. Ni, H. Li and J. Jing, *J. Lumin.*, 2018, **196**, 379–386 b) P. S. Nayab and M. Shkir, *Sens. Actuators B*, 2017, **251**, 951–957 (c) Q. Chen and Z. Fang, *Spectrochim. Acta Part A*, 2018, **193**, 226–234.

(3.33) Sheldrick, G. M. SAINT, Version 6.02, SADABS, Version 2.03, Bruker AXS Inc., Madison, Wisconsin, **2002**.

(3.34) Sheldrick, G. M. SADABS: Software for Empirical Absorption Correction, University of Gottingen, Institute fur Anorganische Chemieder Universitat, Gottingen, Germany, **1999-2003**.

(3.35) Sheldrick, G. M. Crystal structure refinement with *SHELXL*. *Acta Cryst.* 2015, *C71*, 3–8.

(3.36) H. A. Benesi and J. H. Hildebrand, *J. Am. Chem. Soc.*, 1949, **71**, 2703–2707.

(3.37) M. J. Frisch, G. W. Trucks, H. B. Schlegel, G. E. Scuseria, M. A. Robb, J. R. Cheeseman, G. Scalmani, V. Barone, B. Mennucci, G. A. Petersson, H. Nakatsuji, M. Caricato, X. Li, H. P. Hratchian, A. F. Izmaylov, J. Bloino, G. Zheng, J. L. Sonnenberg, M. Hada, M. Ehara, K. Toyota, R. Fukuda, J. Hasegawa, M. Ishida, T. Nakajima, Y. Honda, O. Kitao, H. Nakai, T. Vreven, J. A. Montgomery, Jr., J. E. Peralta, F. Ogliaro, M. Bearpark, J. J. Heyd, E. Brothers, K. N. Kudin, V. N. Staroverov, R. Kobayashi, J. Normand, K. Raghavachari, A. Rendell, J. C. Burant, S. S. Iyengar, J. Tomasi, M. Cossi, N. Rega, J. M. Millam, M. Klene, J. E. Knox, J. B. Cross, V. Bakken, C. Adamo, J. Jaramillo, R. Gomperts, R. E. Stratmann, O. Yazyev, A. J. Austin, R. Cammi, C. Pomelli, J. W. Ochterski, R. L. Martin, K. Morokuma, V. G. Zakrzewski, G. A. Voth, P. Salvador, J. J. Dannenberg, S. Dapprich, A. D. Daniels, O. Farkas, J. B. Foresman, J. V. Ortiz, J. Cioslowski and D. J. Fox, GAUSSIAN09, Revision D.01, Gaussian Inc., Wallingford, CT, 2009.

(3.38) A. D. Becke, *J. Chem. Phys.*, 1993, **98**, 5648–5652.

- (3.39) C. Lee, W. Yang and R. G. Parr, *Phys. Rev. B: Condens. Matter Mater. Phys.*, 1988, **37**, 785–789.
- (3.40) P. J. Hay and W. R. Wadt, *J. Chem. Phys.*, 1985, **82**, 270–283.
- (3.41) W. R. Wadt and P. J. Hay, *J. Chem. Phys.*, 1985, **82**, 284–298.
- (3.42) R. Bauernschmitt and R. Ahlrichs, *Chem. Phys. Lett.*, 1996, **256**, 454–464.
- (3.43) R. E. Stratmann, G. E. Scuseria and M. J. Frisch, *J. Chem. Phys.*, 1998, **109**, 8218–8224.
- (3.44) M. E. Casida, C. Jamorski, K. C. Casida and D. R. Salahub, *J. Chem. Phys.*, 1998, **108**, 4439–4449.
- (3.45) V. Barone and M. Cossi, *J. Phys. Chem. A*, 1998, **102**, 1995–2001.
- (3.46) M. Cossi and V. Barone, *J. Chem. Phys.*, 2001, **115**, 4708–4717.
- (3.47) M. Cossi, N. Rega, G. Scalmani and V. Barone, *J. Comput. Chem.*, 2003, **24**, 669–681.
- (3.48) N. M. O’Boyle, A. L. Tenderholt and K. M. Langner, *J. Comput. Chem.*, 2008, **29**, 839–845.
- (3.49) A. B. Pradhan, S. K. Mandal, S. Banerjee, A. Mukherjee, S. Das, A. R. K. Bukhsh and A. Saha, *Polyhedron*, 2015, **94**, 75–82.
- (3.50) A. Dreuw and M. Head-Gordon, *Chem. Rev.*, 2005, **105**, 4009–4037.

Chapter 4

2-hydroxy-5-methylisophthalaldehyde based fluorescent-colorimetric chemosensor for dual detection of Zn^{2+} and Cu^{2+} with high sensitivity and application in live cell imaging

Abstract

A 2-hydroxy-5-methylisophthalaldehyde (DFP) based Schiff-base ligand (**HL4.1**) was successfully developed as a fluorescent and colorimetric chemosensor for dual detection of Zn²⁺ and Cu²⁺ ions in HEPES buffer medium (H₂O: Methanol = 9:1 (v/v), pH = 7.4). Interestingly, in presence of Zn²⁺ around 16 times increment in fluorescence intensity and in presence of Cu²⁺ ~174 times decrease in fluorescence intensity has been observed. The 1:2 binding modes for both **HL4.1**-Zn²⁺/Cu²⁺ complexes are proved by fluorescence measurements, ESI-MS analysis and DFT-Calculations. The reversibility and regeneration process of **HL4.1** are also established using Na₂EDTA. It has been observed that Chemosensor **HL4.1** exhibits a rapid change in fluorescence intensity within pH range 6-8 against Zn²⁺ and Cu²⁺ ions. Low detection limit was found to be 1.059×10⁻⁹(M) and 3.53×10⁻⁹ (M) for Zn²⁺ and Cu²⁺ ions respectively, also suggests that the chemosensor **HL4.1** has great potential to detect Zn²⁺ and Cu²⁺ ions in environmental and biological studies.

4.1 Introduction

Chemosensors that can selectively detect the presence of both environmentally and biologically important metal ions through the naked eye and optical responses has received significant attention.^{4.1} Environmentally and biologically significant metal ions could be detected using different traditional analytical techniques such as voltammetric methods, inductively coupled plasma mass spectrometry (ICP-MS), ion selective electrodes and atomic absorption/ emission spectrometry. In comparison to above techniques colorimetric and fluorescent methods are more advantageous due to their ease of measurement, excellent selectivity, high sensitivity, simplicity and rapid response time.^{4.2-4.7} Fluorescent-sensing mechanisms that have been extensively investigated are photo induced electron transfer (PET), the rigidity effect, fluorescence resonance energy transfer (FRET), excimer/excimer formation/ extinction, photo-induced charge transfer (PCT), and less frequently, excited-state proton transfer (ESPT). Colorimetric method is extensively used mainly naked-eye detection of the element without any use of a spectroscopic instrument.^{4.8-4.11} Among various cations commonly present in our human body, Zn²⁺ and Cu²⁺ are the second and third most abundant transition element found after iron(III). Both metal ions play critical roles in biology, and they most often present as cofactors in diverse enzymes; however, improper regulation of their storage is also connected to serious disorders. The average zinc and copper ion concentrations required for human growth and development are in the order of 15 mg/L and 0.1 mg/L, respectively. Excess copper is toxic and environmental pollutant. However, its deficiency or over-load is associated with a series of disorders such as anemia, liver damage in infants, Wilson disease, Parkinson's disease, Alzheimer's disease, Menkes syndrome etc.^{4.12-4.14} Similarly, zinc(II) deficiency is associated with growth retardation, neurological disorder, such as Parkinson and Alzheimer's diseases, eye lesion, skin problems and different immunological defense related decrease.^{4.15,4.16} Therefore, the monitoring and imaging of

these elements are important for biological research as well as clinical diagnosis. Regarding detection of Zn²⁺ ion the greatest challenge is to discriminate Zn²⁺ from Cd²⁺.^{4,17} Both are present in the same group of the periodic table with similar photophysical properties. A large number of Zn²⁺ and Cu²⁺ detecting chemosensors are reported in literature, still there is a great need to develop simple and effective chemosensors for their dual detection.

The DFP framework has been an ideal candidate for the construction of different type fluorescent chemosensors. In this work we have synthesized and characterized a DFP based chemosensor (**HL4.1**). **HL4.1** detects both the ions colorimetrically as well as through fluorescent techniques. The detection of both the ions by our receptor (**HL4.1**) has been examined by absorption spectroscopy, emission spectroscopy, DFT calculation, ESI-MS experiment and ¹³C and ¹H-NMR. **HL4.1** shows a colour change from light yellow to green in presence of Zn²⁺ and light yellow to colorless in presence of Cu²⁺ ions under visible light. It exhibits an increment of about 16 times in the emission intensity in the presence of one equivalent of Zn²⁺ ions upon excitation at 410 nm. On the other hand upon addition of one equivalent of Cu²⁺ emission intensity of the chemosensor has been decreased by ~174 times. This is due to paramagnetic nature of Cu²⁺. The LOD of the chemosensor molecule against Zn²⁺ and Cu²⁺ are 1.059×10⁻⁹(M) and 3.53×10⁻⁹ (M) respectively. This chemosensor also exhibits cell permeability and intracellular Cu²⁺ and Zn²⁺ ions sensing in MDA-MB-468 cells.

The main advantage of this dual chemosensor is its easy synthesis procedure which is not only economic but also less time consuming. It has very high binding constant towards both of the ions and limit of detection values for both the ions is in nano molar range. We have performed all the experiments in aqueous-methanolic medium (9:1, v/v, HEPES buffer pH=7.4) which further justify its biological cell imaging application.

4.2 Experimental section

4.2.1 Materials and physical measurements

All reagent or analytical grade chemicals and solvents were purchased from commercial sources and used without further purification. Elemental analysis for C, H and N was carried out using a Perkin–Elmer 240C elemental analyzer. Infrared spectra (400–4000 cm⁻¹) were recorded from KBr pellets on a Nicolet Magna IR 750 series-II FTIR spectrophotometer. Absorption spectra were measured using a Cary 60 spectrophotometer (Agilent) with a 1-cm-path-length quartz cell. Electron spray ionization mass (ESI-MS positive) spectra were recorded on a MICROMASS Q-TOF mass spectrometer. Emission spectra were collected using Fluoromax-4 spectrofluorimeter at room temperature (298 K) in HEPES buffer at pH=7.4 solution under degassed condition. Fluorescence lifetime was measured using a time-resolved spectrofluorometer from IBH, UK. Measurements of ¹H NMR spectra were conducted using a Bruker 300 spectrometer D₂O solvent.

4.2.2 Synthesis of 2-hydroxy-5-methylisophthalaldehyde (DFP)

2-hydroxy-5-methylisophthalaldehyde (DFP) was prepared by following a standard literature procedure.^{4,18}

4.2.3 Synthesis of chemosensor [HL4.1=4-methyl-2,6-bis((E)-((2-(piperazin-1-yl)ethyl)imino)methyl)phenol]

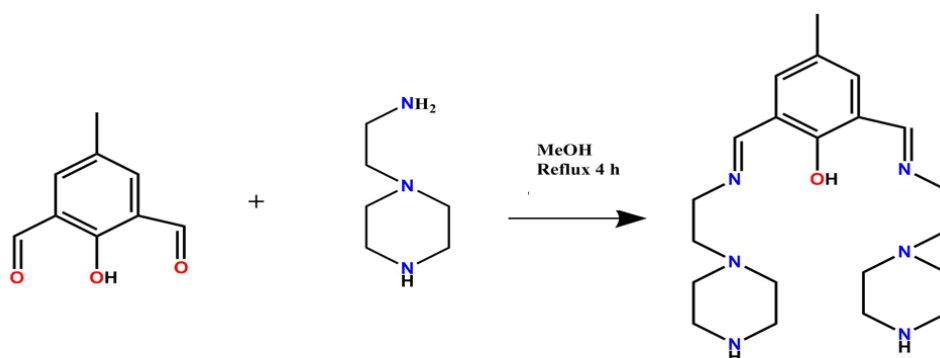
A mixture of 2-hydroxy-5-methylisophthalaldehyde (2.0 mmol, 0.3283 g) and 1-(2-aminoethyl)piperazine (4.0 mmol, 0.516 g) was heated to reflux for *ca.* 4 h in methanol solvent (**Scheme 4.1**). Yellow coloured gummy mass was obtained after evaporation of the solvent.

Yield: 0.335 g (87%). Anal. Calc. for C₂₁H₃₄N₆O: C 65.25%; H 8.87%; N 21.74%. Found: C 65.18%; H 8.48%; N 21.49%. IR (cm⁻¹, KBr): $\nu(\text{C}=\text{N})$ 1634s; $\nu(\text{C}-\text{H})$ 779s. ESI-MS

(positive) in MeOH: The base peak was detected at $m/z = 387.18$, corresponding to [HL4.1+1]⁺. UV-Vis, λ_{\max} (nm), (ϵ (dm³mol⁻¹cm⁻¹)) in HEPES buffer at pH= 7.4: 440 (6229).

¹H NMR (d₆-DMSO, 300 MHz) δ ppm: 2.17 (Ar-CH₃) (s, 3H), 2.42 (-CH₂) (s, 4H), 3.60 (-CH₂) (s, 4H), 2.27 (-CH₂) (s, 8H), 2.58 (-CH₂) (s, 8H), 7.41 (ArH) (m, 2H), 8.50 (-CH=N) (s, 2H).

¹³C NMR (d₆-DMSO, 75 MHz) δ ppm: 20.35 (-CH₃), 45.89-59.39 (-CH₂), 121.44-161.75 (Ar-C), 160.76 (-CH=N) .



Scheme 4.1 Route of synthesis of chemosensor (HL4.1).

4.2.4 Synthesis of complex [Zn₂(L4.1)(OH₂)(OH)(NO₃)](NO₃) (4.1)

A 2 mL methanolic solution of zinc nitrate hexahydrate (2.0 mmol, 0.5948 g) was added drop wise to 20 mL methanolic solution of HL4.1 (1.0 mmol, 0.386 g) followed by addition of triethylamine (2.0 mmol, ~0.4 mL) and the resultant reaction mixture was stirred for *ca.* 1 h. Yellow coloured solid mass was obtained in high yield after slow evaporation of the solvent (Scheme 4.2).

Yield: 0.589 g (85%). Anal. Calc. for C₂₁H₃₈N₈O₁₀Zn₂: C 36.38%; H 5.52%; N 16.16%. Found: C 36.17%; H 5.35%; N 16.84%. IR (cm⁻¹, KBr): ν (C=N) 1632s; ν (NO₃⁻)1321s; ν (C-H) 781 s. ESI-MS (positive) in MeOH: The base peak was detected at $m/z = 638.00$,

corresponding to $[\text{Zn}_2(\mathbf{L4.1})(\text{OLi})(\text{H}_2\text{O})]^+$. UV-Vis, λ_{max} (nm), (ϵ ($\text{dm}^3\text{mol}^{-1}\text{cm}^{-1}$)) in HEPES buffer at pH= 7.4: 410(6975).

¹H NMR (d_6 -DMSO, 300 MHz) δ ppm: 2.16 (Ar-CH₃) (s, 3H), 2.48 (-CH₂) (s, 4H), 2.55 (-CH₂) (s, 8H), 2.89 (-CH₂) (s, 8H), 7.46 (ArH) (m, 2H), 8.57 (-CH=N) (s, 2H).

¹³C NMR (d_6 -DMSO, 75 MHz) δ ppm: 19.94 (-CH₃), 49.07-58.51(-CH₂), 121.37-168.16 (Ar-C), 166.62 (-CH=N) .

4.2.5 Synthesis of complex $[\text{Cu}_2(\mathbf{L4.1})(\text{OH}_2)(\text{OH})(\text{NO}_3)](\text{NO}_3)$ (4.2)

A 2 mL methanolic solution of copper nitrate trihydrate (2.0 mmol, 0.5912g) was added drop wise to 20 mL methanolic solution of **HL4.1** (1.0 mmol, 0.386 g) followed by addition of triethylamine (2.0 mmol, ~0.4 mL) and the resultant reaction mixture was stirred for *ca.* 1 h. Intense green coloured solid mass was obtained after slow evaporation of the solvent (**Scheme 4.2**).

Yield: 0.585 g (85%). Anal. Calc. for C₂₁H₃₈Cu₂N₈O₁₀: C 36.57%; H 5.55%; N 16.25%. Found: C 36.48%; H 5.31%; N 16.02%. IR (cm^{-1} , KBr): $\nu(\text{C}=\text{N})$ 1627s; $\nu(\text{NO}_3^-)$ 1332s; $\nu(\text{C}-\text{H})$ 750s. ESI-MS (positive) in MeOH: The base peak was detected at $m/z = 634.14$ corresponding to $[\text{Cu}_2(\mathbf{L4.1})(\text{OLi})(\text{H}_2\text{O})]^+$. UV-Vis, λ_{max} (nm), (ϵ ($\text{dm}^3\text{mol}^{-1}\text{cm}^{-1}$)) in HEPES buffer at pH= 7.4: 405(12782).

4.2.6 UV-visible and fluorescence spectroscopic studies

Stock solutions of various ions (1×10^{-3} M) were prepared in deionized water. A stock solution of the chemosensor and (**HL4.1**) (1×10^{-3} M) was prepared in methanol. The solution of **HL4.1** was then diluted to 1×10^{-5} M as per requirement. All the spectroscopic experiments including competitive assay of various cations and anions were performed in aqueous-methanolic HEPES buffer medium at pH 7.4. In titration experiments, 30 μL solution of 1×10^{-3} M **HL4.1** (1×10^{-5} M) was taken in a quartz optical cell of 1.0 cm optical path length,

and the ion stock solutions were added gradually to maintain a concentration of 1×10^{-5} M. Spectroscopic studies of the chemosensor (**HL4.1**) in the presence of different anions were performed in HEPES buffer at pH = 7.4. In competitive assay experiments, the test samples were prepared by interacting appropriate amounts of the cations stock in 3 mL of **HL4.1** solution (1×10^{-5} M).

4.2.7. Binding stoichiometry (Job's plot)

Job's continuation method was employed to find out the binding stoichiometry of the chemosensor with that of Zn²⁺ ions using both absorption and emission spectroscopy. In case of Cu²⁺, we have determined the binding stoichiometry using absorption spectroscopy. At a given temperature (25°C), the absorbance and fluorescence were noted for solutions where the concentrations of both chemosensor and Zn²⁺ ions were varied but the sum of their concentrations was kept constant at 1×10^{-5} M. Relative change in absorbance ($\Delta A/A_0$) and fluorescence ($\Delta I/I_0$) were plotted as a function of mole fraction of chemosensor. The break point in the resulting plot corresponds to the mole fraction of chemosensor in Zn²⁺ complex. From the break point the stoichiometry were estimated. The results reported are average of at least three experiments.

4.2.8 Cell line culture

Triple negative human breast cancer cell line MDA-MB-468 was obtained from National Center for Cell Science (NCCS) Pune, India. The cells were grown in DMEM with 10% FBS (Fetal Bovine Serum), penicillin/streptomycin (100units/ml) at 37°C and 5% CO₂. All the treatments were conducted at 37°C and at a cell density allowing exponential growth.

4.2.9 Cell imaging

The MDA-MB-468 cells were grown in coverslips for 24hrs. After that the cells were either mock-treated or treated with 5 μ M of ligand and 10 μ M Zn²⁺ salt in the presence or absence of

10 μM of Cu²⁺ salt and for 24 hrs at 37°C. The cells were washed with 1×PBS. Then they were mounted on a glass slide and observed under fluorescence microscope (Leica).

4.2.10. Computational method

All computations were performed using the GAUSSIAN09 (G09)^{4.19} software package. For optimization we used the density functional theory method at the B3LYP level^{4.20,4.21} and the standard 6-31+G(d) basis set for C, H, N and O atoms^{4.22,4.23} and the lanL2DZ effective potential (ECP) set of Hay and Wadt^{4.24–4.26} for zinc and copper atoms have been chosen for optimization.

TDDFT calculation was performed with the optimized geometry to ensure only positive eigen values. Time-dependent density functional theory (TDDFT)^{4.27–4.29} was performed using conductor-like polarizable continuum model (CPCM)^{4.30–4.32} and the same B3LYP level and basis sets in methanolic solvent system. GAUSSSUM^{4.33} was used to calculate the fractional contributions of various groups to each molecular orbital.

4.3 Results and discussion

4.3.1 Synthesis and characterization

2-hydroxy-5-methylisophthalaldehyde (DFP) has been synthesized according to a standard procedure.^{4.18} The Schiff base ligand (**HL4.1**) was synthesized in a one pot reaction: 2 equiv. of 1-(2-aminoethyl)piperazine was added to a methanolic solution of 1 equiv. of 2-hydroxy-5-methylisophthalaldehyde (DFP) under ambient condition and then the solution was heated for 4h (**Scheme 4.1**). The product was collected as a semi-solid in good yield and used without further purification. It was thoroughly characterized using different spectroscopic methods (UV-Vis, FT-IR, ¹H NMR, ¹³C NMR) and purity was verified with elemental analysis. In the ESI-mass spectrum of the chemosensor the base peak was found at 387.18 corresponding to [HL+1]⁺ (**Figure 4.1**). In the FT-IR spectrum of **HL4.1** a broad band

at around 3374 cm⁻¹ indicate the presence of phenolic OH group and the band at 1634 cm⁻¹ is attributed to the C=N (for azomethine) stretching frequency (**Figure 4.2**).

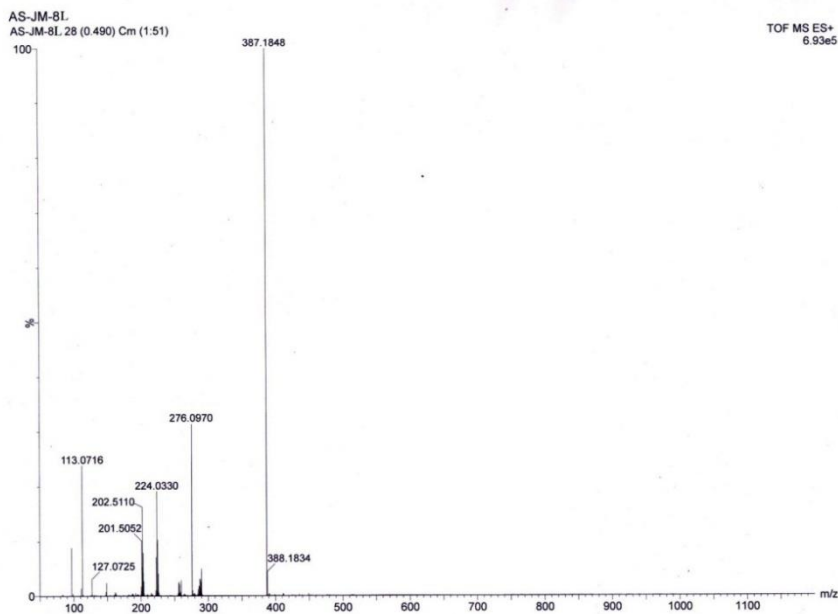


Figure 4.1 ESI-mass spectrum of chemosensor (**HL4.1**).

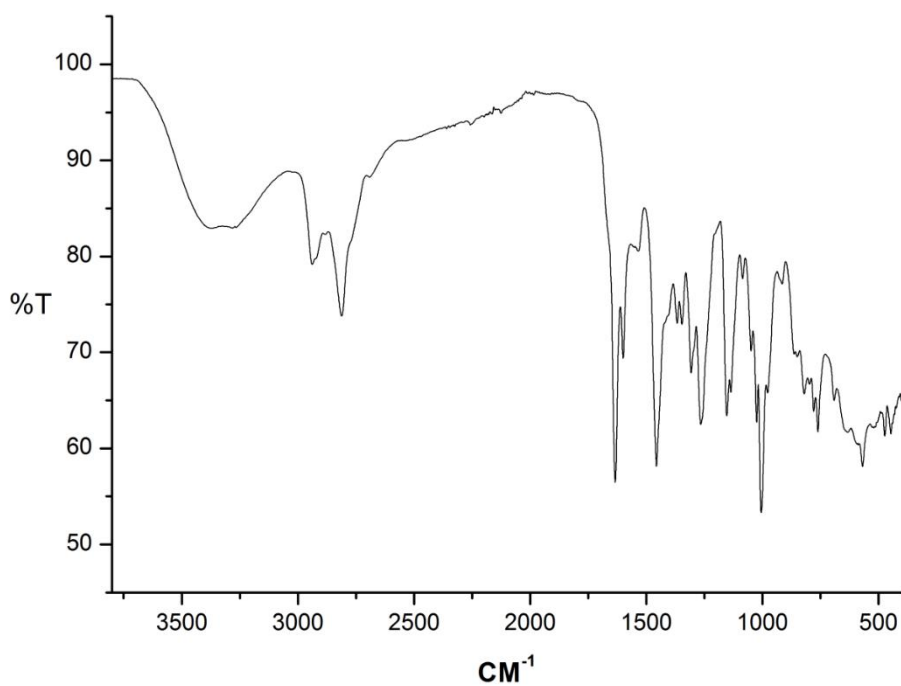
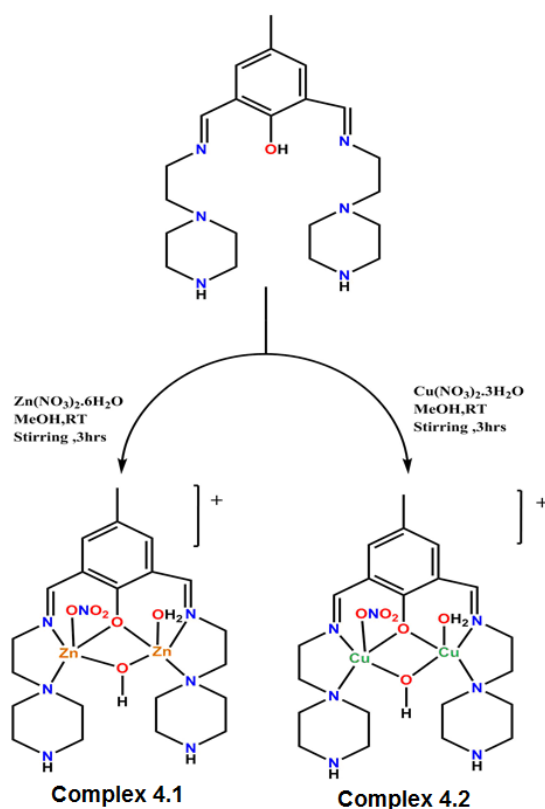


Figure 4.2 FTIR spectrum of chemosensor (**HL4.1**).

HL4.1 react with both Zn(NO₃)₂·6H₂O and Cu(NO₃)₂·3H₂O in 1:2 ratio to produce complex **4.1** and **4.2**, respectively (**Scheme 4.2**). The solid mass of both complexes are isolated in high yield. Both are characterized by elemental and ESI-MS analyses. The experimental and simulated mass spectra of complex **4.1** and **4.2** were well matched with each other at m/z value 638.00 and 634.14 corresponding to molecular ion peak of [Zn₂(L)(OH₂)(OLi)(NO₃)]⁺ and [Cu₂(L)(OH₂)(OLi)(NO₃)]⁺ respectively (**Figures 4.3** and **4.4**). In FT-IR spectrum of complex **4.1** the characteristics stretching frequencies appeared at 1632 cm⁻¹ (νC=N), 781cm⁻¹ (νC-H) and 1321cm⁻¹ ((νNO₃⁻), asymmetric stretch), respectively. Similarly, in case of complex **4.2** the characteristics stretching frequencies appeared at 1627cm⁻¹ ν(C=N), 750cm⁻¹ν(C-H) and 1332 cm⁻¹ (ν(NO₃⁻), asymmetric stretch)) respectively. It is important to mention that although both the complexes are previously reported by Das et al.,^{4,34} chemosensing behavior of **HL4.1** has been explored by us.



Scheme 4.2. Route of synthesis of complexes **4.1** and **4.2**.

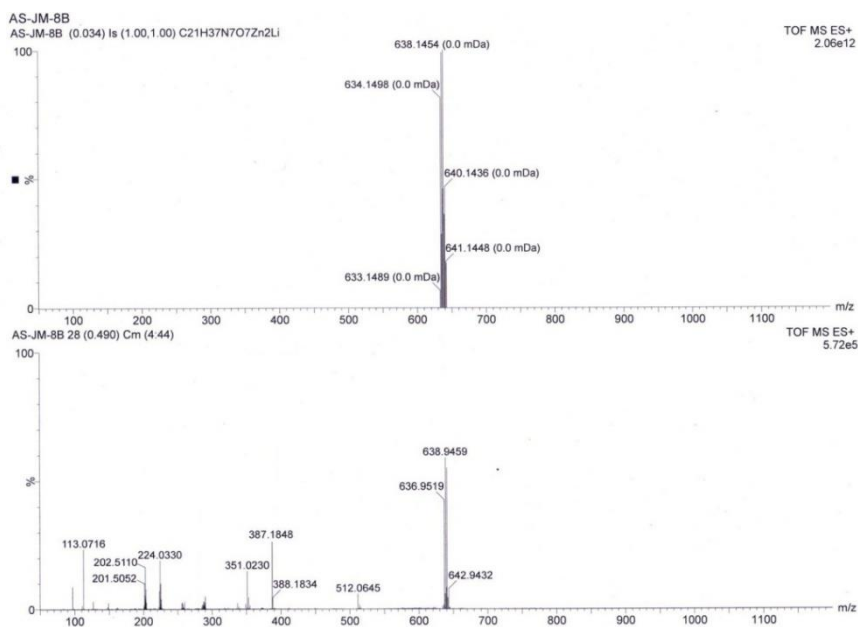


Figure 4.3 ESI-mass spectrum of complex **4.1** [Above = Simulated pattern and Below = Experimental pattern].

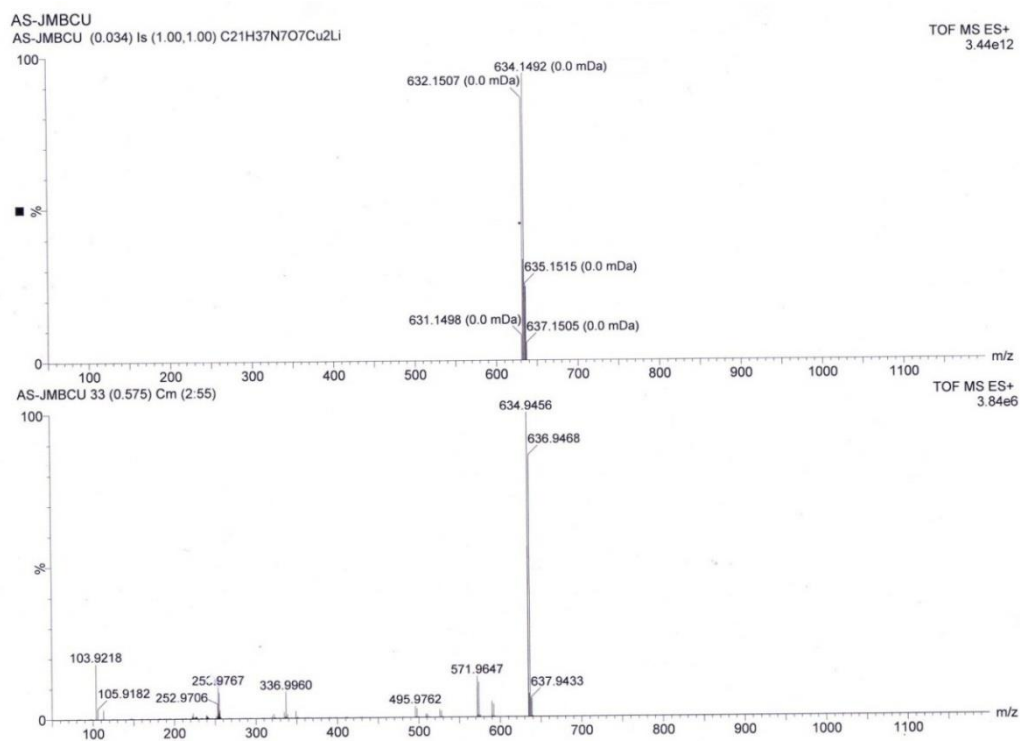


Figure 4.4 ESI-mass spectrum of complex **4.2** [Above = Simulated pattern and Below = Experimental pattern].

4.3.2 Absorption spectral studies

The UV-vis spectrum of the chemosensor **HL4.1** was first investigated in HEPES buffer at pH 7.4 resulting a well-defined band at 440 nm. The peak is attributed to intra molecular $\pi \rightarrow \pi^*$ or $n \rightarrow \pi^*$ type of transition. In presence of Zn²⁺ and Cu²⁺ there is significant changes in the spectra of **HL** which clearly indicate strong interaction between them. The experiments were performed in the same solvent system. Initially it has been observed that upon 2 μ M addition of Zn²⁺ ions to 10 μ M **HL4.1** solution a rapid hypochromic as well as hypsochromic shift of the original peak of **HL4.1** was observed. Upon gradual increase of Zn²⁺ ions concentration (0-20 μ M), the peak at 440 nm disappears with concomitant appearance of a new peak at around 410 nm (**Figure 4.5**). No further change was observed above 2.0 equivalent of Zn²⁺. During such process an isosbestic point was observed at 430 nm (**Figure 4.5**). In case of Cu²⁺ ion similar type of changes has been observed. Upon gradual addition of (0-20 μ M) Cu²⁺ ion at a fixed concentration of **HL4.1** (10 μ M) the intensity of the original peaks at 440 nm rapidly decreases and finally disappear with subsequent appearance of a new peak at around 405 nm (**Figure 4.6**). Again saturation in the absorption intensity of peak at 405 nm observed upon addition of 2 equivalent of Cu²⁺ solution. Both the spectra clearly indicate 2:1 binding stoichiometry of the respective ions with the chemosensor which has been further established with the aid of Job's plot analysis (**Figure 4.7**). These results have been further supported by DFT and mass spectral analysis (**Figures 4.3 and 4.4**). Notably, the addition of the cations (Cd²⁺, Hg²⁺, Pb²⁺, Al³⁺, Ag⁺, Mn²⁺, Fe³⁺, Co²⁺, Ni²⁺, Na⁺, K⁺, Mg²⁺ and Ca²⁺) did not change the initial absorption spectrum of the chemosensor appreciably.

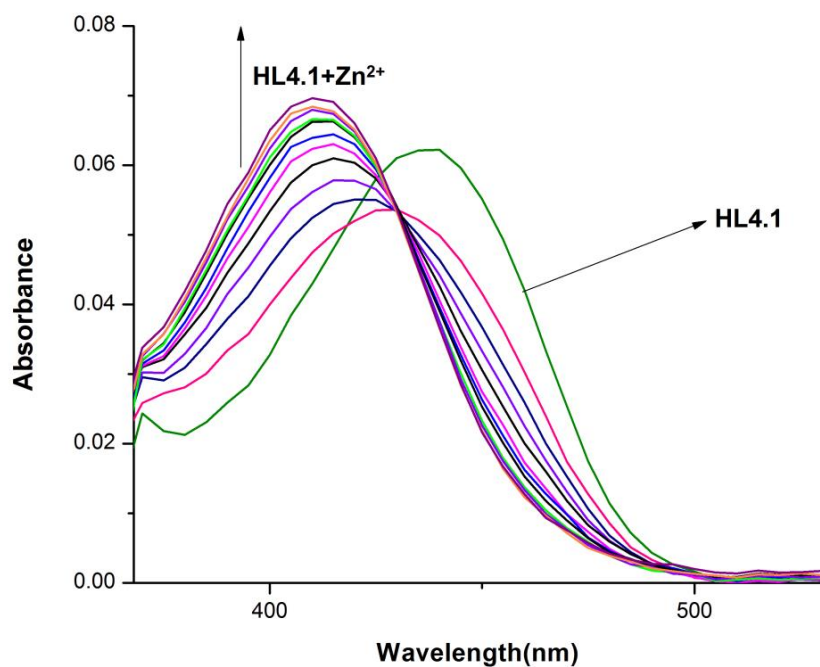


Figure 4.5 Absorption titration of **HL4.1** (10 μM) with gradual addition of Zn²⁺, 0-20 μM in HEPES buffer at pH 7.4.

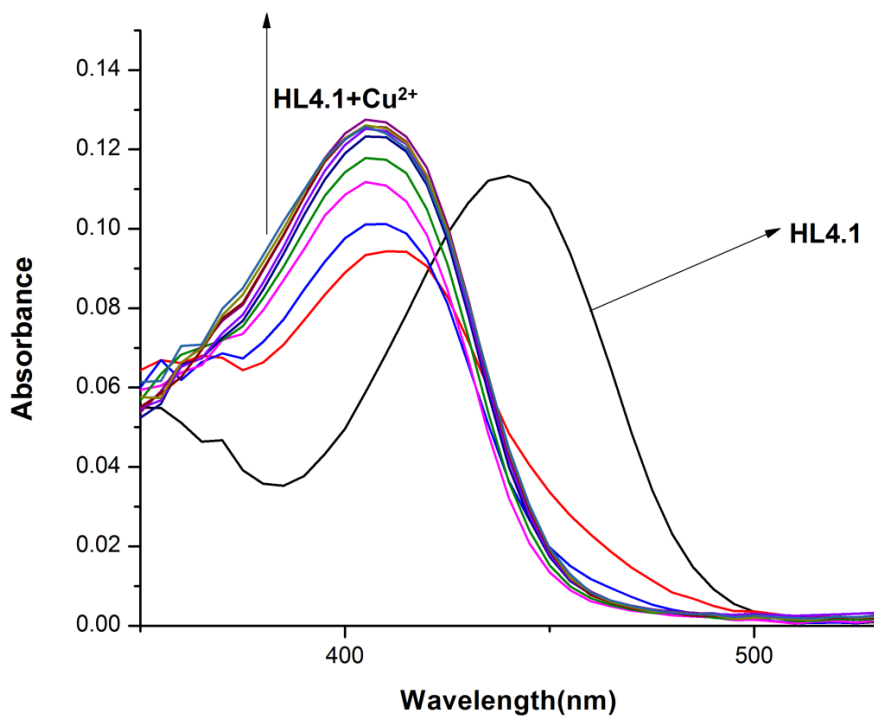


Figure 4.6 Absorption titration of **HL4.1** (10 μM) with gradual addition of Cu²⁺, 0-20 μM in HEPES buffer at pH 7.4.

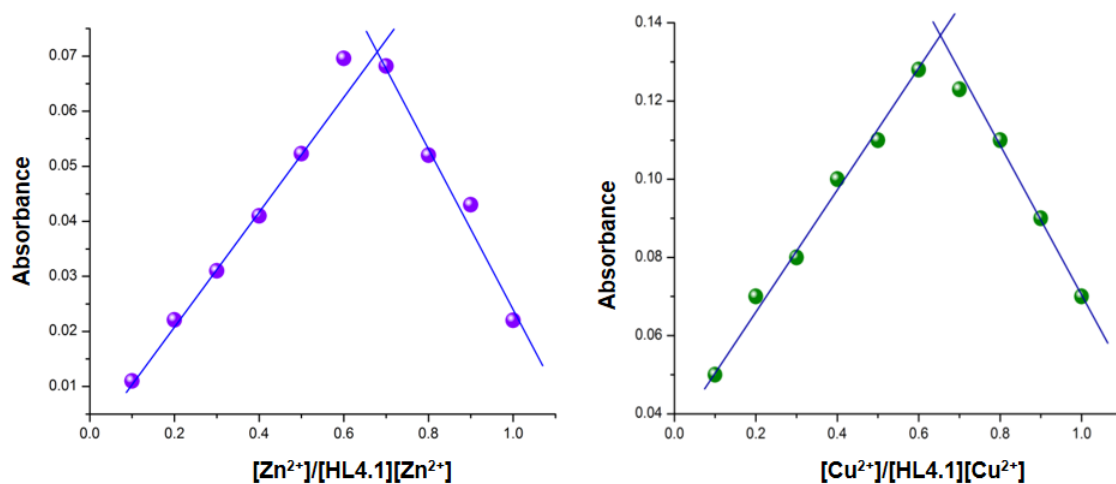


Figure 4.7 2:1 binding stoichiometry has shown by Job's plot of complexes **4.1** and **4.2**. Symbols and solid lines represent the experimental and simulated profiles, respectively.

4.3.3 NMR studies

At first ¹HNMR of the chemosensor (**HL4.1**) has been performed in d₆-DMSO solvent. The spectrum clearly suggests presence of a c₂ symmetry in the molecule. Imine (H-C=N) protons appear as a sharp peak at 8.50 ppm. Aromatic protons appear at 7.41 ppm. Aliphatic protons for aminoethyl moiety appear at 3.60 ppm and 2.42 ppm, respectively, whereas aliphatic protons of piperazine ring system appear at 2.58 ppm and 2.27 ppm, respectively and methyl protons appear at 2.17 ppm. To better understand for complex formation with Zn²⁺ ion, we have performed ¹HNMR titration in certain stoichiometric ratio of **HL4.1** and Zn²⁺ ion in d₆-DMSO solvent. Interestingly, in presence of Zn²⁺ ion all spectra exhibit broadening and splitting of imine, aromatic and aliphatic protons, respectively. Imine (H-C=N) proton shifted to downfield when 1 equivalent of Zn²⁺ is added and it appears at δ = 8.55 ppm. Finally, it shifted to δ = 8.57 ppm when 2 equivalent Zn²⁺ is added. Similarly, aromatic protons appear at 7.44 ppm and 7.46 ppm after addition of 1 and 2 equivalent of Zn²⁺ ion, respectively (**Figure 4.8**).

In ¹³C NMR (d₆-DMSO, 75 MHz) spectrum of **HL4.1**, signals for -CH₃ and -CH₂ carbon atoms appeared at 20.35 and in the range 45.89-59.39, respectively. Aromatic carbon atoms appeared at 121.44, 126.48, 132.68 and 161.75 ppm, respectively. The imine carbon atom appeared at 160.76 ppm (**Figure 4.9**). In case of complex **4.1**, signals for -CH₃ and -CH₂ carbon atoms appeared at 19.94 and in the range 49.07- 58.51, respectively. Aromatic carbon atoms appeared at 121.37-168.15 ppm. Whereas, the imine carbon atom appeared at 166.62 ppm (**Figure 4.10**).

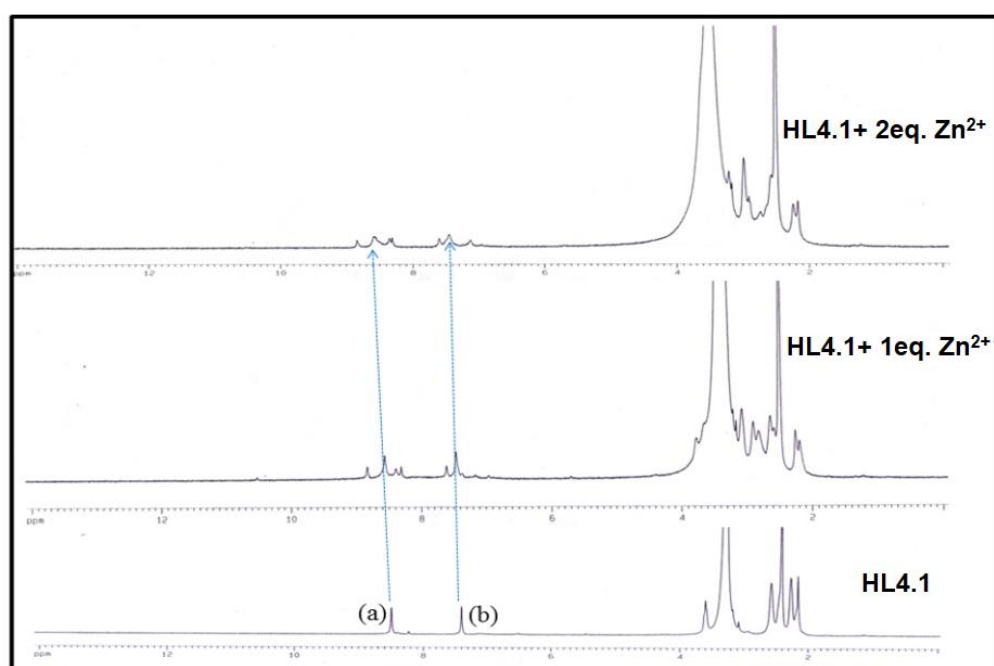


Figure 4.8 ¹H-NMR titration of the free ligand (**HL4.1**) and with the addition of **4.1** and **4.2** equivalent of Zn²⁺ in DMSO-d₆ recorded on a 300 MHz Bruker NMR spectrometer.

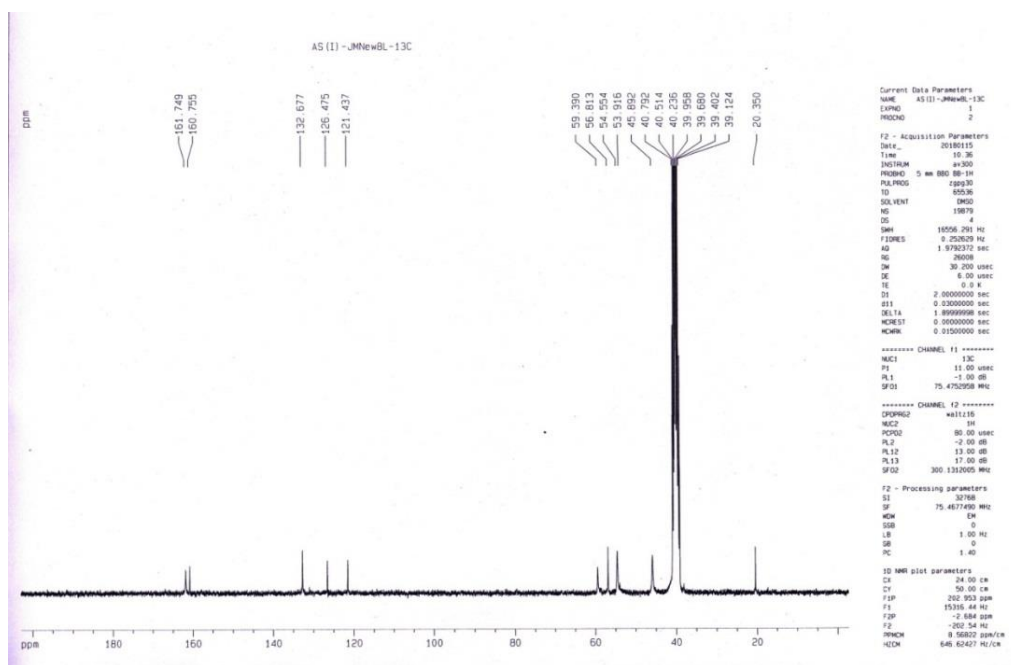


Figure 4.9 ¹³C NMR of HL4.1 in d₆-DMSO solvent.

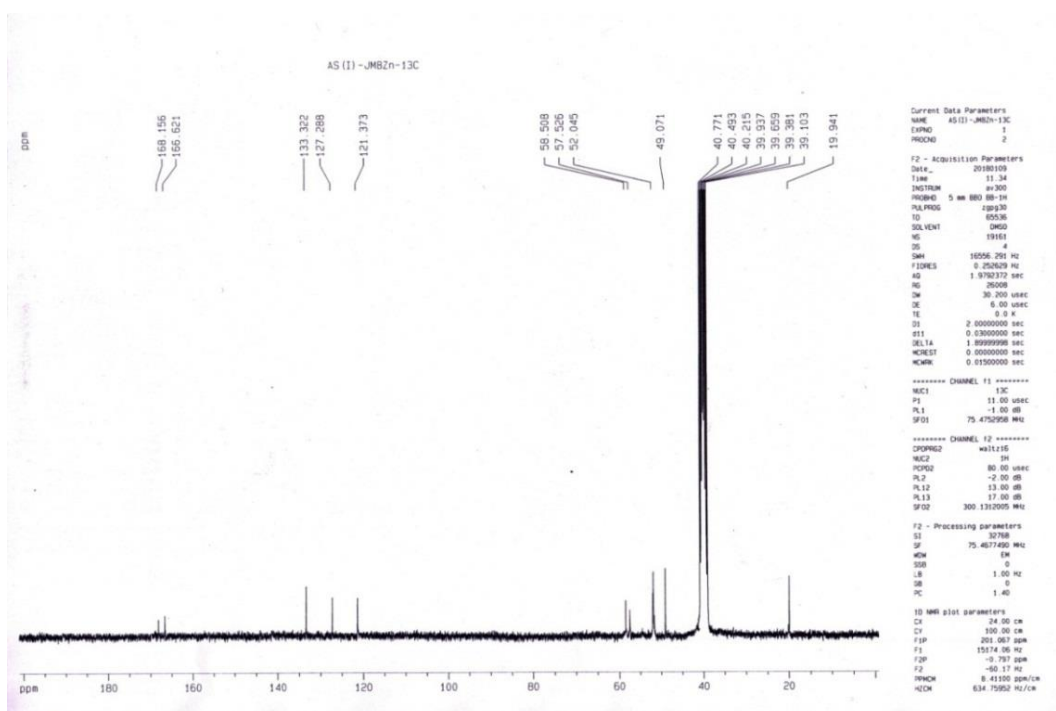


Figure 4.10 ¹³C NMR of complex 4.1 in d₆-DMSO solvent.

4.3.4 Fluorescence properties

Fluorescence experiment also performed in HEPES buffer (pH = 7.4) at ambient conditions. Upon excitation at 440 nm, **HL4.1** exhibits weak fluorescence at 510 nm. This is probably due to PET (Photo induced Electron Transfer) process (**Figure 4.11**). The delocalization of available lone pair on the imine nitrogen atom to the DFP moiety leads to the quenching of the fluorescence. Upon addition of Zn²⁺ ions to **HL4.1** an enormous fluorescence enhancement is observed and the emission band has been blue shifted to 480 nm. The fluorescence enhancement due to Zn²⁺ has a steady growth and finally reaches a maximum at two equivalent of Zn²⁺ with an approximately 16-fold enhancement in the emission intensity. This observation clearly suggests formation of a 1:2 complex. The chelation of Zn²⁺ with O, N donors of **HL4.1** increases the rigidity of the molecular assembly (CHEF effect) via inhibition of free rotation of **HL4.1** around the HC=N bond. Again PET process is eliminated by arresting the lone pair of electrons present in the imine nitrogen. These two effects are jointly responsible for the observed fluorescence enhancement.

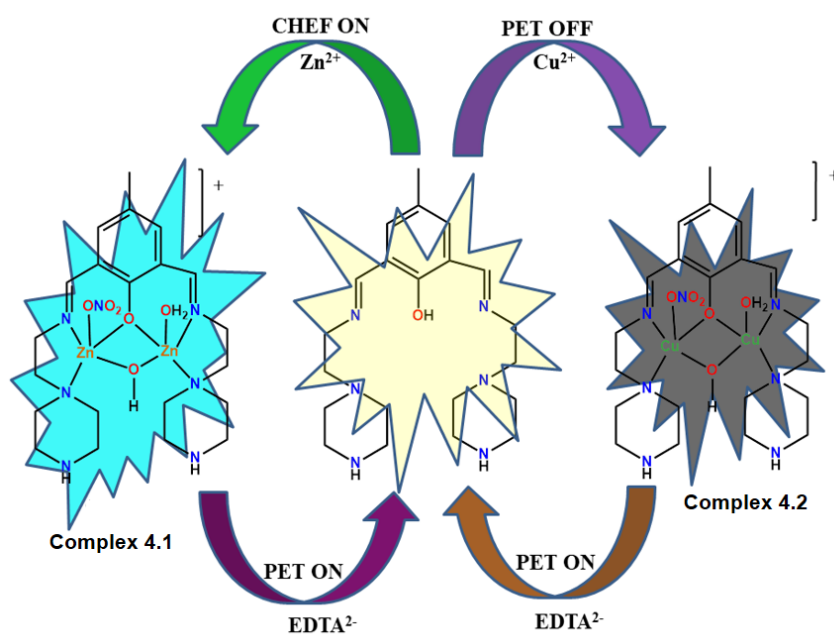


Figure 4.11 Pictorial representation of ‘PET’ and ‘CHEF’ process.

In the inset we have shown a plot of fluorescence intensities at 480 nm (I_{480}) against different concentration of zinc ion (**Figure 4.12**). In the plot the value of (I_{480}) increases with the increasing concentration of Zn²⁺ and a saturation was observed at 2.0 equivalent of added Zn²⁺ which proved 1:2 binding between the probe and Zn²⁺. The sigmoid nature of curve reflects strong interaction between the organic probe and Zn²⁺ ion.

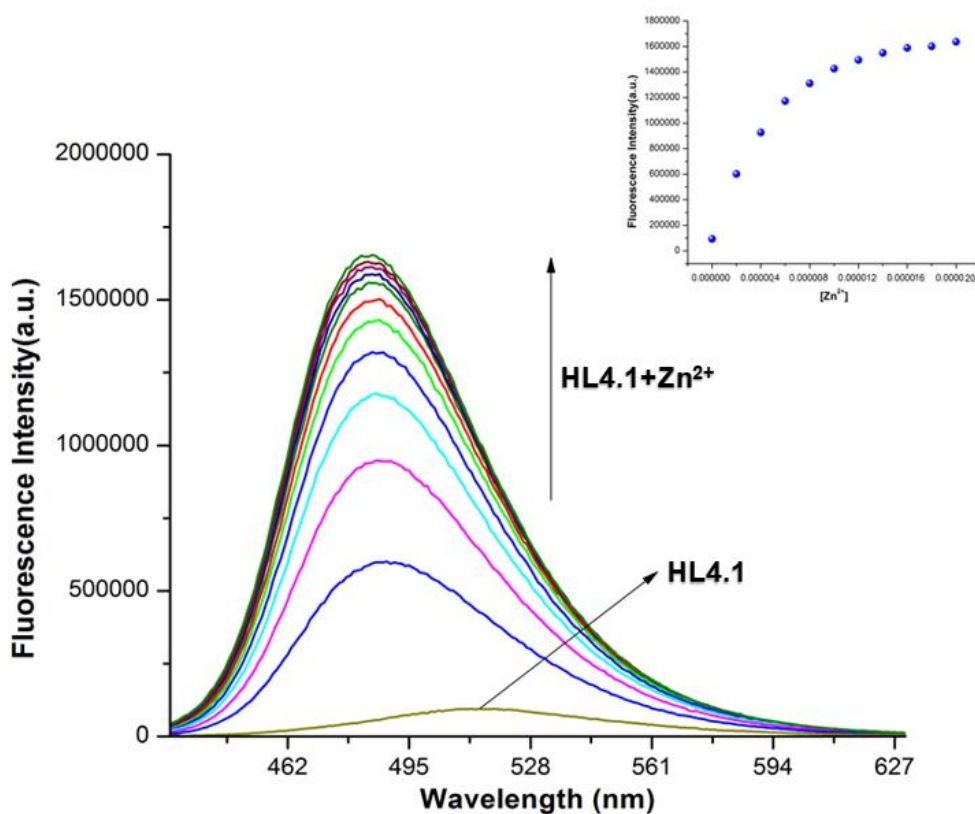


Figure 4.12 Fluorescence titration of **HL4.1** (10 μ M) in HEPES buffer at pH = 7.4 by gradual addition of Zn²⁺ (0–20 μ M) with λ_{em} = 480 nm (1/1 slit). Inset: non-linear plot of fluorescence intensity vs. concentration of Zn²⁺ ion.

On the other hand under identical condition when Cu²⁺ ions (0–20 μ M) were added to the chemosensor solution the fluorescence emission at \sim 510 nm is almost completely quenched (**Figure 4.13**). Such type of (\sim 174 fold) of dramatic quenching in the fluorescence intensity of the chemosensor in presence of Cu²⁺ ion suggests formation of Cu²⁺–probe

complex, thus chelation enhanced quenching (CHEQ) results metal to ligand charge transfer (MLCT) between **HL4.1** and paramagnetic Cu²⁺ ions.^{4,35} Again plot of Fluorescence intensities at 510 nm (I_{510}) vs. concentration of copper ion has been presented in **Figure 4.13** (inset). The sensing character of the probe (I_{510}) decreases with the increasing concentration of Cu²⁺ and the pattern was linear in regarding the concentration of Cu²⁺ in the range of 0–20 μ M (inset), suggesting a 1:2 stoichiometric ratio between **HL4.1** and Cu²⁺.

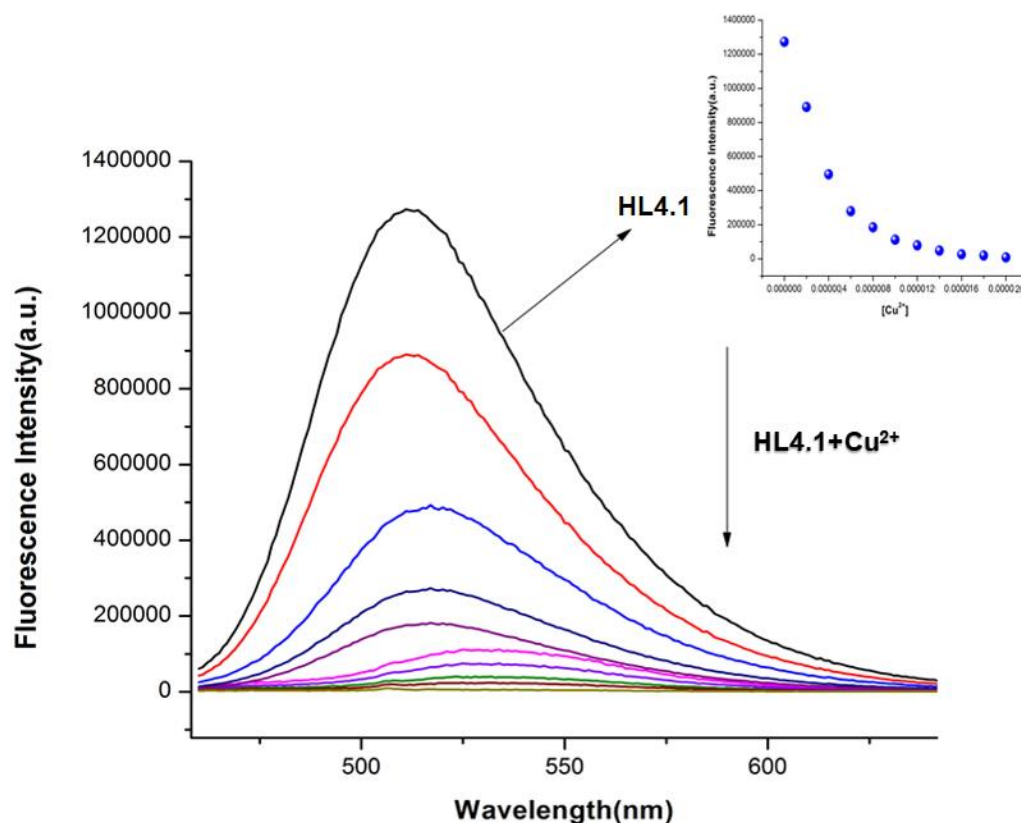


Figure 4.13 Fluorescence titration of **HL4.1** (10 μ M) in HEPES buffer at pH =7.4 by gradual addition of Cu²⁺ (0–20 μ M) with λ_{em} = 510 nm (1/1 slit). Inset: non-linear plot of fluorescence intensity vs. concentration of Cu²⁺ ion.

Binding ability of the chemosensor towards Zn²⁺ and Cu²⁺ ions has been established using Benesi-Hildebrand equation (Equation 1) involving fluorescence titration curve.^{4,36}

$$\frac{F_{max}-F_0}{F_x-F_0} = 1 + \left(\frac{1}{K[C]^n} \right) \quad (1)$$

Where, F_{\max} , F_0 and F_x are fluorescence intensities of **HL4.1** in the presence of metal ions at saturation, free **HL4.1** and any intermediate metal ions concentration, respectively. K is the binding constant of the complexes. Concentrations of Zn²⁺ and Cu²⁺ ions are represented by C and here $n=1$. Then binding constant (K) of the complexes has been determined using the relation, $K = 1/\text{slope}$. A plot of $\frac{F_{\max}-F_0}{F_x-F_0}$ vs $\left(\frac{1}{[C]^1}\right)$ provides the binding constant values as 7.14×10^4 and $2.18 \times 10^5 \text{M}^{-1}$ for Zn²⁺ and Cu²⁺ complexes, respectively (**Figure 4.14** and **4.15**, respectively).

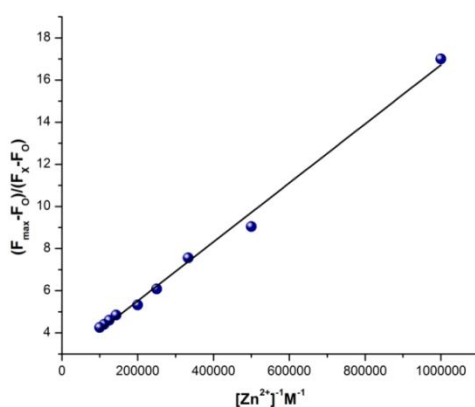


Figure 4.14 Benesi-Hildebrand equation: A plot of $\frac{F_{\max}-F_0}{F_x-F_0}$ vs $\left(\frac{1}{[M]^1}\right)$. Symbols and solid lines represent the experimental and simulated profiles for complex **4.1**, respectively

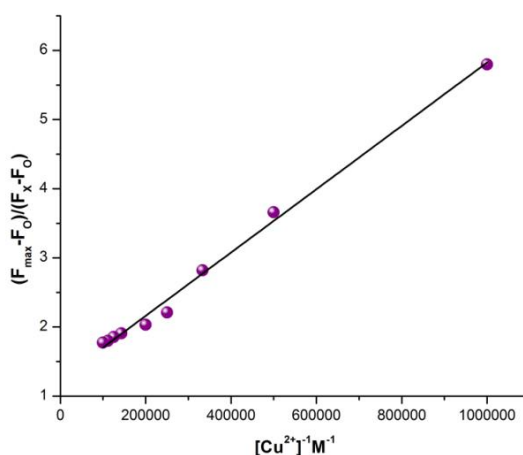


Figure 4.15 Benesi-Hildebrand equation: A plot of $\frac{F_{\max}-F_0}{F_x-F_0}$ vs $\left(\frac{1}{[M]^1}\right)$. Symbols and solid lines represent the experimental and simulated profiles for complex **4.2**, respectively.

To check high selectivity toward the Zn²⁺ and Cu²⁺ over the other competitive species fluorescence titration experiment also performed in presence of different alkali metals (Na⁺ and K⁺), alkali-earth metals (Mg²⁺ and Ca²⁺), and various transition-metal (Mn²⁺, Fe³⁺, Co²⁺, Ni²⁺, Cd²⁺ and Hg²⁺) ions (**Figure 4.16**). It is an important parameter to assess the performance of sensor **HL4.1**. Therefore, the competition as say were performed in the presence of Zn²⁺/Cu²⁺ (2.0 equiv.) mixed with other metal ions (2.0 equiv.) in aqueous media. It has been noted that distinct fluorescence enhancement observed for the mixtures of Zn²⁺ with other metal ions was similar to that caused by Zn²⁺ alone, except for Cu²⁺. The addition of Cu²⁺ to **HL4.1** solution in the presence of Zn²⁺ led to large fluorescence quenching. Here, Cu²⁺ ion detection by **HL4.1** is not influenced by the presence of other competitive metal ions (**Figure 4.17**). Both the competition assay experiments clearly demonstrate high fluorescent recognition of **HL4.1** for Zn²⁺/Cu²⁺ ions over other cations. Binding constant values also support the above explanation. Upon addition of different common anions like S₂O₃²⁻, S²⁻, SO₃²⁻, HSO₄⁻, SO₄²⁻, SCN⁻, N₃⁻, OCN⁻, AsO₄⁻, PO₄³⁻, ClO₄⁻, AcO⁻, Cl⁻, NO₃⁻, P₂O₇⁴⁻, PF₆⁻ and F⁻ in HEPES buffer at pH 7.4 (**Figure 4.18**) chemosensor showed no significant fluorescence enhancement.

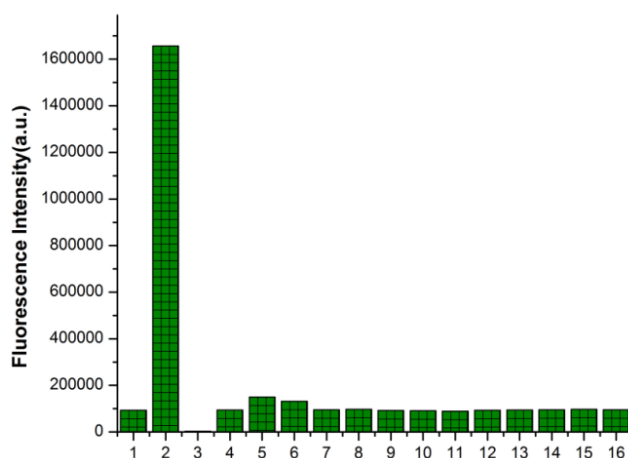


Figure 4.16 Relative fluorescence intensity profile of chemosensor (**HL4.1**) in the presence of different cations in HEPES buffer at pH 7.4. 1=only **HL4.1** (10 μ M); **HL4.1**(10 μ M) +

Mⁿ⁺(20 μM), where Mⁿ⁺=(2–Zn²⁺, 3–Cu²⁺, 4–Ag⁺, 5–Fe³⁺, 6–Hg²⁺, 7–K⁺, 8–Mn²⁺, 9–Na⁺, 10–Ni²⁺, 11–Mg²⁺, 12–Co²⁺, 13–Ca²⁺, 14–Pb²⁺, 15–Cd²⁺ and 16–Cr³⁺).

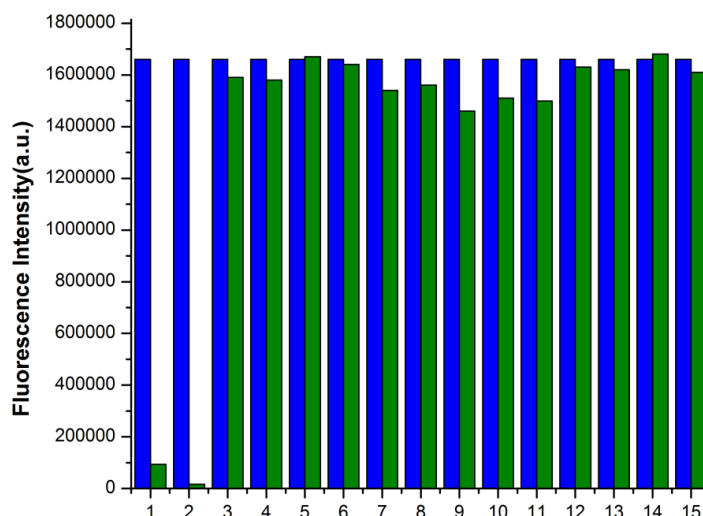


Figure 4.17 Relative fluorescence intensity profile of [HL4.1-Zn²⁺] system in the presence of different cations in HEPES buffer at pH 7.4. 1=only HL4.1 and (2-15)= HL4.1 (10 μM) + Zn²⁺(20 μM) + Mⁿ⁺(20μM), where Mⁿ⁺=(2–Cu²⁺,3–Co²⁺,4–Cr³⁺,5–Fe³⁺,6–Hg²⁺,7–K⁺,8–Mn²⁺,9–Na⁺,10–Ni²⁺,11–Mg²⁺,12–Pb²⁺,13–Ca²⁺,14–Fe²⁺,15–Cd²⁺).

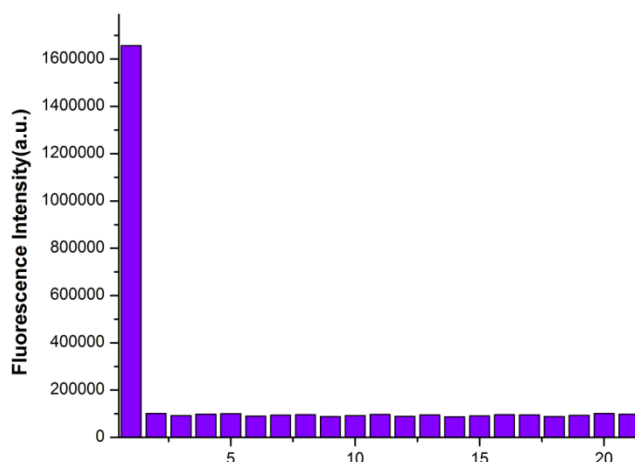


Figure 4.18 Relative fluorescence intensity profile of HL4.1 (10 μM) in the presence of various common anions (50 μM) in HEPES buffer at pH 7.4. 1- HL4.1+Zn²⁺, 2-HL4.1, (3–21)- HL4.1 + Anions, Anions = 3-S₂O₃²⁻, 4-S²⁻, 5-SO₃²⁻, 6- HSO₄⁻, 7- SO₄²⁻, 8-SCN⁻, 9-N₃⁻, 10-OCN⁻, 11-AsO₄³⁻,12-H₂PO₄⁻, 13-HPO₄²⁻, 14-PO₄³⁻, 15-ClO₄⁻, 16-AcO⁻, 17-Cl⁻, 18-NO₃⁻, 19-P₂O₇⁴⁻, 20-PF₆⁻, 21-F⁻.

Interestingly chemosensor **HL4.1** also act as a colorimetric probe for the detection of Zn²⁺ and Cu²⁺ ion. In presence Zn²⁺ ions **HL4.1** exhibits green coloration whereas it is almost colourless in presence of Cu²⁺ ion. Thus, the chemosensor can be used for a selective colorimetric detection of Cu²⁺ and Zn²⁺ ions over other competing metal ions both in environmental and biological fields (**Figure 4.19**).



Figure 4.19 Visual colour changes of chemo sensor (**HL4.1**) (10 μ M) under presence of different metal ions (2 equivalent) in HEPES buffer (pH 7.4). The images in below row and above row were taken under visible light and UV light respectively. Where 1= only **HL4.1**, 2,3,4,5,6,7,8,9,10,11,12,13,14 and 15= **HL4.1**+ Zn²⁺, Cu²⁺, Cd²⁺, Pb²⁺, Hg²⁺, Mn²⁺, Fe³⁺, Co²⁺, Ni²⁺, K⁺, Na⁺, Mg²⁺, Ca²⁺ and Al³⁺ respectively.

Reversibility and regeneration are the two important aspects for real time application of the chemosensor. The experiment was performed in presence of sodium salt of ethylenediaminetetraacetic acid (Na₂EDTA) solution. In case of **HL4.1**-Zn²⁺ complex solution after addition of two equivalent of Na₂EDTA colour changes from green to light yellow with obvious decrease in fluorescence intensity. While, the addition of two equivalent

EDTA to **HL4.1**-Cu²⁺ complex solution an enhancement of emission intensity and finally a light yellow colour indicates the regeneration of the free **HL4.1** (Figure 4.20).



Figure 4.20 Visual colour changes in reversibility experiments. For (A) and (B), 1= Only **HL4.1** (10µM), 2= **HL4.1** (10µM) + Zn²⁺ (20µM), 3= **HL4.1** (10µM) + Zn²⁺ (20µM) + EDTA²⁻ (20µM) under UV and normal light, respectively. For (C) and (D), 1= Only **HL4.1** (10µM), 2= **HL4.1** (10µM) + Cu²⁺ (20µM), 3= **HL4.1** (10µM) + Cu²⁺ (20µM) + EDTA²⁻(20µM) under UV and normal light, respectively.

Limit of detection (LOD) of the chemosensor towards Cu²⁺ and Zn²⁺ ions are calculated using 3σ method.^{4,37} The detection limit of the chemosensor for both the ions are 1.05 × 10⁻⁹ M and 3.53 × 10⁻⁹ M, respectively. In case of Cu²⁺ ion the LOD value is lower than the WHO recommended level for Cu²⁺(2.0 mg/L),^{4,38,4,39} which clearly suggests that this chemosensor can quantitatively detect of Cu²⁺ in HEPES buffer (pH=7.4) media.

The effect of pH on the fluorescence response of the chemosensor **HL4.1** and **HL4.1**-Zn²⁺ and **HL4.1**-Cu²⁺ complexes are examined over a wide range. In case of free **HL4.1** fluorescence intensity remain unchanged in the pH range 2–6 after that from pH 6–11 a slight

enhancement in fluorescence intensity has been observed (**Figure 4.21**). In presence of Zn²⁺ ions change of fluorescence initially in pH range 2–6 fluorescence is almost identical to that of the free ligand. This suggests no complex formation at acidic condition. Upon gradual increase of pH 7–8 a sudden enhancement in fluorescence intensity indicates formation of Zn-complex. Further increase of pH value from 8–11 fluorescence intensity remains unchanged. When Cu²⁺ is added, fluorescence intensity the resultant fluorescence intensity is less compare to free **HL4.1** from pH 3 to 6. In pH 6 to 11 the decrease in fluorescence intensity is more pronounced. The result signifies that the complex formation takes place above pH 6. The pH experiment suggests that **HL4.1** can act as a selective fluorescent probe to recognize both Zn²⁺ and Cu²⁺ ion in presence of other metal ions in biological system under physiological condition.

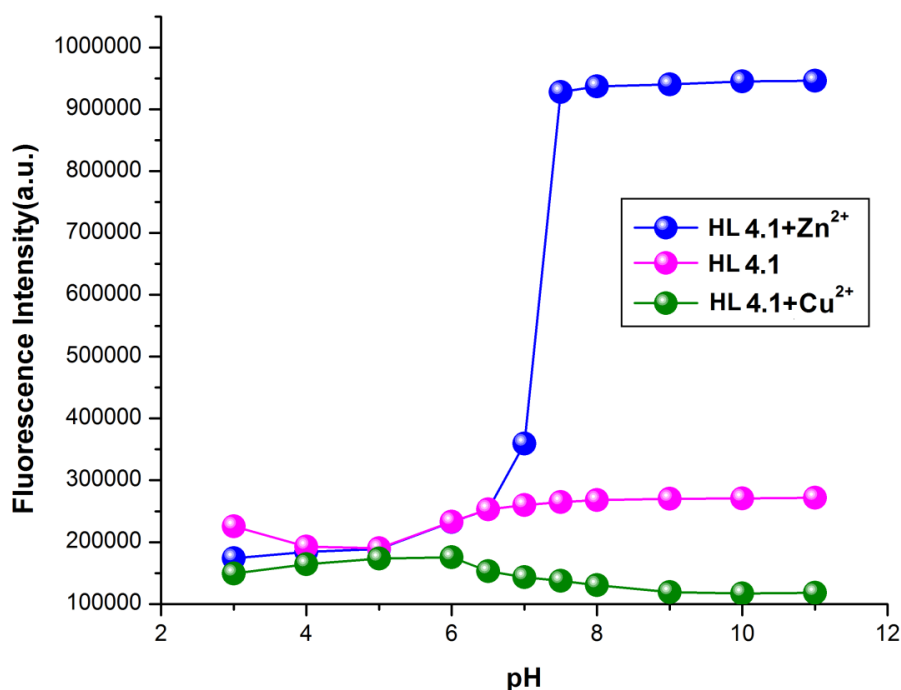


Figure 4.21 Fluorescence intensity of **HL4.1** (10 μ M) in the absence and presence of Zn²⁺ and Cu²⁺ ions (20 μ M) at various pH values in HEPES buffer.

4.3.5 Life time and quantum yield measurements

Lifetime experiment for the chemosensor (**HL4.1**) and complex **4.1** were studied at 298 K in HEPES buffer (pH= 7.4). The average fluorescence decay life time has been measured of the chemosensor and complex **4.1** using the given formula ($\tau_f = a_1\tau_1 + a_2\tau_2$, where a_1 and a_2 are relative amplitude of decay process). The average fluorescence lifetime of the chemosensor and complex **4.1** are 3.12 and 4.96 nS, respectively (**Figure 4.22**, **Table 4.1**).

Fluorescence quantum yield (Φ) has been calculated by the using following formula:

$$\Phi_{\text{sample}} = \left\{ \frac{(\text{OD}_{\text{standard}} \times A_{\text{sample}} \times \eta_{\text{sample}}^2)}{(\text{OD}_{\text{sample}} \times A_{\text{standard}} \times \eta_{\text{standard}}^2)} \right\} \times \Phi_{\text{standard}}$$

Where, A is the area under the emission spectral curve, OD is the optical density of the compound at the excitation wavelength and η is the refractive index of the solvent. Here the value of Φ_{standard} is taken as 0.52 (for Quinine Sulfate).

The values of Φ for **HL4.1** and **HL4.1-Zn²⁺** complexes are found to be 0.036 and 0.39, respectively (**Table 4.1**). The fluorescence quantum yield (Φ) of **HL4.1-Zn²⁺** complex is 10.83 fold greater than free **HL4.1**.

Table 4.1 Data of lifetime (τ_f) and quantum yield (Φ) of **HL4.1** and complex **4.1**.

	τ_f (ns) (average)	χ^2	Φ
HL4.1	3.199	1.0107	0.036
Complex 4.1	4.960	1.1149	0.39

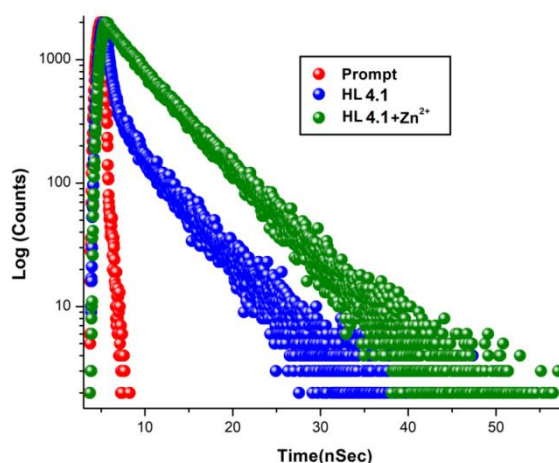


Figure 4.22 Time-resolved fluorescence decay curves (logarithm of normalized intensity vs time in ns) of **HL4.1** in the absence (●) and presence (●) of Zn²⁺ ion, (●) indicates decay curve for the scattered.

4.3.6 Cell imaging

The fluorescence microscopy study is performed to ensure the cellular uptake of ligand and Zn²⁺ salt. A strong green fluorescent signal is observed under the microscope. After the addition of Cu²⁺ salt, the fluorescent signal disappears (**Figure 4.23**).

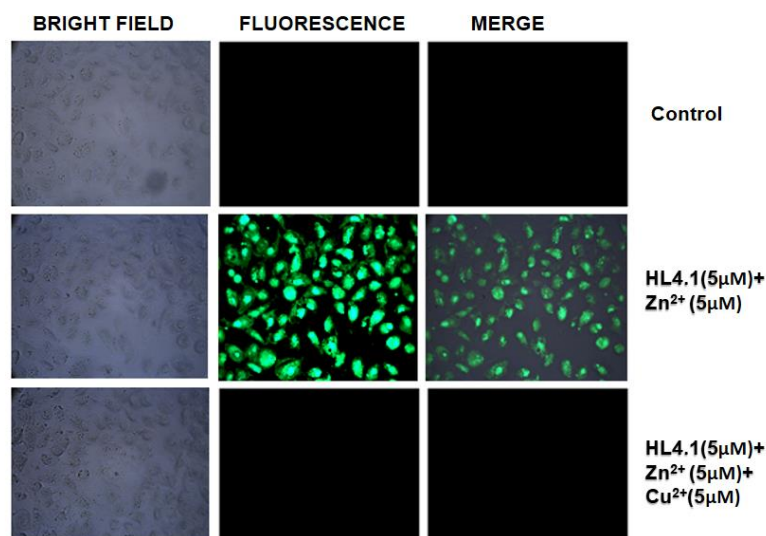


Figure 4.23 Bright field, fluorescence and merged microscopic images of untreated MDA-MB-468 (Control), cells treated with **HL4.1** (5 μM) + Zn²⁺(10μM) and with **HL4.1** (5 μM) + Zn²⁺(10μM) + Cu²⁺(10μM).

4.3.7 DFT study

DFT and TDDFT studies were performed to further support structural and electronic parameters of complexes. For both complexes bond distances and bond angles of the optimized structures are well matched with that of previously reported analogous complexes.³⁴ Furthermore TDDFT study was performed to understand nature, origin and contribution of M.O.s of electronic transitions. It also gives idea of quantity of energy associated with every individual transition. When individual M.O. is concerned the contribution from both ligand and metal center has been computed. So, DFT and TDDFT analysis plays important role to support and understand structural and electronic parameters of complexes.

Here, geometry optimization of **HL4.1**, $[\text{Zn}_2(\text{L4.1})(\text{OH}_2)(\text{OH})(\text{NO}_3)]^+$ and $[\text{Cu}_2(\text{L})(\text{OH}_2)(\text{OH})(\text{NO}_3)]^+$ has been performed using DFT/B3LYP method. The energy minimized structure of complexes **4.1** and **4.2** are shown in **Figure 4.24**. Some selected bond distances and bond angles of both complexes are listed in **Table 4.2**. Theoretical calculations showed that electron density in LUMO of **HL4.1** is mainly distributed over the phenyl ring and imine nitrogen atoms, whereas, electron density in HOMO is mainly distributed over one of the pipyrazine moiety. In complex **4.1**, electron density in both LUMO and HOMO are completely ligand based which follow the same trend to that of free chemosensor **HL4.1** and contribution from metal centers is nil (**Figure 4.25**). In case of complex **4.2**, electron density in LUMO is distributed over the metal centers, Schiff base ligand and coligands and electron density of HOMO is again distributed mainly over one of the pipyrazine moiety (**Figure 4.25**). Energy of some selected M.O. of **HL4.1**, complex **4.1** and **4.2** are given in **Table 4.3** and **4.4**.

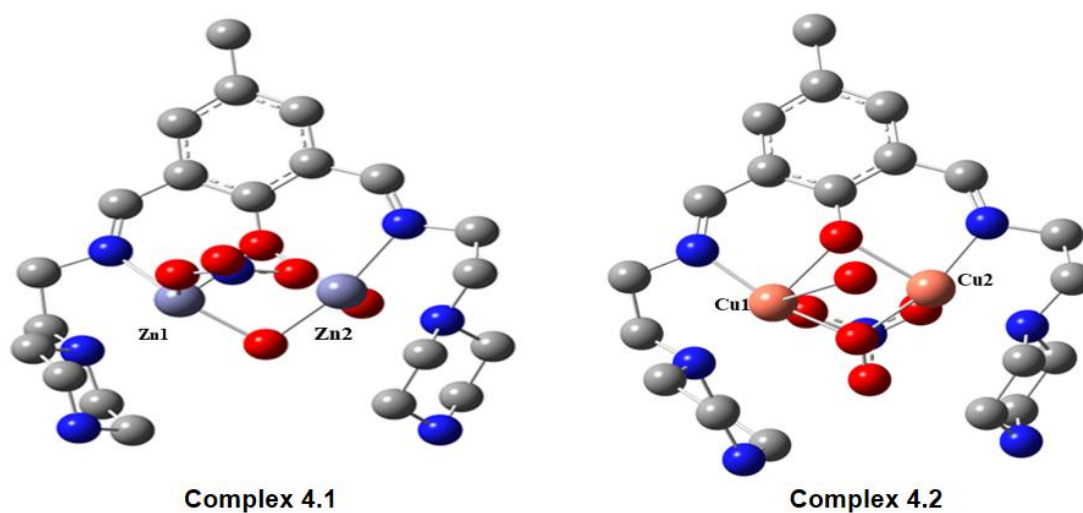


Figure 4.24 DFT optimized structure of complexes **4.1** and **4.2**. H atoms are omitted for clarity.

Table 4.2 Bond lengths (Å) and bond angles (°) of optimized structure of [Zn₂(L4.1)(NO₃)(OH)(OH₂)]⁺ and [Cu₂(L4.1)(NO₃)(OH)(OH₂)]⁺ (B3LYP/6-31+G(d) basis set).

Complex 4.1	Calculated	Complex 4.2	Calculated
Zn1-N _{imine}	2.125	Cu1-N _{imine}	1.982
Zn1-O _{phenoxido}	2.205	Cu1-O _{phenoxido}	2.109
Zn1-O _{nitrate}	2.057	Cu1-O _{nitrate}	2.248
Zn2-N _{imine}	2.146	Cu2-N _{imine}	1.976
Zn2-O _{phenoxido}	2.180	Cu2-O _{phenoxido}	2.150
Zn2-O _{nitrate}	2.171	Cu2-O _{nitrate}	2.229
Zn1... Zn2	3.028	Cu1... Cu2	3.047
N _{imine} - Zn1-O _{phenoxido}	81.290	N _{imine} - Cu1-O _{phenoxido}	87.409
N _{imine} - Zn2-O _{phenoxido}	83.194	N _{imine} - Cu2-O _{phenoxido}	86.577

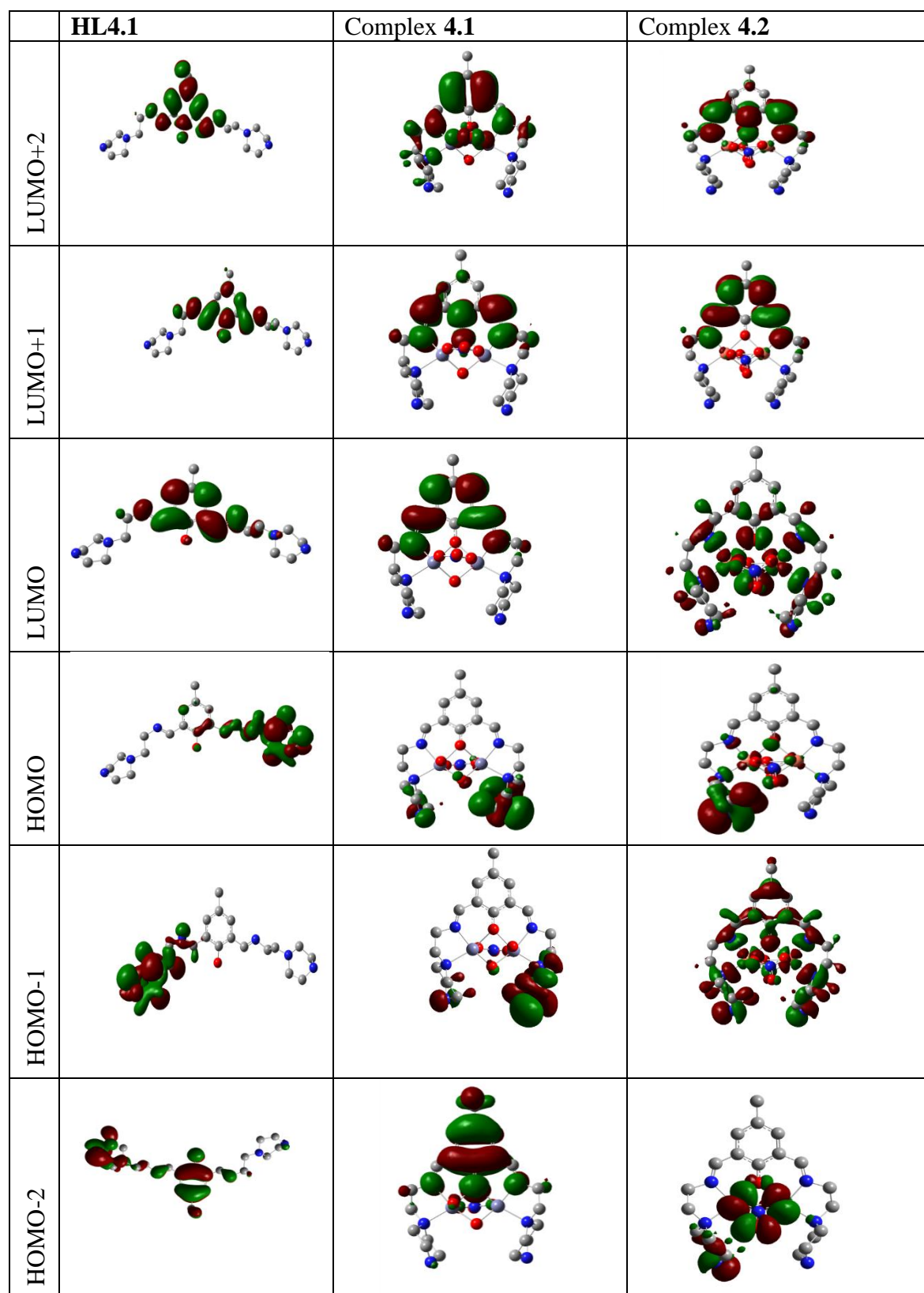


Figure 4.25 Selected contour plots of molecular orbitals of **HL4.1** and complexes **4.1** and **4.2**.

Table 4.3 Energy (eV) of selected M.O.s of the chemosensor (**HL4.1**).

HL4.1	
	Energy(eV)
LUMO+5	2.07
LUMO+4	1.98
LUMO+3	1.43
LUMO+2	0.88
LUMO+1	-0.49
LUMO	-1.35
HOMO	-5.21
HOMO-1	-5.28
HOMO-2	-5.84
HOMO-3	-5.91
HOMO-4	-5.93
HOMO-5	-6.31

Table 4.4 Energy (eV) and composition (%) of selected M.O.s of complexes **4.1** and **4.2**.

M.O.s	complex 4.1			complex 4.2		
	Energy(eV)	% Metal	% Ligand	Energy(eV)	% Metal	% Ligand
LUMO+5	-2.84	0	100	-5.83	16	83
LUMO+4	-3.49	3	1	-6.46	62	37
LUMO+3	-4.58	0	100	-7.37	72	26
LUMO+2	-5.14	0	100	-7.94	57	35
LUMO+1	-8.51	0	67	-8.27	73	13
LUMO	-8.77	-1	101	-8.62	57	30
HOMO	-9.31	-1	101	-9.25	8	90
HOMO-1	-9.36	0	95	-9.51	26	68
HOMO-2	-9.43	-2	50	-9.72	43	40
HOMO-3	-9.77	-5	101	-9.95	71	23
HOMO-4	-9.92	-5	102	-10.19	77	17
HOMO-5	-9.95	-2	102	-10.39	29	22

4.3.8 TDDFT study

Electronic transitions in **HL4.1**, Complex **4.1** and **4.2** are theoretically studied using TDDFT where B3LYP/CPCM method is used with same basis sets in water. Calculated electronic transitions are given in **Tables 4.5** and **4.6**. Theoretical calculations show that in **HL4.1** intense absorption bands appear at 455 and 449 nm respectively for ligand based $\pi-\pi^*$

transition. Major transitions are HOMO-4→LUMO (54%), and HOMO-4→LUMO+1 (43%) respectively. For complex **4.1** major peaks appear at 357, 331, 327 nm respectively and main transitions are HOMO→LUMO (97%), HOMO-1→LUMO (89%) and HOMO-2→LUMO (91%), respectively (**Figure 4.26**). For complex **4.2** the intense absorption bands around 396 and 391 nm corresponding to HOMO→LUMO+1 (94%) and HOMO-3→LUMO (44%) transitions, respectively (**Figure 4.27**). The spectra of electronic transitions obtained from computation for the chemosensor (**HL4.1**), complexes **4.1** and **4.2** are found to be comparable with that of experimental data.

Theoretical calculations of the emission spectra of both ligand (**HL4.1**) and complex **4.1** are performed by optimizing the triplet state (T1), using same basis set. The emission wavelength obtained from the computation is very much comparable with that of experimental data. All the relevant data are given in **Table 4.6**. The emission band of the chemosensor (**HL4.1**) at 510 nm was theoretically obtained at 520.65 nm with major key transitions, HOMO-3 (β)→LUMO+2(β) (82%) and HOMO-2(α)→LUMO+1(α) (18%), respectively. Whereas for the complex **4.1**, the emission band at 480 nm was theoretically obtained at 468.62 with major key transitions, HOMO(α)→LUMO+3(α)(10%), HOMO-9(β)→LUMO(β) (15%) and HOMO-7(β)→LUMO(β), (45%) respectively.

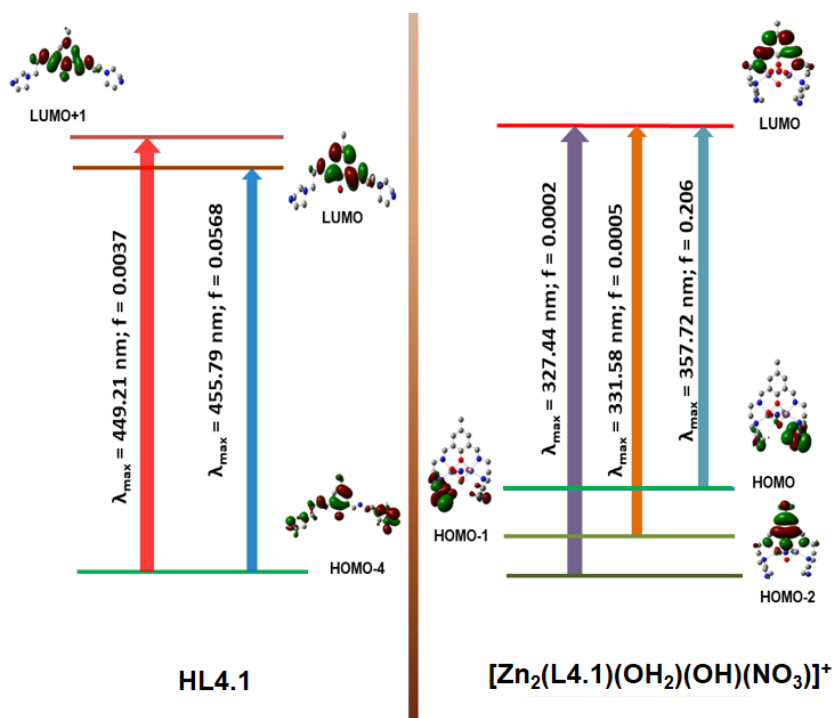


Figure 4.26 Pictorial representation of vertical transition of chemosensor (HL4.1) and complex 4.1.

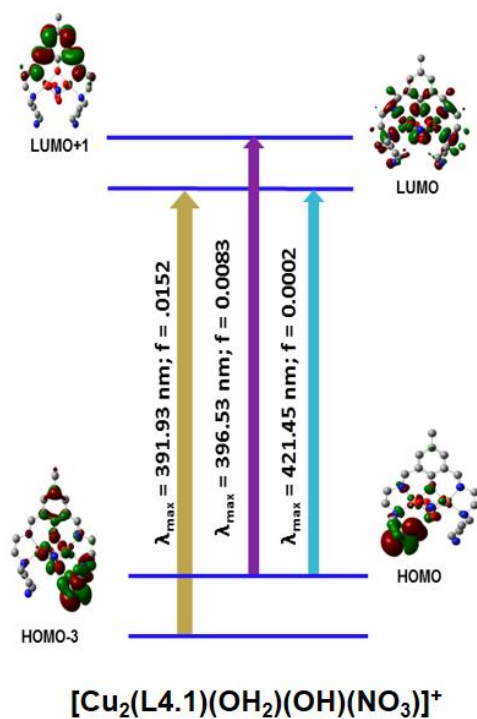


Figure 4.27 Pictorial representation of vertical transition of complex 4.2.

Table 4.5 Electronic transition calculated by TDDFT using B3LYP/CPCM method in methanol solvent of Ligand (**HL4.1**), [Zn₂(**L4.1**)(NO₃) (OH)(OH₂)]⁺ and [Cu₂(**L4.1**)(NO₃) (OH)(OH₂)]⁺.

	E _{excitation} (ev)	λ _{excitation} (nm)	Key transition	Character
Ligand (HL4.1)	2.72	455.7875	HOMO-5 → L+1 (16%), HOMO-4 → LUMO (54%)	π → π*(L)
	2.76	449.2149	HOMO-5 → LUMO (27%), HOMO-4 → LOMO+1 (43%)	π → π*(L)
	3.06	405.0684	HOMO-6 → LUMO (27%), HOMO-5 → LUMO+1 (27%), HOMO-4 → LUMO (38%)	π (L) → π*(L)
	3.13	395.0526	HOMO-6 → LUMO+1 (15%), HOMO-5 → LUMO (27%), HOMO-4 → LUMO+1 (48%)	π (L) → π*(L)
[Zn ₂ (L4.1)(NO ₃) (OH)(OH ₂)] ⁺	3.46	357.7233	HOMO → LUMO (97%)	π (L) → π*(L)
	3.73	331.5860	HOMO-1 → LUMO (89%)	π (L) → π*(L)
	3.78	327.4351	HOMO-2 → LUMO (91%)	π (L) → π*(L)
	4.13	300.1654	HOMO → LOMO+1 (98%)	π (L) → π*(L)
[Cu ₂ (L4.1)(NO ₃) (OH)(OH ₂)] ⁺	2.94	421.4539	HOMO → LUMO (50%), HOMO-3 → LUMO (10%), HOMO-1 → LUMO (15%)	π → π*(L)
	3.12	396.5309	HOMO → LOMO+1 (94%)	π (L) → π*(L)
	3.16	391.9306	HOMO-1 → LUMO (13%), HOMO-4 → LUMO (15%), HOMO-3 → LUMO (44%), HOMO-2 → LUMO (16%)	π (L) → π*(L)
	3.31	373.9506	HOMO-5 → LUMO (28%), HOMO-1 → LUMO (11%), HOMO-1 → LUMO (11%)	π (L) → π*(L)

Table 4.6 Emission spectrum calculated by TDDFT using B3LYP basis set for Ligand (**HL4.1**) and $[Zn_2(L4.1)(NO_3)(OH)(OH_2)]^+$.

	$E_{excitation}$ (ev)	$\lambda_{emission}(nm)$	Excited State	Osc. Strength (f)	Key transition
Ligand (HL4.1)	2.3434	520.65	8	0.0031	HOMO-2(α) \rightarrow LUMO+1 (α)(18%) HOMO-3(β) \rightarrow LUMO+2(β) (82%)
$[Zn_2(L4.1)(NO_3)(OH)(OH_2)]^+$	2.65	468.62	11	0.0053	HOMO(α) \rightarrow LUMO+3(α)(10%) HOMO-9 (β) \rightarrow LUMO(β) (15%) HOMO-7(β) \rightarrow LUMO(β) (45%)

4.4 Conclusion

In summary, we have successfully developed a dual Schiff base fluorescent and colorimetric chemosensor **HL4.1** as a promising analytical tool for the detection of Zn^{2+} and Cu^{2+} in mixed organo – aqueous (1:9) solution. In this work both Zn^{2+} and Cu^{2+} are detected in nano molar scale and the LOD values are 1.059×10^{-9} (M) and 3.53×10^{-9} (M) respectively. **HL4.1** exhibit around 16 times increment in fluorescence intensity in presence of Zn^{2+} and ~174 times decrease in fluorescence intensity in presence of Cu^{2+} . **HL4.1** form 1:2 complex with both metal ions which have been established by fluorescence measurements, ESI-MS analysis and DFT-Calculations. The values of binding constant are 7.14×10^4 and $2.18 \times 10^5 M^{-1}$ for Zn^{2+} and Cu^{2+} complexes, respectively. In fluorescence competition assay experiments

Cu²⁺ replace Zn²⁺ in presence of **HL4.1**. Moreover, the sensors can be completely regenerated from **L4.1-Zn** and **L4.1-Cu** complexes by addition of Na₂EDTA solution. A rapid change in fluorescence intensity of **HL4.1** within pH range 6-8 against Zn²⁺ and Cu²⁺ ions establish its application in real-time quantitative detection of Zn²⁺ and Cu²⁺ ions in water samples and biological systems.

4.5 References

- (4.1) (a) S. Mizukami, T. Nagano, Y. Urano, A. Odani and K. A. Kikuchi, *J. Am. Chem. Soc.*, 2002, **124**, 3920-3925; (b) R. M. Duke, E. B. Veale, F. M. Pfeffer, P. E. Kruger and T. Gunnlaugsson, *Chem. Soc. Rev.* 2010, **39**, 3936-3953; (c) J. Shao, H. Lin and H. K. Lin, *Talanta* 2008, **75**, 1015-1020; (d) B. Kuswandi, W. Verboom and D.N. Reinhoudt, *Sensors* 2006, **6**, 978-1017; (e) K. Ghosh and S. Adhikari, *Tetrahedron Lett.* 2006, **47**, 8165-8169; (f) A. K. Jain, J. Raison, R. Kumar and S. Jain, *Int. J. Environ. Anal. Chem.*, 2007, **87**, 553-563; (g) G. A. E. Mostafa, *Int. J. Environ. Anal. Chem.*, 2008, **88**, 435-446; (h) M. T. Oms, P. A. C. Jongejan, A. C. Veltkamp, G. P. Wyers and J. Slanina, *Int. J. Environ. Anal. Chem.*, 1996, **62**, 207-218.
- (4.2) A. P. S. Gonzales, M. A. Firmino, C. S. Nomura, F. R. P. Rocha, P. V. Oliveira and I. Gaubeur, *Anal. Chim. Acta*, 2009, **636**, 198.
- (4.3) J. P. Lafleur, R. Lam, H. M. Chan and E.D. Salin, *J. Anal. At. Spectrom.*, 2005, **20**, 1315.
- (4.4) Z. Zhu, Z. Liu, H. Zheng and S. Hu, *J. Anal. At. Spectrom.*, 2010, **25**, 697.
- (4.5) H. N. Kim, W. X. Ren, J. S. Kim and J. Yoon, *Chem. Soc. Rev.*, 2012, **41**, 3210.
- (4.6) Z. X. Wang, Y.-X. Guo and S.-N. Ding, *Microchim. Acta*, 2015, **182**, 2223.
- (4.7) P. Sianglam, S. Kulchat, T. Tuntulani and W. Ngeontae, *Spectrochim. Acta, Part A*, 2017, **183**, 408.

- (4.8) S. Wang, Z. Chen, L. Chen, R. Liu and L. Chen, *Analyst*, 2013, **138**, 2080–2084.
- (4.9) C. Li, Y. Zhoua, Y. Li, X. Konga, C. Zoua and C. Weng, *Anal. Chim. Acta*, 2013, **774**, 79–84.
- (4.10) S. Kim, J. Kim, N. H. Lee, H. H. Jang and M. S. Han, *Chem. Commun.*, 2011, **47**, 10299–10301.
- (4.11) H. Zhou, J. Wang, Y. Chen, W. Xi, Z. Zheng, D. Xu, Y. Cao, G. Liu, W. Zhu, J. Wu and Y. Tian, *Dyes Pigm.*, 2013, **98**, 1–10.
- (4.12) K. J. Barnham, C. L. Masters and A. I. Bush, *Nat. Rev. Drug Discovery*, 2004, **3**, 205–214.
- (4.13) E. Gaggelli, H. Kozlowski, D. Valensin and G. Valensin, *Chem. Rev.*, 2006, **106**, 1995–2044.
- (4.14) P. G. Welsh, J. Lipton, C. A. Mebane and J. C. A. Marr, *Ecotoxicol. Environ. Saf.*, 2008, **69**, 199–208.
- (4.15) H. Scherz and E. Kirchhoff, *Sens. Actuators B*, 2006, **19**, 420–433.
- (4.16) J. M. Flinn, D. Hunter, D. H. Linkous, A. Lanzirotti, L. N. Smith, J. Brightwell and B. F. Jones, *Physiol. Behav.*, 2005, **83**, 793–803.
- (4.17) (a) R. Azadbakht, H. Keypour, H. A. Rudbari, A. H. Md. Zaheri and S. Menati, *J. Lumin.*, 2012, **132**, 1860; (b) H. Song, S. Rajendiran, E. Koo, B. K. Min, S. K. Jeong, T. D. Thangadurai and S. Yoon, *J. Lumin.*, 2012, **132**, 3089; (c) S. Kotha, D. Goyal, S. Banerjee and A. Datta, *Analyst*, 2012, **137**, 2871.
- (4.18) R. R. Gagne, C. L. Spiro, T. J. Smith, C. A. Hamann, W. R. Thies and A. K. Schiemke, *J. Am. Chem. Soc.*, 1981, **103**, 4073–4081.
- (4.19) M. J. Frisch, G. W. Trucks, H. B. Schlegel, G. E. Scuseria, M. A. Robb, J. R. Cheeseman, G. Scalmani, V. Barone, B. Mennucci, G.A. Petersson, H. Nakatsuji, M.

Caricato, X. Li, H. P. Hratchian, A. F. Izmaylov, J. Bloino, G. Zheng, J. L. Sonnenberg, M. Hada, M. Ehara, K. Toyota, R. Fukuda, J. Hasegawa, M. Ishida, T. Nakajima, Y. Honda, O. Kitao, H. Nakai, T. Vreven, J. A. Montgomery, Jr., J. E. Peralta, F. Ogliaro, M. Bearpark, J. J. Heyd, E. Brothers, K. N. Kudin, V. N. Staroverov, R. Kobayashi, J. Normand, K. Raghavachari, A. Rendell, J. C. Burant, S. S. Iyengar, J. Tomasi, M. Cossi, N. Rega, J. M. Millam, M. Klene, J. E. Knox, J. B. Cross, V. Bakken, C. Adamo, J. Jaramillo, R. Gomperts, R. E. Stratmann, O. Yazyev, A. J. Austin, R. Cammi, C. Pomelli, J. W. Ochterski, R. L. Martin, K. Morokuma, V. G. Zakrzewski, G. A. Voth, P. Salvador, J. J. Dannenberg, S. Dapprich, A. D. Daniels, Ö. Farkas, J. B. Foresman, J. V. Ortiz, J. Cioslowski and D. J. Fox, GAUSSIAN09, Revision D.01, Gaussian Inc. Wallingford, CT, 2009.

(4.20) A. D. Becke, *J. Chem. Phys.*, 1993, **98**, 5648-5652.

(4.21) C. Lee, W. Yang and R. G. Parr, *Phys. Rev.*, B 1988, **37**, 785-789.

(4.22) P. J. Hay and W. R. Wadt, *J. Chem. Phys.*, 1985, **82**, 270-283.

(4.23) W. R. Wadt and P. J. Hay, *J. Chem. Phys.*, 1985, **82**, 284-298.

(4.24) P. J. Hay and W. R. Wadt, *J. Chem. Phys.*, 1985, **82**, 299-310.

(4.25) G. A. Petersson, A. Bennett, T. G. Tensfeldt, M. A. Al-Laham, W. A. Shirley and J. Mantzaris, *J. Chem. Phys.*, 1988, **89**, 2193-2218.

(4.26) G. A. Petersson and M. A. Al-Laham, *J. Chem. Phys.*, 1991, **94**, 6081-6090.

(4.27) R. Bauernschmitt and R. Ahlrichs, *Chem. Phys. Lett.*, 1996, **256**, 454-464.

(4.28) R. E. Stratmann, G. E. Scuseria and M. J. Frisch, *J. Chem. Phys.*, 1998, **109**, 8218-8224.

- (4.29) M. E. Casida, C. Jamorski, K.C. Casida and D.R. Salahub, *J. Chem. Phys.* 1998, **108**, 4439-4449.
- (4.30) V. Barone and M. Cossi, *J. Phys. Chem. A.* 1998, **102**, 1995-2001.
- (4.31) M. Cossi, and V. Barone, *J. Chem. Phys.* 2001, **115**, 4708-4717.
- (4.32) M. Cossi, N. Rega, G. Scalmani, V. Barone, *J. Comput. Chem.* 2003, **24**, 669-681.
- (4.33) N. M. O'Boyle, A. L. Tenderholt and K. M. Langner, *J. Comput. Chem.* 2008, **29**, 839-845.
- (4.34) (a) A. Guha, T. Chattopadhyay, N. D. Paul, M. Mukherjee, S. Goswami, T. K. Mondal and E. Zangrandoand, D. Das, *Inorg. Chem.* 2012, **51**, 8750–8759; (b) K. S. Banu, T. Chattopadhyay, A. Banerjee, S. Bhattacharya, E. Suresh, M. Nethaji, E. Zangrandoand and D. Das, *Inorg. Chem.* 2008, **47**, 7083-7093.
- (4.35) M. Kumar, R. Kumar, V. Bhalla, P. R. Sharma, T. Kaur and Y. Qurishi, *Dalton Trans.* 2012, **41**, 408-412.
- (4.36) (a) H. A. Benesi and J. H. Hildebrand, *J. Am. Chem. Soc.* 1949, **71**, 2703–2707; (b) S. Banerjee, P. Brandão and A. Saha, *RSC Advances.* 2016, **6**, 101924–101936.
- (4.37) A. B. Pradhan, S. K. Mandal, S. Banerjee, A. Mukherjee, S. Das, A. R. K. Bukhsh and A. Saha, *Polyhedron.* 2015, **94**, 75-82.
- (4.38) Y. R. Kim, H. J. Kim, J. S. Kimn and H. Kim, *Adv. Mater.* 2008, **20**, 4428-4432.
- (4.39) M. Z. Tian, M. M. Hu, J. L. Fan, X. J. Peng, J. Y. Wang, S. G. Sun and R. Zhang, *Bioorg. Med. Chem. Lett.* 2013, **23**, 2916-2919.

Chapter 5

Aza-crown based macrocyclic probe design for "PET-off" multi-Cu²⁺ responsive and "CHEF-on" multi-Zn²⁺ sensor: application in biological cell imaging, and theoretical studies

Abstract

The work represents a rare example of an aza-crown based macrocyclic chemosensor **H₂DTC5.1** [**H₂DTC5.1** = 1,16-dihydroxy-tetraaza-30-crown-8] for selective detection of both Zn²⁺ and Cu²⁺ in HEPES buffer medium (pH 7.4). **H₂DTC5.1** exhibits fluorescence response for both Zn²⁺ and Cu²⁺ ions. The reversibility of the chemosensor in its binding with Zn²⁺ and Cu²⁺ ions is also examined using a Na₂EDTA solution. **H₂DTC5.1** exhibits chelation-enhanced fluorescence (CHEF) effect in the presence of Zn²⁺ ions and quenching effect (CHEQ) in the presence of paramagnetic Cu²⁺ ions. Furthermore, the geometry and spectral properties of **H₂DTC5.1** and the chemosensor bound to Zn²⁺ has been studied by DFT and TDDFT calculations. The limit of detection (LOD) values are 0.11 × 10⁻⁹ M and 0.27 × 10⁻⁹ M for Cu²⁺ and Zn²⁺, respectively. The formation constants for the Zn²⁺ and Cu²⁺ complexes have been measured by pH-potentiometry in 0.15 M NaCl 70:30 (v/v) water:ethanol at 298.1 K. UV-Vis absorption and fluorometric spectral data, pH-potentiometric titrations indicate 1:1 and 2:1 metal: chemosensor species. In the solid state **H₂DTC5.1** is able to accommodate up to four metal ions as proved by the crystal structures of the complexes [Zn₄(**DTC5.1**)(OH₂)(NO₃)₄] (**5.1**) and {[Cu₄(**DTC5.1**)(OCH₃)₂(NO₃)₄].H₂O}_n (**5.2**). **H₂DTC5.1** can be used as a potential chemosensor for monitoring Zn²⁺ and Cu²⁺ ions in biological and environmental media with outstanding accuracy and precision. The propensity of **H₂DTC5.1** to detect intracellular Cu²⁺ and Zn²⁺ ions in the triple negative human breast cancer cell line, MDA-MB-468 and in HeLa cells has been done by fluorescence cell imaging.

5.1 Introduction

The design and construction of new chemosensors capable of detecting selectively and with high sensitivity various metal ions and anions have received immense importance in analysis, biological processes, environmental studies, etc.^{5.1,5.2} Among the various chemosensors reported so far, dual chemosensors that can detect species both colorimetrically and fluorimetrically deserve special mention. The colorimetric technique allows naked eye detection of the color change of a given species without application of sophisticated instruments. On the other hand, luminescent techniques are one of the non-destructive instrumental processes with the lowest cost, easier operation, fastest response time, and highest selectivity and sensitivity.^{5.3-5.6} Moreover, the development of single sensors for multiple analytes is a challenging task. Such type of process is more efficient and less expensive than individual analysis methods.^{5.7} Therefore, both colorimetric and fluorescent chemosensors for the detection of zinc and copper ions are very important as they are the second most and third most essential elements present in the human body and participate in many physiological processes. Zn²⁺ ions are present in the biological systems either in a tightly bound form or in a labile form. Labile Zn²⁺ ions act as a neurotransmitter^{5.8,5.9} and play important roles in apoptosis,^{5.10} regulation of gene expression and insulin secretion.^{5.11} The bound Zn²⁺ ions are present as a structural cofactor in many metalloproteins, such as SOD (superoxide dismutase), carbonic anhydrase and carboxypeptidase.^{5.12,5.13} It has been observed that disruption of Zn²⁺ homeostasis is associated with many neurological disorders such as Alzheimer's disease, Parkinson's disease, epilepsy and amyotrophic lateral sclerosis.^{5.14,5.15} Cu²⁺ ions play crucial roles in blood formation processes and in the functioning of various enzymes like superoxide dismutase, cytochrome c oxidase, tyrosinase, etc.^{5.16} However, Cu²⁺ ion deficiency or over-load can result in liver damage in infants,

Parkinson's disease, Alzheimer's disease, amyotrophic lateral sclerosis (ALS), Menkes and Wilson diseases, etc.^{5.17–5.23}

Up to date a significant number of papers on fluorescence chemosensors used for the detection of Cu²⁺ and Zn²⁺ ions have been reported. Previously reported chemosensors face shortcomings regarding their sensitivity, selectivity, detection limit, interference from other metal ions and low solubility in aqueous solution, etc.^{5.24} A survey of the literature reveals that cyclic systems such as crown ethers, cryptands or cyclodextrins are capable of selectively detecting cations owing to their restricted cavity size and flexibility.^{5.24p,5.25} In this work the Schiff base ligand is a macrocyclic L8X2 type of system. There are very few examples with similar macrocyclic L8X2 arrangement with two donor atoms are present in the literature.^{5.26}

In our continuous endeavor for the preparation of dual-chemosensors,^{5.27} we are reporting an aza-crown based fluorescence probe capable of sensing Zn²⁺ and Cu²⁺ ions with a significant 25 nm emission wavelength difference. Here, the 1,16-dihydroxy-tetraaza-30-crown-8 based Schiff base ligand (**H₂DTC5.1**) has been designed so that the phenoxido oxygen, ethereal oxygen and imine nitrogen atoms of the tetraaza-30-crown-8 can simultaneously coordinate the cations. **H₂DTC5.1** exhibits "turn on" fluorescence towards Zn²⁺ ions and "turn off" fluorescence towards Cu²⁺ in water:methanol (9:1, v/v, 10 mM HEPES buffer, pH 7.4) mixture. We also demonstrate that this sensor is capable of detecting Zn²⁺ even in the presence of large amounts of Cd²⁺ and Hg²⁺ ions. In the presence of Zn²⁺ a 7-fold enhancement of emission intensity has been observed, whereas for Cu²⁺ the emission intensity quenches by ~55-fold. The quenching effect is probably due to the paramagnetic nature of Cu²⁺. The LOD of the chemosensor for Zn²⁺ and Cu²⁺ ions are 0.11×10⁻⁹ M and 0.27×10⁻⁹ M, respectively. Binding modes of both the metal ions with **H₂DTC5.1** (complex **5.1** and complex **5.2**) have been established by X-ray crystallography. This biocompatible

chemosensor also exhibits cell permeability and senses intracellular Cu²⁺ and Zn²⁺ ions in the breast cancer cell line *MDA-MB-468* as well as cervical cancer cell line *HeLa*.

5.2 Experimental section

5.2.1 Materials and physical measurements

All reagent or analytical grade chemicals and solvents were purchased from commercial sources and used without further purification. Elemental analysis for C, H and N was carried out using a Perkin–Elmer 240C elemental analyzer. Infrared spectra (400–4000 cm⁻¹) were recorded from KBr pellets on a Nicolet Magna IR 750 series-II FTIR spectrophotometer. Absorption spectra were measured using a sensitive UV-vis spectrophotometer (UV-2450 spectrophotometer (Shimadzu, Japan)) equipped with a double beam light source with a 1-cm-path-length quartz cell. Electron spray ionization mass (ESI-MS⁺) spectra were recorded on a MICROMASS Q-TOF spectrometer. Emission spectra were collected using Fluoromax-4 spectrofluorometer at room temperature (298 K) under degassed condition. Fluorescence lifetime was measured using a time-resolved spectrofluorometer from IBH, UK. Measurements of ¹H and ¹³C NMR spectra were conducted using BRUKER 400 and BRUKER 300 spectrometers, respectively.

Caution! Perchlorate ion is an extreme oxidizing agent and laboratory hazard. Only a small amount of sample should be prepared and handled with great care.^{5.28}

5.2.2 X-ray crystallography

Single crystal X-ray data of complexes **5.1** and **5.2** were collected on a Bruker SMART APEX-II CCD diffractometer using graphite mono chromated Mo K α radiation ($\lambda = 0.71073$ Å) at room temperature. Data processing, structure solution, and refinement were performed using Bruker Apex-II suite program. All available reflections in $2\theta_{\max}$ range were harvested and corrected for Lorentz and polarization factors with Bruker SAINT plus.^{5.29} Reflections

were then corrected for absorption, inter-frame scaling, and other systematic errors with SADABS.^{5.30} The structures were solved by the direct methods and refined by means of full matrix least-square technique based on F^2 with SHELX-2017/1 software package.^{5.31} All the non hydrogen atoms were refined with anisotropic thermal parameters. C-H hydrogen atoms were inserted at geometrical positions with $U_{\text{iso}} = 1/2U_{\text{eq}}$ to those they are attached. Crystal data and details of data collection and refinement for **5.1** and **5.2** are summarized in Table **5.1**.

Table 5.1. Crystal parameters and selected refinement details for complexes **5.1** and **5.2**.

Complex	5.1	5.2
Empirical formula	C ₃₀ H ₂₂ N ₈ O ₂₀ Zn ₄	C ₃₂ H ₄₄ Cu ₄ N ₈ O ₂₁
Formula weight	1076.03	1130.91
Temperature (K)	273(2)	273(2)
Crystal system	Monoclinic	Monoclinic
Space group	C2	P2 ₁ /n
<i>a</i> (Å)	18.896(5)	11.0489(10)
<i>b</i> (Å)	11.439(3)	21.4323(19)
<i>c</i> (Å)	9.999(3)	19.6369(19)
α (°)	90	90.00
β (°)	99.604(6)	93.811(3)
γ (°)	90	90.00
Volume (Å ³)	2130.9(10)	4639.8(7)
Z	2	4
D_{calc} (g cm ⁻³)	1.686	1.619
Absorption coefficient (mm ⁻¹)	2.310	1.893
<i>F</i> (000)	1088	2304
θ Range for data collection (°)	2.066-27.368	2.079-27.154
Reflections collected	9002	66046
Independent reflection / R_{int}	3351/ 0.0488	4737/0.1220
Data / restraints / parameters	4714/1/298	10232/0/620
Goodness-of-fit on F^2	1.077	1.063
Final <i>R</i> indices [$I > 2\sigma(I)$]	R1 = 0.0677, wR2 = 0.1747	R1 = 0.0748, wR2 = 0.1706
<i>R</i> indices (all data)	R1 = 0.1052, wR2 = 0.1962	R1 = 0.1768, wR2 = 0.2181
Largest diff. peak / hole (e Å ⁻³)	1.490/ -0.584	0.769/-0.596

5.2.3 Synthesis of 2,6-diformyl-4-methylphenol (DFP)

2,6-diformyl-4-methylphenol (DFP) was prepared by following a standard literature procedure.^{5.32}

5.2.4 Synthesis of chemosensor 1,16-dihydroxy-tetraaza-30-crown-8 (H₂DTC5.1)

A mixture of 2,6-diformyl-4-methylphenol (2.0 mmol, 0.3283 g) and 1,2-bis(2-aminoethoxy)ethane (2.0 mmol, 0.296 g) was heated to reflux for 3 h in methanol solvent. Yellow color gummy mass was obtained after evaporation of the solvent.

Yield: 0.486g (88%). Anal. Calc. for C₃₀H₄₀N₄O₆: C 65.20%; H 7.30%; N 10.14%. Found: C 65.55%; H 7.51%; N 10.01%. IR (cm⁻¹, KBr): $\nu(\text{C}=\text{N})$ 1635s; $\nu(\text{C}-\text{H})$ 778s. ESI-MS⁺ in MeOH: The base peak was detected at $m/z = 553.30$, corresponding to [H₂DTC5.1+H]⁺. UV-Vis, λ_{max} (nm), (ϵ (dm³mol⁻¹cm⁻¹)) in 10 mM HEPES buffer at pH= 7.4: 445 (47086).

¹H NMR (DMSO-*d*₆, 400 MHz) δ ppm: 2.19 (Ar-CH₃) (d, 6H, $J = 3.2$ Hz), 3.52 (-CH₂) (d, 8H, $J = 15.2$ Hz), 3.62 (-CH₂) (d, 16H, $J = 5.6$ Hz), 7.44 (ArH) (d, 4H, $J = 9.6$ Hz), 8.49 (-CH=N) (d, 4H, $J = 12.4$ Hz), 14.20 (Ar-OH) (s, 2H).

¹H NMR (CDCl₃, 400 MHz) δ ppm: 2.25 (Ar-CH₃) (t, 6H, $J_1 = 3.6$ Hz, $J_2 = 4.4$ Hz,), 3.58-3.67 (-CH₂) (m, 8H), 3.69-3.77 (-CH₂) (m, 16H), 7.39 (ArH) (s, 4H), 8.47 (-CH=N) (s, 4H), 13.84 (Ar-OH) (s, 2H).

¹³C NMR (DMSO-*d*₆, 75 MHz) δ ppm: 20.26 (-CH₃), 59.97, 70.58 70.75 (-CH₂), 121.36, 127.39, 132.30, 159.34 (Ar-C), 162.29 (-CH=N).

5.2.5 Synthesis of complex (5.1) [Zn₄(DTC5.1)(OH)₂(NO₃)₄]

A 2 mL methanolic solution of zinc nitrate hexahydrate (4.0 mmol, 1.189g) was added drop wise to 20 mL methanolic solution of H₂DTC5.1 (1.0 mmol, 0.552g) followed by addition of triethylamine (2.0 mmol, 0.202g) and the resultant reaction mixture was stirred for ca. 3 h. Yellow color solid mass was obtained in high yield after slow evaporation of the

solvent. This yellow color solid mass was dissolved in N,N-dimethylformamide (DMF)-methanol mixture (v/v, 1:9) and carefully layered with diethyl ether. Yellow color block shape crystals were obtained after a few days.

Yield: 0.847g (78%). Anal. Calc. for C₃₀H₄₀N₈O₂₀Zn₄: C 32.93%; H 3.68%; N 10.24%. Found: C 33.06%; H 3.49%; N 10.38%. IR (cm⁻¹, KBr): $\nu(\text{C}=\text{N})$ 1630s; $\nu(\text{NO}_3^-)$ 1300s; $\nu(\text{C}-\text{H})$ 773 s. ESI-MS⁺ in MeOH: The base peak was detected at $m/z = 1032.96$, corresponding to [Zn₄(DTC5.1)(OH)₂(NO₃)₃]⁺. UV-Vis, λ_{max} (nm), (ϵ (dm³mol⁻¹cm⁻¹)) in 10 mM HEPES buffer at pH= 7.4: 415(44272).

¹H NMR (DMSO-*d*₆, 400 MHz) δ ppm: 2.21 ppm (-CH₃) (s, 3H) and 2.29 ppm (-CH₃) (s, 3H), 7.93 (-CH=N) (d, 1H, $J = 6.8$ Hz), 8.01 (-CH=N) (s, 1H), 8.28 (-CH=N) (d, 1H, $J = 10.4$ Hz), 8.48 (-CH=N) (d, 1H, $J = 12.4$ Hz), 3.1-4.0 (-CH₂) (m, 24H), 6.96 ppm (s), 7.10 ppm (s), 7.16 (s), 7.39 ppm (s), 7.52 ppm (d, 1H, $J = 12.00$ Hz), 7.65 ppm (s) (Ar-H, 4H).

¹³C NMR (DMSO-*d*₆, 75 MHz) δ ppm: 19.36, 19.43 (-CH₃), 58.59, 61.06, 61.23, 61.82, 68.51, 69.41, 70.06, 70.09, 71.47, 71.91, 73.67, 74.07 (-CH₂), 120.44, 121.00, 121.18, 121.50, 121.59, 123.87, 124.20, 139.21, 141.46, 141.50, 163.19, 165.71 (Ar-C), 166.04, 167.82, 170.44, 172.94 (-CH=N).

5.2.6 Synthesis of complex (5.2) {[Cu₄(DTC5.1)(OCH₃)₂(NO₃)₄].H₂O}_n

A 2 mL methanolic solution of copper nitrate trihydrate (4.0 mmol, 0.966g) was added drop wise to 20 mL methanolic solution of H₂DTC5.1 (1.0 mmol, 0.552g) followed by addition of triethylamine (2.0 mmol, 0.202g) and the resultant reaction mixture was stirred for ca. 3 h. Green color solid mass was obtained after slow evaporation of the solvent. This green color solid mass was dissolved in DMF-methanol mixture (v/v, 1:9) and carefully layered with diethyl ether. Green color block shape crystals were obtained after a few days.

Yield: 0.858g (76%). Anal. Calc. for C₃₂H₄₆Cu₄N₈O₂₁: C 33.93%; H 3.92 %; N 9.91%. Found: C 34.10%; H 3.77%; N 10.06%. IR (cm⁻¹, KBr): $\nu(\text{C}=\text{N})$ 1625s; $\nu(\text{NO}_3^-)$ 1300s; $\nu(\text{C}-\text{H})$ 770s. ESI-MS⁺ in MeOH: The base peak was detected at $m/z = 1170.00$ corresponding to [Cu₄(**DTC5.1**)(OCH₃)₂(NO₃)₄+CH₃OH+Na]⁺. UV-Vis, λ_{max} (nm), (ϵ (dm³mol⁻¹cm⁻¹)) in 10 mM HEPES buffer at pH= 7.4: 410(42065).

5.2.7 UV-visible and fluorescence spectroscopic studies

Stock solutions of various ions (1×10^{-3} M) were prepared in deionized water. A stock solution of the chemosensor (**H₂DTC5.1**) (1×10^{-3} M) was prepared in methanol. The solution of **H₂DTC5.1** was then diluted to 1×10^{-5} M as per requirement by HEPES buffer (10 mM, pH = 7.4). All the spectroscopic experiments including competitive assay of various cations and anions were performed in organic-aqueous HEPES buffer (10 mM, water:methanol 9:1(v/v)) medium at pH 7.4. In titration experiments, 30 μL solution of (1×10^{-3} M) **H₂DTC5.1** was taken for 3000 μL in a quartz optical cell of 1.0 cm optical path length and the ion stock solutions were gradually added to it. Spectroscopic studies of the chemosensor (**H₂DTC5.1**) in the presence of different anions were performed in HEPES buffer (10 mM, water:methanol 9:1(v/v)) at pH = 7.4. In competitive assay experiments, the test samples were prepared by interacting appropriate amounts of the cations stock. The values of the equilibrium constants were obtained using the program HypSpec2014.^{5,33,5,34}

5.2.8 EMF measurements

The pH-potentiometric titrations were carried out at 298.1 ± 0.1 K using 0.15 M NaCl in EtOH:H₂O 30:70 v/v as supporting electrolyte in a reaction vessel (capacity 70 cm³) water-thermostatted and argon presaturated containing a separated pH glass electrode (Metrohm 6.0150.100). This reaction vessel is connected through a salt bridge (NaCl 0.5M) to a reference cell filled with NaCl 0.15M, containing the reference electrode (Metrohm 6.0726.107 Ag/AgCl reference electrode in 3M KCl solution). The titration device used was a

905 Titrand controlled from a PC running the software Tiamo 2.3.

The measurement procedure consisted in a monotonic titration in which a fixed volume of titrand (carbonate-free 0.1M NaOH) was added to the reaction vessel. The measured e.m.f. was monitored over time and registered when the measured drift is lower than 0.2 mV/min. Then, the next volume of titrand was added automatically and the cycle repeated until the predefined total volume of titrand had been added. The experimental e.m.f. values were not corrected for the liquid junction potential because this effect was negligible in the pH range investigated.

Prior to the titration, the glass electrode was calibrated as a hydrogen ion concentration probe by titration of previously standardized amounts of HCl in EtOH:H₂O 30:70 v/v with CO₂-free NaOH solutions, and the equivalent point was determined by the Gran's method,^{5,35,5.36} which gives the standard potential, E° , and the ionic product of water ($pK_w = 14.10(1)$). At least two titrations were performed for each one of the studied systems. The titrations were treated separately without finding discrepancies in the values obtained for the constants. The final values of the constants were obtained by merging the individual titrations and fitting them together. Further details of the experimental procedure are afforded in the Supplementary Materials.

The software HYPERQUAD^{5.37} was used to process the data and calculate both the protonation and stability constants.

5.2.9 Cell culture

Triple negative human breast cancer cell line MDA-MB-468, human cervical cancer cells, HeLa and human lung fibroblast cells, WI38 was obtained from National Center for Cell Science (NCCS) Pune, India. The cells were grown in DMEM with 10% FBS (Fetal Bovine Serum), penicillin/streptomycin (100 units/ml) at 37°C and 5%CO₂. All the treatments were conducted at 37°C and at a cell density allowing exponential growth.

5.2.10 Cell imaging

In order to follow the real conditions, HeLa cells were grown in coverslips for 24hrs. Then the cells were either mock-treated or treated with Zn²⁺ (20 μM) ions for 24hrs at 37°C, after that H₂DTC5.1 (5μM) was added to it in the presence or absence of Cu²⁺ (20μM) ions for another 24hrs at 37°C. In another set of experiment MDA-MB-468 cells were grown in coverslips for 24hrs. Then the cells were either mock-treated or treated with 5μM of ligand (H₂DTC5.1) and 20μM Zn²⁺ salt in the presence or absence of 20μM of Cu²⁺ salt for 24hrs at 37°C. Both the cells were washed with 1×PBS. Then they were mounted on a glass slide and observed under fluorescence microscope (Leica) with a filter having excitation of 450-500 nm (blue) and an emission of 500-570 nm (green).

5.2.11 Cell survivability assay

Cell survivability of H₂DTC5.1 was studied for human lung fibroblast cells, WI38 (non-cancerous cells), MDA-MB-468 and HeLa (cancerous cells) following reported procedure.^{5,38} In brief, viability of these cells after exposure to various concentrations of ligand were assessed by MTT assay. The cells were seeded in 96-well plates at 1×10^4 cells per well and exposed to ligand at concentrations of 0 μM, 20 μM, 40 μM, 60 μM, 80 μM, 100 μM for 24 hrs. The resulting formazan crystals were dissolved in an MTT solubilization buffer and the absorbance was measured at 570 nm by using a spectrophotometer (BioTek) and the value was compared with control cells. The cell cytotoxicity of the complexes towards the cancer cells MDA-MB-468 and HeLa were also envisaged following the above mentioned MTT assay protocol. Another set of experiment was performed by MTT assay by keeping the ligand concentration same (5 μM) and varying Zn²⁺ and Cu²⁺ ions at a maximum concentration of 50 μM.

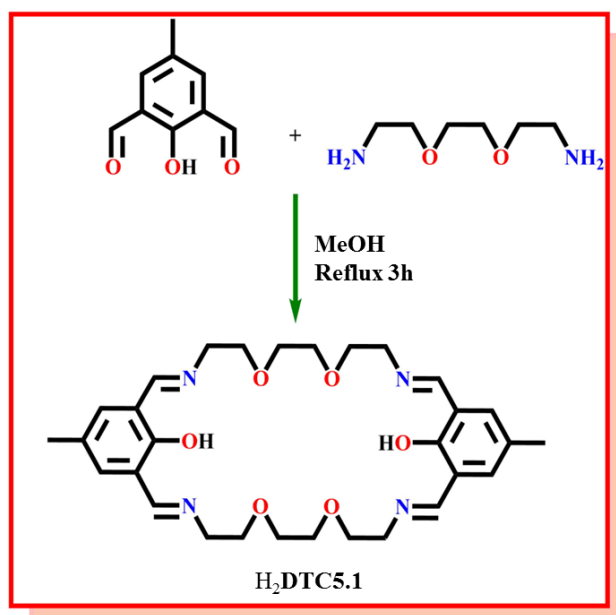
5.2.12 Computational method

The compounds were initially optimized at the B3LYP/6-31+G* level of theory in their singlet ground state (S₀).^{5.39} To obtain theoretical UV-Vis parameters, we performed the time-dependent DFT (TDDFT)^{5.40} calculations using the same level of theory associated with the conductor-like polarizable continuum model (CPCM).^{5.41} For the complexes and ligands (keto and enol forms), we calculated 60 singlet–singlet transition using their ground S₀ state geometries and using the conductor-like polarizable continuum model. The calculated electronic density plots for the frontier molecular orbitals were prepared by using the Gauss View 5.0 software. All the calculations were performed with the Gaussian 09 software package.^{5.42}

5.3 Results and discussion

5.3.1 Synthesis and characterization

2,6-Diformyl-4-methylphenol (DFP) has been prepared following a standard procedure.^{5.32} 1,2-Bis(2-aminoethoxy)ethane was mixed with 2,6-Diformyl-4-methylphenol (DFP) in 1:1 molar ratio in methanol under refluxing condition (**Scheme 5.1**) to generate the Schiff base ligand (H₂DTC**5.1**). The compound was obtained as a semi-solid in good yield and used without further purification. It was thoroughly characterized using different spectroscopic methods (UV-Vis, FT-IR and ¹H, ¹³C NMR) and by elemental analysis. The base peak in the ESI-MS⁺ spectrum was found at $m/z = 553.30$, corresponding to [H₂DTC**5.1**+H]⁺ (**Figure 5.1**). In the FT-IR spectrum, a broad band at around 3415 cm⁻¹ indicates the presence of the phenolic–OH group and the band at 1635 cm⁻¹ is attributed to the C=N (for azomethine) stretching frequency (**Figure 5.2**).



Scheme 5.1 Route of synthesis of chemosensor H₂DTC5.1.

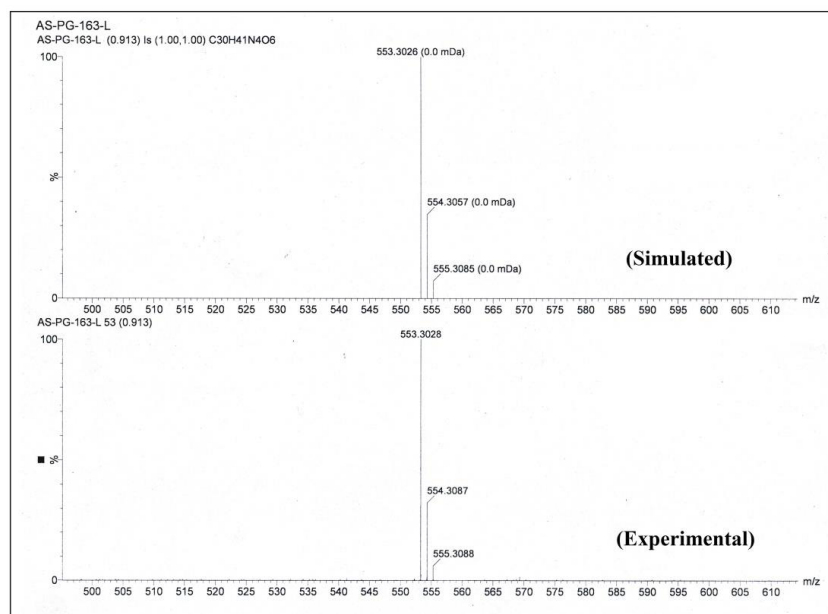


Figure 5.1. ESI-mass spectrum of chemosensor H₂DTC5.1.

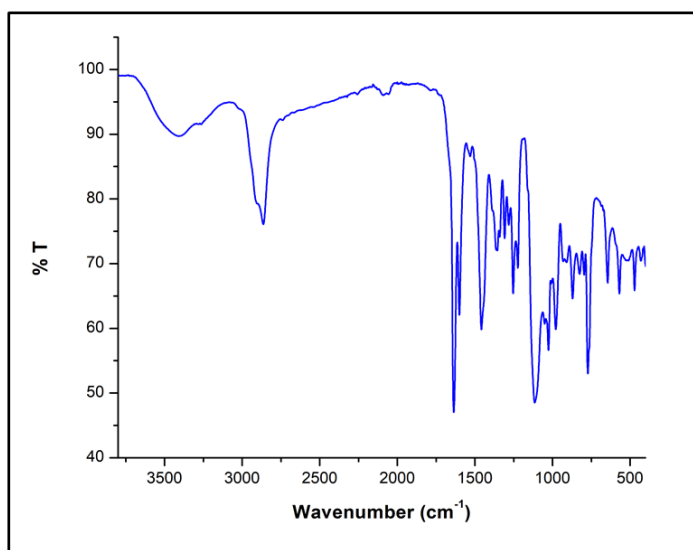
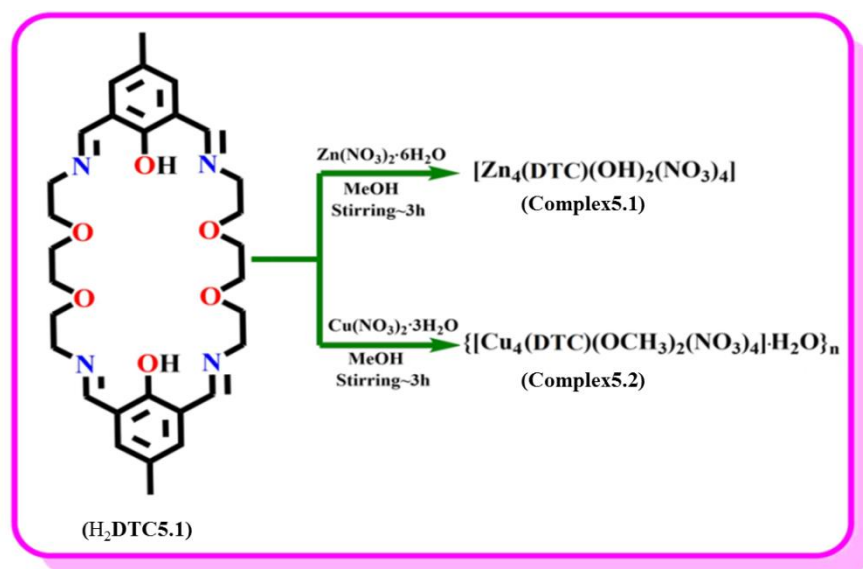


Figure 5.2 FTIR spectrum of chemosensor H₂DTC5.1.

H₂DTC5.1 reacts with both Zn(NO₃)₂·6H₂O and Cu(NO₃)₂·3H₂O in 1:4 ratio to produce complexes **5.1** and **5.2**, respectively (**Scheme 5.2**). Both complexes crystallize from DMF-methanol (v/v, 1:9)/diethylether solvent mixture. They are characterized by X-ray crystallography, elemental analysis and ESI-MS⁺. The experimentally observed peaks at *m/z* 1032.96 and 1170.00 correspond to the molecular ion peaks of [Zn₄(DTC5.1)(OH)₂(NO₃)₃]⁺ and [Cu₄(DTC5.1)(OCH₃)₂(NO₃)₄+CH₃OH+Na]⁺, respectively. In the FT-IR spectrum of **5.1**, characteristics stretching frequencies appear at 1630 cm⁻¹ ν(C=N), 773 cm⁻¹ ν(C-H) and 1300 cm⁻¹ (ν(NO₃⁻), asymmetric stretch), respectively (**Figure 5.3(a)**). Similarly, in the case of **5.2**, characteristics stretching frequencies appear at 1625 cm⁻¹ ν(C=N), 770 cm⁻¹ ν(C-H) and 1300 cm⁻¹ (ν(NO₃⁻), asymmetric stretch)), respectively (**Figure 5.3(b)**). It is important to note that although the ligand and its zinc complex using Zn(ClO₄)₂ were previously reported by N. Maekawa,^{5,43} the chemosensing behavior of H₂DTC5.1 towards Zn²⁺ and Cu²⁺ ions has been explored by us for the first time.



Scheme 5.2 Route of synthesis of complexes **5.1** and **5.2**.

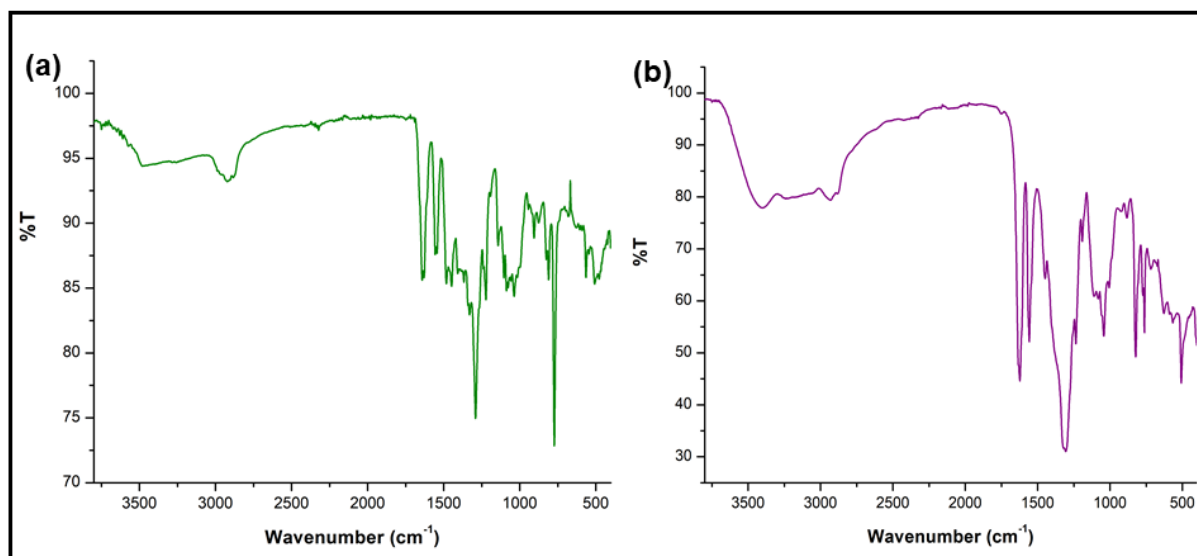


Figure 5.3 FTIR spectrum of (a) complex **5.1** and (b) complex **5.2**.

5.3.2 Crystal structure description of complex **5.1**

The tetranuclear Zn²⁺ complex, [Zn₄(DTC5.1)(OH)₂(NO₃)₄] crystallized in monoclinic form with C₂ space group (**Table 5.1**). The crystal structural of **1** is shown in **Figure 5.4(a)**. Selected bond distances and angles are collected in **Table 5.2**. The asymmetric unit consists of half of the molecule; a further C₂ symmetry operation generates the whole molecule. In **5.1** the macrocyclic ligand H₂DTC5.1 binds four Zn²⁺ ions, Zn1, Zn1a, Zn2 and Zn2a. For simplicity, we only describe the coordination environment around Zn1 and Zn2.

The two zinc centers (Zn1 and Zn2) are doubly bridged by a phenoxido oxygen (O1) of the macrocyclic ligand and a hydroxide anion (O4). Zn1 is additionally coordinated by the imine nitrogen (N1) and the ethereal oxygen atom (O2) of the macrocyclic ligand and an oxygen atom (O6) of a nitrate ion. The monodentate binding mode of nitrate ion has been established by using the M–O distance (Δd) and M–O–N bond angle ($\Delta\theta$)^{5.44} [$\Delta d < 0.3 \text{ \AA}$; $\Delta\theta < 14^\circ$ for bidentate; $0.3 \text{ \AA} < \Delta d < 0.6 \text{ \AA}$; $14^\circ < \Delta\theta < 28^\circ$ for anisobidentate; $\Delta d > 0.6 \text{ \AA}$ $\Delta\theta > 28^\circ$ for monodentate]. Here, the values of Δd and $\Delta\theta$ are 0.68 \AA and 32.7° , respectively. The Addison parameter (τ)^{5.45} for the Zn1 center is found to be 0.5, suggesting an intermediate geometry between square pyramidal and trigonal bipyramidal. The Zn–N_{imino} and Zn–O_{phenoxido} bond distances are $1.993(11) \text{ \AA}$ (Zn1–N1) and $2.044(8) \text{ \AA}$ (Zn1–O1), respectively. The other Zn–O distances are $2.333(10) \text{ \AA}$ (Zn1–O2) and $1.961(10) \text{ \AA}$ (Zn1–O4) and $2.008(10) \text{ \AA}$ (Zn1–O6), respectively. The Zn2 centre is coordinated by phenoxido oxygen (O1), hydroxide ion (O4), imine nitrogen (N2) and another symmetry related hydroxide ion (O4a). The nitrate ion coordinate to the metal centre in an anisobidentate fashion [$\Delta d = 0.33 \text{ \AA}$; $\Delta\theta = 14^\circ$]. The Zn–O bond distances vary from $1.980(9)$ to $2.394(18) \text{ \AA}$. The equatorial angles vary from $56.3(6)^\circ$ to $106.6(4)^\circ$. The axial O4–Zn2–N2 angle is $163.6(4)^\circ$.

5.3.3 Crystal structure description of complex 5.2

Complex 5.2 crystallized in monoclinic form with $P2_1/n$ space group (Table 5.1). Figure 5.4(b) shows the asymmetric unit of 5.2. Selected bond distances and angles are collected in Table 5.2. It is best described as a 1D network (Figure 5.5) of $[\text{Cu}_4(\text{DTC5.1})(\text{OCH}_3)_2(\text{NO}_3)_4] \cdot \text{H}_2\text{O}$ asymmetric units, where the asymmetric units are connected through a pair of $\mu_{1,1}$ bridging nitrate ions and $\mu_{1,1,1}$ bridging methoxide ions. The asymmetric unit consists of a deprotonated macrocyclic ligand, four copper centers (Cu1, Cu2, Cu3 and Cu4, respectively), two methoxide ions, four nitrate ions and a water molecule of crystallization. Cu1, Cu2 and Cu3, Cu4 are doubly bridged by phenoxido oxygen and

methoxide ion. Both Cu1 and Cu4 have perfect square pyramidal geometry (Addison parameter, τ is 0.05 for Cu1 center and 0.03 for Cu4 center)³¹ where they are equatorially coordinated by imine nitrogen (N6 for Cu1 and N2 for Cu4), phenoxido oxygen (O1 for Cu1 and O4 for Cu4), methoxide ion (O19 for Cu1 and O20 for Cu4) and nitrate ion (O11 for Cu1 and O17 for Cu4) of the same asymmetric unit and axially coordinated with another methoxide ion (O20a for Cu1 and O19a for Cu4) of other asymmetric unit. In the 1D chain, these two nitrate ions binds Cu2 and Cu4; Cu1 and Cu3 centers in an anisobidentate fashion [$\Delta d \sim 0.49 \text{ \AA}$]. The Cu-N bond lengths are found to be 1.969(6) and 1.955(6) \AA for Cu1 and Cu4, respectively, whereas the Cu-O bond lengths vary within the range 1.928(5)-2.559 \AA . Both Cu2 and Cu3 centers are bound with phenoxido oxygen (O1 for Cu2 and O4 for Cu3), an imine nitrogen (N5 for Cu2 and N1 for Cu3), methoxide ion (O19 for Cu2 and O2 for Cu3) and a monodentate nitrate ion ($\Delta d = 0.78 \text{ \AA}$ for Cu2 and $\Delta d = 0.61 \text{ \AA}$ for Cu3). The axial N-Cu-O angles vary within the range $166.22(18)^\circ$ - $168.7(2)^\circ$. The Cu-N bond lengths vary from 1.926(6) to 1.946(6) \AA , whereas the Cu-O bond lengths vary within the range 1.9286(9)-2.6747 \AA . The Cu1-Cu2 and Cu3-Cu4 distances are 3.019(13) and 3.0173(13) \AA , respectively.

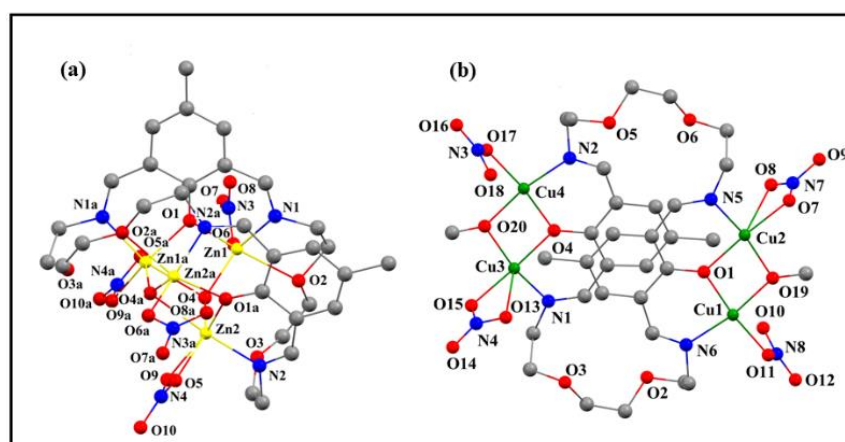


Figure 5.4 (a) Crystal structure of complex **5.1** (ball and stick model) and (b) asymmetric unit of complex **5.2** (ball and stick model). H atoms and solvent molecules are omitted for clarity.

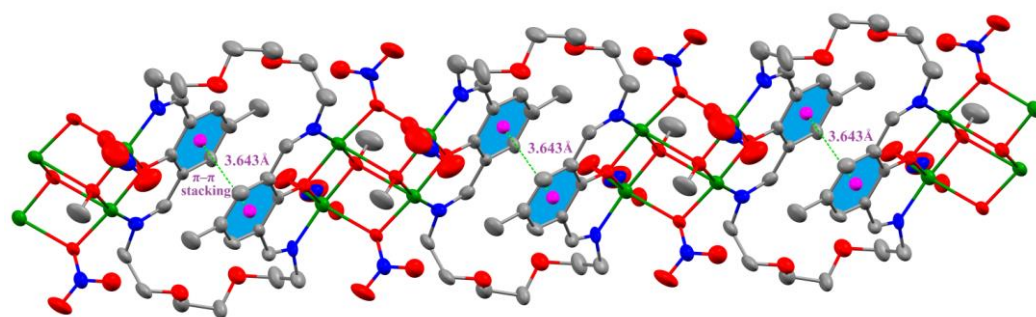


Figure 5.5 One dimensional chain structure of complex **5.2** with π - π face-to-face stacking along 'a' axis.

Table 5.2 Selected Bond lengths (Å) and Bond angles (°) for complexes **5.1** and **5.2**.

Complex 5.1				Complex 5.2			
Zn1-O1	2.044(8)	O1-Zn1-O2	163.1(4)	Cu1-O1	1.945(4)	Cu3-O15	1.982(5)
Zn1-O2	2.333(10)	O1-Zn1-O4	83.3(4)	Cu1-O11	1.974(5)	Cu3-O20	1.9286(9)
Zn1-O4	1.961(10)	O2-Zn1-O4	97.7(4)	Cu1-O19	1.928(5)	Cu3-O11a	2.463(0)
Zn1-O6	2.008(10)	N1-Zn1-O1	89.2(4)	Cu1-O20a	2.551(0)	Cu3-N1	1.926(6)
Zn1-N1	1.993(11)	N1-Zn1-O2	78.0(4)	Cu1-N6	1.969(6)	Cu4-O4	1.951(4)
Zn2-O1	1.992(10)	N1-Zn1-O4	134.1(4)	Cu2-O1	1.964(9)	Cu4-O17	1.972(5)
Zn2-O4	1.980(9)	O4-Zn2-O1	106.6(4)	Cu2-O7	1.969(5)	Cu4-O20	1.937(10)
Zn2-O4a	2.347(10)	O1-Zn2-O5	90.9(5)	Cu2-O8	2.747(0)	Cu4-O19a	2.559(0)
Zn2-O5	2.394(18)	O4-Zn2-O4a	82.5(4)	Cu2-O17a	2.464(0)	Cu4-N2	1.955(6)
Zn2-O9	2.080(12)	O4-Zn2-O9	101.7(5)	Cu2-O19	1.931(0)	Cu1-Cu2	3.019(13)
Zn2-N2	2.054(12)	O5-Zn2-O9	56.3(6)	Cu2-N5	1.946(6)	Cu3-Cu4	3.0173(13)
N2-Zn2-O4	163.6(4)			Cu3-O4	1.957(5)	O19-Cu2-N5	168.7(2)
				Cu3-O13	2.591(0)	O20-Cu3-N1	166.22(18)

5.3.4 NMR studies

¹H NMR of H₂DTC5.1 was recorded in DMSO-*d*₆ and CDCl₃ (Figures 5.6 and 5.7, respectively). In DMSO-*d*₆, the imine (H-C=N) protons appear as a sharp doublet peak at 8.49 ppm ($J = 12.4$ Hz). The aromatic protons appear at 7.44 ppm ($J = 9.6$ Hz) and the aliphatic ones at 3.62 ppm (d, $J = 5.6$ Hz) and 3.52 ppm (d, $J = 15.2$ Hz). A broad signal at 14.21 ppm corresponds to the phenolic protons (Figure 5.6). In the case of 5.1, due to coordination with Zn²⁺, the imine protons appear at 7.93 ppm (d, $J = 6.8$ Hz), 8.01 ppm (s), 8.28 ppm (d, $J = 10.4$ Hz) and 8.48 ppm (d, $J = 12.4$ Hz), and the aromatic protons at 6.96 ppm (s), 7.10 ppm (s), 7.16 ppm (s), 7.39 ppm (s), 7.52 ppm (d, $J = 12.0$ Hz) and 7.65 ppm (s) respectively. A broad multiplet in the range 3.1- 4.0 ppm indicates presence of aliphatic protons. Methyl protons appear at 2.21 ppm (s) and 2.29 ppm (s) (Figure 5.8).

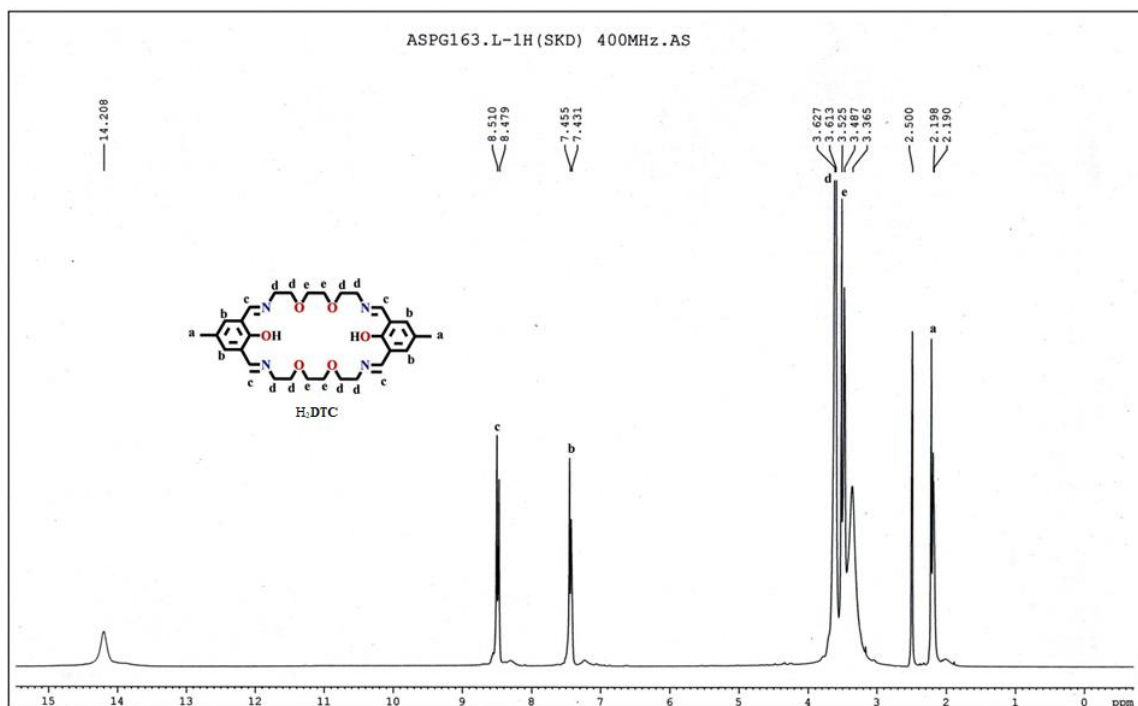


Figure 5.6 ¹H NMR spectrum of (H₂DTC5.1) in DMSO-*d*₆.

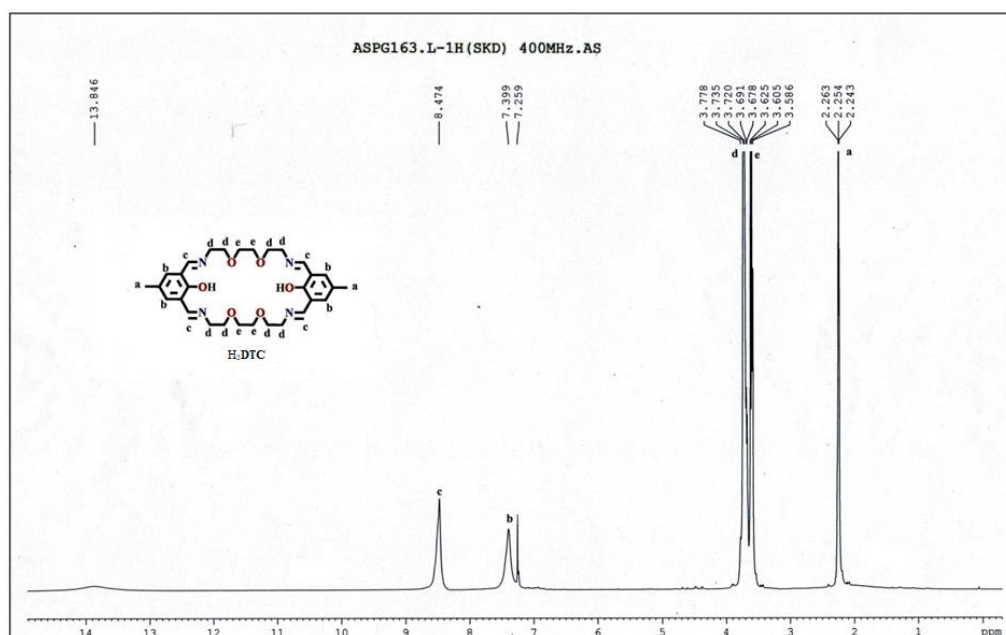


Figure 5.7 ¹H NMR spectrum of H₂DTC5.1 in CDCl₃.

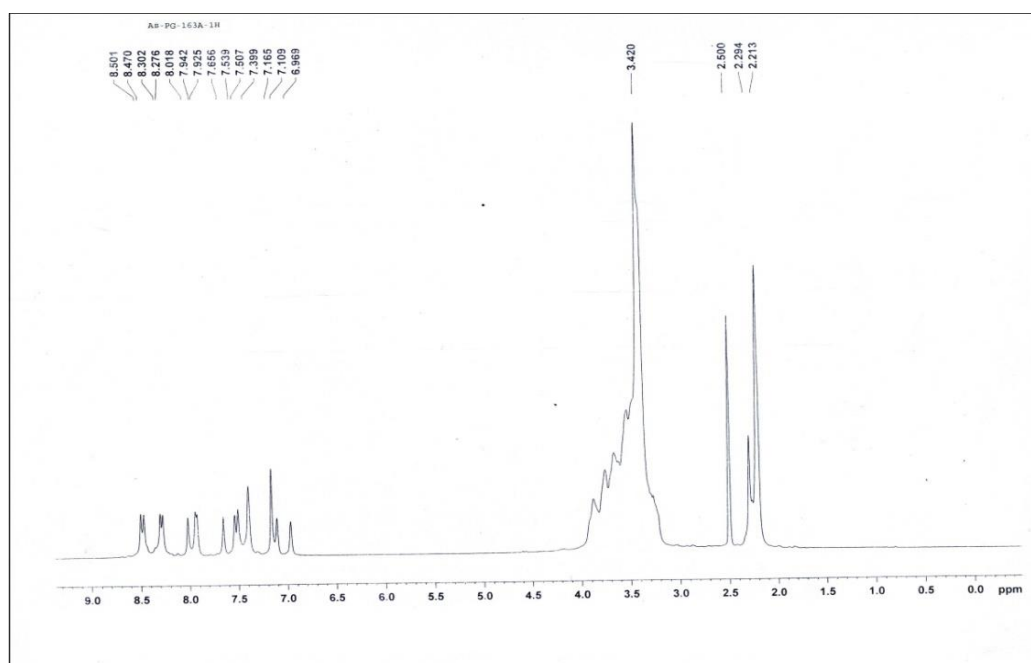


Figure 5.8 ¹H NMR spectrum of complex 5.1 in DMSO-*d*₆.

¹³C NMR spectrum of H₂DTC5.1 was performed in DMSO-*d*₆ (**Figure 5.9**). The imine carbon atoms appear at 162.29 ppm whereas aromatic carbon atoms appear in the range 121.36-159.34 ppm. The signals of the aliphatic carbon atoms appear from 59.97 to 70.75 and that of the methyl carbon atoms at 20.26 ppm. In the ¹³C NMR spectrum of **1** recorded in DMSO-*d*₆ (**Figure 5.10**), the signals of the imine and aromatic carbon atoms appear in the

166.04-172.94 ppm and 120.44-165.71 ppm ranges, respectively. Methylene and methyl carbon atoms are observed in the range 58.59-74.07 ppm and 19.36-19.43 ppm, respectively. We have also performed a ¹H NMR titration of H₂DTC5.1 with Zn²⁺ in DMSO-*d*₆. Upon gradual addition of Zn²⁺, the signal of the OH protons disappears due to the coordination of the metal. Again, in the presence of 3 equivalent or above Zn²⁺ ions significant splitting with downfield shift of aromatic protons from 7.44 ppm to 6.96 ppm, 7.09 ppm, 7.15 ppm, 7.38 ppm, 7.51 ppm and 7.64 ppm (in the presence of 3 equivalent or above Zn²⁺ ions) and imine protons (H-C=N) from, 8.49 ppm to 7.92 ppm, 8.00 ppm, 8.27 ppm and 8.47 ppm is noticed, confirming the metal ion coordination with the imine nitrogens. Similarly, splitting in the spectral pattern of aliphatic protons from, 3.62 ppm and 3.52 ppm to a multiplet (3.46–3.96 ppm) in the presence of metal ions suggests coordination of oxygen atoms of the aza crown part with Zn²⁺ centers. Interestingly, the methyl protons also exhibit a significant change in spectral pattern (from, 2.19 ppm to 2.22 ppm and 2.25 ppm) under such condition (**Figure 5.11**). X-ray crystallographic data of **5.1** also justify the above ¹H NMR titration data.

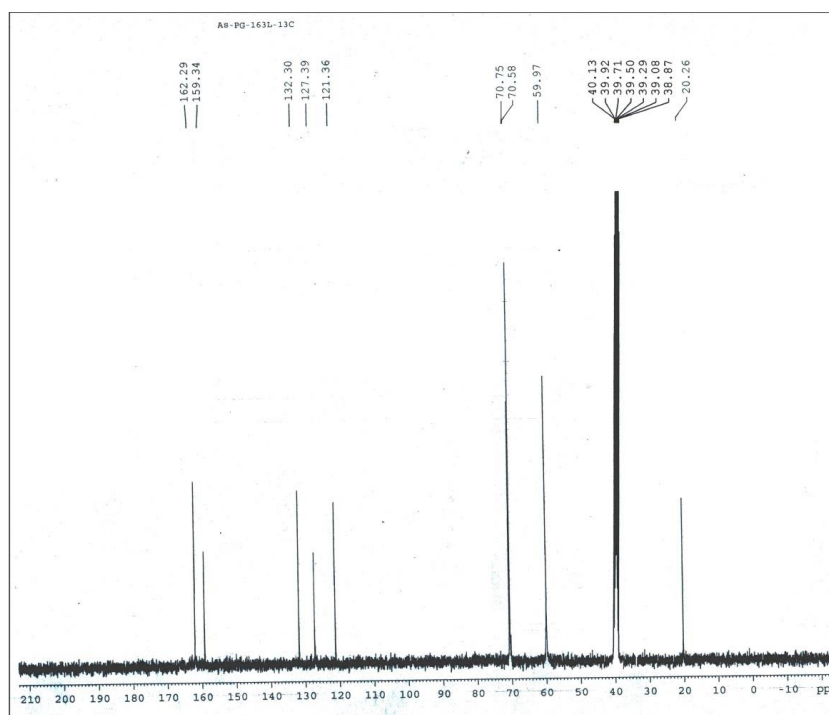


Figure 5.9 ¹³C NMR spectrum of H₂DTC5.1 in DMSO-*d*₆.

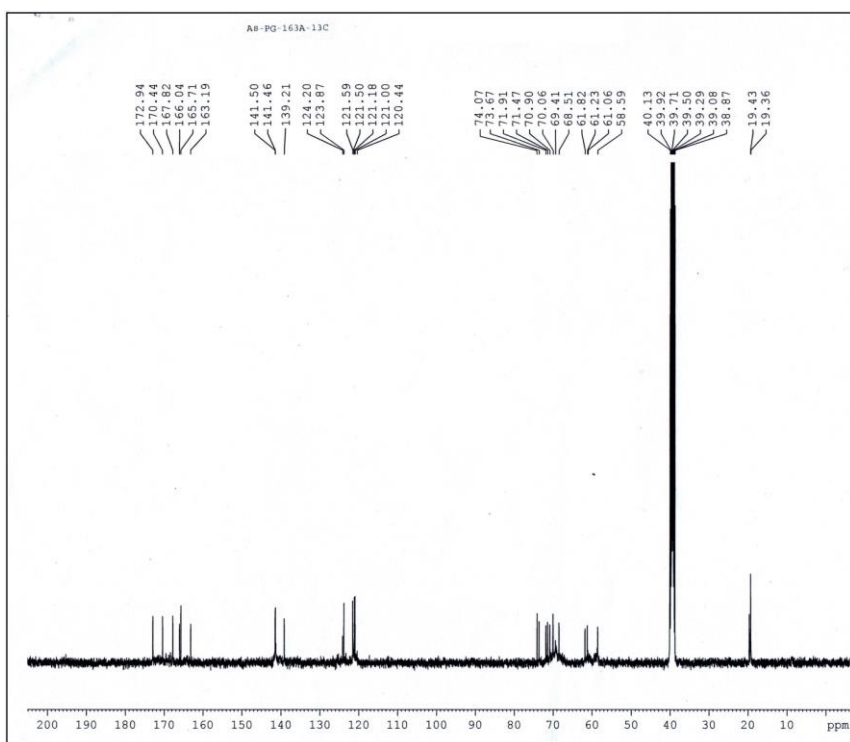


Figure 5.10 ¹³C NMR spectrum of complex **5.1** in DMSO-*d*₆.

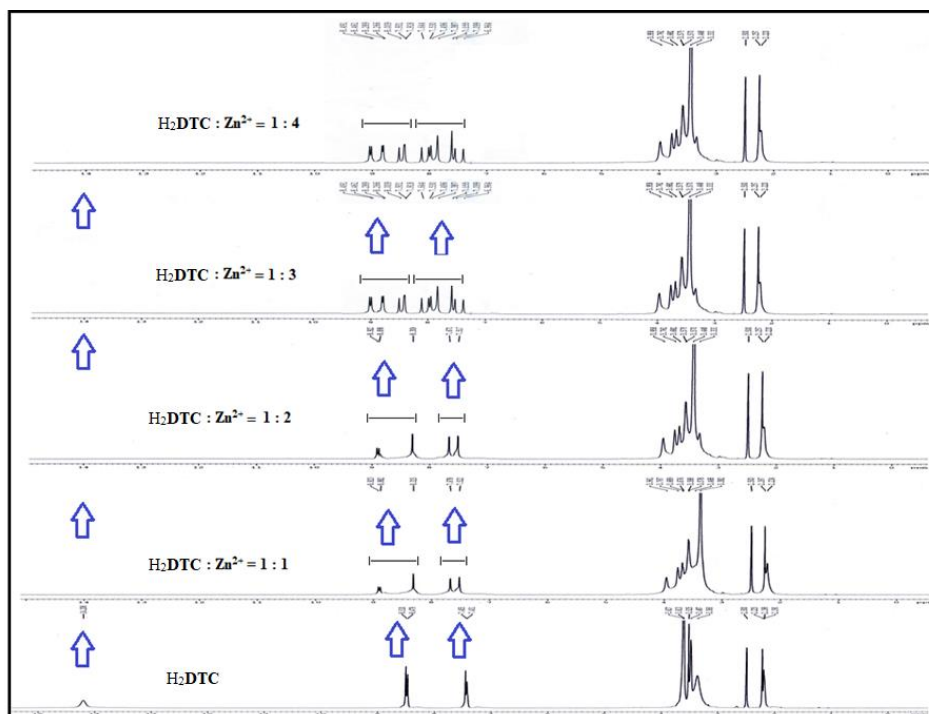


Figure 5.11 ¹H-NMR titration of the free ligand (**H₂DTC5.1**) and with the addition of 1.0, 2.0, 3.0 and 4.0 equivalent of Zn²⁺ in DMSO-*d*₆ recorded on a 400 MHz BRUKER NMR spectrometer.

5.3.5 Absorption spectral studies

The UV-Vis spectrum of H₂DTC5.1 in 10 mM HEPES buffer at pH 7.4 shows a well-defined band at 445 nm. The peak is attributed to an intramolecular $\pi \rightarrow \pi^*$ or $n \rightarrow \pi^*$ transition. Three different sequences of absorption changes for H₂DTC5.1 were noticed with increasing concentration of Zn²⁺ or Cu²⁺ until the intensity saturated in the presence of 4.3 equiv. of the metal ions (**Figure 5.12**). By gradual addition of Cu²⁺ up to 1.0 equiv. in the buffer containing H₂DTC5.1 (10 μ M), the 445-nm absorption band for H₂DTC5.1 was shown to deplete gradually with the concomitant formation of gradually blue shifted absorption intensities maximally up to \sim 424 nm by maintaining isosbestic wavelength at \sim 428 nm (**Figure 5.12** (I-A)). Although the absorption change continued by further addition of Cu²⁺ until 4.3 equiv., only a small blue shifting from 424 nm to 413 nm was detected (**Figure 5.12** (I-B and I-C, respectively)). However, the absorbance change overs from 1.0 to 2.0 equivalents and that of 2.0 until 4.3 equivalents follow two separate isosbestic wavelengths at \sim 417 and \sim 393 nm, respectively. No further absorption change was observed above 4.3 equiv. of Cu²⁺. With the increasing addition of 4.3 equivalents of Zn²⁺, the absorption of H₂DTC5.1 gradually blue shifted up to \sim 413 nm, and most interestingly and similarly to Cu²⁺, the absorption changes exhibited three separate isosbestic wavelengths at \sim 434 nm, \sim 420 nm and \sim 413 nm in the Zn²⁺ equivalents ranges of 0–1.0, 1.0–2.0 and 2.0–4.3, respectively (**Figure 5.12** (II-A, II-B and II-C)). The consecutive appearance of three separate isosbestic wavelengths for the two metal ions suggests the presence of species with different stoichiometric ratios in equilibrium condition. Unfortunately, their overlapping intensities did not allow us to identify their stoichiometries accurately.

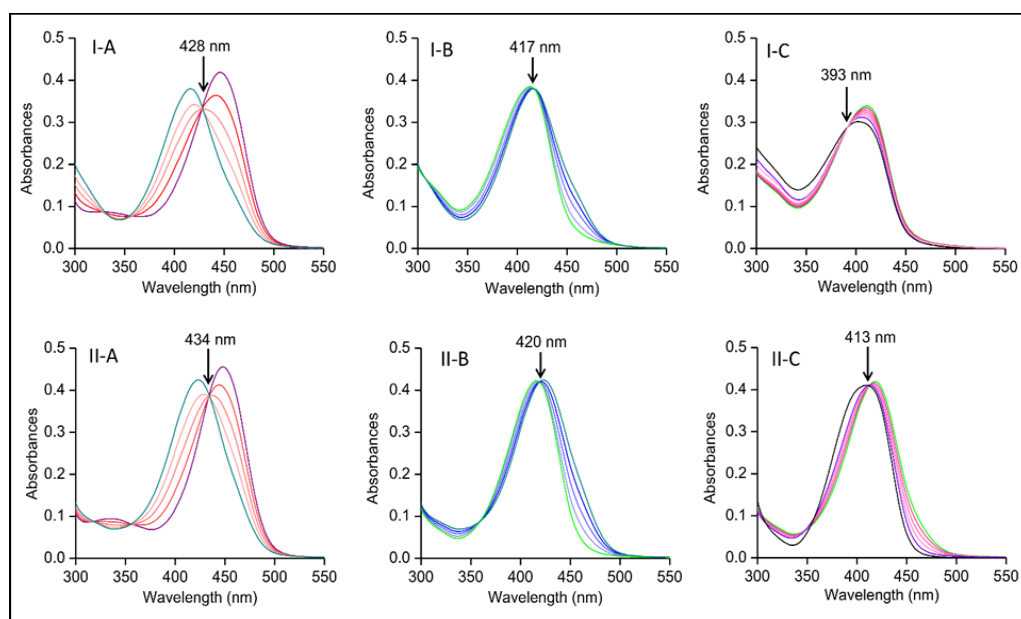


Figure 5.12 Absorption spectra of H₂DTC5.1 (10 μM) in the presence of (I) Cu²⁺ (0–4.30 equiv.) and (II) Zn²⁺ (0–4.30 equiv.) in HEPES buffer (10 mM) at pH 7.4: in absence (purple in A) and presence of 0.25–0.75 equiv. (red in A), 1.0 equiv. (dark cyan in A and B), 1.25–1.75 equiv. (blue in B), 2.0 equiv. (green in B and C), 2.25–4.0 equiv. (pink) and 4.3 equiv. (violet in C) of metal ions. The absorption spectra with gradual increase of Zn²⁺ or Cu²⁺ concentrations are shown by deep-to-light color (red: A; blue, B; pink: C). The spectra of (II-C) complex **5.1** and (I-C) complex **5.2** (40 μM each) are depicted by black lines for comparison. The isosbestic absorption wavelengths are indicated by arrows.

5.3.6 ESI-MS⁺ analysis

ESI-MS⁺ studies have been performed in 1:1, 2:1 and 4:1 metal ion: H₂DTC5.1 (metal ion: Zn²⁺ or Cu²⁺) molar ratio. In case of Zn²⁺, *m/z* peaks appear at 615.15 for 1:1 ratio and 814.16 for 2:1 ratio, suggesting formation of [Zn(HDTC5.1)]⁺ and [Zn₂(DTC5.1)(NO₃)₂+Li]⁺ complexes in water–methanol (9:1, v/v) mixture (**Figure 5.13(a)** and **5.13(b)**, respectively). Similarly, in the presence of Cu²⁺ ions, for the 1:1 and 2:1 ratio, peaks appear at 614.13 and 739.01, which corresponds to [Cu(HDTC5.1)]⁺ and [Cu₂(DTC5.1)(NO₃)₂]⁺, respectively (**Figure 5.14(a)** and **5.14(b)**). When the mass

spectrometric studies are carried out with 4:1 metal to ligand molar ratios, peaks are observed at 1032.96 for Zn²⁺ and 1170.00 for Cu²⁺ corresponding to [Zn₄(DTC5.1)(OH)₂(NO₃)₃]⁺ and [Cu₄(DTC5.1)(OCH₃)₂(NO₃)₄+CH₃OH+Na]⁺ molecular ion, respectively (Figure 5.13(c) and 5.14(c), respectively). Moreover, the experimentally obtained ESI-MS⁺ data nicely match with their simulated patterns.

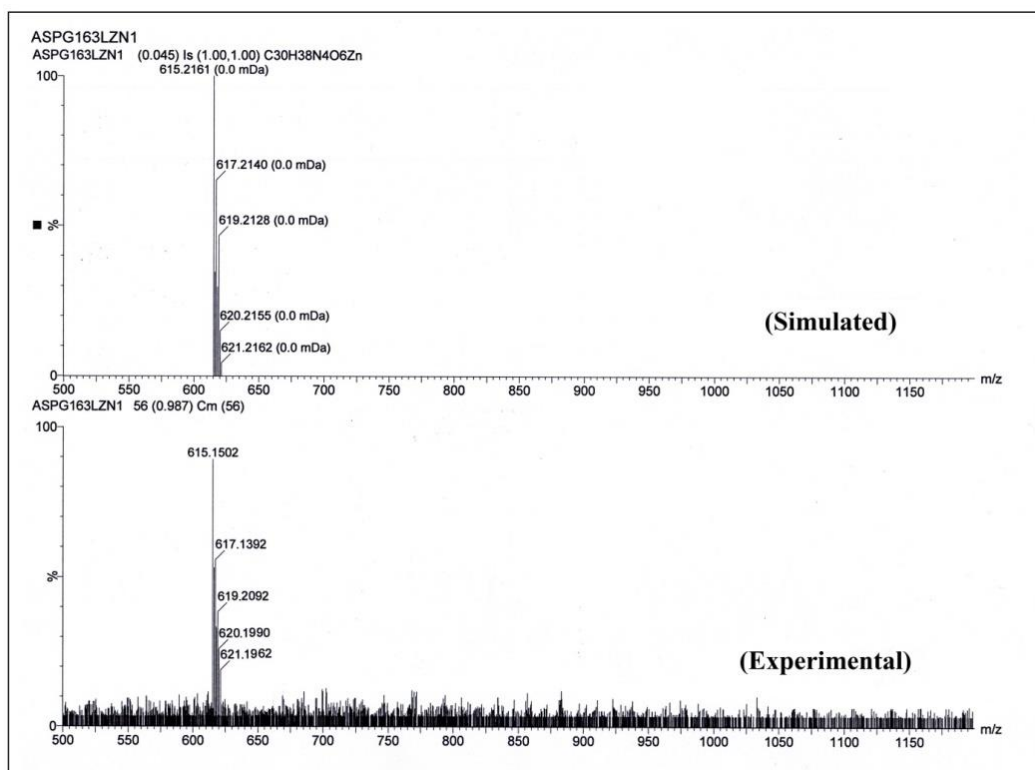


Figure 5.13(a) ESI-mass spectrum of [Zn(HDTC5.1)]⁺ system. The experimental graph is obtained after adding one equivalent Zn²⁺ solution to the H₂DTC5.1 (one equivalent) solution.

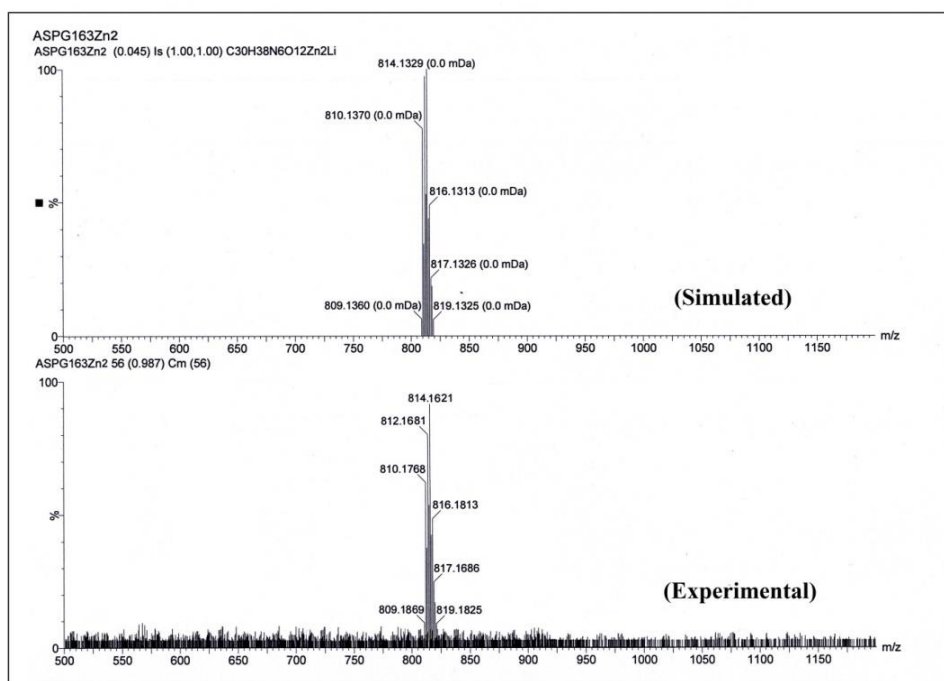


Figure 5.13(b) ESI-mass spectrum of $[\text{Zn}_2(\text{DTC5.1})(\text{NO}_3)_2+\text{Li}]^+$ system. The experimental graph is obtained after adding two equivalent Zn^{2+} solution to the $\text{H}_2\text{DTC5.1}$ (one equivalent) solution.

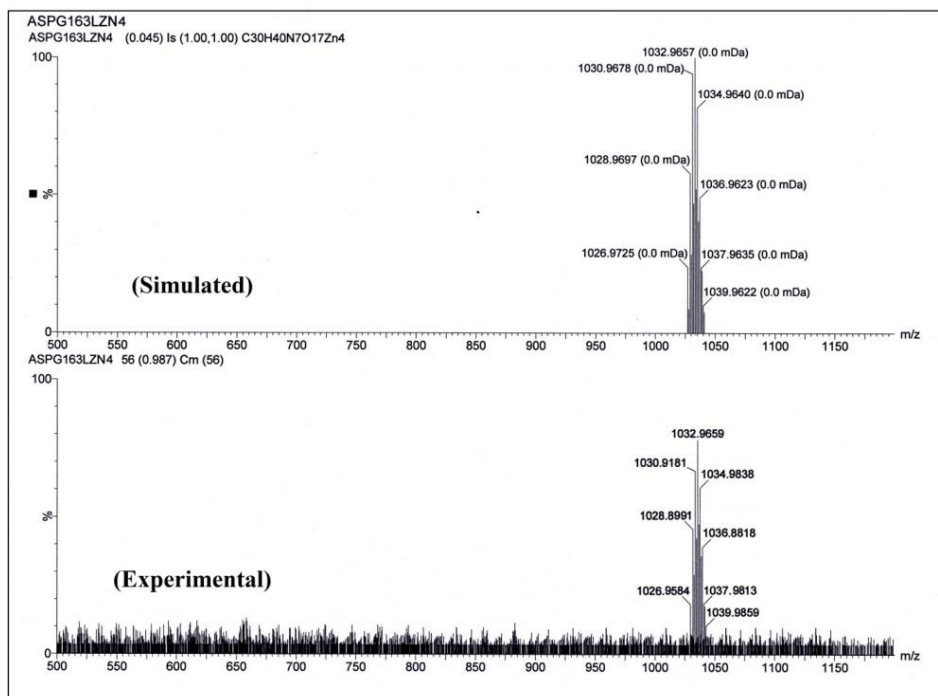


Figure 5.13(c) ESI-mass spectrum of $[\text{Zn}_4(\text{DTC5.1})(\text{OH})_2(\text{NO}_3)_3]^+$ system. The experimental graph is obtained after adding four equivalent Zn^{2+} solution to the $\text{H}_2\text{DTC5.1}$ (one equivalent) solution.

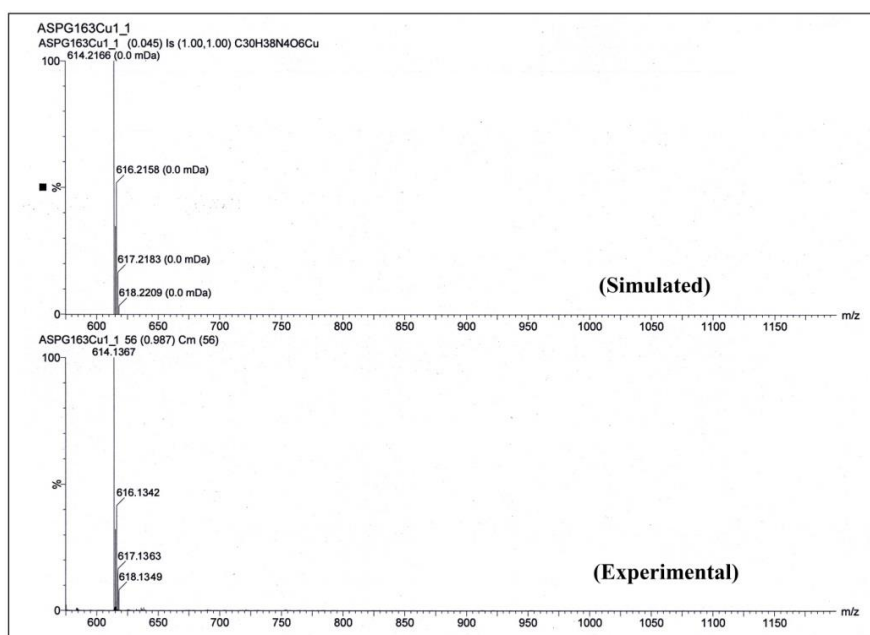


Figure 5.14(a) ESI-mass spectrum of $[\text{Cu}(\text{HDTC5.1})]^+$ system. The experimental graph is obtained after adding one equivalent Cu^{2+} solution to the $\text{H}_2\text{DTC5.1}$ (one equivalent) solution.

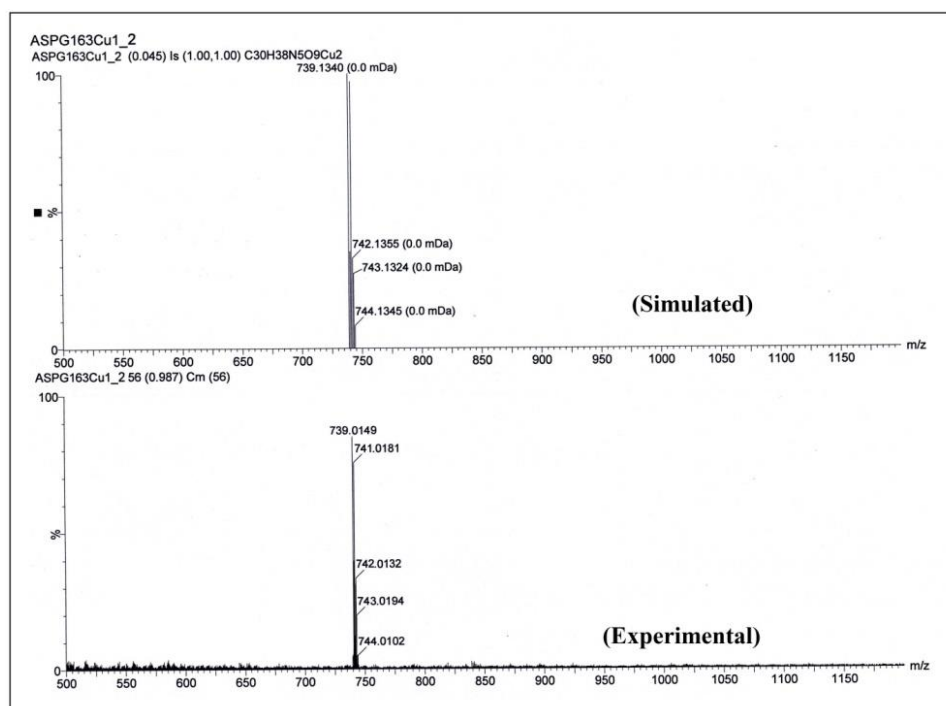


Figure 5.14(b) ESI-mass spectrum of $[\text{Cu}_2(\text{DTC5.1})(\text{NO}_3)]^+$ system. The experimental graph is obtained after adding two equivalent Cu^{2+} solution to the $\text{H}_2\text{DTC5.1}$ (one equivalent) solution.

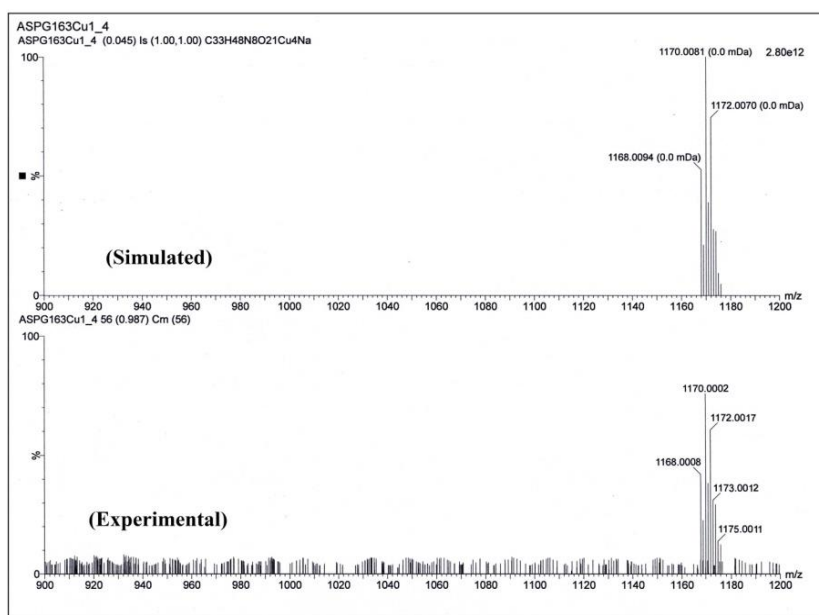


Figure 5.14(c) ESI-mass spectrum of $[\text{Cu}_4(\text{DTC})(\text{OCH}_3)_2(\text{NO}_3)_4+\text{CH}_3\text{OH}+\text{Na}]^+$ system. The experimental graph is obtained after adding four equivalent Cu^{2+} solution to the H_2DTC (one equivalent) solution.

5.3.7 Fluorescence properties

Fluorescence experiments were performed in 10 mM HEPES buffer (pH = 7.4) at ambient conditions. Upon excitation at 445 nm, $\text{H}_2\text{DTC5.1}$ exhibits weak fluorescence at 500 nm. This is probably due to a photoinduced electron transfer process (PET). The delocalization of the available lone pair on the imine nitrogen atom to the DFP moiety leads to the quenching of the fluorescence.

Upon addition of Zn^{2+} to $\text{H}_2\text{DTC5.1}$, the emission at 475 nm (excitation wavelength 415 nm) greatly enhanced accompanied by a blue shift of 25 nm (**Figure 5.15a**). The fluorescence enhancement due to Zn^{2+} ions has a systematic growth of about 7-fold up to four equiv. of Zn^{2+} , although small fluorescence increase is still perceptible at higher Zn^{2+} concentration. The chelation of Zn^{2+} with phenoxido O, imine N atoms of the aromatic part as well as O atoms of the macrocyclic aza-crown part of $\text{H}_2\text{DTC5.1}$ increases the rigidity of the molecular assembly (CHEF effect) via inhibition of free rotation of $\text{H}_2\text{DTC5.1}$ around the

H–C=N bond. Again PET process is hindered by arresting the lone pair of electron present in the imine nitrogen. These two effects are jointly responsible for the observed fluorescence enhancement.

In the case of Cu²⁺, its gradual addition (up to a maximum of four equivalents) to a chemosensor solution completely quenches the fluorescence at ~500 nm (**Figure 5.15c**). Such a dramatic quenching of the fluorescence (~55 fold) (CHEQ) can be attributed to a ligand to metal charge transfer (LMCT) between H₂DTC5.1 and the paramagnetic Cu²⁺ ions.^{5,46} The plot of fluorescence intensity at 500 nm (I₅₀₀) vs. molar ratio ([Cu²⁺]/[H₂DTC5.1]) in **Figure 5.15d** shows that the quenching is maximum for ~ 1:2 H₂DTC5.1: Cu²⁺ stoichiometric ratio.

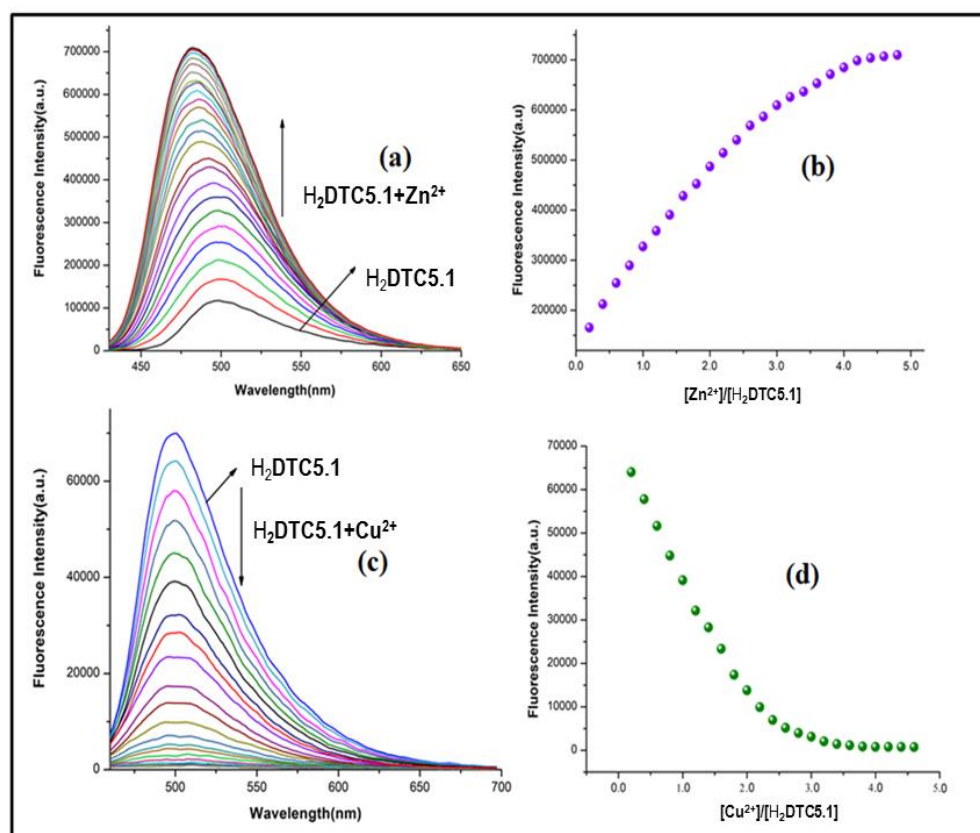


Figure 5.15 Fluorescence titration of H₂DTC5.1 (10 μM) with gradual addition of Zn²⁺/ Cu²⁺ (0–48 μM) in HEPES buffer (10 mM) at pH 7.4 and corresponding fluorescence intensities versus molar ratio plot.

Selectivity of H₂DTC5.1 toward Zn²⁺ and Cu²⁺ over other competitive species was examined by fluorescence titration experiments in the presence of different alkali metals (Na⁺ and K⁺), alkaline-earth metals (Mg²⁺ and Ca²⁺), and various transition-metal ions (Mn²⁺, Fe³⁺, Co²⁺, Ni²⁺, Cu⁺, Cd²⁺ and Hg²⁺) (**Figure 5.16**). In UV chamber, H₂DTC5.1 exhibits a bluish-green fluoresce in presence of Zn²⁺ ion (**Figure 5.17**). Upon addition of different common anions like sodium salts of S₂O₃²⁻, S²⁻, SO₃²⁻, HSO₄⁻, SO₄²⁻, SCN⁻, N₃⁻, OCN⁻, AsO₄³⁻, PO₄³⁻, ClO₄⁻, AcO⁻, Cl⁻, NO₃⁻, P₂O₇⁴⁻ (PPI), PF₆⁻, F⁻, L-Cysteine and glutathione (**Figure 5.18**) in HEPES buffer (10 mM) at pH 7.4 to the chemosensor, no significant fluorescence enhancement was noticed. The competition assay experiments were performed individually for Zn²⁺ (4.0 equiv.) and Cu²⁺ ions (4.0 equiv.) and in the presence of other metal ions (5.0 equiv.) and common anions in a similar solvent system. As shown in **Figure 5.19**, the addition of other metal ions, except Cu²⁺, does not alter significantly the emission of the system Zn²⁺-H₂DTC5.1. However, the addition of Cu²⁺ to an H₂DTC5.1 solution in the presence of Zn²⁺ led to large fluorescence quenching (**Figures 5.19** and **5.20(a)**) in agreement with the higher stability of the Cu²⁺ complexes. Such type of displacement highly corroborates the Irving-Williams series, according to which Cu²⁺ ions have greater tendency of replacing Zn²⁺ ions to form a more stable Cu²⁺-probe complex. Binding constant values also support the above observation. Interestingly, the presence of Cu⁺ ions did not exhibit such type of fluorescence quenching. The effective ionic radii of Cu⁺, Cu²⁺ and Zn²⁺ are 77 pm, 73 pm and 74 pm, respectively. Therefore, charge to radius ratio values of Zn²⁺ and Cu²⁺ ions are comparable and significantly differ from Cu⁺ ions, which initiates selectivity of H₂DTC5.1 towards Zn²⁺ and Cu²⁺ ions. Cu²⁺ ion detection by H₂DTC5.1 is not influenced by the presence of other competitive metal ions including Zn²⁺ ion (**Figures 5.20(b)** and **5.21**).

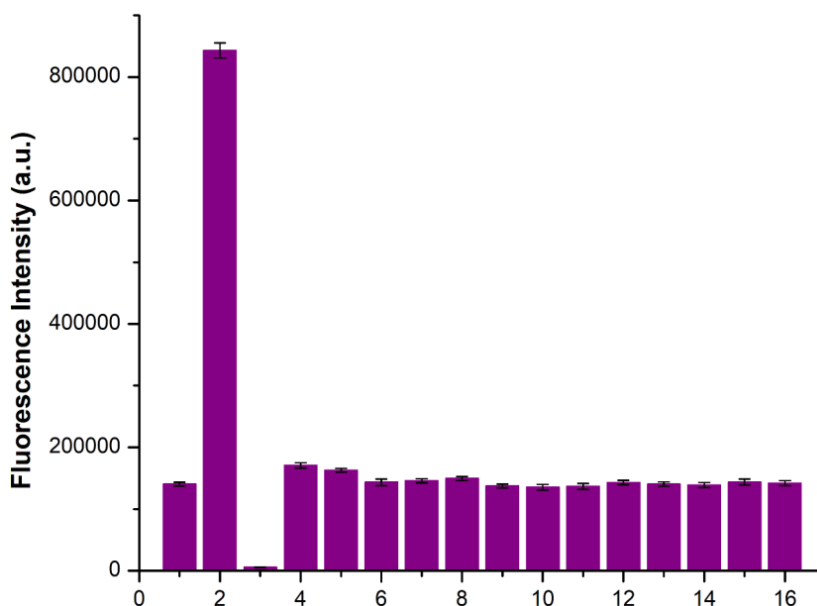


Figure 5.16 Relative fluorescence intensity profile of chemosensor **H₂DTC5.1** in the presence of different cations in HEPES buffer (10mM) at pH 7.4. 1=only **H₂DTC5.1** (10 μ M); **H₂DTC5.1** (10 μ M) + M^{n+} (40 μ M), where M^{n+} =(2–Zn²⁺, 3–Cu²⁺, 4–Ag⁺, 5–Fe³⁺, 6–Hg²⁺, 7–K⁺, 8–Mn²⁺, 9–Na⁺, 10–Ni²⁺, 11–Mg²⁺, 12–Co²⁺, 13–Ca²⁺, 14–Pb²⁺, 15–Cd²⁺ and 16–Cr³⁺).



Figure 5.17 Color changes of chemosensor **H₂DTC5.1** (10 μ M) in the presence of different metal ions (4 equiv.) in HEPES buffer (10 mM, pH 7.4). The images were taken under UV light. Where, 1= only **H₂DTC5.1**, 2-16 = **H₂DTC5.1** + Zn²⁺, Cu²⁺, Cd²⁺, Pb²⁺, Hg²⁺, Mn²⁺, Fe³⁺, Co²⁺, Ni²⁺, Cr³⁺, K⁺, Na⁺, Mg²⁺, Ca²⁺ and Al³⁺, respectively.

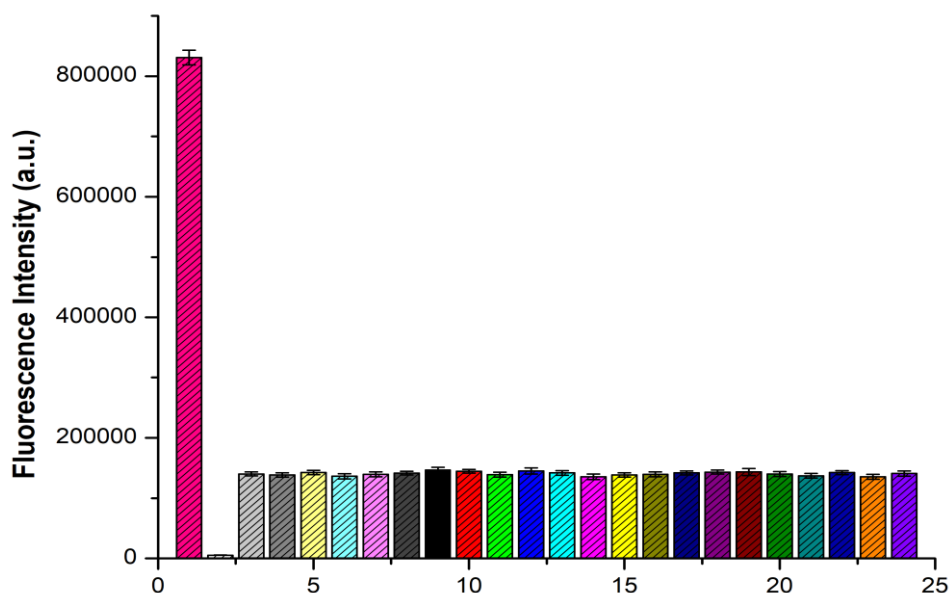


Figure 5.18 Relative fluorescence intensity profile of H₂DTC5.1 (10 μM) in the presence of various common anions (40 μM) in HEPES buffer (10 mM) at pH 7.4. 1- H₂DTC5.1+Zn²⁺, 2- H₂DTC5.1+Cu²⁺, 3-H₂DTC5.1, (4–24)- H₂DTC5.1 + Anions, Anions = 3-S₂O₃²⁻, 4-S²⁻, 5-SO₃²⁻, 6-HSO₄⁻, 7-SO₄²⁻, 8-SCN⁻, 9-N₃⁻, 10-OCN⁻, 11-AsO₄³⁻, 12-H₂PO₄⁻, 13-HPO₄²⁻, 14-PO₄³⁻, 15-ClO₄⁻, 16-AcO⁻, 17-Cl⁻, 18-NO₃⁻, 19-P₂O₇⁴⁻, 20-PF₆⁻, 21-F⁻ 22-L-Cysteine, 23-Glutathione, 24-P₂O₇⁴⁻.

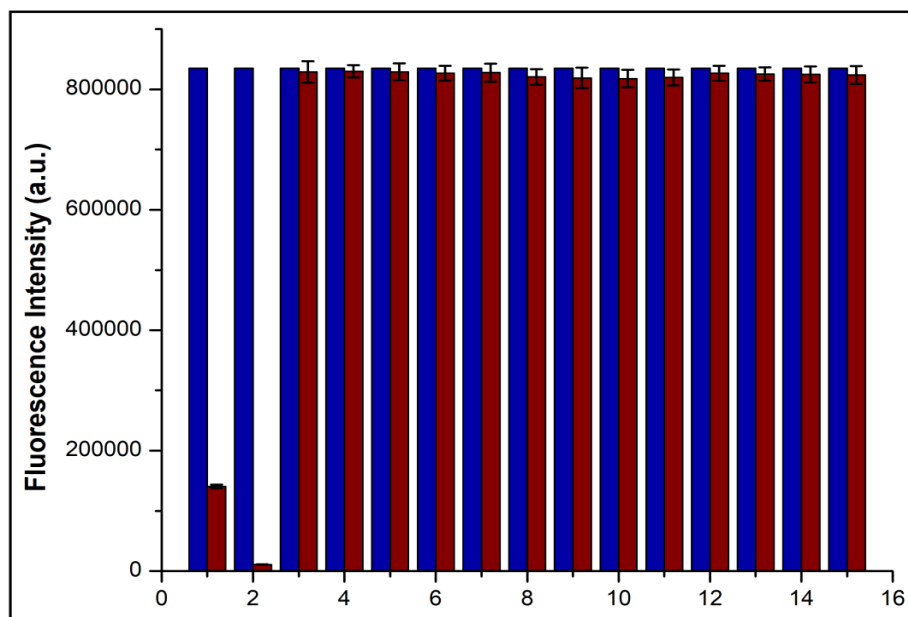


Figure 5.19 Relative fluorescence intensity profile of [DTC5.1-Zn²⁺] system in the presence of different cations in 10 mM HEPES buffer at pH 7.4. 1=only H₂DTC5.1 (10 μM) and (2-

15)= H₂DTC5.1 (10 μM) + Zn²⁺(40 μM) + Mⁿ⁺ (50μM), where Mⁿ⁺=(2–Cu²⁺, 3–Co²⁺, 4–Cr³⁺, 5–Fe³⁺, 6–Hg²⁺, 7–K⁺, 8–Mn²⁺, 9–Na⁺, 10–Ni²⁺, 11–Mg²⁺, 12–Pb²⁺, 13–Ca²⁺, 14–Fe²⁺, 15–Cd²⁺). Blue bars indicate [H₂DTC5.1 (10 μM) + Zn²⁺ (40 μM)] whereas brown bars indicate [H₂DTC5.1 (10 μM) + Zn²⁺ (40 μM) + other cations (50 μM), (except 1)].

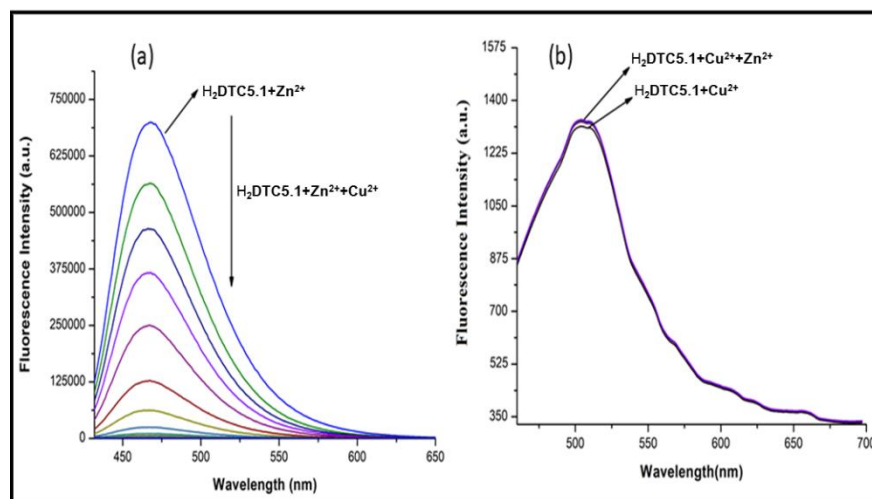


Figure 5.20 Fluorescence titration of (a) [H₂DTC5.1+Zn²⁺] system ([H₂DTC5.1] = 10μM; [Zn²⁺] = 40μM) with gradual addition of Cu²⁺ (40μM); (b) [H₂DTC5.1+Cu²⁺] system ([H₂DTC5.1] = 10μM; [Cu²⁺] = 40μM) with gradual addition of Zn²⁺ (40μM) in HEPES buffer (10 mM) medium at pH 7.4.

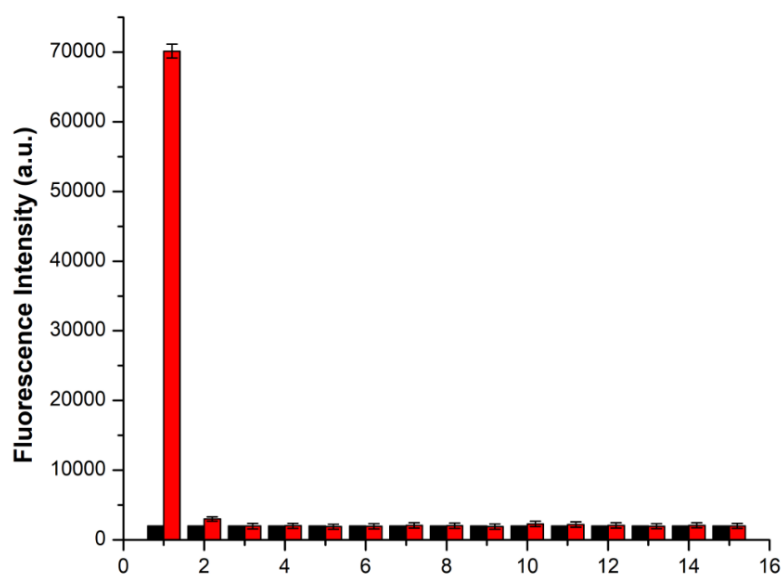


Figure 5.21 Relative fluorescence intensity profile of [DTC5.1-Cu²⁺] system in the presence of different cations in HEPES buffer medium (10 mM) at pH 7.4. 1=only H₂DTC (10 μM)

and (2-15)= **H₂DTC5.1** (10 μ M) + Cu²⁺(40 μ M) + Mⁿ⁺ (50 μ M), where Mⁿ⁺=(2–Zn²⁺, 3–Co²⁺, 4–Cr³⁺, 5–Fe³⁺, 6–Hg²⁺, 7–K⁺, 8–Mn²⁺, 9–Na⁺, 10–Ni²⁺, 11–Mg²⁺, 12–Pb²⁺, 13–Ca²⁺, 14–Fe²⁺, 15–Cd²⁺). Black bars indicate [**H₂DTC5.1** (10 μ M) + Cu²⁺ (40 μ M)] whereas red bars indicate [**H₂DTC5.1** (10 μ M) + Cu²⁺ (40 μ M) + other cations (50 μ M), (except 1)].

In competition assay experiments towards common anions, we have also studied the binding behavior of chemosensor-Zn²⁺ receptor towards PPI and the binding behavior of chemosensor-Cu²⁺ receptor towards biothiols such as L-Cysteine and glutathione. In chemosensor-Zn²⁺ receptor the fluorescence emission only slightly quenched in the presence of a large excess of PPI (40 equiv.) (**Figure 5.22**). Similarly, in the case of chemosensor-Cu²⁺ receptor, glutathione exhibits little fluorescence enhancement (**Figure 5.23**). Therefore the competition assay experiment demonstrates high fluorescent recognition of **H₂DTC5.1** for Zn²⁺ and Cu²⁺ ions over other cations and anions.

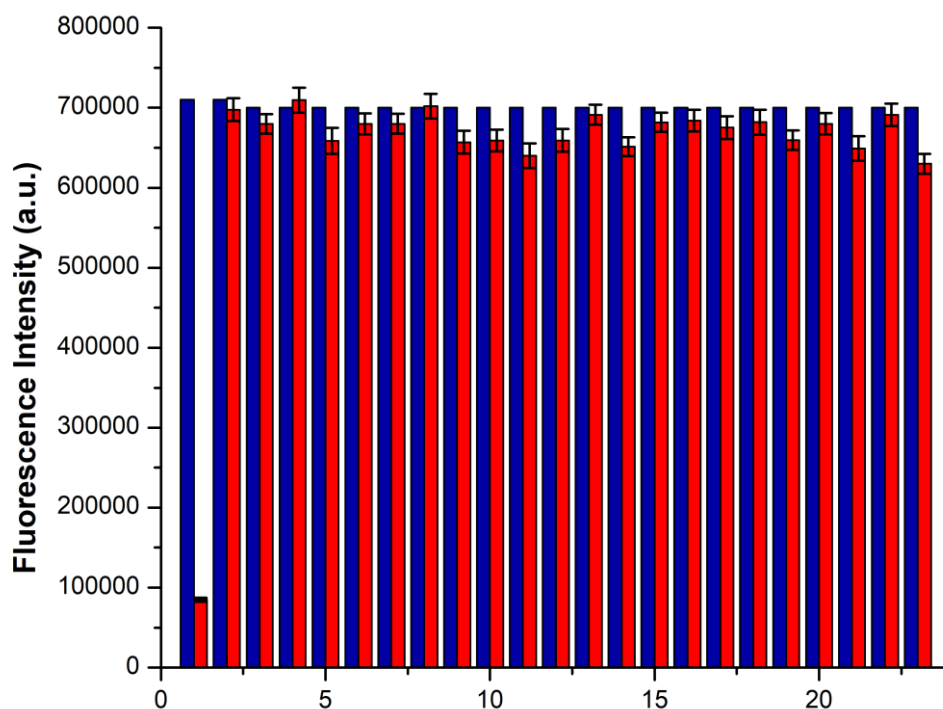


Figure 5.22 Relative fluorescence intensity profile of [**DTC5.1**-Zn²⁺] system in the presence of different anions in HEPES buffer medium (10 mM) at pH 7.4. 1=only **H₂DTC5.1** (10 μ M) and (2-22)= **H₂DTC5.1** (10 μ M) + Zn²⁺(40 μ M) + Anions (50 μ M), Anions = 3–S₂O₃²⁻, 4–S²⁻

, 5-SO₃²⁻, 6-HSO₄⁻, 7-SO₄²⁻, 8-SCN⁻, 9-N₃⁻, 10-OCN⁻, 11-AsO₄³⁻, 12-H₂PO₄⁻, 13-HPO₄²⁻, 14-PO₄³⁻, 15-ClO₄⁻, 16-AcO⁻, 17-NO₃⁻, 18-F⁻, 19-PF₆⁻, 20-L-Cysteine, 21-Glutathione, 22-P₂O₇⁴⁻, 23-large excess P₂O₇⁴⁻ (40 times greater with respect to Zn²⁺ ion concentration). Blue bars indicate [H₂DTC5.1 (10 μM) + Zn²⁺ (40 μM)] whereas red bars indicate [H₂DTC5.1 (10 μM) + Zn²⁺ (40 μM) + other anions (50 μM), (except 1 and 23)].

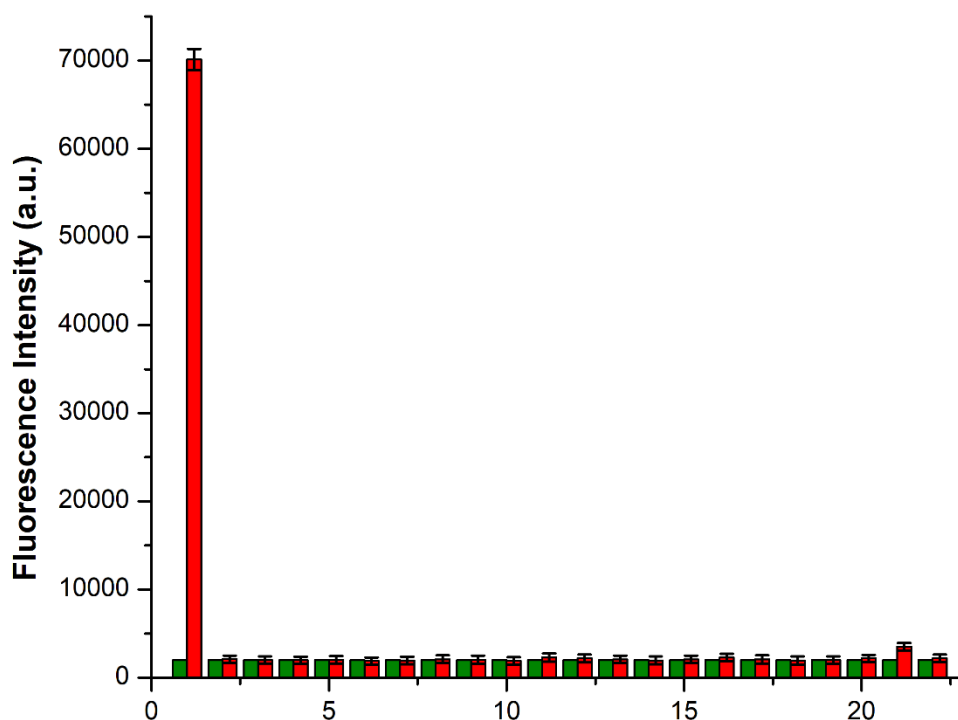


Figure 5.23 Relative fluorescence intensity profile of [DTC5.1-Cu²⁺] system in the presence of different anions in HEPES buffer medium (10 mM) at pH 7.4. 1=only H₂DTC5.1 (10 μM) and (2-22)= H₂DTC (10 μM) + Cu²⁺(40 μM) + Anions (50 μM), Anions 3-S₂O₃²⁻, 4-S²⁻, 5-SO₃²⁻, 6-HSO₄⁻, 7-SO₄²⁻, 8-SCN⁻, 9-N₃⁻, 10-OCN⁻, 11-AsO₄³⁻, 12-H₂PO₄⁻, 13-HPO₄²⁻, 14-PO₄³⁻, 15-ClO₄⁻, 16-AcO⁻, 17-NO₃⁻, 18-F⁻, 19-PF₆⁻, 20-L-Cysteine, 21-Glutathione and 22-P₂O₇⁴⁻. Green bars indicate [H₂DTC5.1 (10 μM) + Cu²⁺ (40 μM)] whereas red bars indicate [H₂DTC (10 μM) + Cu²⁺ (40 μM) + other anions (50 μM), (except 1)].

Furthermore, solid state fluorescence spectroscopic studies of H₂DTC5.1, complex 5.1 and complex 5.2 (Figure 5.24) reveal enhancement of fluorescence intensity in 5.1 and quenching of fluorescence intensity in 5.2 in comparison with H₂DTC5.1.

Reversibility and regeneration are two important aspects for real time application of a chemosensor. The experiments were performed in the presence of sodium salt of ethylenediaminetetraacetic acid (Na₂EDTA) solution. In the case of DTC5.1–Zn²⁺ solution, after addition of four equivalents of Na₂EDTA change its color from bluish-green to light yellow with an obvious decrease in fluorescence intensity. However, the addition of four equivalents of Na₂EDTA to a DTC5.1–Cu²⁺ solution, leads to an enhancement of emission intensity that along with the appearance of a light yellow color indicates the regeneration of the free H₂DTC5.1 (Figure 5.25).

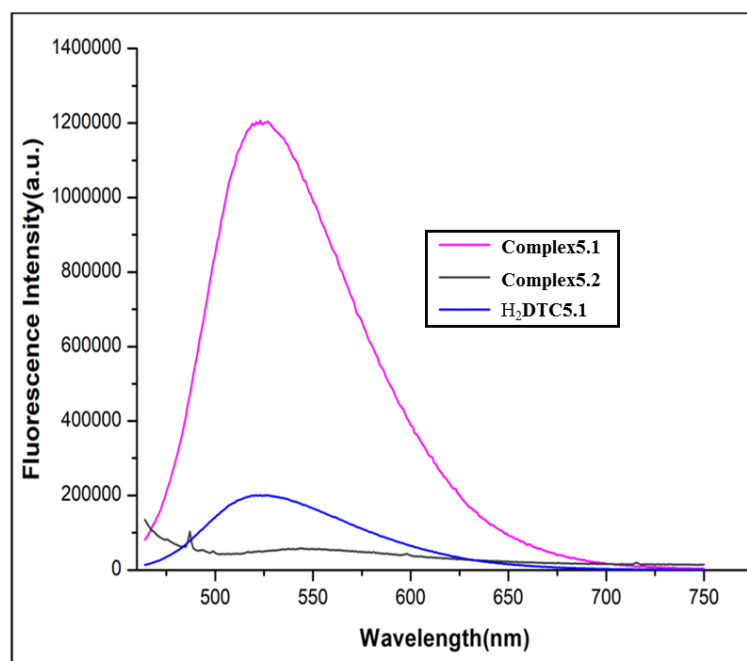


Figure 5.24 Solid state fluorescence spectra of H₂DTC5.1, complexes 5.1 and 5.2.

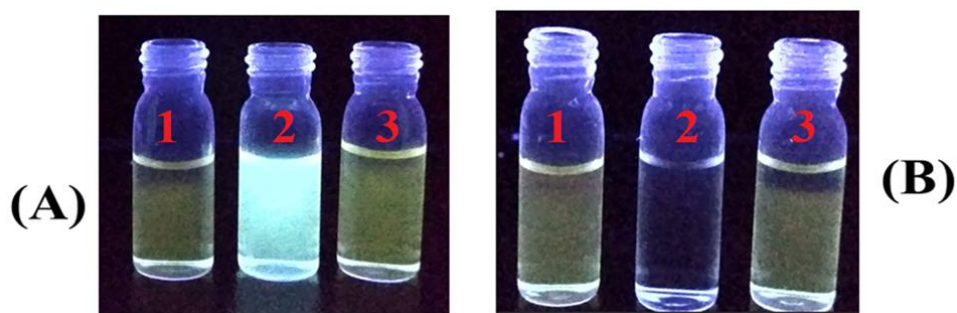


Figure 5.25 Color changes in reversibility experiments under UV light. For (A), 1= Only H₂DTC5.1 (10μM), 2= H₂DTC5.1 (10μM) + Zn²⁺ (40μM), 3= H₂DTC5.1 (10μM) + Zn²⁺ (40μM) + EDTA²⁻(40μM). For (B), 1= Only H₂DTC5.1 (10μM), 2= H₂DTC5.1 (10μM) + Cu²⁺ (40μM), 3= H₂DTC5.1 (10μM) + Cu²⁺ (40μM) + EDTA²⁻(40μM).

The average concentration of Cu²⁺ in blood is 100–150 μg/L and the total concentration of Zn²⁺ ions in mammalian cells is in the range 100–500 μM.^{5.47,5.48} The lower limit of detection (LOD) of the chemosensor towards Cu²⁺ and Zn²⁺ was calculated using the 3σ method.^{5.49} The values obtained, 0.11 × 10⁻⁹ M for Cu²⁺ and 0.27 × 10⁻⁹ M for Zn²⁺, clearly suggest that this chemosensor can detect quantitatively both Cu²⁺ and Zn²⁺ ions in real sample analysis.

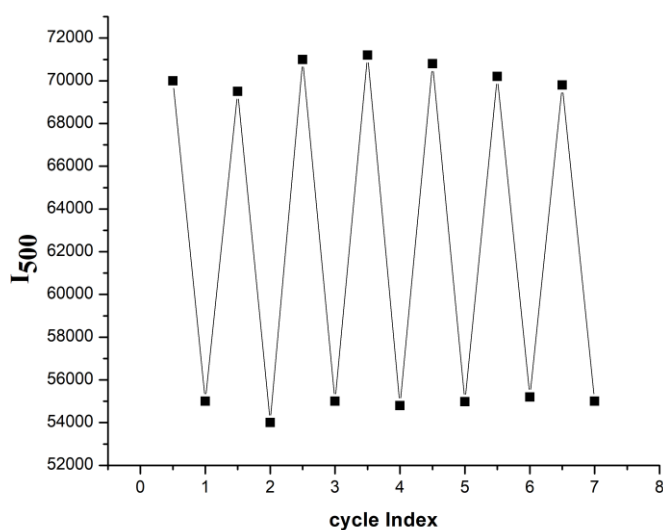


Figure 5.26 Fluorescence reversibility experiment of H₂DTC5.1 between pH 4 and 10.

Stability of chemosensor is examined by reversibility experiment^{5.50} (Figure 5.26). It clearly shows that the chemosensor is well stable in a wide range of pH (pH 4-10) and it can only be dissociated in strong acidic condition (Figure 5.27).

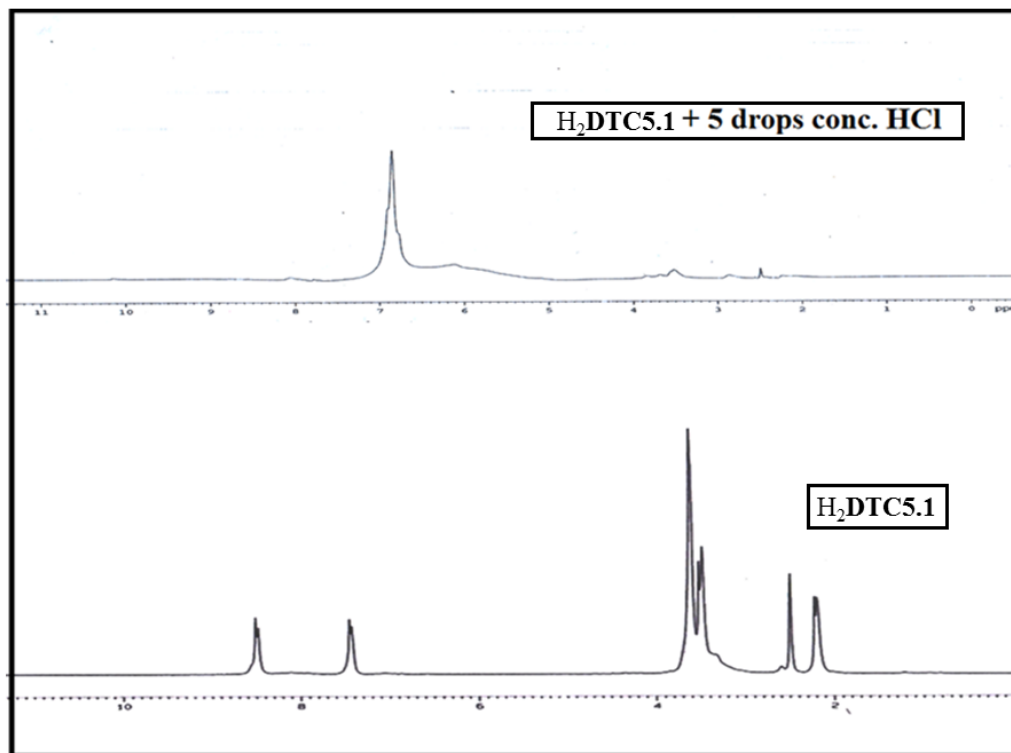


Figure 5.27 ¹H NMR spectra of H₂DTC5.1 in presence of concentrated HCl (total volume of solution is 500 μL) in DMSO-*d*₆ solvent.

Figure 5.28 shows the effect of pH on the fluorescence response of the free H₂DTC5.1 and of the systems Zn²⁺:H₂DTC5.1 and Cu²⁺:H₂DTC5.1 in 4:1 molar ratio. Free H₂DTC5.1 has weak fluorescence at acidic pH that increases slightly from pH 3 to 6 and, then decreases at more basic pH values. The weak emission of the free ligand can be attributed to a PET process that becomes more intense at basic pH when the phenol groups deprotonate (see the distribution diagram). Deprotonation of the phenol groups would extend the electron delocalization to the p-conjugated system formed by the aromatic rings and the C=N (imino) groups, decreasing thereby the emission intensity. While the addition of Zn²⁺ does not lead to any increase in fluorescence at acidic pH values, at pH values above 7, it

produces a large increase in fluorescence (CHEF effect). On the contrary, Cu²⁺ quenches the fluorescence of H₂DTC5.1 throughout all the pH range assayed, particularly at basic pH values, due to the chelation to the metal (CHEQ effect). Above findings suggests that the phenols groups present in H₂DTC5.1 are too basic, they don't dissociate readily, or reprotonate readily enough; thus undergoes deprotonation easily.

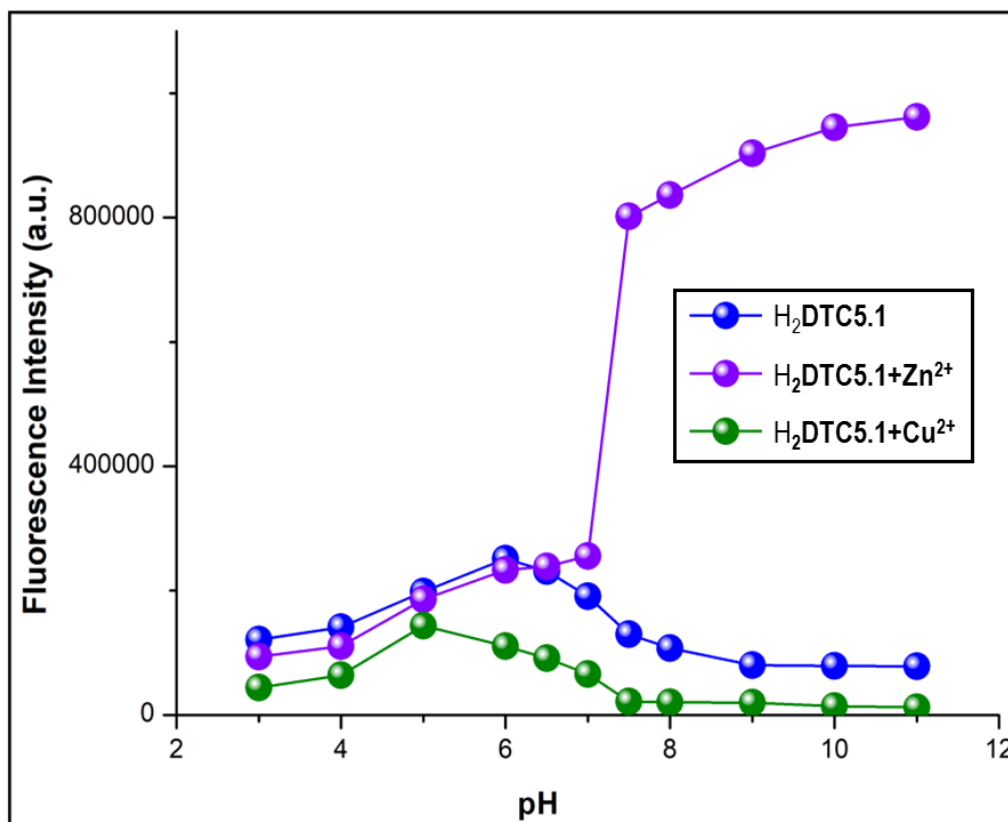


Figure 5.28 Fluorescence intensity of H₂DTC5.1 (10 μM) in the absence and presence of Zn²⁺ and Cu²⁺ ions (40 μM) at various pH values in HEPES buffer (10 mM).

5.3.8 Life time and quantum yield measurements

Lifetime experiments for the H₂DTC5.1 and complexes **5.1** and **5.2** were studied at 298 K in HEPES buffer (10 mM, pH 7.4). The average fluorescence decay lifetimes of H₂DTC5.1 and complexes **5.1** and **5.2** have been determined by using the formula $\tau_f = a_1\tau_1 + a_2\tau_2$, where a_1 and a_2 are the relative amplitudes of the decay process. The average fluorescence lifetime of the H₂DTC5.1, complex **5.1** and complex **5.2** are 1.90, 2.68 and 0.44

ns, respectively (Figure 5.29 and Table 5.3). We unable to obtain phosphorescence intensity apparently due to low fluorescence lifetime values.

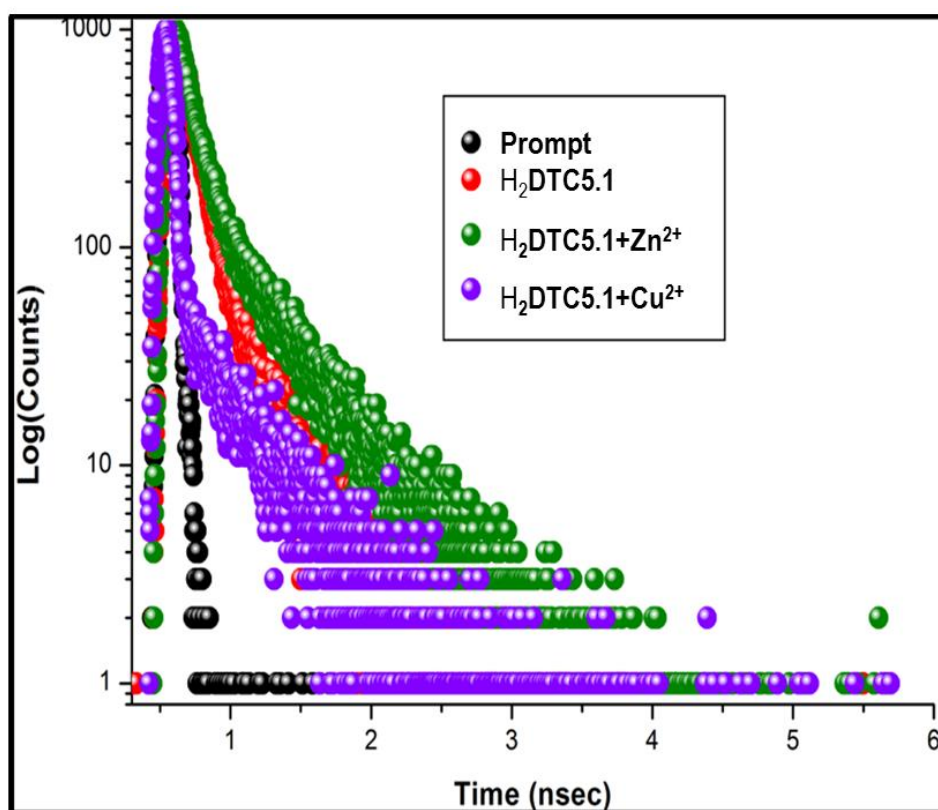


Figure 5.29 Time-resolved fluorescence decay curves (logarithm of normalized intensity vs time in ns) of H₂DTC5.1 in the absence metal ions (●), presence of Zn²⁺ ion (●), presence of Cu²⁺ ion (●) and (●) indicates decay curve for the scattered.

The fluorescence quantum yield (Φ) has been calculated by using the following formula:

$$\Phi_{\text{sample}} = \left\{ \frac{(\text{OD}_{\text{standard}} \times A_{\text{sample}} \times \eta_{\text{sample}}^2)}{(\text{OD}_{\text{sample}} \times A_{\text{standard}} \times \eta_{\text{standard}}^2)} \right\} \times \Phi_{\text{standard}}$$

Where A is the area under the emission spectral curve, OD is the optical density of the compound at the excitation wavelength and η is the refractive index of the solvent. The standard used was quinine sulfate with $\Phi_{\text{standard}} = 0.52$.

The values of Φ for H₂DTC5.1, and for the DTC5.1–Zn²⁺ and DTC5.1–Cu²⁺ complexes are found to be 0.059, 0.28 and 0.0014, respectively (Table 5.3). The fluorescence quantum yield (Φ) of H₂DTC5.1–Zn²⁺ complex is 4.7 fold greater than that of free

H₂DTC5.1. Low fluorescence decay lifetime and quantum yield of complex **5.2** is due to the quenching effect of Cu²⁺ ions.

Table 5.3 Data of lifetime (τ_f) and quantum yield (Φ) of H₂DTC5.1, complex **5.1** and complex **5.2**.

	τ_f (ns) (average)	χ^2	Φ
H ₂ DTC5.1	1.90	0.99380	0.059
Complex 5.1	2.68	1.01279	0.280
Complex 5.2	0.44	1.00342	0.0014

5.3.9 pH-potentiometric titrations

(a) Acid-base behaviour

The *emf* data obtained by titrating H₂DTC5.1 EtOH:H₂O 30:70 v/v solutions in 0.15 M NaCl at 298.1 K with NaOH aqueous solutions were analysed with the HYPERQUAD^{5.37} suite programs. For additional experimental data, pH range covered and fitting parameters, see in **Tables 5.4** to **5.6**. The pH range used for determining the protonation constants was 6 - 11. Further studies were carried out from pH=3 in order to rule out additional protonation steps. A total of four protonation constants were found (see **Table 5.7** and **Figure 5.30**). The first and second protonation constant values are very close between them and should occur at opposite sides of the macrocycle. Attending to the literature data,^{5.51,5.52} there are some crystal structures where the proton is shared between the phenolate groups and the neighbouring imino groups. It is reasonable to suggest that this might also happen in solution. The next two protonations would produce a reorganisation of the protons since, as evidenced in the crystal structure of a related ligand,^{5.53} all four protons at this stage would be placed at the imino groups. A hydrogen bond network between the phenolate and the imino groups would be

contributing to the observed reorganization.

Table 5.4 Information for potentiometric data used in protonation constants fitting.

Curve 1	pH range	6.03-10.60
	data points	76
Curve 2	pH range	9.26 -10.63
	data points	106

Table 5.5 Information for potentiometric data used in zinc(II) interaction studies.

Curve 1	pH range	6.51-10.82
	data points	87
Curve 2	pH range	6.07-10.18
	data points	86

Table 5.6 Information for potentiometric data used in copper(II) interaction studies.

Curve 1	pH range	4.55-10.75
	data points	95
Curve 2	pH range	5.44-10.74
	data points	119

Table 5.7 Logarithms of the stepwise protonation constants for **DTC5.1**, in NaCl 0.15M H₂O : EtOH 70:30 v/v at 298(1) K.

Reaction	log ₁₀ <i>K</i>
$\text{DTC5.1}^{2-} + \text{H}^+ \rightleftharpoons \text{HDTC5.1}^-$	9.81(3) ^a
$\text{HDTC5.1}^- + \text{H}^+ \rightleftharpoons \text{H}_2\text{DTC5.1}$	9.41(2)
$\text{H}_2\text{DTC5.1} + \text{H}^+ \rightleftharpoons \text{H}_3\text{DTC5.1}^+$	8.83(2)
$\text{H}_3\text{DTC5.1}^+ + \text{H}^+ \rightleftharpoons \text{H}_4\text{DTC5.1}^{2+}$	7.51(3)

(a) Numbers in parenthesis are standard deviation on last significant figure

(b) Interaction with Cu²⁺ and Zn²⁺

The interaction of H₂DTC5.1 with Cu²⁺ and Zn²⁺ is studied by means of pH-potentiometric titrations performed with M²⁺: H₂DTC5.1 mole ratios varying from 1:1 to 4:1 in the same solvent mixture and electrolyte as the protonation studies. The introduction in the model of M²⁺: H₂DTC5.1 species of 3:1 and 4:1 stoichiometry do not lead to any improvement in the fitting and, therefore, such stoichiometries are discarded. The titrations only reveal the formation of complex species of 1:1 and 2:1 M²⁺: H₂DTC5.1 stoichiometry (see **Tables 5.8** and **5.9**). Moreover, in the titrations carried out with 3:1 and 4:1 Cu²⁺:H₂DTC5.1 mole ratio, some formation of Cu²⁺ hydroxide was observed at basic pH values. The final models collected in **Table 5.8** show for Cu²⁺, formation of mononuclear [Cu(H_xDTC5.1)]^{2+x} species with *x* varying from 2 to 0, as well as of the non-hydroxylated binuclear species [Cu₂(DTC5.1)]²⁺ and the hydroxylated ones [Cu₂(DTC5.1)(OH)]⁺ and [Cu₂(DTC5.1)(OH)₂]. The distribution diagrams (**Figure 5.31**) show that while for 1:1 Cu²⁺: H₂DTC5.1 mole ratio the mononuclear species prevail throughout all the pH range studied, for 2:1 ratio the binuclear hydroxylated species are quantitatively formed in solution above pH 7. As shown in **Table 5.8**, the stability constant for the formation of the [Cu(DTC5.1)] complex is almost nine orders of magnitude higher than that for the stepwise formation of the [Cu₂(DTC5.1)]²⁺ binuclear species, which may be associated to the fact that there is a larger number of donor atoms involved in the coordination of the first metal ion. The coordination of the second metal should bring about a rearrangement of the ligand and a reorganisation of the coordination sphere with bond breaking and reforming, so that each metal ion occupies one of the sites of the ligand. This low coordination number is reflected in the very low p*K_a* value (p*K_a* = 5.87) associated to the formation of the monohydroxylated binuclear complexes. This p*K_a* supports, on the other hand, that the hydroxide anion is behaving as a bridging ligand between the metal centers.

As with copper, in the case of zinc no stoichiometry higher than 2:1 could be derived from the pH-potentiometric studies (**Figure 5.32**) where in the y-axis the percent complex formation with respect to the total metal contents is represented as a function of pH. Mononuclear complexes have stoichiometries $[\text{Zn}(\text{H}_x\text{DTC5.1})]^{x+}$ with x varying from 4 to 0 and $[\text{Zn}_2(\text{DTC5.1})(\text{OH})_y]^{(4-y)}$ hydroxylated binuclear ones with $y = 1-3$. As expected, the Zn^{2+} complexes of **DTC5.1** have lower stability constants than those of copper as exemplified in **Table 5.8** by the five orders of magnitude lower stability of $[\text{Zn}(\text{DTC5.1})]$ with respect to $[\text{Cu}(\text{DTC5.1})]$ (**Table 5.9**). As shown in the distribution diagram, the hydroxylated species predominate in solution above $\text{pH} = 7.4$ for Zn^{2+} : **DTC5.1** 2:1 molar ratio.

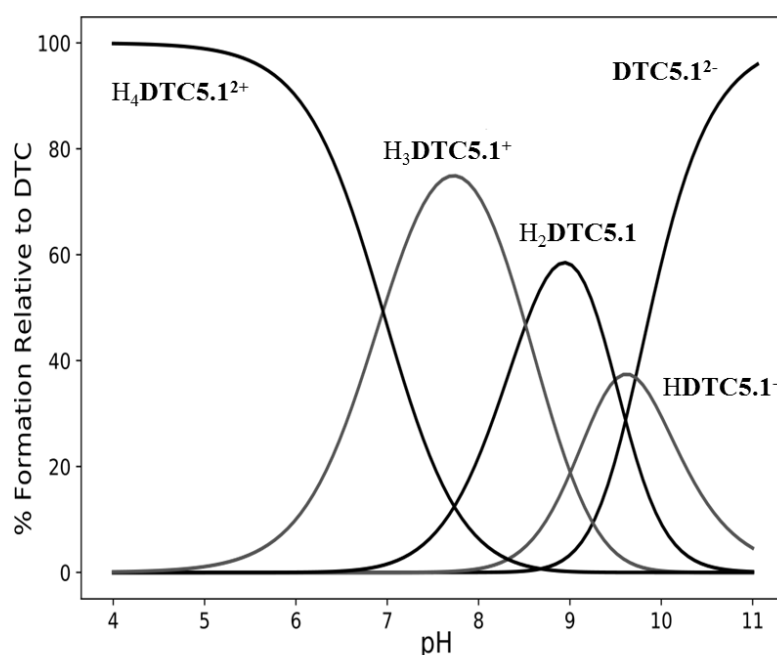


Figure 5.30 Species distribution for the system **DTC5.1** in NaCl 0.15M (EtOH 30%).
 $[\text{DTC5.1}] = 1\text{mM}$

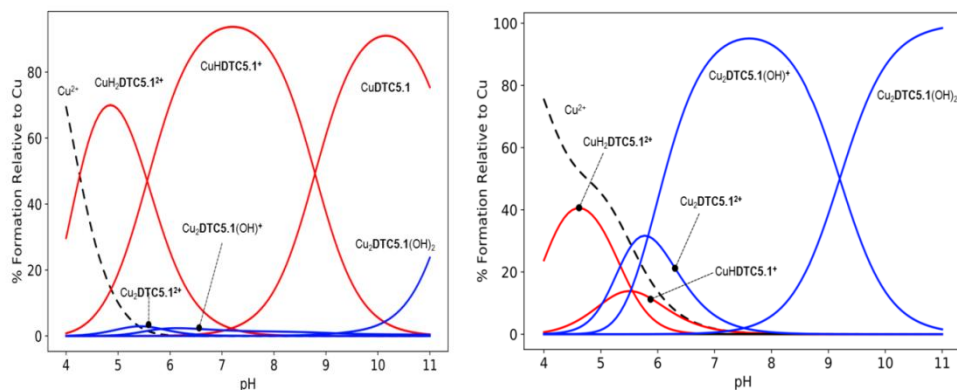


Figure 5.31 Species distribution for the system **DTC5.1** with Cu²⁺ in NaCl 0.15M (EtOH 30%). [**DTC5.1**] = 1mM, [Cu²⁺] = 1 mM (left) or [Cu²⁺] = 2 mM (right). Mononuclear species shown in red, binuclear species shown in blue.

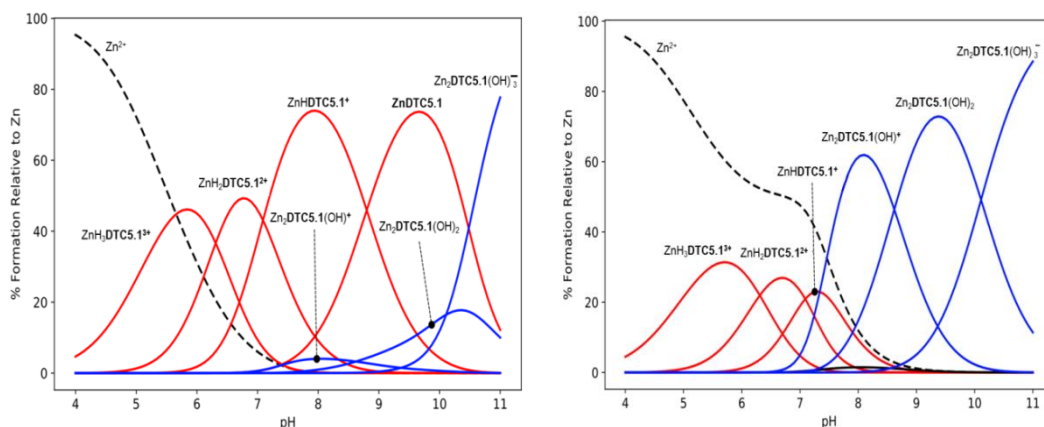


Figure 5.32 Species distribution for the system **DTC5.1** with Zn²⁺ in NaCl 0.15M (EtOH 30%). [**DTC5.1**] = 1mM, [Zn²⁺] = 1 mM (left) or [Zn²⁺] = 2 mM (right). Mononuclear species shown in red, binuclear species shown in blue.

Table 5.8 Logarithm of Stability constants for **DTC5.1** with Cu²⁺, in NaCl 0.15M EtOH 30% at 298(1)K.

Reaction	log ₁₀ <i>K</i>
$\text{DTC5.1}^{2-} + \text{Cu}^{2+} \rightleftharpoons \text{CuDTC5.1}$	15.88(6) ^a
$\text{HDTC5.1}^{-} + \text{Cu}^{2+} \rightleftharpoons \text{CuHDTC5.1}^{+}$	14.86(5)
$\text{H}_2\text{DTC5.1} + \text{Cu}^{2+} \rightleftharpoons \text{CuH}_2\text{DTC5.1}^{2+}$	11.03(6)
$\text{CuDTC5.1} + \text{Cu}^{2+} \rightleftharpoons \text{Cu}_2\text{DTC5.1}^{2+}$	6.57(5)
$\text{Cu}_2\text{DTC5.1}^{2+} + \text{H}_2\text{O} \rightleftharpoons \text{Cu}_2(\text{OH})\text{DTC5.1}^{+} + \text{H}^{+}$	-5.86(7)
$\text{Cu}_2(\text{OH})\text{DTC5.1}^{+} + \text{H}_2\text{O} \rightleftharpoons \text{Cu}_2(\text{OH})_2\text{DTC5.1} + \text{H}^{+}$	-9.17(8)

(a) Numbers in parenthesis represent standard deviation on last significant figure

Table 5.9 Logarithm of Stability constants for **DTC5.1** with Zn²⁺, in NaCl 0.15M EtOH 30% at 298(1)K.

Reaction	log ₁₀ <i>K</i>
$\text{DTC5.1}^{2-} + \text{Zn}^{2+} \rightleftharpoons \text{ZnDTC5.1}$	11.24(5) ^a
$\text{HDTC5.1}^{-} + \text{Zn}^{2+} \rightleftharpoons \text{ZnHDTC5.1}^{+}$	10.39(6)
$\text{H}_2\text{DTC5.1} + \text{Zn}^{2+} \rightleftharpoons \text{ZnH}_2\text{DTC5.1}^{2+}$	8.00(6)
$\text{H}_3\text{DTC5.1}^{+} + \text{Zn}^{2+} \rightleftharpoons \text{ZnH}_3\text{DTC5.1}^{3+}$	5.67(9)
$\text{DTC5.1}^{2-} + 2 \text{Zn}^{2+} + \text{H}_2\text{O} \rightleftharpoons \text{Zn}_2(\text{OH})\text{DTC5.1}^{+} + \text{H}^{+}$	8.31(7)
$\text{Zn}_2(\text{OH})\text{DTC5.1}^{+} + \text{H}_2\text{O} \rightleftharpoons \text{Zn}_2(\text{OH})_2\text{DTC5.1} + \text{H}^{+}$	-8.66(3)
$\text{Zn}_2(\text{OH})_2\text{DTC5.1} + \text{H}_2\text{O} \rightleftharpoons \text{Zn}_2(\text{OH})_3\text{DTC5.1}^{-} + \text{H}^{+}$	-10.2(1)

(a) Numbers in parenthesis represent standard deviation on last significant figure.

5.3.10 Stability constants determination from UV-Vis and fluorometric titrations

UV-Vis and fluorescence titrations were performed adding up to four equivalents of either Cu²⁺ or Zn²⁺ to a 10 μM water solution of H₂DTC5.1 in HEPES buffer (pH=7.4) (Figures 5.12 and 5.15). The data were analyzed with the software HypSpec2014^{5.33,5.34} and the best fitting model was chosen with the same criteria as for the pH-potentiometric data. The equilibrium constants obtained are conditional constants for the experimental conditions used at pH=7.4.

For Cu²⁺, the UV-Vis titrations revealed the formation of species of 1:1 and 2:1 Cu²⁺ : H₂DTC5.1 stoichiometry with values of the successive constants of 6.17(3) and 4.76(2). In the case of Zn²⁺ we could only fit the constant for the 1:1 complex at this pH with a value of log K = 5.83(8). Indeed, the distribution diagram calculated with the constants derived from the pH-potentiometric studies at the concentrations used in the UV-Vis titration (*vide supra*) reveals that only mononuclear species are formed at pH = 7.4, the binuclear species would be forming at higher pH values. Similar conclusions are drawn from the emission studies. As stated above, addition of Cu²⁺ in water produces a strong quenching. The profile of the titration and the analysis of the data support the formation of complexes of 1:1 and 2:1 Cu²⁺ : H₂DTC5.1 stoichiometry (**Figure 5.33**). However, in the case of Zn²⁺ titration, a CHEF effect is observed. As commented above the coordination of the 3d¹⁰ Zn²⁺ ion would prevent the photoinduced electron transfer from the imine lone pairs to the excited fluorophore to occur. The values of the constants obtained from the fluorescence studies (Cu²⁺; log K₁ = 6.085(1), log K₂ = 5.86(2); Zn²⁺, log K₁ = 6.032(8)) agree reasonably well with the UV-Vis and the effective constants (log K_{eff} = Σ [MH_xDTC5.1]^{x+} / [(Σ (H_xDTC5.1)^(x-2)][M²⁺]) determined at pH 7.4 from the potentiometric data. The above binding constant values suggest that the effect of solvent composition on metal-ligand binding properties can be considered to be negligibly small. To support the fact, we have performed a fluorometric titration by using ethanol instead of methanol and maintain the ratio i.e., water:ethanol = 7:3 (v/v). A similar observation has been found that has been depicted in **figure 5.34**.

The above experimental data reveal that the lower stoichiometries (1:1; 1:2 for Cu²⁺ and 1:1 for Zn²⁺) of chemosensor-metal are the most stable components in solution phase. Again, by X-ray crystallography we have established higher stoichiometry (1:4) in solid phase. This is probably due to macrocyclic nature of the chemosensor, H₂DTC5.1 which can accommodate metal ions (Zn²⁺ and Cu²⁺) in different stoichiometry, from 1:1 to 1:4 depending on reaction

condition. Experiments performed in solution phase probably unable to identify higher stoichiometries due to their low stabilities. Presence of different weak interactions ($\pi\cdots\pi$, CH $\cdots\pi$ and hydrogen bond) and nitrate ions facilitates the stabilization of higher stoichiometry complexes in solid phase.

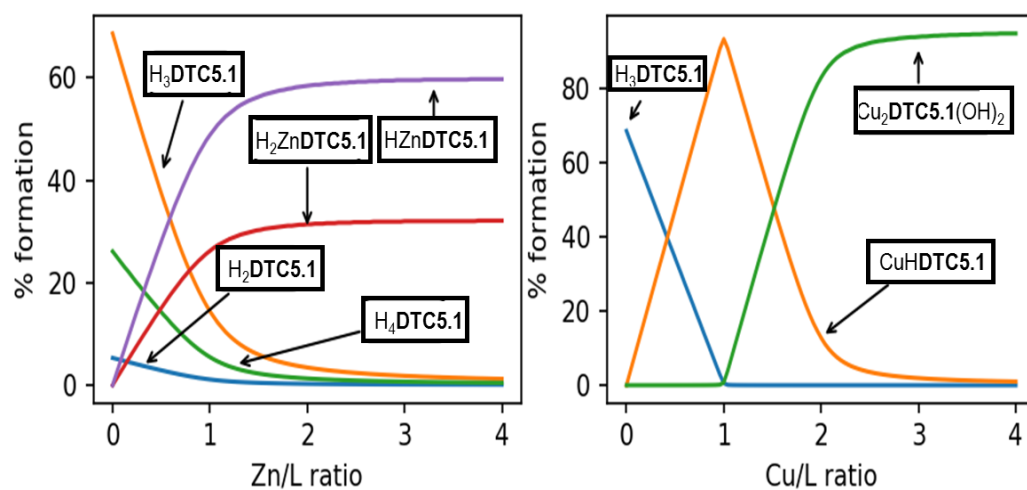


Figure 5.33 Simulated species distribution for the fluorometric titrations ($[H_2DTC5.1]=10\mu M$, $[M]=0$ to $40\mu M$, $pH=7.4$) using formation constants obtained from potentiometric titrations (**Tables 5.8** and **5.9**). Species with formation lower than 5% not represented.

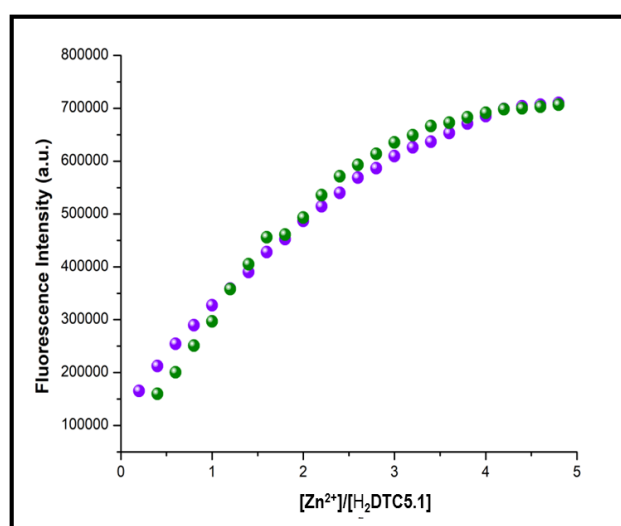


Figure 5.34 Fluorescence intensities versus molar ratio plot obtain from fluorescence spectra of H_2DTC ($10\mu M$) with gradual addition of Zn^{2+} ($0-48\mu M$) in HEPES buffer (10 mM) at pH

7.4 (violet colour represent the titration was carried out in water-methanol (9:1, v/v) mixture and green colour represent the same titration was carried out in water-ethanol (7:3, v/v) mixture).

5.3.11 Cell imaging study

In order to follow the real condition, fluorescence microscopy was used to study the cellular uptake of Zn²⁺ (20 μM) in the cells and a solution of the ligand (5 μM). A promiscuous green fluorescent signal is observed under the microscope that immediately disappears after the incorporation of Cu²⁺ (20 μM) (**Figure 5.35**). The same result was observed in the cellular uptake study of a solution of the ligand (5 μM) and Zn²⁺ (20 μM) simultaneously in presence or absence of Cu²⁺ (20 μM) (**Figure 5.36**). Thus, we can conclude that the cells readily internalize the Zn²⁺ complex producing promiscuous green fluorescence, which is immediately quenched after the addition of Cu²⁺. The nM detection sensitivity order for probe H₂DTC5.1 did not permitted to detect ultra-trace amount of Zn²⁺ or Cu²⁺ (~10⁻¹⁸–10⁻¹³ M) in human cells.^{5.54}

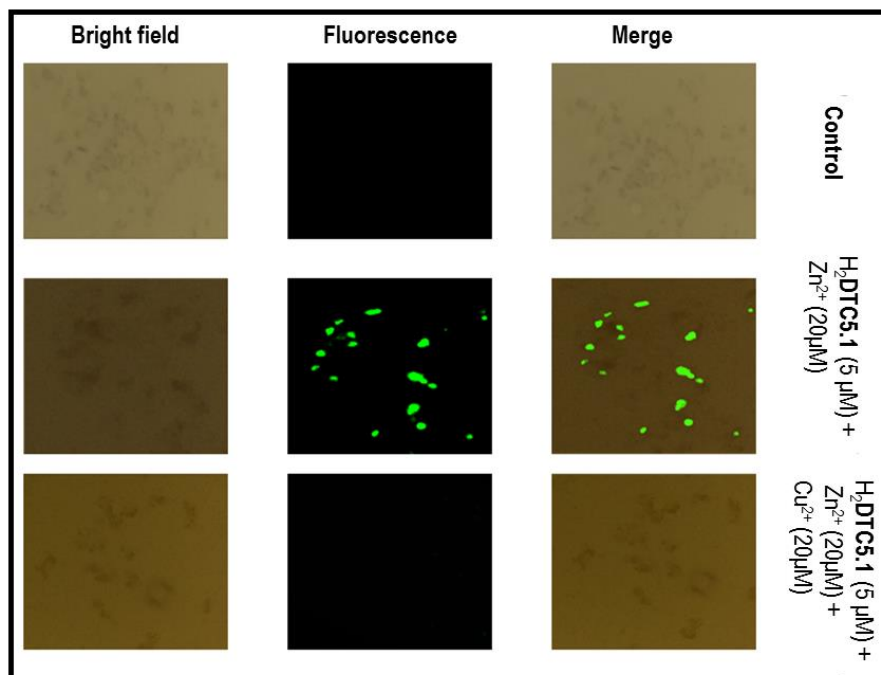


Figure 5.35 Bright field, fluorescence and merged microscopic images of untreated HeLa

(Control), cells treated with Zn²⁺ (20μM) + H₂DTC5.1 (5μM) and with Zn²⁺ (20μM) + H₂DTC5.1 (5μM) + Cu²⁺ (20μM).

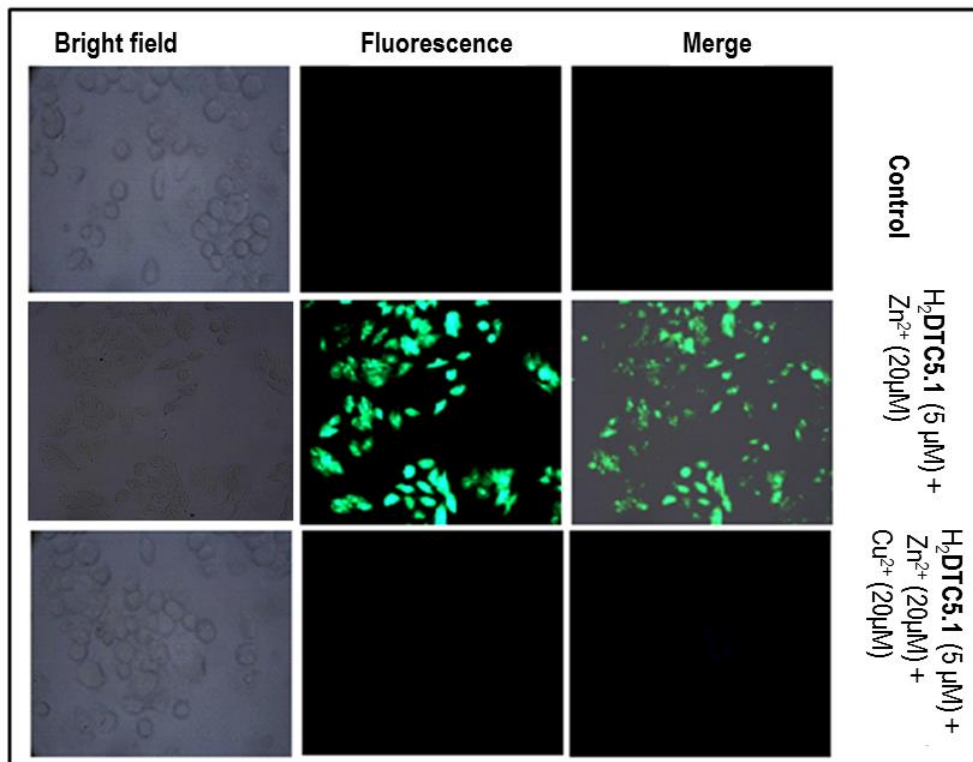


Figure 5.36 Bright field, fluorescence and merged microscopic images of untreated MDA-MB-468 (Control), cells treated with H₂DTC5.1 (5 μM) + Zn²⁺ (20μM) and with H₂DTC5.1 (5 μM) + Zn²⁺ (20μM) + Cu²⁺ (20μM).

5.3.12 Cell survival assay of H₂DTC5.1

The purpose of doing cytotoxicity assay is to explore the possibility of toxic effect of the ligand. The cytotoxicity assay clearly determines whether the ligand exerts any significant adverse effect on the cells. The percentage of survivability is a clear indication of the effects of a particular ligand on the cells. Hence higher bar graph percentage indicates biocompatibility whereas the lower bar graph percentage indicates enhanced mortality of the cells. The *in vitro* cytotoxicity of the H₂DTC5.1 is estimated for estimating the biocompatibility on WI38 (non-cancerous cells), MDA-MB-468 and HeLa (cancerous cells) cell line. The cells were treated with the different concentrations (0μM-100μM) of ligand for 24 h and followed by MTT assay. It is observed that the ligand exhibits no significant toxicity

in all the three cell lines even when treated with high concentrations (**Figures 5.37 and 5.38**, respectively). In addition, no appreciable increase of cytotoxicity (cell survival > 80%) was detected in the presence of experimental Zn²⁺ and Cu²⁺ concentration (20μM-50μM) (**Figure 5.39**), presumably H₂DTC5.1 could scavenge the metals and protect the cell. Henceforth we can conclude that the ligand is biocompatible and might be conducive for biological application.

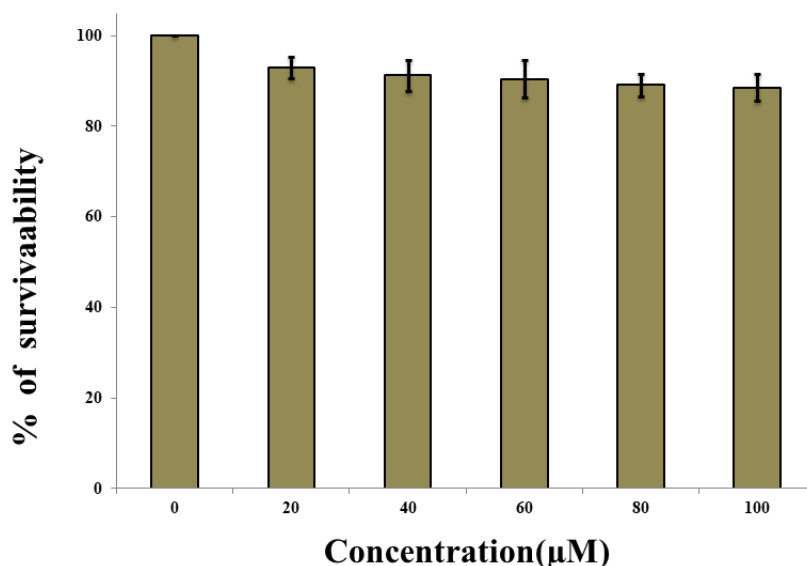


Figure 5.37 Cell survivability of WI38 cells exposed to H₂DTC5.1.

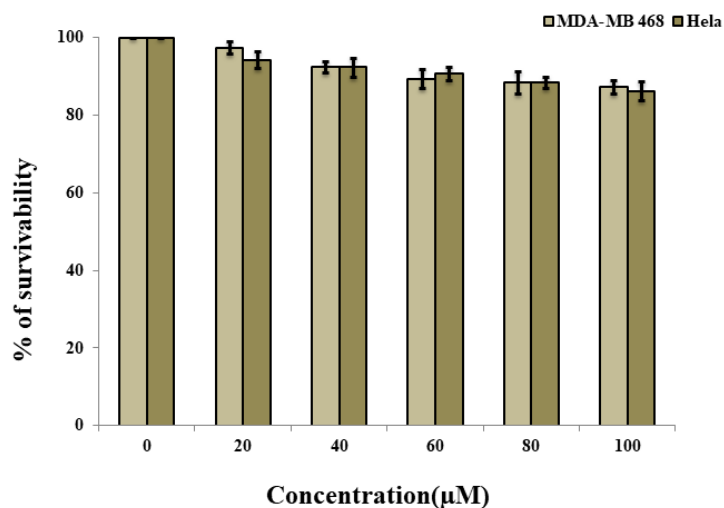


Figure 5.38 Cell survivability of MDA-MB 468 and HeLa cells exposed to H₂DTC5.1.

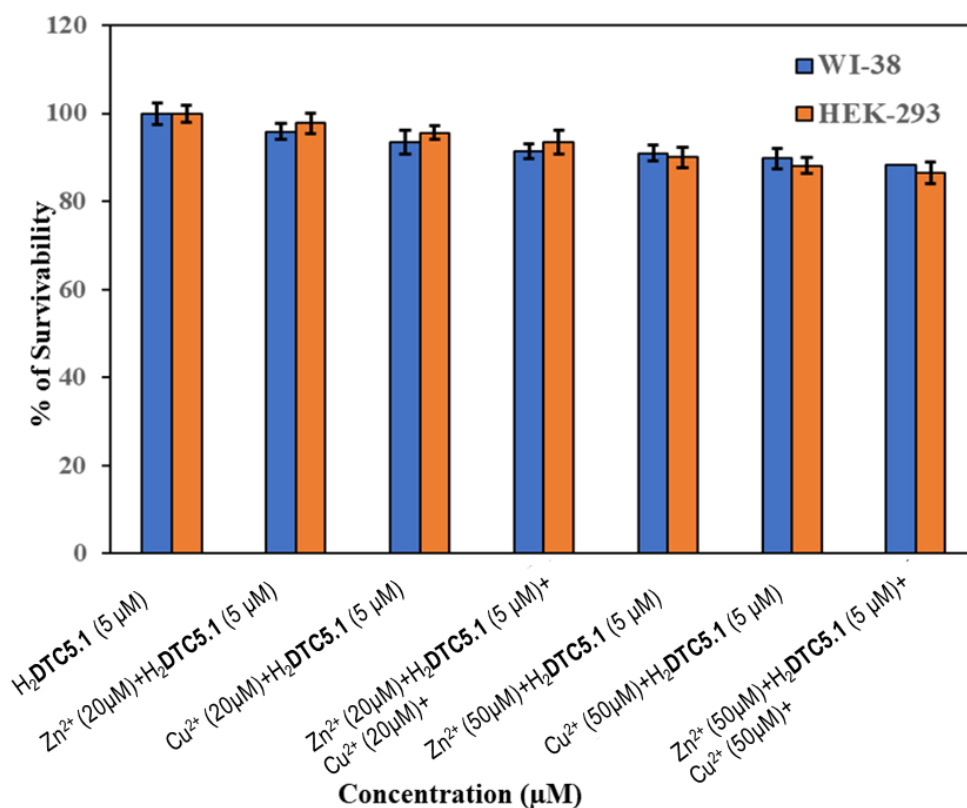


Figure 5.39 Cell survivability of WI38 and HEK-293 cells exposed to H₂DTC with Zn²⁺ and Cu²⁺ ions.

5.3.13 Computational study of the ligand

The UV-Vis absorption spectrum of the ligand was studied at room temperature in water: methanol (9:1, v/v, (10 mM) HEPES buffer pH=7.4). Experimentally the ligand shows one peak at 445 nm and we have computed using the TDDFT methodology the absorption energy associated, along with the oscillator strength and the main configurations. The ligand was studied for three possible tautomeric forms (**Scheme 5.2**). The experimental UV spectrum of the ligand is probably composed by the absorption bands of bis-keto form at room temperature because this tautomer is the most stable (2.2 kcal/mol more stable than the bis-enol form). Consequently, we only describe the TD-DFT study of the bis-keto. Moreover, the lowest lying absorption band computed for the *bis-keto* tautomer ($\lambda = 447$ nm) is in excellent agreement with the experimental one ($\lambda_{\text{exp}} = 445$ nm).

In the ground state the HOMO is basically composed by the six-membered rings and the conjugated exocyclic C=C and C=O bonds. The HOMO-1 and HOMO have the same energy (-5.330 eV). Similarly, the LUMO is basically composed by the π -systems, including the exocyclic C=C bond and the conjugated lone pair of the nitrogen atoms. The energy difference between the HOMO and LUMO is 2.969 eV. The calculated lowest lying absorption band is located at 447 nm for the *bis*-keto form of ligand (see **Figure 5.40**). This absorption band can be assigned to the S₀→S₁ transition and attributed to two electronic transitions: HOMO→LUMO (50%) and HOMO-1→LUMO+1 (50%). The theoretical value is in very good agreement with the experimental absorption value ($\lambda_{\text{exp}} = 445 \text{ nm}$) thus confirming the existence of the *bis*-keto form in solution.

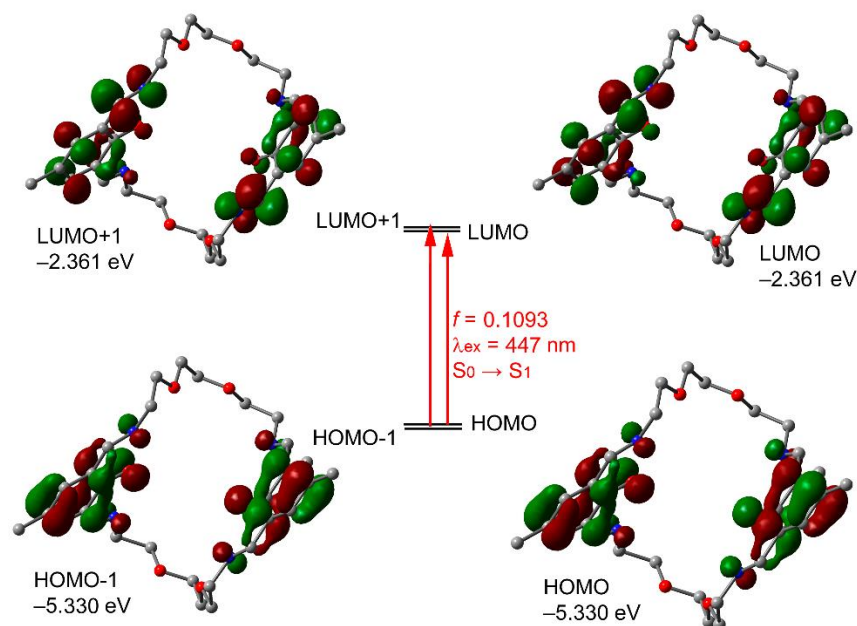


Figure 5.40 Molecular orbitals involved in the UV-Vis absorption of the *bis*-keto form of the ligand at the B3LYP/6-31+G* level of theory.

We have also performed the TD-DFT study of the Zn-complex. Unfortunately, the Cu-complex was not possible to analyze using the TD-DFT calculations likely due to the quintuplet nature of the ground state (high spin configuration). However, the PET-OFF

behavior observed only for the Cu²⁺ complex can be explained in terms of the conformation adopted by the ligand in this complex, as revealed by X-ray experiments. That is, a perfect π - π face-to-face stacking only observed in the Cu²⁺ complex (see **Figure 5.5**) provides a suitable explanation for the quenching of fluorescence in the ligand upon complexation.

In the ground state (S_0) of the Zn²⁺ complex, the HOMO is composed by two phenolic aromatic moieties of the ligands and the conjugated C=N bonds (**Figure 5.41a**). The LUMO is basically composed by the antibonding C=N π orbital. The energy difference between the HOMO and LUMO is 2.741 eV. To get better insight into the experimental absorption values TDDFT calculations were done for the complex on the basis of the X-ray geometry. The calculated absorption energy associated with its oscillator strength, the main configurations and their assignments of the lowest-lying transition in Zn²⁺ complex are given in **Figure 5.41**. This singlet \rightarrow singlet absorption band corresponds to the $S_0 \rightarrow S_3$ excitation (3.1002 eV, $\lambda = 400$ nm and $f = 0.0966$). This single excitation can be attributed to HOMO-2 \rightarrow LUMO, and HOMO \rightarrow LUMO transitions (**Figure 5.41b**), that can be assigned to $\pi(L) \rightarrow \pi^*(L)$ transitions with ILCT character. The experimental value ($\lambda_{\text{exp}} = 413$ nm) is in reasonable agreement with the theoretical one (400 nm). The essential contribution is the HOMO \rightarrow LUMO excitation configuration which is fluorophore-based, and consequently, the fluorescence originates from this transition. The atomic orbitals of the metal center are not involved in the transition and most of the HOMO and LUMO in the Zn(II) complex resemble those of the free sensor. In fact, only a slight alteration of the electron distribution in the LUMO is observed (smaller contribution of the aromatic ring and larger contribution of the imidic bond with respect to the free ligand) that likely explains the chelate enhanced fluorescence.

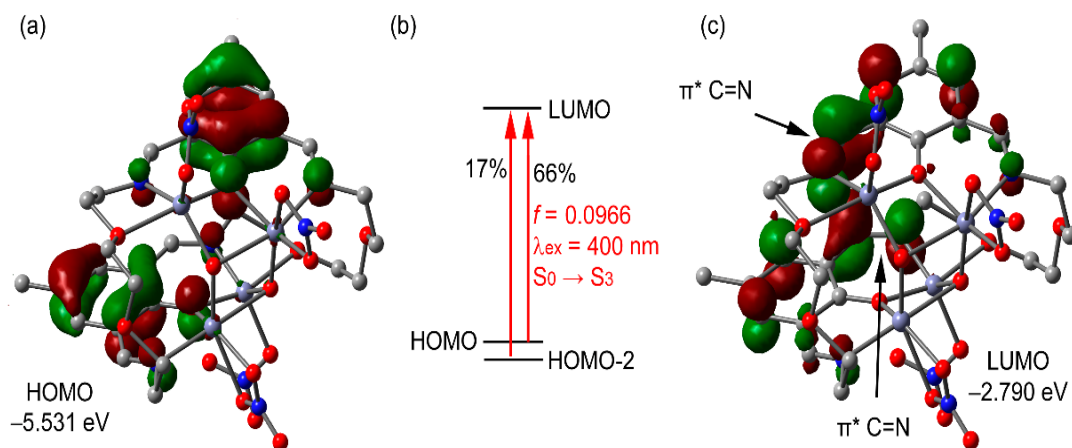


Figure 5.41 (a,c) Plot of the HOMO and LUMO. (b) Frontier molecular orbitals involved in the lowest lying observable UV-Vis absorption of complex **5.1**.

5.4 Conclusion

In summary, we have successfully developed a unique multifunctional aza-crown based Schiff base, **H₂DTC5.1** as a “turn-on” fluorescence receptor for Zn²⁺ ion and “turn-off” for Cu²⁺ ion. In case of Zn²⁺, the fluorescence enhancement originates from the coordination of deprotonated receptor (**DTC5.1²⁻**) through the imine nitrogen, phenoxido oxygen and oxygen atoms of tetraaza-30-crown-8 (CHEF effect). Whereas, addition of Cu²⁺ ions to **H₂DTC5.1** completely quenches the fluorescence response due to ligand to metal charge transfer (LMCT) between **H₂DTC5.1** and the paramagnetic Cu(II) ions (chelation enhanced quenching, CHEQ).

The macrocyclic nature of the chemosensor directs the accommodation of more than one metal centres in the ligand system. pH-potentiometric titrations confirm 1:1 and 2:1 binding stoichiometry between the metal ions (Zn²⁺ and Cu²⁺) and the chemosensor in dilute solutions with a high water content. Interestingly, 1:4, **H₂DTC5.1** : metal, binding stoichiometry has been established in solid phase using X-ray crystallography. The presence of higher number of metal centers and nitrate ions probably play a crucial role in their

isolation in solid phase. Also, different supramolecular interactions like strong $\pi\cdots\pi$ stacking facilitate the crystallization process.

Reversibility and regeneration of the chemosensor have been examined in the presence of Na₂EDTA. Metal-chemosensor complexation is further studied by DFT and TDDFT calculations. We are also successful to reveal its practical application by performing bio-imaging study of H₂DTC**5.1** using MDA-MB-468 cells. Furthermore, the probe is applied to detect intracellular Zn²⁺ and Cu²⁺ in live cells with no significant cytotoxicity.

5.5 References

- (5.1) X. H. Qian and Z. C. Xu, *Chem. Soc. Rev.* 2015, **44**, 4487–4493.
- (5.2) Y. Yang, Q. Zhao, W. Feng and F. Li, *Chem. Rev.* 2013, **113**, 192–270.
- (5.3) M. Li, X. J. Jiang, H. H. Wu, H. L. Lu, H. Y. Li, H. Xu, S. Q. Zang and T. C. W. Mak, *Dalton Trans.* 2015, **44**, 17326–17334.
- (5.4) L. Wang, D. D. Ye, W.X. Li, Y. Y. Liu, L. H. Li, W. L. Zhang and L. Ni, *Spectrochim. Acta A*, 2017, **183**, 291–297.
- (5.5) G. Chen, Z. Guo, G. Zeng and L. Tang, *Analyst.* 2015, **140**, 5400–5443.
- (5.6) Quang, D. T.; Kim, J. S. Fluoro- and Chromogenic Chemodosimeters for Heavy Metal Ion Detection in Solution and Biospecimens. *Chem. Rev.*, 2010, **110**, 6280–6301.
- (5.7) L. Tang, F. Li, M. Liu and R. Nandhakumar, *Spectrochim. Acta A.*, 2011, **78**, 1168–1172.
- (5.8) S. C. Burdette and S. J. Lippard, *Coord. Chem. Rev.*, 2001, **216**, 333–361.
- (5.9) S. L. Sensi, P. Paoletti, A. I. Bush and I. Sekler, *Nat. Rev. Neurosci.*, 2009, **10**, 780–791.
- (5.10) S. J. Lippard and J. M. Berg, *Principles of Bioinorganic Chemistry*. University Science Books: Mill Valley, **1994**.
- (5.11) G. K. Andrews, *Biometals.*, 2001, **14**, 223–237.
- (5.12) J. M. Berg and Y. Shi, *Science*, 1996, **271**, 1081–1085.
- (5.13) J. E. Coleman, *Curr. Opin. Chem. Biol.*, 1998, **2**, 222–234.
- (5.14) A. I. Bush, W. H. Pettingell, G. Multhaup, M. D. Paradis, J. P. Vonsattel, J. F. Gusella, K. Beyreuther, C. L. Masters and R. E. Tanzi, *Science*, 1994, **265**, 1464–1467.
- (5.15) A. I. Bush and R. E. Tanzi, *Proc. Natl. Acad. Sci. U. S. A.*, 2002, **99**, 7317–7319.

- (5.16) H. Tapiero, D. M. Townsend and K. D. Tew, *Biomed.Pharmacother*, 2003, **57**, 386–398.
- (5.17) D. J. Waggoner, T. B. Bart and J. D. Gitlin, *Neurobiol. Dis.*, 1999, **6**, 221–230.
- (5.18) P. G. Georgopoulos, A. Roy, M. J. Yonone-Lioy, R. E. Opiekun and P. J. Lioy, *J. Toxicol. Environ. Health Part B*, 2001, **4**, 341–394.
- (5.19) C. M. Lim, M. A. Cater, J. F. Mercer and S. L. Fontaine, *Biochem. Biophys. Res. Commun.*, 2006, **348**, 428–436.
- (5.20) C. D. Syme, R. C. Nadal, S. E. Rigby and J. H. Viles, *J. Biol. Chem.*, 2004, **279**, 18169–18177.
- (5.21) G. Manfredi and Z. Xu, *Mitochondrion.*, 2005, **5**, 77–87.
- (5.22) J. Valentine, B. G. Hart and J. R. Winkler, *Proc. Natl. Acad. Sci. U. S. A.*, 2008, **130**, 6898–6899.
- (5.23) G. Meloni, P. Faller and M. Vasak, *J. Biol. Chem.*, 2007, **282**, 16068–16078.
- (5.24) (a) A. Helal, S. H. Lee, S. H. Kim and H. S. Kim, *Tetrahedron Letters*, 2010, **51**, 3531–3535. (b) S. Khatua, J. Kang and D. G. Churchill, *New J. Chem.*, 2010, **34**, 1163–1169. (c) X. Zhou, B. Yu, Y. Guo, X. Tang, H. Zhang and W. Liu, *Inorg. Chem.*, 2010, **49**, 4002–4007. (d) Y. Zhang, X. Guo, W. Si, L. Jia and X. Qian *Org. Lett.*, 2008, **10**, 473–476. (e) Y. Mikata, A. Yamanaka, A. Yamashita and S. Yano, *Inorganic Chemistry*, 2008, **47**, 7295–7301. (f) Y. Mikata, M. Wakamatsu, A. Kawamura, N. Yamanaka, S. Yano, A. Odani, K. Morihiro and S. Tamotsu, *Inorganic Chemistry*, 2006, **45**, 9262–9268. (g) Y. Mikata, K. Kawata, S. Iwatsuki and H. Konno, *Inorg. Chem.*, 2012, **51**, 1859–1865. (h) P. D. Zalewski, I. J. Forbes, R. F. Seamark, R. Borlinghaus, W. H. Betts, S. F. Lincoln and A. D. Ward, *Chem. Biol.*, 1994, **1**, 153–161. (i) B. A. Wong, S. Friedle and S. J. Lippard, *Inorg. Chem.*, 2009, **48**, 7009–7011. (j) P. Rivera-Fuentes, A. T. Wrobel, M. L. Zastrow, M. Khan, J. Georgiou, T. T. Luyben, J. C. Roder, K. Okamoto and S. J. Lippard, *Chem. Sci.*, 2015, **6**,

- 1944–1948. (k) J. M. Goldberg, F. Wang, C. D. Sessler, N. W. Vogler, D. Y. Zhang, W. H. Loucks, T. Tzounopoulos and S. J. Lippard, *J. Am. Chem. Soc.*, 2018, **140**, 2020–2023. (l) K. Komatsu, Y. Urano, H. Kojima and T. Nagano, *J. Am. Chem. Soc.*, 2007, **129**, 13447–13454. (m) M. Taki, J. L. Wolford and T. V. O'Halloran, *J. Am. Chem. Soc.*, 2004, **126**, 712–713. (n) T. Koike, T. Watanabe, S. Aoki, E. Kimura and M. Shiro, *J. Am. Chem. Soc.*, 1996, **118**, 12696–12703. (o) X. Yan, J. J. Kim, H. S. Jeong, Y. K. Moon, Y. K. Cho, S. Ahn, S. B. Jun, H. Kim and Y. You, *Inorg. Chem.*, 2017, **56**, 4332–4346. (p) A. K. Bhanja, C. Patra, S. Mondal, S. Mishra, K. D. Saha and C. Sinha, *Sensors and Actuators B*, 2017, **252**, 257–267.
- (5.25) (a) B. P. Vrajesh, *An Introduction of Crown Ether Schiff Bases & Its Applications*. LAP Lambert Academic Publishing. (b) M. Hiraoka (Ed), *Elsevier Science*, 1992. (c) D. A. Safin, M. G. Babashkina and Y. Garcia, *Dalton Trans.*, 2013, **42**, 1969–1972. (d) Shu-lan Cai, Fa-mei Feng and Fu-an Liu, *Journal of Dispersion Science and Technology*, 2016, **37**, 1170–1177.
- (5.26) (a) I. A. Kahwa, S. Folkes, D. J. Williams, S. V. Ley, C. A. O'Mahoney and G. L. McPherson, *J. CHEM. SOC. CHEM. COMMUN.*, 1989, 1531–1533. (b) K. D. Matthews, I. A. Kahwa and D. J. Williams, *Inorg. Chem.* 1994, **33**, 1382–1387. (c) H. Plenio, R. Diodone and D. Badura, *Angew. Chem. Int. Ed. Engl.*, 1997, **36**, 156–158. (d) L. Tei, M. Arca, M. C. Aragoni, A. Bencini, A. J. Blake, C. Caltagirone, F. A. Devillanova, P. Fornasari, A. Garau, F. Isaia, V. Lippolis, M. Schroder, S. J. Teat and B. Valtancoli, *Inorg. Chem.*, 2003, **42**, 8690–8701.
- (5.27) (a) J. Mandal, P. Ghorai, K. Pal, P. Karmakar and A. Saha, *Journal of Luminescence*, 2019, **205**, 14–22. (b) P. Ghorai, S. Banerjee, D. Nag, S. K. Mukhopadhyay and A. Saha, *Journal of Luminescence*, 2019, **205**, 197–209.
- (5.28) D. G. Churchill, *J. Chem. Educ.*, 2006, **83**, 1798–1803.

- (5.29) G. M. Sheldrick, SAINT, Version 6.02, SADABS, Version 2.03, Bruker AXS Inc., Madison, Wisconsin, 2002.
- (5.30) G. M. Sheldrick, SADABS: Software for Empirical Absorption Correction, University of Gottingen, Institute fur Anorganische Chemieder Universitat, Gottingen, Germany, 1999-2003.
- (5.31) G. M. Sheldrick, *ActaCryst.*, 2015, **C71**, 3-8.
- (5.32) R. R. Gagne, C. L. Spiro, T. J. Smith, C. A. Hamann, W. R. Thies and A. K. Schiemke, *J. Am. Chem. Soc.*, 1981, **103**, 4073–4081.
- (5.33) P. Gans, A. Sabatini and A. Vacca, *Annali di Chimica*, 1999, **89**, 45–49.
- (5.34) L. Alderighi, P. Gans, A. Ienco, D. Peters, A. Sabatini and A. Vacca, *Coord. Chem. Rev.*, 1999, **184**, 311–318.
- (5.35) G. Gran, *Analyst*, 1952, **77**, 661–671.
- (5.36) F. J. C. Rossotti and H. Rossotti, *J. Chem. Educ.*, 1965, **42**, 375.
- (5.37) P. Gans, A. Sabatini and A. Vacca, *Talanta*, 1996, **43**, 1739–1753.
- (5.38) (a) A. Pramanik, D. Laha, S. Chattopadhyay, S. K. Dash, S. Roy, P. Pramanik and P. Karmakar, *Materials Science and Engineering C*, 2016, **65**, 327–337. (b) D. Laha, A. Pramanik, S. Chattopadhyay, S. K. Dash, S. Roy, P. Pramanik, P. Karmakar, *RSC Adv.*, 2015, **5**, 68169–68178.
- (5.39) J. P. Perdew, *Phys. Rev. B*, 1986, **33**, 8822-8824.
- (5.40) (a) M. E. Casida, C. Jamoroski, K. C. Casida and D. R. Salahub, *J. Chem. Phys.*, 1998, **108**, 4439–4449. (b) R. E. Stratmann, G. E. Scuseria and M. J. Frisch, *J. Chem. Phys.*, 1998, **109**, 8218–8224. (c) R. Bauernschmitt and R. Ahlrichs, *Chem. Phys. Lett.*, 1996, **256**, 454–464.

(5.41) (a) M. Cossi, N. Rega, G. Scalmani and V. Barone, *J. Comput. Chem.*, 2003, **24**, 669–681. (b) M. Cossi and V. Barone, *J. Chem. Phys.*, 2001, **115**, 4708–4717. (c) V. Barone and M. Cossi, *J. Phys. Chem. A*, 1998, **102**, 1995–2001.

(5.42) M. J. Frisch, G.W. Trucks, H. B. Schlegel, G.E. Scuseria, M. A. Robb, J. R. Cheeseman, G. Scalmani, V. Barone, B. Mennucci, G.A. Petersson, H. Nakatsuji, M. Caricato, X. Li, H. P. Hratchian, A. F. Izmaylov, J. Bloino, G. Zheng, J. L. Sonnenberg, M. Hada, M. Ehara, K. Toyota, R. Fukuda, J. Hasegawa, M. Ishida, T. Nakajima, Y. Honda, O. Kitao, H. Nakai, T. Vreven, J. A. Montgomery, Jr. J. E. Peralta, F. Ogliaro, M. Bearpark, J. J. Heyd, E. Brothers, K. N. Kudin, V. N. Staroverov, R. Kobayashi, J. Normand, K. Raghavachari, A. Rendell, J. C. Burant, S.S. Iyengar, J. Tomasi, M. Cossi, N. Rega, J. M. Millam, M. Klene, J.E. Knox, J. B. Cross, V. Bakken, C. Adamo, J. Jaramillo, R. Gomperts, R. E. Stratmann, O. Yazyev, A. J. Austin, R. Cammi, C. Pomelli, J. W. Ochterski, R. L. Martin, K. Morokuma, V. G. Zakrzewski, G. A. Voth, P. Salvador, J. J. Dannenberg, S. Dapprich, A. D. Daniels, Ö. Farkas, J. B. Foresman, J. V. Ortiz, J. Cioslowski and D. J. Fox, GAUSSIAN09, Revision D.01, Gaussian Inc. Wallingford, CT, 2009.

(5.43) (a) N. M.S. Maekawa, Thesis, University of the Ryukyus, Okinawa, **1999**. (b) Y. Miyazato, E. Asato, M. Ohba and T. Wada, *Chem. Soc. Jpn.* 2012, **85**, 895–901.

(5.44) (a) A. Panja, T. Matsuo, S. Nagao and S. Hirota, *Inorg. Chem.*, 2011, **50**, 11437–11445. (b) G. Parkin, *Chem. Rev.*, 2004, **104**, 699–767.

(5.45) A. W. Addison, T. N. Rao, J. Reedjik, J. V. Rijn, C. G. Verschoor, *Dalton Trans.*, 1984, 1349–1356.

(5.46) M. Kumar, R. Kumar, V. Bhalla, P. R. Sharma, T. Kaur, Y. Qurishi, *Dalton Trans.*, 2012, **41**, 408–412.

(5.47) W. T. Tak and S. C. Yoon, *J. Nephrol.*, 2001, **20**, 863–871.

- (5.48) D. J. Eide, *Biochim. Biophys. Acta*, 2006, **1763**, 711–722.
- (5.49) A. B. Pradhan, S. K. Mandal, S. Banerjee, A. Mukherjee, S. Das, A. R. K. Bukhsh and A. Saha, *Polyhedron*, 2015, **94**, 75–82.
- (5.50) J. Mandal, P. Ghorai, P. Brandao, K. Pal, P. Karmakar and A.Saha, *New J. Chem.*, 2018, **42**, 19818–19826.
- (5.51) M. Tumer, N. Deligonul, A. Golcu, E. Akgun, M. Dolaz, H. Demirelli and M. Digrak, *Transition Metal Chemistry*, 2006, **31**, 1–12.
- (5.52) H. Demirelli, M. Tumer and A. Golcu, *Chem. Soc. Jpn.*, 2006, **79**, 867–875.
- (5.53) D. Esteban-Gómez, C. Platas-Iglesias, F. Avecilla, A. de Blas and T. Rodríguez-Blas, *Eur. J. Inorg. Chem.*, 2007, **12**, 1635–1643.
- (5.54) H. Tapiero, D. M. Townsend and K. D. Tew, *Biomed Pharmacother*, 2003, **57**, 386–398.

Chapter 6

**Two pyridoxal derived Schiff base
chemosensors design for
fluorescence turn-on sensing of
Zn(II) ion in pure aqueous medium**

Abstract

Here, we have prepared two pyridoxal-based chemosensors (**HL6.1** and **HL6.2**) by reacting 2,2'-Thiobis(ethylamine)/1,2-Bis(2-aminoethoxy)ethane together with pyridoxal hydrochloride under ambient condition which are highly selective towards Zn(II) ion. Both the ligands and their Zn(II) bound complexes have been characterized by different spectroscopic studies, ESI-MS and CHN analyses. Absorbance and fluorescence properties of the chemosensors were investigated in pure aqueous solution (HEPES buffer at pH= 7.4) and found upto 20 times fluorescence enhancement in presence of Zn(II) ion. Chemosensors exhibit very weak fluorescence intensity (0.03 and 0.05) which enhance significantly (7-fold) upon addition of zinc ion (0.21 and 0.24). Low LOD values for zinc ion (7.47×10^{-8} M and 6.95×10^{-8} M) make the chemosensors ideal candidate for real life and biological applications. 1 : 1 **L6.1/6.2**: Zn complex binding stoichiometry has been achieved by Job's plot analysis and binding constant of complex **6.1** and **6.2** are found to be 1.5×10^5 and 1.46×10^5 M⁻¹. Theoretical calculations are performed in order to study binding mode of the chemosensors around Zn(II) center. In complex **6.1** coordination number around Zn(II) center is four and it has distorted tetrahedral geometry where sulphur (S) atom from the aliphatic part remains uncoordinated. In complex **6.2** coordination number around Zn(II) center is six and it has distorted octahedral geometry. In cell imaging study both the chemosensors are used to detect zinc ion in Human cervical cancer cell line HeLa grown in tissue culture.

6.1 Introduction

Zinc (II) is the second most abundant heavy metal ion found in the human body after Fe(III/II).^{6.1} Zn is present as a cofactor in many metalloproteins and metalloenzymes such as, zinc finger proteins (ZFPs), histone deacetylases (HDACs) and carbonic anhydrases (CAs).^{6.2} and it regulates some of the essential cellular functions,^{6.1} like gene expression,^{6.3} apoptosis^{6.4} and neurotransmission.^{6.5} It is found as free or loosely bound chelatable form in the brain,^{6.6} pancreas,^{6.7} and spermatozoa.^{6.8} Monitoring of this “free zinc” has great physiological prominence.^{6.9} In transgenic mouse model mobile zinc was used for detection and monitoring the development of prostate cancer.^{6.10} Lack of zinc ions within human body cause several diseases associated with mental retardation and digestive dysfunction because the majority of biological zinc ions are tightly sequestered by proteins.^{6.11} On the other hand, excess “free zinc” is responsible for severe neurological disorders such as Alzheimer's and Parkinson's diseases.^{6.12} Thus monitoring Zn(II) in biological processes suggest great demand in the design and development of efficient systems which can selectively and sensitively detect Zn(II) in living systems. Several analytical methods such as nuclear magnetic resonance (NMR), electron paramagnetic resonance (EPR), and electronic absorption spectroscopy is ineffective^{6.5} for detection of Zn(II) owing to its closed-shell [Ar]3d¹⁰ electronic configuration. Use of Atomic absorption spectroscopy for selective and sensitive detection of Zn(II) is disadvantageous due to its destructive nature.^{6.13} On the contrary use of fluorescent probes as fluorescence detection, i.e. fluorescence spectroscopy is most effective tool for sensing application showing its high sensitivity, selectivity, easy visualization, short response time for detection and realtime bio-imaging.^{6.14} Some commonly used receptors to detect Zn(II) ion are Dipicolylamine (DPA), coumarin, quinoline, bipyridine, triazole, imino diacetic acid, acyclic and cyclic polyamines, and Schiff-bases.^{6.15–6.20} Presence of nitrogen atoms of the above mentioned receptors serve as good binding sites for Zn(II) center. Zn(II)

bound receptor in presence of different fluorophoric units can induce effective signal transduction through a variety of photo-physical mechanisms.

Pyridoxal is one of the water-soluble naturally occurring vitamer of vitamin B6. Pyridoxal 5'-phosphate (PLP) is most active form of vitamin B6 which participates in more than 140 enzymatic reactions in our body like decarboxylation, transamination and racemization.^{6.21-6.23} Pyridoxal is also used as anticancer agent.^{6.24} It has been widely used in the areas of sensing and biosensing due to its bioactivity, solubility in aqueous medium, chelating ability, attractive photophysical properties and easy structural modifications.

In our continuous endeavour for design and synthesis of chemosensors for detection of different metal ions, we have synthesized two pyridoxal based Schiff-base ligands for selective detection of Zn(II) ions in pure aqueous medium. Schiff-based chemosensors are weakly fluorescent due to C=N bond isomerization and phenolic protons based excited-state intramolecular proton transfer (ESIPT) processes.^{6.25} Different spectroscopic techniques, elemental and ESI-MS⁺ analysis are deployed to study interaction between Zn²⁺ and chemosensors. Jobs plot analysis proves 1:1 metal:chemosensor binding stoichiometry. In presence of Zn²⁺ a 20-fold enhancement of emission intensity has been observed. The LOD values of the probes towards Zn²⁺ are 7.47×10^{-8} M and 6.95×10^{-8} M, respectively, lower than the WHO's guideline (76.5 μ M). Both the chemosensors exhibit large Stokes shift (~100 nm) in presence of Zn²⁺ ion. Cell imaging studies along with MTT assay signify its importance in the field of biology.

6.2 Experimental Section

6.2.1 Materials and physical measurements

All reagent or analytical grade chemicals and solvents were purchased from commercial sources and used without further purification. Elemental analysis for C, H and N was carried out using a Perkin–Elmer 240C elemental analyzer. Infrared spectra ($400\text{--}4000\text{ cm}^{-1}$) were recorded from KBr pellets on a Nicolet Magna IR 750 series-II FTIR spectrophotometer. Absorption spectra were measured using a Cary 60 spectrophotometer (Agilent) with a 1-cm-path-length quartz cell. Electron spray ionization mass (ESI-MS positive) spectra were recorded on a MICROMASS Q-TOF mass spectrometer. Emission spectra were collected using Fluoromax-4 spectrofluorimeter at room temperature (298 K) in HEPES buffer at pH= 7.4 solution under degassed condition. Fluorescence lifetime was measured using a time-resolved spectrofluorometer from IBH, UK. Measurements of ^1H NMR spectra were conducted using Bruker 400 and Bruker 300 spectrometer d_6 -DMSO solvent.

6.2.2 Synthesis of chemosensor HL6.1 [HL6.11=4,4'-(thiobis(ethane-2,1-diyl))bis(azanylylidene))bis(methanylylidene))bis(5-(hydroxymethyl)-2-methylpyridin-3ol)]

Pyridoxal hydrochloride (0.203 g, 1 mmol) and sodium acetate (0.328 g, 4 mmol) was stirred 30 minutes in 20 mL methanol solution. Then the solution was filtered and 5ml methanolic solution of 2,2'-Thiobis(ethylamine) (0.060 g, 0.5 mmol) was added. The mixture was stirred for 4 hours. After, evaporation of solvent yellow colored gummy mass was obtained.

Yield: 0.234 g (89%). Anal. Calc. for $\text{C}_{20}\text{H}_{26}\text{N}_4\text{O}_4\text{S}$: C 57.40%; H 6.26%; N 13.39%. Found: C 57.28%; H 6.28%; N 13.30%. IR (cm^{-1} , KBr): $\nu(\text{C}=\text{N})$ 1631s; $\nu(\text{O}-\text{H})$ 3362s(**Figure 6.1**).

ESI-MS (positive) in MeOH: The base peak was detected at $m/z = 419.13$, corresponding to $[\text{HL6.1}+1]^+$ (Figure 6.2). UV-Vis, λ_{max} (nm), (ϵ ($\text{dm}^3\text{mol}^{-1}\text{cm}^{-1}$)) in HEPES buffer at pH= 7.4: 335 (19953).

^1H NMR (d_6 -DMSO, 300 MHz) δ ppm: 8.93(-CH=N) (s, 1H), 7.85 (ArH) (s, 1H), 4.63(-CH₂) (s, 2H), 3.91- 3.87 (-CH₂) (t, 2H), 2.96- 2.91 (-CH₂) (t, 2H), 2.36 (Ar-CH₃) (s, 3H) (Figure 6.3).

^{13}C NMR (d_6 -DMSO, 75 MHz) δ ppm: 165.09 (-CH=N), 119.28-155.03 (Ar-C), 58.74 (-CH₂), 58.20 (-CH₂), 47.08 (-CH₂), 19.16 (-CH₃) (Figure 6.4).

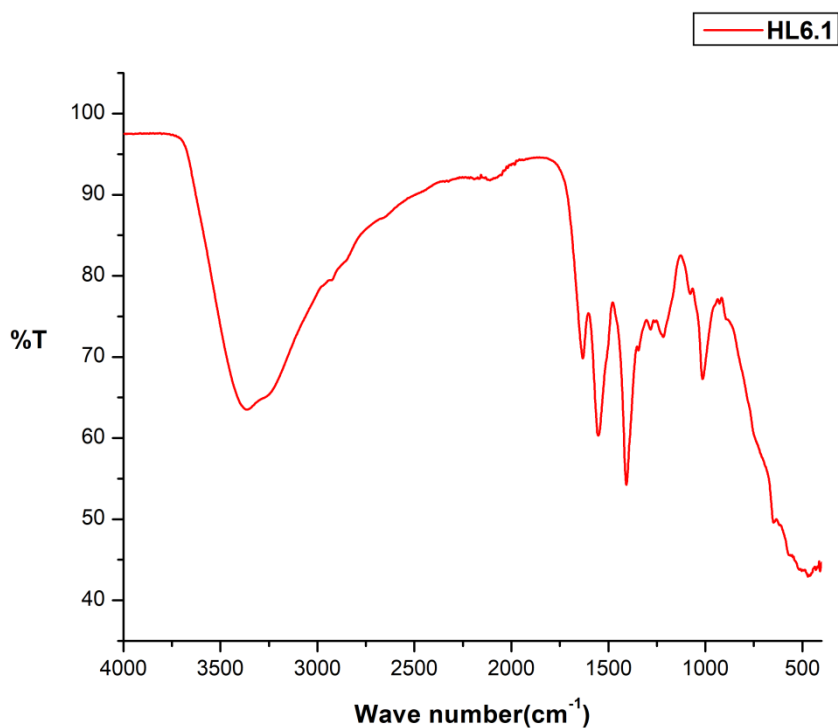


Figure 6.1 FTIR spectrum of chemosensor (HL6.1).

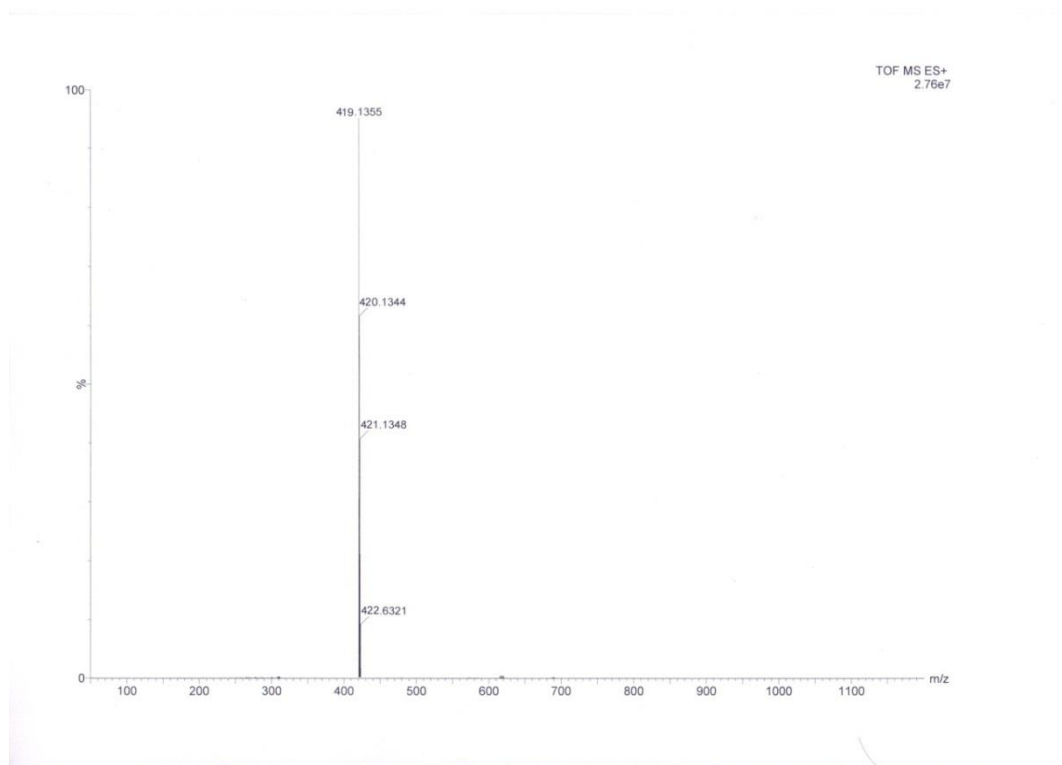


Figure 6.2 ESI-mass spectrum of chemosensor (HL6.1).

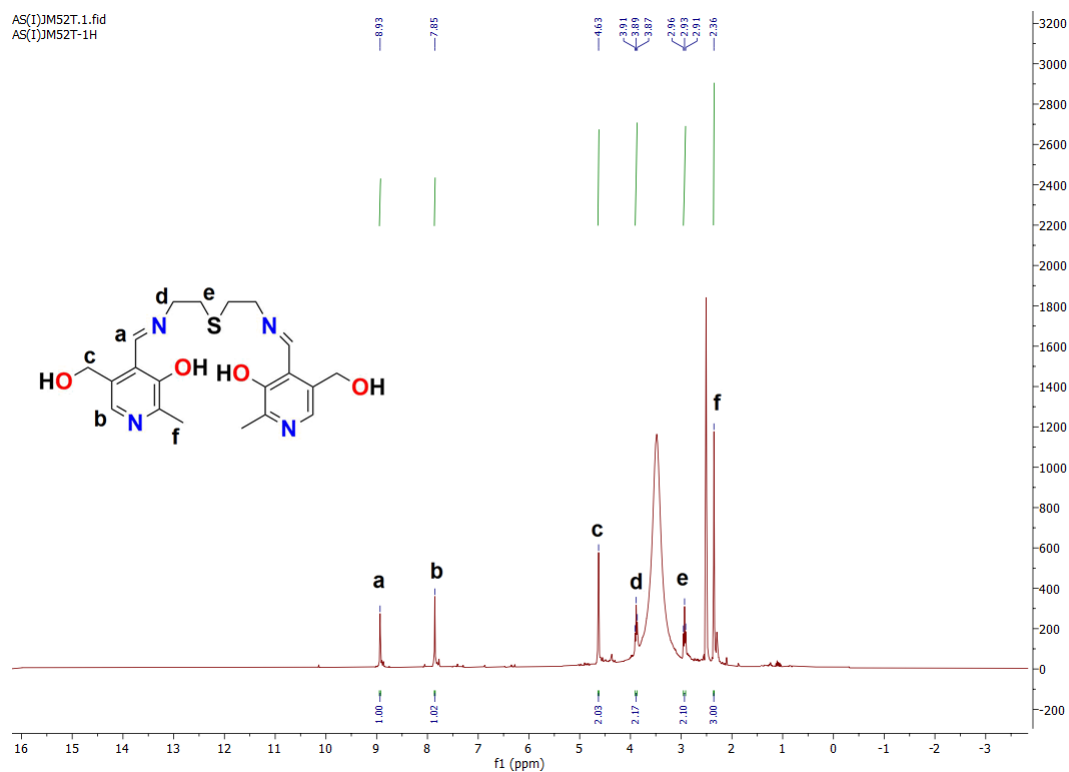


Figure 6.3 ^1H NMR of HL6.1 in d_6 -DMSO solvent.

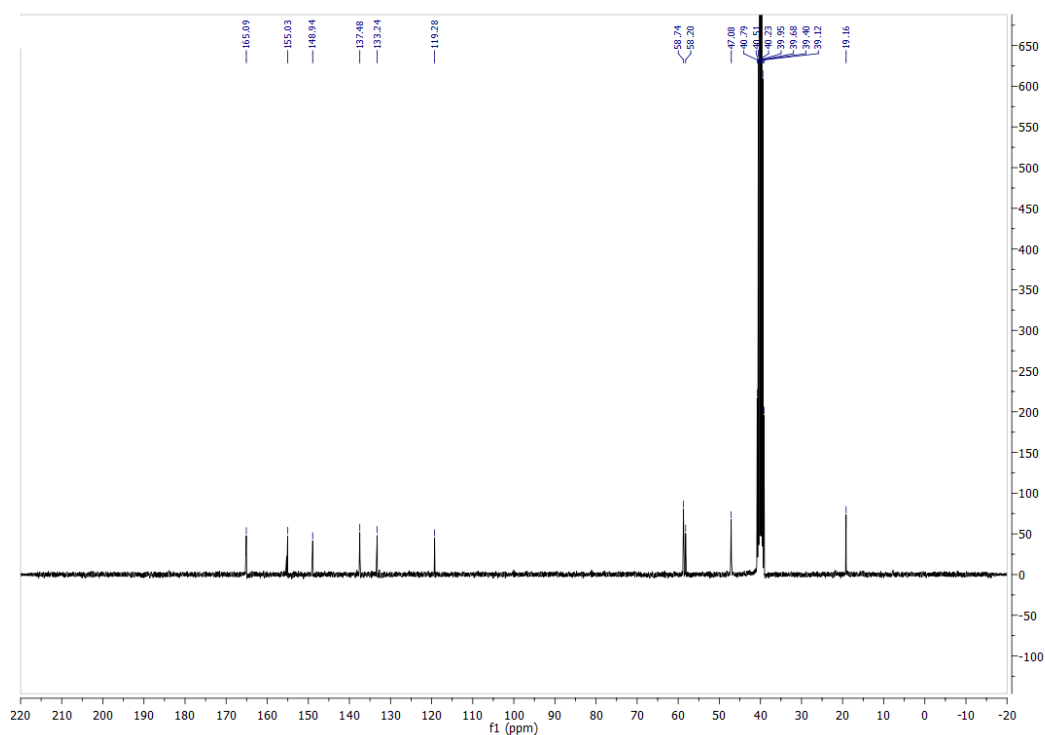


Figure 6.4 ^{13}C NMR of **HL6.1** in d_6 -DMSO solvent.

6.2.3 Synthesis of chemosensor **HL6.2** [**HL6.2**=4,4'-(5,8-dioxa-2,11-diazadodeca-1,11-diene-1,12-diyl)bis(5-(hydroxymethyl)-2-methylpyridin-3-ol)]

Pyridoxal hydrochloride (0.203 g, 1 mmol) and sodium acetate (0.328 g, 4 mmol) was stirred 30 minutes in 20 mL methanol solution. Then the solution was filtered and 5ml methanolic solution of 1,2-Bis(2-aminoethoxy)ethane (0.074 g, 0.5 mmol) was added. The mixture was stirred for 4 hours. After, evaporation of solvent yellow colored gummy mass was obtained.

Yield: 0.256 g (92%). Anal. Calc. for $\text{C}_{22}\text{H}_{30}\text{N}_4\text{O}_6$: C 59.18%; H 6.77%; N 12.55%. Found: C 59.08%; H 6.70%; N 12.49%. IR (cm^{-1} , KBr): $\nu(\text{C}=\text{N})$ 1635s; $\nu(\text{O}-\text{H})$ 3364s (**Figure 6.5**).

ESI-MS (positive) in MeOH: The base peak was detected at $m/z = 447.11$, corresponding to [**HL6.2**+1] $^+$ (**Figure 6.6**). UV-Vis, λ_{max} (nm), (ϵ ($\text{dm}^3\text{mol}^{-1}\text{cm}^{-1}$)) in HEPES buffer at pH=7.4: 335 (18296).

^1H NMR (d_6 -DMSO, 300 MHz) δ ppm: 8.87(-CH=N) (s, 1H) , 7.86 (ArH) (s, 1H), 4.63 (-CH₂) (s, 2H) 3.81-3.57 (-CH₂) (m, 6H), 2.35 (Ar-CH₃) (s, 3H) (**Figure 6.7**).

^{13}C NMR (d_6 -DMSO, 75 MHz) δ ppm: 165.05 (-CH=N), 155.01-119.32 (Ar-C), 70.13 (-CH₂), 58.67 (-CH₂), 58.15 (-CH₂), 19.11(-CH₃) (**Figure 6.8**).

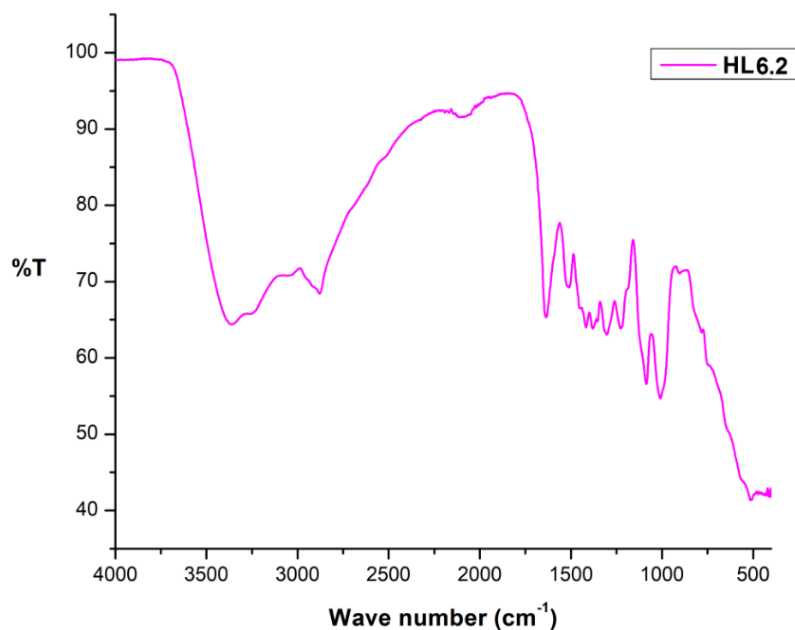


Figure 6.5 FTIR spectrum of chemosensor (**HL6.2**).

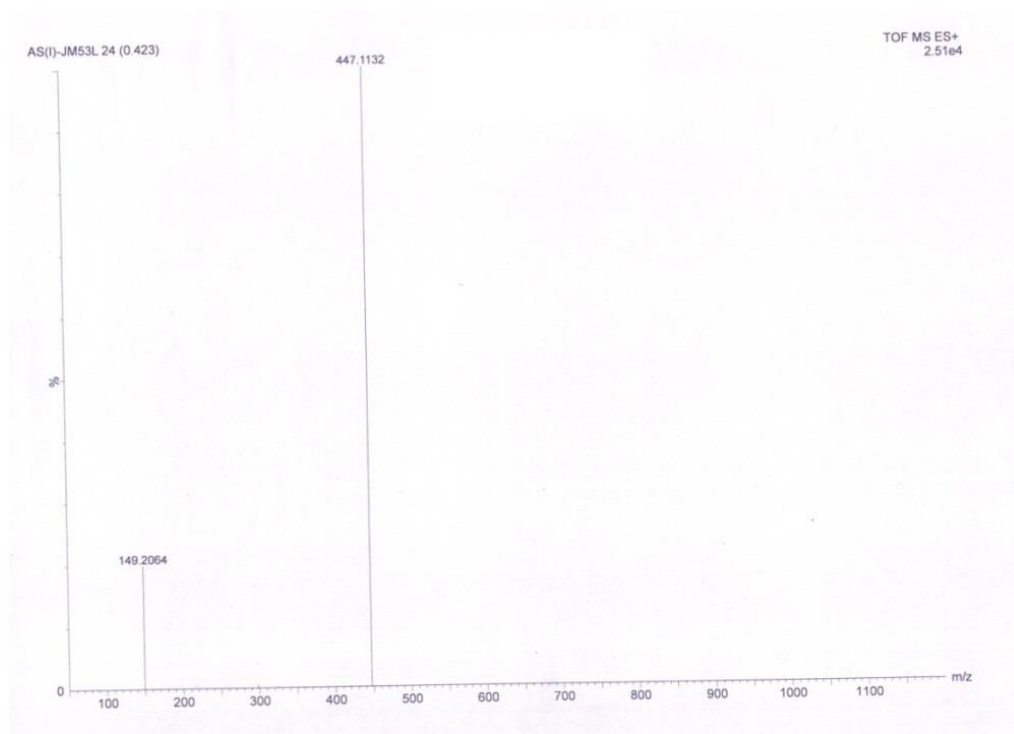


Figure 6.6 ESI-mass spectrum of chemosensor (**HL6.2**).

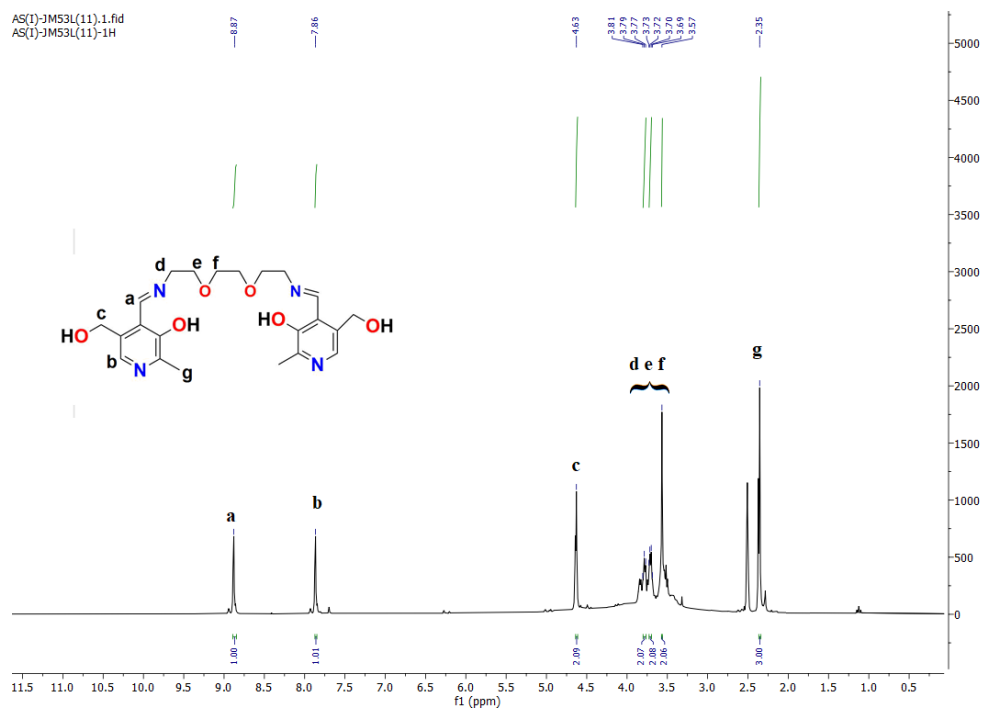


Figure 6.7 ^1H NMR of **HL6.2** in d_6 -DMSO solvent.

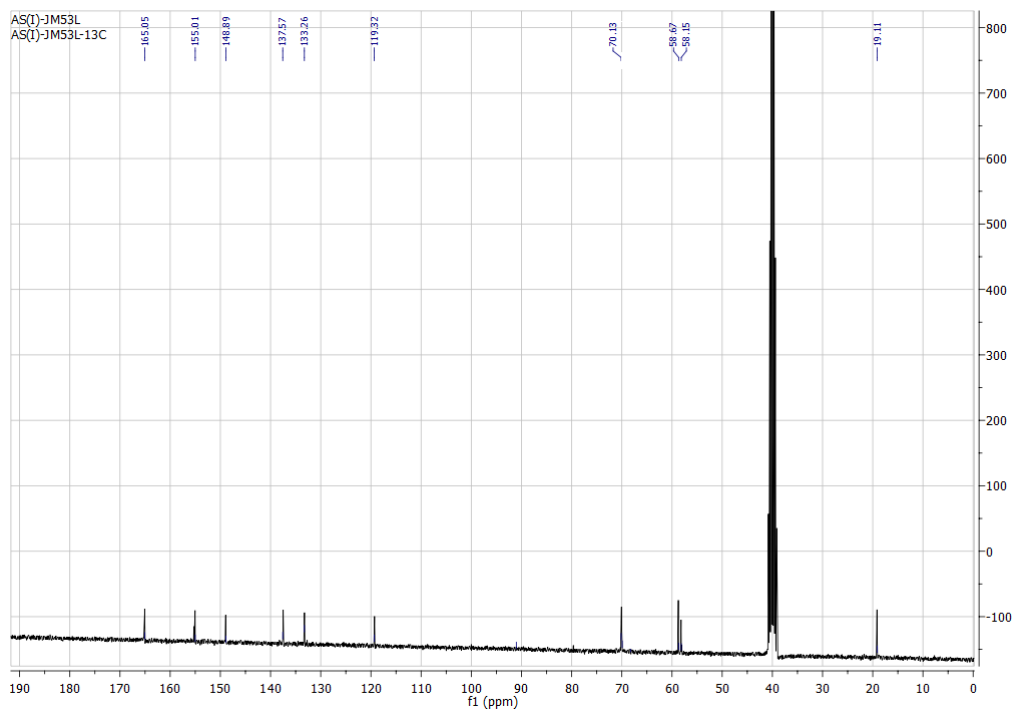


Figure 6.8 ^{13}C NMR of **HL6.2** in d_6 -DMSO solvent.

6.2.4 Synthesis of complex (6.1)

A 2 mL methanolic solution of zinc nitrate hexahydrate (1.0 mmol, 0.297 g) was added drop wise to 20 mL methanolic solution of **HL6.1** (1.0 mmol, 0.418 g) followed by addition of triethylamine (2.0 mmol, ~0.4 mL) and the resultant reaction mixture was stirred for ca. 4 h. Yellow coloured solid mass was obtained in high yield after slow evaporation of the solvent.

Yield: 0.607 g (85%). Anal. Calc. for $C_{20}H_{24}N_4O_4SZn$: C 49.85%; H 5.02%; N 11.63%.

Found: C 49.78%; H 4.98%; N 11.59%. IR (cm^{-1} , KBr): $\nu(C-O)$ 1021s, $\nu(C=N)$ 1626s; $\nu(O-H)$ 3372s (**Figure 6.9**). ESI-MS (positive) in MeOH: The base peak was detected at $m/z = 597.42$, corresponding to $[ZnL6.1(CH_3CN)_2(H_2O)+1]^+$ (**Figure 6.10**). UV-Vis, λ_{max} (nm), (ϵ ($dm^3mol^{-1}cm^{-1}$)) in HEPES buffer at pH= 7.4: 385(20895).

1H NMR (d_6 -DMSO, 300 MHz) δ ppm: 2.37 (Ar- CH_3) (s, 3H), 2.94-4.54 ($-CH_2$) (6H), 7.55-7.93 (ArH) (m, 2H), 8.85-9.03 ($-CH=N$) (s, 2H) (**Figure 6.11**).

^{13}C NMR (d_6 -DMSO, 75 MHz) δ ppm: 20.57 ($-CH_3$), 46.25-60.37($-CH_2$), 117.66-168.97 (Ar-C), 175.46 ($-CH=N$) (**Figure 6.12**).

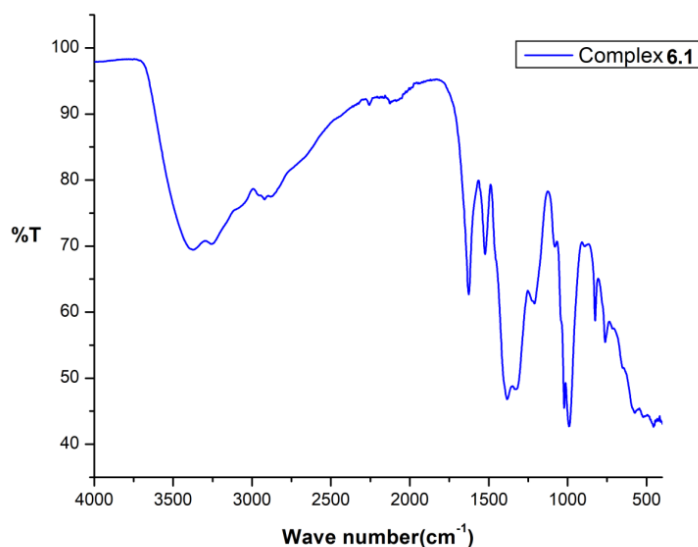


Figure 6.9 FTIR spectrum of complex **6.1**.

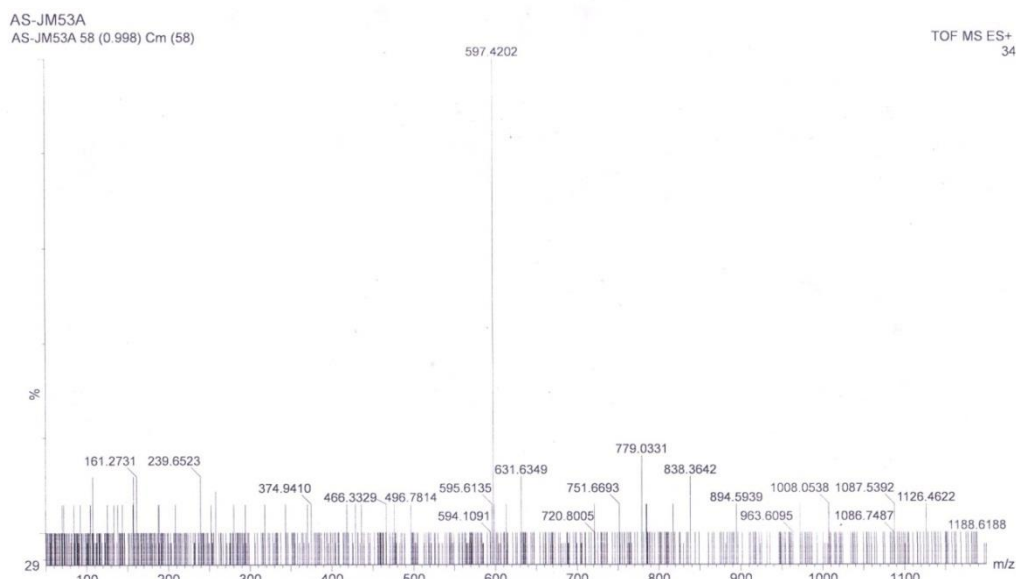


Figure 6.10 ESI-mass spectrum of complex 6.1.

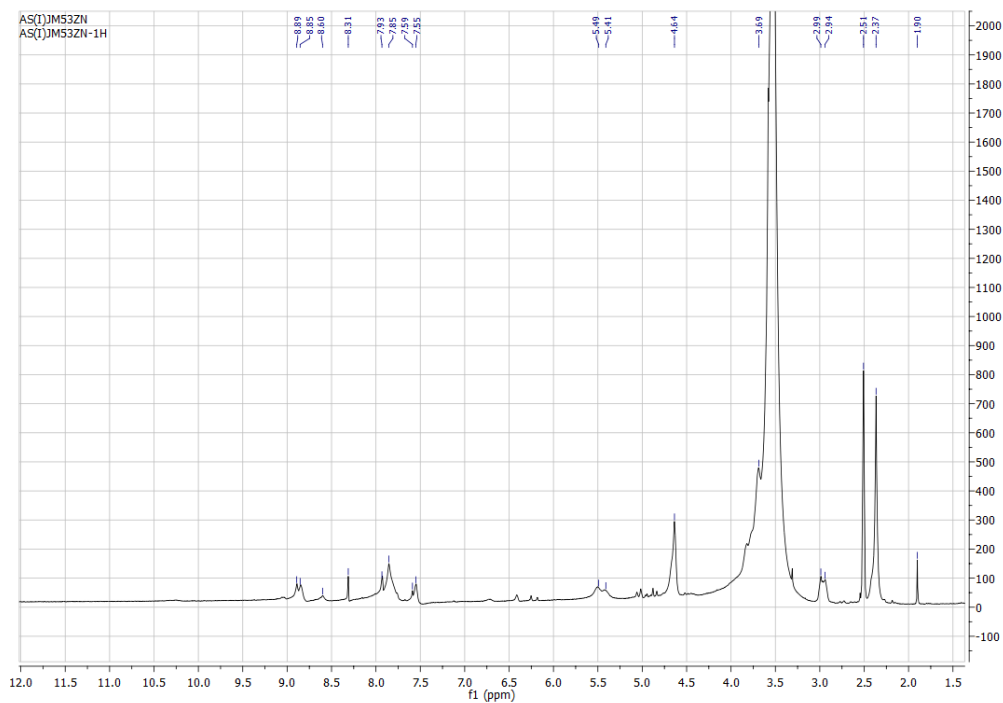


Figure 6.11 ^1H NMR of complex 6.1 in d_6 -DMSO solvent.

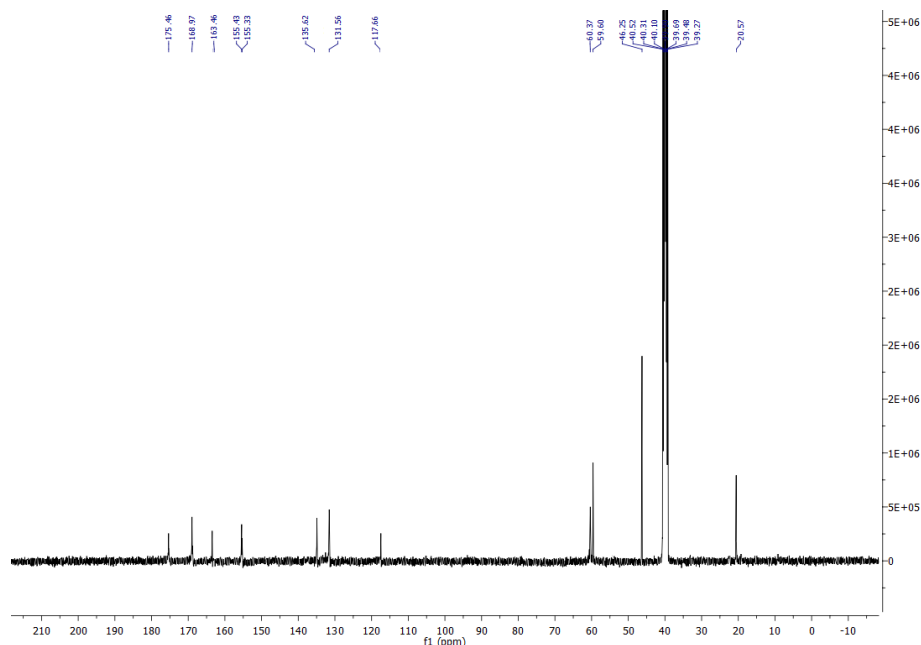


Figure 6.12 ^{13}C NMR of complex **6.1** in d_6 -DMSO solvent.

6.2.5 Synthesis of complex (6.2)

A 2 mL methanolic solution of zinc nitrate hexahydrate (1.0 mmol, 0.297 g) was added drop wise to 20 mL methanolic solution of **HL6.2** (1.0 mmol, 0.446 g) followed by addition of triethylamine (2.0 mmol, ~0.4 mL) and the resultant reaction mixture was stirred for ca. 4 h. Yellow coloured solid mass was obtained in high yield after slow evaporation of the solvent. Yield: 0.647 g (87%). Anal. Calc. for $\text{C}_{22}\text{H}_{28}\text{N}_4\text{O}_6\text{Zn}$: C 51.83%; H 5.54%; N 10.99%. Found: C 51.78%; H 5.48%; N 10.93%. IR (cm^{-1} , KBr): $\nu(\text{C-O})$ 1071s, $\nu(\text{C=N})$ 1623s; $\nu(\text{O-H})$ 3432s(**Figure 6.13**). ESI-MS (positive) in MeOH: The base peak was detected at $m/z = 608.61$, corresponding to $[\text{ZnL6.2}(\text{CH}_3\text{CN})(\text{H}_2\text{O})_2+\text{Na}]^+$ (**Figure 6.14**). UV-Vis, λ_{max} (nm), (ϵ ($\text{dm}^3\text{mol}^{-1}\text{cm}^{-1}$)) in HEPES buffer at pH= 7.4: 385(19958).

^1H NMR (d_6 -DMSO, 300 MHz) δ ppm: 9.03-8.85 (-CH=N) (m, 1H), 7.93-7.55 (ArH) (m, 1H), 4.64 (-CH₂) (s, 2H), 3.81-3.53 (-CH₂) (m, 8H), 2.37 (Ar-CH₃) (s, 3H) (**Figure 6.15**).

^{13}C NMR (d_6 -DMSO, 75 MHz) δ ppm: 19.25 (-CH₃), 59.60-70.22(-CH₂), 117.46-168.97 (Ar-C), 175.34 (-CH=N) (**Figure 6.16**).

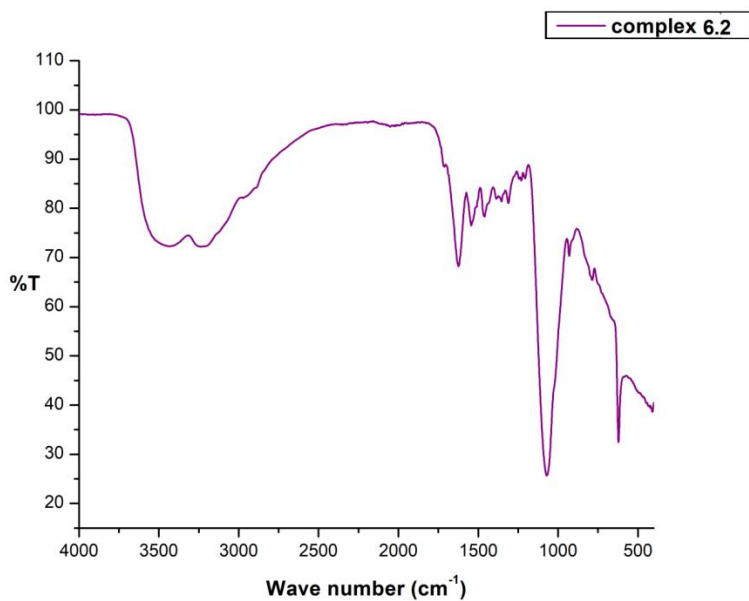


Figure 6.13 FTIR spectrum of complex 6.2.

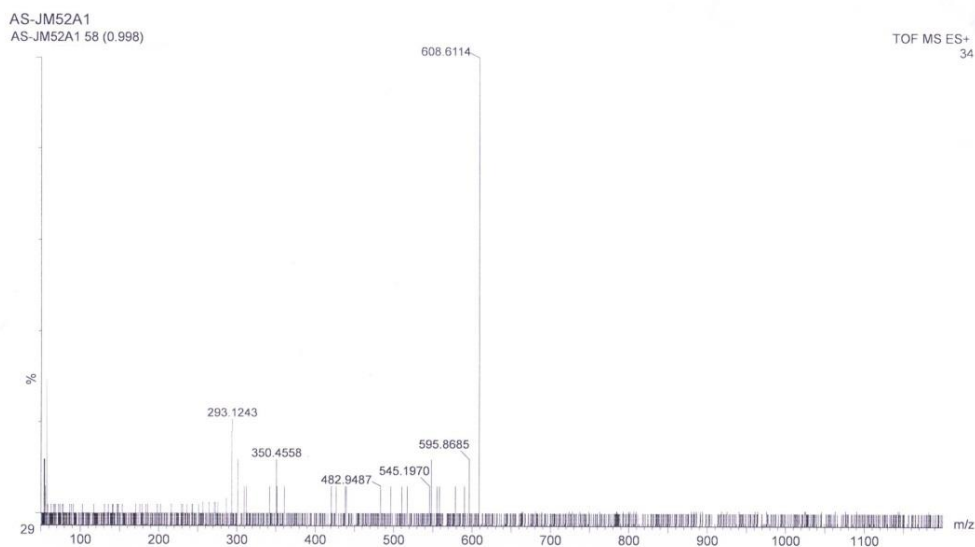


Figure 6.14 ESI-mass spectra of complex 6.2.

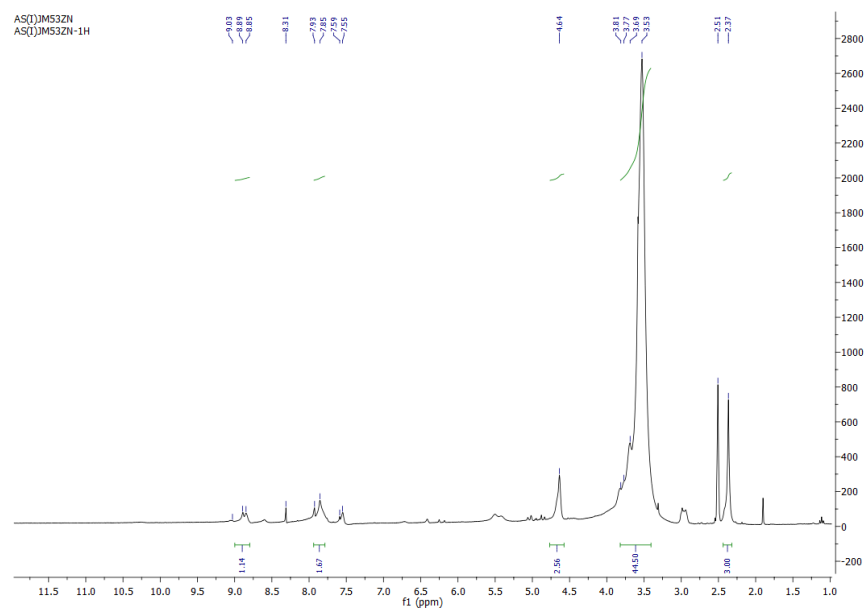


Figure 6.15 ^1H NMR of complex **6.2** in d_6 -DMSO solvent.

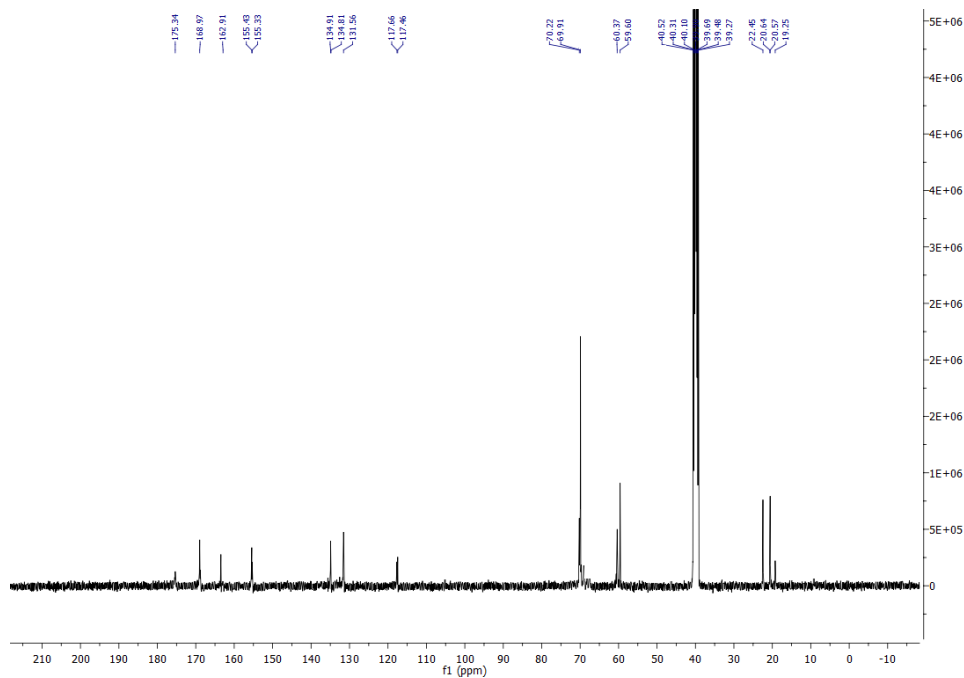


Figure 6.16 ^{13}C NMR of complex **6.2** in d_6 -DMSO solvent.

6.2.6 UV-visible and fluorescence spectroscopic studies

Stock solutions of various ions (1×10^{-3} M) were prepared in deionized water. A stock solution of the chemosensors (**HL6.1** and **HL6.2**) (1×10^{-3} M) were prepared in methanol. The

solution of **HL6.1** and **HL6.2** were then diluted to 1×10^{-5} M as per requirement. All the spectroscopic experiments including competitive assay of various cations and anions were performed in aqueous HEPES buffer medium at pH 7.4. In titration experiments, 30 μ L solution of 1×10^{-3} M **HL6.1** and **HL6.2** (1×10^{-5} M) were taken in a quartz optical cell of 1.0 cm optical path length, and the ion stock solutions were added gradually to maintain a concentration of 1×10^{-5} M. Spectroscopic studies of the chemosensors (**HL6.1** and **HL6.2**) in the presence of different anions were performed in HEPES buffer at pH = 7.4. In competitive assay experiments, the test samples were prepared by interacting appropriate amounts of the cations stock in 3 mL of **HL6.1** and **HL6.2** solution (1×10^{-5} M).

6.2.7 Binding stoichiometry (Job's plot)

Job's continuation method was employed to find out the binding stoichiometry of the chemosensor with that of Zn^{2+} ions using both absorption and emission spectroscopy. At a given temperature (25°C), the absorbance and fluorescence were noted for solutions where the concentrations of both chemosensor and Zn^{2+} ions were varied but the sum of their concentrations was kept constant at 1×10^{-5} M. Relative change in absorbance ($\Delta A/A_0$) were plotted as a function of mole fraction of chemosensor. The break point in the resulting plot corresponds to the mole fraction of chemosensor in Zn^{2+} complex. From the break point the stoichiometry were estimated. The results reported are average of at least three experiments.

6.2.8 Cell culture

Human cervical cancer cell line HeLa was obtained from National Center for Cell Science (NCCS) Pune, India. The cells were grown in DMEM with 10% FBS (Fetal Bovine Serum), penicillin/streptomycin (100units/ml) at 37°C and 5% CO_2 . All the treatments were conducted at 37°C and at a cell density allowing exponential growth.

6.2.9 Cell imaging

The HeLa cells were grown in coverslips for 24hrs. Then the cells were either mock-treated or treated with $10\mu\text{M}$ Zn^{2+} ion for 24hrs at 37°C , after that $10\mu\text{M}$ of ligand was added to it for another 24hrs at 37°C . The cells were washed with $1\times\text{PBS}$ and then they were mounted on a glass slide and observed under fluorescence microscope (Leica).

6.2.10 Computational method

All computations were performed using the GAUSSIAN09 (G09)^{6.27} software package. For optimization we used the density functional theory method at the B3LYP level^{6.28,6.29} and the standard 6-31+G(d) basis set for C, H, N and O atoms^{6.30,6.31} and the lanL2DZ effective potential (ECP) set of Hay and Wadt^{6.32–6.34} for zinc and copper atoms have been chosen for optimization.

TDDFT calculation was performed with the optimized geometry to ensure only positive eigen values. Time-dependent density functional theory (TDDFT)^{6.35–6.37} was performed using conductor-like polarizable continuum model (CPCM)^{6.38–6.40} and the same B3LYP level and basis sets in aqueous solvent system. GAUSSSUM^{6.41} was used to calculate the fractional contributions of various groups to each molecular orbital.

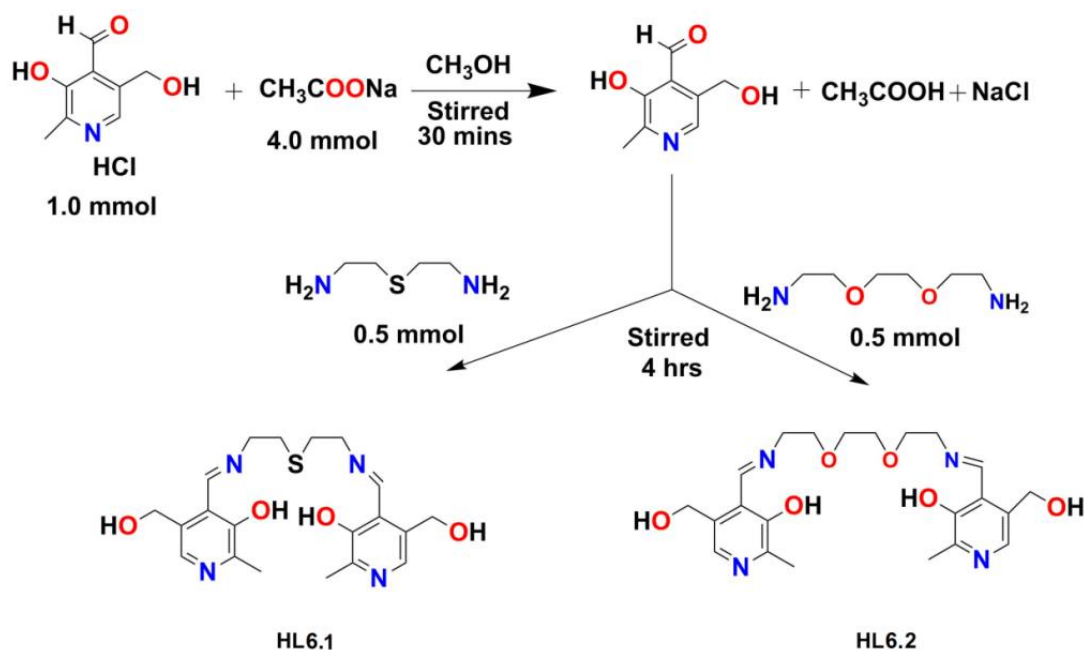
6.3 Results and discussion

6.3.1 Synthesis and characterization

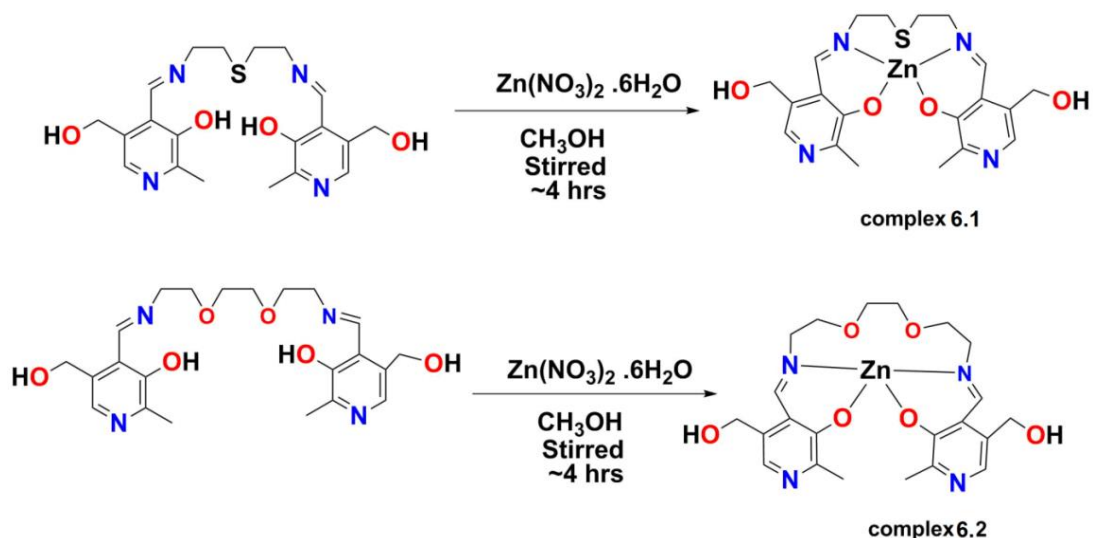
Firstly, the pyridoxal hydrochloride was neutralized with CH_3COONa to keep pH of the methanolic solution 7. Then 2,2'-Thiobis(ethylamine) or 1,2-Bis(2-aminoethoxy)ethane was added to the solution in 2:1 ratio to prepare Schiff base ligands (**HL6.1** and **HL6.2**) under ambient condition (**Scheme 6.1**). The ligands are semi-solid and they used without further purification. Characterization of **HL6.1** and **HL6.2** are done using different spectroscopic techniques (UV-Vis, FT-IR, ^1H NMR, ^{13}C NMR) and elemental analysis. In the

ESI-mass spectrum of the chemosensors the base peak was found at 419.13 and 447.22 corresponding to $[\text{HL6.1}+1]^+$ and $[\text{HL6.2}+1]^+$, respectively (**Figures 6.2** and **6.6**). In the FT-IR spectrum of both **HL6.1** and **HL6.2** a broad band at around 3361 cm^{-1} indicates the presence of phenolic OH group and the band around 1631 cm^{-1} is attributed to the C=N (for azomethine) stretching frequency (**Figures 6.1** and **6.5**).

HL6.1 and **HL6.2** both react with $\text{Zn}(\text{NO}_3)_2 \cdot 6\text{H}_2\text{O}$ in 1:1 ratio to produce complex **6.1** and **6.2**, respectively (**Scheme 6.2**). The solid mass of both complexes are isolated in high yield. Both are characterized by FT-IR, NMR spectroscopy, elemental and ESI-MS analyses. The experimental and simulated mass spectra of complexes are well matched with each other. m/z value 597.42 and 608.61 corresponding to molecular ion peak of $[\text{ZnL6.1}(\text{CH}_3\text{CN})_2(\text{H}_2\text{O})+1]^+$ and $[\text{ZnL6.2}(\text{CH}_3\text{CN})(\text{H}_2\text{O})_2+\text{Na}]^+$, respectively (**Figures 6.10** and **6.14**). In FT-IR spectrum of complex **6.1** and **6.2** the characteristics stretching frequencies appeared around 1021 ($\nu_{\text{C-O}}$), 1626 ($\nu_{\text{C=N}}$), 3372 (ν_{OH}) and 1071 ($\nu_{\text{C-O}}$), 1623 ($\nu_{\text{C=N}}$); 3432 ($\nu_{\text{O-H}}$), respectively (**Figures 6.9** and **6.13**).



Scheme 6.1 Route to the synthesis of chemosensors (**HL6.1** and **HL6.2**).



Scheme 6.2 Route to the synthesis of complexes (6.1 and 6.2).

6.3.2 Absorption spectral studies

In this work all spectroscopic experiments were carried out in deionized water medium in presence of HEPES buffer at pH 7.4. The UV-vis spectrum of both chemosensors (**HL6.1** and **HL6.2**) gives well-defined bands around 333 nm, responsible for intra molecular $\pi \rightarrow \pi^*$ or $n \rightarrow \pi^*$ type of transition. In presence of Zn^{2+} ion a significant change in the spectrum of chemosensors are observed. Upon gradual addition of Zn^{2+} ion solution (0-10 μM), the peak at 335 nm decreases with concomitant appearance of a new peak at around 385 nm (**Figure 6.17**). Bathochromic shift of the peak at 385 nm indicates strong interaction between them. This could be assigned as O^- (phenolate) to Zn^{2+} charge transfer band. No further change was observed above 1.0 equivalent of Zn^{2+} . During such process an isosbestic point was observed at 353 nm. 1:1 binding stoichiometry between the chemosensor and Zn^{2+} ion has been established with the aid of Job's plot analysis (**Figure 6.18**). Importantly, upon addition of other common cations (Cd^{2+} , Hg^{2+} , Pb^{2+} , Al^{3+} , Ag^+ , Mn^{2+} , Fe^{3+} , Co^{2+} , Ni^{2+} , Na^+ , K^+ , Mg^{2+} and Ca^{2+}) did not make appreciable change in the absorption spectrum of the chemosensor.

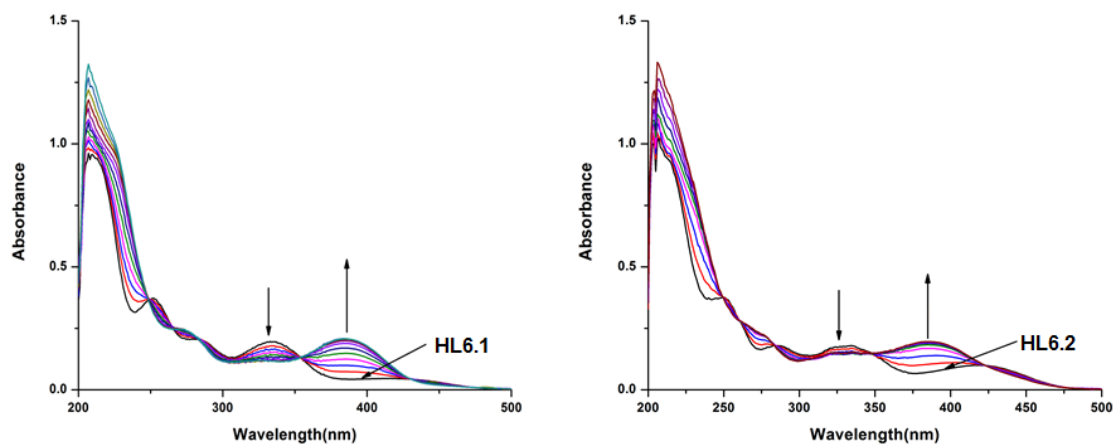


Figure 6.17 Absorption titration of chemosensors (**HL6.1** and **HL6.2**) (10 μM) with gradual addition of Zn^{2+} , 0-10 μM in HEPES buffer at pH 7.4.

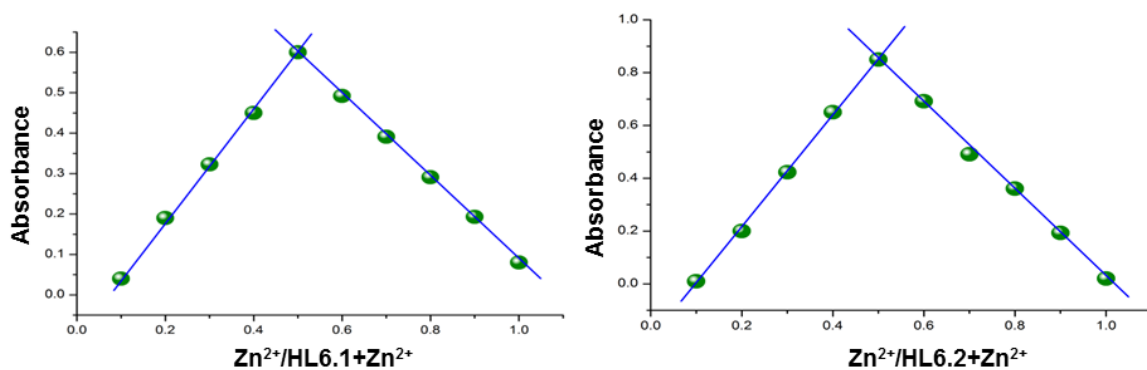


Figure 6.18 1:1 binding stoichiometry has shown by Job's plot of complexes **6.1**(left) and **6.2**(right). Symbols and solid lines represent the experimental and simulated profiles, respectively.

6.3.3 NMR studies

All ^1H and ^{13}C NMR spectrum of chemosensors (**HL6.1** and **HL6.2**) and their Zn-bound compounds (compound **6.1** and **6.2**) are recorded in d_6 -DMSO solvent. The ^1H NMR spectra of chemosensors clearly suggest presence of a c_2 symmetry within the molecule. In **HL6.1** imine (H-C=N) proton appears at 8.93 ppm. Aromatic proton appears as a sharp peak at 7.85 ppm. Aliphatic protons associated with pyridine ring appear at 4.63 ppm whereas aliphatic protons of thiobisethylamine moiety appear at 3.91 ppm to 2.91 ppm and methyl protons appear at 2.36 ppm.

To establish complex formation between Zn^{2+} and chemosensor, we have performed ^1H NMR of complexes **6.1** and **6.2** in d_6 -DMSO solvent. Interestingly, in presence of Zn^{2+} ion broadening, downfield shift and splitting of imine, aromatic and aliphatic protons of **HL6.1** are observed. Imine (H-C=N) proton shifted to downfield and it appears at $\delta = 9.03$ ppm. Similarly, aromatic protons appear at 7.85-7.55 ppm.

In ^{13}C NMR (d_6 -DMSO, 75 MHz) spectrum of **HL6.1**, signals for imine carbon atom appeared at 165.09 ppm. Aromatic carbon atoms appeared within 155.031-19.28 ppm. $-\text{CH}_2$ and $-\text{CH}_3$ carbon atoms appeared at in the range 58.74 -47.08 and 19.16, respectively (**Figure 6.4**). In case of complex **6.1** downfield shift of peaks are observed. Signals for $-\text{CH}_3$ and $-\text{CH}_2$ carbon atoms appeared at 20.57 and in the range 60.37-46.25, respectively. Aromatic carbon atoms appeared in the range of 168.97-117.66 ppm. Whereas, the imine carbon atom appeared at 175.46 ppm (**Figure 6.12**).

6.3.4 Fluorescence properties

Fluorescence experimental so performed in HEPES buffer (pH = 7.4) at ambient conditions. Upon excitation at 385 nm, chemosensor (**HL6.1**) exhibits weak fluorescence at 472 nm. This is probably due to C=N bond isomerization and phenolic protons based excited-

state intramolecular proton transfer (ESIPT) processes.^{6.26} In presence of Zn^{2+} a steady growth of fluorescence enhancement has been observed at 472 nm. Saturation of emission intensity achieved at one equivalent of Zn^{2+} with an approximately 20-fold of enhancement. This observation clearly suggests formation of a 1:1 complex. The chelation of Zn^{2+} with imine nitrogens, phenoxido oxygens of the chemosensor increases rigidity of the molecular assembly (CHEF effect), responsible for fluorescence enhancement (**Figures 6.19** and **6.20**). In case of **HL6.2** similar type of changes has been observed (**Figure 6.21**).

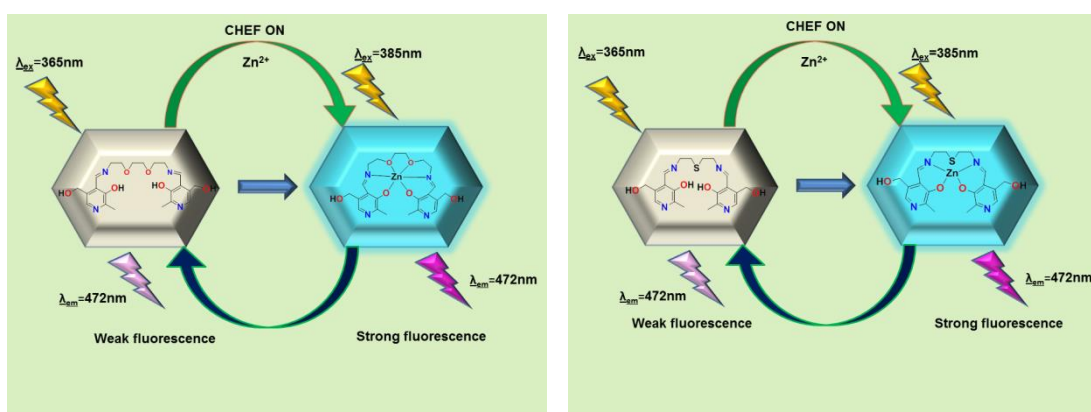


Figure 6.19 Pictorial representation of ‘CHEF’ process.

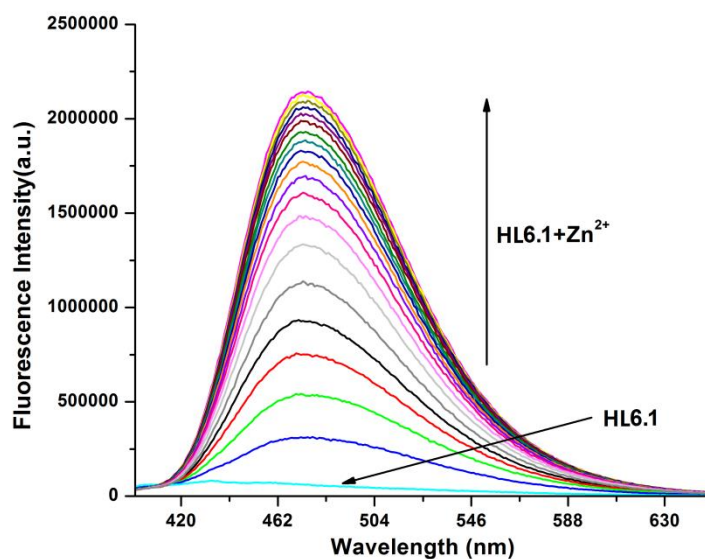


Figure 6.20 Fluorescence titration of **HL6.1** (10 μM) in HEPES buffer at pH =7.4 by gradual addition of Zn^{2+} (0–10 μM) with $\lambda_{\text{em}} = 472$ nm.

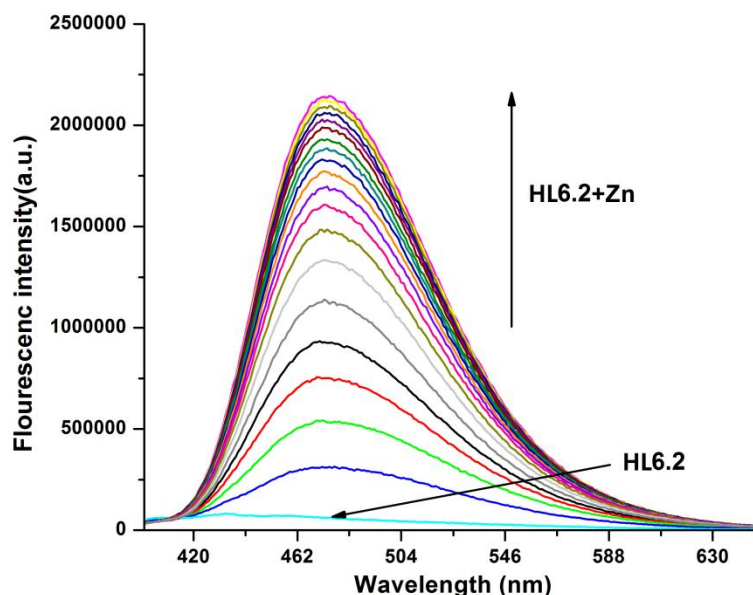


Figure 6.21 Fluorescence titration of **HL6.2** (10 μM) in HEPES buffer at pH = 7.4 by gradual addition of Zn^{2+} (0–10 μM) with $\lambda_{\text{em}} = 472 \text{ nm}$.

Binding ability of the chemosensors toward Zn^{2+} ions has been established using Benesi-Hildebrand equation (Equation 1) involving fluorescence titration curve.^{6.42}

$$\frac{F_{\text{max}} - F_0}{F_x - F_0} = 1 + \left(\frac{1}{K[C]^n} \right) \quad (1)$$

Where, F_{max} , F_0 and F_x are fluorescence intensities of chemosensor in the presence of metal ions at saturation, free chemosensor and any intermediate metal ions concentration, respectively. K is the binding constant of the complexes. Concentrations of Zn^{2+} ions are represented by C and here $n=1$. Then binding constant (K) of the complexes has been determined using the relation, $K = 1/\text{slope}$. A plot of $\frac{F_{\text{max}} - F_0}{F_x - F_0}$ vs $\left(\frac{1}{[C]^1} \right)$ provides the binding constant values as 1.5×10^5 and $1.46 \times 10^5 \text{ M}^{-1}$ for complex **6.1** and complex **6.2**, respectively (**Figure 6.22**).

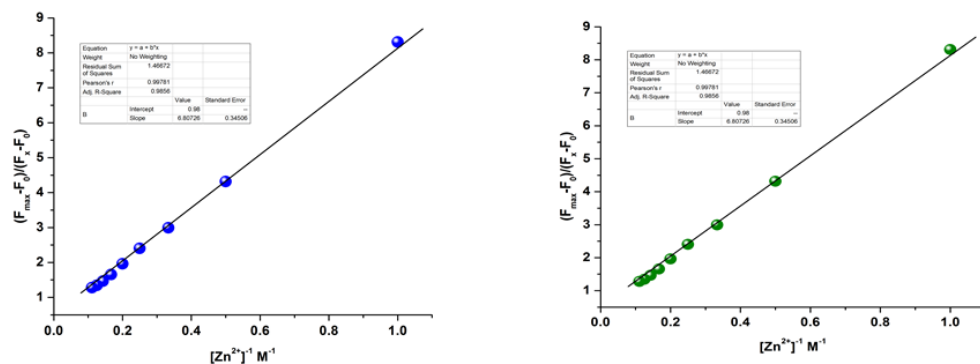


Figure 6.22 Benesi-Hildebrand equation: A plot of $\frac{F_{max}-F_0}{F_x-F_0}$ vs $\left(\frac{1}{[M]}\right)$. Symbols and solid lines represent the experimental and simulated profiles for complexes **6.1** (left) and **6.2** (right), respectively.

Selectivity of the chemosensor towards Zn^{2+} over the other metal ions is checked by performing competitive assay experiment in presence of different alkali metals (Na^+ and K^+), alkali-earth metals (Mg^{2+} and Ca^{2+}), and various transition-metal (Mn^{2+} , Fe^{3+} , Co^{2+} , Ni^{2+} , Cd^{2+} and Hg^{2+}) ions. In competition assay Zn^{2+} (1.0 equiv.) and the **HL6.1/HL6.2** is mixed with excess amount of different metal ions (2.0 equiv.) in aqueous media (buffer). Fluorescence enhancement observed for the mixtures of Zn^{2+} with most of the metal ions except Hg^{2+} , Ni^{2+} and Cu^{2+} where little quenching has been observed (**Figure 6.23**). Competition assay experiment demonstrates high fluorescent recognition of **HL6.1/HL6.2** for Zn^{2+} ions over other cations. Upon addition of different common anions like $S_2O_3^{2-}$, S^{2-} , SO_3^{2-} , HSO_4^- , SO_4^{2-} , SCN^- , N_3^- , OCN^- , AsO_4^- , HPO_4^{2-} , PO_4^{3-} , ClO_4^- , AcO^- , Cl^- , NO_3^- , $P_2O_7^{4-}$, PF_6^- and F^- in HEPES buffer at pH 7.4 chemosensors showed no significant fluorescence enhancement.

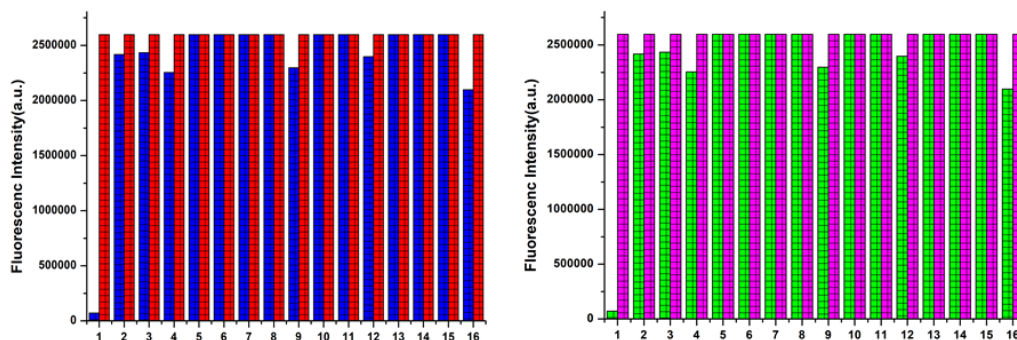


Figure 6.23 Relative fluorescence intensity profile of [HL6.1/HL6.2-Zn²⁺] system in the presence of different cations in HEPES buffer at pH 7.4. 1=only HL6.1/HL6.2 and (2-16)=HL6.1/HL6.2 (10 μM) + Zn²⁺(20 μM) + Mⁿ⁺(20μM), where Mⁿ⁺=(2–Co²⁺,3–Pb²⁺,4–Hg²⁺,5–Mn²⁺,6–Fe²⁺,7–Fe³⁺,8–Co²⁺,9–Ni²⁺,10–K⁺,11–Na⁺,12–Mg²⁺, 13–Ca²⁺,14–Al³⁺,15–Cd²⁺ and 16–Cu²⁺) (left= HL6.1 and right=HL6.2).

Interestingly chemosensors (HL6.1 and HL6.2) also act as a fluorometric probe for the detection of Zn²⁺ ion. In presence Zn²⁺ ions HL6.1 and HL6.2 exhibit blue fluorescence. Thus, the chemosensors can be used for a selective fluorometric detection of Zn²⁺ ions over other competing metal ions both in environmental and biological fields (Figure 6.24).

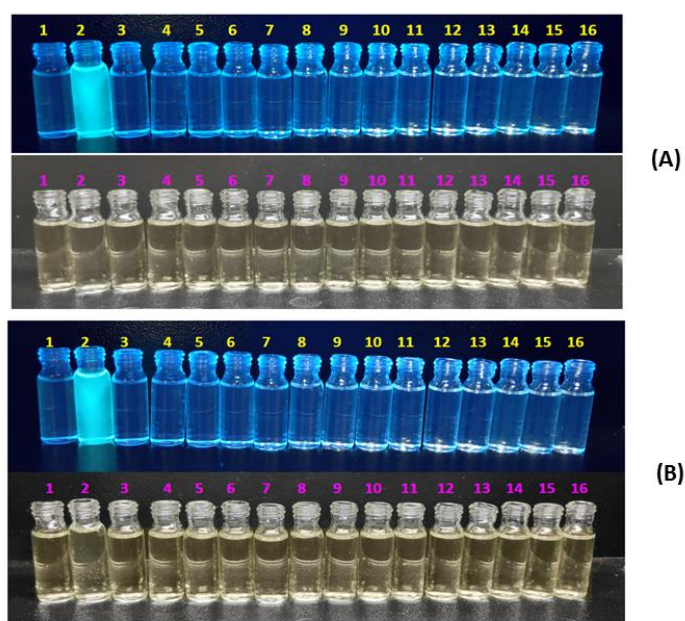


Figure 6.24 Visual colour changes of chemo sensor (HL6.1/HL6.2) (10μM) under presence of different metal ions (2 equivalent) in HEPES buffer (pH 7.4). The images in below row

and above row were taken under visible light and UV light, respectively. Where 1= only **HL6.1/HL6.2**, 2,3,4,5,6,7,8,9,10,11,12,13,14,15 and 16= **HL6.1/HL6.2**+ Zn²⁺, Cu²⁺, Cd²⁺, Pb²⁺, Hg²⁺, Mn²⁺, Fe²⁺, Fe³⁺, Co²⁺, Ni²⁺, K⁺, Na⁺, Mg²⁺, Ca²⁺ and Al³⁺, respectively. (A=**HL6.1** and B=**HL6.2**).

We have also examined reversibility test and regeneration of the free chemosensors, two vital aspects for real time application of the chemosensor. In this experiment a strong chelating ligand, sodium salt of ethylenediaminetetraacetic acid (Na₂EDTA) is added presence of Zn²⁺ ion and chemosensor. In presence of one equiv. of Na₂EDTA fluorescence intensity have changed from sky-blue to colourless with significant decrease in fluorescence intensity confirming generation of free probe. Addition of extra one equivalent metal ion returns back the usual fluorescence intensity (**Figure 6.25**).

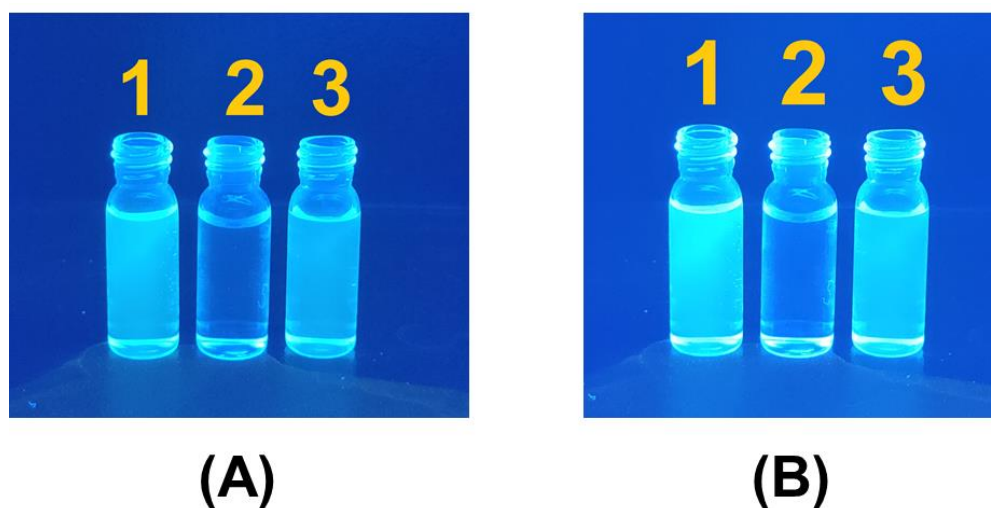


Figure 6.25 Visual colour changes in reversibility experiments. For (A) and (B), 1= chemosensor (**HL6.1/HL6.2**) + Zn²⁺ (10μM), 2= **HL6.1/HL6.2** (10μM) + Zn²⁺ (10μM) + EDTA²⁻(10μM), 3= **HL6.1/HL6.2** (10μM) + Zn²⁺ (10μM) + EDTA²⁻(10μM) + Zn²⁺ (10μM) under UV light, respectively.

Limit of detection (LOD) of the chemosensors towards Zn²⁺ ions are calculated using 3σ method.^{6,43} The detection limit of the chemosensor for both the ions are 7.47×10^{-8} M and 6.95×10^{-8} M, respectively.

The effect of pH on the fluorescence response of the chemosensors **HL6.1** and **HL6.1-Zn²⁺** complexes are examined within range 2-14. Initially free chemosensor exhibits fluorescence property in strong acidic medium (up to pH=3) due to protonation of pyridine nitrogen. Fluorescence property disappears with increase of pH (up to pH=11) (**Figure 6.26**). In presence of Zn²⁺ ions fluorescence gradually increases in pH range 4–6 due to complex formation. Intensity remains constant upto pH=8 suggesting stability of the Zn bound complex. Above pH 9 a sudden decrease in fluorescence intensity suggests dissociation of Zn-complex and generation of free chemosensor. Similar result has been observed in case of **HL6.2**. The pH experiment suggests that **HL6.1** and **HL6.2** can act as a selective fluorescent probe to recognize Zn²⁺ ion in presence of other metal ions in biological system under physiological condition.

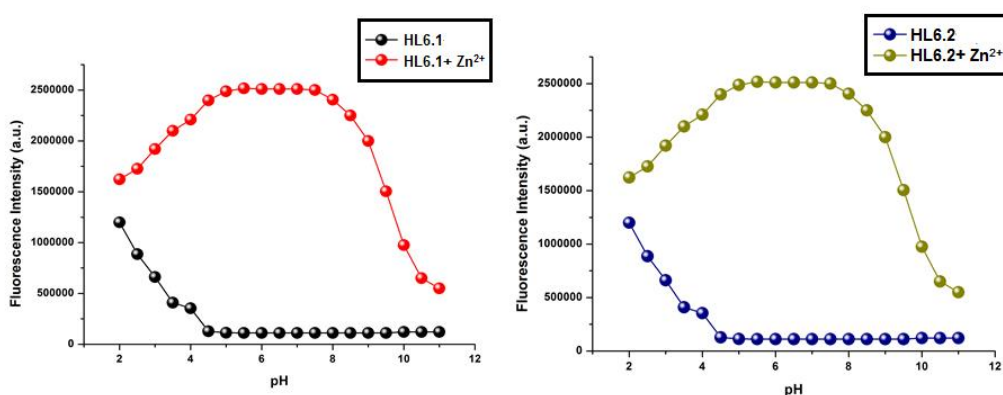


Figure 6.26 Fluorescence intensity of **HL6.1** (left)/**HL6.2** (right) (10 μ M) in the absence and presence of Zn²⁺ ions (10 μ M) at various pH values in HEPES buffer.

6.3.5 Life time and quantum yield measurements

Lifetime experiment for the chemosensors (**HL6.1** and **HL6.2**) and complexes (**6.1-6.2**) were studied at 298 K in HEPES buffer (pH= 7.4). The average fluorescence decay life time has been measured of the chemosensors and complexes using the given formula ($\tau_f = a_1\tau_1 + a_2\tau_2$, where a_1 and a_2 are relative amplitude of decay process). The average

fluorescence lifetime of the chemosensors (**HL6.1** and **HL6.2**), complex **6.1** and complex **6.2** are 2.24 ns, 2.21 ns, 2.54 ns and 3.77 ns, respectively (**Figure 6.27**, **Table 6.1**).

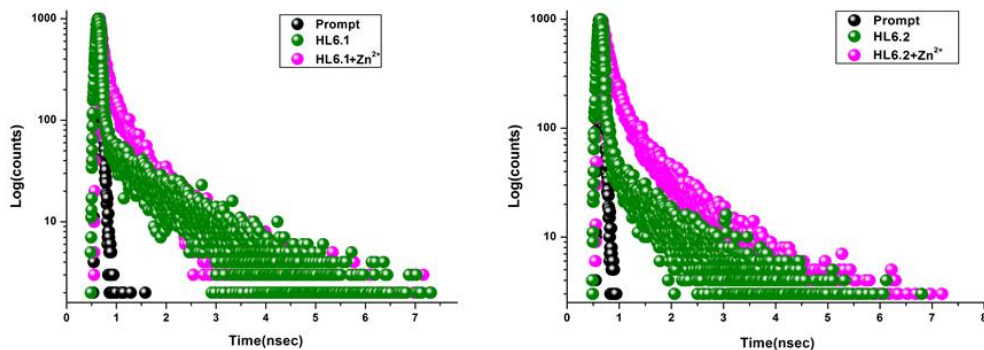


Figure 6.27 Time-resolved fluorescence decay curves (logarithm of normalized intensity vs time in ns) of **HL1** in the absence (●) and presence (●) of Zn^{2+} ion, (●) indicates decay curve for the scattered.

Fluorescence quantum yield (Φ) has been calculated by the using following formula:

$$\Phi_{\text{sample}} = \left\{ \frac{(\text{OD}_{\text{standard}} \times A_{\text{sample}} \times \eta_{\text{sample}}^2)}{(\text{OD}_{\text{sample}} \times A_{\text{standard}} \times \eta_{\text{standard}}^2)} \right\} \times \Phi_{\text{standard}}$$

Where, A is the area under the emission spectral curve, OD is the optical density of the compound at the excitation wavelength and η is the refractive index of the solvent. Here the value of Φ_{standard} is taken as 0.52 (for Quinine Sulfate).

The values of Φ for chemosensors (**HL6.1** and **HL6.2**), complex **6.1** and complex **6.2** are found to be 0.03, 0.05, 0.21 and 0.24, respectively (**Table 6.1**).

Table 6.1 Lifetime, quantum yield, LOD and binding constant values of chemosensors (**HL6.1** and **HL6.2**) and complexes (**6.1** and **6.2**).

	Lifetime (ns) ($\tau_{\text{av.}}$)	Quantum Yield (Φ)	LOD (M)	Binding Constant (M^{-1})
HL6.1	2.24	0.03	-	-
HL6.2	2.21	0.05	-	-
complex 6.1	2.54	0.21	7.47×10^{-8} M	1.50×10^5
complex 6.2	3.77	0.30	6.95×10^{-8} M	1.46×10^5

6.3.6 Cell imaging

The fluorescence microscopy study is performed to ensure the cellular uptake of ligand and Zn^{2+} salt. A strong green fluorescent signal is observed under the microscope (**Figure 6.28**). Thus we can conclude that the cells internalize the complex and producing green signal.

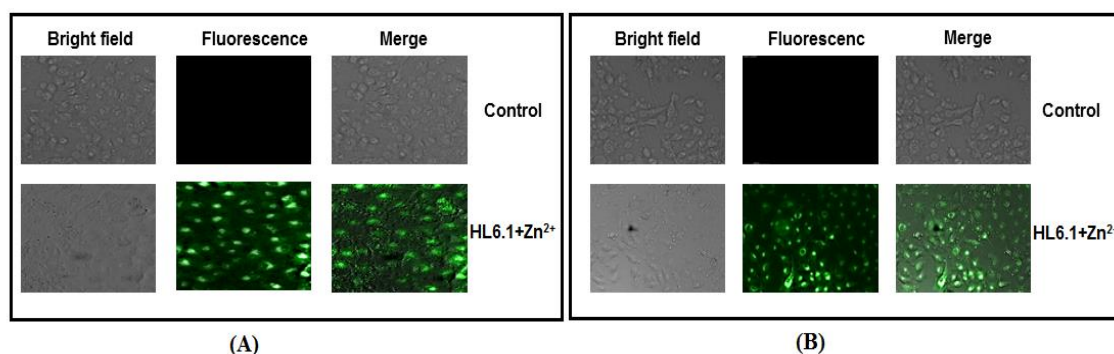


Figure 6.28 Bright field, fluorescence and merged microscopic images of untreated HeLa (Control), cells treated with Zn^{2+} ($10\mu\text{M}$) + **HL6.1** ($10\mu\text{M}$) (A) and Zn^{2+} ($10\mu\text{M}$) + **HL6.2** ($10\mu\text{M}$) (B), respectively

6.3.7 DFT study

DFT studies were performed to support mode of complexation between chemosensors and Zn^{2+} and their structural parameters. Furthermore TDDFT study was performed to understand nature, origin and contribution of M.O.s of electronic transitions. It also gives idea of quantity of energy associated with every individual transition. When individual M.O. is concerned the contribution from both ligand and metal center has been computed. So, DFT and TDDFT analysis plays important role to support and understand structural and electronic parameters of complexes.

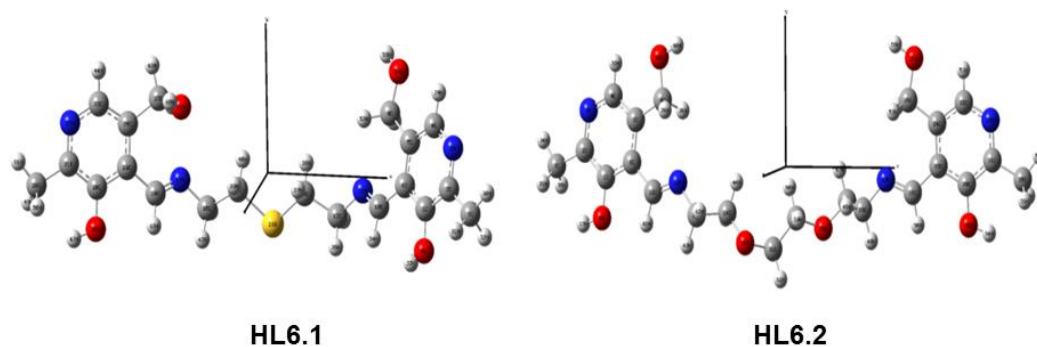


Figure 6.29 optimized structure of **HL6.1** (left) and **HL6.2** (right).

Here, geometry optimization of chemosensors (**HL6.1** and **HL6.2**), complex **6.1** and complex **6.2** has been performed using DFT/B3LYP method. Energy minimized structure of chemosensors (**HL6.1** and **HL6.2**) and complexes (**6.1** and **6.2**) are shown in **Figures 6.29** and **6.30**, respectively. In the optimized structure of Zn^{2+} -**HL6.1**, the metal ion is coordinated with two amine N atoms and two phenoxido O atoms. The S atom of the aliphatic part remains uncoordinated. Whereas in Zn^{2+} -**HL6.2**, apart from amine N atoms and phenoxido O atoms of **HL6.2**, participation of both oxygen atoms result completion of all six coordination sites around the metal center. Some selected bond distances and bond angles of both complexes are listed in **Table 6.2**. For both complexes bond distances and bond angles of the optimized structures are well matched with that of previously reported analogous complexes.^{6.44}

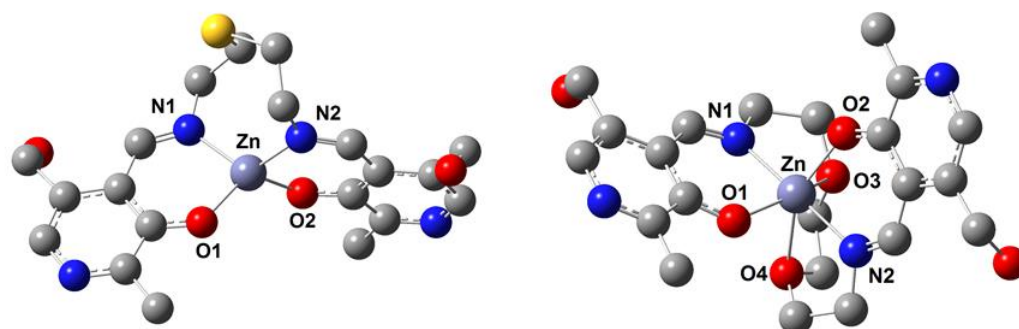
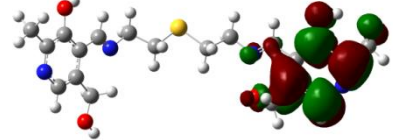

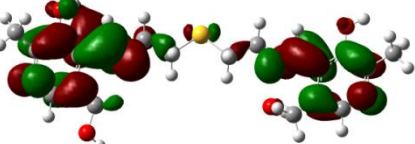
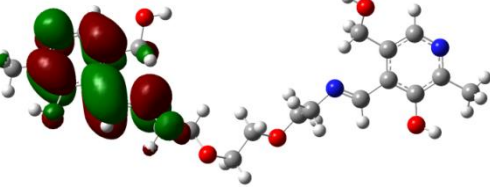
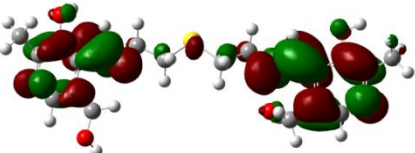
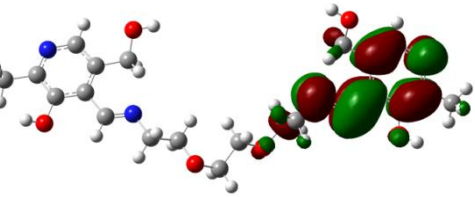
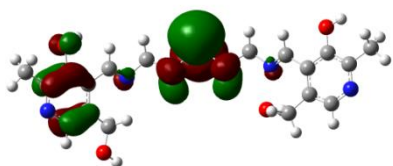
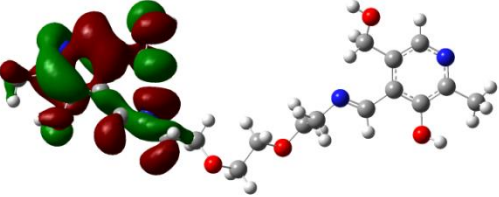


Figure 6.30 optimized structure of **complex 6.1**(left) and **complex 6.2**(right).

In **HL6.1**, electron density in HOMO of is mainly distributed over the aliphatic part, whereas, electron density in LUMO is mainly distributed over both pyridine moiety. In **HL6.2** electron density in both **HOMO** and **LUMO** are distributed over one of the pyridine moiety (**Figure 6.31**). Interestingly in complex **6.1** and **6.2**, electron density in both LUMO and HOMO are completely ligand based where contribution from metal centers is nil (**Figure 6.32**). Energy of some selected M.O. of chemosensors, complex **6.1** and **6.2** are given in **Table 6.3**.

	HL6.1	HL6.2
LUMO+2		
LUMO+1		
LUMO		
HOMO		

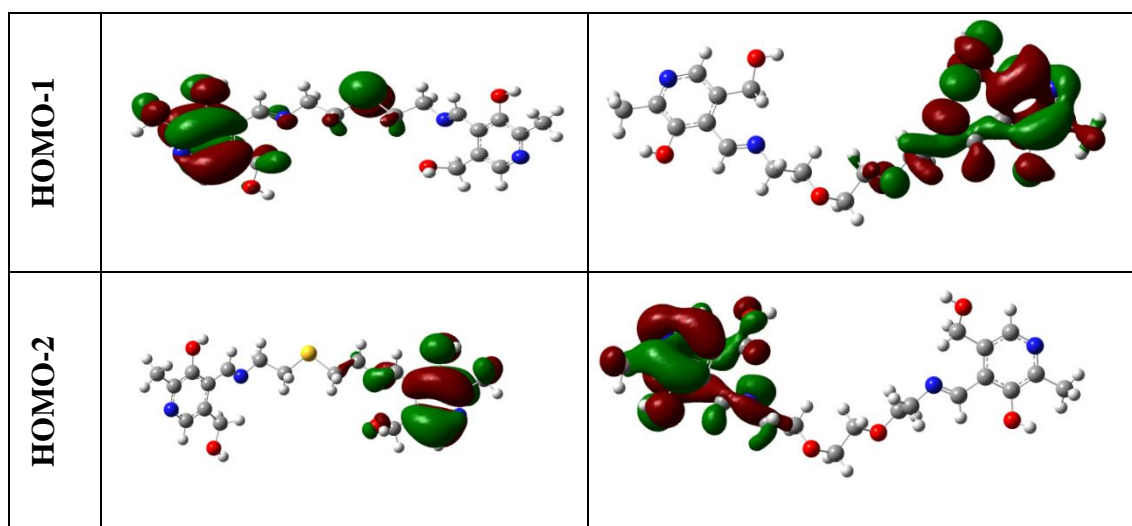
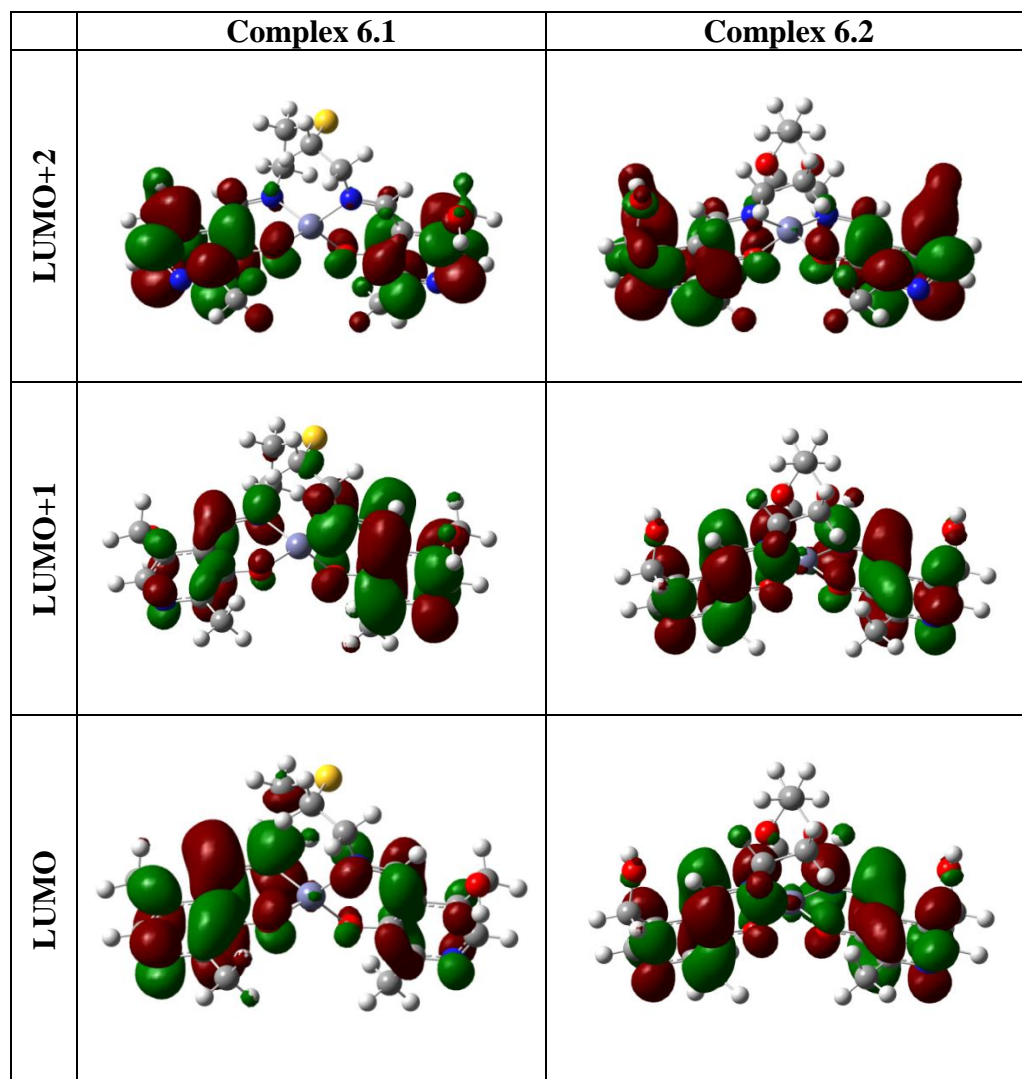


Figure 6.31 Selected contour plots of molecular orbitals of HL6.1 and HL6.2.



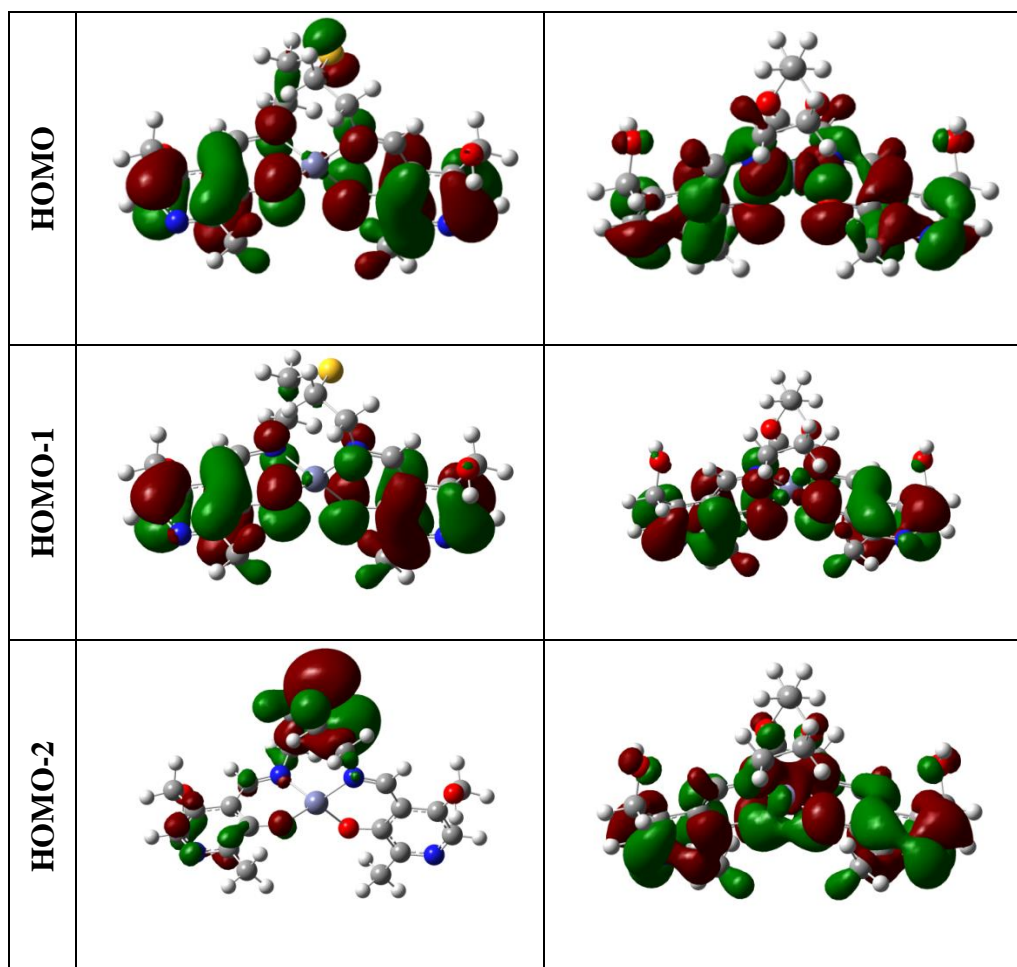


Figure 6.32 Selected contour plots of molecular orbitals of complex **6.1** and complex **6.2**.

Table 6.2 Bond lengths (Å) and bond angles (°) of optimized structure of complex **6.1** and complex **6.2** (B3LYP/6-31+G(d) basis set).

Complex 6.1	Calculated	Complex 6.2	Calculated
Zn-N ₁ / Zn-N ₂	2.05/2.07	Zn-N ₁ /Zn-N ₂	2.14
Zn-O ₁ / Zn-O ₂	1.95/1.96	Zn-O ₁ /Zn-O ₂	2.01
N ₁ -Zn-N ₂	119.07	Zn-O ₃ /Zn-O ₄	2.35
O ₁ -Zn-O ₂	122.85	N ₁ -Zn-O ₁	86.82
N ₁ -Zn-O ₁	92.96	N ₂ -Zn-O ₁	95.11
N ₁ -Zn-O ₂	116.33	N ₁ -Zn-O ₂	75.71

N ₂ -Zn-O ₁	116.44	N ₂ -Zn-O ₂	101.20
		O ₂ -Zn-O ₄	149.83

Table 6.3 Energy (eV) and composition (%) of selected M.O.s of chemosensors and complexes (**6.1** and **6.2**).

M.O.s	HL6.1	HL6.2	Complex6.1	Complex6.2
	Energy(eV)	Energy(eV)	Energy(eV)	Energy(eV)
LUMO+5	0.83	0.65	0.38	0.56
LUMO+4	0.66	0.65	0.31	0.53
LUMO+3	0.19	-0.19	-0.34	-0.22
LUMO+2	-0.24	-0.19	-0.37	-0.22
LUMO+1	-1.62	-1.59	-2.18	-2.01
LUMO	-1.66	-1.61	-2.26	-2.03
HOMO	-6.06	-6.36	-5.99	-5.76
HOMO-1	-6.09	-6.4	-6.06	-5.86
HOMO-2	-6.49	-6.57	-6.43	-6.41
HOMO-3	-6.59	-6.59	-6.67	-6.44
HOMO-4	-6.85	-6.83	-6.68	-7.2
HOMO-5	-6.9	-7.03	-7.36	-7.2

6.3.8 TDDFT study

Electronic transitions in **HL6.1**, **HL6.2**, complex **6.1** and complex **6.2** are theoretically studied using TDDFT were B3LYP/CPCM method is used with same basis sets in water. Calculated electronic transitions are given in **Table 6.4**. Theoretical calculations show that in **HL6.1** and **HL6.2** intense absorption bands appear at 321 and 332 nm, respectively for ligand based $\pi-\pi^*$ transition. Major transitions are HOMO→LUMO (64%), HOMO→L+1 (19%) and HOMO-2→ LUMO+1 (22%), HOMO→LUMO+1 (73%) for **HL6.1** and **HL6.2**, respectively. For complex **6.1** and complex **6.2** major peaks appear at 384 nm and 385 nm, respectively. Main transitions are HOMO→LUMO (78%) and HOMO→LUMO (87%) for complex **6.1** and complex **6.2**, respectively (**Figures 6.33** and **6.32**). The spectra of electronic transitions obtained from computation for the chemosensors (**HL6.1** and **HL6.2**), complexes **6.1** and **6.2** are found to be comparable with that of experimental data.

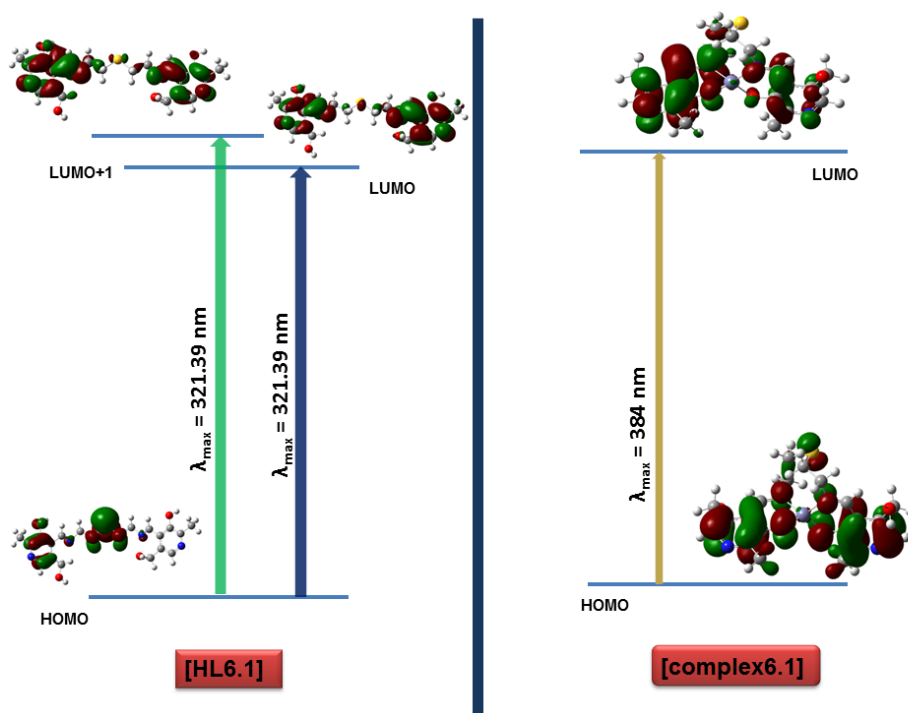


Figure 6.32 Pictorial representation of vertical transition of chemosensor (HL6.1) and complex 6.1.

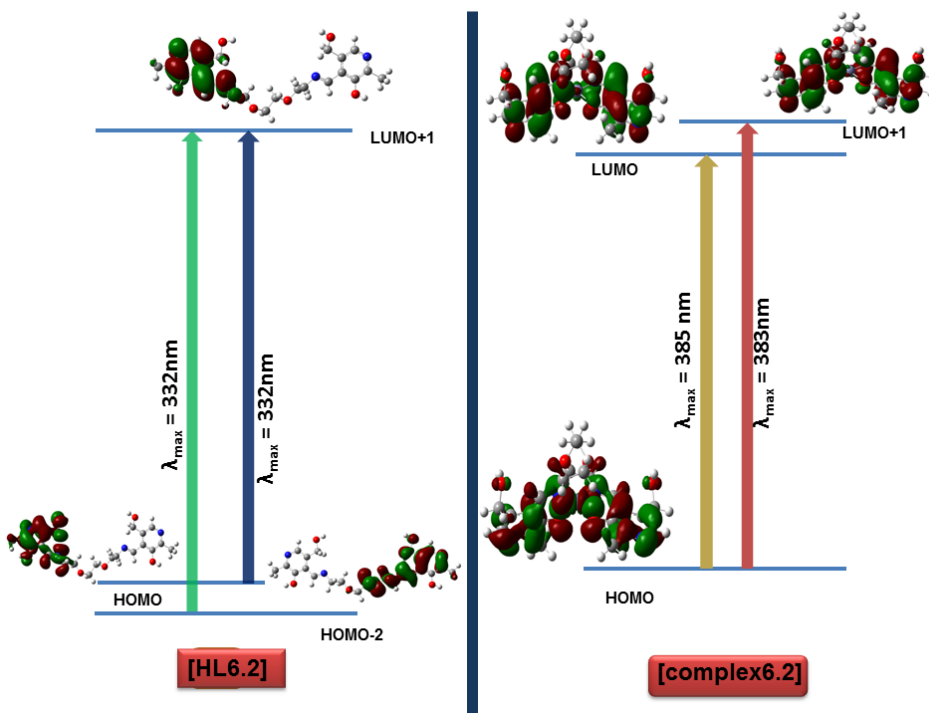


Figure 6.33 Pictorial representation of vertical transition of chemosensor (HL6.2) and complex 6.2.

Table 6.4 Electronic transition calculated by TDDFT using B3LYP/CPCM method in water solvent of chemosensors (**HL6.1** and **HL6.2**) and complexes (**6.1** and **6.2**).

	E _{excitation} (ev)	λ _{excitation} (nm)	Key transition	Transition assigned
HL6.1	31114.66	321	HOMO→LUMO (64%), HOMO→L+1 (19%)	n→π*
	34515.12	268	HOMO-2→LUMO (66%), HOMO-2→LUMO+1 (23%)	π→π*
HL6.2	30118.56	332	HOMO-2→LUMO+1 (22%), HOMO→LUMO+1 (73%)	n→π*
	37904.29	263	HOMO-4→LUMO (83%)	π→π*
Complex6.1	27376.25952	384	HOMO→LUMO (78%)	
Complex6.2	25968.00	385	HOMO→LUMO (87%)	
	26106.73	383	HOMO-1→LUMO (23%), HOMO→LUMO+1 (68%)	

6.4 Conclusion

In summary, we have successfully developed two pyridoxal-based chemosensors (**HL6.1** and **HL6.2**) for selective detection of Zn²⁺ in pure aqueous medium (HEPES buffer at pH= 7.4). Zn²⁺ is detected in around nano molar scale and the LOD values are 7.47×10^{-8} M and 6.95×10^{-8} M respectively. Both **HL6.1** and **HL6.2** exhibit around 20 times increment in fluorescence intensity in presence of Zn²⁺. **HL6.1** and **HL6.2** form 1:1 complex with the metal ion which have been established by fluorescence measurements, ESI-MS analysis and Jobs plot analysis. The values of binding constant are 1.5×10^5 and 1.46×10^5 M⁻¹ for Zn²⁺-**HL6.1/HL6.2** complexes, respectively. Reversibility test and regeneration of the chemosensors are also checked using Na₂EDTA solution. **HL6.1** and **HL6.2** are employed as a sensor to detect zinc ion in Human cervical cancer cell line HeLa grown in tissue culture which showed strong luminescence in the presence of Zn(II).

6.5 References

- (6.1) B. L. Vallee and K. H. Falchuk, *Psychol. Rep.*, 1993, **73**, 79–118.
- (6.2) W. Kaim and B. Schwederski, *Wiley & Sons*, 1994, **4**, 242–272.
- (6.3) A. Klug, *Annu. Rev. Biochem.*, 2010, **79**, 213–231.
- (6.4) A. Adamo, M. Zago, G. Mackenzie, L. Aimo, C. Keen, A. Keenan and P. Oteiza, *Neurotoxic. Res.*, 2010, **17**, 1–14.
- (6.5) K. Tóth, *Annu. Rev. Nutr.*, 2010, **31**, 139–153.
- (6.6) C. J. Frederickson, *Int. Rev. Neurobiol.*, 1989, **31**, 145–238.
- (6.7) P. D. Zalewski, S. H. Millard, I. J. Forbes, O. Kapaniris, A. Slavotinek, W. H. Betts, A. D. Ward, S. F. Lincoln and I. Mahadevan, *J. Histochem. Cytochem.*, 1994, **42**, 877–884.
- (6.8) P. D. Zalewski, X. Jian, L. L. Soon, W. G. Breed, R. F. Seamark, S.F. Lincoln, A. D. Ward and F. Z. Sun, *Reprod. Fertil. Dev.*, 1996, **8**, 1097–1105.
- (6.9) E. P. Huang, *Proc. Natl. Acad. Sci. U. S. A.*, 1997, **94**, 13386–13387.
- (6.10) S. K. Ghosh, P. Kim, X. a. Zhang, S. H. Yun, A. Moore, S. J. Lippard and Z. Medarova, *Cancer Res.*, 2010, **70**, 6119–6127.
- (6.11) A. Krejčel and W. Maret, *J. Biol. Inorg. Chem.*, 2006, **11**, 1049–1062.
- (6.12) (a) A. I. Bush, *Trends Neurosci.*, 2003, **26**, 207–214; (b) D. Noy, I. Solomonov, O. Sinkevich, T. Arad, K. Kjaer and I. Sagi, *J. Am. Chem. Soc.*, 2008, **130**, 1376–1383.
- (6.13) S. Assaf and S.-H. Chung, *Nature*, 1984, **308**, 734–736.

- (6.14) (a) R. Y. Tsien, ed. A. W. Czarnik, *American Chemical Society*, Washington, DC, 1993, pp. 130–146; (b) Y. Xiang, A. J. Tong, P. Y. Jin and Y. Ju, *Org. Lett.*, 2006, **8**, 2863–2866.
- (6.15) E. L. Que, D. W. Domaille and C. J. Chang, *Chem. Rev.*, 2008, **108**, 1517–1549.
- (6.16) A. P. De Silva, H. N. Gunaratne, T. Gunnlaugsson, A. J. Huxley, C. P. McCoy, J. T. Rademacher and T. E. Rice, *Chem. Rev.*, 1997, **97**, 1515–1566.
- (6.17) P. Jiang and Z. Guo, *Coord. Chem. Rev.*, 2004, **248**, 205–229.
- (6.18) P. Carol, S. Sreejith and A. Ajayaghosh, *Chem.–Asian J.*, 2007, **2**, 338–348.
- (6.19) E. Kimura and S. Aoki, *Zinc Biochemistry, Physiology, and Homeostasis*, 2001, 5–18.
- (6.20) N. C. Lim, J. V. Schuster, M. C. Porto, M. A. Tanudra, L. Yao, H. C. Freake and C. Brückner, *Inorg. Chem.*, 2005, **44**, 2018–2030.
- (6.21) P. P. Cohen, *Biochem. J.*, 1939, **33**, 1478–1487.
- (6.22) J. Awapara, R. P. Sandman and C. Hanly, *Arch. Biochem. Biophys.*, 1962, **98**, 520–525.
- (6.23) W. A. Wood and I. C. Gunsalus, *J. Biol. Chem.*, 1951, **190**, 403–416.
- (6.24) (a) D. A. Bender, ed. D. A. Bender, Cambridge University Press, New York, U.S.A, 1992, pp. 223–268; (b) D. A. Bender, J. F. Bowden, W. F. Coulsen, M. R. Dewji, J. Sutton and E. K. Symes, ed. J. E. Leklem and R. D. Reynolds, Alan R. Liss, New York, U.S.A, 1988, pp. 45–49.
- (6.25) (a) J. Mandal, P. Ghorai, K. Pal, T. Bhaumik, P. Karmakar and A. Saha, *ACS Omega*, 2020, **5**, 145–157; (b) J. Mandal, P. Ghorai, K. Pal, P. Karmakar and A. Saha, *Journal of Luminescence*, 2019, **205**, 14–22; (c) P. Ghorai, S. G. Chowdhury, K. Pal, J. Mandal, P.

Karmakar, A. Franconetti, A. Frontera, S. Blasco, E. García-España, P.P. Parui and A. Saha, *Inorganic Chemistry*, 2022, **61**, 1982-1996; (d) J. Mandal, K. Pal, S. G. Chowdhury, P. Karmakar, A. Panja, S. Banerjee and A. Saha, *Dalton Trans.*, 2022, **51**, 15555-155570;

(6.26) S. Mandal, Y. Sikdar, D. K. Maiti, G. P. Maiti, S. K. Mandal, J. K. Biswas and S. Goswami, *RSC Adv.*, 2015, **5**, 72659–72669.

(6.27) M. J. Frisch, G.W. Trucks, H. B. Schlegel, G. E. Scuseria, M. A. Robb, J. R. Cheeseman, G. Scalmani, V. Barone, B. Mennucci, G.A. Petersson, H. Nakatsuji, M. Caricato, X. Li, H. P. Hratchian, A. F. Izmaylov, J. Bloino, G. Zheng, J. L. Sonnenberg, M. Hada, M. Ehara, K. Toyota, R. Fukuda, J. Hasegawa, M. Ishida, T. Nakajima, Y. Honda, O. Kitao, H. Nakai, T. Vreven, J. A. Montgomery, Jr. J. E. Peralta, F. Ogliaro, M. Bearpark, J. J. Heyd, E. Brothers, K. N. Kudin, V. N. Staroverov, R. Kobayashi, J. Normand, K. Raghavachari, A. Rendell, J. C. Burant, S. S. Iyengar, J. Tomasi, M. Cossi, N. Rega, J. M. Millam, M. Klene, J. E. Knox, J. B. Cross, V. Bakken, C. Adamo, J. Jaramillo, R. Gomperts, R. E. Stratmann, O. Yazyev, A. J. Austin, R. Cammi, C. Pomelli, J. W. Ochterski, R. L. Martin, K. Morokuma, V. G. Zakrzewski, G. A. Voth, P. Salvador, J. J. Dannenberg, S. Dapprich, A.D. Daniels, Ö. Farkas, J.B. Foresman, J.V. Ortiz, J. Cioslowski and D. J. Fox, GAUSSIAN09, Revision D.01, Gaussian Inc. Wallingford, CT, 2009.

(6.28) A. D. Becke, *J. Chem. Phys.* 1993, **98**, 5648-5652.

(6.29) C. Lee, W. Yang and R. G. Parr, *Phys. Rev. B*, 1988, **37**, 785-789.

(6.30) P. J. Hay and W. R. Wadt, *J. Chem. Phys.*, 1985, **82**, 270-283.

(6.31) P. J. Hay and W. R. Wadt, *J. Chem. Phys.*, 1985, **82**, 284-298.

(6.32) P. J. Hay and W. R. Wadt, *J. Chem. Phys.*, 1985, **82**, 299-310.

- (6.33) G. A. Petersson, A. Bennett, T. G. Tensfeldt, M. A. Al-Laham, W. A. Shirley and J. Mantzaris, *J. Chem. Phys.*, 1988, **89**, 2193-2218.
- (6.34) G. A. Petersson and M. A. Al-Laham, *J. Chem. Phys.*, 1991, **94**, 6081-6090.
- (6.35) R. Bauernschmitt and R. Ahlrichs, *Chem. Phys. Lett.*, 1996, **256**, 454-464.
- (6.36) R. E. Stratmann, G. E. Scuseria and M. J. Frisch, *J. Chem. Phys.*, 1998, **109**, 8218-8224.
- (6.37) M. E. Casida, C. Jamorski, K. C. Casida and D. R. Salahub, *J. Chem. Phys.*, 1998, **108**, 4439-4449.
- (6.38) V. Barone and M. Cossi, *J. Phys. Chem. A*, 1998, **102**, 1995-2001.
- (6.39) M. Cossi and V. Barone, *J. Chem. Phys.*, 2001, **115**, 4708-4717.
- (6.40) M. Cossi, N. Rega, G. Scalmani and V. Barone, *J. Comput. Chem.*, 2003, **24**, 669-681.
- (6.41) N. M. O'Boyle, A. L. Tenderholt and K. M. Langner, *J. Comput. Chem.*, 2008, **29**, 839-845.
- (6.42) (a) H. A. Benesi and J. H. Hildebrand, *J. Am. Chem. Soc.*, 1949, **71**, 2703-2707; (b) S. Banerjee, P. Brandão and A. Saha, *RSC Advances*, 2016, **6**, 101924-101936.
- (6.43) A. B. Pradhan, S. K. Mandal, S. Banerjee, A. Mukherjee, S. Das, A. R. K. Bukhsh and A. Saha, *Polyhedron*, 2015, **94**, 75-82.
- (6.44) A. Hussain, K. Mariappan, D. C. Cork, L. D. Lewandowski, P. K. Shrestha, S. Giri, X. Wang and A. G. Sykes, *RSC Adv.*, 2021, **11**, 34181-34192.



Appendix-I

**List of Publications
&
Seminar Attended**

List of Publications

1. 2-hydroxy-5-methylisophthalaldehyde based fluorescent-colorimetric chemosensor for dual detection of Zn^{2+} and Cu^{2+} with high sensitivity and application in live cell imaging; **J. Mandal**, P. Ghorai, K. Pal, P. Karmakar, A. Saha; Journal of Luminescence, 2018, **205**, 14-22.
2. An aminoquinoline based biocompatible fluorescent and colourimetric pH sensor designed for cancer cell discrimination; **J. Mandal**, P. Ghorai, P. Brandão, K. Pal, P. Karmakar, A. Saha; New Journal of Chemistry; 2018, **42**, 19818-19826.
3. Development of Rhodamine 6G-Based Fluorescent Chemosensors for Al^{3+} -Ion Detection: Effect of Ring Strain and Substituent in Enhancing Its Sensing Performance; **J. Mandal**, P. Ghorai, K. Pal, T. Bhaumik, P. Karmakar, A. Saha; ACS omega; 2019, **5**, 145-157.
4. Two rhodamine-azo based fluorescent probes for recognition of trivalent metal ions: crystal structure elucidation and biological applications; **J. Mandal**, K. Pal, S. G. Chowdhury, P. Karmakar, A. Panja, S. Banerjee, A. Saha; Dalton Transactions; 2022, **51**, 15555-15570.
5. Aza-Crown-Based Macrocyclic Probe Design for “PET-off” Multi- Cu^{2+} Responsive and “CHEF-on” Multi- Zn^{2+} Sensor: Application in Biological Cell Imaging and Theoretical Studies; P. Ghorai, S. G. Chowdhury, K. Pal, **J. Mandal**, P. Karmakar, A. Franconetti, A. Frontera, S. Blasco, E. García-España, P. P. Parui, A. Saha; Inorganic Chemistry; 2022, **61**, 1982-1996.
6. Two pyridoxal derived Schiff base chemosensors design for fluorescence turn-on sensing of Zn(II) ion in pure aqueous medium; **J. Mandal**, S. G. Chowdhury, P. Karmakar, A. Saha; (manuscript submitted to New Journal of Chemistry)
7. First example of chromone-based Ni(II) coordination polymers with tunable magnetic properties; **J. Mandal**, P. Brandão, S. Benmansour, C. J. Gómez García, A. Saha, (just accepted in Crystal Growth & Design (Manuscript ID: cg-2022-01076z.R1)).

List of Seminar Attended and Presented Poster

1. National Seminar on “*Emerging Trends in Chemistry (ETC-2017)*” Under CAS II Program, organized by Department of Chemistry, Jadavpur University.

Held on February 15, 2017.

2. National Seminar on “*Current Development in Chemical Science (CDCS-2018)*” Under CAS II Program, organized by Department of Chemistry, Jadavpur University.

Held on March 7, 2018.

3. National Seminar on “*Chemical Science: Today and Tomorrow (CSTT-2019)*” Under CAS II Program, organized by Department of Chemistry, Jadavpur University.

Held on March 14, 2019.

4. National Seminar on “*Emerging Trends in Chemical Sciences*” Under CAS II Program, organized by Department of Chemistry, Jadavpur University.

Held on January 07, 2020.

5. National Seminar on “*Recent Trends in Inorganic Chemistry*”, organized by Inorganic Chemistry Section, Department of Chemistry, Jadavpur University.

Held on March 06, 2020.

Appendix-II

THESIS RELATED
PUBLISHED PAPERS

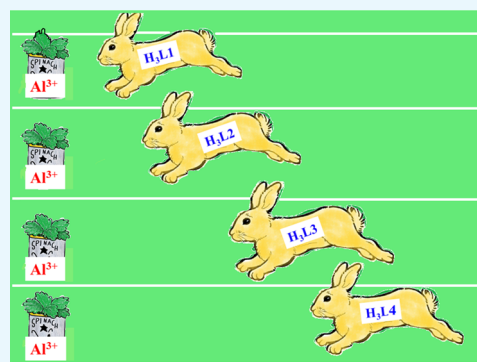
Development of Rhodamine 6G-Based Fluorescent Chemosensors for Al³⁺-Ion Detection: Effect of Ring Strain and Substituent in Enhancing Its Sensing Performance

Jayanta Mandal,[†] Pravat Ghorai,[†] Kunal Pal,[‡] Tanurima Bhaumik,[†] Parimal Karmakar,[‡] and Amrita Saha^{*,†}

[†]Department of Chemistry and [‡]Department of Life Science and Biotechnology, Jadavpur University, Kolkata 700032, India

Supporting Information

ABSTRACT: Four rhodamine 6G-based chemosensors (H₃L1–H₃L4) are designed for selective detection of Al³⁺ ion. They are characterized using various spectroscopic techniques and X-ray crystallography. All absorption and emission spectral studies have been performed in 10 mM *N*-(2-hydroxyethyl)-piperazine-*N'*-ethanesulfonic acid (HEPES) buffer solution at pH 7.4 in H₂O/MeOH (9:1, v/v) at 25 °C. In absorption spectra, chemosensors exhibit an intense band around 530 nm in the presence of Al³⁺ ion. Chemosensors (H₃L1–H₃L4) are nonfluorescent when excited around 490 nm. The presence of Al³⁺ ion enhances the emission intensity (555 nm) many times. The formation of complexes 1–4 is established with the aid of different spectroscopic techniques. The limit of detection value obtained in the nanomolar range confirms the high sensitivity of the probes toward Al³⁺ ion. It has been observed that the presence of aliphatic spacers in the diamine part and different halogen substituents in the salicylaldehyde part strongly influences the selectivity of the chemosensors toward Al³⁺ ion. The propensity of the chemosensors to identify intracellular Al³⁺ ions in triple-negative human breast cancer cell line MDA-MB-468 by fluorescence imaging is also examined in this study.



INTRODUCTION

Metal ions play a crucial role in human life and in the environment. Therefore, their detection is of immense importance to biologists, chemists, and environmentalists.¹ Scientists emerge in the development of new methodologies for recognition of these cations.^{2–5} Design and synthesis of new chemosensors for the selective detection of biologically and environmentally important cations needs a special mention in this context.^{6,7}

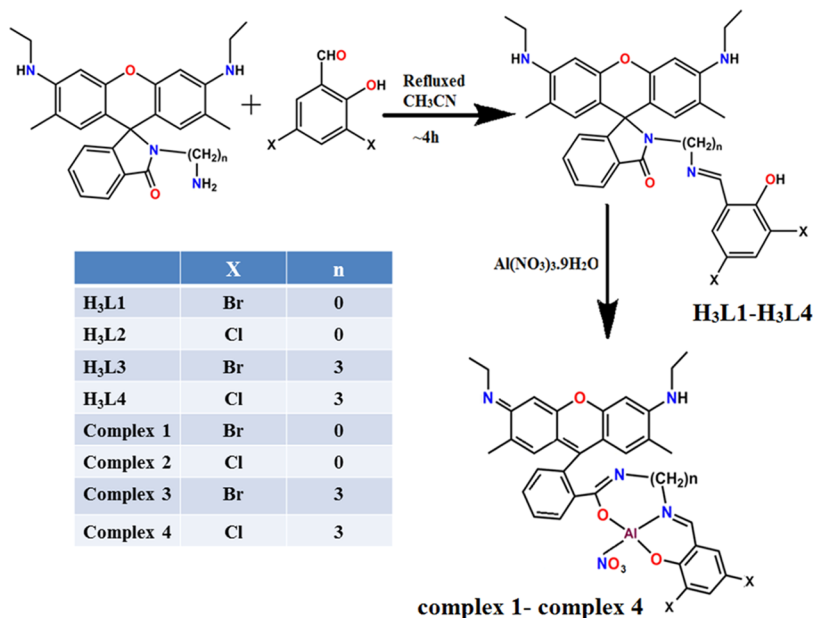
Aluminum is the highest abundant metal in the earth's crust.^{8–10} Materials prepared from aluminum are widely used in our society. They are used in food additives, textile industry, water treatment plants, paper industry, production of light alloys, medicines (antacids), cookware, etc. Aluminum toxicity causes Alzheimer's and Parkinson's diseases.¹¹ Other Al-contaminated diseases are amyotrophic lateral sclerosis, microcytic hypochromic anemia, osteomalacia, and breast cancer.^{12–17} Preparation of chemosensors for the selective detection of Al³⁺ ion is a challenging task owing to its weak coordination ability, strong hydration ability, and interferences from other trivalent ions like Cr³⁺ and Fe³⁺. To date, a considerable number of organic probes for Al³⁺ ion^{18–23} have been synthesized, most of which suffer from some drawbacks like insolubility in aqueous solution, synthetic procedures with multiple steps, poor sensitivity and selectivity with target metal ions, etc.^{24–26} Al³⁺-sensing organic probes consist of important

fluorophoric units like rhodamine, anthraquinone, BODIPY, salicylaldehyde, fluorescein, coumarin, etc.^{27–33} Rhodamine-based chemophores are colorless and nonfluorescent due to the presence of spirolactam ring. The sensing mechanism is basically opening of the spirolactam ring resulting in a strong emission. Low pH or acidic condition also initiates opening of the spirolactam ring. Therefore, selective choice of metal ion can initiate spirolactam ring opening of rhodamine-based probes. A literature study reveals that rhodamine-based probes can selectively detect various metal ions like Al³⁺, Fe³⁺, Cr³⁺, Hg²⁺, Cu²⁺, etc.^{34–43} Some recently reported rhodamine-based important chemosensors are collected in Chart S1 (Supporting Information). Chart S1 clearly shows that chemosensors reported in the present work have certain advantages regarding the crystal structure, real sample analysis, and cell imaging study in comparison to previously reported data.⁴⁴ Yang et al.^{44a} reported two rhodamine-pyrazole-based both colorimetric and turn-on fluorescent chemosensors for dual detection of Ni²⁺ and Al³⁺ ions in alcohol and aqueous DMF medium. Jeong et al.^{44b} synthesized rhodamine-chloronicotinaldehyde-based “OFF–ON” chemosensor for colorimetric and fluorimetric detection of Al³⁺ in acetonitrile medium. Chemate and

Received: July 15, 2019

Accepted: November 14, 2019

Published: December 27, 2019

Scheme 1. Route of Preparation of Chemosensors (H_3L1-H_3L4) and Complexes 1–4

co-workers have used two rhodamine-based OFF–ON fluorescent chemosensors for dual detection of Hg^{2+} and Al^{3+} in aqueous solution.^{44c} Maity and co-workers prepared a rhodamine-1,2,3-triazole-based chemosensor for dual detection of Al^{3+} and fluoride or acetate ions in CH_3OH-H_2O (9:1) medium.^{44d} The above examples did not report crystal structures of the chemosensors and their biological cell imaging studies. In this work, we have successfully elucidated crystal structures of all four chemosensors and also performed their biological studies. In an interesting work, Roy and co-workers synthesized a rhodamine-based dual chemosensor for detection of Al^{3+} and Zn^{2+} ions in *N*-(2-hydroxyethyl)-piperazine-*N'*-ethanesulfonic acid (HEPES) buffer.^{44e} Ghosh and co-workers have prepared a chemosensor using the rhodamine unit for detection and discrimination of Al^{3+} and Hg^{2+} ions in HEPES buffer.^{44f} Alam and co-workers synthesized a rhodamine-based trivalent fluorescent sensor which can selectively detect Fe^{3+} , Al^{3+} , and Cr^{3+} ions in CH_3OH-H_2O (1:1).^{44g} These works clearly show that the chemosensors did not achieve their selectivity toward Al^{3+} ions, whereas our synthesized chemosensors show selectivity only toward Al^{3+} ions. Fu and co-workers^{44h} synthesized a rhodamine 6G-containing fluorescent probe for Al^{3+} ion. Sahana et al. reported a rhodamine–pyrene compound for selective colorimetric and fluorimetric detection of Al^{3+} ion and living cell imaging study.⁴⁴ⁱ In the above chemosensors, the limit of detection (LOD) values are observed in the micromolar range; interestingly, our reported chemosensors give LOD values in the nanomolar range. Roy et al. reported a rhodamine-based fluorescent chemosensor^{44j} for selective detection of Al^{3+} ions in $H_2O/MeOH = 1: 9$ (v/v) medium. Sen and co-workers also reported a rhodamine-based Al^{3+} -ion-sensing organic compound^{44k} in $EtOH$ –water, 1: 3 (v/v) medium. Sahana and group synthesized a rhodamine-based fluorescent probe^{44l} for selective detection of Al^{3+} ions in $EtOH$ –water, 4: 1 (v/v) medium. In all of these examples, medium is mainly organoaqueous, whereas our Al^{3+} -ion-sensing studies are performed in $MeOH$ –water, 1: 9 (v/v) medium.

In this work, we have chosen hydrazine and 1,3-diaminopropane as amines, 3,5-dichlorosalicylaldehyde and 3,5-dibromosalicylaldehyde as aldehydes to prepare four different rhodamine 6G-based chemosensors, H_3L1 , H_3L2 , H_3L3 , and H_3L4 , respectively. All of the four chemosensors selectively detect Al^{3+} both colorimetrically and fluorimetrically. The structure–property relationship is established in this work. Variation of amines and halogen substituents in the salicylaldehyde part controls the extent of selectivity toward Al^{3+} ion. A significant variation in different sensing parameters such as LOD, binding constant, and naked eye detection of Al^{3+} ion is observed during this study. These biocompatible chemosensors (H_3L1-H_3L4) also exhibit cell permeability and sense intracellular Al^{3+} ion present in breast cancer cell line, MDA-MB-468 cells.

RESULTS AND DISCUSSION

Synthesis and Characterization. *N*-(Rhodamine-6G)-lactam-hydrazine and *N*-(Rhodamine-6G)lactam-propylenediamine have been synthesized according to a published procedure.⁴⁵ The chemosensors (H_3L1-H_3L4) are synthesized by the Schiff base condensation reaction using rhodamine-6G-based amine and 3,5-dibromosalicylaldehyde or 3,5-dichlorosalicylaldehyde. They are carefully characterized using different spectroscopy techniques (UV–vis, Fourier transform infrared (FT-IR), and NMR), and the purity is verified with ESI-MS and C, H, N analysis (Figures S1–S5, Supporting Information).

H_3L1-H_3L4 react with $Al(NO_3)_3 \cdot 9H_2O$ in a 1:1 ratio to produce complexes 1–4 (Scheme 1). They are characterized by 1H NMR, ^{13}C NMR, FT-IR spectroscopy, C, H, N analysis, and electrospray ionization mass spectrometry (ESI-MS) analysis. The experimentally obtained ESI-MS data are well matched with their simulated result (Figures S6–S10, Supporting Information). Detail data are presented in Experimental Section.

Crystal Structure Descriptions of Chemosensors (H_3L1-H_3L4). We have successfully developed X-ray-quality crystals of H_3L1 , H_3L2 , and H_3L3 , H_3L4 , which are poorly

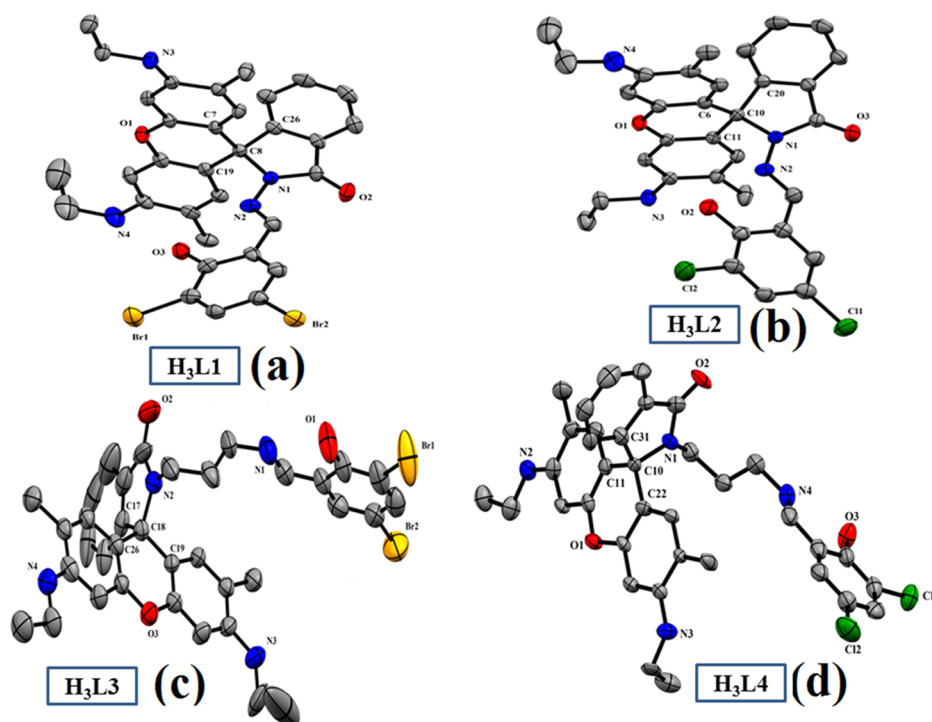


Figure 1. ORTEP view of the chemosensors (a) = $\text{H}_3\text{L1}$, (b) = $\text{H}_3\text{L2}$, (c) = $\text{H}_3\text{L3}$, and (d) = $\text{H}_3\text{L4}$. Atoms are shown as 30% thermal ellipsoids. Here, H atoms are omitted for clarity.

diffracted. $\text{H}_3\text{L1}$ and $\text{H}_3\text{L2}$ are formed with a triclinic crystal system with a $P\bar{1}$ space group, whereas $\text{H}_3\text{L3}$ and $\text{H}_3\text{L4}$ crystals are developed in the monoclinic system with a $P2_1/c$ space group (Table S1). ORTEP views of the chemosensors are shown in Figure 1 ($\text{H}_3\text{L1}$ – $\text{H}_3\text{L4}$, respectively). Important bond distances and bond angles are collected in Tables S2 and S3, respectively (Supporting Information). The organic molecule is nonplanar, and it confirms the Schiff base condensation reaction along with the presence of a spirolactam ring and a xanthenes unit within the molecule. The C–O and C–N bond distances of the chemosensors vary within the range of 1.217–1.381 and 1.274–1.441 Å, respectively.

NMR Studies. All of the chemosensors and Al^{3+} –probe complexes give well-resolved ^1H NMR spectra in $\text{DMSO}-d_6$ solvent. In $\text{H}_3\text{L1}$, the phenolic OH and imine proton appear as a sharp singlets at 11.56 and 8.90 ppm, respectively. Aromatic protons appear in the region 7.94–6.20 ppm. Aliphatic amine (–NH) protons appear as triplet at 5.11 ppm. Aliphatic CH_2 protons appear as quartet at 3.13 ppm. Aromatic CH_3 protons appear as singlet at 1.84 ppm, whereas aliphatic CH_3 protons appear as triplet at 1.20 ppm (Figures S11–S14, Supporting Information).

In complex **1**, the phenolic –OH peak disappears due to complexation and imine proton shifts to downfield and appears as a sharp singlet at 9.30 ppm. We also observe significant changes in the aromatic peak positions and broadening of the peaks due to complexation. During complexation, one NH proton of the aliphatic part disappears and the other appears as a broad peak at 5.11 ppm. Aliphatic CH_2 protons merged with water molecules and appear as multiplet at 3.50 ppm. Aromatic CH_3 protons appear as singlet at 1.87 ppm, and aliphatic CH_3 protons appear as triplet at 1.22 ppm (Figures S15–S18).

All of the chemosensors and probe-bound Al^{3+} complexes give clean ^{13}C NMR spectra in the $\text{DMSO}-d_6$ solvent. In $\text{H}_3\text{L1}$, spirolactam amide carbon appears at 165.58 and phenolic

carbon appears at 164.21 ppm. Imine carbon appears at 161.87 ppm. Aromatic carbons are present in the region 151.88–96.32 ppm. The carbon atom connecting the xanthenes part and the spirolactam ring is sp^3 -hybridized and appears at 66.24 ppm. Aromatic CH_3 carbons appear with double intensity at 37.92 ppm. Aliphatic CH_2 and CH_3 carbons appear with double intensity at 17.44 and 14.59 ppm, respectively (Figures S19–S22, Supporting Information).

In complex **1**, spirolactam amide carbon appears at 167.58, phenolic carbon appears at 165.90 ppm, and imine carbon appears at 163.37 ppm. These three peaks are shifted to downfield due to metal coordination. Aromatic carbons appear within 151.88–96.32 ppm. Since metal coordination results spirolactam ring opening, the sp^3 -hybridized carbon atom connecting the xanthenes part and the spirolactam ring now becomes sp^2 -hybridized and appears at 134.90 ppm. Aromatic CH_3 carbons appear with double intensity at 37.92 ppm. Aliphatic CH_2 and CH_3 carbons appear with double intensity at 17.44 and 14.59 ppm, respectively (Figures S23–S26, Supporting Information).

Absorption Spectral Analysis. The UV–vis spectra of chemosensors ($\text{H}_3\text{L1}$ – $\text{H}_3\text{L4}$) are first examined in 10 mM HEPES buffer solution at pH 7.4 (9:1, water/methanol, v/v). Chemosensors $\text{H}_3\text{L1}$ and $\text{H}_3\text{L2}$ exhibit well-resolved bands at ~ 290 and ~ 345 nm, whereas $\text{H}_3\text{L3}$ and $\text{H}_3\text{L4}$ show a well-defined band at ~ 420 nm. Peaks are represented as $\pi \rightarrow \pi^*$ and $n \rightarrow \pi^*$ type of transitions. Interestingly, upon successive addition of Al^{3+} ions (0–11 μM , 10 mM HEPES buffer solution; pH 7.4; 9:1, water/methanol, v/v) to the chemosensor (10 μM), a new peak appears at ~ 530 nm with significant changes in the spectra of all chemosensors ($\text{H}_3\text{L1}$ – $\text{H}_3\text{L4}$). In $\text{H}_3\text{L1}$ and $\text{H}_3\text{L2}$, absorbance of peaks at ~ 290 and ~ 345 nm gradually increase, whereas in $\text{H}_3\text{L3}$ and $\text{H}_3\text{L4}$, the absorbance of peak at ~ 420 nm gradually decreases (Figures 2 and S27–S29, Supporting Information). In the presence of

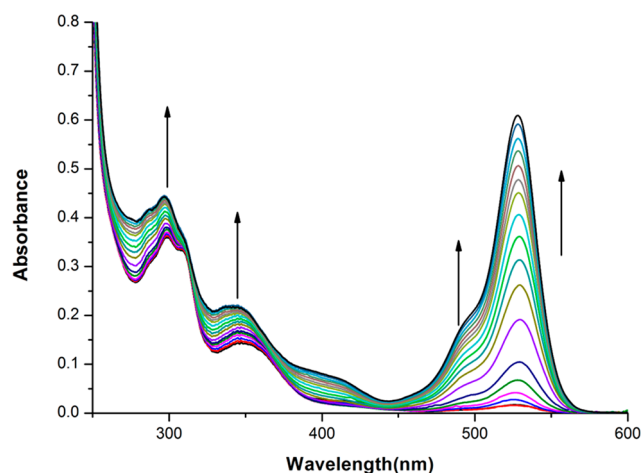


Figure 2. Absorption titration study of $\text{H}_3\text{L1}$ ($10 \mu\text{M}$) with gradual addition of Al^{3+} , $0\text{--}11 \mu\text{M}$ in 10 mM HEPES buffer at $\text{pH } 7.4$.

Al^{3+} , spirolactam ring opening occurs, followed by the coordination of the cation. Here, the Al^{3+} ion binds with phenoxido oxygen, imine nitrogen, and amide oxygen of the chemosensor. Spirolactam ring opening results reorientation of protons within the aromatic ring and consequently removal of one primary amine proton. Generation of a new peak at $\sim 530 \text{ nm}$ in the presence of Al^{3+} ions also confirms structural rearrangement within the organic molecule. The color of the solution turns fluorescent pinkish yellow. Saturation has been observed in the presence of 1.1 equiv of Al^{3+} ions to the chemosensor. The $1:1$ binding stoichiometry of the chemosensors with Al^{3+} ions has been confirmed by Job's plot analysis (Figures S30–S33, Supporting Information). These results have been further supported by ESI-MS analysis. It is important to mention that the addition of different cations (Cd^{2+} , Hg^{2+} , Pb^{2+} , Zn^{2+} , Ag^+ , Mn^{2+} , Fe^{3+} , Co^{2+} , Ni^{2+} , Na^+ , K^+ , Mg^{2+} , and Ca^{2+}) did not change the initial absorption spectrum of the chemosensor appreciably.

Fluorescence Properties Analysis. The experiment is performed in 10 mM HEPES buffer at $\text{pH} = 7.4$ ($9:1$, water/methanol, v/v) at ambient conditions. When excited at 345 nm , probes ($10 \mu\text{M}$) are nonfluorescent. Upon successive addition of Al^{3+} ions ($0\text{--}11 \mu\text{M}$) to the probe, an enormous fluorescence enhancement is observed at 555 nm (Figures 3 and S34–S36, Supporting Information). The fluorescence enhancement has a steady growth and finally reaches a maximum at 1.1 equiv of Al^{3+} ions. In fact, metal ions initiate

opening of spirolactam ring followed by a long conjugation of π -electronic system within the probe (Figure S37). Generation of a fluorescence peak at 555 nm in the presence of Al^{3+} ions also proves the above fact. Interestingly, the values of increment in emission spectra is not equal for all of the probes. In the case of $\text{H}_3\text{L1}$ and $\text{H}_3\text{L2}$, the emission enhancement is 780- and 725-fold , whereas for $\text{H}_3\text{L3}$ and $\text{H}_3\text{L4}$, the enhancement is 425- and 391-fold .

The binding ability of the chemosensors toward Al^{3+} ions has been calculated using the Benesi–Hildebrand equation (eq 1) involving fluorescence titration curve⁴⁶

$$1/(F - F_0) = 1/(F_{\text{max}} - F_0) + (1/K[C])\{1/(F_{\text{max}} - F_0)\} \quad (1)$$

here, F_{max} , F_0 , and F_x are fluorescence intensities of chemosensors ($\text{H}_3\text{L1}\text{--}\text{H}_3\text{L4}$), in the presence of metal ions at saturation, free chemosensors ($\text{H}_3\text{L1}\text{--}\text{H}_3\text{L4}$), and any intermediate metal-ions concentration, respectively. K is denoted as the binding constant of the complexes, and the concentration of Al^{3+} ions is represented by C . The value of binding constant (K) of the complexes has been determined using the relation $K = 1/\text{slope}$. The binding constant values are 8.00×10^5 , 6.90×10^5 , 1.37×10^4 , and $1.03 \times 10^4 \text{ M}^{-1}$, respectively, for the chemosensors $\text{H}_3\text{L1}\text{--}\text{H}_3\text{L4}$ toward Al^{3+} ions (Figures S38–S41, Supporting Information). We have also performed fluorescence titrations of the chemosensors in the presence of Al^{3+} ions in aprotic solvent such as tetrahydrofuran (THF) to determine the binding constant in THF and to compare the difference of binding constant values determined in protic and aprotic solvents. The calculated binding constant values in THF are close to the previously calculated values measured in the HEPES buffer solution ($9:1$, water/methanol, v/v) (Table S4, Figures S38–S45, Supporting Information). Therefore, we can conclude that free chemosensors $\text{H}_3\text{L1}\text{--}\text{H}_3\text{L4}$ do not undergo deprotonation in solution (protic or aprotic). Al^{3+} ions can promote deprotonation of $\text{H}_3\text{L1}\text{--}\text{H}_3\text{L4}$ in both aqueous or nonaqueous solution.

The high selectivity of the chemosensors toward Al^{3+} ions is again established by competition assay experiment. Here, in the presence of chemosensor and Al^{3+} ions (1.0 equiv), different metal ions (Cd^{2+} , Hg^{2+} , Pb^{2+} , Zn^{2+} , Ag^+ , Mn^{2+} , Fe^{3+} , Co^{2+} , Ni^{2+} , Na^+ , K^+ , Mg^{2+} , and Ca^{2+}) (Figures S46–S49, Supporting Information) and common anions ($\text{S}_2\text{O}_3^{2-}$, S^{2-} , SO_3^{2-} , HSO_4^- , SO_4^{2-} , SCN^- , N_3^- , OCN^- , AsO_4^{3-} , H_2PO_4^- , HPO_4^{2-} , PO_4^{3-} , ClO_4^- , AcO^- , NO_3^- , F^- , Cl^- , PF_6^- , and

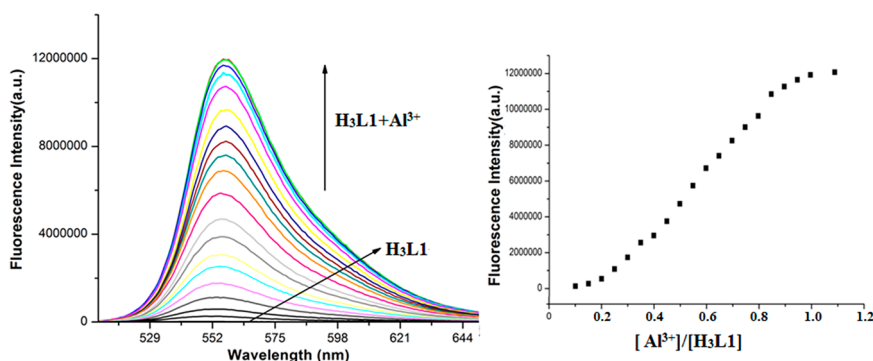


Figure 3. Fluorescence titration of $\text{H}_3\text{L1}$ ($10 \mu\text{M}$) in 10 mM HEPES buffer at $\text{pH} = 7.4$ by successive addition of Al^{3+} ($0\text{--}11 \mu\text{M}$) with $\lambda_{\text{em}} = 555 \text{ nm}$ ($1/1 \text{ slit}$).

$\text{P}_2\text{O}_7^{4-}$) are added in excess amount (4.0 equiv) in 10 mM HEPES buffer solution at pH 7.4. Competition assay experiments clearly express high-fluorescent recognition of chemosensors ($\text{H}_3\text{L1}$ – $\text{H}_3\text{L4}$) for Al^{3+} ions over most of the metal ions and all common anions. It is important to mention that in the presence of Cr^{3+} , Mg^{2+} , Cu^{2+} , and Fe^{3+} ions little quenching in fluorescence intensity has been observed (Figures 4 and S50–S56, Supporting Information).

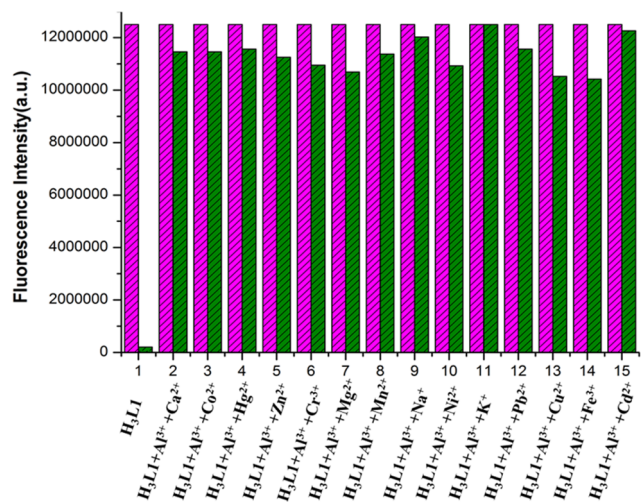


Figure 4. Relative fluorescence intensity diagram of $[\text{H}_3\text{L1}-\text{Al}^{3+}]$ system in the presence of different cations in 10 mM HEPES buffer at pH 7.4. 1 = only $\text{H}_3\text{L1}$ and (2–15) = $\text{H}_3\text{L1}$ (10 μM) + Al^{3+} (10 μM) + M^{n+} (40 μM), where M^{n+} = (2— Ca^{2+} , 3— Co^{2+} , 4— Hg^{2+} , 5— Zn^{2+} , 6— Cr^{3+} , 7— Mg^{2+} , 8— Mn^{2+} , 9— Na^+ , 10— Ni^{2+} , 11— K^+ , 12— Pb^{2+} , 13— Cu^{2+} , 14— Fe^{3+} , 15— Cd^{2+}).

Interestingly, all of the chemosensors, $\text{H}_3\text{L1}$ – $\text{H}_3\text{L4}$, also act as colorimetric probe for selective detection of Al^{3+} ions. In the presence of Al^{3+} ions, all of the probes exhibit fluorescent pinkish yellow coloration, whereas they are almost colorless in the presence of common ions. The intensity of the Al^{3+} chemosensor increases in the order $\text{H}_3\text{L1} > \text{H}_3\text{L2} > \text{H}_3\text{L3} > \text{H}_3\text{L4}$. Thus, the chemosensors will be a good choice for selective colorimetric detection of Al^{3+} ions in both environmental and biological fields (Figures 5 and S57–S59,

Supporting Information). We have used saloon waste water and our laboratory tap water for real sample analysis. Al^{3+} ions present in saloon waste water and laboratory tap water are successfully detected by our chemosensors through the naked eye and under UV lamp (Figure S60, Supporting Information).

Reversibility and regeneration are two important factors for real-time application of the chemosensor. This is tested with the aid of sodium salt of ethylenediaminetetraacetic acid (Na_2EDTA) solution. The fluorescent pinkish yellow color of the probe– Al^{3+} complex disappears after addition of 1 equiv of Na_2EDTA with a simultaneous decrease in fluorescence intensity, which clearly indicates the regeneration of the free chemosensor. Again, addition of Al^{3+} ions to the probe gives back fluorescent pinkish yellow coloration. The whole cycle is repeated for at least five times to establish reversibility and regeneration point (Figure S61, Supporting Information).

Limit of detection (LOD) of the chemosensors toward Al^{3+} ions is estimated using the 3σ method.⁴⁷ The detection limits of the chemosensors ($\text{H}_3\text{L1}$ – $\text{H}_3\text{L4}$) for the Al^{3+} ions are 1.4×10^{-9} , 2.50×10^{-9} , 0.40×10^{-8} , and 0.53×10^{-8} M, respectively.

The effect of pH on chemosensors ($\text{H}_3\text{L1}$ – $\text{H}_3\text{L4}$) both in free condition and in the presence of Al^{3+} ions is studied fluorimetrically. It is well known that in acidic condition, the spirolactam ring of the chemosensor opens. A similar observation is also noticed in the presence of Al^{3+} ions. Therefore, both free chemosensor and chemosensor– Al^{3+} adduct will exhibit high fluorescence intensity at pH 2–4. At pH 5, a sharp decrease in the fluorescence intensity of free chemosensor is observed. After pH 5–11, its fluorescence intensity is very weak and remains unchanged. This observation suggests reconstruction of spirolactam ring in neutral and basic conditions. In the presence of Al^{3+} ions, the fluorescence intensity of the chemosensor decreases slightly at pH 4 and then it maintains a constant value up to pH 8. At pH 9, a sharp decrease in fluorescence intensity of chemosensor is observed. After pH 9–11, a very weak fluorescence intensity is observed. This is probably due to the generation of $\text{Al}(\text{OH})_3$ and free chemosensor at higher pH. Rest of the probes ($\text{H}_3\text{L2}$ – $\text{H}_3\text{L4}$) and probe– Al^{3+} adducts also followed a similar trend in fluorescence intensity at different pH values (Figures 6 and S62–S64, Supporting Information). The pH experiments

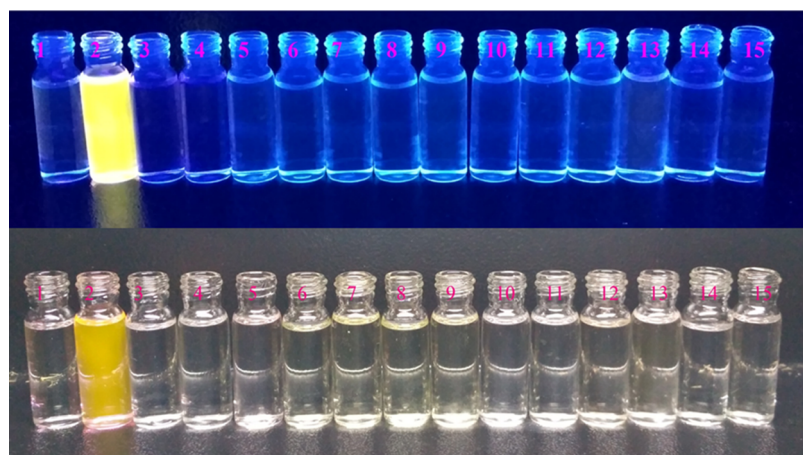


Figure 5. Visual color changes of chemosensor $\text{H}_3\text{L1}$ (10 μM) in the presence of common metal ions (1 equiv) in 10 mM HEPES buffer (pH 7.4). The images in the bottom row and top row were taken under visible light and UV light, respectively, where 1 = only $\text{H}_3\text{L1}$, 2–15 = $\text{H}_3\text{L1}$ + different metal ions (Al^{3+} , Cu^{2+} , Cd^{2+} , Pb^{2+} , Hg^{2+} , Mn^{2+} , Fe^{3+} , Co^{2+} , Ni^{2+} , K^+ , Na^+ , Mg^{2+} , Ca^{2+} , and Zn^{2+} , respectively).

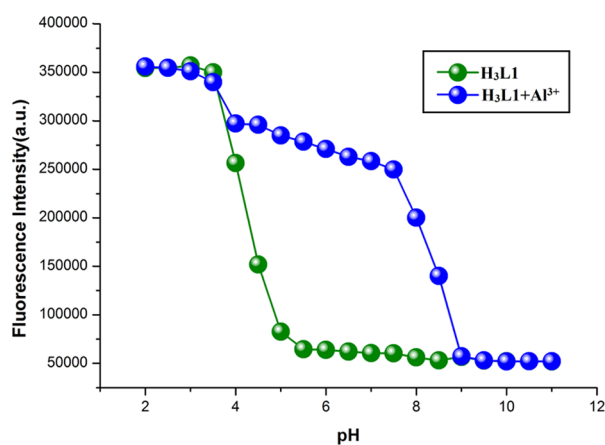


Figure 6. Fluorescence intensity of H₃L1 (10 μM) in the absence and presence of Al³⁺ ions (10 μM) at different pH values in 10 mM HEPES buffer.

show that these chemosensors can act as a selective fluorescent probe to recognize Al³⁺ ions in the presence of other metal ions in a biological system under physiological condition.

Lifetime and Quantum Yield Study. Lifetime measurements for the chemosensors (H₃L1–H₃L4) and complexes 1–4 are studied at 25 °C in 10 mM HEPES buffer (pH = 7.4) medium. The average values of fluorescence decay lifetime of the chemosensors and complexes 1–4 have been measured using the given formula ($\tau_f = a_1\tau_1 + a_2\tau_2$, where a_1 and a_2 are the relative amplitudes of the decay process). The average values of fluorescence lifetime of the chemosensors (H₃L1–H₃L4) and complexes 1–4 are 3.95, 2.56, 1.58, 1.06 ns and 6.8, 4.58, 4.53, 4.38 ns, respectively (Figures S69–S72 and Table S5, Supporting Information).

The fluorescence quantum yield (Φ) has been calculated as follows

$$\Phi_{\text{sample}} = \left\{ \frac{(\text{OD}_{\text{standard}} \times A_{\text{sample}} \times \eta_{\text{sample}}^2)}{(\text{OD}_{\text{sample}} \times A_{\text{standard}} \times \eta_{\text{standard}}^2)} \right\} \times \Phi_{\text{standard}} \quad (2)$$

In the above equation (eq 2), A is the area under the emission spectral curve, OD is the optical density of the compound at the excitation wavelength, and η is the refractive index of the solvent. The Φ_{standard} value is taken as 0.52 (for quinine sulfate).

The values of Φ for H₃L1–H₃L4 and probe–Al³⁺ complexes 1–4 are estimated to be 0.004, 0.003, 0.002, 0.004 and 0.24, 0.18, 0.13, 0.11, respectively (Table S5).

Mechanism of Fluorescence Intensity Enhancement in Chemosensors in the Order H₃L1 > H₃L2 > H₃L3 > H₃L4 in the Presence of Al³⁺ Ions. In this work, the sensing behavior of four rhodamine 6G-based chemosensors toward Al³⁺ ions is explored. The fluorescence intensity of the chemosensors increases abruptly in the presence of Al³⁺ ions due to opening of the spirolactam ring (Scheme 1). This mechanistic process has been supported by spectroscopic techniques such as ¹H, ¹³C NMR, and FT-IR spectroscopy.^{31,34,36–38,40} In the presence of Al³⁺ ions, appreciable changes are observed in their ¹H NMR spectrum of free chemosensors. The presence of Al³⁺ ion initiates spirolactam ring opening followed by rearrangement of double bonds. This results in the disappearance of one aliphatic amine (–NH)

proton. The disappearance of phenolic –OH peak and downfield shift of imine proton (9.30 ppm) establishes coordination of phenoxido oxygen and imine nitrogen atom with the metal center. Changes in the spectral pattern of both aromatic and aliphatic protons are also observed after addition of Al³⁺. In free chemosensor, the carbon atom connecting the xanthene part and the spirolactam ring is sp³-hybridized, and it appears at 66.24 ppm. Interestingly, during metal coordination, spirolactam ring opens, and as a result, the sp³-hybridized carbon atom becomes sp²-hybridized and appears at 134.90 ppm (Figures S23–S26). Free chemosensors exhibit FT-IR stretching frequency of amide “C=O” bond and imine bond at ~1699 and ~1674 cm^{–1}, respectively, which are shifted significantly to lower values and appear at ~1663 and ~1646 cm^{–1}, respectively, after complexation. The sharp –OH peak at 3408 cm^{–1} also disappears after complexation. This observation suggests Al³⁺-ion coordination with phenoxido oxygen, amide oxygen, and imine nitrogen of the chemosensor. Therefore, FT-IR data also supports spirolactam ring opening in the presence of Al³⁺ ion.

All chemosensors are colorless and nonfluorescent in visible light. The presence of Al³⁺ ions initiates opening of the spirolactam ring and the color becomes intense, pinkish yellow. The intensity of color is not similar. In the presence of Al³⁺ ions, the intensity increases in the order H₃L1 > H₃L2 > H₃L3 > H₃L4. Again, H₃L1, H₃L2, H₃L3, and H₃L4 exhibit around 780, 725, 425, and 391 times increase of fluorescence intensity in the presence of Al³⁺ ions, respectively. The LOD values are 1.4 × 10^{–9}, 2.50 × 10^{–9}, 0.40 × 10^{–8}, and 0.53 × 10^{–8} M, respectively. The values of binding constant of the probes toward Al³⁺ ions are 8.00 × 10⁵, 6.90 × 10⁵, 1.37 × 10⁴, and 1.03 × 10⁴ M^{–1}, respectively. Here, enhancement in the fluorescence intensity of the chemosensors in the presence of Al³⁺ ions and binding constant values of the probes toward Al³⁺ ions follow the same order H₃L1 > H₃L2 > H₃L3 > H₃L4. All these facts can be well explained by considering two factors: influence of ring strain during interaction between chemosensors and Al³⁺ ions and electron-withdrawing effect (–I effect) of the halogen substituent present in the chemosensors. Interestingly, the first effect is more pronounced. H₃L1 and H₃L2 form more stable five-membered chelate rings with Al³⁺ ions, whereas H₃L3 and H₃L4 form eight-membered chelate rings in the presence of Al³⁺ ions (Figure S37). Also, in the presence of a bromo substituent, the coordination ability of the imine nitrogen and phenoxido oxygen of the respective chemosensor is relatively high in comparison with a chloro substituent due to the –I effect. Therefore, due to the formation of the most stable H₃L1–Al³⁺ complex, the intensity of the complex solution under visible light is maximum, binding constant is the highest and LOD value is the lowest among four chemosensors.

Biocompatibility Study of the Ligands. The cellular toxicities of the ligands (H₃L1, H₃L2, H₃L3, and H₃L4) are envisaged to determine the compatibility against the normal human lung fibroblast cells, WI-38. The cells are exposed with various concentrations (20–100 μM/mL) of the ligands. Then, the cells are incubated for 24 h and the cellular survivability is determined with the help of the MTT assay. From the results, no significant toxicity is observed even at enhanced concentrations of 100 μM (as seen in Figure S69, Supporting Information). Hence, the results clearly depict the biocompatibility of the ligands and also suggest that these

ligands have the potential to emerge as promising tools for application in biomedical fields.

Cell Imaging. The cellular internalization of the chemosensors ($\text{H}_3\text{L1}$ – $\text{H}_3\text{L4}$) ($10\ \mu\text{M}$) and Al^{3+} salt ($10\ \mu\text{M}$) has been determined with the aid of detailed fluorescence microscopy studies. The fluorescence microscopy images reveal the presence of a promiscuous red fluorescent signal in the microscope (Figure 7). Henceforth, the results suggest

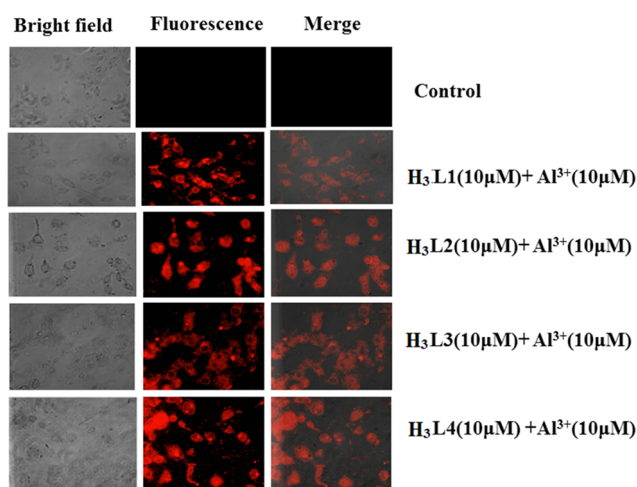


Figure 7. Bright-field, fluorescence, and merged microscopy images of untreated MDA-MB-468 (control) cells in the presence of chemosensor ($\text{H}_3\text{L1}$ – $\text{H}_3\text{L4}$) ($10\ \mu\text{M}$) + Al^{3+} ($10\ \mu\text{M}$).

that the ligands and the Al^{3+} salts are promptly internalized by the cells, which in turn are responsible for the emergence of red fluorescent signal.

Density Functional Theory (DFT) Study. DFT and time-dependent DFT (TDDFT) studies are performed to establish the structural and electronic parameters of probes. Furthermore, to understand the nature, origin, and contribution of M.O.s for electronic transitions, a TDDFT study was performed. This study gives an idea of the quantity of energy associated with every individual transition. In each individual M.O., the contribution from both chemosensor and metal center has been computed. Therefore, DFT and TDDFT analyses play an important role to support and understand structural and electronic parameters of complexes.

Here, the geometry optimization of the chemosensors ($\text{H}_3\text{L1}$ – $\text{H}_3\text{L4}$) has been performed using the DFT/B3LYP process. Some important bond distances and bond angles of all of the chemosensors ($\text{H}_3\text{L1}$ – $\text{H}_3\text{L4}$) are listed in Tables S2 and S3. Energies (eV) of some selected M.O.s are included in Table S6. Contour plots of some selected molecular orbital of the chemosensors are depicted in Figure S70. Theoretical calculations reveal that in $\text{H}_3\text{L1}$, electron density in lowest unoccupied molecular orbital (LUMO) is mainly distributed over the xantheno part and electron density in highest occupied molecular orbital (HOMO) is mainly distributed over the xantheno part and spirolactam ring. In $\text{H}_3\text{L2}$, the electron density in LUMO is mainly distributed over the salicyl part and the spirolactam ring adjacent aromatic moiety and the electron density in HOMO is mainly distributed over the xantheno part. LUMOs of both $\text{H}_3\text{L3}$ and $\text{H}_3\text{L4}$ are mainly salicyl part-based, whereas HOMOs are mainly xantheno moiety-based.

TDDFT Study. Electronic transitions in chemosensors ($\text{H}_3\text{L1}$ – $\text{H}_3\text{L4}$) are theoretically studied using the TDDFT, B3LYP/CPCM method. Important electronic transitions are given in Table S7. In theoretical calculations, for $\text{H}_3\text{L1}$ and $\text{H}_3\text{L2}$, intense absorption bands are found at around 355 and 345 nm, respectively. Major transitions for $\text{H}_3\text{L1}$ are HOMO – 2 \rightarrow LUMO (88%) and HOMO – 1 \rightarrow LUMO (74%) (Figure 8), whereas for $\text{H}_3\text{L2}$, the key transitions are HOMO

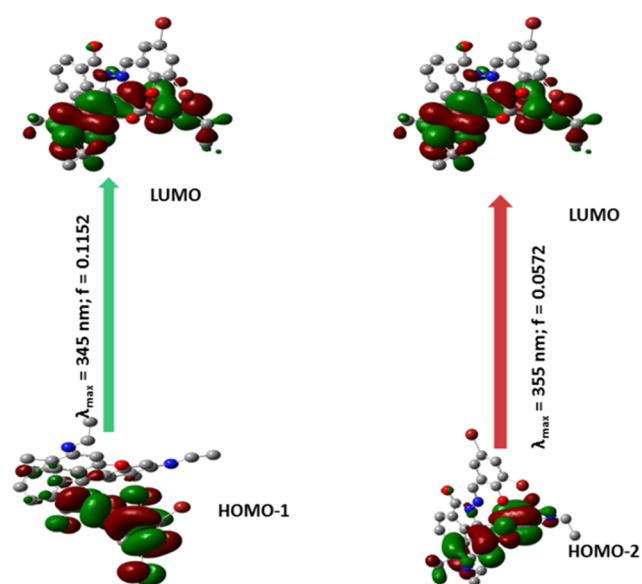


Figure 8. Pictorial representation of key transitions involved in UV-vis absorption of chemosensor $\text{H}_3\text{L1}$.

– 2 \rightarrow LUMO (99%) and HOMO – 3 \rightarrow LUMO (96%), respectively (Figure S71). In the case of $\text{H}_3\text{L3}$ and $\text{H}_3\text{L4}$, two major bands are observed at around 420 and 400 nm, which correspond to the HOMO \rightarrow LUMO (96%) and HOMO – 1 \rightarrow LUMO (95%) ($\text{H}_3\text{L3}$) (Figure S72) and HOMO \rightarrow LUMO (97%) and HOMO – 1 \rightarrow LUMO (96%) ($\text{H}_3\text{L4}$) (Figure S73).

SUMMARY

We have successfully developed four new rhodamine 6G-based fluorescent and colorimetric chemosensors $\text{H}_3\text{L1}$ – $\text{H}_3\text{L4}$ for a rapid and selective detection of Al^{3+} ions. For visualization by the naked eye, the intensity of the color of probe– Al^{3+} ions increases in the order $\text{HL4-Al}^{3+} < \text{HL3-Al}^{3+} < \text{HL2-Al}^{3+} < \text{HL1-Al}^{3+}$. All four chemosensors form a 1:1 complex with Al^{3+} ions, which has been proved by fluorescence measurements, ESI-MS analysis, and NMR studies. In fluorescence competition assay experiments, the selectivity of the probes toward Al^{3+} ions is established. Moreover, the reversibility is also achieved by addition of Na_2EDTA solution. $\text{H}_3\text{L1}$, $\text{H}_3\text{L2}$, $\text{H}_3\text{L3}$, and $\text{H}_3\text{L4}$ exhibit around 780, 725, 425, and 391 times enhancement in fluorescence intensity in the presence of Al^{3+} ions. Al^{3+} is detected in the nanomolar scale, and the LOD values are 1.4×10^{-9} , 2.50×10^{-9} , 0.40×10^{-8} , and 0.53×10^{-8} M, respectively. All of the probes are suitable for real-time quantitative detection of Al^{3+} ions in the field of environmental samples and biological systems. The values of binding constant of the probes toward Al^{3+} ions are 8.00×10^5 , 6.90×10^5 , 1.37×10^4 , and $1.03 \times 10^4\ \text{M}^{-1}$, respectively. In this work, we have also established the influence of ring strain and electron-

withdrawing effect (−I effect) of the halogen substituents present in the chemosensors during interaction between chemosensors and Al^{3+} ions. Interestingly, the first effect is more pronounced compare to the other. The color intensity difference of the probes in the presence of Al^{3+} ions under visible light, different binding constants, quantum yields, and LOD values of the probes toward Al^{3+} ions can be well explained in the light of the above two factors. $\text{H}_3\text{L1}$ and $\text{H}_3\text{L2}$ form more stable five-membered chelate ring with Al^{3+} ions, whereas $\text{H}_3\text{L3}$ and $\text{H}_3\text{L4}$ form an eight-membered chelate ring in the presence of Al^{3+} ions (Figure S37). Also, in the presence of bromo substituent, the coordination ability of the imine nitrogen and phenoxido oxygen of the respective chemosensor is relatively high in comparison to chloro substituent due to less −I effect. We are also successful in revealing its practical application by performing cell imaging study of chemosensors ($\text{H}_3\text{L1}$ – $\text{H}_3\text{L4}$) using MDA-MB-468 cells. Furthermore, the probes are applied to detect intracellular Al^{3+} ions in live cells with no significant cytotoxicity. We have compared different factors like elucidation of crystal structure of the chemosensors, solubility of chemosensors in the aqueous medium for biological and real sample analyses, selectivity of the chemosensors toward Al^{3+} ions, and the nanomolar range of LOD values between chemosensors reported in this work and previously reported results. Interestingly, our chemosensors have successfully covered all of the points mentioned above in comparison to previously reported results presented in Chart S1.

EXPERIMENTAL SECTION

Materials and Physical Measurements Description.

All reagent- or analytical-grade chemicals and solvents were collected from commercial sources and used without further purification. Elemental analysis was carried out using a PerkinElmer 240C elemental analyzer. Infrared spectra (400 – 4000 cm^{-1}) were recorded using KBr pellets on a Nicolet Magna IR 750 series-II FT-IR spectrophotometer. Absorption spectral data were collected using a Cary 60 spectrophotometer (Agilent) with a 1 cm path length quartz cell. Electron spray ionization mass (ESI-MS positive) spectra were noted using a MICROMASS Q-TOF mass spectrometer. A Fluoromax-4 spectrofluorimeter was used to collect emission spectral data at room temperature (298 K) in HEPES buffer at pH = 7.4 solution under degassed condition. A time-resolved spectrofluorometer from IBH, U.K., was used to collect the fluorescence lifetime data, ^1H and ^{13}C NMR spectral data were collected using Bruker 400 and 300 spectrometers in $\text{DMSO-}d_6$ solvent.

X-ray Crystallography. Single-crystal X-ray data of chemosensors ($\text{H}_3\text{L1}$ – $\text{H}_3\text{L4}$) were collected on a Bruker SMART APEX-II CCD diffractometer with the aid of graphite monochromated Mo $K\alpha$ radiation ($\lambda = 0.71073\text{ \AA}$) at room temperature. Data processing, structure solution, and refinement were examined using the Bruker Apex-II suite program. All available reflections data in the $2\theta_{\text{max}}$ range were harvested and corrected for Lorentz and polarization factors with Bruker SAINT plus.⁴⁸ Reflections were then corrected for absorption, interframe scaling, and different systematic errors with SADABS.⁴⁹ The structures were solved by the direct methods and refined with the help of a full-matrix least-squares technique based on F^2 with SHELX-2017/1 software package.⁵⁰ All of the nonhydrogen atoms were refined with anisotropic thermal parameters. C–H hydrogen atoms were

attached at geometrical positions with $U_{\text{iso}} = 1/2U_{\text{eq}}$ to those they are attached. Crystal data and details of data collection and refinement for $\text{H}_3\text{L1}$ – $\text{H}_3\text{L4}$ are collected in Table S1.

Synthesis of *N*-(Rhodamine-6G)lactam-hydrazine and *N*-(Rhodamine-6G)lactam-propylenediamine. *N*-(Rhodamine-6G)lactam-hydrazine and *N*-(Rhodamine-6G)lactam-propylenediamine were prepared by following the literature procedure.⁴⁵

Preparation of Chemosensor ($\text{H}_3\text{L1}$) [$\text{H}_3\text{L1} = 2$ -((3,5-Dibromo-2-hydroxybenzylidene)amino)-3',6'-bis(ethylamino)-2',7'-dimethylspiro[isoindoline-1,9'-xanthen]-3-one]. A mixture of *N*-(Rhodamine-6G)lactam-hydrazine (2.0 mmol, 0.8564 g) and 3,5-dichlorosalicylaldehyde (2.0 mmol, 0.5598 g) was heated in refluxing condition for ca. 4 h in acetonitrile solvent. Very light yellow crystals were collected after evaporation of the solvent.

Yield: 1.008 g (84%). Anal. calcd for $\text{C}_{33}\text{H}_{30}\text{Br}_2\text{N}_4\text{O}_3$: C 57.41%; H 4.38%; N 8.11%. Found: C 57.18%; H 4.30%; N 8.02%. IR (cm^{-1} , KBr): $\nu(\text{C}=\text{N})$ 1621s; $\nu(\text{O}-\text{H})$ 3408s; $\nu(\text{C}=\text{O})$ 1663s (Figure S5). ESI-MS (positive) in MeOH: The molecular ion appeared at $m/z = 691.11$, consistent to [$\text{H}_3\text{L1} + 1$]⁺ (Figure S1). UV-vis, λ_{max} (nm), (ϵ ($\text{dm}^3\text{ mol}^{-1}\text{ cm}^{-1}$)) in HEPES buffer at pH = 7.4: 345 (14020).

^1H NMR (400 MHz, $\text{DMSO-}d_6$) δ ppm: 1.20 (− CH_3) (t, 6H, $J_1 = 7.2\text{ Hz}$, $J_2 = 6.8\text{ Hz}$), 1.84 (Ar- CH_3) (s, 6H), 3.13 (− CH_2) (q, 4H), 5.11 (NH) (t, 2H, $J_1 = 4.8\text{ Hz}$, $J_2 = 5.2\text{ Hz}$), 6.20 (Ar-CH) (s, 2H), 6.34 (Ar-CH) (s, 2H), 7.06 (Ar-CH) (d, 1H, $J = 7.2\text{ Hz}$), 7.53 (Ar-CH) (s, 1H), 7.56–7.72 (Ar-CH) (m, 2H), 7.94 (Ar-CH) (d, 1H, $J = 7.2\text{ Hz}$), 8.90 (− $\text{CH}=\text{N}$) (s, 1H), 11.56 (−OH) (s, 1H) (Figure S11).

^{13}C NMR ($\text{DMSO-}d_6$, 75 MHz) δ ppm: 14.59, 17.44, 37.92, 66.24, 96.32, 104.13, 106.13, 114.16, 119.04, 121.58, 123.78, 124.36, 127.20, 128.26, 129.47, 132.40, 134.90, 136.25, 148.47, 151.48, 151.88, 161.87, 164.27, 166.13 (Figure S19).

Synthesis of Chemosensor ($\text{H}_3\text{L2}$) [$\text{H}_3\text{L2} = 2$ -((3,5-Dichloro-2-hydroxybenzylidene)amino)-3',6'-bis(ethylamino)-2',7'-dimethylspiro[isoindoline-1,9'-xanthen]-3-one]. A mixture of *N*-(Rhodamine-6G)lactam-hydrazine (2.0 mmol, 0.8564 g) and 3,5-dichlorosalicylaldehyde (2.0 mmol, 0.3820 g) was heated in refluxing condition for ca. 4 h in acetonitrile solvent. Very light yellow crystals were collected after evaporation of the solvent.

Yield: 1.200g (87%). Anal. calcd for $\text{C}_{33}\text{H}_{30}\text{Cl}_2\text{N}_4\text{O}_3$: C 65.89%; H 5.03%; N 9.31%. Found: C 65.68%; H 4.88%; N 9.29%. IR (cm^{-1} , KBr): $\nu(\text{C}=\text{N})$ 1619s; $\nu(\text{O}-\text{H})$ 3421s; $\nu(\text{C}=\text{O})$ 1699s (Figure S5). ESI-MS (positive) in MeOH: The base peak appeared at $m/z = 623.18$, corresponding to [$\text{H}_3\text{L2} + 1$]⁺ (Figure S2). UV-vis, λ_{max} (nm), (ϵ ($\text{dm}^3\text{ mol}^{-1}\text{ cm}^{-1}$)) in HEPES buffer (10 mM) at pH = 7.4: 345 (20 440).

^1H NMR (400 MHz, $\text{DMSO-}d_6$) δ ppm: 1.20 (− CH_3) (t, 6H, $J_1 = 7.2\text{ Hz}$, $J_2 = 6.8\text{ Hz}$), 1.84 (Ar- CH_3) (s, 6H), 3.15–3.09 (− CH_2) (m, 4H), 5.11 (NH) (t, 2H, $J = 5.2\text{ Hz}$), 6.20 (Ar-CH) (s, 2H), 6.33 (Ar-CH) (s, 2H), 7.40 (Ar-CH) (s, 1H), 7.51 (Ar-CH) (d, 1H, $J = 7.2\text{ Hz}$), 7.56–7.65 (Ar-CH) (m, 2H), 7.94 (Ar-CH) (d, 1H, $J = 7.2\text{ Hz}$), 8.96 (− $\text{CH}=\text{N}$) (s, 1H), 11.32 (−OH) (s, 1H) (Figure S12).

^{13}C NMR ($\text{DMSO-}d_6$, 75 MHz) δ ppm: 14.59, 17.44, 37.92, 66.24, 96.32, 104.13, 106.13, 114.13, 119.04, 121.58, 123.78, 124.36, 127.20, 128.26, 129.47, 132.40, 134.90, 136.25, 148.47, 151.48, 151.88, 154.27, 166.13 (Figure S20).

Synthesis of Chemosensor ($\text{H}_3\text{L3}$) [$\text{H}_3\text{L3} = 2$ -((3,5-Dibromo-2-hydroxybenzylidene)amino)propyl)-3',6'-bis(ethylamino)-2',7'-dimethylspiro[isoindoline-1,9'-xanthen]-

3-one]. A mixture of *N*-(Rhodamine-6G)lactam-propylenediamine (2.0 mmol, 0.9128 g) and 3,5-dichlorosalicylaldehyde (2.0 mmol, 0.5598 g) was heated in refluxing condition for ca. 4 h in acetonitrile solvent. Yellow crystals were collected after evaporation of the solvent.

Yield: 1.171 g (80%). Anal. calcd for $C_{36}H_{36}Br_2N_4O_3$: C 59.03%; H 4.95%; N 7.65%. Found: C 58.88%; H 4.78%; N 9.29%. IR (cm^{-1} , KBr): $\nu(C=N)$ 1621s; $\nu(O-H)$ 3401s; $\nu(C=O)$ 1663s (Figure S5). ESI-MS (positive) in MeOH: The base peak appeared at $m/z = 755.01$, corresponding to $[H_3L3 + Na]^+$ (Figure S3). UV-vis, λ_{max} (nm), (ϵ ($dm^3 mol^{-1} cm^{-1}$)) in HEPES buffer at pH = 7.4: 420 (47 570).

1H NMR (400 MHz, DMSO- d_6) δ ppm: 1.20 ($-CH_3$) (t, 6H, $J_1 = 9.6$ Hz, $J_2 = 9.2$ Hz), 1.84 (Ar- CH_3) (s, 6H), 2.09 ($-CH_2$) (d, 2H, $J = 16.8$ Hz), 3.13 ($-CH_2$) (q, 4H), 5.11 (NH) (s, 2H), 6.20 (Ar-CH) (s, 2H), 6.34 (Ar-CH) (s, 2H), 7.06 (Ar-CH) (d, 1H, $J = 9.2$ Hz), 7.54 (Ar-CH) (s, 1H), 7.54–7.72 (Ar-CH) (m, 2H), 7.72 (Ar-CH) (s, 1H), 7.95 (Ar-CH) (d, 1H, $J = 8.8$ Hz), 8.90 ($-CH=N$) (s, 1H), 11.66 ($-OH$) (s, 1H) (Figure S13).

^{13}C NMR (DMSO- d_6 , 75 MHz) δ ppm: 14.74, 16.74, 29.11, 37.54, 38.92, 54.60, 65.10, 96.64, 106.06, 107.72, 113.74, 118.00, 118.97, 122.76, 123.89, 128.17, 128.37, 131.16, 132.60, 132.81, 137.90, 147.54, 151.79, 153.42, 160.96, 163.82, 168.52 (Figure S21).

Synthesis of Chemosensor (H_3L4) [$H_3L4 = 2-(3-((3,5-Dichloro-2-hydroxybenzylidene)amino)propyl)-3',6'-bis(ethylamino)-2',7'-dimethylspiro[isoinoline-1,9'-xanthen]-3-one$]. A mixture of *N*-(Rhodamine-6G)lactam-propylenediamine (2.0 mmol, 0.9128 g) and 3,5-dichlorosalicylaldehyde (2.0 mmol, 0.3820 g) was heated in refluxing condition for ca. 4 h in acetonitrile solvent. Yellow crystals were obtained after evaporation of the solvent.

Yield: 1.008 g (84%). Anal. calcd for $C_{36}H_{36}Cl_2N_4O_3$: C 67.18%; H 5.64%; N 8.71%. Found: C 67.18%; H 5.58%; N 8.59%. IR (cm^{-1} , KBr): $\nu(C=N)$ 1634s; $\nu(O-H)$ 3430s; $\nu(C=O)$ 1674s (Figure S5). ESI-MS (positive) in MeOH: The base peak appeared at $m/z = 665.13$, corresponding to $[H_3L4 + Na]^+$ (Figure S4). UV-vis, λ_{max} (nm), (ϵ ($dm^3 mol^{-1} cm^{-1}$)) in HEPES buffer (10 mM) at pH = 7.4: 420 (47 570).

1H NMR (400 MHz, DMSO- d_6) δ ppm: 1.20 ($-CH_3$) (t, 6H, $J_1 = 9.6$ Hz, $J_2 = 9.2$ Hz), 1.84 (Ar- CH_3) (s, 6H), 2.09 ($-CH_2$) (d, 2H, $J = 16.8$ Hz), 3.14 ($-CH_2$) (q, 4H), 5.118 (NH) (s, 2H), 6.21 (Ar-CH) (s, 2H), 6.34 (Ar-CH) (s, 2H), 7.06 (Ar-CH) (d, 1H, $J = 9.2$ Hz), 7.54 (Ar-CH) (s, 1H), 7.54–7.72 (Ar-CH) (m, 2H), 7.72 (Ar-CH) (s, 1H), 7.94 (Ar-CH) (d, 1H, $J = 14.4$ Hz), 8.92 ($-CH=N$) (s, 1H), 11.66 ($-OH$) (s, 1H) (Figure S14).

^{13}C NMR (DMSO- d_6 , 75 MHz) δ ppm: 14.71, 16.72, 29.11, 37.54, 38.92, 54.60, 65.10, 96.65, 106.10, 117.99, 118.68, 121.13, 122.76, 123.61, 123.88, 128.15, 128.38, 128.99, 131.18, 132.57, 147.54, 151.79, 153.43, 159.18, 163.87, 168.49 (Figure S22).

Synthesis of Complex (1) $\{[Al(HL1)(NO_3)] = N-(3,5-Dibromo-2-oxidobenzylidene)-2-(6-(ethylamino)-3-(ethylimino)-2,7-dimethyl-3H-xanthen-9-yl)-benzohydrazonatenitratatoaluminium(III)\}$. A 2 mL methanolic solution of aluminum nitrate nonahydrate (1.0 mmol, 0.375 g) was added carefully to a 20 mL acetonitrile solution of H_3L1 (1.0 mmol, 0.690 g) followed by addition of triethylamine (1.0 mmol, ~ 0.2 mL), and the resultant reaction mixture was stirred for ca. 3 h. A red solid mass was collected in high yield after slow evaporation of the solvent.

Yield: 0.512 g (78%). Anal. calcd for $C_{33}H_{28}AlBr_2N_5O_6$: C 50.99%; H 3.63%; N 9.01%. Found: C 50.55%; H 3.51%; N 8.91%. IR (cm^{-1} , KBr): $\nu(C=N)$ 1601s; $\nu(NO_3^-)$ 1300s and 809s; $\nu(C=O)$ 1655s (Figure S10). ESI-MS (positive) in MeOH: The base peak was observed at $m/z = 778.06$, corresponding to $[Al(HL1)(NO_3) + 1]^+$ (Figure S6). UV-vis, λ_{max} (nm), (ϵ ($dm^3 mol^{-1} cm^{-1}$)) in HEPES buffer at pH = 7.4: 490 (27 500).

1H NMR (400 MHz, DMSO- d_6) δ ppm: 1.22 ($-CH_3$) (t, 6H, $J = 5.6$ Hz), 1.87 (Ar- CH_3) (s, 6H), 3.50 ($-CH_2$) (t, 4H, $J = 5.2$ Hz), 5.11 (NH) (s, 1H), 6.10 (Ar-CH) (s, 2H), 6.27 (Ar-CH) (s, 2H), 6.97–6.95 (Ar-CH) (m, 2H), 7.52–7.50 (Ar-CH) (m, 2H), 7.61 (Ar-CH) (s, 1H), 7.81–7.80 (Ar-CH) (m, 2H), 9.30 ($-CH=N$) (s, 1H) (Figure S15).

^{13}C NMR (DMSO- d_6 , 75 MHz) δ ppm: 14.59, 17.44, 37.92, 96.32, 104.13, 106.13, 114.16, 119.04, 121.58, 123.78, 124.36, 127.20, 128.26, 129.47, 132.40, 134.90, 136.25, 148.47, 151.48, 151.88, 163.37, 165.90, 167.58 (Figure S23).

Synthesis of Complex (2) $\{[Al(HL2)(NO_3)] = N-(3,5-Dichloro-2-oxidobenzylidene)-2-(6-(ethylamino)-3-(ethylimino)-2,7-dimethyl-3H-xanthen-9-yl)-benzohydrazonatenitratatoaluminium(III)\}$. A 2 mL methanolic solution of aluminum nitrate nonahydrate (1.0 mmol, 0.375 g) was added carefully to a 20 mL acetonitrile solution of H_3L2 (1.0 mmol, 0.690 g) followed by addition of triethylamine (1.0 mmol, ~ 0.2 mL), and the resultant reaction mixture was stirred for ca. 3 h. A red solid mass was isolated in high yield after slow evaporation of the solvent.

Yield: 0.512 g (78%). Anal. calcd for $C_{33}H_{28}AlCl_2N_5O_6$: C 50.99%; H 3.63%; N 9.01%. Found: C 50.55%; H 3.51%; N 8.91%. IR (cm^{-1} , KBr): $\nu(C=N)$ 1603s; $\nu(NO_3^-)$ 1300s and 810s; $\nu(C=O)$ 1646s (Figure S10). ESI-MS (positive) in MeOH: The base peak appeared at $m/z = 696.22$, corresponding to $[Al(HL2)(NO_3) + Li]^+$ (Figure S7). UV-vis, λ_{max} (nm), (ϵ ($dm^3 mol^{-1} cm^{-1}$)) in HEPES buffer at pH = 7.4: 415 (19 670).

1H NMR (400 MHz, DMSO- d_6) δ ppm: 1.22 ($-CH_3$) (t, 6H, $J = 5.6$ Hz), 1.87 (Ar- CH_3) (s, 6H), 3.50 ($-CH_2$) (t, 4H, $J = 5.2$ Hz), 5.12 (NH) (s, 1H), 6.12 (Ar-CH) (s, 2H), 6.28 (Ar-CH) (s, 2H), 6.97–6.95 (Ar-CH) (m, 2H), 7.52–7.50 (Ar-CH) (m, 2H), 7.61 (Ar-CH) (s, 1H), 7.82–7.80 (Ar-CH) (m, 2H), 9.33 ($-CH=N$) (s, 1H) (Figure S16).

^{13}C NMR (DMSO- d_6 , 75 MHz) δ ppm: 14.59, 17.44, 37.92, 96.32, 105.10, 106.13, 114.13, 119.04, 121.58, 123.78, 124.36, 127.20, 128.26, 129.47, 132.40, 134.88, 136.25, 149.47, 152.48, 152.90, 162.87, 165.27, 169.13 (Figure S24).

Synthesis of Complex (3) $\{[Al(L3)(NO_3)] = N-(3-((3,5-Dibromo-2-oxidobenzylidene)amino)propyl)-2-(6-(ethylamino)-3-(ethylimino)-2,7-dimethyl-3H-xanthen-9-yl)-benzimidatenitratatoaluminium(III)\}$. A 2 mL methanolic solution of aluminum nitrate nonahydrate (1.0 mmol, 0.375 g) was added carefully to a 20 mL acetonitrile solution of H_3L3 (1.0 mmol, 0.690 g) followed by addition of triethylamine (1.0 mmol, ~ 0.2 mL), and the resultant reaction mixture was stirred for ca. 3 h. A red solid mass was isolated in high yield after slow evaporation of the solvent.

Yield: 0.512 g (78%). Anal. calcd for $C_{36}H_{35}AlBr_2N_5O_6$: C 52.63%; H 4.42%; N 8.53%. Found: C 52.55%; H 4.31%; N 8.47%. IR (cm^{-1} , KBr): $\nu(C=N)$ 1630s; $\nu(NO_3^-)$ 1300s and 811s; $\nu(C=O)$ 773s (Figure S10). ESI-MS (positive) in MeOH: The base peak appeared at $m/z = 822.09$, corresponding to $[Al(HL3)(NO_3) + 1]^+$ (Figure S8). UV-

vis, λ_{\max} (nm), (ϵ ($\text{dm}^3 \text{mol}^{-1} \text{cm}^{-1}$)) in HEPES buffer at pH = 7.4: 490 (28160).

^1H NMR (400 MHz, $\text{DMSO}-d_6$) δ ppm: 1.22 ($-\text{CH}_3$) (t, 6H, $J = 5.6$ Hz), 1.38 ($-\text{CH}_2$) (t, 2H, $J_1 = 5.6$ Hz, $J_2 = 5.2$ Hz), 1.87 (Ar- CH_3) (s, 6H), 2.62 ($-\text{CH}_2$) (d, 2H, $J = 3.6$ Hz), 3.05 ($-\text{CH}_2$) (t, 2H, $J_1 = 4.2$ Hz, $J_2 = 4.5$ Hz), 3.13 ($-\text{CH}_2$) (q, 4H), 5.11 (NH) (t, 1H), 6.01 (Ar-CH) (s, 2H), 6.20 (Ar-CH) (s, 2H), 6.97–6.96 (Ar-CH) (m, 2H), 7.52–7.50 (Ar-CH) (m, 2H), 7.61 (Ar-CH) (s, 1H), 7.82–7.80 (Ar-CH) (m, 2H), 9.32 ($-\text{CH}=\text{N}$) (s, 1H) (Figure S17).

^{13}C NMR ($\text{DMSO}-d_6$, 75 MHz) δ ppm: 14.74, 16.74, 29.21, 37.54, 38.92, 54.80, 96.64, 106.06, 107.72, 113.74, 118.00, 118.97, 122.76, 123.89, 128.17, 128.37, 131.16, 132.60, 132.81, 137.90, 147.54, 151.79, 153.42, 160.96, 163.82, 168.52 (Figure S25).

Synthesis of Complex (4) $\{\text{[Al(HL4)(NO}_3\text{)]} = N\text{-}(3\text{-}((3,5\text{-Dichloro-2-oxidobenzylidene)amino)propyl)\text{-}2\text{-}(6\text{-}(ethylamino)\text{-}3\text{-}(ethylimino)\text{-}2,7\text{-dimethyl-3H-xanthen-9-yl)-benzimidatenitratoaluminium(III))\}$. A 2 mL methanolic solution of aluminum nitrate nonahydrate (1.0 mmol, 0.375 g) was added carefully to a 20 mL acetonitrile solution of $\text{H}_3\text{L4}$ (1.0 mmol, 0.690 g) followed by addition of triethylamine (1.0 mmol, ~ 0.2 mL), and the resultant reaction mixture was stirred for ca. 3 h. A red solid mass was isolated in high yield after slow evaporation of the solvent.

Yield: 0.512 g (78%). Anal. calcd for $\text{C}_{36}\text{H}_{35}\text{AlCl}_2\text{N}_5\text{O}_6$: C 59.02%; H 4.95%; N 9.56%. Found: C 58.85%; H 4.81%; N 9.21%. IR (cm^{-1} , KBr): $\nu(\text{C}=\text{N})$ 1621s; $\nu(\text{NO}_3^-)$ 1310s and 813s; $\nu(\text{C}=\text{O})$ 1634s (Figure S10). ESI-MS (positive) in MeOH: The base peak appeared at $m/z = 732.16$, corresponding to $[\text{Al(HL4)(NO}_3\text{)} + 1]^+$ (Figure S9). UV-vis, λ_{\max} (nm), (ϵ ($\text{dm}^3 \text{mol}^{-1} \text{cm}^{-1}$)) in HEPES buffer at pH = 7.4: 490 (13 019).

^1H NMR (400 MHz, $\text{DMSO}-d_6$) δ ppm: 1.29 ($-\text{CH}_3$) (t, 6H $J = 4.2$ Hz), 1.38 ($-\text{CH}_2$) (t, 2H $J_1 = 4.2$ Hz, $J_2 = 4.5$ Hz), 1.87 (Ar- CH_3) (s, 6H), 2.62 ($-\text{CH}_2$) (d, 2H, $J = 3.6$ Hz), 3.05 ($-\text{CH}_2$) (t, 2H, $J_1 = 4.2$ Hz, $J_2 = 4.5$ Hz), 3.13 ($-\text{CH}_2$) (q, 4H), 5.11 (NH) (s, 1H), 6.10 (Ar-CH) (s, 2H), 6.27 (Ar-CH) (s, 2H), 6.97–6.94 (Ar-CH) (m, 2H), 7.52–7.50 (Ar-CH) (m, 2H), 7.61 (Ar-CH) (s, 1H), 7.87–7.85 (Ar-CH) (m, 2H), 9.35 ($-\text{CH}=\text{N}$) (s, 1H) (Figure S18).

^{13}C NMR ($\text{DMSO}-d_6$, 75 MHz) δ ppm: 14.71, 16.72, 29.11, 37.54, 54.60, 96.65, 106.10, 117.99, 118.68, 121.13, 122.76, 123.61, 123.88, 128.15, 128.38, 128.99, 131.88, 132.57, 147.74, 151.59, 153.73, 160.18, 164.57, 169.45 (Figure S26).

UV-Visible and Fluorescence Spectroscopy Experiment. Stock solutions of different ions (1×10^{-3} M) were prepared in a deionized water medium. A stock solution of the chemosensors ($\text{H}_3\text{L1-H}_3\text{L4}$) (1×10^{-3} M) was prepared in methanol medium. The chemosensors ($\text{H}_3\text{L1-H}_3\text{L4}$) solution was then diluted to 1×10^{-5} M as per requirement. A competitive assay of various cations and anions and other spectroscopic experiments were performed in aqueous methanolic HEPES buffer (10 mM) medium at pH 7.4. In the competitive assay experiments, the test samples were prepared by mixing appropriate amounts of the cations stock in 3 mL of chemosensors ($\text{H}_3\text{L1-H}_3\text{L4}$) solution (1×10^{-5} M).

Binding Stoichiometry (Job's Plot) Studies. Binding stoichiometry of the chemosensors with that of Al^{3+} ions is determined by Job's continuation method using absorption spectroscopy. At 25 °C, the absorbance was recorded for solutions where the concentrations of both chemosensor and Al^{3+} ions are varied but the sum of their concentrations was

kept constant at 1×10^{-5} M, i.e., relative change in absorbance ($\Delta A/A_0$) against mole fraction of chemosensor. The break point in the resulting plot represents the mole fraction of chemosensor in the Al^{3+} complex. From the break point, the stoichiometry was determined. The final results reported were an average of at least three experiments.

Cell Culture. The triple-negative breast cancer cells of human origin, MDA-MB-468, are procured from the National Center for Cell Science (NCCS) Pune, India. The cells were cultured in an enriched cell culture medium, Dulbecco's modified Eagle's medium (DMEM), supplemented with 10% fetal bovine serum (FBS) and a mixture of appropriate antibiotics (streptomycin and penicillin at a dose of 100 units/mL). The cells were incubated at a temperature of 37 °C and in the prevalence of 5% CO_2 .

Cell Visualization Studies. The human breast cancer cells, MDA-MB-468, were cultured on coverslips for a period of 24 h. Then, these cells were either left untreated or were exposed to a dose of ligands (10 μM) and Al^{3+} salt (10 μM). These treated cells were then incubated for 24 h at a temperature of 37 °C. Afterward, the cells were thoroughly washed with the help of $1 \times \text{PBS}$. Ultimately, the cells were envisaged with the help of a fluorescence microscope (Leica) following the mounting of the cells on a glass slide.

Computational Method. All computations were studied using the GAUSSIAN09 (G09)⁵¹ software package. For optimization process, we used the density functional theory method at the B3LYP level,^{52,53} and the standard 6-31+G(d) basis set for C, H, N, and O atoms^{54,55} and the lanL2DZ effective potential (ECP) set of Hay and Wadt^{56–58} for aluminum atoms have been selected for optimization.

TDDFT calculation was studied with the optimized geometry to ensure only positive eigen values. Time-dependent density functional theory (TDDFT)^{59–61} was examined using conductor-like polarizable continuum model (CPCM)^{62–64} and the same B3LYP level and basis sets in methanolic solvent system. GAUSSSUM⁶⁵ was utilized to calculate the fractional contributions of various groups to each molecular orbital.

■ ASSOCIATED CONTENT

● Supporting Information

The Supporting Information is available free of charge at <https://pubs.acs.org/doi/10.1021/acsomega.9b02181>.

CCDC 1916757, 1916768, 1916759, and 1938716 include the supplementary crystallographic data for chemosensors ($\text{H}_3\text{L1-H}_3\text{L4}$), respectively (PDF)

[H3L1 \(CIF\)](#)

[H3L2 \(CIF\)](#)

[H3L3 \(CIF\)](#)

[H3L4 \(CIF\)](#)

■ AUTHOR INFORMATION

Corresponding Author

*E-mail: asaha@chemistry.jdvu.ac.in, amritasahachemju@gmail.com. Tel: +91-33-24572146.

ORCID

Amrita Saha: 0000-0001-9357-801X

Notes

The authors declare no competing financial interest.

ACKNOWLEDGMENTS

A.S. gratefully acknowledges the financial support of this work by the DST, India (Sanction No. SB/FT/CS-102/2014, dated July 18, 2015), and RUSA 2.0, Government of India (Sanction No. R-11/262/19, dated March 08, 2019).

REFERENCES

- (1) Du, J.; Hu, M. M.; Fang, J. L.; Peng, X. J. Fluorescent chemodosimeters using “mild” chemical events for the detection of small anions and cations in biological and environmental media. *Chem. Soc. Rev.* **2012**, *41*, 4511–4535.
- (2) Gonz ales, A. P. S.; Firmino, M. A.; Nomura, C. S.; Rocha, F. R. P.; Oliveira, P. V.; Gaubeur, I. Peat as a Natural Solid-phase for Copper Preconcentration and Determination in a Multicommutated Flow System Coupled to Flame Atomic Absorption Spectrometry. *Anal. Chim. Acta* **2009**, *636*, 198–204.
- (3) Pathirathna, P.; Yang, Y. Y.; Forzley, K.; McElmurry, S. P.; Hashemi, P. Fast-scan Deposition-stripping Voltammetry at Carbon-fiber Microelectrodes: Real-time, Subsecond, Mercury Free Measurements of Copper. *Anal. Chem.* **2012**, *84*, 6298–6302.
- (4) Becker, J. S.; Zoriy, M. V.; Pickhardt, C.; Palomero-Gallagher, N.; Zilles, K. Imaging of Copper, Zinc, and Other Elements in Thin Section of Human Brain Samples (Hippocampus) by Laser Ablation Inductively Coupled Plasma Mass Spectrometry. *Anal. Chem.* **2005**, *77*, 3208–3216.
- (5) Liu, Y.; Liang, P.; Guo, L. Nanometer Titanium Dioxide Immobilized on Silica Gel as Sorbent for Preconcentration of Metal Ions Prior to their Determination by Inductively Coupled Plasma Atomic Emission Spectrometry. *Talanta* **2005**, *68*, 25–30.
- (6) Zhou, Y.; Zhang, Y.; Yoon, J. F. Fluorescence and colorimetric chemosensors for fluoride-ion detection. *Chem. Rev.* **2014**, *114*, 5511–5571.
- (7) Zhang, J. F.; Zhou, Y.; Yoon, J.; Kim, J. S. Recent progress in fluorescent and colorimetric chemosensors for detection of precious metal ions (silver, gold and platinum ions). *Chem. Soc. Rev.* **2011**, *40*, 3416–3429.
- (8) Muller, G.; Bernuzzi, V.; Desor, D.; et al. Developmental alterations in offspring of female rats orally intoxicated by aluminum lactate at different gestation periods. *Teratology* **1990**, *42*, 253–261.
- (9) Golub, M.; Donald, J. M.; et al. Effects of aluminum ingestion on spontaneous motor activity of mice. *Neurotoxicol. Teratol.* **1989**, *11*, 231–235.
- (10) Williams, R. J. P. Recent aspects of aluminium chemistry and biology: a survey. *Coord. Chem. Rev.* **2002**, *228*, 93–97.
- (11) Yokel, R. A. Aluminum chelation principles and recent advances. *Coord. Chem. Rev.* **2002**, *228*, 97–113.
- (12) Baral, M.; Sahoo, S. K.; Kanungo, B. K. J. Tripodal amine catechol ligands: a fascinating class of chelators for aluminium(III). *J. Inorg. Biochem.* **2008**, *102*, 1581–1688.
- (13) Kawahara, M.; Muramoto, K.; Kobayashi, K.; Mori, H.; Kroda, Y. Aluminum promotes the aggregation of Alzheimer’s amyloid beta-protein in vitro. *Biochem. Biophys. Res. Commun.* **1994**, *198*, 531–535.
- (14) Paik, S. R.; Lee, J. H.; Kim, D. H.; Chang, C. S.; Kim, J. Aluminum-induced structural alterations of the precursor of the non-A beta component of Alzheimer’s disease amyloid. *Arch. Biochem. Biophys.* **1997**, *344*, 325–334.
- (15) Lin, J. L.; Kou, M. T.; Leu, M. L. Effect of long-term low-dose aluminum-containing agents on hemoglobin synthesis in patients with chronic renal insufficiency. *Nephron* **1996**, *74*, 33–38.
- (16) Good, P. F.; Olanow, C. W.; Perl, D. P. Neuromelanin-containing neurons of the substantia nigra accumulate iron and aluminum in Parkinson’s disease: a LAMMA study. *Brain Res.* **1992**, *593*, 343–346.
- (17) Darbre, P. D. Aluminium, antiperspirants and breast cancer. *J. Inorg. Biochem.* **2005**, *99*, 1912–1919.
- (18) Singha, D. K.; Mahata, P. Highly selective and sensitive luminescence turn-on-based sensing of Al³⁺ ions in aqueous medium using a MOF with freefunctional sites. *Inorg. Chem.* **2015**, *54*, 6373–6379.
- (19) Diao, Q.; Ma, P.; Lv, L.; Li, T.; Sun, Y.; Wang, X.; Song, D. A water-soluble and reversible fluorescent probe for Al³⁺ and F⁻ in living cells. *Sens. Actuators, B* **2016**, *229*, 138–144.
- (20) Naskar, B.; Modak, R.; Sikdar, Y.; Maiti, D. K.; Bauz a, A.; Frontera, A.; Katarkar, A.; Chaudhuri, K.; Goswami, S. Fluorescent sensing of Al³⁺ by benzophenone based Schiff base chemosensor and live cell imaging applications: impact of keto-enol tautomerism. *Sens. Actuators, B* **2017**, *239*, 1194–1204.
- (21) Gupta, V. K.; Singh, A. K.; Kumawat, L. K. Thiazole Schiff base turn-on fluorescent chemosensor for Al³⁺ ion. *Sens. Actuators, B* **2014**, *195*, 98–108.
- (22) Gupta, V. K.; Mergu, N.; Kumawat, L. K.; Singh, A. K. A reversible fluorescence off–on–off sensor for sequential detection of aluminum and acetate/fluoride ions. *Talanta* **2015**, *144*, 80–89.
- (23) Gupta, V. K.; Jain, A. K.; Maheshwari, G. Aluminum (III) selective potentiometric sensor based on morin in poly (vinyl chloride) matrix. *Talanta* **2007**, *72*, 1469–1473.
- (24) Ding, Y.; Zhu, W.; Xu, Y.; Qian, X. A small molecular fluorescent sensor functionalized silica microsphere for detection and removal of mercury, cadmium, and lead ions in aqueous solutions. *Sens. Actuators, B* **2015**, *220*, 762–771.
- (25) Wan, X.; Liu, T.; Liu, H.; Gu, L.; Yao, Y. Cascade OFF–ON–OFF fluorescent probe: dual detection of trivalent ions and phosphate ions. *RSC Adv.* **2014**, *4*, 29479–29484.
- (26) Wang, L.; Li, H.; Cao, D. A new photoresponsive coumarin-derived Schiff base: chemosensor selectively for Al³⁺ and Fe³⁺ and fluorescence turn-on under room light. *Sens. Actuators, B* **2013**, *181*, 749–755.
- (27) Lu, Y.; Huang, S.; Liu, Y.; He, S.; Zhao, L.; Zeng, X. Highly Selective and Sensitive Fluorescent Turn-on Chemosensor for Al³⁺ Based on a Novel Photoinduced Electron Transfer Approach. *Org. Lett.* **2011**, *13*, 5274–5277.
- (28) (a) Tachapermporn, Y.; Thavornpradit, S.; Charoenpanich, A.; Sirirak, J.; Burgess, K.; Wanichacheva, N. Near-infrared aza-BODIPY fluorescent probe for selective Cu²⁺ detection and its potential in living cell imaging. *Dalton Trans.* **2017**, *46*, 16251–16256. (b) Liu, T.; Dong, Y.; Wan, X.; Li, W.; Yao, Y. An easy and accessible water-soluble sensor for the distinctive fluorescence detection of Zn²⁺ and Al³⁺ ions. *RSC Adv.* **2015**, *5*, 76939–76942.
- (29) (a) Hou, L.; Feng, J.; Wang, Y.; Dong, C.; Shuang, S.; Wang, Y. Single fluorescein-based probe for selective colorimetric and fluorometric dual sensing of Al³⁺ and Cu²⁺. *Sens. Actuators, B* **2017**, *247*, 451–460. (b) Qin, J.-C.; Fan, L.; Wang, B.-D.; Yang, Z.-Y.; Li, T.-R. The design of a simple fluorescent chemosensor for Al³⁺/Zn²⁺ via two different approaches. *Anal. Methods.* **2015**, *7*, 716–722.
- (30) Chen, X.; Pradhan, T.; Wang, F.; Kim, J. S.; Yoon, J. Fluorescent Chemosensors Based on Spiroring-Opening of Xanthenes and Related Derivatives. *Chem. Rev.* **2012**, *112*, 1910–1956.
- (31) Kim, H. N.; Lee, M. H.; Kim, H. J.; Kim, J. S.; Yoon, J. A new trend in rhodamine-based chemosensors: application of spirolactam ring-opening to sensing ions. *Chem. Soc. Rev.* **2008**, *37*, 1465–1472.
- (32) Dujols, V.; Ford, F.; Czarnik, A. W. A Long-Wavelength Fluorescent Chemodosimeter Selective for Cu(II) Ion in Water. *J. Am. Chem. Soc.* **1997**, *119*, 7386–7387.
- (33) Quang, D. T.; Kim, J. S. Fluoro- and Chromogenic Chemodosimeters for Heavy Metal Ion Detection in Solution and Biospecimens. *Chem. Rev.* **2010**, *110*, 6280–6301.
- (34) Li, X.-M.; Zhao, R.-R.; Yang, Y.; Lv, X. W.; Wei, Y.-L.; Tan, R.; Zhang, J.-F.; Zhou, Y. A Rhodamine-based fluorescent sensor for chromium ions and its application in bioimaging. *Chin. Chem. Lett.* **2017**, *28*, 1258–1261.
- (35) Kwon, J. Y.; Jang, Y. J.; Lee, Y. J.; Kim, K. M.; Seo, M. S.; Nam, W.; Yoon, J. A Highly Selective Fluorescent Chemosensor for Pb²⁺. *J. Am. Chem. Soc.* **2005**, *127*, 10107–10111.
- (36) Wang, Y.; Chang, H.-Q.; Wu, W.-N.; Mao, X.-J.; Zhao, X.-L.; Yang, Y.; Xu, Z.-Q.; Xu, Z.-H.; Jia, L. A highly sensitive and selective colorimetric and off–on fluorescent chemosensor for Cu²⁺ based on

- rhodamine 6G hydrazide bearing thiosemicarbazide moiety. *J. Photochem. Photobiol. A* **2017**, *335*, 10–16.
- (37) Alam, R.; Bhowmick, R.; Islam, A. S. M.; katarkar, A.; Chaudhuri, K.; Ali, M. A rhodamine based fluorescent trivalent sensor (Fe^{3+} , Al^{3+} , Cr^{3+}) with potential applications for live cell imaging and combinational logic circuits and memory devices. *New J. Chem.* **2017**, *41*, 8359–8369.
- (38) Jeong, J. W.; Rao, B. A.; Son, Y.-A. Rhodamine-chloronicotinaldehyde-based “OFF–ON” chemosensor for the colorimetric and fluorescent determination of Al^{3+} ions. *Sens. Actuators, B* **2015**, *208*, 75–84.
- (39) Gupta, V. K.; Mergu, N.; Kumawat, L. K. Tunable photoluminescence of water-soluble AgInZnS –graphene oxide (GO) nanocomposites and their application in-vivo bioimaging. *Sens. Actuators, B* **2016**, *223*, 101–113.
- (40) Ku, K.-S.; Muthukumar, P.; Angupillai, S.; Son, Y.-A. A new rhodamine 6 G based chemosensor for trace level Al^{3+} and its thin film application in 100% aqueous medium. *Sens. Actuators, B* **2016**, *236*, 184–191.
- (41) Hou, L.; Feng, J.; Wang, Y.; Dong, C.; Shuang, S.; Wang, Y. Single fluorescein-based probe for selective colorimetric and fluorometric dual sensing of Al^{3+} and Cu^{2+} . *Sens. Actuators, B* **2017**, *247*, 451–460.
- (42) Maniyazagan, M.; Mariadasse, R.; Nachiappan, M.; Jeyakanthan, J.; Lokanath, N. K.; Naveen, S.; Sivaraman, G.; Muthuraja, P.; Manisankar, P.; Stalin, T. Synthesis of rhodamine based organic nanorods for efficient chemosensor probe for Al (III) ions and its biological applications. *Sens. Actuators, B* **2018**, *254*, 795–804.
- (43) Huang, Q.; Zhang, Q.; Wang, E.; Zhou, Y.; Qiao, H.; Pang, L.; Yu, F. A new “off-on” fluorescent probe for Al^{3+} in aqueous solution based on rhodamine B and its application to bioimaging. *Spectrochim. Acta, Part A* **2016**, *152*, 70–76.
- (44) (a) Yang, G.; Meng, X.; Fang, S.; Wang, L.; Wang, Z.; Wang, F.; Duan, H.; Hao, A. Two novel pyrazole-based chemosensors: “naked-eye” colorimetric recognition of Ni^{2+} and Al^{3+} in alcohol and aqueous DMF media. *New J. Chem.* **2018**, *42*, 14630–14641. (b) Jeong, J. W.; Rao, B. A.; Son, Y. Rhodamine-chloronicotinaldehyde-based “OFF–ON” chemosensor for the colorimetric and fluorescent determination of Al^{3+} ions. *Sens. Actuators, B* **2015**, *208*, 75–84. (c) Chemate, S.; Sekar, N. A new rhodamine based OFF–ON fluorescent chemosensors for selective detection of Hg^{2+} and Al^{3+} in aqueous media. *Sens. Actuators, B* **2015**, *220*, 1196–1204. (d) Maity, S. B.; Bharadwaj, P. K. A Chemosensor Built with Rhodamine Derivatives Appended to an Aromatic Platform via 1,2,3-Triazoles: Dual Detection of Aluminum(III) and Fluoride/Acetate Ions. *Inorg. Chem.* **2013**, *52*, 1161–1163. (e) Roy, A.; Shee, U.; Mukherjee, A.; Mandal, S. K.; Roy, P. Rhodamine-Based Dual Chemosensor for Al^{3+} and Zn^{2+} Ions with Distinctly Separated Excitation and Emission Wavelengths. *ACS Omega* **2019**, *4*, 6864–6875. (f) Ghosh, M.; Mandal, S.; Ta, S.; Das, D. Detection and discrimination of Al^{3+} and Hg^{2+} using a single probe: Nano-level determination, human breast cancer cell (MCF7) imaging, binary logic gate development and sea fish sample analysis. *Sens. Actuators, B* **2017**, *249*, 339–347. (g) Alam, R.; Bhowmick, R.; Islam, A. S. M.; katarkar, A.; Chaudhuri, K.; Ali, M. A rhodamine based fluorescent trivalent sensor (Fe^{3+} , Al^{3+} , Cr^{3+}) with potential applications for live cell imaging and combinational logic circuits and memory devices. *New J. Chem.* **2017**, *41*, 8359–8369. (h) Fu, Y.; Jiang, X.-J.; Zhu, Y.-Y.; Zhou, B.-J.; Zang, S.-Q.; Tang, M.-S.; Zhang, H.-Y.; Maka, T. C. W. A new fluorescent probe for Al^{3+} based on rhodamine 6G and its application to bioimaging. *Dalton Trans.* **2014**, *43*, 12624–12632. (i) Sahana, A.; Banerjee, A.; Lohar, S.; Banik, A.; Mukhopadhyay, S. K.; Safin, D. A.; Babashkina, M. G.; Bolte, M.; Garcia, Y.; Das, D. FRET based tri-color emissive rhodamine–pyrene conjugate as an Al^{3+} selective colorimetric and fluorescence sensor for living cell imaging. *Dalton Trans.* **2013**, *42*, 13311–13314. (j) Roy, A.; Mukherjee, R.; Dam, B.; Dam, S.; Roy, P. A rhodamine-based fluorescent chemosensor for Al^{3+} : is it possible to control the metal ion selectivity of a rhodamine-6G based chemosensor. *New J. Chem.* **2018**, *42*, 8415–8425. (k) Sen, B.; Mukherjee, M.; Banerjee, S.; Pal, S.; Chattopadhyay, P. A rhodamine-based ‘turn-on’ Al^{3+} ion-selective reporter and the resultant complex as a secondary sensor for F^- ion are applicable to living cell staining. *Dalton Trans.* **2015**, *44*, 8708–8717. (l) Sahana, A.; Banerjee, A.; Lohar, S.; Sarkar, B.; Mukhopadhyay, S. K.; Das, D. Rhodamine-Based Fluorescent Probe for Al^{3+} through Time-Dependent PET–CHEF–FRET Processes and Its Cell Staining Application. *Inorg. Chem.* **2013**, *52*, 3627–3633. (45) Yang, X. F.; Guo, X. Q.; Zhao, Y. B. Development of a novel rhodamine-type fluorescent probe to determine peroxyxynitrite. *Talanta* **2002**, *57*, 883–890. (46) Benesi, H. A.; Hildebrand, J. H. A Spectrophotometric Investigation of the Interaction of Iodine with Aromatic Hydrocarbons. *J. Am. Chem. Soc.* **1949**, *71*, 2703–2707. (47) Pradhan, A. B.; Mandal, S. K.; Banerjee, S.; Mukherjee, A.; Das, S.; Bukhsh, A. R. K.; Saha, A. A highly selective fluorescent sensor for zinc ion based on quinoline platform with potential applications for cell imaging studies. *Polyhedron* **2015**, *94*, 75–82. (48) Sheldrick, G. M. *S.A.I.N.T., version 6.02, S.A.D.A.B.S., version 2.03*; Bruker AXS Inc.: Madison, Wisconsin, 2002. (49) Sheldrick, G. M. *S.A.D.A.B.S. Software for Empirical Absorption Correction*; University of Gottingen, Institute fur Anorganische Chemieder Universitat: Gottingen, Germany, 1999–2003. (50) Sheldrick, G. M. Crystal structure refinement with SHELXL. *Acta Cryst.* **2015**, *C71*, 3–8. (51) Frisch, M. J.; Trucks, G. W.; Schlegel, H. B.; Scuseria, G. E.; Robb, M. A.; Cheeseman, J. R.; Scalmani, G.; Barone, V.; Mennucci, B.; Petersson, G. A.; Nakatsuji, H.; Caricato, M.; Li, X.; Hratchian, H. P.; Izmaylov, A. F.; Bloino, J.; Zheng, G.; Sonnenberg, J. L.; Hada, M.; Ehara, M.; Toyota, K.; Fukuda, R.; Hasegawa, J.; Ishida, M.; Nakajima, T.; Honda, Y.; Kitao, O.; Nakai, H.; Vreven, T.; Montgomery, J. A., Jr.; Peralta, J. E.; Ogliaro, F.; Bearpark, M.; Heyd, J.; Brothers, J. E.; Kudin, K. N.; Staroverov, V. N.; Kobayashi, R.; Normand, J.; Raghavachari, K.; Rendell, A.; Burant, J. C.; Iyengar, S. S.; Tomasi, J.; Cossi, M.; Rega, N.; Millam, J. M.; Klene, M.; Knox, J. E.; Cross, J. B.; Bakken, V.; Adamo, C.; Jaramillo, J.; Gomperts, R.; Stratmann, R. E.; Yazyev, O.; Austin, A. J.; Cammi, R.; Pomelli, C.; Ochterski, J. W.; Martin, R. L.; Morokuma, K.; Zakrzewski, V. G.; Voth, G. A.; Salvador, P.; Dannenberg, J. J.; Dapprich, S.; Daniels, A. D.; Farkas, Ö.; Foresman, J. B.; Ortiz, J. V.; Cioslowski, J.; Fox, D. J. *Gaussian 09*, revision D.01; Gaussian Inc.: Wallingford, CT, 2009. (52) Becke, A. D. Density-functional thermochemistry. III. The role of exact exchange. *J. Chem. Phys.* **1993**, *98*, 5648–5652. (53) Lee, C.; Yang, W.; Parr, R. G. Development of the Colle-Salvetti correlation-energy formula into a functional of the electron density. *Phys. Rev. B* **1988**, *37*, 785–789. (54) Hay, P. J.; Wadt, W. R. Ab initio effective core potentials for molecular calculations. Potentials for K to Au including the outermost core orbitals. *J. Chem. Phys.* **1985**, *82*, 270–283. (55) Wadt, W. R.; Hay, P. Ab initio effective core potentials for molecular calculations. Potentials for main group elements Na to Bi. *J. Chem. Phys.* **1985**, *82*, 284–298. (56) Hay, P. J.; Wadt, W. R. Ab initio effective core potentials for molecular calculations. Potentials for K to Au including the outermost core orbitals. *J. Chem. Phys.* **1985**, *82*, 299–310. (57) Petersson, G. A.; Bennett, A.; Tensfeldt, T. G.; Al-Laham, M. A.; Shirley, W. A.; Mantzaris, J. A complete basis set model chemistry. I. The total energies of closed-shell atoms and hydrides of the first-row elements. *J. Chem. Phys.* **1988**, *89*, 2193–2218. (58) Petersson, G. A.; Al-Laham, M. A. A complete basis set model chemistry. II. Open-shell systems and the total energies of the first-row atoms. *J. Chem. Phys.* **1991**, *94*, 6081–6090. (59) Bauernschmitt, R.; Ahlrichs, R. Treatment of electronic excitations within the adiabatic approximation of time dependent density functional theory. *Chem. Phys. Lett.* **1996**, *256*, 454–464. (60) Stratmann, R. E.; Scuseria, G. E.; Frisch, M. An efficient implementation of time-dependent density-functional theory for the calculation of excitation energies of large molecules. *J. Chem. Phys.* **1998**, *109*, 8218–8224.

(61) Casida, M. E.; Jamorski, C.; Casidaand, K. C.; Salahub, D. R. Density- and density-matrix-based coupled Kohn–Sham methods for dynamic polarizabilities and excitation energies of molecules. *J. Chem. Phys.* **1998**, *108*, 4439–4449.

(62) Barone, V.; Cossi, M. Quantum Calculation of Molecular Energies and Energy Gradients in Solution by a Conductor Solvent Model. *J. Phys. Chem. A* **1998**, *102*, 1995–2001.

(63) Cossi, M.; Barone, V. Time-dependent density functional theory for molecules in liquid solutions. *J. Chem. Phys.* **2001**, *115*, 4708–4717.

(64) Cossi, M.; Rega, N.; Scalmani, G.; Barone, V. Energies, structures, and electronic properties of molecules in solution with the C-PCM solvation model. *J. Comput. Chem.* **2003**, *24*, 669–681.

(65) O’Boyle, N. M.; Tenderholt, A. L.; Langner, K. M. cclib: a library for package-independent computational chemistry algorithms. *J. Comput. Chem.* **2008**, *29*, 839–845.

Cite this: *Dalton Trans.*, 2022, **51**, 15555

Two rhodamine-azo based fluorescent probes for recognition of trivalent metal ions: crystal structure elucidation and biological applications†

Jayanta Mandal,^a Kunal Pal,^b Sougata Ghosh Chowdhury,^b Parimal Karmakar,^{id b} Anangamohan Panja,^{id c} Snehasis Banerjee^{id d} and Amrita Saha^{id *a}

Two rhodamine and azo based chemosensors (**HL1** = (3',6'-bis(ethylamino)-2-((2-hydroxy-3-methoxy-5-(phenyldiazenyl)benzylidene)amino)-2',7'-dimethylspiro[isoinidoline-1,9'-xanthen]-3-one) and **HL2** = (3',6'-bis(ethylamino)-2-(((2-hydroxy-3-methoxy-5-(*p*-tolylidiazanyl)benzylidene)amino)-2',7'-dimethylspiro[isoinidoline-1,9'-xanthen]-3-one) have been synthesized for colorimetric and fluorometric detection of three trivalent metal ions, Al³⁺, Cr³⁺ and Fe³⁺. The chemosensors have been thoroughly characterized by different spectroscopic techniques and X-ray crystallography. They are non-fluorescent due to the presence of a spirolactam ring. The trivalent metal ions initiate an opening of the spirolactam ring when excited at 490 nm in Britton–Robinson buffer solution (H₂O/MeOH 1 : 9 v/v; pH 7.4). The opening of the spirolactam ring increases conjugation within the probe, which is supported by an intense fluorescent pinkish-yellow colouration and an enhancement of the fluorescence intensity of the chemosensors by ~400 times in the presence of Al³⁺ and Cr³⁺ ions and by ~100 times in the presence of Fe³⁺ ions. Such a type of enormous fluorescence enhancement is rarely observed in other chemosensors for the detection of trivalent metal ions. A 2 : 1 binding stoichiometry of the probes with the respective ions has been confirmed by Job's plot analysis. Elucidation of the crystal structures of the Al³⁺ bound chemosensors (**1** and **4**) also justifies the 2 : 1 binding stoichiometry and the presence of an open spirolactam ring within the chemosensor framework. The limit of detection (LOD) values for both the chemosensors towards the respective metal ions are in the order of ~10⁻⁹ M which supports their application in the biological field. The biocompatibility of the ligands has been studied with the help of the MTT assay. The results show that no significant toxicity was observed up to 100 μM of chemosensor concentration. The capability of our synthesized chemosensors to detect intracellular Al³⁺, Cr³⁺ and Fe³⁺ ions in the cervical cancer cell line HeLa was evaluated with the aid of fluorescence imaging.

Received 9th February 2022,
Accepted 25th August 2022

DOI: 10.1039/d2dt00399f

rsc.li/dalton

Introduction

Colorimetric and fluorescent chemosensors which are designed for selective detection of metal ions play a crucial role in the development of medicinal and environmental

research.^{1–3} Various techniques such as atomic absorption spectroscopy,⁴ inductively coupled plasma-mass spectroscopy,⁵ plasma emission spectrometry,⁶ neutron activation analysis,⁷ chromatography⁸ and voltammetry⁹ are available for detection of different metal ions in food, biological systems, and environmental and industrial samples. Most of these detection techniques are expensive and users face challenges in sample preparation, instrument handling and their costly maintenance charges. In this regard, the fluorescence study is a highly sensitive, user friendly, low cost and real time monitoring process. Among different metal ions, trivalent metal ions, Al³⁺, Cr³⁺ and Fe³⁺ deserve special mention. Extensive application of these metals in industry and daily life results in their diffusion and contamination in living systems and causes a wide variety of diseases.¹⁰ Aluminium is the most abundant metal in the Earth's crust and used vastly for domestic purposes. The excessive concentration of Al³⁺ in the human body causes myopathy, encephalopathy, microcytic hypochromic

^aDepartment of Chemistry, Jadavpur University, Kolkata-700032, India.
E-mail: amritasahachemju@gmail.com, amrita.saha@jadavpuruniversity.in,
asaha@chemistry.jdvu.ac.in; Tel: +91-33-24572146

^bDepartment of Life Science and Biotechnology, Jadavpur University, Kolkata-700032, India

^cDepartment of Chemistry, Gokhale Memorial Girls' College, 1/1 Harish Mukherjee Road, Kolkata-700020, India

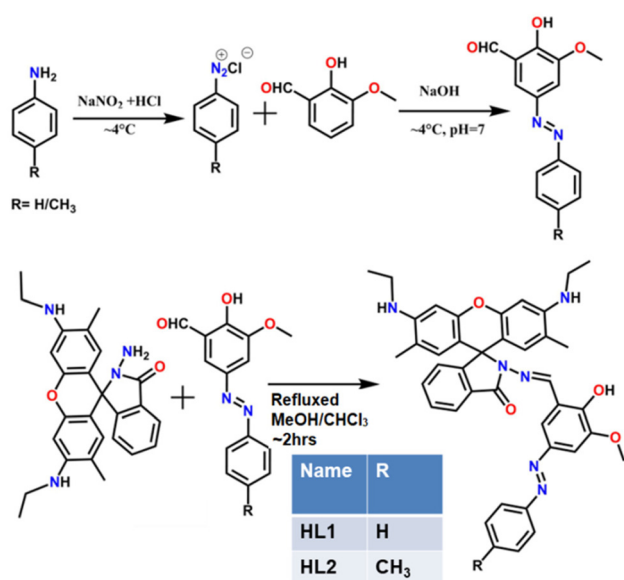
^dDepartment of Higher Education, University Branch, Bikash Bhavan, Salt Lake, Sector-3, Kolkata, 700091, India

† Electronic supplementary information (ESI) available. CCDC 2051844–2051847 for **HL1**, **HL2**, and complexes **1** and **4**, respectively. For ESI and crystallographic data in CIF or other electronic format see DOI: <https://doi.org/10.1039/d2dt00399f>

anemia, Parkinson's disease and Alzheimer's disease.¹¹ Iron is an important dietary element since it is present in the active site of different metalloenzymes which play crucial roles in different physiological processes, such as oxygen uptake,¹² oxygen metabolism,¹³ electron transfer¹⁴ *etc.* Therefore, iron deficiency leads to low blood pressure, anemia, *etc.*,^{15,16} whereas excess iron storage can generate reactive oxygen species, which can damage lipids, proteins and nucleic acids.^{17,18} Cr³⁺ is an essential nutritional trace element for the human body and its deficiency causes cardiovascular disease and diabetes and affects the glucose and lipid metabolism resulting in nervous system disorder.¹⁹ Again, Cr³⁺ from industrial waste causes damage to the environment and living systems. Generally, chemosensors designed for sensing individual metal ions are well known in the literature, but only a handful of examples of dual or multi-metal ion sensing chemosensors are reported. Such a type of chemosensor reduces the synthesis cost and analytical time.

Here, we have demonstrated rhodamine and azo containing fluorescent and colorimetric probes **HL1** and **HL2** [**HL1** = 3',6'-bis(ethylamino)-2-((2-hydroxy-3-methoxy-5-(phenyldiazonyl)benzylidene)amino)-2',7'-dimethylspiro[isindoline-1,9'-xanthen]-3-one and [**HL2** = 3',6'-bis(ethylamino)-2-((2-hydroxy-3-methoxy-5-(*p*-tolylidiazonyl)benzylidene)amino)-2',7'-dimethylspiro[isindoline-1,9'-xanthen]-3-one] for monitoring trivalent ions, Al³⁺, Cr³⁺ and Fe³⁺ (Scheme 1). Common fluorophore units present in fluorescent chemosensors are coumarin, pyrene, 1,8-naphthalimide, rhodamine, squaraine, cyanine, boron dipyrromethene difluoride (BODIPY), nitrobenzofurazan, *etc.* Among them, rhodamine-based chemosensors are capable of both naked eye detection and fluorescence emission. They have excellent photophysical properties with greater photostability, visible wavelength emission, high extinction coefficients and quantum

yields. Their off/on-type of sensing property is owing to their structural properties. The presence of protons or metal ions initiates the opening of their spirolactam ring, resulting in a colorimetric response and strong fluorescence emission.²⁰ In the chemosensors, an azo unit is introduced due to its high photosensitivity and it may also initiate longer conjugation.²¹ Recently, two rhodamine and azo based chemosensors which selectively detect Al³⁺ and Cu²⁺ ions were reported. In the case of Al³⁺, rhodamine 2B and nitro substituted azo units are present in the chemosensor.²² Rhodamine 2B and simple azo units are present in the case of the Cu²⁺ sensor.²³ Interestingly, replacement of the rhodamine 2B unit with a rhodamine 6G unit and a simple azo or methyl substituted azo unit results in chemosensors **HL1** and **HL2** which selectively detect trivalent metal ions. Chemosensors **HL1** and **HL2** exhibit an ~400, ~400 and ~100 times enhancement of fluorescence intensity at 555 nm wavelength in the presence of Al³⁺, Cr³⁺ and Fe³⁺, respectively. The permissible limit of Al³⁺, Cr³⁺ and Fe³⁺ ions in water is 2.9 mg L⁻¹, 0.3 mg L⁻¹, and 0.05 mg L⁻¹, respectively. Therefore, a low detection limit (LOD) of **HL1** and **HL2** against Al³⁺, Cr³⁺ and Fe³⁺ ions (~10⁻⁹ M order) will allow us to use them in real world applications and cell imaging studies. We have successfully elucidated the X-ray crystal structures of both the chemosensors and their Al³⁺ bound complexes. Their X-ray crystal structures confirm the 1 : 2 binding stoichiometry between the metal ion and the chemosensors. The crystal structures of Al³⁺ bound rhodamine-based chemosensor complexes are scarce in the literature. Some recently reported rhodamine-based chemosensors are given in Chart S1²⁴ (ESI[†]). A literature survey on previously reported rhodamine based chemosensors^{24–26} (both single metal ion and multiple metal ion detectors) and other chemosensors^{27–30} (both single metal ion and multiple metal ion sensors) reveals that our reported chemosensors, which simultaneously detect three trivalent metal ions, have certain advantages like easy synthetic procedures involving less expensive chemicals, a high fluorescence enhancement in the presence of metal ions, low LOD values (10⁻⁹ M order), dual sensing character (colorimetric and fluorescence), X-ray structures of both free chemosensors and their metal bound forms and real world and biological applications. One main drawback of these chemosensors is their partial solubility in an aqueous medium.^{31,32,24m}



Scheme 1 Route to preparation of the azo-aldehyde and chemosensors (**HL1** and **HL2**).

Experimental section

Materials and physical measurement description

All reagent or analytical grade chemicals and solvents were collected from commercial sources and used without further purification. Elemental analysis was carried out using a Perkin-Elmer 240C elemental analyzer. Infrared spectra (400–4000 cm⁻¹) were recorded using KBr pellets on a Nicolet Magna IR 750 series-II FTIR spectrophotometer. Absorption spectral data were collected using a Cary 60 spectrophotometer (Agilent) with a 1 cm-path-length quartz cell. Electron spray ionization mass (ESI-MS positive) spectra were recorded using a MICROMASS Q-TOF mass spectrometer. A Fluoromax-4 spec-

trofluorimeter was used to collect emission spectral data at room temperature (298 K) in Britton–Robinson buffer at pH = 7.4 solution under degassed conditions. A time-resolved spectrofluorometer from IBH, UK was used to collect fluorescence lifetime data. ^1H and ^{13}C NMR spectral data were collected using Bruker 300 and Bruker 400 spectrometers in CD_3OD and $\text{DMSO}-d_6$ solvents. Cyclic voltammetric experiments were performed using a PC-controlled PAR model 273A electrochemical system under a nitrogen atmosphere using an Ag/AgCl reference electrode, with a Pt disk working electrode and a Pt wire auxiliary electrode in acetonitrile containing a supporting electrolyte, 0.1 M Bu_4NClO_4 .

X-ray crystallography

Single crystal X-ray data of the chemosensors (**HL1** and **HL2**) were collected on a Bruker SMART APEX-II CCD diffractometer using graphite mono-chromated Mo $\text{K}\alpha$ radiation ($\lambda = 0.71073 \text{ \AA}$) at room temperature. Data processing, structure solution, and refinement were examined using the Bruker Apex-II suite program. All available reflection data in the $2\theta_{\text{max}}$ range were collected and corrected for Lorentz and polarization factors with Bruker SAINT plus.³³ Reflections were then corrected for absorption, inter-frame scaling, and different systematic errors with SADABS.³⁴ The structures were solved by the direct methods and refined with the help of the full matrix least-square technique based on F^2 with the SHELX-2017/1 software package.³⁵ All the non-hydrogen atoms were refined with anisotropic thermal parameters. C–H hydrogen atoms were attached to the geometrical positions with $U_{\text{iso}} = 1/2U_{\text{eq}}$ for those atoms they were attached to. Some restraints were applied when refining disordered DMF molecules and nitrate ions to make it reasonable. One of the dichloromethane molecules present as the solvent of crystallization in **HL1** was highly disordered, which was very difficult to model, and thus their final contribution to the R value was excluded through the SQUEEZE procedure. Similarly in complex **1**, two water and two DMF molecules present as solvents of crystallization are highly disordered and it is very difficult to produce a good model to resolve the issue and thereby their contributions were removed by a squeeze procedure from the final R values. Crystal data and details of data collection and refinement for the chemosensors (**HL1** and **HL2**) and complexes (**1** and **4**) are collected in Table S2.†

Synthesis of *N*-(rhodamine-6G)lactam-hydrazine and azo-aldehydes

N-(Rhodamine-6G)lactam-hydrazine and azo-aldehydes were prepared by following literature procedures.^{24h,21}

Preparation of chemosensor **HL1**

A mixture of *N*-(rhodamine-6G)lactam-hydrazine (2.0 mmol, 0.8564 g) and 2-hydroxy-5-(phenyldiazenyl)benzaldehyde (2.0 mmol, 0.512 g) was heated under refluxing conditions for ca. 2 h in methanol–chloroform (9 : 1, v/v). Light yellow crystals were formed from slow evaporation of the methanol–chloroform solvent mixture.

Yield: 1.094 g (80%). Anal. Calc. for $\text{C}_{42}\text{H}_{40}\text{N}_6\text{O}_4\text{Cl}_6$: C 55.71%; H 4.45%; N 9.28%; Found: C 55.69%; H 4.40%; N 9.26%. IR (cm^{-1} , KBr): $\nu(\text{C}=\text{N})$ 1624s; $\nu(\text{O}-\text{H})$ 3433s; $\nu(\text{C}=\text{O})$ 1690s (Fig. S1†). ESI-MS (positive) in MeOH: the base peak appeared at $m/z = 689.27$, corresponding to $[\text{HL1} + \text{Na}]^+$ (Fig. S2†). UV-Vis, λ_{max} (nm), (ϵ ($\text{dm}^3 \text{ mol}^{-1} \text{ cm}^{-1}$)) in Britton–Robinson buffer at pH = 7.4: 307 (39 020).

^1H NMR (300 MHz, d_6 -DMSO) δ ppm: 1.20 (–CH₃) (t, 6H, $J = 7.2$ Hz), 1.86 (Ar–CH₃) (s, 6H), 3.34–3.099 (–CH₂) (m, 4H), 3.84 (–OCH₃) (s, 3H), 5.09 (NH) (t, 2H, $J_1 = 4.8$ Hz, $J_2 = 5.1$ Hz), 6.23 (Ar–CH) (s, 2H), 6.34 (Ar–CH) (s, 2H), 7.06 (Ar–CH) (d, 1H, $J = 6.2$ Hz), 7.44 (Ar–CH) (s, 1H), 7.49–7.67 (Ar–CH) (m, 4H), 7.82–7.96 (Ar–CH) (m, 3H), 8.32 (Ar–CH₃) (s, 1H), 9.05 (–CH=N) (s, 1H), 11.55 (–OH) (s, 1H) (Fig. S3a†).

^1H NMR (400 MHz, d_4 -CD₃OD) δ ppm: 1.31 (–CH₃) (t, 6H), 1.92 (Ar–CH₃) (s, 6H), 3.21–3.27 (–CH₂) (m, 4H), 3.91 (–OCH₃) (s, 3H), 6.29 (Ar–CH) (s, 2H), 6.49 (Ar–CH) (s, 2H), 7.53–8.29 (Ar–CH) (m, 11H), 8.84 (–CH=N) (s, 1H), 11.54 (–OH) (s, 1H) (Fig. S3b†).

^{13}C NMR (d_6 -DMSO, 75 MHz) δ ppm: 14.62, 17.47, 37.94, 56.36, 66.08, 96.29, 104.06, 104.70, 118.92, 119.28, 119.77, 122.74, 123.63, 124.31, 127.27, 128.71, 128.96, 129.32, 129.85, 131.33, 134.59, 145.06, 146.67, 147.40, 148.39, 149.26, 150.56, 151.47, 151.99, 152.35, 165.25 (Fig. S4†).

Synthesis of chemosensor **HL2**

A mixture of *N*-(rhodamine-6G)lactam-hydrazine (2.0 mmol, 0.8564 g) and 2-hydroxy-3-methoxy-5-(*p*-tolyl diazenyl)benzaldehyde (2.0 mmol, 0.540 g) was heated under refluxing conditions for ca. 2 h in methanol–chloroform (9 : 1, v/v). Light yellow crystals were formed from slow evaporation of the methanol–chloroform solvent mixture.

Yield: 1.201 g (86%). Anal. Calc. for $\text{C}_{42}\text{H}_{41}\text{N}_6\text{O}_4\text{Cl}_3$: C 63.04%; H 5.16%; N 10.50%. Found: C 62.98%; H 5.10%; N 10.46%. IR (cm^{-1} , KBr): $\nu(\text{C}=\text{N})$ 1621s; $\nu(\text{O}-\text{H})$ 3421s; $\nu(\text{C}=\text{O})$ 1696s (Fig. S1†). ESI-MS (positive) in MeOH: the molecular ion peak appeared at $m/z = 681.27$, corresponding to $[\text{HL2} + 1]^+$ (Fig. S5†). UV-Vis, λ_{max} (nm), (ϵ ($\text{dm}^3 \text{ mol}^{-1} \text{ cm}^{-1}$)) in Britton–Robinson buffer (10 mM) at pH = 7.4: 310 (38 440).

^1H NMR (300 MHz, d_6 -DMSO) δ ppm: 1.21 (–CH₃) (t, 6H), 1.86 (Ar–CH₃) (s, 6H), 2.39 (Ar–CH₃) (s, 3H), 3.18–3.09 (–CH₂) (m, 4H), 3.85 (–OCH₃) (s, 3H), 5.09 (NH) (t, 2H, $J_1 = 4.5$ Hz, $J_2 = 5.4$ Hz), 6.22 (Ar–CH) (s, 2H), 6.34 (Ar–CH) (s, 2H), 7.06 (Ar–CH) (d, 1H, $J = 6.6$ Hz), 7.36 (Ar–CH) (d, 2H, $J = 8.4$ Hz), 7.42 (Ar–CH) (s, 1H), 7.65–7.56 (Ar–CH) (m, 2H), 7.75 (Ar–CH) (d, 2H, $J = 8.1$ Hz), 7.94 (Ar–CH) (d, 2H, $J = 6.6$ Hz), 8.32 (Ar–CH) (s, 1H), 9.03 (–CH=N) (s, 1H), 11.51 (–OH) (s, 1H) (Fig. S6a†).

^1H NMR (400 MHz, d_4 -CD₃OD) δ ppm: 1.29 (–CH₃) (t, 6H), 1.92 (Ar–CH₃) (s, 6H), 2.42 (Ar–CH₃) (s, 3H), 3.26–3.21 (–CH₂) (m, 4H), 3.89 (–OCH₃) (s, 3H), 6.26 (Ar–CH) (s, 2H), 6.44 (Ar–CH) (s, 2H), 8.02–7.30 (Ar–CH) (m, 9H), 8.30 (Ar–CH) (s, 1H), 8.82 (–CH=N) (s, 1H), 11.50 (–OH) (s, 1H) (Fig. S6b†).

^{13}C NMR (d_6 -DMSO, 75 MHz) δ ppm: 14.62, 17.47, 21.92, 37.94, 56.36, 66.08, 96.29, 104.06, 104.70, 118.92, 119.28, 119.77, 122.74, 123.63, 124.31, 127.27, 128.71, 128.96, 129.32,

129.85, 131.33, 134.59, 145.06, 146.67, 147.40, 148.39, 149.26, 150.56, 151.47, 151.99, 152.35, 165.27 (Fig. S7†).

Synthesis of [Al(L1)₂](NO₃)·3DMF·2H₂O (1)

Firstly, 2 mL of a methanol solution of aluminum nitrate nonahydrate (1.0 mmol, 0.375 g) was added carefully to 20 mL of a methanol–chloroform (9 : 1, v/v) solution of **HL1** (2.0 mmol, 1.332 g). Then, the reaction mixture was stirred for *ca.* 3 h. Red crystals were collected in high yield after slow evaporation of the methanol–DMF solvent mixture.

Yield: 1.348 g (79%). Anal. Calc. for C₈₉H₉₉AlN₁₆O₁₆: C 63.79%; H 5.95%; N 13.37%; Found: C 63.68%; H 5.86%; N 13.29%. IR (cm⁻¹, KBr): $\nu(\text{C}=\text{N})$ 1601s; $\nu(\text{NO}_3^-)$ 1300s and 809s; $\nu(\text{C}=\text{O})$ 1646s (Fig. S8†). The molecular ion peak appeared at $m/z = 1357.37$ and 679.26, corresponding to [Al(L1)₂]⁺ and [Al(L1)₂ + H]²⁺, respectively (Fig. S9†). UV-Vis, λ_{max} (nm), (ϵ (dm³ mol⁻¹ cm⁻¹)) in Britton–Robinson buffer at pH = 7.4: 525 (59 558).

¹H NMR (400 MHz, d₆-DMSO) δ ppm: 1.20 (–CH₃) (t, 6H, $J = 7.2$ Hz), 1.87 (Ar–CH₃) (s, 6H), 3.12–3.19 (–CH₂) (m, 4H), 5.93 (NH) (s, 1H), 6.29 (Ar–CH) (d, 2H, $J = 6$ Hz), 6.40 (Ar–CH) (d, 2H, $J = 6.3$ Hz), 7.47–7.61 (Ar–CH) (m, 6H), 7.63–7.88 (Ar–CH) (m, 4H), 8.41 (NH) (d, 2H), 9.07 (–CH=N) (s, 1H) (Fig. S10a†).

¹H NMR (400 MHz, d₄-CD₃OD) δ ppm: 1.32 (–CH₃) (t, 6H), 2.09 (Ar–CH₃) (s, 6H), 3.12–3.19 (–CH₂) (m, 4H), 6.53 (NH) (s, 1H), 6.89 (Ar–CH) (d, 4H), 7.42–8.45 (Ar–CH) (m, 10H), 8.90 (–CH=N) (s, 1H) (Fig. S10b†).

¹³C NMR (d₆-DMSO, 75 MHz) δ ppm: 14.55, 17.92, 38.10, 56.35, 96.62, 104.16, 105.21, 118.29, 119.09, 119.67, 122.41, 122.74, 123.63, 124.30, 125.12, 127.34, 128.74, 129.35, 130.33, 134.60, 141.42, 145.08, 148.17, 149.22, 150.23, 150.40, 151.47, 151.91, 156.01, 157.22, 164.47, 168.07 (Fig. S11†).

Synthesis of [Cr(L1)₂](NO₃) (2)

Firstly, 2 mL of a methanol solution of chromium nitrate nonahydrate (1.0 mmol, 0.400 g) was added carefully to 20 mL of a methanol–chloroform (9 : 1, v/v) solution of **HL1** (2.0 mmol, 1.332 g). Then, the reaction mixture was stirred for *ca.* 3 h. Red microcrystals were collected in high yield after slow evaporation of the solvent.

Yield: 1.385 g (80%). Anal. Calc. for C₈₀H₇₄CrN₁₃O₁₁: C 66.74%; H 5.16%; N 12.60%; Found: C 66.65%; H 5.01%; N 12.50%. IR (cm⁻¹, KBr): $\nu(\text{C}=\text{N})$ 1601s; $\nu(\text{NO}_3^-)$ 1300s and 810s; $\nu(\text{C}=\text{O})$ 1655 s (Fig. S8†). The molecular ion peak appeared at $m/z = 1382.51$ and 691.76, corresponding to [Cr(L1)₂]⁺ and [Cr(L1)₂ + H]²⁺, respectively (Fig. S12†). UV-Vis, λ_{max} (nm), (ϵ (dm³ mol⁻¹ cm⁻¹)) in Britton–Robinson buffer at pH = 7.4: 525 (80 235).

Synthesis of [Fe(L1)₂](NO₃) (3)

Firstly, 2 mL of a methanol solution of ferric nitrate nonahydrate (1.0 mmol, 0.404 g) was added carefully to 20 mL of a methanol–chloroform (9 : 1, v/v) solution of **HL1** (2.0 mmol, 1.332 g). Then, the reaction mixture was stirred for *ca.* 3 h. A red powder was collected in high yield after slow evaporation of the solvent.

Yield: 1.302 g (75%). Anal. Calc. for C₈₀H₇₄FeN₁₃O₁₁: C 66.74%; H 5.15%; N 12.56%; Found: C 66.55%; H 5.01%; N 12.41%. IR (cm⁻¹, KBr): $\nu(\text{C}=\text{N})$ 1603s; $\nu(\text{NO}_3^-)$ 1300s and 809s; $\nu(\text{C}=\text{O})$ 1641s (Fig. S8†). The molecular ion peak appeared at $m/z = 1386.51$ and 693.83, corresponding to [Fe(L1)₂]⁺ and [Fe(L1)₂ + H]²⁺, respectively (Fig. S13†). UV-Vis, λ_{max} (nm), (ϵ (dm³ mol⁻¹ cm⁻¹)) in Britton–Robinson buffer at pH = 7.4: 525 (80 470).

Synthesis of [Al(HL2)(L2)](NO₃)₂·4H₂O (4)

Firstly, 2 mL of a methanol solution of aluminum nitrate nonahydrate (1.0 mmol, 0.375 g) was added carefully to 20 mL of a methanol–chloroform (9 : 1, v/v) solution of **HL2** (2.0 mmol, 1.362 g). Then, the reaction mixture was stirred for *ca.* 3 h. Red crystals were collected in high yield after slow evaporation of the solvent.

Yield: 0.802 g (76%). Anal. Calc. for C₈₂H₈₇AlN₁₄O₁₈: C 62.19%; H 5.54%; N 12.38%; Found: C 62.01%; H 5.29%; N 12.07%. IR (cm⁻¹, KBr): $\nu(\text{C}=\text{N})$ 1608s; $\nu(\text{NO}_3^-)$ 1300s and 822s; $\nu(\text{C}=\text{O})$ 1640s (Fig. S14†). The molecular ion peak appeared at $m/z = 1385.58$ and 693.29, corresponding to [Al(L2)₂]⁺ and [Al(L2)₂ + H]²⁺, respectively (Fig. S15†). UV-Vis, λ_{max} (nm), (ϵ (dm³ mol⁻¹ cm⁻¹)) in Britton–Robinson buffer at pH = 7.4: 525 (59 847).

¹H NMR (400 MHz, d₆-DMSO) δ ppm: 1.20 (–CH₃) (t, 6H, $J = 7.2$ Hz), 1.87 (Ar–CH₃) (s, 6H), 2.39 (Ar–CH₃) (s, 3H), 3.12–3.19 (–CH₂) (m, 4H), 5.93 (NH) (s, 1H), 6.29 (Ar–CH) (d, 2H, $J = 6$ Hz), 6.40 (Ar–CH) (d, 2H, $J = 6.3$ Hz), 7.47–7.61 (Ar–CH) (m, 4H), 7.63–7.88 (Ar–CH) (m, 4H), 8.41 (Ar–CH) (d, 1H), 9.07 (–CH=N) (s, 1H) (Fig. S16a†).

¹H NMR (400 MHz, d₄-CD₃OD) δ ppm: 1.34 (–CH₃) (t, 6H), 2.09 (Ar–CH₃) (s, 6H), 2.68 (Ar–CH₃) (s, 3H), 3.04–2.90 (–CH₂) (m, 4H), 6.24 (Ar–CH) (s, 2H), 6.46 (Ar–CH) (s, 2H), 7.43–8.18 (Ar–CH) (m, 10H), 8.45 (Ar–CH) (d, 1H), 8.99 (–CH=N) (s, 1H) (Fig. S16b†).

¹³C NMR (d₆-DMSO, 75 MHz) δ ppm: 14.55, 17.91, 21.91, 38.10, 56.34, 96.60, 104.16, 105.01, 118.99, 119.09, 119.67, 122.41, 122.74, 123.63, 124.30, 125.12, 127.34, 128.74, 129.35, 130.33, 134.60, 141.46, 145.08, 148.17, 149.23, 150.23, 150.40, 151.47, 151.91, 156.01, 157.25, 164.27, 168.27 (Fig. S17†).

Synthesis of [Cr(L2)₂](NO₃) (5)

Firstly, 2 mL of a methanol solution of chromium nitrate nonahydrate (1.0 mmol, 0.400 g) was added carefully to 20 mL of a methanol–chloroform (9 : 1, v/v) solution of **HL2** (2.0 mmol, 1.362 g). Then, the reaction mixture was stirred for *ca.* 3 h. Red coloured microcrystals were collected in high yield after slow evaporation of the solvent.

Yield: 1.448 g (82%). Anal. Calc. for C₈₂H₇₈CrN₁₃O₁₁: C 66.84%; H 5.34%; N 12.36%; Found: C 66.75%; H 5.28%; N 12.31%. IR (cm⁻¹, KBr): $\nu(\text{C}=\text{N})$ 1600s; $\nu(\text{NO}_3^-)$ 1312s and 811s; $\nu(\text{C}=\text{O})$ 1641s (Fig. S14†). The molecular ion peak appeared at $m/z = 1411.55$ and 706.28, corresponding to [Cr(L2)₂]⁺ and [Cr(L2)₂ + H]²⁺, respectively (Fig. S18†). UV-Vis, λ_{max} (nm), (ϵ (dm³ mol⁻¹ cm⁻¹)) in Britton–Robinson buffer at pH = 7.4: 525 (80 235).

Synthesis of [Fe(L2)₂](NO₃) (6)

Firstly, 2 mL of a methanol solution of ferric nitrate nonahydrate (1.0 mmol, 0.404 g) was added carefully to 20 mL of a methanol–chloroform (9 : 1, v/v) solution of **HL2** (2.0 mmol, 1.362 g). Then, the reaction mixture was stirred for *ca.* 3 h. A red coloured powder was collected in high yield after slow evaporation of the solvent.

Yield: 1.377 g (78%). Anal. Calc. for C₈₂H₇₈FeN₁₃O₁₁: C 66.66%; H 5.32%; N, 12.32%; Found: C 66.55%; H 5.25%; N 12.30%; IR (cm⁻¹, KBr): $\nu(\text{C}=\text{N})$ 1605s; $\nu(\text{NO}_3^-)$ 1300s and 812s; $\nu(\text{C}=\text{O})$ 1642s (Fig. S14†). The molecular ion peak appeared at $m/z = 1414.54$ and 707.77, corresponding to [Fe(L2)₂]⁺ and [Fe(L2)₂ + H]²⁺, respectively (Fig. S19†). UV-Vis, λ_{max} (nm), (ϵ (dm³ mol⁻¹ cm⁻¹)) in Britton–Robinson buffer at pH = 7.4: 525 (82 471).

UV-visible and fluorescence spectroscopic experiment

Stock solutions of different ions (1×10^{-3} M) were prepared in deionized water medium. A stock solution of the chemosensors (**HL1** and **HL2**) (1×10^{-3} M) was prepared in methanol medium. The chemosensor (**HL1** and **HL2**) solution was then diluted to 1×10^{-5} M as per requirements. Competitive assays of various cations and anions and other spectroscopic experiments were performed in aqueous-methanol Britton–Robinson buffer (10 mM) medium at pH 7.4. In competitive assay experiments, the test samples were prepared by mixing appropriate amounts of the cation stock in 3 mL of the chemosensor (**HL1** and **HL2**) solution (1×10^{-5} M).

Binding stoichiometry (Job's plot) studies

Binding stoichiometry of the chemosensors with Al³⁺, Cr³⁺ and Fe³⁺ ions was determined by Job's continuous variation method using absorption spectroscopy. At 25 °C temperature, the absorbance was recorded for the solutions where the concentrations of both chemosensors and Al³⁺, Cr³⁺ and Fe³⁺ ions were varied but the sum of their concentrations was kept constant at 1×10^{-5} M. The relative change in absorbance ($\Delta A/A_0$) was plotted against mole fraction. The break point in the resulting plot represents the mole fraction of the chemosensor in the Al³⁺, Cr³⁺ and Fe³⁺ complexes. From the break point the stoichiometry was determined. The final results were the average of at least three experiments.

Protocol of real sample analysis

A stock solution of the chemosensors (**HL1** and **HL2**) (1×10^{-2} M) was prepared in methanol:H₂O (9 : 1) medium. 3 mL of the real sample (saloon waste water or laboratory tap water) was taken in a vial and 3 μ L stock solution of the chemosensors (**HL1** or **HL2**) was added to it. An instantaneous colour change was observed. After that, we recorded the images of the vials under a UV-lamp and visible light.

Cell culture

The cervical cancer cell line HeLa was procured from the National Center for Cell Science (NCCS) Pune, India. The cells

were cultured in an enriched cell culture medium, DMEM (Dulbecco's modified Eagle medium), supplemented with 10% FBS (fetal bovine serum) and a mixture of appropriate antibiotics (streptomycin and penicillin) at a dose of 100 units per ml. The cells were incubated at a temperature of 37 °C and in the prevalence of 5% CO₂.

Cell internalisation studies

The cervical cancer cell line HeLa was cultured on coverslips for a period of 24 h. Then these cells were either left untreated or were exposed to a dose of ligands (10 μ M) and Al³⁺ salt (5 μ M), Cr³⁺ salt (5 μ M), and Fe³⁺ salts (5 μ M). These treated cells were then incubated for 24 h at a temperature of 37 °C. Afterwards the cells were thoroughly washed with the help of 1 \times PBS. Finally the cells were mounted on a glass slide and visualized with the aid of a fluorescent microscope (Leica).

Computational method

All computations were performed using the GAUSSIAN 09 (G09)³⁷ software package. For optimization, we used the density functional theory method at the CAM-B3LYP level^{38,39} and the standard 6-31+G(d) basis set for C, H, N and O atoms.^{40,41} TDDFT calculations were performed with the optimized geometry to ensure only positive eigen values. Time-dependent density functional theory (TDDFT)^{42–44} was performed using the conductor-like polarizable continuum model (CPCM)^{45–47} and the same CAM-B3LYP level and basis sets in a methanol solvent system. GAUSSSUM⁴⁸ was used to calculate the fractional contributions of various groups to each molecular orbital.

Results and discussion

Synthesis and characterization

N-(Rhodamine-6G)lactam-hydrazine and azo-aldehyde were prepared following the published procedures.^{24h,21} The Schiff base condensation reaction between rhodamine-6G based amine and 2-hydroxy-5-(phenyldiazenyl)benzaldehyde or 2-hydroxy-3-methoxy-5-(*p*-tolyl diazenyl)benzaldehyde finally generated the chemosensors, **HL1** and **HL2**, respectively (Scheme 1). Different spectroscopic techniques (UV-Vis, FT-IR and NMR), X-ray crystallography, ESI-mass and elemental analysis were utilized for their complete characterization (Fig. S1–S21; ESI†).

The reaction between M(NO₃)₃·9H₂O (where, M³⁺ = Al³⁺, Cr³⁺ and Fe³⁺) and **HL1/HL2** in a 1 : 2 ratio produced complexes **1–6**, respectively. They were characterized by ¹H NMR, ¹³C NMR, FT-IR spectroscopy, X ray-crystallography, and C, H and N analyses. In ESI-MS analysis, both the chemosensors exhibit the base peak at m/z 689.27 and 681.27, corresponding to [**HL1** + Na]⁺ and [**HL2** + 1]⁺, respectively. All six complexes **1–6** exhibit ESI-MS peaks at 1357.37, 1382.60, 1386.51, 1385.51, 1411.49, and 1414.64 corresponding to the [M(L1/L2)₂]⁺ (where M = Al, Cr, Fe) species. Interestingly, all the experimental data are well matched with their simulated patterns.

Crystal structure descriptions of the chemosensors (HL1 and HL2)

X ray-crystallographic analysis reveals that **HL1** is crystallized in the monoclinic system with the $P2_1/c$ space group, while **HL2** in the triclinic system with the $P\bar{1}$ space group (Table S2†). The crystal structure of chemosensor **HL1** is presented in Fig. 1, while that of **HL2** is depicted in Fig. S20.† Both chemosensors are non planar and their crystal structures confirm imine bond formation, and the presence of a spiroactam ring, xanthene unit and azo chromophore within the molecules. The C–O and C–N bond distances of **HL1** vary within the ranges 1.220–1.425 Å and 1.280–1.494 Å, respectively.

Crystal structure descriptions of complexes 1 and 4

The crystals of complex **1** were developed from a methanol–DMF solvent mixture whereas, the crystals of complex **4** were collected from a chloroform–methanol solvent mixture. Complex **4** crystallized in the triclinic system with space group $P\bar{1}$ where the asymmetric unit consists of two complex cations and four non-coordinating nitrate anions together with four water molecules as the solvent of crystallization. The crystal structure of one of the complex cations is shown in Fig. 2. Crystallographic data are collected in Table S2† and important bond lengths and angles are given in Table S3.† The crystal structure of complex **4** confirms the presence of an open spiroactam ring within the chemosensor and 2 : 1 binding stoichiometry between the chemosensor and the Al^{3+} ion. The structures of the complex cations in the asymmetric unit are similar and the structure of only one unit is briefly described here. In the complex cations, the metal centre is distorted octahedral being coordinated with two imine N-atoms (N4 and N10), two phenoxide O-atoms (O3 and O7) of both ligands and two O-atoms of open spiroactam amide (O2 and O6) of the

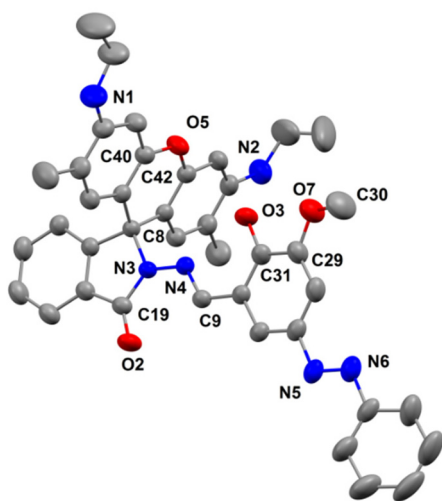


Fig. 1 Crystal structure of chemosensor **HL1**. Atoms are shown as 30% thermal ellipsoids. H atoms and the solvent molecule are omitted for clarity.

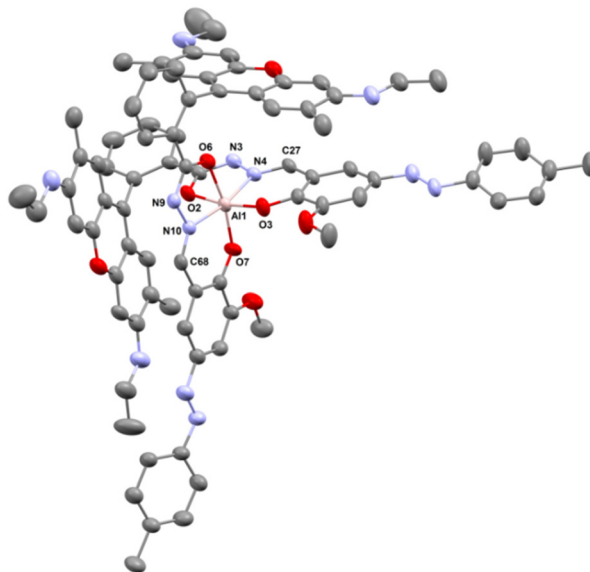


Fig. 2 Crystal structure of one of the complex cations of **4**. Atoms are shown as 30% thermal ellipsoids. H atoms are omitted for clarity.

chemosensor in a meridional fashion. The Al^{3+} – $O_{phenoxide}$, Al^{3+} – N_{imine} bond distances vary within the ranges 1.807–1.929 (3) Å, 1.811–1.863(2) Å and 1.957–2.000(3) Å, respectively. In complex **4**, spiroactam amide is present in amide form in one chemosensor and in iminolate form in the other one. The presence of both amide and iminolate forms of spiroactam amide is further supported by shorter C–O (C67–O6, 1.247(5) Å) and longer C–N (C67–N9, 1.348(6) Å) bond distances in one chemosensor unit and relatively long C–O (C26–O2, 1.297(5) Å) and short C–N (C26–N3, 1.323(5) Å) bond distances in another chemosensor unit. The azo bonds (N11–N12 and N5–N6) exhibit double bond character with distances of 1.265(6) Å and 1.277(6) Å, repetitively. In the complex the azo bound phenyl ring is slightly twisted with respect to the phenolate ring. The dihedral angles between these two phenyl rings are 21.91° and 36.92° for complex **4** (Fig. 2).

Complex **1** crystallizes in the same crystal system as complex **4** does but the asymmetric unit of complex **1** consists of a complex cation, comprising an Al^{3+} ion and two chemosensors, and one non-coordinating nitrate anion. Three DMF and two water molecules are also present as solvents of crystallization. In complex **1**, spiroactamide is present exclusively in iminolate form. The presence of the iminolate form is confirmed by longer C–O (C10–O1 = 1.290 Å, C11–O2 = 1.291 Å) and shorter C–N (C10–N10 = 1.312 Å, C11–N2 = 1.307 Å) bond distances within the complex cation (Fig. S21 and Table S3; ESI†).

NMR studies

All 1H NMR spectra are recorded in $DMSO-d_6$ solvent. The 1H NMR spectrum of **HL2** is discussed as a representative example. Here, both phenolic –OH and imine proton appear as sharp singlets at 11.51 and 9.04 ppm, respectively. Aromatic

protons appear as singlets at 8.32 and 7.42 ppm, representing the azo-aromatic part, and doublets at 7.74 and 7.36 ppm, representing the *O*-vanillin part. Aromatic protons adjacent to the spirolactam ring appear as doublets at 7.94 and 7.06 ppm and multiplets within 7.65–7.56 ppm. Aromatic protons present in the xanthene part appear as sharp singlets with double intensity at 6.34 and 6.22 ppm. Aliphatic amine (–NH) protons appear as a triplet at 5.09 ppm. Aromatic –OCH₃ protons appear as a singlet at 3.84 ppm. Aliphatic CH₂ protons appear as a multiplet within 3.18–3.09 ppm. Aromatic CH₃ protons appear as singlets at 2.39 and 1.85 ppm, whereas aliphatic CH₃ protons appear as a triplet at 1.21 ppm (Fig. S6†). The ¹H NMR spectrum data of **HL1** are collected in the Experimental section (Fig. S3; ESI†).

Both Al³⁺-probe complexes (**1** and **4**) give clean and similar types of ¹H NMR spectra in DMSO-*d*₆ solvent. In complex **4**, the coordination of metal with the chemosensors results in the disappearance of the phenolic –OH proton, whereas the position of the imine proton (singlet, 9.08 ppm) remains almost unchanged. We also observe a downfield shift of aromatic protons and broadening of the peaks. Aromatic protons adjacent to the open spirolactam ring, azo-aromatic moiety and *o*-vanillin part appear as multiplets within the range 7.96–7.47 ppm. Protons present in the xanthene part appear as doublets at 6.40 and 6.29 ppm, respectively. Aliphatic CH₂ protons appear as a multiplet within 3.19–3.12 ppm and aromatic OCH₃ protons (merged with water molecules) appear as a multiplet within the 3.90–3.69 ppm range. During complexation one aliphatic –NH proton disappears, and the other aliphatic amine gets protonated (–NH₂⁺) and appears at 5.93 ppm. In complex **4**, the amide group is present in imino-late form in one chemosensor and amide form in another chemosensor for which the proton appears at 8.42 ppm. Interestingly, the positions of aromatic and aliphatic CH₃ protons are almost unchanged upon complexation (2.39, 1.87 and 1.20 ppm, respectively) (Fig. S12; ESI†). The ¹H NMR spectral data of complex **1** are collected in the Experimental section (Fig. S9; ESI†).

¹³C NMR spectra are also recorded in DMSO-*d*₆ solvent and collected in the Experimental section. In **HL2**, spirolactam amide carbon appears at 165.25 and phenolic carbon appears at 152.35 ppm. Imine carbon appears at 151.99 ppm. In complex **4**, metal coordination results in a downfield shift of the spirolactam amide carbon, phenolic carbon and imine carbon positions at 168.27, 164.27 and 157.25 ppm respectively. In the free chemosensor, the carbon atom connecting the xanthene part and spirolactam ring is sp³ hybridized and appears at 66.08 ppm. Al³⁺ coordination results in spirolactam ring opening, therefore, the carbon atom connecting the xanthene part and spirolactam ring shows changed hybridization from sp³ to sp² and appears at 141.46 ppm. Interestingly, the positions of the OCH₃ carbon, aliphatic CH₂ and CH₃ carbon atoms remain almost unchanged (appear at 56.34, 17.91 and 14.54 ppm, respectively) both in the free and Al³⁺ bound chemosensor (Fig. S11 and S17; ESI†).

We have also performed ¹H NMR titration in DMSO-*d*₆ solvent. Gradual addition of Al³⁺ (0–2 equivalent) to the chemosensor (**HL1/HL2**) solution shows gradual disappearance of the phenolic-OH proton and aliphatic-NH proton confirming the opening of the spirolactam ring followed by complexation through phenoxide oxygen, amide oxygen and imine nitrogen atoms. Broadening of both aromatic and aliphatic protons is also observed during this titration process (Fig. S22 and S23; ESI†). Since all the sensing experiments are performed in methanol:water solution, we have performed ¹H NMR of the free chemosensors and complexes **1** and **4** in CD₃OD. Well resolved NMR spectra are presented in the Experimental section and ESI (Fig. S10b and S16b†).

Absorption spectral analysis

The UV-Vis spectra of the chemosensors (**HL1** and **HL2**) are first examined in 10 mM Britton–Robinson buffer solution at pH 7.4 (1:9, water: methanol, v/v). Chemosensors **HL1** and **HL2** exhibit well-resolved bands at ~307 and ~360 nm, responsible for π → π* and n → π* types of transitions. Interestingly upon successive addition of Al³⁺, Fe³⁺ and Cr³⁺ ions (0–6 μM, 10 mM Britton–Robinson buffer solution; pH 7.4; 1:9, water: methanol, v/v) to the chemosensor (10 μM), a new peak appears at ~525 nm with significant changes in the spectra of all chemosensors (**HL1** and **HL2**). In the case of Fe³⁺, an additional peak appears at ~395 nm (Fig. 3 and S24; ESI†). The presence of Al³⁺, Cr³⁺ and Fe³⁺ ions initiates spirolactam ring opening followed by the coordination with the chemosensors, resulting in its colour change from faint yellow to intense fluorescent yellowish pink in visible light. Spirolactam ring opening increases the delocalization of π electrons within the ligand framework followed by charge transfer transitions. Saturation has been observed in the presence of 0.5 equivalents of trivalent metal ions to the chemosensors. The 2:1 binding stoichiometry of the chemosensors with Al³⁺, Cr³⁺ and Fe³⁺ ions has been confirmed by Job's plot analysis at λ = 525 nm (Fig. 4 and S25, ESI†). Addition of different cations (Cd²⁺, Hg²⁺, Pb²⁺, Zn²⁺, Ag⁺, Mn²⁺, Fe²⁺, Co²⁺, Ni²⁺, Na⁺, K⁺, Mg²⁺, Cu²⁺, Ca²⁺, As³⁺, Ga³⁺, In³⁺, Tl³⁺ and citric acid) did not change the absorption spectrum of the chemosensors appreciably under similar experimental conditions (Fig. S26 and S27, ESI†). We have also performed UV-Vis spectroscopic studies of the chemosensors in a series of different solvents such as EtOH, DMSO, THF, MeCN and EtOH–H₂O (9:1, v/v), DMSO–H₂O (9:1, v/v), HEPES buffer in MeOH–H₂O (9:1) but no solvatochromic behavior was observed in the case of both chemosensors (Fig. S28, ESI†).

Fluorescence property analysis

Both chemosensors (10 μM) are non-fluorescent when excited at 360 nm in 10 mM Britton–Robinson buffer (1:9, water: methanol, v/v; pH = 7.4) medium. The exposure of trivalent metal ions (Al³⁺, Cr³⁺ and Fe³⁺ ions; 0–6 μM) to the probe results in great fluorescence enhancement at 555 nm (Fig. 5 and S29; ESI†). Fluorescence increases steadily and reaches a

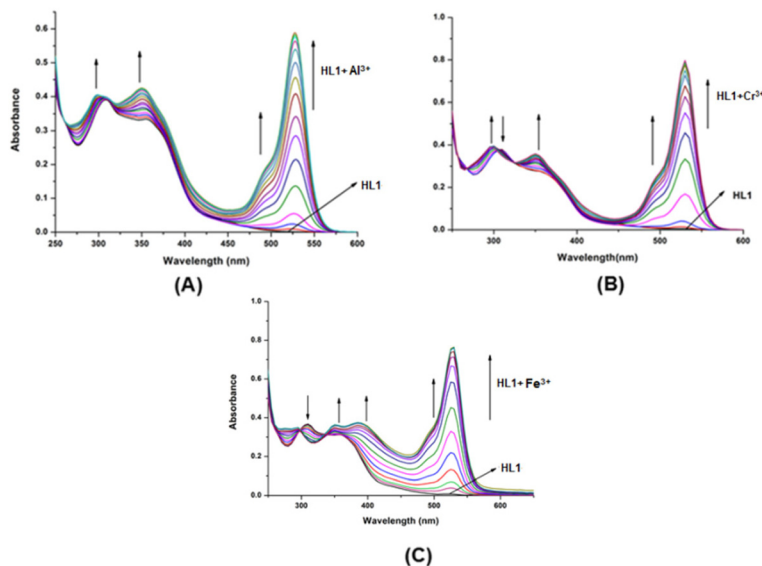


Fig. 3 Absorption titration study of HL1 (10 μM) with gradual addition of metal ions (Al^{3+} , Cr^{3+} and Fe^{3+}) (A–C) 0–6 μM in 10 mM Britton–Robinson buffer at pH 7.4.

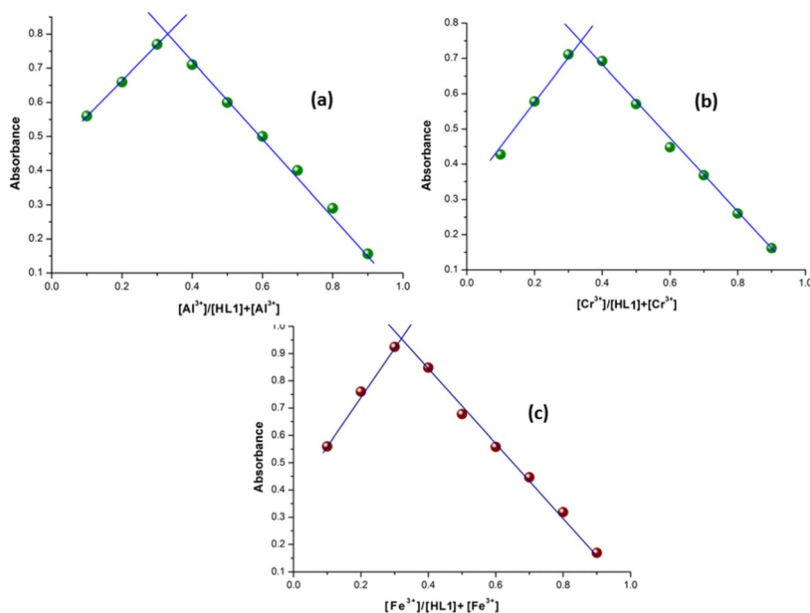


Fig. 4 2 : 1 (ligand : metal) binding stoichiometry is shown by Job's plot of complexes 1–3 (a–c) (at $\lambda = 525 \text{ nm}$). Symbols and solid lines represent the experimental and simulated profiles, respectively.

maximum at 0.5 equivalents of every trivalent metal ion. Free chemosensors are non-fluorescent due to the presence of the closed spirolactam ring. Opening of the spirolactam ring and metal coordination with imine N-atoms, phenoxide O-atoms and O-atoms of open spirolactam amide initiate fluorescence enhancement. In the case of Al^{3+} and Cr^{3+} the emission enhancement is ~ 400 fold, whereas for Fe^{3+} the enhancement is ~ 100 fold.

Binding ability of the chemosensors towards Al^{3+} , Cr^{3+} and Fe^{3+} ions has been calculated using the Benesi–

Hildebrand equation (eqn (1)) involving the fluorescence titration curve.³⁶

$$1/(F - F_0) = 1/(F_{\text{max}} - F_0) + (1/K[C])\{1/(F_{\text{max}} - F_0)\} \quad (1)$$

Here, F_{max} , F_0 and F_x represent fluorescence intensities of each chemosensor (**HL1/HL2**) in the presence of metal ions at saturation, free chemosensors (**HL1/HL2**) and any intermediate metal ion concentration, respectively. K is denoted as the

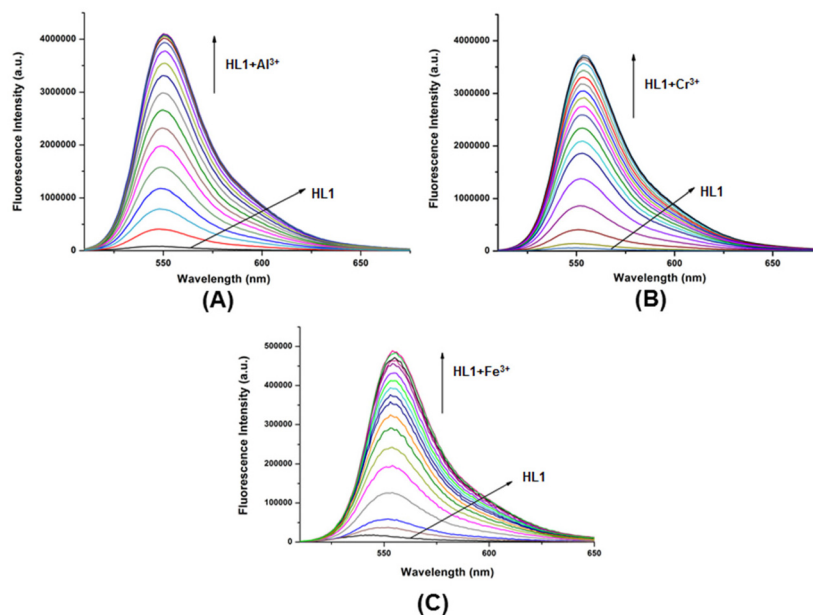


Fig. 5 Fluorescence titration of **HL1** (10 μM) in 10 mM Britton–Robinson buffer at pH = 7.4 by successive addition of metal ions (Al^{3+} , Cr^{3+} and Fe^{3+}) (A–C) (0–6 μM) with $\lambda_{\text{em}} = 555 \text{ nm}$.

binding constant of the complexes and the concentration of the respective metal ion is represented by C . The value of the binding constant (K) has been determined using the relation, $K = 1/\text{slope}$. The binding constant values are $5.14 \times 10^5 \text{ M}^{-2}$, $4.91 \times 10^5 \text{ M}^{-2}$, and $3.37 \times 10^4 \text{ M}^{-2}$ and $5.03 \times 10^5 \text{ M}^{-2}$, $4.86 \times 10^5 \text{ M}^{-2}$, and $3.95 \times 10^4 \text{ M}^{-2}$, respectively for the chemosensors **HL1** and **HL2** towards Al^{3+} , Cr^{3+} and Fe^{3+} ions (Fig. 6 and S30; ESI[†]).

High selectivity of the chemosensors toward respective metal ions (Al^{3+} , Cr^{3+} and Fe^{3+}) is again established by the competition assay experiment. Here in the presence of the chemosensors and respective metal (Al^{3+} , Cr^{3+} and Fe^{3+}) ions, (0.5 equiv.) different metal ions (Cd^{2+} , Hg^{2+} , Pb^{2+} , Zn^{2+} , Ag^+ , Mn^{2+} , Fe^{2+} , Co^{2+} , Ni^{2+} , Na^+ , K^+ , Mg^{2+} , Cu^{2+} , Ca^{2+} , As^{3+} , Ga^{3+} , In^{3+} and Tl^{3+}) (Fig. 7 and S31–S35; ESI[†]) and common anions ($\text{S}_2\text{O}_3^{2-}$, S^{2-} , SO_3^{2-} , HSO_4^- , SO_4^{2-} , SCN^- , N_3^- , OCN^- , AsO_4^{3-} , H_2PO_4^- , HPO_4^{2-} , PO_4^{3-} , ClO_4^- , AcO^- , NO_3^- , F^- , Cl^- , PF_6^- , $\text{P}_2\text{O}_7^{4-}$ and ROS such as NaOCl , KO_2 , H_2O_2) are added in excess (10.0 equiv.) in 10 mM Britton–Robinson buffer solution at pH 7.4. Competition assay experiments clearly express high fluorescence recognition of the chemosensors (**HL1** and **HL2**) for Al^{3+} , Cr^{3+} and Fe^{3+} ions over most of the metal ions and all common anions (Fig. S36–S41; ESI[†]).

Interestingly both the chemosensors, **HL1** and **HL2**, also act as colorimetric probes for selective detection of Al^{3+} , Cr^{3+} and Fe^{3+} ions. The Al^{3+} , Cr^{3+} and Fe^{3+} ions exhibit fluorescent pinkish yellow colouration in the presence of both probes. Some common cations show light yellow colouration in the presence of the chemosensors. The intensity of the chemosensors increases in the order $\text{Al}^{3+} \approx \text{Cr}^{3+} > \text{Fe}^{3+}$. Thus, the chemosensors will be a good choice for colorimetric detection of Al^{3+} , Cr^{3+} and Fe^{3+} ions both in environmental and biological fields (Fig. 8 and S42; ESI[†]).

The on-field applicability of these colorimetric sensors has also been tested. We have performed paper strip experiments to support colorimetric and fluorescence sensing abilities of both the chemosensors. We have used saloon waste water and our laboratory tap water for real sample analysis. The presence of Al^{3+} ions in saloon waste water and laboratory tap water is successfully detected by our chemosensors with the naked eye and under a UV-lamp (Fig. S43 and S44, ESI[†]). Although the chemosensors have low solubility in water, the use of aqueous-methanol solutions of **HL1/HL2** in the system and low LOD values of the chemosensors help this type of detection. Both the chemosensors are highly photostable. In the photostability experiments, 10^{-3} M aqueous solutions of **HL1** and **HL2** were irradiated with tungsten lamp light (emission in the 400–700 nm range, power 60 W/220 V) over a period of one hour. Interestingly, the fluorescence intensity of the chemosensors remains unchanged over a period of time (Fig. S45 and S46, ESI[†]).

Limit of detection (LOD) values of the chemosensors towards Al^{3+} , Cr^{3+} and Fe^{3+} ions are estimated using the 3σ method.⁴⁹ The detection limit values of the chemosensors (**HL1** and **HL2**) for Al^{3+} , Cr^{3+} and Fe^{3+} ions are $2.86 \times 10^{-8} \text{ M}$, $2.67 \times 10^{-8} \text{ M}$, $5.62 \times 10^{-6} \text{ M}$, $2.78 \times 10^{-8} \text{ M}$, $2.61 \times 10^{-8} \text{ M}$ and $6.14 \times 10^{-6} \text{ M}$, respectively.

The effect of pH on chemosensors (**HL1** and **HL2**) both under free conditions and in the presence of Al^{3+} , Cr^{3+} and Fe^{3+} ions is studied fluorometrically. It is well known that under acidic conditions, the spiro lactam ring of the chemosensor opens. A similar observation is also made in the presence of Al^{3+} , Cr^{3+} and Fe^{3+} ions. Therefore, both free chemosensor and chemosensor- Al^{3+} , Cr^{3+} , and Fe^{3+} adducts exhibit high fluorescence intensity at pH 2–4. At pH 5, a sharp

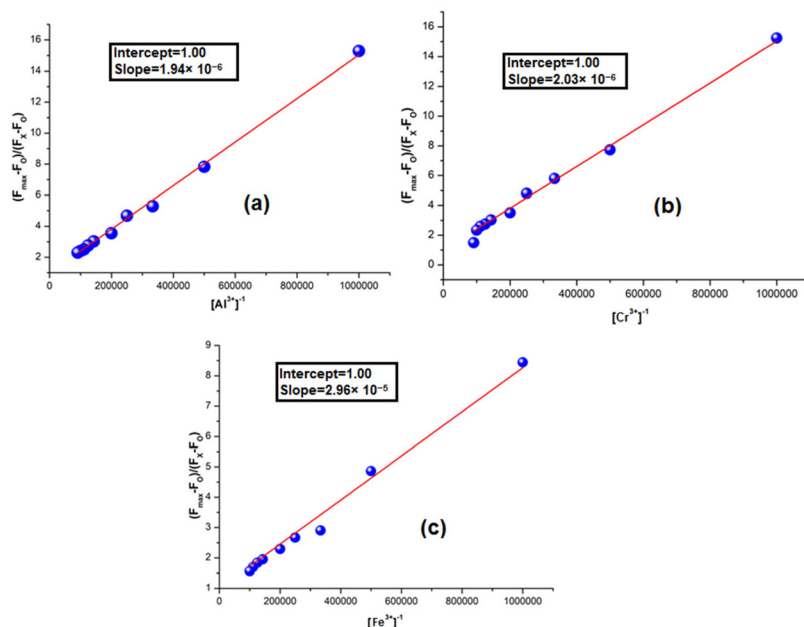


Fig. 6 Benesi–Hildebrand plot for complexes 1–3 (a–c). The plot is obtained after adding 5 μM Al^{3+} , Cr^{3+} and Fe^{3+} solution to the HL1 solution (10 μM) (in 10 mM HEPES buffer medium, pH 7.4).

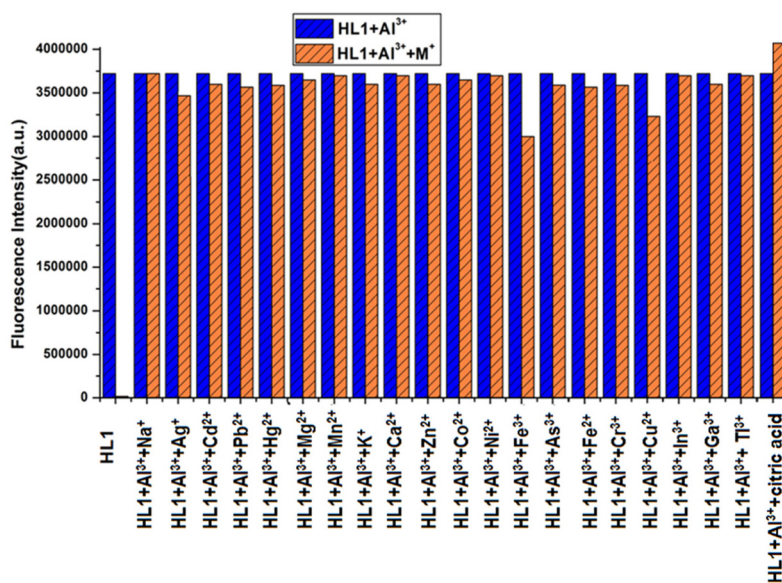


Fig. 7 Relative fluorescence intensity diagram of the $[\text{HL1-Al}^{3+}]$ system in the presence of different cations in 10 mM Britton–Robinson buffer at pH 7.4.

decrease in the fluorescence intensity of the free chemosensor is observed. Above pH 5 to pH 11 its fluorescence intensity is very weak and remains unchanged. This observation suggests the reconstruction of the spirolactam ring under neutral and basic conditions. In the presence of Al^{3+} , Cr^{3+} and Fe^{3+} ions, the fluorescence intensity of the chemosensor decreases a little above pH 4 and then it maintains a constant value up to pH 8. At pH 9 a sharp decrease in the fluorescence intensity of the chemosensor is observed. Above pH 9 to pH 11, very weak

fluorescence intensity is observed. This is probably due to the generation of metal hydroxide and the free chemosensor at higher pH (Fig. 9 and S47; ESI[†]). Interestingly, the effect of pH is more pronounced in the case of the Fe^{3+} -chemosensor adduct. The pH experiment shows that these chemosensors can act as a selective fluorescent probe for the detection of Al^{3+} , Cr^{3+} and Fe^{3+} ions in the presence of other metal ions in biological systems under physiological conditions.

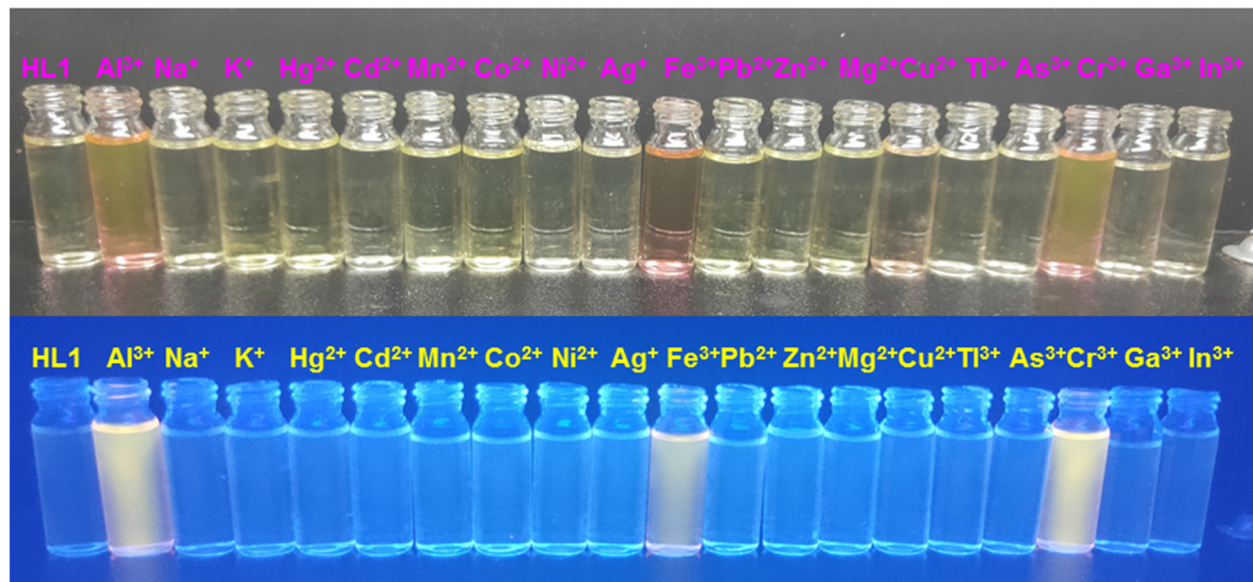


Fig. 8 Visual colour changes of chemosensor HL1 (10 μM) in the presence of common metal ions (0.5 equivalent) in 10 mM Britton–Robinson buffer (pH 7.4). The images in the above row and below row were recorded under visible light and UV light respectively.

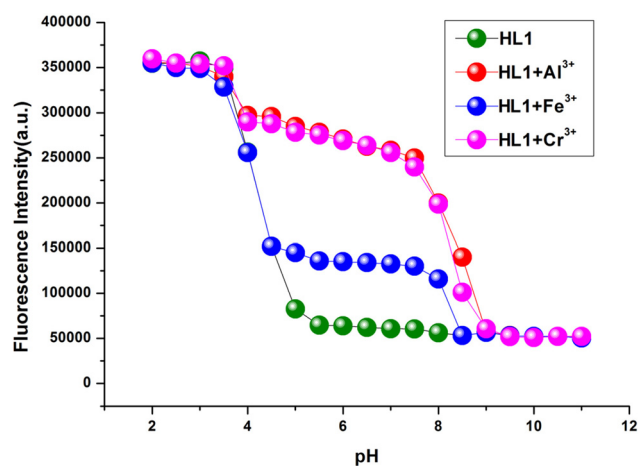


Fig. 9 Fluorescence intensity of HL1 (10 μM) in the absence and presence of metal ions (Al^{3+} , Cr^{3+} and Fe^{3+}) (5 μM) at different pH values in 10 mM Britton–Robinson buffer.

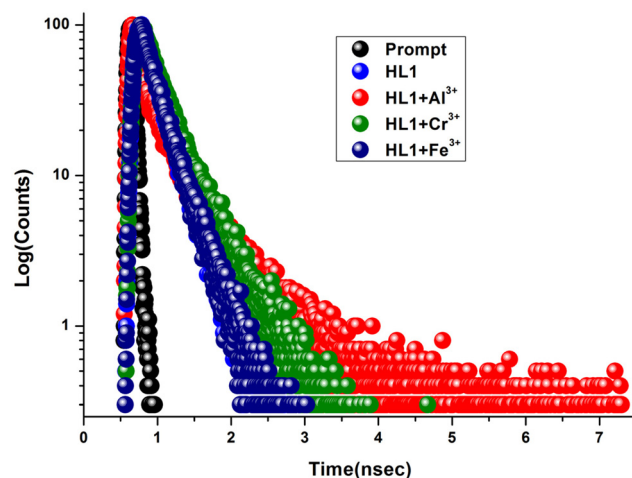


Fig. 10 Time-resolved fluorescence decay curves (logarithm of normalized intensity vs. time in ns) of HL1.

Life time and quantum yield study

Lifetime measurements for the chemosensors (**HL1** and **HL2**) and complexes **1–6** are performed at 25 °C in 10 mM Britton–Robinson buffer (pH = 7.4) medium. The average values of fluorescence decay life time of the chemosensors and complexes **1–6** have been measured using the given formula ($\tau_f = a_1\tau_1 + a_2\tau_2$, where a_1 and a_2 are the relative amplitude of the decay process). The average values of fluorescence lifetime of the chemosensors (**HL1** and **HL2**) and complexes **1–6** are 2.26 and 2.21 ns and 4.56, 3.77, 2.14, 4.24, 3.59 and 2.12 ns, respectively (Fig. 10, S48 and Table S1; ESI†).

The fluorescence quantum yield (Φ) has been calculated as follows:

$$\Phi_{\text{sample}} = \left\{ \frac{(\text{OD}_{\text{standard}} \times A_{\text{sample}} \times \eta_{\text{sample}}^2)}{(\text{OD}_{\text{sample}} \times A_{\text{standard}} \times \eta_{\text{standard}}^2)} \right\} \times \Phi_{\text{standard}}$$

In the above equation, A is the area under the emission spectral curve, OD is the optical density of the compound at the excitation wavelength and η is the refractive index of the solvent. The Φ_{standard} value is taken as 0.52 (for quinine sulfate).

The values of Φ for **HL1** and **HL2** and complexes **1–6** are estimated to be 0.005 and 0.006 and 0.26, 0.24, 0.02, 0.25, 0.23, and 0.02 respectively (Table S1†).

Mechanism of fluorescence intensity enhancement in the chemosensors in the presence of trivalent metal ions

Free chemosensors are non-fluorescent due to the presence of the spirolactam ring. The fluorescence intensity of the chemosensor increases ~ 400 times in the presence of Al^{3+} and Cr^{3+} ions and ~ 100 times in the presence of Fe^{3+} ions due to the opening of its spirolactam ring followed by complexation with the respective metal ions. ^1H , ^{13}C NMR and FT-IR spectroscopy and X-ray crystallographic techniques are used to explain the mechanistic pathway. The crystal structures of complexes **1** and **4** prove the presence of an open spirolactam ring in the Al^{3+} bound chemosensors. The presence of phenoxide oxygen, amide oxygen and imine nitrogen in the coordination environment is also observed in the crystal structures. In the ^1H NMR spectra of the free chemosensors, a phenolic $-\text{OH}$ peak, and imine and aliphatic $-\text{NH}$ protons appear around 11.5 and 9.0 and 5.0 ppm. Whereas, in the presence of Al^{3+} ions the disappearance of the phenolic $-\text{OH}$ peak and aliphatic $-\text{NH}$ proton, and the downfield shift of imine protons and aromatic protons, establish the opening of spirolactam ring and coordination of phenoxide oxygen and imine nitrogen atoms with the metal center. In the ^{13}C NMR spectra of the free chemosensor, the sp^3 hybridized carbon atom connecting the xanthene part and spirolactam ring appears at 66.08 ppm. Interestingly, the spirolactam ring opening followed by metal coordination results in a change of sp^3 hybridization into sp^2 hybridization and a new peak appears at 141.46 ppm (Fig. S11 and S17; ESI†). In the FT-IR spectrum, the free chemosensors exhibit stretching frequency of the amide $\text{C}=\text{O}$ bond and imine bond at ~ 1696 and ~ 1621 cm^{-1} , respectively. These values are shifted significantly to lower values and appear at ~ 1640 and ~ 1600 cm^{-1} , respectively for all metal bound complexes (complexes **1–6**). Apart from that a sharp $-\text{OH}$ peak appears around 3500 cm^{-1} in the free chemosensor and it also disappears after complexation. Such types of changes in the FT-IR spectral pattern again confirm the opening of the spirolactam ring and coordination of phenoxide oxygen, imine nitrogen and amide oxygen atoms with the metal centers. Therefore, using the above spectroscopic and X-ray crystallographic results, we can easily establish the coordination of the metal centers ($\text{Al}^{3+}/\text{Cr}^{3+}/\text{Fe}^{3+}$) with the chemosensor followed by charge transfer within the ligand framework resulting in strong colorimetric changes and great fluorescence enhancement.

Biocompatibility study of the ligands

The cellular toxicity of the ligands (**HL1** and **HL2**) was envisaged to determine the compatibility against the normal human lung fibroblast cells, WI-38. The cells were exposed with various concentrations (20 – 100 μM ml^{-1}) of the ligands. Then the cells were incubated for 24 h and then the cellular survivability was determined with the help of the MTT assay.

From the results, no significant toxicity was observed even at enhanced concentrations of 100 μM (as seen in Fig. S49; ESI†). Hence the results clearly depict the biocompatibility of the ligands and also suggest that these ligands have potential to emerge as promising tools for application in biomedical fields.

Cell imaging

The cellular internalization of the chemosensors (**HL1** and **HL2**) (10 μM) and Cr^{3+} salt (5 μM), Fe^{3+} salt (5 μM) and Al^{3+} salt (5 μM) has been investigated in detail with the aid of fluorescence microscopy studies. The images obtained from fluorescence microscopy shows a distinct red fluorescent signal (Fig. 11 and S50; ESI†). Hence the results suggest that the ligands and the Cr^{3+} salt (5 μM), Fe^{3+} salt (5 μM), and Al^{3+} salts (5 μM) are promptly internalized by the cells which in turn is responsible for the emergence of a red fluorescent signal.

DFT and TDDFT study

We have performed DFT and TDDFT studies to support the structure of the chemosensors. The TDDFT studies also help to understand the nature, origin and contribution of the FMOs which are involved in the electronic transitions, and quantity of energy associated with each transition. Here, the optimization of **HL1** and **HL2** was performed using DFT with the Coulomb attenuating method CAM-B3LYP (Fig. S51†). The optimized energies (eV) of some selected FMOs are presented in Table S5.† The contour plots of some selected molecular orbitals of the chemosensors are presented in Fig. S52 (ESI†). Both the ligands **HL1** and **HL2** can exist in keto or enol form in solution. The results show that in the keto and enol forms of **HL1** and only the keto form of **HL2**, the electron density in

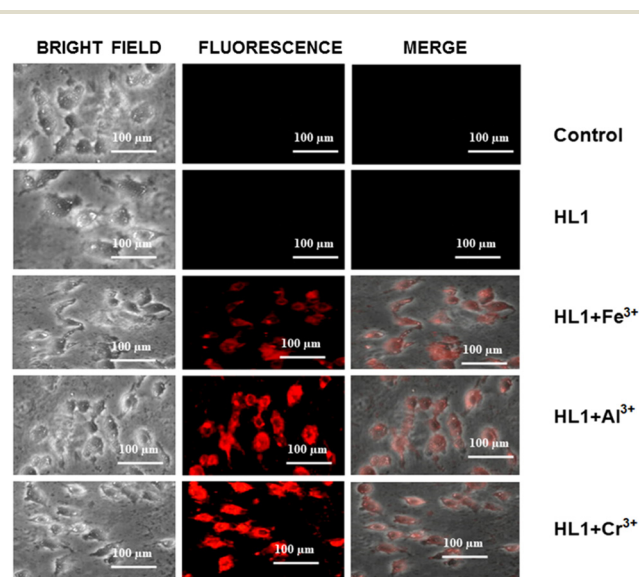


Fig. 11 Bright field, fluorescence and merged microscopic images of untreated HeLa (control) cells in the presence of the chemosensor (**HL1**) (10 μM) + M^{3+} (Al^{3+} , Cr^{3+} and Fe^{3+}) (5 μM).

the HOMO and LUMO is distributed over the azo aromatic part. In the case of the enol form of **HL2**, the electron density in the HOMO and LUMO is mainly distributed on the rhodamine part.

In TDDFT, the CAM-B3LYP/CPCM method was used with the same basis sets in methanol. The calculated electronic transitions are presented in Table S6.† The theoretical calculations showed that the keto and enol form of both chemosensors exhibit intense absorption bands at around 310 and 365 nm for the ligand based $\pi \rightarrow \pi^*$ and $n \rightarrow \pi^*$ transitions, respectively, which are well matched with experimental observations. The major transitions for **HL1** are H-2 \rightarrow L (89%) and H-2 \rightarrow L+1 (56%) (for enol form) and H-2 \rightarrow L (83%), H \rightarrow L+1 (80%), and H-9 \rightarrow L+1 (27%) (for keto form), whereas for **HL2**, the key transitions are H-2 \rightarrow L (89%) and H-2 \rightarrow L+1 (53%) (for enol form) and H \rightarrow L (86%), H \rightarrow L+1 (84%), and H-9 \rightarrow L+1 (32%) (for keto form) (Fig. 12).

To investigate the mechanism of emission behavior of the Al-complex, the structures of the S_0 and S_1 states were optimized at the DFT level using the Coulomb attenuating method CAM-B3LYP hybrid functional and the split-valence 6-31+G(d)

basis set for all atoms. Time dependent DFT (TD-DFT) approaches over 60 states to compute the vertical excitations also using the CAM-B3LYP functional to minimize deviations in charge-transfer excitation energies.⁵⁰ To avoid the computational time, we have truncated the structure slightly of the Al-complex as shown in the cartesian coordinates in the ESI.† The solvation effects were applied *via* a conductor-like screening model (CPCM) using methanol as the solvent.

The results show that the two strong low-energy transitions are associated with H-2 to L+2 (58%) at 525 nm ($f = 0.48$ a.u.) and H-2 to L+3 (63%) at 519 nm ($f = 0.45$ a.u.). This is in good agreement with the experimental results at 555 nm. Further analyses (Table 1 and Fig. 13) of these FMOs show that H-2 is localized (93%) on the azo aromatic part of the chemosensor (1st part, marked with red colour) (see Fig. 14), L+2 is localized (96%) on the open spirolactam ring of the rhodamine unit (2nd part, marked with sky colour), and L+3 is delocalized over both the open spirolactam ring of the rhodamine part (1st part, marked with green colour) (72%) and the azo aromatic part of the chemosensor (2nd part, marked with blue colour) (22%). Thus, the peak at 525 nm originated from an electron

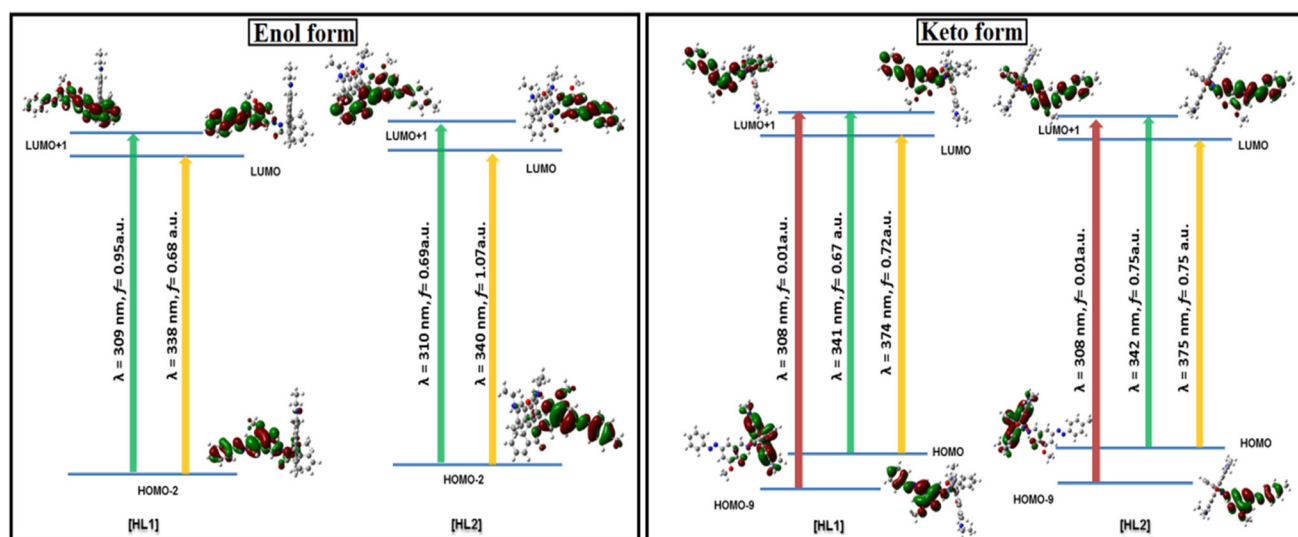


Fig. 12 Pictorial representation of key transitions of chemosensors HL1 and HL2.

Table 1 Composition (%) of the FMOs in terms of the central metal and the fragments of the attached ligands for the Al-complex

FMOs	Energy (eV)	Al	1 st part		2 nd part	
			Azo (red)	Rhodamine (green)	Azo (blue)	Rhodamine (sky)
L+3	-1.75	0	1	72	22	5
L+2	-1.91	0	0	0	3	96
L+1	-2.62	0	1	1	27	71
LUMO	-3.83	0	0	30	20	49
HOMO	-4.13	0	0	29	21	50
H-1	-4.28	0	0	0	100	0
H-2	-4.8	0	93	5	0	1
H-3	-5.17	1	77	19	1	3

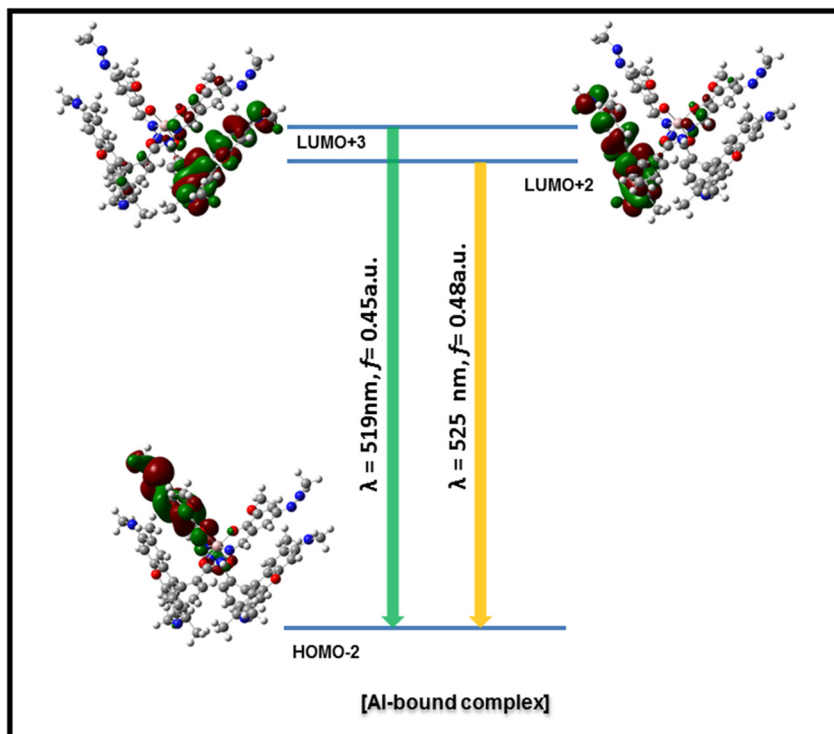


Fig. 13 Pictorial representation of the lowest energy vertical excitation of the Al-bound complex.

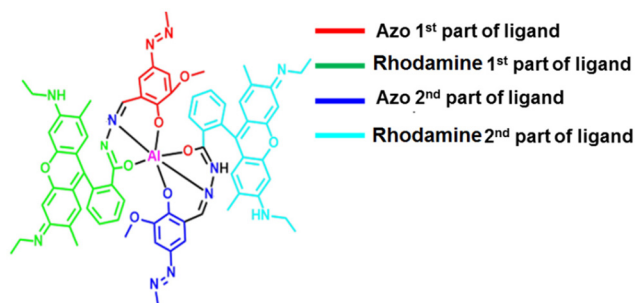


Fig. 14 Naming of fragments of the Al-bound complex as used in Table 1.

transition from the azo aromatic part (marked with red colour) to the rhodamine part (marked with sky colour) of chemosensors. Another peak at 519 nm can be assigned to a transition from the azo part of the ligand (marked with red colour) to both the fragments: the rhodamine (marked with green colour) and azo aromatic part of chemosensors (marked with blue colour).

Natural transition orbital (NTO) study

Additionally, analysis on the electronic structure of the excited states employing NTO representation showed that the S1 state can be mainly characterized by intra-ligand charge-transfer (ILCT) transitions, by populating the highest-occupied (HO) NTO and the lowest-unoccupied (LU)NTO which describe the hole and the excited electron state, respectively. The charge

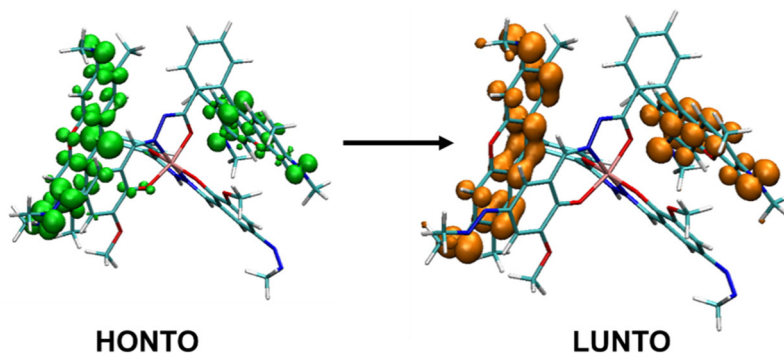


Fig. 15 The HONTO and LUNTO of the strongest low-energy emission.

transfer index (Δr) values between the HONTO and LUNTO, and hole–electron overlapping indices (σ_s) were calculated to identify the charge transition in the excited-states. The Δr value is a quantitative measure of charge-transfer (CT) length of electron excitation; higher Δr indices and smaller σ_s indices imply a longer CT distance, whereas, smaller Δr values and larger σ_s values are indicators of local-excitation. Here, the computed values of Δr and σ_s are 2.47 Å and 0.51 which indicate that the fluorophore originated from the charge transfer within the Schiff base. As shown in Fig. 15, both HONTOs and LUNTOs are mainly localized on the ligand Schiff base.

Therefore, theoretical studies clearly reveal that in metal bound chemosensors, the presence of the metal ion (Al^{3+}) initiates opening of the spirolactam ring of the chemosensor followed by charge transfer within the ligand framework resulting in strong colorimetric changes and great fluorescence enhancement.

Conclusions

Here, we have reported two new fluorescent and colorimetric chemosensors containing rhodamine 6G and azo units (**HL1** and **HL2**) which selectively detect trivalent metal ions Al^{3+} , Cr^{3+} and Fe^{3+} . The crystal structures of both chemosensors show a closed spirolactam ring, which makes them non-fluorescent. Both chemosensors form 2 : 1 complexes with trivalent metal ions which have been established by Job's plots. The crystal structures of Al^{3+} bound chemosensors prove the presence of an open spirolactam ring resulting in visual colouration and enhancement of the fluorescence intensity of the system. Al^{3+} and Cr^{3+} ions exhibit an ~ 400 times enhancement of fluorescence intensity in the presence of chemosensors, whereas an ~ 100 times enhancement has been observed in the case of Fe^{3+} ions. Such a huge enhancement of fluorescence intensity is rarely observed in other trivalent metal ion sensing chemosensors. The LOD values of the trivalent ions Al^{3+} , Cr^{3+} and Fe^{3+} are 2.86×10^{-8} M, 2.67×10^{-8} M, and 5.62×10^{-6} M, and 2.78×10^{-8} M, 2.61×10^{-8} M, and 6.14×10^{-6} M, respectively. The values of the binding constant of the probes towards the respective metal (Al^{3+} , Cr^{3+} and Fe^{3+}) ions are $5.14 \times 10^5 \text{ M}^{-2}$, $4.91 \times 10^5 \text{ M}^{-2}$, and $3.37 \times 10^4 \text{ M}^{-2}$ and $5.03 \times 10^5 \text{ M}^{-2}$, $4.86 \times 10^5 \text{ M}^{-2}$, and $3.95 \times 10^4 \text{ M}^{-2}$, respectively. We are also successful in revealing its practical application by performing the cell imaging study of chemosensors (**HL1** and **HL2**) using HeLa cells. Furthermore, the probes are applied to detect intracellular Al^{3+} , Cr^{3+} and Fe^{3+} ions in live cells with no significant cytotoxicity. A comparison of different experimental findings like crystal structure elucidation of free chemosensors and their metal (particularly Al^{3+}) bound complexes, biological applications, LOD values, enhancement of fluorescence intensity in the presence of metal ions *etc.* of chemosensors reported earlier with the present probes (Chart S1[†]) has been performed. Interestingly, our chemosensors have successfully met most of the criteria especially the crystal structure study of Al^{3+} bound chemosensor complexes which are rare in the literature.

Conflicts of interest

There are no conflicts of interest to declare.

Acknowledgements

A. S. gratefully acknowledges the financial support of this work by the DST, India (sanction no. SB/FT/CS-102/2014, dated – 18.07.2015) and RUSA 2.0, Government of India (sanction no. R-11/262/19, dated – 08.03. 2019). J. M. heartily acknowledges the UGC, Government of India for his RGNF fellowship (Registration ID: RGNF-2017-18-SC-WES-33748).

References

- J. S. Kim and D. T. Quang, *Chem. Rev.*, 2007, **107**, 3780–3799.
- H. N. Kim, M. H. Lee, H. J. Kim, J. S. Kim and J. Yoon, *Chem. Soc. Rev.*, 2008, **37**, 1465–1472.
- X. Chen, T. Pradhan, F. Wang, J. S. Kim and J. Yoon, *Chem. Rev.*, 2012, **112**, 1910–1956.
- Y. Yamini, N. Alizadeh and M. Shamsipur, *Anal. Chim. Acta*, 1997, **355**, 69–74.
- C. F. Harrington, S. A. Merson and T. M. D. D'Silva, *Anal. Chim. Acta*, 2004, **505**, 247–254.
- S. L. C. Ferreira, A. S. Queiroz, M. S. Fernandes and H. C. dos Santos, *Spectrochim. Acta, Part B*, 2002, **57**, 1939–1950.
- J. C. Yu, J. M. Lo and K. M. Wai, *Anal. Chim. Acta*, 1983, **154**, 307–312.
- A. Ali, H. Shen and X. Yin, *Anal. Chim. Acta*, 1998, **369**, 215–223.
- A. Bobrowski, K. Nowak and J. Zarebski, *Anal. Bioanal. Chem.*, 2005, **382**, 1691–1697.
- W. Shoty, D. Weiss, P. Appleby, A. Cheburkin, R. Frei and M. Gloor, *Science*, 1998, **281**, 1635–1640.
- V. K. Gupta, A. K. Jain and G. Maheshwari, *Talanta*, 2007, **72**, 1469–1473.
- G. C. Kabat and T. E. Rohan, *Cancer, Causes Control*, 2007, **118**, 1047–1053.
- P. Aisen, C. Enns and M. Wessling-Resnick, *Int. J. Biochem. Cell Biol.*, 2001, **33**, 940–959.
- K. J. Hintze and E. C. Theil, *Proc. Natl. Acad. Sci. U. S. A.*, 2005, **102**, 15048–15052.
- L. Huang, F. Hou, J. Cheng, P. Xi, F. Chen, D. Bai and Z. Zeng, *Org. Biomol. Chem.*, 2012, **10**, 9634–9638.
- H. Kim, K. B. Kim, E. J. Song, I. H. Hwang, J. Y. Noh, P.-G. Kim, K.-D. Jeong and C. Kim, *Inorg. Chem. Commun.*, 2013, **36**, 72–76.
- J. Wang, D. Zhang, Y. Liu, P. Ding, C. Wang, Y. Ye and Y. Zhao, *Sens. Actuators, B*, 2014, **191**, 344–350.
- P. Xie, F. Guo, R. Xia, Y. Wang, D. Yao, G. Yang and L. Xie, *J. Lumin.*, 2014, **145**, 849–854.
- H. Wu, P. Zhou, J. Wang, L. Zhao and C. Duan, *New J. Chem.*, 2009, **33**, 653.

- 20 X. Q. Chen, T. Pradhan, F. Wang, J. S. Kim and J. Y. Yoon, *Chem. Rev.*, 2012, **112**, 1910–1956.
- 21 (a) S. Banerjee, A. Dey, P. Ghorai, P. Brandao, J. Ortega-Castro, A. Frontera, P. P. Ray and A. Saha, *New J. Chem.*, 2018, **42**, 13430–13441; (b) M. Yang, W. Meng, X. Liu, N. Su, J. Zhou and B. Yang, *RSC Adv.*, 2014, **4**, 22288–22293.
- 22 S. Mabhai, M. Dolai, S. Dey, A. Dhara, B. Das and A. Jana, *New J. Chem.*, 2018, **42**, 10191–10201.
- 23 M. Yang, W. Meng, X. Liu, N. Su, J. Zhou and B. Yang, *RSC Adv.*, 2014, **4**, 22288–22293.
- 24 (a) S. Samanta, T. Ray, F. Haque and G. Das, *J. Lumin.*, 2016, **171**, 13–18; (b) S. Paul, A. Manna and S. Goswami, *Dalton Trans.*, 2015, **44**, 11805–11810; (c) S. Dey, S. Sarkar, D. Maity and P. Roy, *Sens. Actuators, B*, 2017, **246**, 518–534; (d) A. Roy, S. Das, S. Sacher, S. K. Mandal and P. Roy, *Dalton Trans.*, 2019, **48**, 17594–17604; (e) R. Alam, R. Bhowmick, A. S. M. Islam, A. Katarkar, K. Chaudhuri and M. Ali, *New J. Chem.*, 2017, 8359–8369; (f) D. Singha, T. Das, L. Satyanarayana, P. Roy and M. Nandi, *New J. Chem.*, 2019, **43**, 15563–15574; (g) D. Das, R. Alam, A. Katarkar and M. Ali, *Photochem. Photobiol. Sci.*, 2019, **18**, 242–252; (h) X. Tang, Y. Wang, J. Han, L. Ni, H. Zhang, C. Li, J. Lid and Y. Qiu, *Dalton Trans.*, 2018, **47**, 3378–3387; (i) D. Das, R. Alam and M. Ali, *Analyst*, 2022, **147**, 471–479; (j) D. Singha, A. Pal, H. Uyama, P. Roy and M. Nandi, *Dalton Trans.*, 2021, **50**, 12478–12494; (k) N. Dey, N. Kumari and S. Bhattacharya, *Tetrahedron*, 2021, **85**, 132007; (l) Y. Fu, X. J. Jiang, Y. Y. Zhu, B. J. Zhou, S. Q. Zang, M. S. Tang, H. Y. Zhang and T. C. W. Mak, *Dalton Trans.*, 2014, **43**, 12624–12632; (m) J. Qiu, C. Zhong, M. Liu, Y. Yuan, H. Zhu and Y. Gao, *New J. Chem.*, 2021, **45**, 5184–51949; (n) S. Das, P. P. Das, J. W. Walton, K. Ghoshal, L. Patra and M. Bhattacharyya, *New J. Chem.*, 2021, **45**, 1853–1862; (o) C. Kan, X. Wang, X. Shao, L. Wu, S. Qiu and J. Zhu, *New J. Chem.*, 2021, **45**, 8918–8924; (p) Z. Qin, W. Su, P. Liu, J. Ma, Y. Zhang and T. Jiao, *ACS Omega*, 2021, **6**, 25040–25048; (q) J. Mandal, P. Ghorai, K. Pal, T. Bhaumik, P. Karmakar and A. Saha, *ACS Omega*, 2020, **5**, 145–157.
- 25 A. Hazra, P. Ghosh and P. Roy, *Spectrochim. Acta, Part A*, 2022, **271**, 120905.
- 26 A. Hazra and P. Roy, *Anal. Chim. Acta*, 2022, **1193**, 339378.
- 27 M. B. Maitya, B. Dutta, A. Rahaman, N. Sahu, D. P. Mandal, S. Bhattacharjee and C. Sinha, *J. Mol. Struct.*, 2022, **1250**, 131870.
- 28 T. T. Liu, S. J. Li, H. Fu, Z. N. Tian, X. J. Sun and Z. Y. Xing, *Journal of Photochemistry & Photobiology, A: Chemistry*, 2020, **403**, 112865.
- 29 S. O. Tumay, A. Senocak and A. Mermer, *New J. Chem.*, 2021, **45**, 18400–18411.
- 30 R. Kaushik, R. Sakla, N. Kumar, A. Ghosh, V. D. Ghule and D. A. Jose, *Sens. Actuators, B*, 2021, **328**, 129026.
- 31 L. Hou, T. Liu, Y. Gong, J. Li, C. Deng, C. Zhang, Y. Wang, S. Shuang and W. Liang, *New J. Chem.*, 2020, **44**, 19642–19649.
- 32 (a) L. Wang, W. Li, W. Zhi, Y. Wang, J. Han, Z. Cao, L. Ni, H. Li and J. Jing, *J. Lumin.*, 2018, **196**, 379–386; (b) P. S. Nayab and M. Shkir, *Sens. Actuators, B*, 2017, **251**, 951–957; (c) Q. Chen and Z. Fang, *Spectrochim. Acta, Part A*, 2018, **193**, 226–234.
- 33 G. M. Sheldrick, *SAINT, Version 6.02, SADABS, Version 2.03*, Bruker AXS Inc., Madison, Wisconsin, 2002.
- 34 G. M. Sheldrick, *SADABS: Software for Empirical Absorption Correction*, University of Gottingen, Institute fur Anorganische Chemieder Universitat, Gottingen, Germany, 1999–2003.
- 35 G. M. Sheldrick, Crystal structure refinement with SHELXL, *Acta Crystallogr., Sect. C: Struct. Chem.*, 2015, **71**, 3–8.
- 36 H. A. Benesi and J. H. Hildebrand, *J. Am. Chem. Soc.*, 1949, **71**, 2703–2707.
- 37 M. J. Frisch, G. W. Trucks, H. B. Schlegel, G. E. Scuseria, M. A. Robb, J. R. Cheeseman, G. Scalmani, V. Barone, B. Mennucci, G. A. Petersson, H. Nakatsuji, M. Caricato, X. Li, H. P. Hratchian, A. F. Izmaylov, J. Bloino, G. Zheng, J. L. Sonnenberg, M. Hada, M. Ehara, K. Toyota, R. Fukuda, J. Hasegawa, M. Ishida, T. Nakajima, Y. Honda, O. Kitao, H. Nakai, T. Vreven, J. A. Montgomery Jr., J. E. Peralta, F. Ogliaro, M. Bearpark, J. J. Heyd, E. Brothers, K. N. Kudin, V. N. Staroverov, R. Kobayashi, J. Normand, K. Raghavachari, A. Rendell, J. C. Burant, S. S. Iyengar, J. Tomasi, M. Cossi, N. Rega, J. M. Millam, M. Klene, J. E. Knox, J. B. Cross, V. Bakken, C. Adamo, J. Jaramillo, R. Gomperts, R. E. Stratmann, O. Yazyev, A. J. Austin, R. Cammi, C. Pomelli, J. W. Ochterski, R. L. Martin, K. Morokuma, V. G. Zakrzewski, G. A. Voth, P. Salvador, J. J. Dannenberg, S. Dapprich, A. D. Daniels, O. Farkas, J. B. Foresman, J. V. Ortiz, J. Cioslowski and D. J. Fox, *GAUSSIAN09, Revision D.01*, Gaussian Inc., Wallingford, CT, 2009.
- 38 A. D. Becke, *J. Chem. Phys.*, 1993, **98**, 5648–5652.
- 39 C. Lee, W. Yang and R. G. Parr, *Phys. Rev. B: Condens. Matter Mater. Phys.*, 1988, **37**, 785–789.
- 40 P. J. Hay and W. R. Wadt, *J. Chem. Phys.*, 1985, **82**, 270–283.
- 41 W. R. Wadt and P. J. Hay, *J. Chem. Phys.*, 1985, **82**, 284–298.
- 42 R. Bauernschmitt and R. Ahlrichs, *Chem. Phys. Lett.*, 1996, **256**, 454–464.
- 43 R. E. Stratmann, G. E. Scuseria and M. J. Frisch, *J. Chem. Phys.*, 1998, **109**, 8218–8224.
- 44 M. E. Casida, C. Jamorski, K. C. Casida and D. R. Salahub, *J. Chem. Phys.*, 1998, **108**, 4439–4449.
- 45 V. Barone and M. Cossi, *J. Phys. Chem. A*, 1998, **102**, 1995–2001.
- 46 M. Cossi and V. Barone, *J. Chem. Phys.*, 2001, **115**, 4708–4717.
- 47 M. Cossi, N. Rega, G. Scalmani and V. Barone, *J. Comput. Chem.*, 2003, **24**, 669–681.
- 48 N. M. O’Boyle, A. L. Tenderholt and K. M. Langner, *J. Comput. Chem.*, 2008, **29**, 839–845.
- 49 A. B. Pradhan, S. K. Mandal, S. Banerjee, A. Mukherjee, S. Das, A. R. K. Bukhsh and A. Saha, *Polyhedron*, 2015, **94**, 75–82.
- 50 A. Dreuw and M. Head-Gordon, *Chem. Rev.*, 2005, **105**, 4009–4037.



2-hydroxy-5-methylisophthalaldehyde based fluorescent-colorimetric chemosensor for dual detection of Zn^{2+} and Cu^{2+} with high sensitivity and application in live cell imaging

Jayanta Mandal^a, Pravat Ghorai^a, Kunal Pal^b, Parimal Karmakar^b, Amrita Saha^{a,*}

^a Department of Chemistry, Jadavpur University, Kolkata 700032, India

^b Department of Life Science and Biotechnology, Jadavpur University, Kolkata 700032, India

ARTICLE INFO

Keywords:

Schiff base
 Zn^{2+} and Cu^{2+} sensor
 Spectroscopic analysis
 Cell imaging
 DFT calculations

ABSTRACT

A 2-hydroxy-5-methylisophthalaldehyde (HMP) based Schiff-base ligand (HL) was successfully developed as a fluorescent and colorimetric chemosensor for dual detection of Zn^{2+} and Cu^{2+} ions in HEPES buffer medium (H_2O :Methanol = 9:1 (v/v), pH = 7.4). Interestingly, in presence of Zn^{2+} around 16 times increment in fluorescence intensity and in presence of Cu^{2+} ~ 174 times decrease in fluorescence intensity has been observed. The 1:2 binding modes for both HL- Zn^{2+} / Cu^{2+} complexes are proved by fluorescence measurements, ESI-MS analysis and DFT-Calculations. The reversibility and regeneration process of HL are also established using Na_2EDTA . It has been observed that Chemosensor HL exhibits a rapid change in fluorescence intensity within pH range 6–8 against Zn^{2+} and Cu^{2+} ions. Low detection limit was found to be 1.059×10^{-9} (M) and 3.53×10^{-9} (M) for Zn^{2+} and Cu^{2+} ions respectively. These values also suggest that the chemosensor HL has great potential to detect Zn^{2+} and Cu^{2+} ions in environmental and biological studies.

1. Introduction

Chemosensors that can selectively detect the presence of both environmentally and biologically important metal ions through the naked eye and optical responses has received significant attention [1]. Environmentally and biologically significant metal ions could be detected using different traditional analytical techniques such as voltammetric methods, inductively coupled plasma mass spectrometry (ICP-MS), ion selective electrodes and atomic absorption/emission spectrometry. In comparison to above techniques colorimetric and fluorescent methods are more advantageous due to their ease of measurement, excellent selectivity, high sensitivity, simplicity and rapid response time [2–7]. Fluorescent-sensing mechanisms that have been extensively investigated are photo induced electron transfer (PET), the rigidity effect, fluorescence resonance energy transfer (FRET), excimer/exciple formation/ extinction, photo-induced charge transfer (PCT), and less frequently, excited-state proton transfer (ESPT). Colorimetric method is extensively used mainly naked-eye detection of the element without any use of a spectroscopic instrument [8–11]. Among various cations commonly present in our human body, Zn^{2+} and Cu^{2+} are the second and third most abundant transition element found after iron(III). Both metal ions play critical roles in biology, and they most often present as

cofactors in diverse enzymes; however, improper regulation of their storage is also connected to serious disorders. The average zinc and copper ion concentrations required for human growth and development are in the order of 15 mg/L and 0.1 mg/L, respectively. Excess copper is toxic and environmental pollutant. However, its deficiency or over-load is associated with a series of disorders such as anemia, liver damage in infants, Wilson disease, Parkinson's disease, Alzheimer's disease, Menkes syndrome etc [12–14]. Similarly, zinc(II) deficiency is associated with growth retardation, neurological disorder, such as Parkinson and Alzheimer's diseases, eye lesion, skin problems and different immunological defense related decrease [15,16]. Therefore, the monitoring and imaging of these elements are important for biological research as well as clinical diagnosis. Regarding detection of Zn^{2+} ion the greatest challenge is to discriminate Zn^{2+} from Cd^{2+} [17]. Both are present in the same group of the periodic table with similar photo-physical properties. A large number of Zn^{2+} and Cu^{2+} detecting chemosensors are reported in literature, still there is a great need to develop simple and effective chemosensors for their dual detection.

The HMP framework has been an ideal candidate for the construction of different type fluorescent chemosensors (chart S1). A careful literature survey of chemosensors based on isophthalaldehyde and its derivatives reveal that most of the chemosensors selectively detect only

* Corresponding author.

E-mail address: amritasahachemju@gmail.com (A. Saha).

Zn^{2+} ion (chart S1, see ref. 3S, 5S-7S, 9S). There are some chemosensors which detect both Zn^{2+} and other ions like Cd^{2+} , Mg^{2+} , Al^{3+} and H_2S [1S,2S,8S,10S]. Among these some are dual chemosensors i.e. both colorimetric as well as fluorometric sensor. Most of the chemosensors work in organic-aqueous solvent mixture and are responsive towards biological systems. Apart from that only few isophthalaldehyde based chemosensors are known which selectively detect both Zn^{2+} and Cu^{2+} ions. Prof. Pombeiro and his group had synthesized an isophthalaldehyde based chemosensor which fluorimetrically detect both Zn^{2+} and Cu^{2+} ions in methanol solvent [4S]. In one of our recent work we have reported an isophthalaldehyde based chemosensor which act as both colorimetric as well as fluorometric sensor for dual detection of Zn^{2+} and Cu^{2+} ions in organo aqueous solvent [16S].

In this work we have synthesized and characterized a HMP based chemosensor (**HL**). **HL** detects both the ions colorimetrically as well as through fluorescent techniques. The detection of both the ions by our receptor (**HL**) has been examined by absorption spectroscopy, emission spectroscopy, DFT calculation, ESI-MS experiment and ^{13}C and ^1H NMR spectroscopy. **HL** shows a color change from light yellow to green in presence of Zn^{2+} and light yellow to colorless in presence of Cu^{2+} ions under visible light. It exhibits an increment of about 16 times in the emission intensity in the presence of one equivalent of Zn^{2+} ions upon excitation at 410 nm. On the other hand upon addition of one equivalent of Cu^{2+} emission intensity of the chemosensor has been decreased by ~ 174 times. This is due to paramagnetic nature of Cu^{2+} . The LOD of the chemosensor molecule against Zn^{2+} and Cu^{2+} are 1.059×10^{-9} (M) and 3.53×10^{-9} (M) respectively. This chemosensor also exhibits cell permeability and intracellular Cu^{2+} and Zn^{2+} ions sensing in MDA-MB-468 cells.

The main advantage of this dual chemosensor is its easy synthesis procedure which is not only economic but also less time consuming. It has very high binding constant towards both of the ions and limit of detection values for both the ions is in nano molar range. We have performed all the experiments in aqueous-methanolic medium (9:1, v/v, HEPES buffer pH = 7.4) which further justify its biological cell imaging application.

2. Experimental section

2.1. Materials and physical measurements

All reagent or analytical grade chemicals and solvents were purchased from commercial sources and used without further purification. Elemental analysis for C, H and N was carried out using a Perkin–Elmer 240 C elemental analyzer. Infrared spectra ($400\text{--}4000\text{ cm}^{-1}$) were recorded from KBr pellets on a Nicolet Magna IR 750 series-II FTIR spectrophotometer. Absorption spectra were measured using a Cary 60 spectrophotometer (Agilent) with a 1-cm-path-length quartz cell. Electron spray ionization mass (ESI-MS positive) spectra were recorded on a MICROMASS Q-TOF mass spectrometer. Emission spectra were collected using Fluoromax-4 spectrofluorimeter at room temperature (298 K) in HEPES buffer at pH = 7.4 solution under degassed condition. Fluorescence lifetime was measured using a time-resolved spectrofluorometer from IBH, UK. Measurements of ^1H NMR spectra were conducted using a Bruker 300 spectrometer D_2O solvent.

2.2. Synthesis of 2-hydroxy-5-methylisophthalaldehyde (HMP)

2-hydroxy-5-methylisophthalaldehyde (HMP) was prepared by following a standard literature procedure [18].

2.3. Synthesis of Chemosensor [HL = 4-methyl-2,6-bis((E)-((2-(piperazin-1-yl)ethyl)imino)methyl)phenol]

A mixture of 2-hydroxy-5-methylisophthalaldehyde (2.0 mmol, 0.3283 g) and 1-(2-aminoethyl) piperazine (4.0 mmol, 0.516 g) was

heated to reflux for ca. 4 h in methanol solvent. Yellow colored gummy mass was obtained after evaporation of the solvent.

Yield: 0.335 g (87%). Anal. Calc. for $\text{C}_{21}\text{H}_{34}\text{N}_6\text{O}$: C 65.25%; H 8.87%; N 21.74%. Found: C 65.18%; H 8.48%; N 21.49%. IR (cm^{-1} , KBr): $\nu(\text{C}=\text{N})$ 1634 s; $\nu(\text{C}-\text{H})$ 779 s. ESI-MS (positive) in MeOH: The base peak was detected at $m/z = 387.18$, corresponding to $[\text{HL} + 1]^+$. UV-Vis, λ_{max} (nm), (ϵ ($\text{dm}^3\text{mol}^{-1}\text{cm}^{-1}$)) in HEPES buffer at pH = 7.4: 440 (6229), 230 (38740).

^1H NMR (d_6 -DMSO, 300 MHz) δ ppm: 2.17 (Ar- CH_3) (s, 3H), 2.42 ($-\text{CH}_2$) (s, 4H), 3.60 ($-\text{CH}_2$) (s, 4H), 2.27 ($-\text{CH}_2$) (s, 8H), 2.58 ($-\text{CH}_2$) (s, 8H), 7.41 (ArH) (m, 2H), 8.50 ($-\text{CH}=\text{N}$) (s, 2H).

^{13}C NMR (d_6 -DMSO, 75 MHz) δ ppm: 20.35 ($-\text{CH}_3$), 45.89–59.39 ($-\text{CH}_2$), 121.44–161.75 (Ar-C), 160.76 ($-\text{CH}=\text{N}$).

2.4. Synthesis of complex $[\text{Zn}_2(\text{L})(\text{OH}_2)(\text{OH})(\text{NO}_3)](\text{NO}_3)(1)$

A 2 mL methanolic solution of zinc nitrate hexahydrate (2.0 mmol, 0.5948 g) was added drop wise to 20 mL methanolic solution of **HL** (1.0 mmol, 0.386 g) followed by addition of triethylamine (2.0 mmol, ~ 0.4 mL) and the resultant reaction mixture was stirred for ca. 3 h. Yellow colored solid mass was obtained in high yield after slow evaporation of the solvent.

Yield: 0.589 g (85%). Anal. Calc. for $\text{C}_{21}\text{H}_{38}\text{N}_8\text{O}_{10}\text{Zn}_2$: C 36.38%; H 5.52%; N 16.16%. Found: C 36.17%; H 5.35%; N 16.84%. IR (cm^{-1} , KBr): $\nu(\text{C}=\text{N})$ 1632 s; $\nu(\text{NO}_3^-)$ 1321 s; $\nu(\text{C}-\text{H})$ 781 s. ESI-MS (positive) in MeOH: The base peak was detected at $m/z = 638.00$, corresponding to $[\text{Zn}_2(\text{L})(\text{OLi})(\text{H}_2\text{O})]^+$. UV-Vis, λ_{max} (nm), (ϵ ($\text{dm}^3\text{mol}^{-1}\text{cm}^{-1}$)) in HEPES buffer at pH = 7.4: 410(6975).

^1H NMR (d_6 -DMSO, 300 MHz) δ ppm: 2.16 (Ar- CH_3) (s, 3H), 2.48 ($-\text{CH}_2$) (s, 4H), 2.55 ($-\text{CH}_2$) (s, 8H), 2.89 ($-\text{CH}_2$) (s, 8H), 7.46 (ArH) (m, 2H), 8.57 ($-\text{CH}=\text{N}$) (s, 2H).

^{13}C NMR (d_6 -DMSO, 75 MHz) δ ppm: 19.94 ($-\text{CH}_3$), 49.07–58.51 ($-\text{CH}_2$), 121.37–168.16 (Ar-C), 166.62 ($-\text{CH}=\text{N}$).

2.5. Synthesis of complex $[\text{Cu}_2(\text{L})(\text{OH}_2)(\text{OH})(\text{NO}_3)](\text{NO}_3)(2)$

A 2 mL methanolic solution of copper nitrate trihydrate (2.0 mmol, 0.5912 g) was added drop wise to 20 mL methanolic solution of **HL** (1.0 mmol, 0.386 g) followed by addition of triethylamine (2.0 mmol, ~ 0.4 mL) and the resultant reaction mixture was stirred for ca. 3 h. Intense green colored solid mass was obtained after slow evaporation of the solvent.

Yield: 0.585 g (85%). Anal. Calc. for $\text{C}_{21}\text{H}_{38}\text{Cu}_2\text{N}_8\text{O}_{10}$: C 36.57%; H 5.55%; N 16.25%. Found: C 36.48%; H 5.31%; N 16.02%. IR (cm^{-1} , KBr): $\nu(\text{C}=\text{N})$ 1627 s; $\nu(\text{NO}_3^-)$ 1332 s; $\nu(\text{C}-\text{H})$ 750 s. ESI-MS (positive) in MeOH: The base peak was detected at $m/z = 634.14$ corresponding to $[\text{Cu}_2(\text{L})(\text{OLi})(\text{H}_2\text{O})]^+$. UV-Vis, λ_{max} (nm), (ϵ ($\text{dm}^3\text{mol}^{-1}\text{cm}^{-1}$)) in HEPES buffer at pH = 7.4: 405(12782), 620 (696).

2.6. UV-visible and fluorescence spectroscopic studies

Stock solutions of various ions (1×10^{-3} M) were prepared in deionized water. A stock solution of the chemosensor and (**HL**) (1×10^{-3} M) was prepared in methanol. The solution of **HL** was then diluted to 1×10^{-5} M as per requirement. All the spectroscopic experiments including competitive assay of various cations and anions were performed in aqueous- methanolic HEPES buffer medium at pH 7.4. In titration experiments, 30 μL solution of 1×10^{-3} M **HL** (1×10^{-5} M) was taken in a quartz optical cell of 1.0 cm optical path length, and the ion stock solutions were added gradually to maintain a concentration of 1×10^{-5} M. Spectroscopic studies of the chemosensor (**HL**) in the presence of different anions were performed in HEPES buffer at pH = 7.4. In competitive assay experiments, the test samples were prepared by interacting appropriate amounts of the cations stock in 3 mL of **HL** solution (1×10^{-5} M).

2.7. Binding stoichiometry (Job's plot)

Job's continuation method was employed to find out the binding stoichiometry of the chemosensor with that of Zn^{2+} ions using both absorption and emission spectroscopy. In case of Cu^{2+} , we have determined the binding stoichiometry using absorption spectroscopy. At a given temperature (25 °C), the absorbance and fluorescence were noted for solutions where the concentrations of both chemosensor and Zn^{2+} ions were varied but the sum of their concentrations was kept constant at 1×10^{-5} M. Relative change in absorbance ($\Delta A/A_0$) and fluorescence ($\Delta I/I_0$) were plotted as a function of mole fraction of chemosensor. The break point in the resulting plot corresponds to the mole fraction of chemosensor in Zn^{2+} complex. From the break point the stoichiometry were estimated. The results reported are average of at least three experiments.

2.8. Cell line culture

Triple negative human breast cancer cell line MDA-MB-468 was obtained from National Center for Cell Science (NCCS) Pune, India. The cells were grown in DMEM with 10% FBS (Fetal Bovine Serum), penicillin/streptomycin (100units/mL) at 37 °C and 5%CO₂. All the treatments were conducted at 37 °C and at a cell density allowing exponential growth.

2.9. Cell Imaging

The MDA-MB-468 cells were grown in coverslips for 24hrs. After that the cells were either mock-treated or treated with 5 μ M of ligand and 10 μ M Zn^{2+} salt in the presence or absence of 10 μ M of Cu^{2+} salt and for 24hrs at 37 °C. The cells were washed with $1 \times$ PBS. Then they were mounted on a glass slide and observed under fluorescence microscope (Leica).

2.10. Computational method

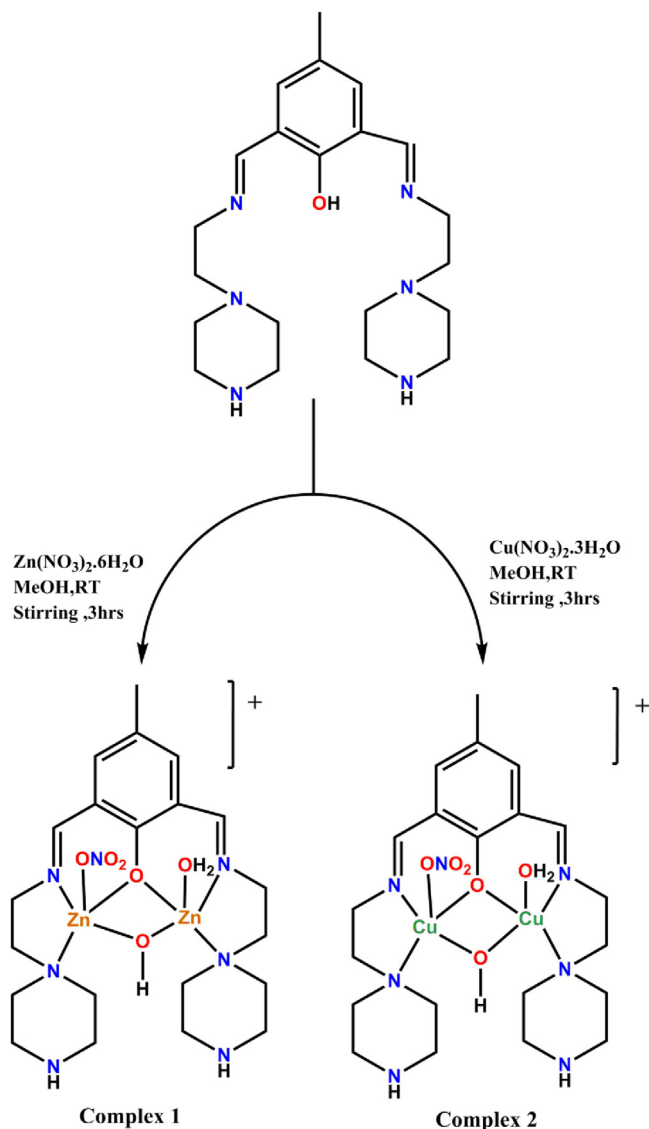
All computations were performed using the GAUSSIAN09 (G09) [19] software package. For optimization we used the density functional theory method at the B3LYP level [20,21] and the standard 6–31 + G(d) basis set for C, H, N and O atoms [22,23] and the lanL2DZ effective potential (ECP) set of Hay and Wadt [24–26] for zinc and copper atoms have been chosen for optimization.

TDDFT calculation was performed with the optimized geometry to ensure only positive eigen values. Time-dependent density functional theory (TDDFT) [27–29] was performed using conductor-like polarizable continuum model (CPCM)[30–32] and the same B3LYP level and basis sets in methanolic solvent system. GAUSSSUM [33] was used to calculate the fractional contributions of various groups to each molecular orbital.

3. Results and discussion

3.1. Synthesis and characterization

2-hydroxy-5-methylisophthalaldehyde (HMP) has been synthesized according to a standard procedure [18]. The Schiff base ligand (HL) was synthesized in a one pot reaction: 2 equiv. of 1-(2-aminoethyl)piperazine was added to a methanolic solution of 1 equiv. of 2-hydroxy-5-methylisophthalaldehyde (HMP) under ambient condition and then the solution was heated for 4 h (Scheme S1). The product was collected as a semi-solid in good yield and used without further purification. It was thoroughly characterized using different spectroscopic methods (UV–Vis, FT-IR, ¹H NMR, ¹³C NMR) and purity was verified with elemental analysis. In the ESI-mass spectrum of the chemosensor the base peak was found at 387.18 corresponding to $[HL + 1]^+$ (Fig. S1). In the FT-IR spectrum of HL a broad band at around 3374 cm^{-1} indicate the



Scheme 1. Route of synthesis of complexes 1 and 2.

presence of phenolic OH group and the band at 1634 cm^{-1} is attributed to the C=N (for azomethine) stretching frequency (Fig. S2).

HL react with both $Zn(NO_3)_2 \cdot 6H_2O$ and $Cu(NO_3)_2 \cdot 3H_2O$ in 1:2 ratio to produce complex 1 and 2 respectively (Scheme 1). The solid mass of both complexes are isolated in high yield. Both are characterized by elemental and ESI-MS analyses. The experimental and simulated mass spectra of complex 1 and 2 were well matched with each other at m/z value 638.00 and 634.14 corresponding to molecular ion peak of $[Zn_2(L)(OH_2)(OLi)(NO_3)]^+$ and $[Cu_2(L)(OH_2)(OLi)(NO_3)]^+$ respectively (Fig. S3–S4, ESI). The obtained data were strongly supported by previously reported crystallographic result [34]. The data suggested that in both complexes metal centers (Zn(II) or Cu(II)) are bridged by phenoxido oxygen atom of the deprotonated chemosensor (L⁻) and hydroxido ion. They are also coordinated with imine nitrogen and amine donor from the piperazine ring. One metal center coordinated with oxygen atom of nitrate ion and water molecule is attached with another metal center giving rise to a distorted square pyramidal geometry around the metal center. In FT-IR spectrum of complex 1 the characteristics stretching frequencies appeared at 1632 cm^{-1} ($\nu(C=N)$), 781 cm^{-1} ($\nu(C-H)$) and 1321 cm^{-1} ($\nu(NO_3^-)$, asymmetric stretch), respectively. Similarly, in case of complex 2 the characteristics stretching frequencies appeared at 1627 cm^{-1} ($\nu(C=N)$), 750 cm^{-1} ($\nu(C-H)$) and 1332

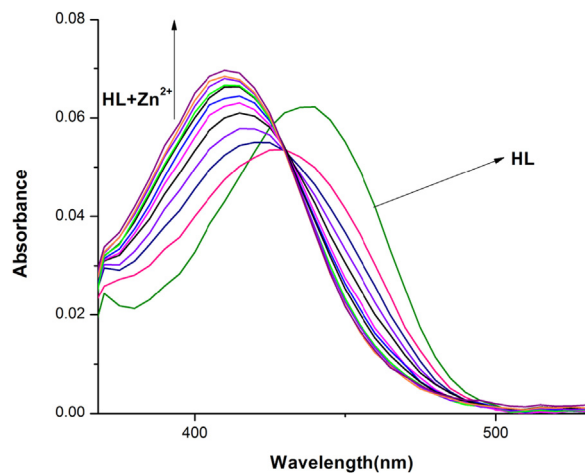


Fig. 1. Absorption titration of HL (10 μM) with gradual addition of Zn^{2+} , 0–20 μM in HEPES buffer at pH 7.4.

cm^{-1} ($\nu(\text{NO}_3^-)$, asymmetric stretch)) respectively. It is important to mention that although both the complexes are previously reported by Das et al. [34], chemosensing behavior of HL has been explored by us.

3.2. Absorption spectral studies

The UV–vis spectrum of the chemosensor HL was first investigated in HEPES buffer at pH 7.4 resulting well-defined bands at 230 nm and 440 nm respectively (Fig. S5). These peaks are attributed to intramolecular $\pi \rightarrow \pi^*$ and $n \rightarrow \pi^*$ type of transitions. In presence of Zn^{2+} and Cu^{2+} there are significant changes in the spectra of HL which clearly indicate strong interaction between them. The experiments were performed in the same solvent system. Initially it has been observed that upon 2 μM addition of Zn^{2+} ions to 10 μM HL solution a rapid hypsochromic shift of the original peak of HL was observed. Upon gradual increase of Zn^{2+} ions concentration (0–20 μM), the peak at 440 nm disappears with concomitant appearance of a new peak at around 410 nm (Fig. 1). No further change was observed above 2.0 equivalent of Zn^{2+} . During such process an isobestic point was observed at 430 nm (Fig. 1). In case of Cu^{2+} ion similar type of changes has been observed. Upon gradual addition of (0–20 μM) Cu^{2+} ion at a fixed concentration of HL (10 μM) the intensity of the original peaks at 440 nm rapidly decreases and finally disappear with subsequent appearance of a new peak at around 405 nm (Fig. 2). Again saturation in the absorption intensity of peak at 405 nm observed upon addition of

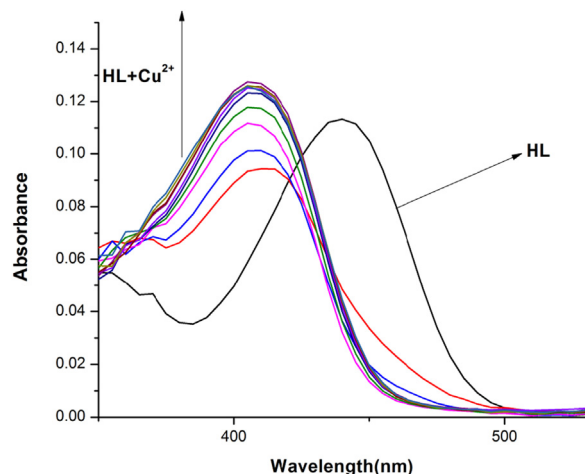


Fig. 2. Absorption titration of HL (10 μM) with gradual addition of Cu^{2+} , 0–20 μM in HEPES buffer at pH 7.4.

2.0 equivalent of Cu^{2+} solution. Both the spectra clearly indicate 2:1 binding stoichiometry of the respective ions with the chemosensor which has been further established with the aid of Job's plot analysis (Fig. 3 and Fig. S6). These results have been further supported by DFT and mass spectral analysis. Notably, the addition of the cations (Cd^{2+} , Hg^{2+} , Pb^{2+} , Al^{3+} , Ag^+ , Mn^{2+} , Fe^{3+} , Co^{2+} , Ni^{2+} , Na^+ , K^+ , Mg^{2+} and Ca^{2+}) and anions ($\text{S}_2\text{O}_3^{2-}$, S^{2-} , SO_3^{2-} , HSO_4^- , SO_4^{2-} , SCN^- , N^{3-} , OCN^- , AsO_4^{3-} , PO_4^{3-} , ClO_4^- , CH_3COO^- , Cl^- , NO_3^- , $\text{P}_2\text{O}_7^{4-}$, PF_6^- and F^-) did not change the initial absorption spectrum of the chemosensor appreciably.

3.3. NMR studies

At first ^1H NMR of the chemosensor (HL) has been performed in d_6 -DMSO solvent. The spectrum clearly suggests presence of a c_2 symmetry in the molecule. Imine (H-C=N) protons appear as a sharp peak at 8.50 ppm. Aromatic protons appear at 7.41 ppm. Aliphatic protons for aminoethyl moiety appear at 3.60 ppm and 2.42 ppm, respectively, whereas aliphatic protons of piperazine ring system appear at 2.58 ppm and 2.27 ppm, respectively and methyl protons appear at 2.17 ppm (Fig. S7).

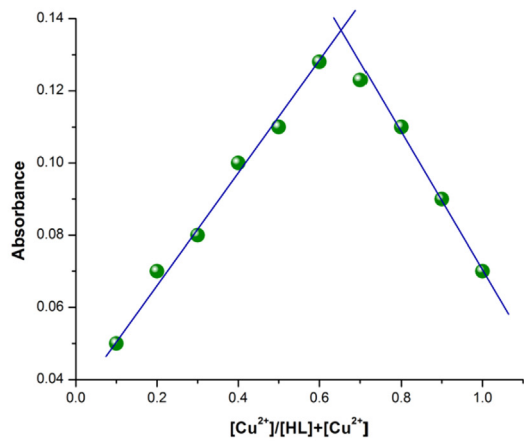
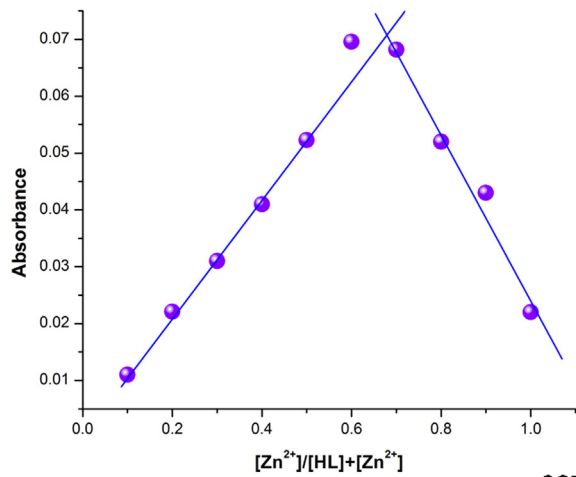
To better understand of complex formation with Zn^{2+} ion, we have performed ^1H NMR titration in certain stoichiometric ratio of HL and Zn^{2+} ion in d_6 -DMSO solvent. Interestingly, in presence of Zn^{2+} ion all spectra exhibit broadening and splitting of imine, aromatic and aliphatic protons, respectively. Imine (H-C=N) proton shifted to down-field when 1.0 equivalent of Zn^{2+} is added and it appears at $\delta = 8.55$ ppm. Finally, it shifted to $\delta = 8.57$ ppm when 2.0 equivalent Zn^{2+} is added. Similarly, aromatic protons appear at 7.44 ppm and 7.46 ppm after addition of 1.0 and 2.0 equivalent of Zn^{2+} ion, respectively (Fig. 4).

In ^{13}C NMR (d_6 -DMSO, 75 MHz) spectrum of HL, signals for $-\text{CH}_3$ and $-\text{CH}_2$ carbon atoms appeared at 20.35 and in the range 45.89–59.39, respectively. Aromatic carbon atoms appeared at 121.44, 126.48, 132.68 and 161.75 ppm, respectively. The imine carbon atom appeared at 160.76 ppm (Fig. S8). In case of complex 1, signals for $-\text{CH}_3$ and $-\text{CH}_2$ carbon atoms appeared at 19.94 and in the range 49.07–58.51, respectively. Aromatic carbon atoms appeared in the range of 121.37–168.15 ppm. Whereas, the imine carbon atom appeared at 166.62 ppm (Fig. S9).

3.4. Fluorescence properties

Fluorescence experiment also performed in HEPES buffer (pH = 7.4) at ambient conditions. Upon excitation at 440 nm, HL exhibits weak fluorescence at 510 nm. This is probably due to PET (Photoinduced Electron Transfer) process (Fig. 5) [see ref. 1S, 3S, 5S, 13S, Chart S1]. The delocalization of available lone pair on the imine nitrogen atom to the HMP moiety leads to the quenching of the fluorescence. Upon addition of Zn^{2+} ions to HL an enormous fluorescence enhancement is observed and the emission band has been blue shifted to 480 nm. The enhancement in intensity of HL gets saturated upon addition of two equiv. of Zn^{2+} ions. There is an approximately 16-fold enhancement in the emission intensity of HL in the presence of two equiv. of Zn^{2+} ions. This observation clearly suggests formation of a 1:2 complex. The chelation of Zn^{2+} with O, N donors of HL increases the rigidity of the molecular assembly (CHEF effect) via inhibition of free rotation of HL around the HC=N bond. Again PET process is eliminated by arresting the lone pair of electrons present in the imine nitrogen. These two effects are jointly responsible for the observed fluorescence enhancement.

In the inset we have shown a plot of fluorescence intensities at 480 nm (I_{480}) against different concentration of zinc ion (Fig. 6). In the plot the value of (I_{480}) increases with the increasing concentration of Zn^{2+} and a saturation was observed at 2.0 equivalent of added Zn^{2+} which proved 1:2 binding between the probe and Zn^{2+} . The sigmoid



297

Fig. 3. 2:1 binding stoichiometry has shown by Job's plot of complexes 1 and 2, respectively. Symbols and solid lines represent the experimental and simulated profiles, respectively.

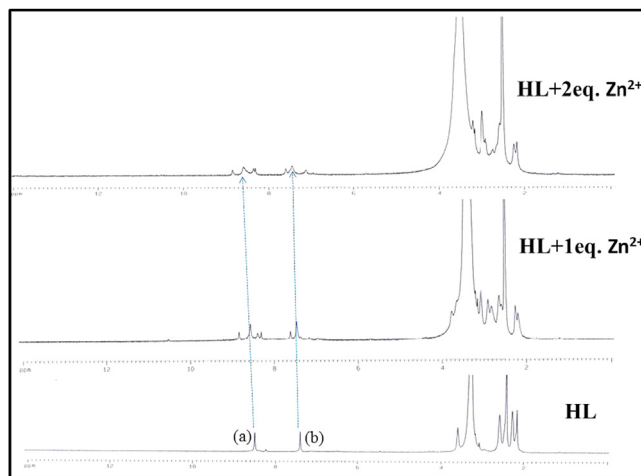


Fig. 4. ¹H NMR titration of the free ligand (HL) and with the addition of 1.0 and 2.0 equivalent of Zn²⁺ in DMSO-d₆ recorded on a 300 MHz Bruker NMR spectrometer.

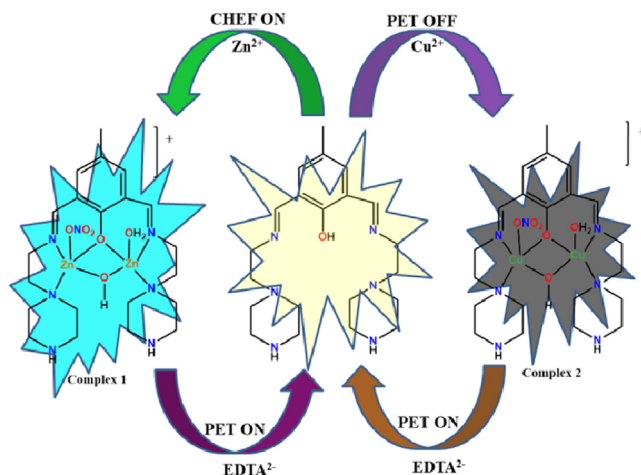


Fig. 5. Pictorial representation of 'PET' and 'CHEF' process.

nature of curve reflects strong interaction between the organic probe and Zn²⁺ ion.

On the other hand under identical condition when Cu²⁺ ions

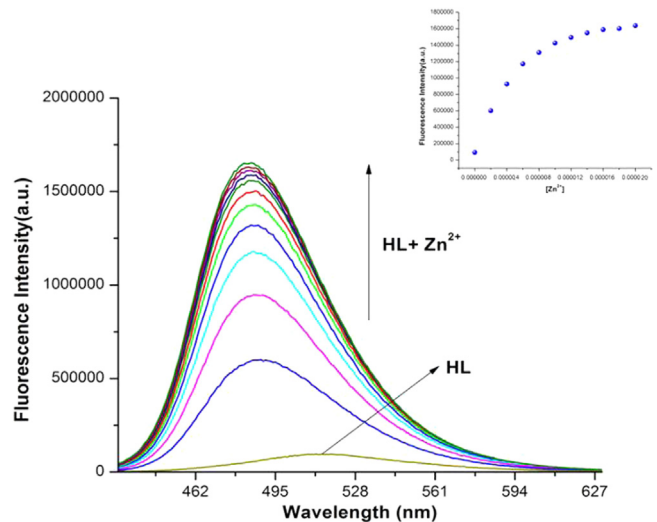


Fig. 6. Fluorescence titration of HL (10 μM) in HEPES buffer at pH = 7.4 by gradual addition of Zn²⁺ (0–20 μM) with λ_{em} = 480 nm (1/1 slit). Inset: non-linear plot of fluorescence intensity vs. concentration of Zn²⁺ ion.

(0–20 μM) were added to the chemosensor solution the fluorescence emission at ~ 510 nm is almost completely quenched (Fig. 7). Such type of (~ 174 fold) of dramatic quenching in the fluorescence intensity of the chemosensor in presence of Cu²⁺ ion suggests formation of Cu²⁺ probe complex, thus chelation enhanced quenching (CHEQ) results metal to ligand charge transfer (MLCT) between HL and paramagnetic Cu²⁺ ions [35]. Again plot of Fluorescence intensities at 510 nm (I₅₁₀) vs. concentration of copper ion has been presented in Fig. 7 (inset). The sensing character of the probe (I₅₁₀) decreases with the increasing concentration of Cu²⁺ and the pattern was linear in regarding the concentration of Cu²⁺ in the range of 0–20 μM (inset), suggesting a 1:2 stoichiometric ratio between HL and Cu²⁺.

Binding ability of the chemosensor towards Zn²⁺ and Cu²⁺ ions has been established using Benesi-Hildebrand equation (Eq. (1)) involving fluorescence titration curve [36].

$$\frac{F_{max} - F_0}{F_x - F_0} = 1 + \left(\frac{1}{K[C]^n} \right) \quad (1)$$

where, F_{max}, F₀ and F_x are fluorescence intensities of HL in the presence of metal ions at saturation, free HL and any intermediate metal ions concentration, respectively. K is the binding constant of the complexes.

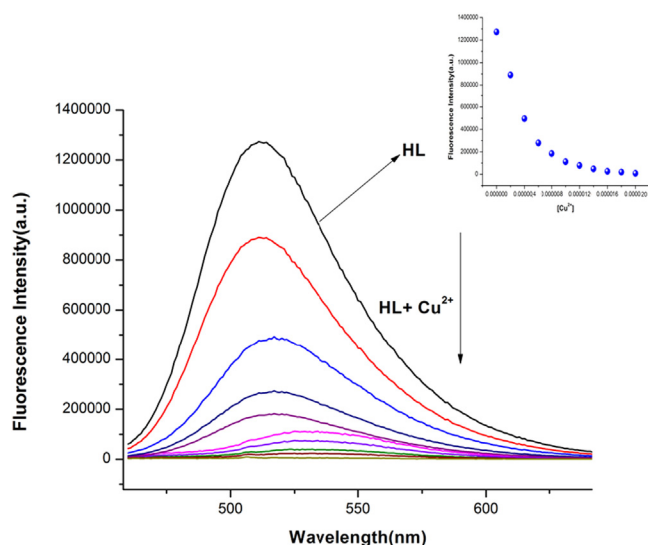


Fig. 7. Fluorescence titration of HL (10 μM) in HEPES buffer at pH = 7.4 by gradual addition of Cu^{2+} (0–20 μM) with $\lambda_{\text{em}} = 510 \text{ nm}$ (1/1 slit). Inset: non-linear plot of fluorescence intensity vs. concentration of Cu^{2+} ion.

Concentrations of Zn^{2+} and Cu^{2+} ions are represented by C and here $n = 1$. Then binding constant (K) of the complexes has been determined using the relation, $K = 1/\text{slope}$. A plot of $\frac{F_{\text{max}} - F_0}{F_x - F_0}$ vs $\left(\frac{1}{[\text{C}]^1}\right)$ provides the binding constant values as $7.14 \times 10^4 \text{ M}^{-1}$ and $2.18 \times 10^5 \text{ M}^{-1}$ for Zn^{2+} and Cu^{2+} complexes, respectively (Fig. S10 and S11, respectively).

To check high selectivity toward the Zn^{2+} and Cu^{2+} over the other competitive species fluorescence titration experiment also performed in presence of different alkali metals (Na^+ and K^+), alkaline-earth metals (Mg^{2+} and Ca^{2+}), and various transition-metal (Mn^{2+} , Fe^{3+} , Co^{2+} , Ni^{2+} , Cd^{2+} and Hg^{2+}) ions (Fig. S12). It is an important parameter to assess the performance of sensor HL. Therefore, the competition assay were performed in the presence of $\text{Zn}^{2+}/\text{Cu}^{2+}$ (2.0 equiv.) mixed with other metal ions (2.0 equiv.) in organo - aqueous media. It has been noted that distinct fluorescence enhancement observed for the mixtures of Zn^{2+} with other metal ions except for Cu^{2+} . The addition of Cu^{2+} to HL solution in the presence of Zn^{2+} leads to large fluorescence quenching. Here, Cu^{2+} ion detection by HL is not influenced by the presence of other competitive metal ions (Fig. 8). Both the competition assay experiments clearly demonstrate high fluorescent recognition of HL for $\text{Zn}^{2+}/\text{Cu}^{2+}$ ions over other cations. Binding constant values also

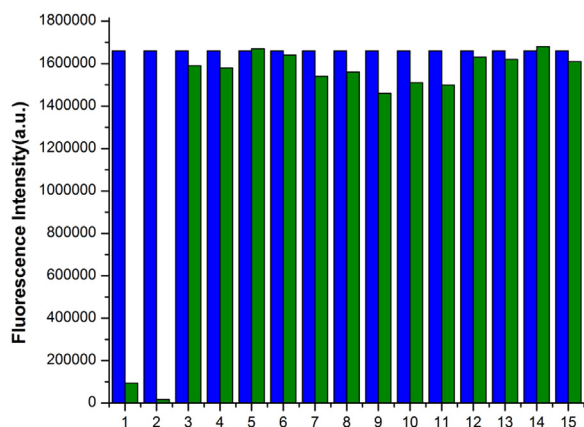


Fig. 8. Relative fluorescence intensity profile of $[\text{HL-Zn}^{2+}]$ system in the presence of different cations in HEPES buffer at pH 7.4. 1 = only HL and (2–15) = HL (10 μM) + Zn^{2+} (20 μM) + M^{n+} (20 μM), where $\text{M}^{n+} = (2-\text{Cu}^{2+}, 3-\text{Co}^{2+}, 4-\text{Cr}^{3+}, 5-\text{Fe}^{3+}, 6-\text{Hg}^{2+}, 7-\text{K}^+, 8-\text{Mn}^{2+}, 9-\text{Na}^+, 10-\text{Ni}^{2+}, 11-\text{Mg}^{2+}, 12-\text{Pb}^{2+}, 13-\text{Ca}^{2+}, 14-\text{Fe}^{2+}, 15-\text{Cd}^{2+})$.

support the above explanation. Upon addition of different common anions like $\text{S}_2\text{O}_3^{2-}$, S^{2-} , SO_3^{2-} , HSO_4^- , SO_4^{2-} , SCN^- , N_3^- , OCN^- , AsO_4^- , PO_4^{3-} , ClO_4^- , CH_3COO^- , Cl^- , NO_3^- , $\text{P}_2\text{O}_7^{4-}$, PF_6^- and F^- in HEPES buffer at pH 7.4 (Fig. S13) chemosensor showed no significant fluorescence enhancement.

Interestingly chemosensor HL also act as a colorimetric probe for the detection of Zn^{2+} and Cu^{2+} ion. In presence Zn^{2+} ions HL exhibits greenish blue coloration whereas it is almost colorless in presence of Cu^{2+} ion. Thus, the chemosensor can be used for a selective colorimetric detection of Cu^{2+} and Zn^{2+} ions over other competing metal ions both in environmental and biological fields (Fig. 9).

Reversibility and regeneration are the two important aspects for real time application of the chemosensor. The experiment was performed in presence of sodium salt of ethylene diamine tetraacetic acid (Na_2EDTA) solution. In case of HL- Zn^{2+} complex solution after addition of two equivalent of Na_2EDTA color changes from green to light yellow with obvious decrease in fluorescence intensity. While, the addition of two equivalent EDTA to HL- Cu^{2+} complex solution an enhancement of emission intensity and finally a light yellow color indicates the regeneration of the free HL (Fig. S14).

Limit of detection (LOD) of the chemosensor towards Cu^{2+} and Zn^{2+} ions are calculated using 3σ method [37]. The detection limit of the chemosensor for both the ions is $1.05 \times 10^{-9} \text{ M}$ and $3.53 \times 10^{-9} \text{ M}$, respectively. In case of Cu^{2+} ion the LOD value is lower than the WHO recommended level for Cu^{2+} (2.0 mg/L), [38,39] which clearly suggests that this chemosensor can quantitatively detect of Cu^{2+} in HEPES buffer (pH = 7.4) media.

The effect of pH on the fluorescence response of the chemosensor HL and HL- Zn^{2+} and HL- Cu^{2+} complexes are examined over a wide range. In case of free HL fluorescence intensity remain unchanged in the pH range 2–6 after that from pH 6–11 a slight enhancement in fluorescence intensity has been observed (Fig. 10). In presence of Zn^{2+} ions change of fluorescence initially in pH range 2–6 fluorescence is almost identical to that of the free ligand. This suggests no complex formation at acidic condition. Upon gradual increase of pH 7–8 a sudden enhancement in fluorescence intensity indicates formation of Zn-complex. Further increase of pH value from 8–11 fluorescence intensity remains unchanged. When Cu^{2+} is added, the resultant fluorescence intensity is less compare to free HL in pH 2-6. In pH 6–11 the decrease in fluorescence intensity is more pronounced. The result signifies that the complex formation takes place above pH 6. The pH experiment suggests that HL can act as a selective fluorescent probe to recognize both Zn^{2+} and Cu^{2+} ion in presence of other metal ions in biological system under physiological condition2

3.5. Life time and quantum yield measurements

Lifetime experiment for the chemosensor (HL) and complex 1 were studied at 298 K in HEPES buffer (pH = 7.4). The average fluorescence decay life time has been measured of the chemosensor and complex 1 using the given formula ($\tau_f = a_1\tau_1 + a_2\tau_2$, where a_1 and a_2 are relative amplitude of decay process). The average fluorescence lifetime of the chemosensor and complex 1 are 3.12 ns and 4.96 ns, respectively (Fig. 11, Table S1).

Fluorescence quantum yield (Φ) has been calculated by using the following formula:

$$\Phi_{\text{sample}} = \left\{ \frac{(\text{OD}_{\text{standard}} \times A_{\text{sample}} \times \eta_{\text{sample}}^2)}{(\text{OD}_{\text{sample}} \times A_{\text{standard}} \times \eta_{\text{standard}}^2)} \right\} \times \Phi_{\text{standard}}$$

where, A is the area under the emission spectral curve, OD is the optical density of the compound at the excitation wavelength and η is the refractive index of the solvent. Here the value of Φ_{standard} is taken as 0.52 (for Quinine Sulfate).

The values of Φ for HL and HL- Zn^{2+} complexes are found to be 0.036 and 0.39, respectively (Table S1). The fluorescence quantum



Fig. 9. Visual color changes of chemo sensor (**HL**) ($10\ \mu\text{M}$) under presence of different metal ions (2.0 equivalent) in HEPES buffer ($\text{pH } 7.4$). The images in below row and above row were taken under visible light and UV light respectively. Where 1 = only **HL**, 2, 3, 4, 5, 6, 7, 8, 9, 10, 11, 12, 13, 14 and 15 = **HL** + Zn^{2+} , Cu^{2+} , Cd^{2+} , Pb^{2+} , Hg^{2+} , Mn^{2+} , Fe^{3+} , Co^{2+} , Ni^{2+} , K^+ , Na^+ , Mg^{2+} , Ca^{2+} and Al^{3+} respectively.

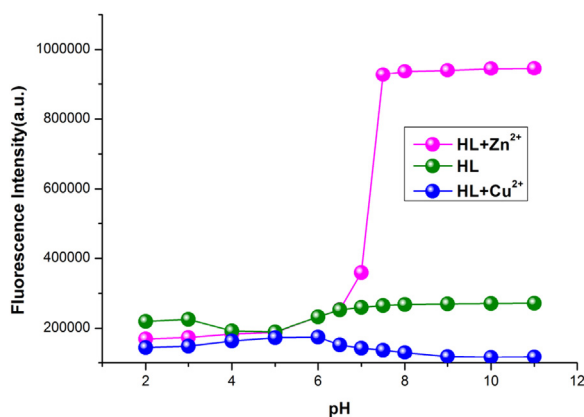


Fig. 10. Fluorescence intensity of **HL** ($10\ \mu\text{M}$) in the absence and presence of Zn^{2+} and Cu^{2+} ions ($20\ \mu\text{M}$) at various pH values in HEPES buffer.

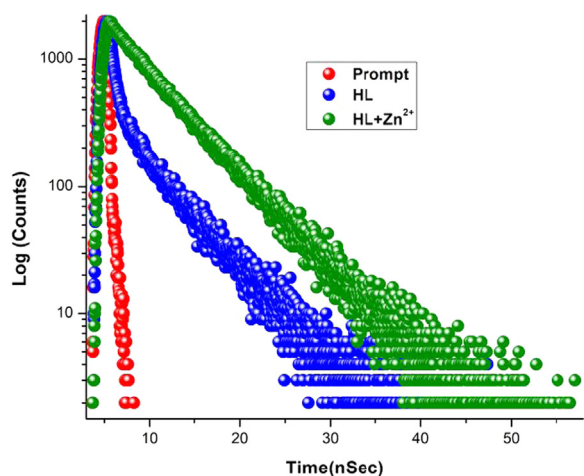


Fig. 11. Time-resolved fluorescence decay curves (logarithm of normalized intensity vs time in ns) of **HL** in the absence (●) and presence (●) of Zn^{2+} ion, (●) indicates decay curve for the scattered.

yield (Φ) of **HL**- Zn^{2+} complex is 10.83 fold greater than free **HL**.

3.6. Cell imaging

A cell imaging experiment is performed with MDA-MB 468 cells in order to demonstrate the efficacy of the ligand and Zn^{2+} salt to serve as a luminescent bio-probe. The MDA-MB 468 cells are fluorescently labeled by the ligand and Zn^{2+} salt and immediately after the cells emit strong green fluorescent signal under the microscope. Thus the ligand

and Zn^{2+} salt are well permeable to the cells. Additionally, no apparent morphological anomalies of the cells were observed. Perhaps the ligand and Zn^{2+} salt have no immediate toxic effect on the cells at the concentration we used. The mock-treated cells exhibited no fluorescence. But immediately after the addition of Cu^{2+} salt to the labeled cells, the cells no longer emit any signal due to the quenching of the fluorescent signal by the Cu^{2+} salt (Fig. 12).

3.7. DFT study

DFT and TDDFT studies were performed to further support structural and electronic parameters of complexes. For both complexes bond distances and bond angles of the optimized structures are well matched with that of previously reported analogous complexes [34]. Furthermore TDDFT study was performed to understand nature, origin and contribution of M.O.s in electronic transitions. It also gives idea of quantity of energy associated with every individual transition. When individual M.O. is concerned the contribution from both ligand and metal center has been computed. So, DFT and TDDFT analysis plays important role to support and understand structural and electronic parameters of complexes.

Here, geometry optimization of **HL**, $[\text{Zn}_2(\text{L})(\text{OH})_2(\text{OH})(\text{NO}_3)]^+$ and $[\text{Cu}_2(\text{L})(\text{OH})_2(\text{OH})(\text{NO}_3)]^+$ has been performed using DFT/B3LYP method. The energy minimized structure of complexes 1 and 2 are shown in Fig S15 and S16, respectively. Some selected bond distances and bond angles of both complexes are listed in Table S2. Theoretical calculations showed that electron density in LUMO of **HL** is mainly distributed over the phenyl ring and imine nitrogen atoms, whereas, electron density in HOMO is mainly distributed over one of the pipyrazine moiety. In complex 1, electron density in both LUMO and HOMO are completely ligand based which follow the same trend to that of free chemosensor **HL** and contribution from metal centers is nil (Fig. S17). In case of complex 2, electron density in LUMO is distributed over the metal centers, Schiff base ligand and coligands and electron density of HOMO is again distributed mainly over one of the pipyrazine moiety (Fig. S17). Energy of some selected M.O. of **HL**, complex 1 and 2 are given in Table S3-S5. Mulliken charge distribution showed positive charge on both zinc and copper ions for complexes 1 and 2 and they are presented in Table S6.

3.8. TDDFT study

Electronic transitions in **HL**, Complex 1 and 2 are theoretically studied using TDDFT were B3LYP/CPCM method is used with same basis sets in water. Calculated electronic transitions are given in Table S7. Theoretical calculations show that in case of **HL** intense absorption bands appear at 455 and 449 nm respectively for $n\text{-}\pi^*$ transition. Major transitions are HOMO-4 \rightarrow LUMO (54%), and HOMO-4 \rightarrow LUMO+1 (43%) respectively. For complex 1 major peaks appear at 357, 331, 327 nm respectively and

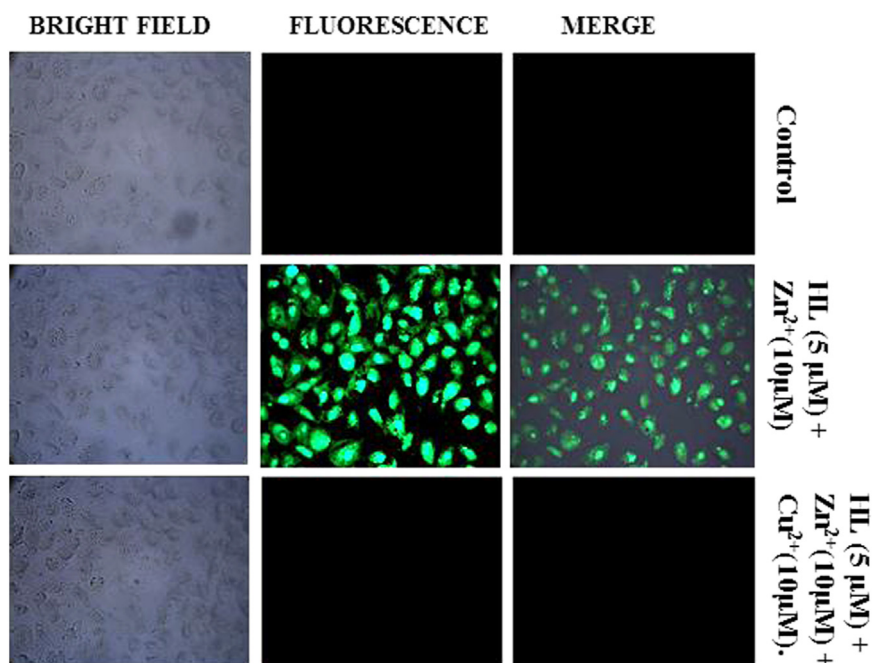


Fig. 12. Bright field, fluorescence and merged microscopic images of untreated MDA-MB-468 (Control), cells treated with HL (5 μM) + Zn^{2+} (10 μM) and with HL (5 μM) + Zn^{2+} (10 μM) + Cu^{2+} (10 μM).

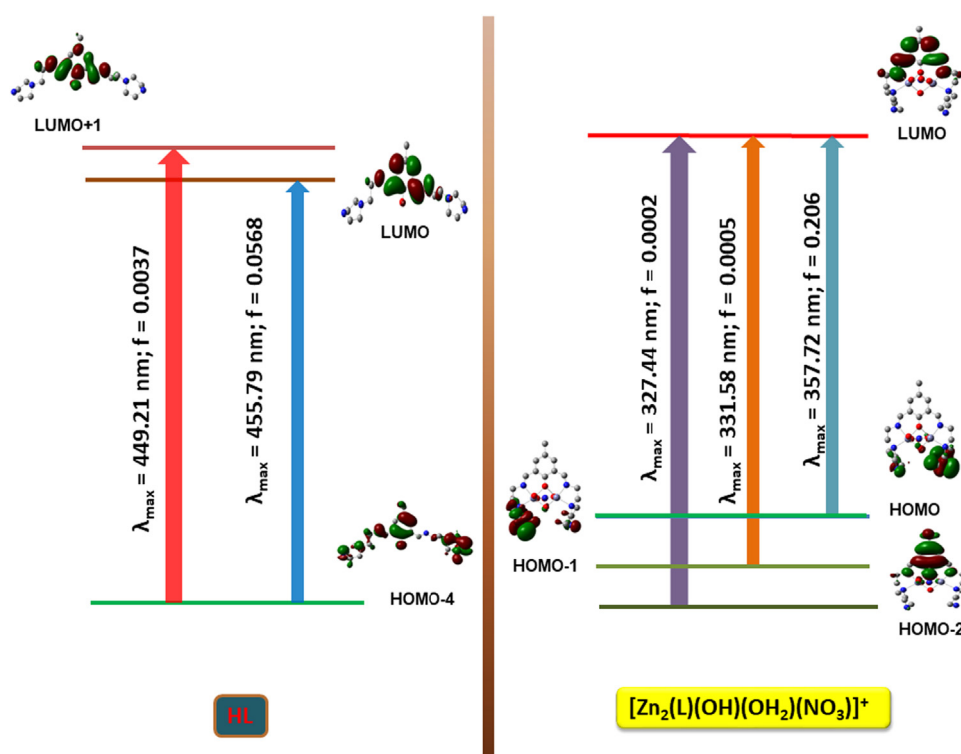


Fig. 13. Pictorial representation of vertical transition of chemosensor (HL) and complex 1.

main transitions are HOMO \rightarrow LUMO (97%), HOMO-1 \rightarrow LUMO (89%) and HOMO-2 \rightarrow LUMO (91%), respectively (Fig. 13). For complex 2 the intense absorption bands around 396 and 391 nm corresponding to HOMO \rightarrow LUMO + 1 (94%) and HOMO-3 \rightarrow LUMO (44%) transitions, respectively (Fig. 14). The spectra of electronic transitions obtained from computation for the chemosensor (HL), complexes 1 and 2 are found to be comparable with that of experimental data.

Theoretical calculations of the emission spectra of both ligand (HL) and complex 1 are performed by optimizing the triplet state (T1), using

same basis set. The emission wavelength obtained from the computation is very much comparable with that of experimental data. All the relevant data are given in Table S8. The emission band of the chemosensor (HL) at 510 nm was theoretically obtained at 520.65 nm with major key transitions, HOMO-3 (β) \rightarrow LUMO + 2(β) (82%) and HOMO-2(α) \rightarrow LUMO + 1(α) (18%), respectively. Whereas for the complex 1, the emission band at 480 nm was theoretically obtained at 468.62 with major key transitions, HOMO(α) \rightarrow LUMO + 3(α) (10%), HOMO-9(β) \rightarrow LUMO(β) (15%) and HOMO-7(β) \rightarrow LUMO(β), (45%) respectively.

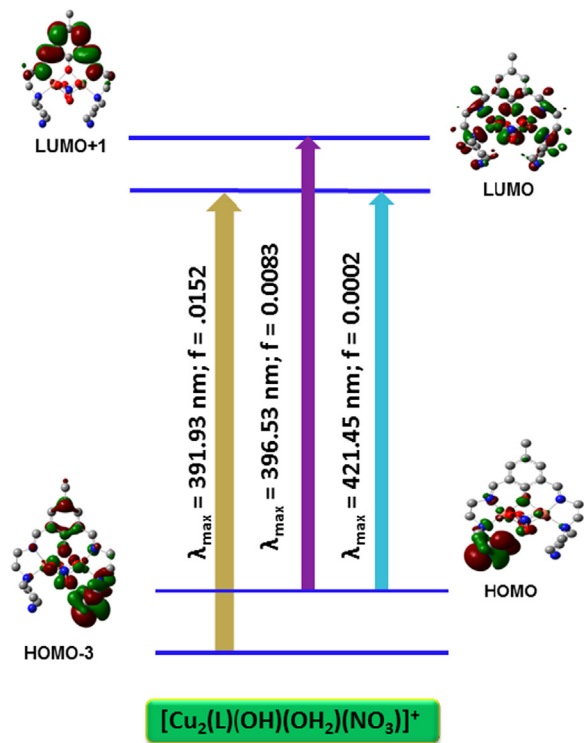


Fig. 14. Pictorial representation of vertical transition of complex 2.

4. Summary

In summary, we have successfully developed a dual Schiff base fluorescent and colorimetric chemosensor **HL** as a promising analytical tool for the detection of Zn^{2+} and Cu^{2+} ions in mixed organo – aqueous (1:9) solution. In this work both Zn^{2+} and Cu^{2+} are detected in nano molar scale and the LOD values are $1.059 \times 10^{-9}(\text{M})$ and $3.53 \times 10^{-9}(\text{M})$ respectively. **HL** exhibit around 16 times increment in fluorescence intensity in presence of Zn^{2+} and ~ 174 times decrease in fluorescence intensity in presence of Cu^{2+} . **HL** form 1:2 complex with both metal ions which have been established by fluorescence measurements, ESI-MS analysis and DFT-Calculations. The values of binding constant are $7.14 \times 10^4 \text{M}^{-1}$ and $2.18 \times 10^5 \text{M}^{-1}$ for Zn^{2+} and Cu^{2+} complexes, respectively. In fluorescence competition assay experiment Cu^{2+} replace Zn^{2+} in presence of **HL**. Moreover, the sensors can be completely regenerated from L-Zn and L-Cu complexes by addition of Na_2EDTA solution. A rapid change in fluorescence intensity of **HL** within pH range 6–8 against Zn^{2+} and Cu^{2+} ions establish its application in real-time quantitative detection of Zn^{2+} and Cu^{2+} ions in water samples and biological systems.

Acknowledgments

A. S. gratefully acknowledges the financial support of this work by the The Department of Science & Technology (DST), India (Sanction No. SB/FT/CS-102/2014, dated- 18.07.2015).

Conflicts of interest

There are no conflicts of interest to declare.

Appendix A. Supporting information

Supplementary data associated with this article can be found in the online version at <https://doi.org/10.1016/j.jlumin.2018.08.080>.

References

- [1] (a) S. Mizukami, T. Nagano, Y. Urano, A. Odani, K.A. Kikuchi, *J. Am. Chem. Soc.* 124 (2002) 3920–3925; (b) R.M. Duke, E.B. Veale, F.M. Pfeffer, P.E. Kruger, T. Gunnlaugsson, *Chem. Soc. Rev.* 39 (2010) 3936–3953; (c) J. Shao, H. Lin, H.K. Lin, *Talanta* 75 (2008) 1015–1020; (d) B. Kuswandi, W. Verboom, D.N. Reinhoudt, *Sensors* 6 (2006) 978–1017; (e) K. Ghosh, S. Adhikari, *Tetrahedron Lett.* 47 (2006) 8165–8169; (f) A.K. Jain, J. Raisoni, R. Kumar, S. Jain, *Int. J. Environ. Anal. Chem.* 87 (2007) 553–563; (g) G.A.E. Mostafa, *Int. J. Environ. Anal. Chem.* 88 (2008) 435–446; (h) M.T. Oms, P.A.C. Jongejan, A.C. Veltkamp, G.P. Wyers, J. Slanina, *Int. J. Environ. Anal. Chem.* 62 (1996) 207–218.
- [2] A.P.S. Gonzales, M.A. Firmino, C.S. Nomura, F.R.P. Rocha, P.V. Oliveira, I. Gaubeur, *Anal. Chim. Acta* 636 (2009) 198.
- [3] J.P. Lafleur, R. Lam, H.M. Chan, E.D. Salin, *J. Anal. At. Spectrom.* 20 (2005) 1315.
- [4] Z. Zhu, Z. Liu, H. Zheng, S. Hu, *J. Anal. At. Spectrom.* 25 (2010) 697.
- [5] H.N. Kim, W.X. Ren, J.S. Kim, J. Yoon, *Chem. Soc. Rev.* 41 (2012) 3210.
- [6] Z.X. Wang, Y.-X. Guo, S.-N. Ding, *Microchim. Acta* 182 (2015) 2223.
- [7] P. Sianglam, S. Kulchat, T. Tuntulani, W. Ngontae, *Spectrochim. Acta, Part A* 183 (2017) 408.
- [8] S. Wang, Z. Chen, L. Chen, R. Liu, L. Chen, *Analyst* 138 (2013) 2080–2084.
- [9] C. Li, Y. Zhou, Y. Li, X. Konga, C. Zoua, C. Weng, *Anal. Chim. Acta* 774 (2013) 79–84.
- [10] S. Kim, J. Kim, N.H. Lee, H.H. Jang, M.S. Han, *Chem. Commun.* 47 (2011) 10299–10301.
- [11] H. Zhou, J. Wang, Y. Chen, W. Xi, Z. Zheng, D. Xu, Y. Cao, G. Liu, W. Zhu, J. Wu, Y. Tian, *Dyes Pigments* 98 (2013) 1–10.
- [12] K.J. Barnham, C.L. Masters, A.I. Bush, *Nat. Rev. Drug Discov.* 3 (2004) 205–214.
- [13] E. Gaggelli, H. Kozłowski, D. Valensin, G. Valensin, *Chem. Rev.* 106 (2006) 1995–2044.
- [14] P.G. Welsh, J. Lipton, C.A. Mebane, J.C.A. Marr, *Ecotoxicol. Environ. Saf.* 69 (2008) 199–208.
- [15] H. Scherz, E. Kirchoff, *Sens. Actuators B* 19 (2006) 420–433.
- [16] J.M. Flinn, D. Hunter, D.H. Linkous, A. Lanzirotti, L.N. Smith, J. Brightwell, B.F. Jones, *Physiol. Behav.* 83 (2005) 793–803.
- [17] (a) R. Azadbakht, H. Keypour, H.A. Rudbari, A.H. Md. Zaheri, S. Menati, *J. Lumin.* 132 (2012) 1860; (b) H. Song, S. Rajendiran, E. Koo, B.K. Min, S.K. Jeong, T.D. Thangadurai, S. Yoon, *J. Lumin.* 132 (2012) 3089; (c) S. Kotha, D. Goyal, S. Banerjee, A. Datta, *Analyst* 137 (2012) 2871.
- [18] R.R. Gagne, C.L. Spiro, T.J. Smith, C.A. Hamann, W.R. Thies, A.K. Schiemke, *J. Am. Chem. Soc.* 103 (1981) 4073–4081.
- [19] M.J. Frisch, G.W. Trucks, H.B. Schlegel, G.E. Scuseria, M.A. Robb, J.R. Cheeseman, G. Scalmani, V. Barone, B. Mennucci, G.A. Petersson, H. Nakatsuji, M. Caricato, X. Li, H.P. Hratchian, A.F. Izmaylov, J. Bloino, G. Zheng, J.L. Sonnenberg, M. Hada, M. Ehara, K. Toyota, R. Fukuda, Y. Hasegawa, M. Ishida, T. Nakajima, Y. Honda, O. Kitao, H. Nakai, T. Vreven, J.A. Montgomery, Jr., J.E. Peralta, F. Ogliaro, M. Bearpark, J.J. Heyd, E. Brothers, K.N. Kudin, V.N. Staroverov, R. Kobayashi, J. Normand, K. Raghavachari, A. Rendell, J.C. Burant, S.S. Iyengar, J. Tomasi, M. Cossi, N. Rega, J.M. Millam, M. Klene, J.E. Knox, J.B. Cross, V. Bakken, C. Adamo, J. Jaramillo, R. Gomperts, R.E. Stratmann, O. Yazyev, A.J. Austin, R. Cammi, C. Pomelli, J.W. Ochterski, R.L. Martin, K. Morokuma, V.G. Zakrzewski, G.A. Voth, P. Salvador, J.J. Dannenberg, S. Dapprich, A.D. Daniels, Ö. Farkas, J.B. Foresman, J.V. Ortiz, J. Cioslowski, D.J. Fox, GAUSSIAN09, Revision D.01, Gaussian Inc., Wallingford, CT, 2009.
- [20] A.D. Becke, *J. Chem. Phys.* 98 (1993) 5648–5652.
- [21] C. Lee, W. Yang, R.G. Parr, *Phys. Rev. B* 37 (1988) 785–789.
- [22] P.J. Hay, W.R. Wadt, *J. Chem. Phys.* 82 (1985) 270–283.
- [23] W.R. Wadt, P.J. Hay, *J. Chem. Phys.* 82 (1985) 284–298.
- [24] P.J. Hay, W.R. Wadt, *J. Chem. Phys.* 82 (1985) 299–310.
- [25] G.A. Petersson, A. Bennett, T.G. Tensfeldt, M.A. Al-Laham, W.A. Shirley, J. Mantzaris, *J. Chem. Phys.* 89 (1988) 2193–2218.
- [26] G.A. Petersson, M.A. Al-Laham, *J. Chem. Phys.* 94 (1991) 6081–6090.
- [27] R. Bauernschmitt, R. Ahlrichs, *Chem. Phys. Lett.* 256 (1996) 454–464.
- [28] R.E. Stratmann, G.E. Scuseria, M.J. Frisch, *J. Chem. Phys.* 109 (1998) 8218–8224.
- [29] M.E. Casida, C. Jamorski, K.C. Casidaand, D.R. Salahub, *J. Chem. Phys.* 108 (1998) 4439–4449.
- [30] V. Barone, M. Cossi, *J. Phys. Chem. A* 102 (1998) 1995–2001.
- [31] M. Cossiani, V. Barone, *J. Chem. Phys.* 115 (2001) 4708–4717.
- [32] M. Cossi, N. Rega, G. Scalmani, V. Barone, *J. Comput. Chem.* 24 (2003) 669–681.
- [33] N.M. O’Boyle, A.L. Tenderholt, K.M. Langner, *J. Comput. Chem.* 29 (2008) 839–845.
- [34] (a) A. Guha, T. Chattopadhyay, N.D. Paul, M. Mukherjee, S. Goswami, T.K. Mondal, E. Zangrandoand, D. Das, *Inorg. Chem.* 51 (2012) 8750–8759; (b) K.S. Banu, T. Chattopadhyay, A. Banerjee, S. Bhattacharya, E. Suresh, M. Nethaji, E. Zangrando, D. Das, *Inorg. Chem.* 47 (2008) 7083–7093.
- [35] M. Kumar, R. Kumar, V. Bhalla, P.R. Sharma, T. Kaur, Y. Qurishi, *Dalton Trans.* 41 (2012) 408–412.
- [36] (a) H.A. Benesi, J.H. Hildebrand, *J. Am. Chem. Soc.* 71 (1949) 2703–2707; (b) S. Banerjee, P. Brandão, A. Saha, *RSC Adv.* 6 (2016) 101924–101936.
- [37] A.B. Pradhan, S.K. Mandal, S. Banerjee, A. Mukherjee, S. Das, A.R.K. Bukhsh, A. Saha, *Polyhedron* 94 (2015) 75–82.
- [38] Y.R. Kim, H.J. Kim, J.S. Kim, H. Kim, *Adv. Mater.* 20 (2008) 4428–4432.
- [39] M.Z. Tian, M.M. Hu, J.L. Fan, X.J. Peng, J.Y. Wang, S.G. Sun, R. Zhang, *Bioorg. Med. Chem. Lett.* 23 (2013) 2916–2919.

Aza-Crown-Based Macrocyclic Probe Design for “PET-off” Multi-Cu²⁺ Responsive and “CHEF-on” Multi-Zn²⁺ Sensor: Application in Biological Cell Imaging and Theoretical Studies

Pravat Ghorai, Sougata Ghosh Chowdhury, Kunal Pal, Jayanta Mandal, Parimal Karmakar, Antonio Franconetti, Antonio Frontera, Salvador Blasco, Enrique García-España, Partha Pratim Parui, and Amrita Saha*



Cite This: <https://doi.org/10.1021/acs.inorgchem.1c03141>



Read Online

ACCESS |



Metrics & More

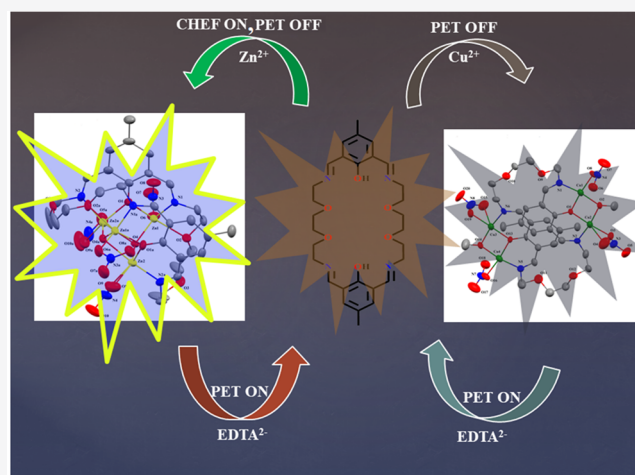


Article Recommendations



Supporting Information

ABSTRACT: The work represents a rare example of an aza-crown-based macrocyclic chemosensor, H₂DTC (H₂DTC = 1,16-dihydroxy-tetraaza-30-crown-8) for the selective detection of both Zn²⁺ and Cu²⁺ in HEPES buffer medium (pH 7.4). H₂DTC exhibits a fluorescence response for both Zn²⁺ and Cu²⁺ ions. The reversibility of the chemosensor in its binding with Zn²⁺ and Cu²⁺ ions is also examined using a Na₂EDTA solution. H₂DTC exhibits a chelation-enhanced fluorescence (CHEF) effect in the presence of Zn²⁺ ions and a quenching effect (CHEQ) in the presence of paramagnetic Cu²⁺ ions. Furthermore, the geometry and spectral properties of H₂DTC and the chemosensor bound to Zn²⁺ have been studied by DFT and TDDFT calculations. The limit of detection (LOD) values are 0.11 × 10⁻⁹ and 0.27 × 10⁻⁹ M for Cu²⁺ and Zn²⁺, respectively. The formation constants for the Zn²⁺ and Cu²⁺ complexes have been measured by pH-potentiometry in 0.15 M NaCl in 70:30 (v:v) water:ethanol at 298.1 K. UV-vis absorption and fluorometric spectral data and pH-potentiometric titrations indicate 1:1 and 2:1 metal:chemosensor species. In the solid state H₂DTC is able to accommodate up to four metal ions, as proved by the crystal structures of the complexes [Zn₄(DTC)(OH)₂(NO₃)₄] (1) and {[Cu₄(DTC)(OCH₃)₂(NO₃)₄]·H₂O}_n (2). H₂DTC can be used as a potential chemosensor for monitoring Zn²⁺ and Cu²⁺ ions in biological and environmental media with outstanding accuracy and precision. The propensity of H₂DTC to detect intracellular Cu²⁺ and Zn²⁺ ions in the triple negative human breast cancer cell line MDA-MB-468 and in HeLa cells has been determined by fluorescence cell imaging.



INTRODUCTION

The design and construction of new chemosensors capable of detecting various metal ions and anions selectively with high sensitivity have received immense attention in analyses, biological processes, environmental studies, etc.^{1,2} Among the various chemosensors reported so far, dual chemosensors that can detect species both colorimetrically and fluorimetrically deserve special mention. The colorimetric technique allows the naked-eye detection of the color change of a given species without the application of sophisticated instruments. On the other hand, luminescence techniques are some of the nondestructive instrumental processes with the lowest cost, easier operation, fastest response time, and highest selectivity and sensitivity.^{3–6} Moreover, the development of single sensors for multiple analytes is a challenging task. Such a process is more efficient and less expensive than individual analysis methods.⁷ Therefore, both colorimetric and fluores-

cent chemosensors for the detection of zinc and copper ions are very important, as they are the second most and third most essential elements present in the human body and participate in many physiological processes. Zn²⁺ ions are present in biological systems either in a tightly bound form or in a labile form. Labile Zn²⁺ ions act as neurotransmitters^{8,9} and play important roles in apoptosis,¹⁰ regulation of gene expression, and insulin secretion.¹¹ The bound Zn²⁺ ions are present as a structural cofactor in many metalloproteins, such as SOD (superoxide dismutase), carbonic anhydrase, and carboxypep-

Received: October 9, 2021

tidase.^{12,13} It has been observed that the disruption of Zn²⁺ homeostasis is associated with many neurological disorders such as Alzheimer's disease, Parkinson's disease, epilepsy, and amyotrophic lateral sclerosis.^{14,15} Cu²⁺ ions play crucial roles in blood formation processes and in the functioning of various enzymes such as superoxide dismutase, cytochrome *c* oxidase, tyrosinase, etc.¹⁶ However, Cu²⁺ ion deficiency or overload can result in liver damage in infants, Parkinson's disease, Alzheimer's disease, amyotrophic lateral sclerosis (ALS), Menkes and Wilson diseases, etc.^{17–23}

To date significant numbers of papers on fluorescence chemosensors used for the detection of Cu²⁺ and Zn²⁺ ions have been reported (chart S1). Previously reported chemosensors face shortcomings with regard to their sensitivity, selectivity, detection limit, interference from other metal ions, low solubility in aqueous solution, etc.²⁴ A survey of the literature reveals that cyclic systems such as crown ethers, cryptands, and cyclodextrins are capable of selectively detecting cations due to their restricted cavity size and flexibility.^{24p,25} In this work the Schiff base ligand is a macrocyclic L8X2 type of system. There are very few examples in the literature of a similar macrocyclic L8X2 arrangement with two donor atoms being present.²⁶

In our continuing endeavors in the preparation of dual chemosensors,²⁷ we report an aza-crown-based fluorescence probe capable of sensing Zn²⁺ and Cu²⁺ ions with a significant 25 nm emission wavelength difference. Here, a 1,16-dihydroxy-tetraaza-30-crown-8-based Schiff base ligand (H₂DTC) has been designed so that the phenoxido oxygen, ethereal oxygen, and imine nitrogen atoms of the tetraaza-30-crown-8 group can simultaneously coordinate the cations. H₂DTC exhibits “turn on” fluorescence toward Zn²⁺ ions and “turn off” fluorescence toward Cu²⁺ in a water/methanol (9/1, v/v, 10 mM HEPES buffer, pH 7.4) mixture. We also demonstrate that this sensor is capable of detecting Zn²⁺ even in the presence of large amounts of Cd²⁺ and Hg²⁺ ions. In the presence of Zn²⁺ a 7-fold enhancement in emission intensity has been observed, whereas for Cu²⁺ the emission intensity is quenched by ~55-fold. The quenching effect is probably due to the paramagnetic nature of Cu²⁺. The LOD values of the chemosensor for Zn²⁺ and Cu²⁺ ions are 0.11 × 10^{−9} and 0.27 × 10^{−9} M, respectively. The binding modes of both the metal ions with H₂DTC (complexes 1 and 2) have been established by X-ray crystallography. This biocompatible chemosensor also exhibits cell permeability and senses intracellular Cu²⁺ and Zn²⁺ ions in the breast cancer cell line MDA-MB-468 as well as the cervical cancer cell line HeLa.

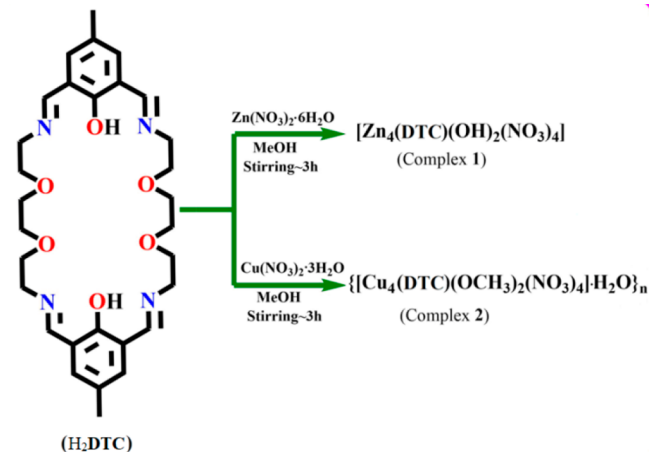
RESULTS AND DISCUSSION

Synthesis and Characterization. 2,6-Diformyl-4-methylphenol (DFP) has been prepared following a standard procedure.²⁸ 1,2-Bis(2-aminoethoxy)ethane was mixed with 2,6-diformyl-4-methylphenol (DFP) in a 1:1 molar ratio in methanol under reflux (Scheme S1 in the Supporting Information) to generate the Schiff base ligand H₂DTC. The compound was obtained as a semisolid in good yield and was used without further purification. It was thoroughly characterized using different spectroscopic methods (UV–vis, FT-IR, and ¹H and ¹³C NMR) and by elemental analysis. The base peak in the ESI-MS⁺ spectrum was found at *m/z* 553.30, corresponding to [H₂DTC + H]⁺ (Figure S1 in the Supporting Information). In the FT-IR spectrum, a broad band at around 3415 cm^{−1} indicates the presence of the phenolic –OH group

and the band at 1635 cm^{−1} is attributed to the C=N (for azomethine) stretching frequency (Figure S2 in the Supporting Information).

H₂DTC reacts with both Zn(NO₃)₂·6H₂O and Cu(NO₃)₂·3H₂O in a 1:4 ratio to produce complexes 1 and 2, respectively (Scheme 1). Both complexes crystallize from a DMF/methanol

Scheme 1. Route of Synthesis of Complexes 1 and 2



(v/v, 1/9)/diethyl ether solvent mixture. They have been characterized by X-ray crystallography, elemental analysis, and ESI-MS⁺. The experimentally observed peaks at *m/z* 1032.96 and 1170.00 correspond to the molecular ion peaks of [Zn₄(DTC)(OH)₂(NO₃)₃]⁺ and [Cu₄(DTC)(OCH₃)₂(NO₃)₄ + CH₃OH + Na]⁺, respectively. In the FT-IR spectrum of 1, characteristic stretching frequencies appear at 1630 cm^{−1} (ν(C=N)), 773 cm^{−1} (ν(C–H)), and 1300 cm^{−1} (ν(NO₃), asymmetric stretch), respectively (Figure S3a in the Supporting Information). Similarly, in the case of 2, characteristic stretching frequencies appear at 1625 cm^{−1} (ν(C=N)), 770 cm^{−1} (ν(C–H)), and 1300 cm^{−1} (ν(NO₃), asymmetric stretch), respectively (Figure S3b in the Supporting Information). It is important to note that, although the ligand and its zinc complex using Zn(ClO₄)₂ were previously reported by Maekawa,²⁹ the chemosensing behavior of H₂DTC toward Zn²⁺ and Cu²⁺ ions has been explored by us for the first time.

Crystal Structure Description of Complex 1. The tetranuclear Zn²⁺ complex [Zn₄(DTC)(OH)₂(NO₃)₄] crystallized in a monoclinic form with space group C₂ (Table S1 in the Supporting Information). The crystal structure of 1 is shown in Figure 1a. Selected bond distances and angles are collected in Table S2 in the Supporting Information. The asymmetric unit consists of half of the molecule; a further C₂ symmetry operation generates the whole molecule. In 1 the macrocyclic ligand H₂DTC binds four Zn²⁺ ions: Zn1, Zn1a, Zn2, and Zn2a. For simplicity, we only describe the coordination environment around Zn1 and Zn2. The two zinc centers Zn1 and Zn2 are doubly bridged by a phenoxido oxygen (O1) of the macrocyclic ligand and a hydroxide anion (O4). Zn1 is additionally coordinated by the imine nitrogen (N1), the ethereal oxygen atom (O2) of the macrocyclic ligand, and an oxygen atom (O6) of a nitrate ion. The monodentate binding mode of nitrate ion has been established by using the M–O distance (Δ*d*) and M–O–N bond angle (Δθ)³⁰ (Δ*d* < 0.3 Å and Δθ < 14° for bidentate; 0.3 Å < Δ*d* <

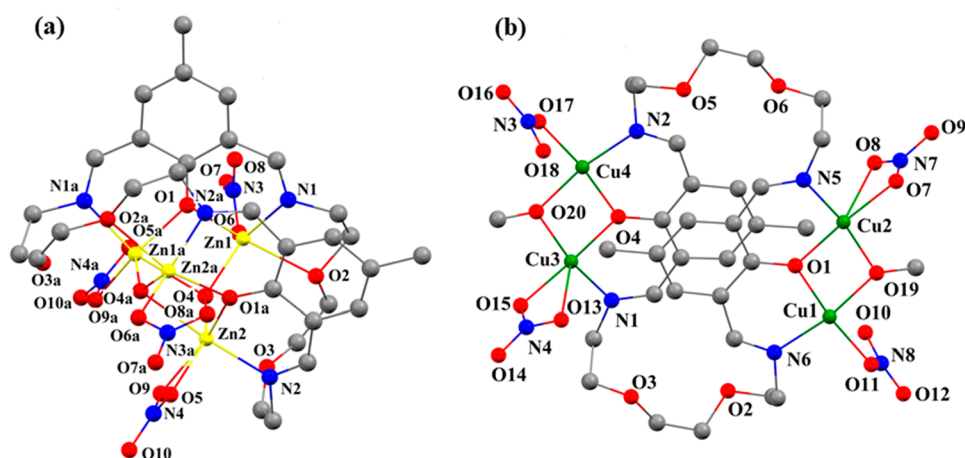


Figure 1. (a) Crystal structure of complex 1 (ball and stick model) and (b) asymmetric unit of complex 2 (ball and stick model). H atoms and solvent molecules are omitted for clarity.

0.6 Å and $14^\circ < \Delta\theta < 28^\circ$ for anisobidentate; $\Delta d > 0.6$ Å and $\Delta\theta > 28^\circ$ for monodentate). Here, the values of Δd and $\Delta\theta$ are 0.68 Å and 32.7° , respectively. The Addison parameter (τ)³¹ for the Zn1 center is found to be 0.5, suggesting a geometry intermediate between square pyramidal and trigonal bipyramidal. The Zn–N_{imino} and Zn–O_{phenoxido} bond distances are 1.993(11) Å (Zn1–N1) and 2.044(8) Å (Zn1–O1), respectively. The other Zn–O distances are 2.333(10) Å (Zn1–O2), 1.961(10) Å (Zn1–O4), and 2.008(10) Å (Zn1–O6), respectively. The Zn2 center is coordinated by a phenoxido oxygen (O1), a hydroxide ion (O4), an imine nitrogen (N2) and another symmetry-related hydroxide ion (O4a). The nitrate ion coordinates to the metal center in an anisobidentate fashion ($\Delta d = 0.33$ Å; $\Delta\theta = 14^\circ$). The Zn–O bond distances vary from 1.980(9) to 2.394(18) Å. The equatorial angles vary from 56.3(6) to 106.6(4) $^\circ$. The axial O4–Zn2–N2 angle is 163.6(4) $^\circ$.

Crystal Structure Description of Complex 2. Complex 2 crystallized in a monoclinic form with space group $P2_1/n$ (Table S1 in the Supporting Information). Figure 1b shows the asymmetric unit of 2. Selected bond distances and angles are collected in Table S2 in the Supporting Information. It is best described as a 1D network (Figure S4 in the Supporting Information) of asymmetric $[\text{Cu}_4(\text{DTC})(\text{OCH}_3)_2(\text{NO}_3)_4] \cdot \text{H}_2\text{O}$ units, where the asymmetric units are connected through a pair of $\mu_{1,1}$ bridging nitrate ions and $\mu_{1,1,1}$ bridging methoxide ions. The asymmetric unit consists of a deprotonated macrocyclic ligand, four copper centers (Cu1, Cu2, Cu3, and Cu4, respectively), two methoxide ions, four nitrate ions, and a water molecule of crystallization. Cu1, Cu2 and Cu3, Cu4 are doubly bridged by a phenoxido oxygen and a methoxide ion. Both Cu1 and Cu4 have a perfect square-pyramidal geometry (the Addison parameter, τ , is 0.05 for the Cu1 center and 0.03 for the Cu4 center),³¹ where they are equatorially coordinated by an imine nitrogen (N6 for Cu1 and N2 for Cu4), a phenoxido oxygen (O1 for Cu1 and O4 for Cu4), a methoxide ion (O19 for Cu1 and O20 for Cu4), and a nitrate ion (O11 for Cu1 and O17 for Cu4) of the same asymmetric unit and axially coordinated with another methoxide ion (O20a for Cu1 and O19a for Cu4) of another asymmetric unit. In the 1D chain, these two nitrate ions bind Cu2, Cu4 and Cu1, Cu3 centers in an anisobidentate fashion ($\Delta d \approx 0.49$ Å). The Cu–N bond lengths are found to be 1.969(6) and 1.955(6) Å for

Cu1 and Cu4, respectively, whereas the Cu–O bond lengths vary within the range 1.928(5)–2.559 Å. The Cu2 and Cu3 centers are both bound with a phenoxido oxygen (O1 for Cu2 and O4 for Cu3), an imine nitrogen (N5 for Cu2 and N1 for Cu3), a methoxide ion (O19 for Cu2 and O2 for Cu3), and a monodentate nitrate ion ($\Delta d = 0.78$ Å for Cu2 and $\Delta d = 0.61$ Å for Cu3). The axial N–Cu–O angles vary within the range 166.22(18)–168.7(2) $^\circ$. The Cu–N bond lengths vary from 1.926(6) to 1.946(6) Å, whereas the Cu–O bond lengths vary within the range 1.9286(9)–2.6747 Å. The Cu1–Cu2 and Cu3–Cu4 distances are 3.019(13) and 3.0173(13) Å, respectively.

NMR Studies. The ^1H NMR spectrum of H_2DTC was recorded in $\text{DMSO-}d_6$ and CDCl_3 (Figures S5 and S6, respectively, in the Supporting Information). In $\text{DMSO-}d_6$, the imine (H–C=N) protons appear as a sharp doublet peak at 8.49 ppm ($J = 12.4$ Hz). The aromatic protons appear at 7.44 ppm ($J = 9.6$ Hz) and the aliphatic protons at 3.62 ppm (d, $J = 5.6$ Hz) and 3.52 ppm (d, $J = 15.2$ Hz). A broad signal at 14.21 ppm corresponds to the phenolic protons (Figure S5 in the Supporting Information). In the case of 1, due to coordination with Zn^{2+} , the imine protons appear at 7.93 ppm (d, $J = 6.8$ Hz), 8.01 ppm (s), 8.28 ppm (d, $J = 10.4$ Hz), and 8.48 ppm (d, $J = 12.4$ Hz) and the aromatic protons at 6.96 ppm (s), 7.10 ppm (s), 7.16 ppm (s), 7.39 ppm (s), 7.52 ppm (d, $J = 12.0$ Hz), and 7.65 ppm (s), respectively. A broad multiplet in the range 3.1–4.0 ppm indicates the presence of aliphatic protons. Methyl protons appear at 2.21 ppm (s) and 2.29 ppm (s) (Figure S7 in the Supporting Information).

The ^{13}C NMR spectrum of H_2DTC was recorded in $\text{DMSO-}d_6$ (Figure S8 in the Supporting Information). The imine carbon atoms appear at 162.29 ppm, whereas aromatic carbon atoms appear in the range 121.36–159.34 ppm. The signals of the aliphatic carbon atoms appear from 59.97 to 70.75 ppm and that of the methyl carbon atoms at 20.26 ppm. In the ^{13}C NMR spectrum of 1 recorded in $\text{DMSO-}d_6$ (Figure S9 in the Supporting Information), the signals of the imine and aromatic carbon atoms appear in the 166.04–172.94 and 120.44–165.71 ppm ranges, respectively. Methylene and methyl carbon atoms are observed in the ranges 58.59–74.07 and 19.36–19.43 ppm, respectively. We have also performed a ^1H NMR titration of H_2DTC with Zn^{2+} in $\text{DMSO-}d_6$. Upon gradual addition of Zn^{2+} , the signal of the OH protons

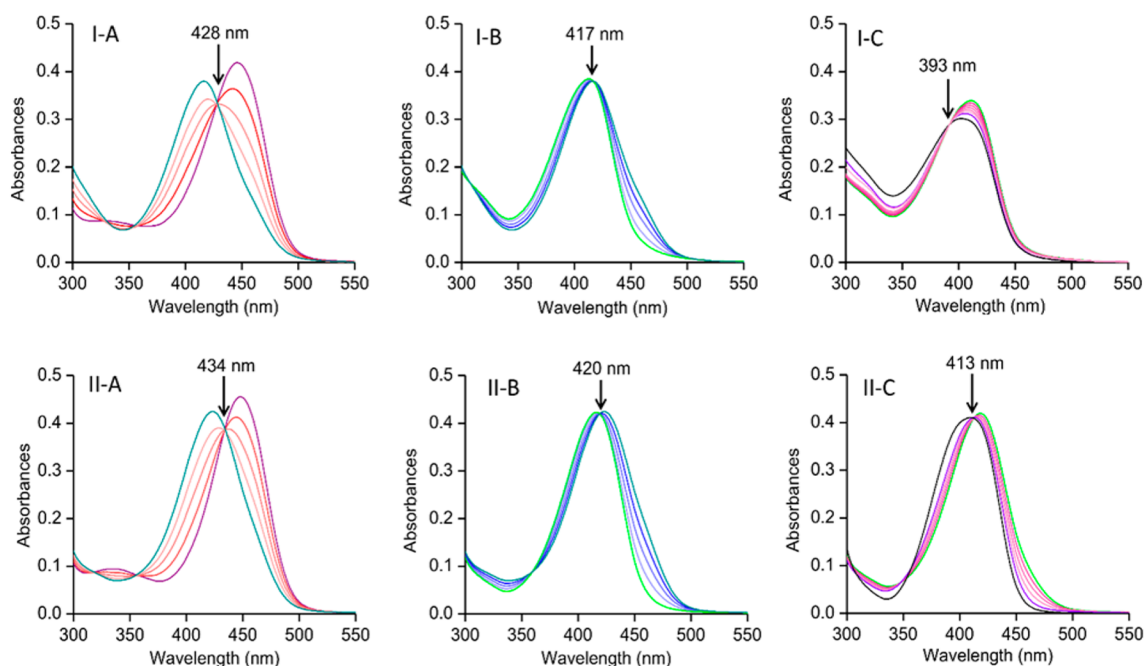


Figure 2. Absorption spectra of H_2DTC ($10 \mu\text{M}$) in the presence of (I) Cu^{2+} (0–4.30 equiv) and (II) Zn^{2+} (0–4.30 equiv) in HEPES buffer (10 mM) at pH 7.4: in the absence (purple in A) and presence of 0.25–0.75 equiv (red in A), 1.0 equiv (dark cyan in A and B), 1.25–1.75 equiv (blue in B), 2.0 equiv (green in B and C), 2.25–4.0 equiv (pink), and 4.3 equiv (violet in C) of metal ions. The absorption spectra with the gradual increase of Zn^{2+} or Cu^{2+} concentrations are shown by deep to light colors (red, A; blue, B; pink, C). The spectra of (II-C) complex 1 and (I-C) complex 2 ($40 \mu\text{M}$ each) are depicted by black lines for comparison. The isosbestic absorption wavelengths are indicated by arrows.

disappears due to the coordination of the metal. Again, in the presence of 3 equiv or above of Zn^{2+} ions significant splitting with downfield shift of aromatic protons from 7.44 ppm to 6.96, 7.09, 7.15, 7.38, 7.51, and 7.64 ppm and imine protons (H–C=N) from 8.49 ppm to 7.92, 8.00, 8.27, and 8.47 ppm is noticed, confirming the metal ion coordination with the imine nitrogens. Similarly, splitting in the spectral pattern of aliphatic protons from 3.62 and 3.52 ppm to a multiplet (3.46–3.96 ppm) in the presence of metal ions suggests the coordination of oxygen atoms of the aza-crown part with Zn^{2+} centers. Interestingly, the methyl protons also exhibit a significant change in spectral pattern (from 2.19 ppm to 2.22 and 2.25 ppm) under such a condition (Figure S10 in the Supporting Information). X-ray crystallographic data of 1 also justify the above ^1H NMR titration data.

Absorption Spectra Studies. The UV–vis spectrum of H_2DTC in 10 mM HEPES buffer at pH 7.4 shows a well-defined band at 445 nm. The peak is attributed to an intramolecular $\pi \rightarrow \pi^*$ or $n \rightarrow \pi^*$ transition. Three different sequences of absorption changes for H_2DTC were noticed with an increasing concentration of Zn^{2+} or Cu^{2+} until the intensity saturated in the presence of 4.3 equiv of the metal ions (Figure 2). By gradual addition of Cu^{2+} up to 1.0 equiv in the buffer containing H_2DTC ($10 \mu\text{M}$), the 445 nm absorption band for H_2DTC was shown to be gradually depleted with the concomitant formation of gradually blue shifted absorption intensities maximally up to ~ 424 nm by maintaining the isosbestic wavelength at ~ 428 nm (Figure 2 (I-A)). Although the absorption change continued by further addition of Cu^{2+} until 4.3 equiv, only a small blue shift from 424 to 413 nm was detected (Figure 2 (I-B and I-C, respectively)). However, the absorbance change from 1.0 to 2.0 equiv and that from 2.0 to 4.3 equiv follow two separate isosbestic wavelengths at ~ 417 and ~ 393 nm, respectively. No further absorption change was

observed above 4.3 equiv of Cu^{2+} . With the increasing addition of 4.3 equiv of Zn^{2+} , the absorption of H_2DTC gradually blue shifted up to ~ 413 nm, and most interestingly and similarly to Cu^{2+} , the absorption changes exhibited three separate isosbestic wavelengths at ~ 434 , ~ 420 , and ~ 413 nm in the Zn^{2+} ranges of 0–1.0, 1.0–2.0 and 2.0–4.3 equiv, respectively (Figure 2 (II-A, II-B, and II-C)). The consecutive appearance of three separate isosbestic wavelengths for the two metal ions suggests the presence of species with different stoichiometric ratios under equilibrium conditions. Unfortunately, their overlapping intensities did not allow us to identify their stoichiometries accurately.

ESI-MS⁺ Analysis. ESI-MS⁺ studies have been performed with 1:1, 2:1, and 4:1 metal ion: H_2DTC (metal ion: Zn^{2+} or Cu^{2+}) molar ratios. In the case of Zn^{2+} , m/z peaks appear at 615.15 for the 1:1 ratio and 814.16 for the 2:1 ratio, suggesting the formation of $[\text{Zn}(\text{HDTC})]^+$ and $[\text{Zn}_2(\text{DTC})(\text{NO}_3)_2 + \text{Li}]^+$ complexes in a water/methanol (9/1, v/v) mixture (Figure S11a,b, respectively, in the Supporting Information). Similarly, in the presence of Cu^{2+} ions, for the 1:1 and 2:1 ratios, peaks appear at 614.13 and 739.01, which correspond to $[\text{Cu}(\text{HDTC})]^+$ and $[\text{Cu}_2(\text{DTC})(\text{NO}_3)]^+$, respectively (Figure S12a,b, respectively, in the Supporting Information). When the mass spectrometric studies were carried out with a 4:1 metal to ligand molar ratio, peaks were observed at 1032.96 for Zn^{2+} and 1170.00 for Cu^{2+} corresponding to $[\text{Zn}_4(\text{DTC})(\text{OH})_2(\text{NO}_3)_3]^+$ and $[\text{Cu}_4(\text{DTC})(\text{OCH}_3)_2(\text{NO}_3)_4 + \text{CH}_3\text{OH} + \text{Na}]^+$ molecular ions, respectively (Figures S11c and S12c, respectively, in the Supporting Information). Moreover, the experimentally obtained ESI-MS⁺ data nicely match with their simulated patterns.

Fluorescence Properties. Fluorescence experiments were performed in 10 mM HEPES buffer (pH 7.4) under ambient conditions. Upon excitation at 445 nm, H_2DTC exhibits weak

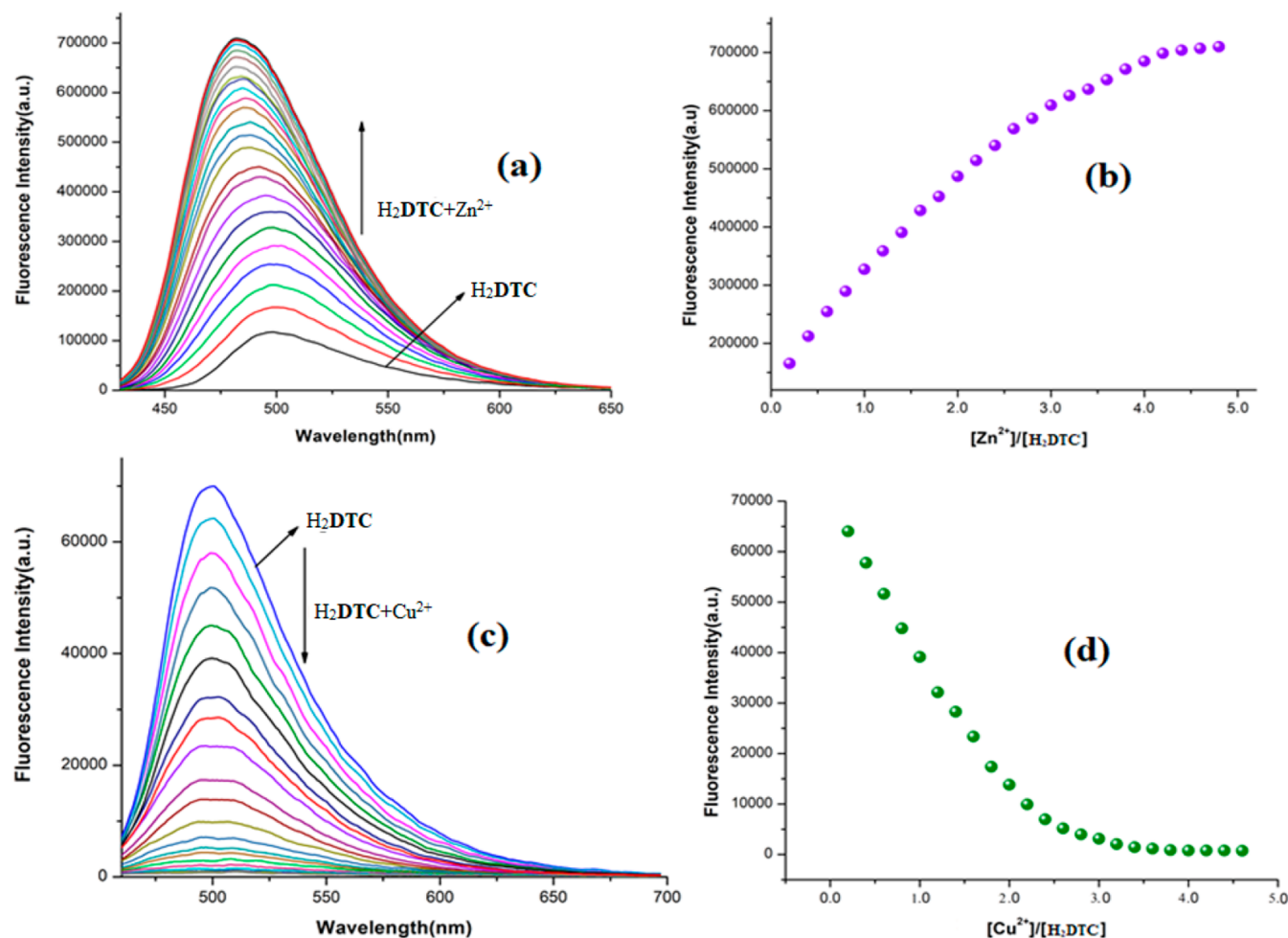


Figure 3. Fluorescence titration of H₂DTC (10 μ M) with gradual addition of Zn²⁺/Cu²⁺ (0–48 μ M) in HEPES buffer (10 mM) at pH 7.4 and corresponding fluorescence intensity versus molar ratio plot.



Figure 4. Color changes of the chemosensor H₂DTC (10 μ M) in the presence of different metal ions (4 equiv) in HEPES buffer (10 mM, pH 7.4). The images were taken under UV light. Legend: 1, only H₂DTC; 2–16, H₂DTC + Zn²⁺, Cu²⁺, Cd²⁺, Pb²⁺, Hg²⁺, Mn²⁺, Fe³⁺, Co²⁺, Ni²⁺, Cr³⁺, K⁺, Na⁺, Mg²⁺, Ca²⁺, and Al³⁺, respectively.

fluorescence at 500 nm. This is probably due to a photoinduced electron transfer process (PET). The delocalization of the available lone pair on the imine nitrogen atom to the DFP moiety leads to the quenching of the fluorescence.

Upon addition of Zn²⁺ to H₂DTC, the emission at 475 nm (excitation wavelength 415 nm) was greatly enhanced, accompanied by a blue shift of 25 nm (Figure 3a). The fluorescence enhancement due to Zn²⁺ ions has a systematic growth of about 7-fold up to 4 equiv of Zn²⁺, although a small fluorescence increase is still perceptible at higher Zn²⁺ concentrations. The chelation of Zn²⁺ with phenoxido O and imine N atoms of the aromatic part as well as O atoms of the

macrocyclic aza-crown part of H₂DTC increases the rigidity of the molecular assembly (CHEF effect) via inhibition of the free rotation of H₂DTC around the H–C=N bond. Again a PET process is hindered by arresting the lone pair of electrons present on the imine nitrogen. These two effects are jointly responsible for the observed fluorescence enhancement.

In the case of Cu²⁺, its gradual addition (up to a maximum of 4 equiv) to a chemosensor solution completely quenches the fluorescence at \sim 500 nm (Figure 3c). Such a dramatic quenching of the fluorescence (\sim 55-fold) (CHEQ) can be attributed to a ligand to metal charge transfer (LMCT) between H₂DTC and the paramagnetic Cu²⁺ ions.³² The plot

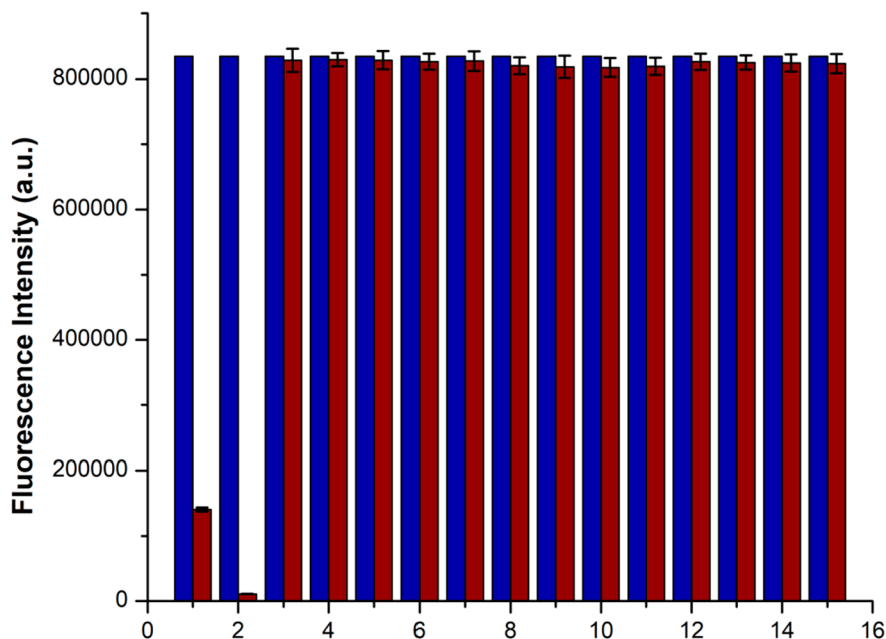


Figure 5. Relative fluorescence intensity profile of the [DTC–Zn²⁺] system in the presence of different cations in 10 mM HEPES buffer at pH 7.4. Legend: 1, only H₂DTC (10 μM), 2–15, H₂DTC (10 μM) + Zn²⁺ (40 μM) + Mⁿ⁺ (50 μM), where Mⁿ⁺ = (Cu²⁺ (2), Co²⁺ (3), Cr³⁺ (4), Fe³⁺ (5), Hg²⁺ (6), K⁺ (7), Mn²⁺ (8), Na⁺ (9), Ni²⁺ (10), Mg²⁺ (11), Pb²⁺ (12), Ca²⁺ (13), Fe²⁺ (14), Cd²⁺ (15)). Blue bars indicate H₂DTC (10 μM) + Zn²⁺ (40 μM), whereas brown bars indicate H₂DTC (10 μM) + Zn²⁺ (40 μM) + other cations (50 μM) (except for 1).

of fluorescence intensity at 500 nm (I_{500}) vs molar ratio ($[Cu^{2+}]/[H_2DTC]$) in Figure 3d shows that the quenching is at a maximum for an ~1:2 H₂DTC:Cu²⁺ stoichiometric ratio.

The selectivity of H₂DTC toward Zn²⁺ and Cu²⁺ over other competitive species was examined by fluorescence titration experiments in the presence of different alkali metal (Na⁺ and K⁺), alkaline-earth metal (Mg²⁺ and Ca²⁺), and transition-metal ions (Mn²⁺, Fe³⁺, Co²⁺, Ni²⁺, Cu⁺, Cd²⁺, and Hg²⁺) (Figure S13 in the Supporting Information). In a UV chamber, H₂DTC exhibits a bluish green fluorescence in the presence of Zn²⁺ ions (Figure 4). Upon the addition of different common anions such as sodium salts of S₂O₃²⁻, S²⁻, SO₃²⁻, HSO₄⁻, SO₄²⁻, SCN⁻, N₃⁻, OCN⁻, AsO₄³⁻, PO₄³⁻, ClO₄⁻, AcO⁻, Cl⁻, NO₃⁻, P₂O₇⁴⁻ (PPi), PF₆⁻, F⁻, L-cysteine, and glutathione (Figure S14 in the Supporting Information) in HEPES buffer (10 mM) at pH 7.4 to the chemosensor, no significant fluorescence enhancement was noticed. Competition assay experiments were performed individually for Zn²⁺ (4.0 equiv) and Cu²⁺ ions (4.0 equiv) and in the presence of other metal ions (5.0 equiv) and common anions in a similar solvent system. As shown in Figure 5, the addition of other metal ions, except Cu²⁺, does not significantly alter the emission of the system Zn²⁺-H₂DTC. However, the addition of Cu²⁺ to an H₂DTC solution in the presence of Zn²⁺ led to large fluorescence quenching (Figure 5 and Figure S15a in the Supporting Information), in agreement with the higher stability of the Cu²⁺ complexes. Such a type of displacement highly corroborates the Irving–Williams series, according to which Cu²⁺ ions have a greater tendency of replacing Zn²⁺ ions to form a more stable Cu²⁺-probe complex. Binding constant values also support the above observation. Interestingly, the presence of Cu⁺ ions did not exhibit such a type of fluorescence quenching. The effective ionic radii of Cu⁺, Cu²⁺, and Zn²⁺ are 77, 73, and 74 pm, respectively. Therefore, the charge to radius ratio values of Zn²⁺ and Cu²⁺ ions are comparable and significantly differ from that of Cu⁺ ions,

which initiates the selectivity of H₂DTC toward Zn²⁺ and Cu²⁺ ions. Cu²⁺ ion detection by H₂DTC is not influenced by the presence of other competitive metal ions, including Zn²⁺ ions (Figures S15b and S16 in the Supporting Information).

In competition assay experiments toward common anions, we have also studied the binding behavior of the chemosensor–Zn²⁺ receptor toward PPi and the binding behavior of the chemosensor–Cu²⁺ receptor toward biothiols such as L-cysteine and glutathione. In the chemosensor–Zn²⁺ receptor the fluorescence emission was only slightly quenched in the presence of a large excess of PPi (40 equiv) (Figure S17 in the Supporting Information). Similarly, in the case of the chemosensor–Cu²⁺ receptor, glutathione exhibits little fluorescence enhancement (Figure S18 in the Supporting Information). Therefore, the competition assay experiment demonstrates a high fluorescence recognition of H₂DTC for Zn²⁺ and Cu²⁺ ions over other cations and anions.

Furthermore, solid-state fluorescence spectroscopic studies of H₂DTC and complexes 1 and 2 (Figure S19 in the Supporting Information) reveal the enhancement of fluorescence intensity in 1 and the quenching of fluorescence intensity in 2 in comparison with H₂DTC.

Reversibility and regeneration are two important aspects for the real-time application of a chemosensor. The experiments were performed in the presence of a solution of the sodium salt of ethylenediaminetetraacetic acid (Na₂EDTA). In the case of the DTC–Zn²⁺ solution, after addition of 4 equiv of Na₂EDTA the color changes from bluish green to light yellow with an obvious decrease in fluorescence intensity. However, the addition of 4 equiv of Na₂EDTA to a DTC–Cu²⁺ solution leads to an enhancement of emission intensity that along with the appearance of a light yellow color indicates the regeneration of the free H₂DTC (Figure S20 in the Supporting Information).

The average concentration of Cu²⁺ in blood is 100–150 μg/L, and the total concentration of Zn²⁺ ions in mammalian cells

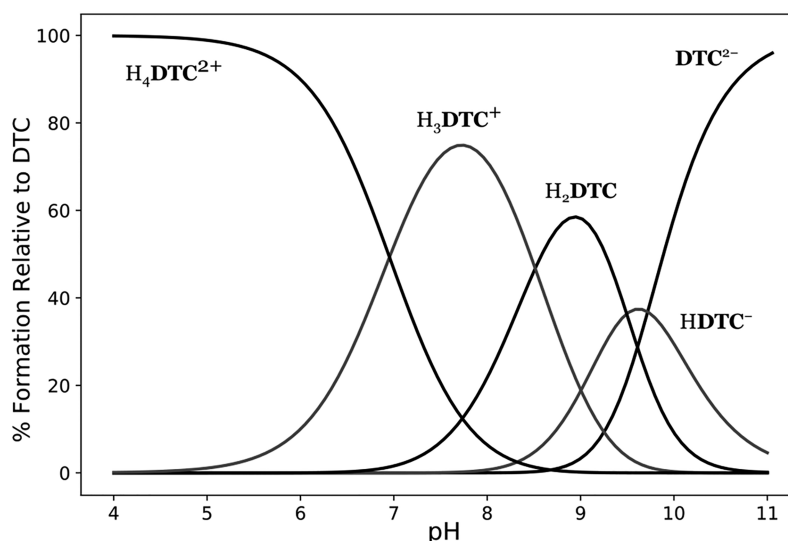


Figure 6. Species distribution for the system DTC in 0.15 M NaCl (EtOH 30%). [DTC] = 1 mM.

is in the range 100–500 μM .^{33,34} The lower limit of detection (LOD) of the chemosensor toward Cu^{2+} and Zn^{2+} was calculated using the 3σ method.³⁵ The values obtained, 0.11×10^{-9} M for Cu^{2+} and 0.27×10^{-9} M for Zn^{2+} , clearly suggest that this chemosensor can quantitatively detect both Cu^{2+} and Zn^{2+} ions in the analysis of a real sample.

The stability of the chemosensor was examined by a reversibility experiment³⁶ (Figure S21 in the Supporting Information). It clearly shows that the chemosensor is quite stable in a wide range of pH (pH 4–10) and it can only be dissociated under strongly acidic conditions (Figure S22 in the Supporting Information).

Figure S23 in the Supporting Information shows the effect of pH on the fluorescence response of the free H_2DTC and of the systems $\text{Zn}^{2+}:\text{H}_2\text{DTC}$ and $\text{Cu}^{2+}:\text{H}_2\text{DTC}$ with a 4:1 molar ratio. Free H_2DTC has weak fluorescence at acidic pH that increases slightly from pH 3 to 6 and then decreases at more basic pH values. The weak emission of the free ligand can be attributed to a PET process that becomes more intense at basic pH when the phenol groups are deprotonated (see the distribution diagram). Deprotonation of the phenol groups would extend the electron delocalization to the π -conjugated system formed by the aromatic rings and the $\text{C}=\text{N}$ (imino) groups, thereby decreasing the emission intensity. While the addition of Zn^{2+} does not lead to any increase in fluorescence at acidic pH values, at pH values above 7, it produces a large increase in fluorescence (CHEF effect). In contrast, Cu^{2+} quenches the fluorescence of H_2DTC throughout the entire pH range assayed, particularly at basic pH values, due to the chelation to the metal (CHEQ effect). The above findings suggest that the phenol groups present in H_2DTC are too basic, do not dissociate readily, or reprotonate readily enough and thus easily undergo deprotonation.

Lifetime and Quantum Yield Measurements. Lifetime experiments for the H_2DTC and complexes **1** and **2** were studied at 298 K in HEPES buffer (10 mM, pH 7.4). The average fluorescence decay lifetimes of H_2DTC and complexes **1** and **2** have been determined by using the formula $\tau_f = a_1\tau_1 + a_2\tau_2$, where a_1 and a_2 are the relative amplitudes of the decay process. The average fluorescence lifetime of H_2DTC , and complexes **1** and **2** are 1.90, 2.68, and 0.44 ns, respectively

(Figure S24 and Table S3 in the Supporting Information). We were unable to obtain the phosphorescence intensity apparently due to low fluorescence lifetime values.

The fluorescence quantum yield (Φ) was calculated by using the formula

$$\Phi_{\text{sample}} = \left\{ \frac{(\text{OD}_{\text{standard}} \times A_{\text{sample}} \times \eta_{\text{sample}}^2)}{(\text{OD}_{\text{sample}} \times A_{\text{standard}} \times \eta_{\text{standard}}^2)} \right\} \times \Phi_{\text{standard}}$$

where A is the area under the emission spectral curve, OD is the optical density of the compound at the excitation wavelength, and η is the refractive index of the solvent. The standard used was quinine sulfate with $\Phi_{\text{standard}} = 0.52$.

The values of Φ for H_2DTC and for the $\text{DTC}-\text{Zn}^{2+}$ and $\text{DTC}-\text{Cu}^{2+}$ complexes were found to be 0.059, 0.28 and 0.0014, respectively (Table S3 in the Supporting Information). The fluorescence quantum yield (Φ) of the $\text{H}_2\text{DTC}-\text{Zn}^{2+}$ complex is 4.7-fold greater than that of free H_2DTC . The low fluorescence decay lifetime and quantum yield of complex **2** is due to the quenching effect of Cu^{2+} ions.

pH-Potentiometric Titrations. Acid–Base Behavior. The EMF data obtained by titrating H_2DTC EtOH/ H_2O 30/70 v/v solutions in 0.15 M NaCl (EtOH 30%) at 298.1 K with NaOH aqueous solutions were analyzed with the HYPERQUAD³⁷ suite programs. For additional experimental data, the pH range covered, and fitting parameters, see Tables S4–S6 in the Supporting Information. The pH range used for determining the protonation constants was 6–11. Further studies were carried out from pH 3 in order to rule out additional protonation steps. A total of four protonation constants were found (see Table S7 in the Supporting Information and Figure 6). The first and second protonation constant values are very close and should occur at opposite sides of the macrocycle. According to the literature data,^{38,39} there are some crystal structures where a proton is shared between phenolate groups and the neighboring imino groups. It is reasonable to suggest that this might also happen in solution. The next two protonations would produce a reorganization of the protons since, as was evidenced in the crystal structure of a related ligand,⁴⁰ all four protons at this stage would be placed at the imino groups. A hydrogen-bond

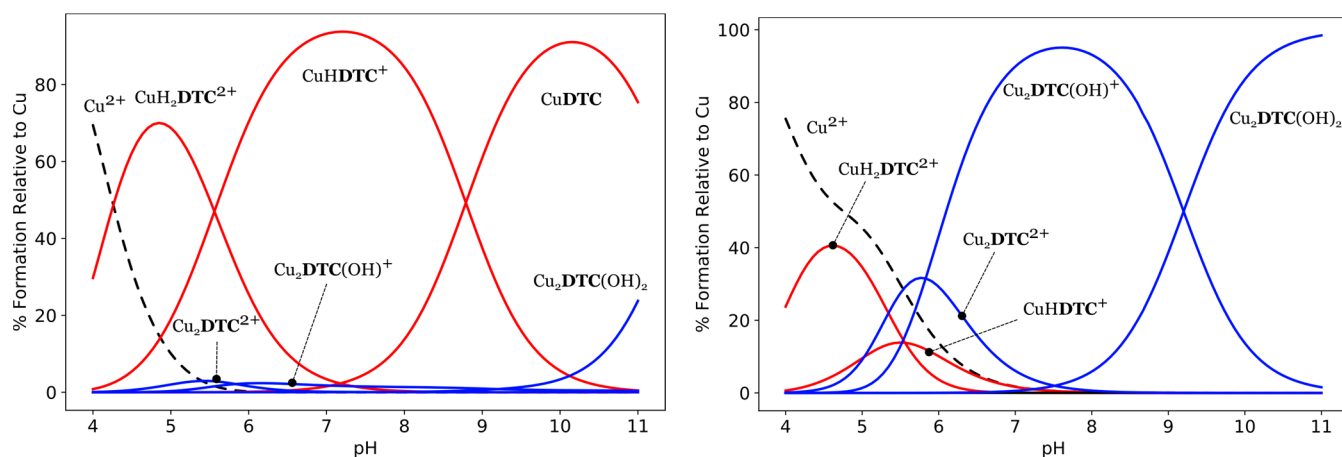


Figure 7. Species distribution for the system DTC with Cu^{2+} in NaCl 0.15 M (EtOH 30%). $[\text{DTC}] = 1 \text{ mM}$, $[\text{Cu}^{2+}] = 1 \text{ mM}$ (left), and $[\text{Cu}^{2+}] = 2 \text{ mM}$ (right). Mononuclear species are shown in red, and binuclear species are shown in blue.

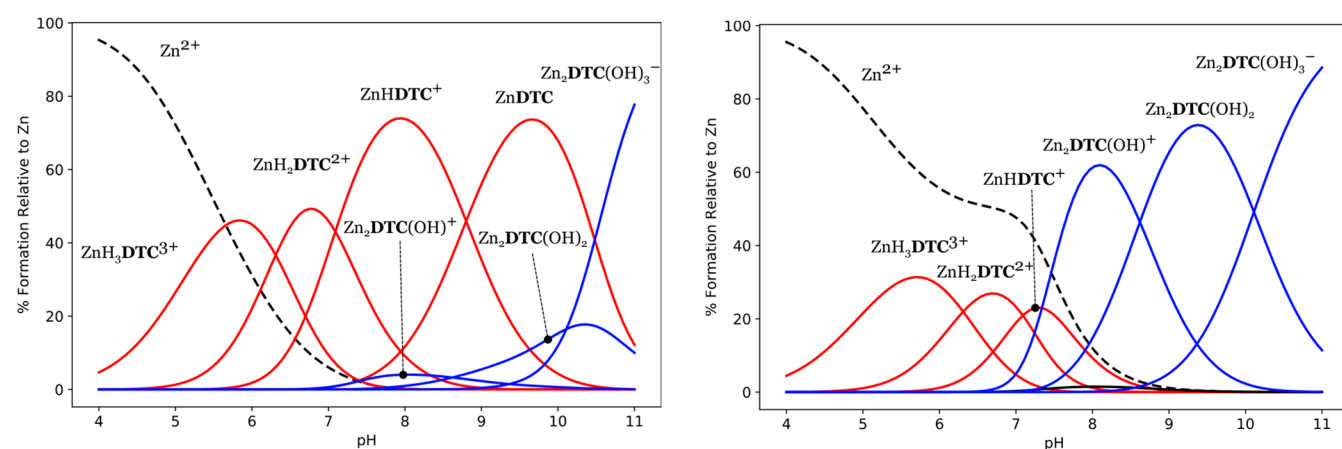


Figure 8. Species distribution for the system DTC with Zn^{2+} in 0.15 M NaCl (EtOH 30%). $[\text{DTC}] = 1 \text{ mM}$, $[\text{Zn}^{2+}] = 1 \text{ mM}$ (left), and $[\text{Zn}^{2+}] = 2 \text{ mM}$ (right). Mononuclear species are shown in red, and binuclear species are shown in blue.

network between the phenolate and the imino groups would contribute to the observed reorganization.

Interaction with Cu^{2+} and Zn^{2+} . The interaction of H_2DTC with Cu^{2+} and Zn^{2+} was studied by means of pH-potentiometric titrations performed with $\text{M}^{2+}:\text{H}_2\text{DTC}$ mole ratios varying from 1:1 to 4:1 in the same solvent mixture and electrolyte as in the protonation studies. The introduction in the model of $\text{M}^{2+}:\text{H}_2\text{DTC}$ species with 3:1 and 4:1 stoichiometry did not lead to any improvement in the fitting and, therefore, such stoichiometries were discarded. The titrations only revealed the formation of complex species of 1:1 and 2:1 $\text{M}^{2+}:\text{H}_2\text{DTC}$ stoichiometry (see Tables S8 and S9 in the Supporting Information). Moreover, in the titrations carried out with 3:1 and 4:1 $\text{Cu}^{2+}:\text{H}_2\text{DTC}$ mole ratios, some formation of Cu^{2+} hydroxide was observed at basic pH values. The final models collected in Table S8 show for Cu^{2+} the formation of mononuclear $[\text{Cu}(\text{H}_x\text{DTC})]^{2+x}$ species with x varying from 2 to 0, as well as of the nonhydroxylated binuclear species $[\text{Cu}_2(\text{DTC})]^{2+}$ and the hydroxylated species $[\text{Cu}_2(\text{DTC})(\text{OH})]^+$ and $[\text{Cu}_2(\text{DTC})(\text{OH})_2]$. The distribution diagrams (Figure 7) show that, while for the 1:1 $\text{Cu}^{2+}:\text{H}_2\text{DTC}$ mole ratio the mononuclear species prevail throughout the entire pH range studied, for a 2:1 ratio the binuclear hydroxylated species are quantitatively formed in solution above pH 7. As shown in Table S8, the stability

constant for the formation of the $[\text{Cu}(\text{DTC})]$ complex is almost 9 orders of magnitude higher than that for the stepwise formation of the $[\text{Cu}_2(\text{DTC})]^{2+}$ binuclear species, which may be associated with the fact that there is a larger number of donor atoms involved in the coordination of the first metal ion. The coordination of the second metal should bring about a rearrangement of the ligand and a reorganization of the coordination sphere with bond breaking and re-forming, so that each metal ion occupies one of the sites of the ligand. This low coordination number is reflected in the very low $\text{p}K_a$ value ($\text{p}K_a = 5.87$) associated with the formation of the monohydroxylated binuclear complexes. This $\text{p}K_a$ value supports, on the other hand, that the hydroxide anion is behaving as a bridging ligand between the metal centers.

As with copper, in the case of zinc no stoichiometry higher than 2:1 could be derived from the pH-potentiometric studies (Figure 8), where for the y axis the percent complex formation with respect to the total metal content is represented as a function of pH. Mononuclear complexes have the stoichiometries $[\text{Zn}(\text{H}_x\text{DTC})]^{x+}$ with x varying from 4 to 0 and $[\text{Zn}_2(\text{DTC})(\text{OH})_y]^{4-y}$ hydroxylated binuclear complexes with y varying from 1 to 3. As expected, the Zn^{2+} complexes of DTC have lower stability constants than those of copper, as exemplified in Table S8 by the 5 orders of magnitude lower stability of $[\text{Zn}(\text{DTC})]$ with respect to $[\text{Cu}(\text{DTC})]$ (Table

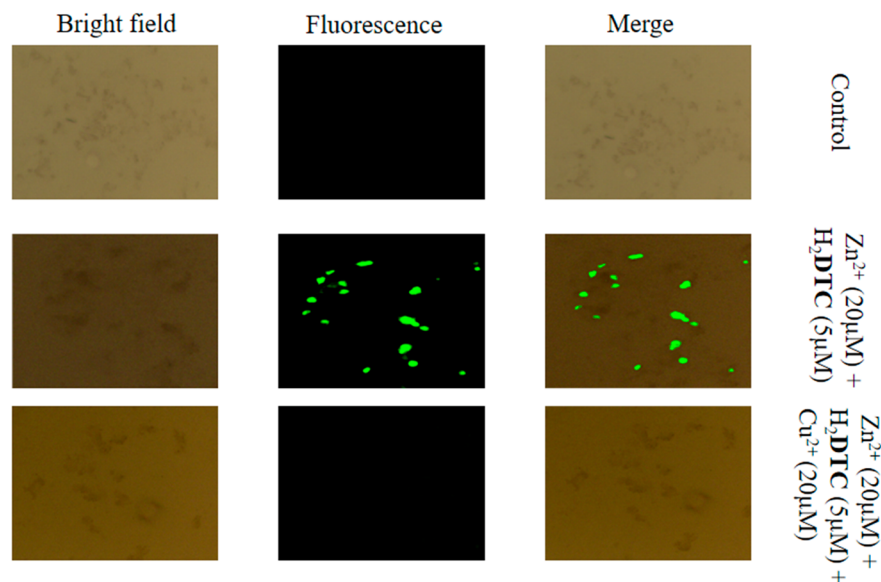


Figure 9. Bright field, fluorescence, and merged microscopic images of untreated HeLa (Control) cells and cells treated with Zn^{2+} ($20 \mu\text{M}$) + H_2DTC ($5 \mu\text{M}$) and with Zn^{2+} ($20 \mu\text{M}$) + H_2DTC ($5 \mu\text{M}$) + Cu^{2+} ($20 \mu\text{M}$).

S9). As shown in the distribution diagram, the hydroxylated species predominate in solution above pH 7.4 for a 2:1 $\text{Zn}^{2+}:\text{DTC}$ molar ratio.

Stability Constant Determination from UV–Vis and Fluorometric Titrations. UV–vis and fluorescence titrations were performed by adding up to 4 equiv of either Cu^{2+} or Zn^{2+} to a $10 \mu\text{M}$ water solution of H_2DTC in HEPES buffer (pH 7.4) (Figures 2 and 3). The data were analyzed with the software HypSpec2014,^{41,42} and the best-fitting model was chosen with the same criteria as for the pH-potentiometric data. The equilibrium constants obtained are conditional constants for the experimental conditions used at pH 7.4.

For Cu^{2+} , the UV–vis titrations revealed the formation of species of 1:1 and 2:1 $\text{Cu}^{2+}:\text{H}_2\text{DTC}$ stoichiometries with values of the successive constants being 6.17(3) and 4.76(2), respectively. In the case of Zn^{2+} we could only fit the constant for the 1:1 complex at this pH with a value of $\log K = 5.83(8)$. Indeed, the distribution diagram calculated with the constants derived from the pH-potentiometric studies at the concentrations used in the UV–vis titration (*vide supra*) reveals that only mononuclear species are formed at pH 7.4; the binuclear species forms at higher pH values. Similar conclusions were drawn from the emission studies. As stated above, addition of Cu^{2+} in water produces a strong quenching. The profile of the titration and the analysis of the data support the formation of 1:1 and 2:1 complexes of $\text{Cu}^{2+}:\text{H}_2\text{DTC}$ stoichiometry (Figure S25 in the Supporting Information). However, in the case of the Zn^{2+} titration, a CHEF effect is observed. As noted above, the coordination of the $3d^{10}$ Zn^{2+} ion would prevent the photoinduced electron transfer from the imine lone pairs to the excited fluorophore from occurring. The values of the constants obtained from the fluorescence studies (Cu^{2+} , $\log K_1 = 6.085(1)$, $\log K_2 = 5.86(2)$; Zn^{2+} , $\log K_1 = 6.032(8)$) agree reasonably well with the UV–vis and the effective constants ($\log K_{\text{eff}} = \sum [\text{MH}_x\text{DTC}]^{x+} / [(\sum (\text{H}_x\text{DTC})^{x-2} [\text{M}^{2+}])]$) determined at pH 7.4 from the potentiometric data. The above binding constant values suggest that the effect of solvent composition on the metal–ligand binding properties can be considered to be negligibly small.

To support this fact, we performed a fluorometric titration by using ethanol instead of methanol and maintained the water/ethanol mixture at 7/3 (v/v). A similar observation was found and is depicted in Figure S26 in the Supporting Information.

The above experimental data reveal that the lower stoichiometries (1:1 and 1:2 for Cu^{2+} and 1:1 for Zn^{2+}) of chemosensor to metal are the most stable components in the solution phase. Again, by X-ray crystallography we have established a higher stoichiometry (1:4) in the solid phase. This is probably due to the macrocyclic nature of the chemosensor H_2DTC , which can accommodate metal ions (Zn^{2+} and Cu^{2+}) in different stoichiometries from 1:1 to 1:4 depending on the reaction conditions. Experiments performed in the solution phase were probably unable to identify higher stoichiometries due to their low stabilities. The presence of different weak interactions ($\pi\cdots\pi$, $\text{CH}\cdots\pi$, and hydrogen bonds) and nitrate ions facilitates the stabilization of higher stoichiometry complexes in the solid phase.

Cell Imaging Study. In order to follow the real conditions, fluorescence microscopy was used to study the cellular uptake of Zn^{2+} ($20 \mu\text{M}$) in cells and a solution of the ligand ($5 \mu\text{M}$). A promiscuous green fluorescence signal is observed under the microscope that immediately disappears after the incorporation of Cu^{2+} ($20 \mu\text{M}$) (Figure 9). The same result was observed in the cellular uptake study of a solution of the ligand ($5 \mu\text{M}$) and Zn^{2+} ($20 \mu\text{M}$) simultaneously in the presence or absence of Cu^{2+} ($20 \mu\text{M}$) (Figure S27 in the Supporting Information). Thus, we can conclude that the cells readily internalize the Zn^{2+} complex, producing promiscuous green fluorescence, which is immediately quenched after the addition of Cu^{2+} . The nanomolar detection sensitivity order for the probe H_2DTC did not permit the detection of ultratrace amounts of Zn^{2+} or Cu^{2+} ($\sim 10^{-18}$ – 10^{-13} M) in human cells.⁴³

Cell Survival Assay of H_2DTC . The purpose of doing a cytotoxicity assay is to explore the possibility of toxic effects of the ligand. A cytotoxicity assay clearly determines whether the ligand exerts any significant adverse effect on the cells. The percentage of survivability is a clear indication of the effects of a particular ligand on the cells. Hence, a higher bar graph

percentage indicates biocompatibility, whereas a lower bar graph percentage indicates enhanced mortality of the cells. The *in vitro* cytotoxicity of H₂DTC was determined to estimate the biocompatibility with WI-38 (noncancerous cells) and MDA-MB-468 and HeLa (cancerous cells) cell lines. The cells were treated with different concentrations (0–100 μM) of the ligand for 24 h and followed by an MTT assay. It is observed that the ligand exhibits no significant toxicity in all three cell lines even when they are treated with high concentrations of H₂DTC (Figures S28 and S29, respectively, in the Supporting Information). In addition, no appreciable increase in cytotoxicity (cell survival >80%) was detected in the presence of experimental Zn²⁺ and Cu²⁺ concentrations (20–50 μM) (Figure S30 in the Supporting Information); presumably H₂DTC could scavenge the metals and protect the cell. Hence, we can conclude that the ligand is biocompatible and might be conducive for biological applications.

Computational Study of the Ligand. The UV–vis absorption spectrum of the ligand was studied at room temperature in water/methanol (9/1 v/v, 10 mM HEPES buffer, pH 7.4). Experimentally the ligand shows one peak at 445 nm, and we have computed using the TDDFT methodology the associated absorption energy, along with the oscillator strength and the main configurations. The ligand was studied for three possible tautomeric forms (Scheme S2 in the Supporting Information). The experimental UV spectrum of the ligand is probably composed of the absorption bands of the bis-keto form at room temperature because this tautomer is the most stable (2.2 kcal/mol more stable than the bis-enol form). Consequently, we only describe the TD-DFT study of the bis-keto form. Moreover, the lowest lying absorption band computed for the bis-keto tautomer ($\lambda = 447$ nm) is in excellent agreement with the experimental band ($\lambda_{\text{exp}} = 445$ nm).

In the ground state the HOMO is basically composed of the six-membered rings and the conjugated exocyclic C=C and C=O bonds. The HOMO-1 and HOMO have the same energy (−5.330 eV). Similarly, the LUMO is basically composed of the π systems, including the exocyclic C=C bond and the conjugated lone pair of the nitrogen atoms. The energy difference between the HOMO and LUMO is 2.969 eV. The calculated lowest-lying absorption band is located at 447 nm for the bis-keto form of ligand (see Figure 10). This absorption band can be assigned to an S₀ → S₁ transition and attributed to two electronic transitions: HOMO → LUMO (50%) and HOMO-1 → LUMO+1 (50%). The theoretical value is in very good agreement with the experimental absorption value ($\lambda_{\text{exp}} = 445$ nm), thus confirming the existence of the bis-keto form in solution.

We have also performed a TD-DFT study of the Zn complex. Unfortunately, it was not possible to analyze the Cu complex using the TD-DFT calculations, likely due to the quintuplet nature of the ground state (high-spin configuration). However, the PET-OFF behavior observed only for the Cu²⁺ complex can be explained in terms of the conformation adopted by the ligand in this complex, as revealed by X-ray experiments. That is, a perfect π – π face-to-face stacking only observed in the Cu²⁺ complex (see Figure S4 in the Supporting Information) provides a suitable explanation for the quenching of fluorescence in the ligand upon complexation.

In the ground state (S₀) of the Zn²⁺ complex, the HOMO is composed of two phenolic aromatic moieties of the ligands and

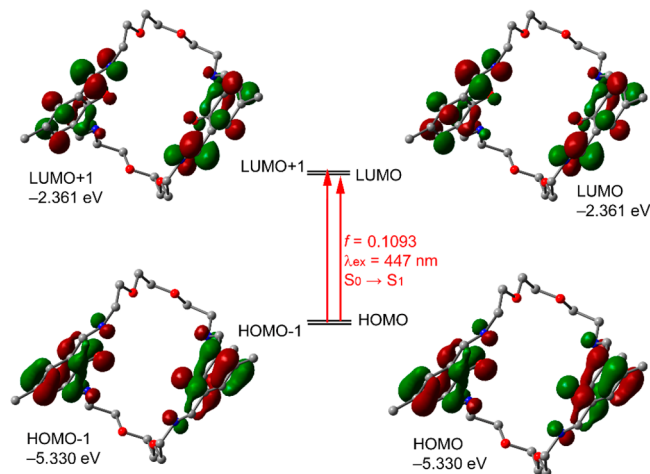


Figure 10. Molecular orbitals involved in the UV–vis absorption of the bis-keto form of the ligand at the B3LYP/6-31+G* level of theory.

the conjugated C=N bonds (Figure 11a). The LUMO is basically composed of the antibonding C=N π orbital. The energy difference between the HOMO and LUMO is 2.741 eV. To get a better insight into the experimental absorption values TDDFT calculations were carried out for the complex on the basis of the X-ray geometry. The calculated absorption energy associated with its oscillator strength, the main configurations, and their assignments of the lowest-lying transition in the Zn²⁺ complex are given in Figure 11. This singlet → singlet absorption band corresponds to the S₀ → S₃ excitation (3.1002 eV, $\lambda = 400$ nm, and $f = 0.0966$). This single excitation can be attributed to HOMO-2 → LUMO and HOMO → LUMO transitions (Figure 11b), which can be assigned to $\pi(L) \rightarrow \pi^*(L)$ transitions with ILCT character. The experimental value ($\lambda_{\text{exp}} = 413$ nm) is in reasonable agreement with the theoretical value (400 nm). The essential contribution is the HOMO → LUMO excitation configuration, which is fluorophore-based, and consequently the fluorescence originates from this transition. The atomic orbitals of the metal center are not involved in the transition, and most of the HOMO and LUMO in the Zn(II) complex resemble those of the free sensor. In fact, only a slight alteration of the electron distribution is observed in the LUMO (smaller contribution of the aromatic ring and larger contribution of the imidic bond with respect to the free ligand), which likely explains the chelate-enhanced fluorescence.

SUMMARY

In summary, we have successfully developed a unique multifunctional aza-crown-based Schiff base, H₂DTC, as a “turn-on” fluorescence receptor for Zn²⁺ ions and “turn-off” receptor for Cu²⁺ ions. In the case of Zn²⁺, the fluorescence enhancement originates from the coordination of the deprotonated receptor (DTC²⁻) through the imine nitrogen, phenoxido oxygen, and oxygen atoms of tetraaza-30-crown-8 (CHEF effect). However, the addition of Cu²⁺ ions to H₂DTC completely quenches the fluorescence response due to ligand to metal charge transfer (LMCT) between H₂DTC and the paramagnetic Cu(II) ions (chelation-enhanced quenching, CHEQ).

The macrocyclic nature of the chemosensor directs the accommodation of more than one metal center in the ligand

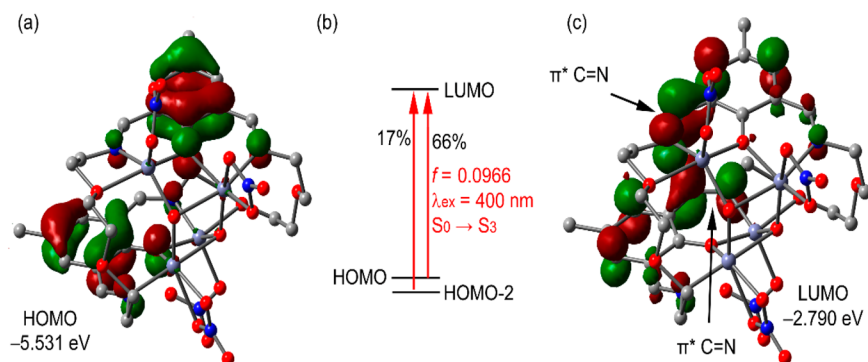


Figure 11. (a, c) Plots of the HOMO and LUMO. (b) Frontier molecular orbitals involved in the lowest-lying observable UV–vis absorption of complex **1**.

system. pH-potentiometric titrations confirm 1:1 and 2:1 binding stoichiometries between the metal ions (Zn^{2+} and Cu^{2+}) and the chemosensor in dilute solutions with a high water content. Interestingly, the 1:4 H_2DTC :metal binding stoichiometry has been established in the solid phase using X-ray crystallography. The presence of a higher number of metal centers and nitrate ions probably plays a crucial role in their isolation in the solid phase. Also, different supramolecular interactions such as strong $\pi\cdots\pi$ stacking facilitate the crystallization process.

The reversibility and regeneration of the chemosensor have been examined in the presence of Na_2EDTA . The metal–chemosensor complexation was further studied by DFT and TDDFT calculations. We were also successful in reveal the practical application of the chemosensor by performing a bioimaging study of H_2DTC using MDA-MB-468 cells. Furthermore, the probe was applied to detect intracellular Zn^{2+} and Cu^{2+} in live cells with no significant cytotoxicity.

EXPERIMENTAL SECTION

Materials and Physical Measurements. All reagent or analytical grade chemicals and solvents were purchased from commercial sources and used without further purification. Elemental analyses for C, H, and N were carried out using a Perkin–Elmer 240C elemental analyzer. Infrared spectra ($400\text{--}4000\text{ cm}^{-1}$) were recorded from KBr pellets with a Nicolet Magna IR 750 series-II FTIR spectrophotometer. Absorption spectra were measured using a sensitive UV–vis spectrophotometer (UV-2450 spectrophotometer (Shimadzu, Japan)) equipped with a double-beam light source with a 1 cm path length quartz cell. Electron spray ionization mass (ESI-MS⁺) spectra were recorded with a MICROMASS Q-TOF spectrometer. Emission spectra were collected using a Fluoromax-4 spectrofluorometer at room temperature (298 K) under degassed conditions. The fluorescence lifetime was measured using a time-resolved spectrofluorometer from IBH, UK. Measurements of ^1H and ^{13}C NMR spectra were conducted using BRUKER 400 and BRUKER 300 spectrometers, respectively.

Caution! Perchlorate ion is an extreme oxidizing agent and laboratory hazard. Only a small amount of the sample should be prepared, and it should be handled with great care.⁴⁴

X-ray Crystallography. Single-crystal X-ray data of complexes **1** and **2** were collected on a Bruker SMART APEX-II CCD diffractometer using graphite-monochromated $\text{Mo K}\alpha$ radiation ($\lambda = 0.71073\text{ \AA}$) at room temperature. Data processing, structure solution, and refinement were performed using the Bruker Apex-II program suite. All available reflections in the $2\theta_{\text{max}}$ range were harvested and corrected for Lorentz and polarization factors with Bruker SAINT plus.⁴⁵ Reflections were then corrected for absorption, interframe scaling, and other systematic errors with SADABS.⁴⁶ The structures were solved by direct methods and refined by means of a

full-matrix least-squares technique based on F^2 with the SHELX-2017/1 software package.⁴⁷ All of the non-hydrogen atoms were refined with anisotropic thermal parameters. C–H hydrogen atoms were inserted at geometric positions with U_{iso} being 1/2 of the U_{eq} values of the atoms to which they were attached. Crystal data and details of data collection and refinement for **1** and **2** are summarized in Table S1 in the Supporting Information.

Synthesis of 2,6-Diformyl-4-methylphenol (DFP). 2,6-Diformyl-4-methylphenol (DFP) was prepared by following a standard literature procedure.²⁸

Synthesis of the Chemosensor 1,16-Dihydroxy-tetraaza-30-crown-8 (H_2DTC). A mixture of 2,6-diformyl-4-methylphenol (2.0 mmol, 0.3283 g) and 1,2-bis(2-aminoethoxy)ethane (2.0 mmol, 0.296 g) was heated to reflux for 3 h in methanol solvent. A yellow gummy mass was obtained after evaporation of the solvent.

Yield: 0.486 g (88%). Anal. Calcd for $\text{C}_{30}\text{H}_{40}\text{N}_4\text{O}_6$: C, 65.20; H, 7.30; N, 10.14. Found: C, 65.55; H, 7.51; N, 10.01. IR (cm^{-1} , KBr): $\nu(\text{C}=\text{N})$ 1635s; $\nu(\text{C}-\text{H})$ 778s. ESI-MS⁺ in MeOH: the base peak was detected at m/z 553.30, corresponding to $[\text{H}_2\text{DTC}+\text{H}]^+$. UV–vis (λ_{max} (nm) (ϵ ($\text{dm}^3\text{ mol}^{-1}\text{ cm}^{-1}$)), in 10 mM HEPES buffer at pH=7.4): 445 (47086). ^1H NMR ($\text{DMSO}-d_6$, 400 MHz; δ , ppm): 2.19 (Ar- CH_3) (d, 6H, $J = 3.2$ Hz), 3.52 ($-\text{CH}_2$) (d, 8H, $J = 15.2$ Hz), 3.62 ($-\text{CH}_2$) (d, 16H, $J = 5.6$ Hz), 7.44 (ArH) (d, 4H, $J = 9.6$ Hz), 8.49 ($-\text{CH}=\text{N}$) (d, 4H, $J = 12.4$ Hz), 14.20 (Ar-OH) (s, 2H). ^1H NMR (CDCl_3 , 400 MHz; δ , ppm): 2.25 (Ar- CH_3) (t, 6H, $J_1 = 3.6$ Hz, $J_2 = 4.4$ Hz), 3.58–3.67 ($-\text{CH}_2$) (m, 8H), 3.69–3.77 ($-\text{CH}_2$) (m, 16H), 7.39 (ArH) (s, 4H), 8.47 ($-\text{CH}=\text{N}$) (s, 4H), 13.84 (Ar-OH) (s, 2H). ^{13}C NMR ($\text{DMSO}-d_6$, 75 MHz; δ , ppm): 20.26 ($-\text{CH}_3$), 59.97, 70.58 70.75 ($-\text{CH}_2$), 121.36, 127.39, 132.30, 159.34 (Ar-C), 162.29 ($-\text{CH}=\text{N}$).

Synthesis of the Complex $[\text{Zn}_4(\text{DTC})(\text{OH})_2(\text{NO}_3)_4]$ (1**).** A 2 mL methanolic solution of zinc nitrate hexahydrate (4.0 mmol, 1.189 g) was added dropwise to 20 mL of a methanolic solution of H_2DTC (1.0 mmol, 0.552 g) followed by the addition of triethylamine (2.0 mmol, 0.202 g), and the resultant reaction mixture was stirred for ca. 3 h. A yellow solid mass was obtained in high yield after slow evaporation of the solvent. This yellow solid mass was dissolved in an *N,N*-dimethylformamide (DMF)/methanol mixture (v/v, 1/9) and carefully layered with diethyl ether. Yellow block-shaped crystals were obtained after a few days.

Yield: 0.847g (78%). Anal. Calcd for $\text{C}_{30}\text{H}_{40}\text{N}_8\text{O}_{20}\text{Zn}_4$: C, 32.93; H, 3.68; N, 10.24. Found: C, 33.06; H, 3.49; N, 10.38. IR (cm^{-1} , KBr): $\nu(\text{C}=\text{N})$ 1630s; $\nu(\text{NO}_3^-)$ 1300s; $\nu(\text{C}-\text{H})$ 773 s. ESI-MS⁺ in MeOH: the base peak was detected at m/z 1032.96, corresponding to $[\text{Zn}_4(\text{DTC})(\text{OH})_2(\text{NO}_3)_3]^+$. UV–vis (λ_{max} (nm) (ϵ ($\text{dm}^3\text{ mol}^{-1}\text{ cm}^{-1}$)) in 10 mM HEPES buffer at pH 7.4): 415 (44272). ^1H NMR ($\text{DMSO}-d_6$, 400 MHz; δ , ppm): 2.21 ppm ($-\text{CH}_3$) (s, 3H), 2.29 ($-\text{CH}_3$) (s, 3H), 7.93 ($-\text{CH}=\text{N}$) (d, 1H, $J = 6.8$ Hz), 8.01 ($-\text{CH}=\text{N}$) (s, 1H), 8.28 ($-\text{CH}=\text{N}$) (d, 1H, $J = 10.4$ Hz), 8.48 ($-\text{CH}=\text{N}$) (d, 1H, $J = 12.4$ Hz), 3.1–4.0 ($-\text{CH}_2$) (m, 24H), 6.96 (s), 7.10 (s), 7.16 (s), 7.39 (s), 7.52 (d, 1H, $J = 12.00$ Hz), 7.65 (s) (Ar-H, 4H). ^{13}C NMR ($\text{DMSO}-d_6$, 75 MHz; δ , ppm): 19.36, 19.43

($-\text{CH}_3$), 58.59, 61.06, 61.23, 61.82, 68.51, 69.41, 70.06, 70.09, 71.47, 71.91, 73.67, 74.07 ($-\text{CH}_2$), 120.44, 121.00, 121.18, 121.50, 121.59, 123.87, 124.20, 139.21, 141.46, 141.50, 163.19, 165.71 (Ar-C), 166.04, 167.82, 170.44, 172.94 ($-\text{CH}=\text{N}$).

Synthesis of the Complex $[\text{Cu}_4(\text{DTC})(\text{OCH}_3)_2(\text{NO}_3)_4]\cdot\text{H}_2\text{O}$, (2). A 2 mL methanolic solution of copper nitrate trihydrate (4.0 mmol, 0.966 g) was added dropwise to 20 mL of a methanolic solution of H_2DTC (1.0 mmol, 0.552 g) followed by addition of triethylamine (2.0 mmol, 0.202 g), and the resultant reaction mixture was stirred for ca. 3 h. A green solid mass was obtained after slow evaporation of the solvent. This green solid mass was dissolved in a DMF/methanol mixture (v/v, 1/9) and carefully layered with diethyl ether. Green block-shaped crystals were obtained after a few days.

Yield: 0.858 g (76%). Anal. Calcd for $\text{C}_{33}\text{H}_{46}\text{Cu}_4\text{N}_3\text{O}_{21}$: C, 33.93; H, 3.92; N, 9.91. Found: C, 34.10; H, 3.77; N, 10.06. IR (cm^{-1} , KBr): $\nu(\text{C}=\text{N})$ 1625s; $\nu(\text{NO}_3^-)$ 1300s; $\nu(\text{C}-\text{H})$ 770s. ESI-MS⁺ in MeOH: the base peak was detected at m/z 1170.00 corresponding to $[\text{Cu}_4(\text{DTC})(\text{OCH}_3)_2(\text{NO}_3)_4 + \text{CH}_3\text{OH} + \text{Na}]^+$. UV-vis (λ_{max} (nm) (ϵ ($\text{dm}^3 \text{mol}^{-1} \text{cm}^{-1}$)) in 10 mM HEPES buffer at pH 7.4): 410 (42065).

UV-Visible and Fluorescence Spectroscopic Studies. Stock solutions of various ions (1×10^{-3} M) were prepared in deionized water. A stock solution of the chemosensor H_2DTC (1×10^{-3} M) was prepared in methanol. The solution of H_2DTC was then diluted to 1×10^{-5} M as per requirements by HEPES buffer (10 mM, pH 7.4). All of the spectroscopic experiments including a competitive assay of various cations and anions were performed in organic/aqueous HEPES buffer (10 mM, water/methanol 9/1 (v/v)) medium at pH 7.4. In titration experiments, 30 μL of a solution of 1×10^{-3} M H_2DTC was taken up to 3000 μL in a quartz optical cell of 1.0 cm optical path length, and the ion stock solutions were gradually added to it. Spectroscopic studies of the chemosensor H_2DTC in the presence of different anions were performed in HEPES buffer (10 mM, water/methanol 9/1 (v/v)) at pH 7.4. In competitive assay experiments, the test samples were prepared by using appropriate amounts of the cation stock solutions. The values of the equilibrium constants were obtained using the program HypSpec2014.^{41,42}

EMF Measurements. The pH-potentiometric titrations were carried out at 298.1 ± 0.1 K using 0.15 M NaCl in EtOH/ H_2O 30/70 v/v as the supporting electrolyte in a reaction vessel (capacity 70 cm^3) that was thermostated with water and presaturated with argon containing a separated pH glass electrode (Metrohm 6.0150.100). This reaction vessel was connected through a salt bridge (NaCl 0.5 M) to a reference cell filled with NaCl 0.15 M, containing the reference electrode (Metrohm 6.0726.107 Ag/AgCl reference electrode in 3 M KCl solution). The titration device used was a 905 Titrand apparatus controlled by a PC running the software Tiamo 2.3.

The measurement procedure consisted of a monotonic titration in which a fixed volume of the titrand (carbonate-free 0.1 M NaOH) was placed in the reaction vessel. The measured EMF was monitored over time and registered when the measured drift was lower than 0.2 mV/min. Then, the next volume of the titrand was added automatically and the cycle was repeated until the predefined total volume of the titrand had been added. The experimental EMF values were not corrected for the liquid junction potential because this effect was negligible in the pH range investigated.

Prior to the titration, the glass electrode was calibrated as a hydrogen ion concentration probe by the titration of previously standardized amounts of HCl in EtOH/ H_2O 30/70 v/v with CO_2 -free NaOH solutions, and the equivalent point was determined by the Gran method,^{48,49} which gives the standard potential, E° , and the ionic product of water ($\text{p}K_w = 14.10(1)$). At least two titrations were performed for each of the studied systems. The titrations were treated separately without finding discrepancies in the values obtained for the constants. The final values of the constants were obtained by merging the individual titrations and fitting them together. Further details of the experimental procedure are given in the Supporting Information.

The software HYPERQUAD⁵⁷ was used to process the data and calculate both the protonation and stability constants.

Cell Culture. The triple negative human breast cancer cell line MDA-MB-468, the human cervical cancer cell line HeLa, and the human lung fibroblast cell line WI-38 were obtained from the National Center for Cell Science (NCCS), Pune, India. The cells were grown in DMEM with 10% fetal bovine serum and penicillin/streptomycin (100 units/mL) at 37 °C and 5% CO_2 . All the treatments were conducted at 37 °C and with a cell density allowing exponential growth.

Cell Imaging. In order to follow the real conditions, HeLa cells were grown in cover slips for 24 h. Then the cells were either mock-treated or treated with Zn^{2+} (20 μM) ions for 24 h at 37 °C; after that H_2DTC (5 μM) was added to them in the presence or absence of Cu^{2+} (20 μM) ions for another 24 h at 37 °C. In another set of experiments MDA-MB-468 cells were grown in cover slips for 24 h. Then the cells were either mock-treated or treated with 5 μM of ligand (H_2DTC) and 20 μM of the Zn^{2+} salt in the presence or absence of 20 μM of the Cu^{2+} salt for 24 h at 37 °C. Both types of cells were washed with $1 \times \text{PBS}$. Then they were mounted on a glass slide and observed under a fluorescence microscope (Leica) with a filter having an excitation of 450–500 nm (blue) and an emission of 500–570 nm (green).

Cell Survivability Assay. The cell survivability of H_2DTC was studied for human lung fibroblast cells WI-38 (noncancerous cells) and MDA-MB-468 and HeLa (cancerous cells) following a reported procedure.⁵⁰ In brief, the viability of these cells after exposure to various concentrations of ligand was assessed by an MTT assay. The cells were seeded in 96-well plates at 1×10^4 cells per well and exposed to the ligand at concentrations of 0, 20, 40, 60, 80, and 100 μM for 24 h. The resulting formazan crystals were dissolved in an MTT solubilization buffer, the absorbance was measured at 570 nm by using a spectrophotometer (BioTek), and the value was compared with that of control cells. The cell cytotoxicity of the complexes toward the cancer cells MDA-MB-468 and HeLa were also determined by following the aforementioned MTT assay protocol. Another set of experiments was performed with an MTT assay by keeping the ligand concentration the same (5 μM) and varying Zn^{2+} and Cu^{2+} ions to a maximum concentration of 50 μM .

Computational Methods. The compounds were initially optimized at the B3LYP/6-31+G* level of theory in their singlet ground state (S_0).⁵¹ To obtain theoretical UV-vis parameters, we performed time-dependent DFT (TD-DFT)⁵² calculations using the same level of theory associated with the conductor-like polarizable continuum model (CPCM).⁵³ For the complexes and ligands (keto and enol forms), we calculated 60 singlet-singlet transition using their ground S_0 state geometries and using the conductor-like polarizable continuum model. The calculated electronic density plots for the frontier molecular orbitals were prepared by using the Gauss View 5.0 software. All of the calculations were performed with the Gaussian 09 software package.⁵⁴

■ ASSOCIATED CONTENT

SI Supporting Information

The Supporting Information is available free of charge at <https://pubs.acs.org/doi/10.1021/acs.inorgchem.1c03141>.

Additional tables and figures as described in the text and details of the calculations (PDF)

Accession Codes

CCDC 1884738–1884739 contain the supplementary crystallographic data for this paper. These data can be obtained free of charge via www.ccdc.cam.ac.uk/data_request/cif, or by emailing data_request@ccdc.cam.ac.uk, or by contacting The Cambridge Crystallographic Data Centre, 12 Union Road, Cambridge CB2 1EZ, UK; fax: +44 1223 336033.

AUTHOR INFORMATION

Corresponding Author

Amrita Saha – Department of Chemistry, Jadavpur University, Kolkata 700032, India; orcid.org/0000-0001-9357-801X; Phone: +91-33-24572941; Email: amritasahachemju@gmail.com

Authors

Pravat Ghorai – Department of Chemistry, Jadavpur University, Kolkata 700032, India
Sougata Ghosh Chowdhury – Department of Life Science and Biotechnology, Jadavpur University, Kolkata 700032, India
Kunal Pal – Department of Life Science and Biotechnology, Jadavpur University, Kolkata 700032, India
Jayanta Mandal – Department of Chemistry, Jadavpur University, Kolkata 700032, India
Parimal Karmakar – Department of Life Science and Biotechnology, Jadavpur University, Kolkata 700032, India
Antonio Franconetti – Department of Chemistry, Universitat de les Illes Balears, 07122 Palma de Mallorca, Balears, Spain
Antonio Frontera – Department of Chemistry, Universitat de les Illes Balears, 07122 Palma de Mallorca, Balears, Spain; orcid.org/0000-0001-7840-2139
Salvador Blasco – Institute of Molecular Sciences, Universitat de València, 46980 Paterna, Valencia, Spain
Enrique García-España – Institute of Molecular Sciences, Universitat de València, 46980 Paterna, Valencia, Spain; orcid.org/0000-0002-4601-6505
Partha Pratim Parui – Department of Chemistry, Jadavpur University, Kolkata 700032, India; orcid.org/0000-0002-2674-7458

Complete contact information is available at:
<https://pubs.acs.org/10.1021/acs.inorgchem.1c03141>

Notes

The authors declare no competing financial interest.

ACKNOWLEDGMENTS

A.S. gratefully acknowledges the financial support of this work by the DST of India (Sanction No. SB/FT/CS-102/2014, dated 18.07.2015). A.F. thanks the MINECO/AEI from Spain for a “Juan de la Cierva” contract. We thank the MINECO/AEI from Spain for financial support (project number CTQ2017-85821-R and PID2019-110751RB-I00, RED2018-102331-T, FEDER funds). We are grateful to the CTI (UIB) for free allocation of computer time.

REFERENCES

- (1) Qian, X. H.; Xu, Z. C. Fluorescence imaging of metal ions implicated in diseases. *Chem. Soc. Rev.* **2015**, *44*, 4487–4493.
- (2) Yang, Y.; Zhao, Q.; Feng, W.; Li, F. Luminescent Chemosensors for Bioimaging. *Chem. Rev.* **2013**, *113*, 192–270.
- (3) Li, M.; Jiang, X. J.; Wu, H. H.; Lu, H. L.; Li, H. Y.; Xu, H.; Zang, S. Q.; Mak, T. C. W. A dual functional probe for “turn-on” fluorescence response of Pb²⁺ and colorimetric detection of Cu²⁺ based on a rhodamine derivative in aqueous media. *Dalton Trans.* **2015**, *44*, 17326–17334.
- (4) Wang, L.; Ye, D. D.; Li, W. X.; Liu, Y. Y.; Li, L. H.; Zhang, W. L.; Ni, L. Fluorescent and colorimetric detection of Fe(III) and Cu(II) by a difunctional rhodamine-based probe. *Spectrochim. Acta, Part A* **2017**, *183*, 291–297.
- (5) Chen, G.; Guo, Z.; Zeng, G.; Tang, L. Fluorescent and colorimetric sensors for environmental mercury detection. *Analyst.* **2015**, *140*, 5400–5443.
- (6) Quang, D. T.; Kim, J. S. Fluoro- and Chromogenic Chemosensors for Heavy Metal Ion Detection in Solution and Biospecimens. *Chem. Rev.* **2010**, *110*, 6280–6301.
- (7) Tang, L.; Li, F.; Liu, M.; Nandhakumar, R. Single sensor for two metal ions: colorimetric recognition of Cu²⁺ and fluorescent recognition of Hg²⁺. *Spectrochim. Acta, Part A* **2011**, *78*, 1168–1172.
- (8) Burdette, S. C.; Lippard, S. J. IC334 — golden edition of coordination chemistry reviews. Coordination chemistry for the neurosciences. *Coord. Chem. Rev.* **2001**, *216*, 333–361.
- (9) Sensi, S. L.; Paoletti, P.; Bush, A. I.; Sekler, I. Zinc in the physiology and pathology of the CNS. *Nat. Rev. Neurosci.* **2009**, *10*, 780–791.
- (10) Lippard, S. J.; Berg, J. M. *Principles of Bioinorganic Chemistry*; University Science Books: 1994.
- (11) Andrews, G. K. Cellular zinc sensors: MTF-1 regulation of gene expression. *Biometals.* **2001**, *14*, 223–237.
- (12) Berg, J. M.; Shi, Y. The galvanization of biology: a growing appreciation for the roles of zinc. *Science.* **1996**, *271*, 1081–1085.
- (13) Coleman, J. E. Zinc enzymes. *Curr. Opin. Chem. Biol.* **1998**, *2*, 222–234.
- (14) Bush, A. I.; Pettingell, W. H.; Multhaup, G.; Paradis, M. D.; Vonsattel, J. P.; Gusella, J. F.; Beyreuther, K.; Mastersand, C. L.; Tanzi, R. E. Rapid induction of Alzheimer A beta amyloid formation by zinc. *Science.* **1994**, *265*, 1464–1467.
- (15) Bush, A. I.; Tanzi, R. E. The galvanization of β -amyloid in Alzheimer's disease. *Proc. Natl. Acad. Sci. U. S. A.* **2002**, *99*, 7317–7319.
- (16) Tapiero, H.; Townsend, D. M.; Tew, K. D. Trace elements in human physiology and pathology Copper. *Biomed.Pharmacother.* **2003**, *57*, 386–398.
- (17) Waggoner, D. J.; Bart, T. B.; Gitlin, J. D. The Role of Copper in Neurodegenerative Disease. *Neurobiol. Dis.* **1999**, *6*, 221–230.
- (18) Georgopoulos, P. G.; Roy, A.; Yonone-Lioy, M. J.; Opiekun, R. E.; Lioy, P. J. Environmental copper: Its dynamics and human exposure issues. *J. Toxicol. Environ. Health Part B* **2001**, *4*, 341–394.
- (19) Lim, C. M.; Cater, M. A.; Mercer, J. F.; Fontaine, S. L. Copper-dependent interaction of glutaredoxin with the N termini of the copper-ATPases (ATP7A and ATP7B) defective in Menkes and Wilson diseases. *Biochem. Biophys. Res. Commun.* **2006**, *348*, 428–436.
- (20) Syme, C. D.; Nadal, R. C.; Rigby, S. E.; Viles, J. H. Copper binding to the amyloid-beta (A β) peptide associated with Alzheimer's disease: folding, coordination geometry, pH dependence, stoichiometry, and affinity of A β -(1–28): insights from a range of complementary spectroscopic techniques. *J. Biol. Chem.* **2004**, *279*, 18169–18177.
- (21) Manfredi, G.; Xu, Z. Mitochondrial dysfunction and its role in motor neuron degeneration in ALS. *Mitochondrion.* **2005**, *5*, 77–87.
- (22) Lee, J. C.; Gray, H. B.; Winkler, J. R. Copper(II) binding to alpha-synuclein, the Parkinson's protein. *J. Am. Chem. Soc.* **2008**, *130*, 6898–6899.
- (23) Meloni, G.; Faller, P.; Vasak, M. Redox Silencing of Copper in Metal-linked Neurodegenerative Disorders REACTION OF Zn²⁺ METALLOTHIONEIN-3 WITH Cu²⁺ IONS. *J. Biol. Chem.* **2007**, *282*, 16068–16078.
- (24) (a) Helal, A.; Lee, S. H.; Kim, S. H.; Kim, H.-S. Dual-signaling fluorescent chemosensor based on bisthiazole derivatives. *Tetrahedron Lett.* **2010**, *51*, 3531–3535. (b) Khatua, S.; Kang, J.; Churchill, D. G. Direct dizinc displacement approach for efficient detection of Cu²⁺ in aqueous media: acetate versus phenolate bridging platforms. *New J. Chem.* **2010**, *34*, 1163–1169. (c) Zhou, X.; Yu, B.; Guo, Y.; Tang, X.; Zhang, H.; Liu, W. Both Visual and Fluorescent Sensor for Zn²⁺ Based on Quinoline Platform. *Inorg. Chem.* **2010**, *49*, 4002–4007. (d) Zhang, Y.; Guo, X.; Si, W.; Jia, L.; Qian, X. Ratiometric and Water-Soluble Fluorescent Zinc Sensor of Carboxamidoquinoline with an Alkoxyethylamino Chain as Receptor. *Org. Lett.* **2008**, *10*, 473–476. (e) Mikata, Y.; Yamanaka, A.; Yamashita, A.; Yano, S.

- Isoquinoline-Based TQEN Family as TPEN-Derived Fluorescent Zinc Sensors. *Inorg. Chem.* **2008**, *47*, 7295–7301. (f) Mikata, Y.; Wakamatsu, M.; Kawamura, A.; Yamanaka, N.; Yano, S.; Odani, A.; Morihiro, K.; Tamotsu, S. Methoxy-Substituted TQEN Family of Fluorescent Zinc Sensors. *Inorg. Chem.* **2006**, *45*, 9262–9268. (g) Mikata, Y.; Kawata, K.; Iwatsuki, S.; Konno, H. Zinc-Specific Fluorescent Response of Tris(isoquinolylmethyl)amines (isoTQAs). *Inorg. Chem.* **2012**, *51*, 1859–1865. (h) Zalewski, P. D.; Forbes, I. J.; Seamark, R. F.; Borlinghaus, R.; Betts, W. H.; Lincoln, S. F.; Ward, A. D. Flux of intracellular labile zinc during apoptosis (gene-directed cell death) revealed by a specific chemical probe, Zinquin. *Chem. Biol.* **1994**, *1*, 153–161. (i) Wong, B. A.; Friedle, S.; Lippard, S. J. Subtle Modification of 2,2-Dipicolylamine Lowers the Affinity and Improves the Turn-On of Zn(II)-Selective Fluorescent Sensors. *Inorg. Chem.* **2009**, *48*, 7009–7011. (j) Rivera-Fuentes, P.; Wrobel, A. T.; Zastrow, M. L.; Khan, M.; Georgiou, J.; Luyben, T. T.; Roder, J. C.; Okamoto, K.; Lippard, S. J. A far-red emitting probe for unambiguous detection of mobile zinc in acidic vesicles and deep tissue. *Chem. Sci.* **2015**, *6*, 1944–1948. (k) Goldberg, J. M.; Wang, F.; Sessler, C. D.; Vogler, N. W.; Zhang, D. Y.; Loucks, W. H.; Tzounopoulos, T.; Lippard, S. J. Photoactivatable Sensors for Detecting Mobile Zinc. *J. Am. Chem. Soc.* **2018**, *140*, 2020–2023. (l) Komatsu, K.; Urano, Y.; Kojima, H.; Nagano, T. Development of an Iminocoumarin-Based Zinc Sensor Suitable for Ratiometric Fluorescence Imaging of Neuronal Zinc. *J. Am. Chem. Soc.* **2007**, *129*, 13447–13454. (m) Taki, M.; Wolford, J. L.; O'Halloran, T. V. Emission Ratiometric Imaging of Intracellular Zinc: Design of a Benzoxazole Fluorescent Sensor and Its Application in Two-Photon Microscopy. *J. Am. Chem. Soc.* **2004**, *126*, 712–713. (n) Koike, T.; Watanabe, T.; Aoki, S.; Kimura, E.; Shiro, M. A Novel Biomimetic Zinc(II)-Fluorophore, Dansylamideethyl-Pendant Macrocyclic Tetraamine_{1,4,7,10} Tetraazacyclododecane (Cyclen). *J. Am. Chem. Soc.* **1996**, *118*, 12696–12703. (o) Yan, X.; Kim, J. J.; Jeong, H. S.; Moon, Y. K.; Cho, Y. K.; Ahn, S.; Jun, S. B.; Kim, H.; You, Y. Low-Affinity Zinc Sensor Showing Fluorescence Responses with Minimal Artifacts. *Inorg. Chem.* **2017**, *56*, 4332–4346. (p) Bhanja, A. K.; Patra, C.; Mondal, S.; Mishra, S.; Saha, K. D.; Sinha, C. Macrocyclic azacrown chromogenic reagent to Al³⁺ and fluorescence sensor for Zn²⁺ and Al³⁺ along with live cell application and logic operation. *Sens. Actuators, B* **2017**, *252*, 257–267.
- (25) (a) Vrajesh, B. P. *An Introduction of Crown Ether Schiff Bases & Its Applications*; LAP Lambert Academic: 2015. (b) *Crown Ethers and Analogous Compounds*; Hiraoka, M., Ed.; Elsevier Science: 1992. (c) Safin, D. A.; Babashkina, M. G.; Garcia, Y. Crown ether-containing Schiff base as a highly efficient “turn-on” fluorescent sensor for determination and separation of Zn²⁺ in water. *Dalton Trans.* **2013**, *42*, 1969–1972. (d) Cai, S.-l.; Feng, F.-m.; Liu, F.-a. Function of the Metallomicelle from an Aza-Crown Ether Complex with an Acetamide Branch as a Highly Potent Promoter of Phosphate Diester Hydrolytic Cleavage. *J. Dispersion Sci. Technol.* **2016**, *37*, 1170–1177.
- (26) (a) Kahwa, I. A.; Folkers, S.; Williams, D. J.; Ley, S. V.; O'Mahoney, C. A.; McPherson, G. L. The First Crystal and Molecular Structure of Lanthanide Homodinuclear Macrocyclic Complexes showing Metal-Metal Pair Interactions. *J. CHEM. SOC. CHEM. COMMUN.* **1989**, 1531–1533. (b) Matthews, K. D.; Kahwa, I. A.; Williams, D. J. Preparation, Structure, and Luminescence of Dinuclear Lanthanide Complexes of a Novel Imine-Amine Phenolate Macrocyclic. *Inorg. Chem.* **1994**, *33*, 1382–1387. (c) Plenio, H.; Diodone, R.; Badura, D. Synthesis and Coordination Chemistry of Fluorine-Containing Cages. *Angew. Chem., Int. Ed. Engl.* **1997**, *36*, 156–158. (d) Tei, L.; Arca, M.; Aragoni, M. C.; Bencini, A.; Blake, A. J.; Caltagirone, C.; Devillanova, F. A.; Fornasari, P.; Garau, A.; Isaia, F.; Lippolis, V.; Schroder, M.; Teat, S. J.; Valtancoli, B. Coordination Chemistry of a New Cofacial Binucleating Macropolycycle Derived from 1,4,7-Triazacyclononane. *Inorg. Chem.* **2003**, *42* (26), 8690–8701.
- (27) (a) Mandal, J.; Ghorai, P.; Pal, K.; Karmakar, P.; Saha, A. 2-hydroxy-5-methylisophthalaldehyde based fluorescent-colorimetric chemosensor for dual detection of Zn²⁺ and Cu²⁺ with high sensitivity and application in live cell imaging. *J. Lumin.* **2019**, *205*, 14–22.
- (b) Ghorai, P.; Banerjee, S.; Nag, D.; Mukhopadhyay, S. K.; Saha, A. Design and synthesis of a novel fluorescent-colorimetric chemosensor for selective detection of Zn(II) and Cu(II) ions with applications in live cell imaging and molecular logic gate. *J. Lumin.* **2019**, *205*, 197–209.
- (28) Gagne, R. R.; Spiro, C. L.; Smith, T. J.; Hamann, C. A.; Thies, W. R.; Schiemke, A. K. The synthesis, redox properties, and ligand binding of heterobinuclear transition-metal macrocyclic ligand complexes. Measurement of an apparent delocalization energy in a mixed-valent copper(I) copper(II) complex. *J. Am. Chem. Soc.* **1981**, *103*, 4073–4081.
- (29) (a) Maekawa, N. M.S. Thesis, University of the Ryukyus, Okinawa, 1999. (b) Miyazato, Y.; Asato, E.; Ohba, M.; Wada, T. Synthesis and Characterization of a Tetracopper(II) Complex Having a [Cu₄(μ₄-O)] Framework Stabilized by the Tetranucleating Macrocyclic Ligand. *Bull. Chem. Soc. Jpn.* **2012**, *85*, 895–901.
- (30) (a) Panja, A.; Matsuo, T.; Nagao, S.; Hirota, S. DNA Cleavage by the Photocontrolled Cooperation of Zn^{II} Centers in an Azobenzene-Linked Dizinc Complex. *Inorg. Chem.* **2011**, *50*, 11437–11445. (b) Parkin, G. Synthetic Analogues Relevant to the Structure and Function of Zinc Enzymes. *Chem. Rev.* **2004**, *104*, 699–767.
- (31) Addison, A. W.; Rao, T. N.; Reedijk, J.; Rijn, J. V.; Verschoor, C. G. Synthesis, structure, and spectroscopic properties of copper(II) compounds containing nitrogen–sulphur donor ligands; the crystal and molecular structure of aqua[1,7-bis(N-methylbenzimidazol-2'-yl)-2,6-dithiaheptane]copper(II) perchlorate. *J. Chem. Soc., Dalton Trans.* **1984**, 1349–1356.
- (32) Kumar, M.; Kumar, R.; Bhalla, V.; Sharma, P. R.; Kaur, T.; Qurishi, Y. Thiocalix[4]arene based fluorescent probe for sensing and imaging of Fe³⁺ ions. *Dalton Trans.* **2012**, *41*, 408–412.
- (33) Tak, W. T.; Yoon, S. C. Clinical Significance of Blood Level of Zinc and Copper in Chronic Renal Failure Patients. *Korean J. Nephrol.* **2001**, *20*, 863–871.
- (34) Eide, D. J. Zinc transporters and the cellular trafficking of zinc. *Biochim. Biophys. Acta* **2006**, *1763*, 711–722.
- (35) Pradhan, A. B.; Mandal, S. K.; Banerjee, S.; Mukherjee, A.; Das, S.; Bukhsh, A. R. K.; Saha, A. A highly selective fluorescent sensor for zinc ion based on quinoline platform with potential applications for cell imaging studies. *Polyhedron* **2015**, *94*, 75–82.
- (36) Mandal, J.; Ghorai, P.; Brandao, P.; Pal, K.; Karmakar, P.; Saha, A. An aminoquinoline based biocompatible fluorescent and colourimetric pH sensor designed for cancer cell discrimination. *New J. Chem.* **2018**, *42*, 19818–19826.
- (37) Gans, P.; Sabatini, A.; Vacca, A. Investigation of Equilibria in Solution. Determination of Equilibrium Constants with the HYPERQUAD Suite of Programs. *Talanta* **1996**, *43*, 1739–1753.
- (38) Tumer, M.; Deligonul, N.; Golcu, A.; Akgun, E.; Dolaz, M.; Demirelli, H.; Digrak, M. Mixed-ligand Copper(II) Complexes: Investigation of their Spectroscopic, Catalysis, Antimicrobial and Potentiometric Properties. *Transition Metal Chemistry* **2006**, *31*, 1–12.
- (39) Demirelli, H.; Tumer, M.; Golcu, A. Synthesis and Characterization of Polydentate Schiff-Base Ligands and Their Complexes. *Bull. Chem. Soc. Jpn.* **2006**, *79*, 867–875.
- (40) Esteban-Gómez, D.; Platas-Iglesias, C.; Avecilla, F.; de Blas, A.; Rodríguez-Blas, T. Effect of protonation and interaction with anions on a lead(II) complex with a lateral macrobicyclic containing a phenol Schiff-base spacer. *Eur. J. Inorg. Chem.* **2007**, *2007*, 1635–1643.
- (41) Gans, P.; Sabatini, A.; Vacca, A. Determination of Equilibrium Constants from Spectrophotometric Data obtained from Solutions of known pH: The Program pHAB. *Annali di Chimica* **1999**, *89*, 45–49.
- (42) Alderighi, L.; Gans, P.; Ienco, A.; Peters, D.; Sabatini, A.; Vacca, A. Hyperquad simulation and speciation (HySS): a utility program for the investigation of equilibria involving soluble and partially soluble species. *Coord. Chem. Rev.* **1999**, *184*, 311–318.
- (43) Tapiero, H.; Townsend, D. M.; Tew, K. D. Trace elements in human physiology and pathology. *Biomed Pharmacother* **2003**, *57*, 386–398.

- (44) Churchill, D. G. Chemical Structure and Accidental Explosion Risk in the Research Laboratory. *J. Chem. Educ.* **2006**, *83*, 1798–1803.
- (45) Sheldrick, G. M. *SAINT, Ver. 6.02, and SADABS, Ver. 2.03*; Bruker AXS: 2002.
- (46) Sheldrick, G. M. *SADABS: Software for Empirical Absorption Correction*; University of Gottingen: 1999–2003.
- (47) Sheldrick, G. M. Crystal structure refinement with *SHELXL*. *Acta Crystallogr.* **2015**, *C71*, 3–8.
- (48) Gran, G. Determination of the Equivalence Point in Potentiometric Titrations. II. *Analyst* **1952**, *77*, 661–671.
- (49) Rossotti, F. J. C.; Rossotti, H. Potentiometric Titrations Using Gran Plots: A Textbook Omission. *J. Chem. Educ.* **1965**, *42*, 375.
- (50) (a) Pramanik, A.; Laha, D.; Chattopadhyay, S.; Dash, S. K.; Roy, S.; Pramanik, P.; Karmakar, P. An in-vivo study for targeted delivery of copper-organic complex to breast cancer using chitosan polymer nanoparticles. *Materials Science and Engineering C* **2016**, *68*, 327–337. (b) Laha, D.; Pramanik, A.; Chattopadhyay, S.; Dash, S. K.; Roy, S.; Pramanik, P.; Karmakar, P. Folic acid modified copper oxide nanoparticles for targeted delivery in in vitro and in vivo systems. *RSC Adv.* **2015**, *5*, 68169–68178.
- (51) Perdew, J. P. Density-functional approximation for the correlation energy of the inhomogeneous electron gas. *Phys. Rev. B* **1986**, *33*, 8822–8824.
- (52) (a) Casida, M. E.; Jamoroski, C.; Casida, K. C.; Salahub, D. R. Molecular excitation energies to high-lying bound states from time-dependent density-functional response theory: Characterization and correction of the time-dependent local density approximation ionization threshold. *J. Chem. Phys.* **1998**, *108*, 4439–4449. (b) Stratmann, R. E.; Scuseria, G. E.; Frisch, M. J. An efficient implementation of time-dependent density-functional theory for the calculation of excitation energies of large molecules. *J. Chem. Phys.* **1998**, *109*, 8218–8224. (c) Bauernschmitt, R.; Ahlrichs, R. Treatment of electronic excitations within the adiabatic approximation of time dependent density functional theory. *Chem. Phys. Lett.* **1996**, *256*, 454–464.
- (53) (a) Cossi, M.; Rega, N.; Scalmani, G.; Barone, V. Energies, structures, and electronic properties of molecules in solution with the C-PCM solvation model. *J. Comput. Chem.* **2003**, *24*, 669–681. (b) Cossi, M.; Barone, V. Time-dependent density functional theory for molecules in liquid solutions. *J. Chem. Phys.* **2001**, *115*, 4708–4717. (c) Barone, V.; Cossi, M. Quantum Calculation of Molecular Energies and Energy Gradients in Solution by a Conductor Solvent Model. *J. Phys. Chem. A* **1998**, *102*, 1995–2001.
- (54) Frisch, M. J.; Trucks, G. W.; Schlegel, H. B.; Scuseria, G. E.; Robb, M. A.; Cheeseman, J. R.; Scalmani, G.; Barone, V.; Mennucci, B.; Petersson, G. A.; Nakatsuji, H.; Caricato, M.; Li, X.; Hratchian, H. P.; Izmaylov, A. F.; Bloino, J.; Zheng, G.; Sonnenberg, J. L.; Hada, M.; Ehara, M.; Toyota, K.; Fukuda, R.; Hasegawa, J.; Ishida, M.; Nakajima, T.; Honda, Y.; Kitao, O.; Nakai, H.; Vreven, T.; Montgomery, J. A., Jr.; Peralta, J. E.; Ogliaro, F.; Bearpark, M.; Heyd, J. J.; Brothers, E.; Kudin, K. N.; Staroverov, V. N.; Kobayashi, R.; Normand, J.; Raghavachari, K.; Rendell, A.; Burant, J. C.; Iyengar, S. S.; Tomasi, J.; Cossi, M.; Rega, N.; Millam, J. M.; Klene, M.; Knox, J. E.; Cross, J. B.; Bakken, V.; Adamo, C.; Jaramillo, J.; Gomperts, R.; Stratmann, R. E.; Yazyev, O.; Austin, A. J.; Cammi, R.; Pomelli, C.; Ochterski, J. W.; Martin, R. L.; Morokuma, K.; Zakrzewski, V. G.; Voth, G. A.; Salvador, P.; Dannenberg, J. J.; Dapprich, S.; Daniels, A. D.; Farkas, Ö.; Foresman, J. B.; Ortiz, J. V.; Cioslowski, J.; Fox, D. J. *GAUSSIAN 09, Rev. C.01*; Gaussian, Inc.: 2009.



ACS IN FOCUS

Cellulose
Lab-Grown
Diek Erlich & Dorothée Suck

Machine Learning in Chemistry
Jon Paul Janet & Heather J. Kulik

Bacterials
Teresa Cheng Jaramillo & William M. Wuest

ACS In Focus ebooks are digital publications that help readers of all levels accelerate their fundamental understanding of emerging topics and techniques from across the sciences.



pubs.acs.org/series/Infocus

ACS Publications
Most Trusted. Most Cited. Most Read.